1994 IEEE Nonlinear Optics:

Materials, Fundamentals, and Applications

July 25-29, 1994

Hilton Waikoloa Village
Waikoloa, Hawaii

IEEE LASERS AND
LEOS
ELECTRO-OPTICS SOCIETY

OPTICAL SOCIETY
OF AMERICA

1994 IEEE Nonlinear Optics:

Materials, Fundamentals, and Applications

July 25-29, 1994

Hilton Waikoloa Village
Waikoloa, Hawaii

IEEE

OPTICAL SOCIETY
OF AMERICA

i

IEEE

OPTICAL SOCIETY
OF AMERICA

Nonlinear Optics '94

Conference Co-Chairs

Monte Khoshnevisan
*Rockwell International
Science Center,
Thousand Oaks, CA*

Y. Ron Shen
*University of California,
Berkeley, CA*

Program Co-Chairs

Richard Lind
*Hughes Research Labs,
Malibu, CA*

C.L. Tang
*Cornell University,
Ithaca, NY*

Program Committee

Dana Anderson
*JILA University of Colorado,
Boulder, CO*

John Bierlein
*DuPont de Nemours,
Wilmington, DE*

Gary Bjorklund
*IBM Almaden Research Center
San Jose, CA*

Joseph Eberly
*University of Rochester
Rochester, NY*

Martin Fejer
*Stanford University
Stanford, CA*

Athanasios Gavrielldes
*PL/LIDN
Kirtland AFB, NM*

Eric Ippen
*MIT
Cambridge, MA*

Anthony Johnson
*AT&T Bell Laboratories
Holmdel, NJ*

Marc Levenson
*IBM Almaden Research Center
San Jose, CA*

Dave Miller
*AT&T Bell Laboratories,
Holmdel, NJ*

Richard Powell
*University of Arizona
Tucson, AZ*

David Rockwell
*Hughes Research Labs
Malibu, CA*

George Valley
*Hughes Research Labs
Malibu, CA*

Pochl Yeh
*University of California
Santa Barbara, CA*

Eric Van Stryland
*University of Central Florida
Orlando, FL*

David Williams
*Eastman Kodak Co.
Rochester, NY*

Domestic Advisory Committee

Christopher Clayton
*U.S. Air Force Phillips
Laboratory, Kirtland AFB, NM*

L.N. Durvasula
ARPA/DSO, Arlington, VA

Albert Harvey
*National Science Foundation,
Washington, DC*

Iam-Choon Khoo
*Pennsylvania State University,
University Park, PA*

Lou Lome
*BMDO, DTI
Washington, DC*

Herschel S. Pilloff
*Office of Naval Research,
Arlington, VA*

Keith Sage
Rocketdyne, Canoga Park, CA

Howard Schlosssberg
*U.S. Air Force Office of
Scientific Research,
Washington, DC*

William Woody
*U.S. Air Force, Wright
Laboratory, Write Patterson AFB,
OH*

International Advisory Committee

Girish S. Argrarwal
*University of Hyderabad,
Hyderabad, India*

Sien Chi
*National Chiaotung University,
Taiwan, R.O.C.*

Malcolm Dunn
Lochnager, St. Andrews, UK

H.J. Eichler
*Technische Universitat,
Berlin, Germany*

Christos Flytzanis
CNRS Lab, Palaiseau, France

John A. Hermann
DSTO, Salisbury, Australia

Jean-Pierre Huignard
Thomson CSF, Orsay, France

Taisuya Kimura
NTT, Tokyo, Japan

Masahiro Matsuoka
*University of Tokyo,
Minato-ku, Japan*

Henry Van Driel
*University of Toronto, Toronto,
Canada*

Daniel F. Walls
*University of Aukland,
Auckland, New Zealand*

Herbert Walther
*MPI fur Quantenoptik,
Garching, Germany*

Yoshitaka Yamamoto
*Stanford University,
Stanford, CA*

Guo-zeng Yang
*Academy of Sciences, Beijing,
China*

Zhi-ming Zhang
*Funda University, Shanghai,
China*

Table of Contents

MONDAY, JULY 25, 1994

TUESDAY, JULY 26, 1994

WEDNESDAY, JULY 27, 1994

THURSDAY, JULY 28, 1994

FRIDAY, JULY 29, 1994

x

MONDAY, JULY 25

MA: Nonlinear Organic Materials
MB: Novel NLO Effects
MC: Nonlinear Frequency Conversion
MP: Poster Session I

EO POLYMER MATERIALS AND DEVICES: FROM RESEARCH TO REALITY

Rick Lytel
Akzo Electronic Products Inc.
250 C Twin Dolphin Drive
Redwood City, CA 94065
(415) 508-2945

Polymer nonlinear optical materials offer new opportunities in integrated optics[1]. The large electronic hyperpolarizabilities in certain conjugated organic molecules lead to materials with large, ultrafast optical susceptibilities. In particular, electro-optic (EO) poled polymer materials exhibit low dispersion and low dielectric constants. EO polymer materials have been modulated to 40 GHz[2] and exhibit few fundamental limits for ultrafast modulation and switching. Polymeric integrated optic materials also offer great fabrication flexibility. The materials are spin-coatable into high quality, multilayer films, and can be patterned, metallized, and poled. Channel waveguides and integrated optic circuits can be defined by the poling process itself[3], by photochemistry of the EO polymer[4,5], or by a variety of well understood micro-machining techniques. To date, EO polymer materials have been used to fabricate high-speed Mach-Zehnder modulators[6], directional couplers[7], Fabry-Perot etalons[8], and even multitap devices[9]. Recent developments in EO polyimide materials[10,11] show it is possible to achieve sufficient thermal stability of the aligned state to meet both manufacturing and end-use requirements[12] for such devices. The demonstrated performance of EO polymer materials and devices is now beginning to approach that of inorganic materials, as displayed in Figure 1.

The ultimate advantages of EO polymers, however, may extend far beyond the duplication of inorganic devices. Multilayer structures of EO polymers can be fabricated in large area formats (6-8 inch wafers) with high device packing densities. Furthermore, EO polymer devices can be fabricated directly on electronic substrates and assembled with ICs to create a hybrid optoelectronic package. Finally, the substrate itself can serve as a bench for assembly and integration in a manner similar to standard Si waferboard[13].

FIGURE-OF-MERIT	GaAs	Ti-Lithium Niobate	EO Polymers
EO coefficient r (pm/V)	1.5	31	30
Dielectric constant ε	12	28	3.5
Refractive index n	3.5	2.2	1.6
$n^3 r$ (pm/V)	64	330	123
$n^3 r/\varepsilon$ (pm/V)	5.4	12	35
Loss (dB/cm @ λ=1.3 μm)	2	0.2	0.5
Space-BW product (GHz-cm)	>100	10	>100
Voltage-length product (V-cm)	5	5	10

Figure 1. Comparison of different technologies for integrated optic devices

Planar polymer waveguide technologies have the ultimate potential to gain widespread use in essentially every electronic and fiber-optic system application. Passive components will find use as splitters, couplers, multiplexors, and parallel array connectors in trunk, local loop, wide-area,

and local-area networks. Electro-optic polymer devices have the broadest potential. Applications include external modulation of lasers, fast network configuration switches, optical network units in Fiber-to-the-Home (FTTH), modulator arrays for data networks, filters, couplers, multiplexors, digital-analog and analog-digital converters, and pulse-shapers. The market potential for planar polymer waveguides is very large due to low wafer processing costs and potential to achieve low-cost single-mode fiber-attach and packaging. This means polymers may compete well with other technologies in conventional optoelectronic applications.

Polymer technologies offer new, unique opportunities in electronic systems applications that are not available with other technologies. With polymers, high levels of integration have been demonstrated by using multiple levels of waveguides[14] as well as in-plane and out-of-plane mirrors[15]. The potential for low-cost manufacturing, packaging, and assembly arises from the capability to perform hybrid integration of single-mode components using lithographically-defined registration techniques. This could lead to advanced products such as processor multichip modules with high-bandwidth interfaces between CPU and second-level cache, optical mesh routers for massively parallel computers, and 8-12 bit, high-speed A-D's. EO polymers are unique in offering this level of product potential.

Cost, reliability, performance, and availability are the main drivers for obtaining and sustaining long-term interest in polymers by systems users. Polymer reliability is seen by customers as a major issue, particularly for EO poled polymers. Reliability needs to be proved with extensive test data of the packaged components, following the well-known standards for telecom and electronic components, in general. It is important to note that laser diodes have achieved success in the market, despite their propensity for drift, low-yields, limited lifetime, and failure. The market has accepted "correction" methods for laser diode performance, such as thermo-electric coolers, drift compensation circuitry, and elaborate packaging because the total cost of a laser transmitter has been reduced to acceptable levels in many cases. Similar techniques could be applied to polymer devices but will increase their cost and may reduce their reliability.

Major outstanding issues in EO polymer devices include the reduction of DC drift, reduction of loss, and enhancement of thermal stability. To date, all of these issues have been resolved in EO polymer devices, although perhaps not all at the same time. However, the fundamental reasons for drift or poling decay are sufficiently understood to provide enthusiasts and skeptics alike with optimism for the achievement of commercial specifications for the technology.

What about competing technologies? For passive technologies, glass is the main competitor. $LiNbO_3$ and GaAs waveguides, and direct laser modulation provide competition for electro-optic polymers. Underlying all of this is the inertia of electronic systems designers to change their solutions from wires to fiber-based systems: Whenever possible, electronic solutions will be thoroughly examined and selected, if economically feasible and practical. However, high-end communication in all markets is moving toward utilization of the bandwidth offered by optical fiber, and thus the growth of markets for all optoelectronic devices is inevitable. EO polymers will likely share the market with their inorganic counterparts.

With further development, electro-optic polymers have the potential to far-outdistance inorganic materials in figures-of-merit, and, in fact, already do in some key properties, such as length-bandwidth products. Polymers are not likely to ever exhibit insertion loss as low as glass for passive devices. However, intrinsic performance of polymers, measured against other materials, is not sufficient for judging the potential of the technology. Overall production costs, balanced against performance, will determine the utilization of polymer waveguide technologies.

REFERENCES

1. For a thorough current review, see <u>Polymers for Lightwave and Integrated Optics</u>", L.A. Hornak ed. (Marcel Dekker, New York), 1992.
2. C.C. Teng, "Traveling-wave Polymeric Optical Intersity Modulator with more than 40 GHz of 3-dB electrical bandwidth", Appl. Phys. Lett. <u>60</u>, 1538 (1992).
3. J.I. Thackara, G.F. Lipscomb, M.A. Stiller, A.J. Ticknor and R. Lytel, "Poled Electro-optic Waveguide Formation in Thin-film Organic Media", Appl. Phys. Lett. <u>52</u>, 1031 (1988).
4. G. R. Mohlmann, W.H. Horsthuis, C.P. van der Vorst, "Recent Developments in Optically Nonlinear Polymers and Related Electro-Optic Devices," Proc. SPIE <u>1177</u>, 67 (1989).
5. M.B.J. Diemeer, F.M.M. Suyten, E.S. Trammel, A. McDonach, M.J. Copeland, L.J. Jenneskens and W.H.G. Horsthuis, Electronics Letters <u>26</u> (6) 379 (1990).
6. D.G. Girton, S. Kwiatkowski, G.F. Lipscomb, and R. Lytel, "20 GHz Electro-optic Polymer Mach-Zehnder Modulator", Appl. Phys. Lett. <u>58</u>, 1730 (1991).
7. R. Lytel, G.F. Lipscomb, M. Stiller, J.I. Thackara, and A.J. Ticknor, "Organic Integrated Optical Devices", in <u>Nonlinear Optical Effects in Polymers,</u> J. Messier, F. Kajzar, P. Prasad, and D. Ulrich, eds., NATO ASI Series Vol. <u>162</u> (1989), p. 227.
8. C.A. Eldering, A. Knoesen, and S.T. Kowel, "Characterization of Polymeric Electro-optic Films Using Metal Mirror/Electrode Fabry-Perot Etalons", Proc. SPIE <u>1337</u>, 348 (1990).
9. T.E. Van Eck, A.J. Ticknor, R. Lytel, and G.F. Lipscomb, "A Complementary Optical Tap Fabricated in an Electro-optic Polymer Waveguide", Appl. Phys. Lett. <u>58</u>, 1558 (1991).
10. J.W. Wu, J.F. Valley, S. Ermer, E.S. Binkley, J.T. Kenney, G.F. Lipscomb, R. Lytel, "Thermal Stability of Electro-Optic Response in Poled Polyimide Systems", Appl. Phys. Lett., <u>58</u>, 225 (1991).
11. J.F. Valley, J.W. Wu, S. Ermer, M. Stiller, E.S. Binkley, J.T. Kenney, G.F. Lipscomb, and R. Lytel, "Thermoplasticity and Parallel-plate Poling of Electro-optic Polyimide Host Thin Films", Appl. Phys. Lett. <u>60</u>, 160 (1992).
12. R. Lytel and G.F. Lipscomb, "Materials Requirements for Electro-optic Polymers", in <u>Electrical, Optical, and Magnetic Properties of Organic Solid State Materials</u>, Materials Research Society Proceedings Vol. <u>247</u>, 17 (1992).
13. C.A. Armiento, A.J. Negri, M.J. Tabasky, R.A. Boudreau, M.A. Rothman, T.W. Fitzgerald, and P.O. Haugsjaa, "Gigabit Transmitter Array Modules on Silicon Waferboard", IEEE CHMT <u>15</u>, 1072 (1992).
14. T.A. Tumolillo, Jr. and P.R. Ashley, "Multilevel Registered Polymeric Mach-Zehnder Intensity Modulator Array", Appl. Phys. Lett. <u>62</u>, 3068 (1993).
15. B.L. Booth, "Optical Interconnection Polymers", in <u>*Polymers for Lightwave and Integrated Optics*</u>", L.A. Hornak ed. (Marcel Dekker, New York), 1992, pp. 231-266.

Bulk-Type Phase-Matched SHG Devices of Poled Polymers

X.T. Tao, T. Watanabe, H. Ukuda, D.C. Zou, S.Shimoda, H. Sato, and S. Miyata
Falculty of Technology, Tokyo University of Agriculture and Technology

Introduction:

Polymeric second-order nonlinear optical (NLO) materials have been studied extensively in recent years for applications in communication and optical signal processing[1-2]. Most of the earlier works were concerned with the synthesis and the general properties such as nonlinear optical coefficients and temporal stability. Only a few studies have been reported on phase matched second harmonic generation (SHG)[3]. In fact, phase matching is the first important condition to achieve high conversion efficiency of SHG. It has been proposed that the mode dispersion of fundamental and second-harmonic waves was used to achieve phase matching, in which very precise control of film thickness was required. This is not easy for poled polymer films generally obtained by spin-coating. To avoid this difficulty, the use of Cerenkov radiation and non-collinear light path have been proposed. But in all these methods the obtainable SHG conversion efficiency was limited by the small over-lap integrals for different modes. In order to maximize the overlap integral, the quasi-phase matching (QPM)[4] mthods by altering $\chi^{(2)}$ singal or periodic poling have been proposed. But again the precise control of periodicity should be needed, which is also very difficult. Here we describe, for the first time, bulk phase matched second harmonic generation in poled and drawn polymers, polyurea (PU) by using birefringence. The calculated type-I phase-matching characteristics of a drawn PU was confirmed by experiment.

Experiment and results:

1.Sample preparation

The schematic synthesis of polyurea (PU) is shown in Fig. 1.
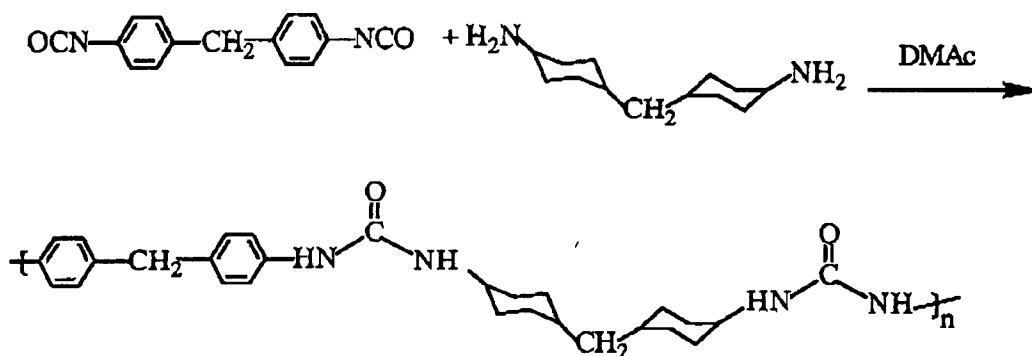
Figure 1. Schematic synthsis of polyurea

2. Polymer geometry and refractive indices

The geometry of polymer and the dispersion of refractive indices vs wavelenths of U1 polymer with draw ratio of 1.4 were shown in Fig.2, and Fig. 3, respectively.
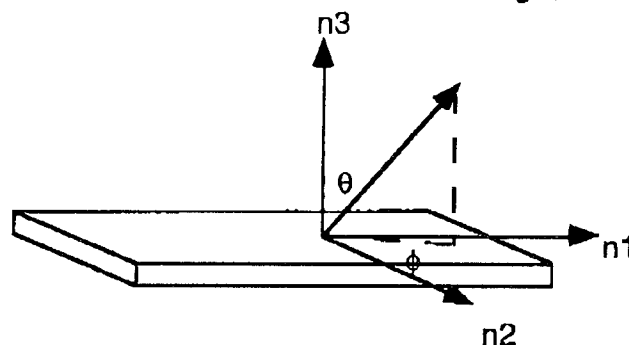
Fig. 2. Geometry of polymer film samples
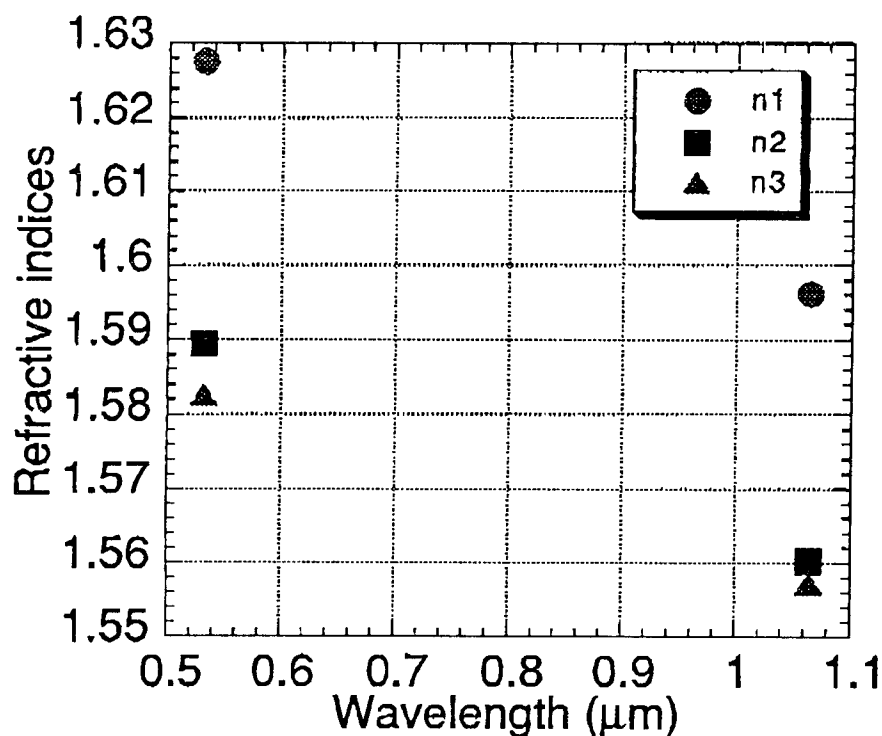
Fig. 3. Refractive indices of poled polymer with draw ratio of 1.4

3.Phase matching experiment

Using the refractive indices of polymer with draw ratio of 1.4, the type I phase matching characteristics has been calculated, the θ and ϕ curve was shown in Fig.4. Cutting a film with $\theta= 90°$ and $\phi= 52.6°$, the phase matched SHG has been observed in experiment by using a Nd:YAG laser with 1064 nm fundamental wavelength, the results were shown in Fig.5.
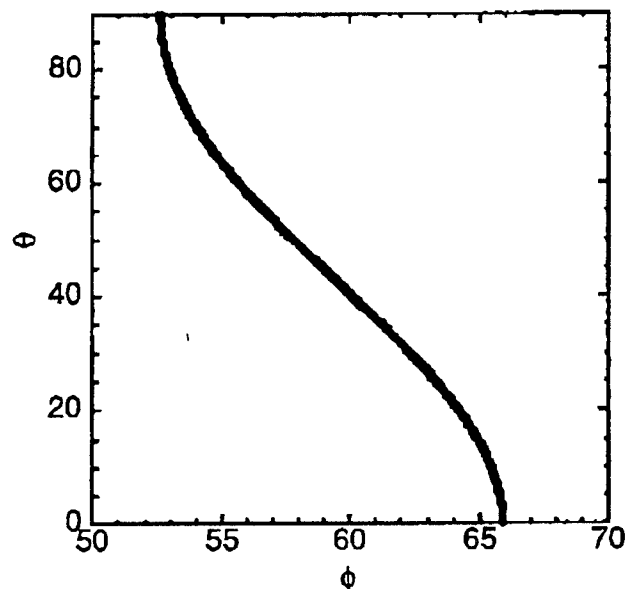
Fig. 4 Type I phase matching curve of polymer with draw ratio of 1.4.
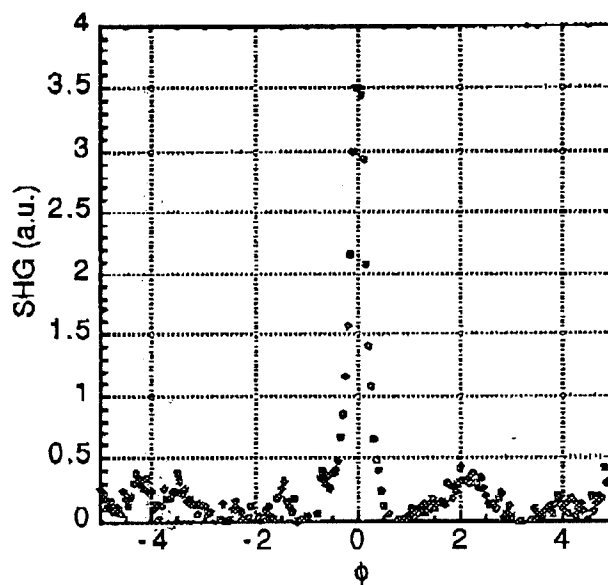
Fig. 5. The dependence of phasematched SHG of polymer on angle ϕ.

Refrences:
(1)   D. S. Chemla, J. Zyss, Eds."Nonlinear optical properties of organic   molecules and crystals" (Academic press New york, 1987)
(2)   S. Miyata, ed."Nonlinear optics, fundamentals, materials and   devices" (North Holland,1992)
(3)   O. Sugihara, T.Kinoshita, M.Okabe, S.Kunioka, Y.Nonaka, and   K.Sasaki, Appl. Optics, 30, 2957 (1991).
(4) M.M.Fejer, G.A.Magel, D.H.Jundt, and R.L.Byer, IEEE J. Quan.Elec. 28, 2631, (1992)

Optical-Loss Reduction and Phase-Matched Second-Harmonic Generation in a Four-Layered Polymeric Waveguide

Koen Clays
Laboratory of Chemical and Biological Dynamics,
Center for Research in Molecular Photonics and Electronics,
Department of Chemistry, University of Leuven,
Celestijnenlaan 200D, B-3001 Leuven, Belgium (tel: +32/16/201015)

Jay S. Schildkraut and David J. Williams
Imaging Research and Advanced Development, Eastman Kodak Company,
Rochester, New York 14650 (tel: +1/716/252-4956).

For a number of important reasons, the waveguide format is advantageous for applications using the nonlinear-optical (NLO) properties of materials.[1] For the realization of a thin film with a higher refractive index, necessary for waveguiding, spin coating this film from a viscous solution of a polymer in a volatile solvent is both simple and inexpensive. For efficient second-harmonic generation in the waveguide format, based on the modal dispersion relations for phase-matching, the overlap integral describing the overlap of the modal field distribution functions $E(z)$ for the fundamental mode m and the harmonic mode n., has to be optimized. The NLO film susceptibility has to be tailored to avoid negative contributions to the overlap integral resulting from a negative part of the modal field from the harmonic mode. In a four-layered waveguide, this can be accomplished by using an additional polymer layer with zero NLO film susceptibility. This additional layer also has lower optical loss, so that the total waveguide loss is also reduced. Finally, the relative thickness of the two polymer films is chosen to fulfil the phase matching condition.[2]

The polymer with the zero NLO film susceptibility used in this study is polystyrene. Two NLO active polymers were used.[3] Their structure, with the NLO chromophore, is shown in Fig. 1. The stilbene polymer (a) has spacers with different lengths (2 or 6 methylene units)between the polymer chain and the stilbene chromophore to prevent semi-crystallinity. The phenyl polymer (b) has a smaller chromophore for reduced absorption in the visible.
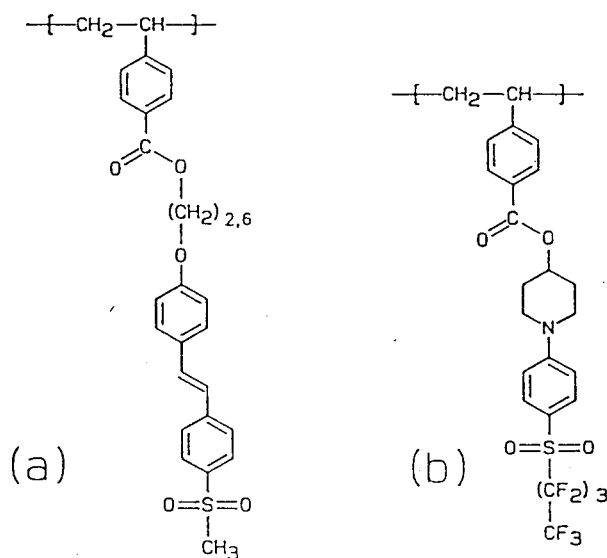
Fig. 1. Molecular structure of the NLO polymers used in the experiments: (a) stilbene NLO polymer; (b) phenyl NLO polymer.

Thin films were prepared by spin coating from a viscous solution of the polymer in the appropriate solvent on a suitable substrate. For the study of the reduction of the linear optical waveguide loss, synthetic fused silica substrates were used. To accurately determine the optical constants of the three polymers used, three-layer waveguides were prepared. The observed coupling angles for waveguiding are related to the real part of the refractive index. The imaginary part was calculated from the waveguide attenuation, determined by measuring the scattered-light intensity profile along the propagation axis. The polystyrene polymer was lossless; the attenuation for the stilbene and phenyl polymer was caused by absorption and not by scattering.

Based on the obtained values for real and imaginary part of the refractive index for the different polymers, we were able to predict the reduction in waveguide loss for the four-layered structure. The predicted values have been experimentally verified. Calculated and measured waveguide losses for a three- and a four-layered waveguide of the phenyl polymer at 457.9 nm are shown in Fig. 2. It is clear that a considerable reduction in loss can be obtained (from 80 down to 1 dB.cm^{-1} for the $m=0$ mode). For SHG with phasematching to the $m=1$ mode, the loss reduction for the latter mode (from 80 to 12 dB.cm^{-1}) is more important.
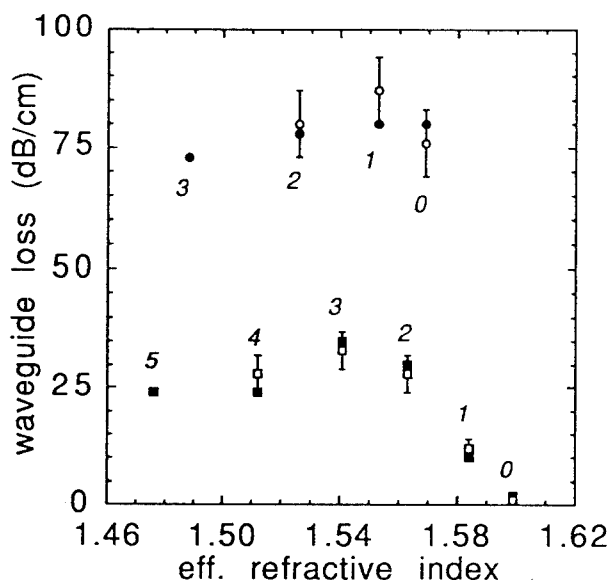
Fig. 2. Dependence of calculated (filled symbols) and experimental (open symbols) waveguide attenuation on mode number for the three-layered (circles) and for the four-layered waveguide structure (squares) at 457.9 nm.

The best quantitative agreement between calculated and experimental loss values is observed when absorption, and not scattering, is the largest cause of the waveguide loss. The modal loss equation takes into account only the absorption losses for the different layers, and not the surface and interface scattering. This contribution to the total waveguide loss becomes especially important when the difference in refractive index is large, and for very thin layers.

For the study of the NLO properties of the polymer waveguides, Pyrex substrates, coated with transparent ITO were used. Corona poling was used to induce the polar order of the NLO chromophores, necessary for second-order NLO effects. The higher glass transition temperature and the lower solubility in apolar solvents for the NLO stilbene and phenyl polymer allowed spincoating and processing of a polystyrene layer on top of an oriented NLO polymer layer. Reduced absorption and SHG in transmission format confirmed the poling and the stability of the NLO layer during processing of the fourth layer. A quadratic dependence of the SHG intensity as a function of fundamental intensity is always observed. The increase in SHG intensity for increasing angle of incidence of the fundamental is typical of the symmetry induced by poling. An increased scatter is observed however, probably due to random variation in layer thicknesses.

A four-layer waveguide was prepared for phasematched SHG to the blue in waveguide format. Based on the dispersion of the refractive index, as determined from prism coupling experiments at different wavelengths, and on the actual physical thickness of the two polymer layers, as measured with the stylus method, the phase-matching wavelength was calculated to be 850 nm. The structure of the waveguide is shown in Fig. 3. Note the match of the nodal plane of the modal field distribution for the second-harmonic $m=1$ mode with the boundary between the polystyrene and the stilbene polymer layer. This construction completely avoids any negative contribution to the overlap integral. Measurements of the SHG intensity as a function of wavelength confirmed the phasematching at the calculated wavelength. The relatively broad phase-matching curve (Fig. 4), correlating very well with the low conversion efficiency ($\eta < 0.001$ %), is believed to be also caused by the random thickness variations.
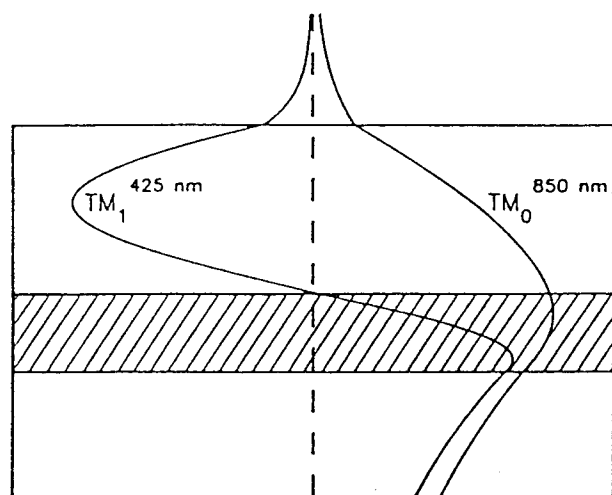
Fig. 3. Structure of the four-layered polymeric waveguide (0.15 mm stilbene NLO polymer film, hatched, covered with a 0.33 mm polystyrene layer) with the thicknesses optimized for phasematching and optimal overlap integral.
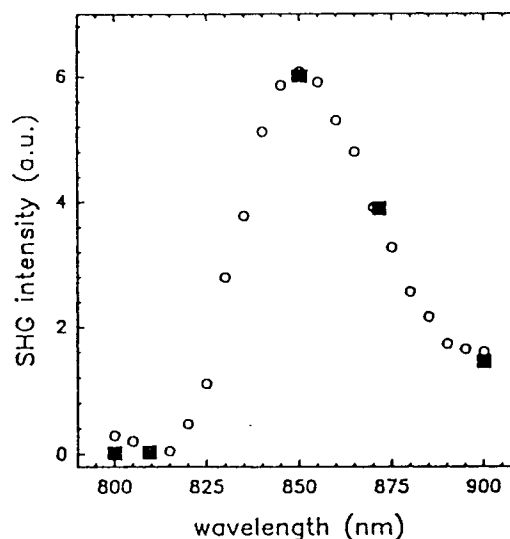
Fig. 4. Wavelength dependence of the SHG intensity generated in the four-layered polymeric waveguide structure. Open circles, calculated; filled squares, experimental values

The observed enhancement as a function of wavelength confirms the phase matching for the four-layered structure. For coherent conversion processes, the intensity is quadratically dependent on the interaction length. This length is mostly determined by the absorption at the second-harmonic wavelength, and, especially for four-layered waveguides, by random thickness variations. A thickness control of 50 nm is believed to be routinely achieved in photoresist formulations. For a single-layer thickness of only 150 nm, the relative thickness variation is important and reduces substantially the interaction length over which phase matching can be maintained. The Langmuir-Blodgett film deposition technique offers a monolayer thickness resolution. This technique has recently been applied to phase-match and optimizes the overlap integral, not by avoiding the negative contribution to the overlap integral, but by inverting the sign of the susceptibility in the region with negative field for the second-harmonic mode.[4] This can only be achieved through the unique features of LB deposition, but this technique requires amphiphilic polymers and time-consuming layer by layer deposition.

references :
1. D. J. Williams, *Introduction to Nonlinear Optical Effects in Molecules and Polymers* (Wiley, New York, 1991)
2. K. Clays, J. S. Schildkraut, and D. J. Williams, *J. Opt. Soc. Am. B* **11**, (1994).
3. D. R. Robello, R. J. Perry, and E. J. Urankar, *Macromolecules* **25**, 2940 (1993).
4. T. L. Penner, H. R. Motschmann, N. J. Armstrong, M. C. Ezenyilimba, and D. J. Williams, *Nature* **367**, 49 (1994).

Large Third-Order Nonlinearities for the Excited States of Diphenylhexatriene and Quaterphenyl Measured Through Time Resolved Degenerate Four-Wave Mixing

M.J. Rosker, H.O. Marcy, and L.F. Warren
Rockwell International Science Center
1049 Camino Dos Rios
Thousand Oaks, CA 91360
805-373-4463

It has been recently suggested[1] and subsequently shown[2,3] that the optical nonlinearity of the first electronically excited state of a conjugated organic molecule can be significantly larger than that of the ground state. The first measurements were made using third harmonic generation ($3\omega \sim 514$ nm) in silicon naphthalocyanine, but the large excited state absorption induced made it difficult to ascertain whether the nonlinearity was the result of a purely non-resonant mechanism. Rodenberger $et\ al.$[3] later used degenerate four-wave mixing (DFWM) at 1.064 μm to probe the nonlinearity of dilute solution of diphenylhexatriene (DPH) after it was excited at 355 nm. An enhancement of nearly two orders of magnitude in $\chi^{(3)}$ value was observed and was purported to be the result of a purely non-resonant electronic effect, in part because the DFWM grating lifetime was observed to decay within the temporal resolution of their experiment (35 ps).

We will report time-resolved studies of the third-order nonlinear optical dynamics of two molecules in their electronically excited states: DPH and quaterphenyl [(Ph)$_4$], another example of a quasi-one-dimensional organic molecule with extended conjugation. These results were obtained using ~120 fs optical pulses for both the UV pump (at ~320 nm) and the visible spectrum DFWM beams (at ~640 nm). While our results are in agreement with those obtained by Rodenberger $et\ al.$[3] for DPH, the ultrafast optical pulses allowed us to resolve the excited state DFWM grating dynamics. The ground-state $\chi^{(3)}$ for (Ph)$_4$ in the solid-state was previously measured to be very small,[4] but the excited state enhancement of the $\chi^{(3)}$ response was as much as an order of magnitude greater than that for DPH. For both of these molecules, components of the DFWM response were observed on both very fast (<120 fs) and slower (>10 ps) time scales.

The DPH sample was made up in a nitrogen glove-bag in anhydrous dioxane (distilled from sodium under N$_2$) at a concentration of 6.5×10^{-3} M; the (Ph)$_4$ sample was similarly prepared to ~1×10^{-4} M. DFWM studies were carried out in the conventional backward counterpropagating pump geometry, with the samples contained in quartz cells of 50 μm path length, which essentially determined the temporal resolution. The optical source was an amplified, mode-locked dye laser producing approximately 120 fs, 600 μJ pulses at 20 Hz at a wavelength of approximately 640 nm. The pump light was generated by frequency doubling (to ~ 320 nm wavelength) a portion of the amplified light in a 1 mm thick KDP crystal. The remaining amplified light formed the basis of the DFWM experiment.

Figures 1 and 2 show the femtosecond time-resolved DFWM response for both samples as a function of the relative delay of the readout beam. No attempt has been made here to subtract out the DWFM signal of the solvent; however, we observed for the (Ph)$_4$ solution that the

ground-state DFWM signal at the concentration used is predominantly due to the dioxane solvent. These results demonstrate that the excited state NLO response is not purely electronic, as was previously suggested for DPH.[3] This is apparent because the transient persists for significantly longer than the pulse. For DPH, the transient fits well to a sum of two exponentials with time constants of 13 ps and ~200 ps. For $(Ph)_4$, the initial grating decay is non-exponential, but later decays with an exponential time constant of 11 ps. Another interesting aspect of this data lies in the apparent turn-on time required after the grating is written for the nonlinearity to develop. For $(Ph)_4$, the maximum DFWM signal is not achieved until almost 1 ps after the grating was written. The turn-on behavior for DPH also shows non-instantaneous response. Such behavior is characteristic of other molecular nonlinearities (e.g., CS_2), and likely indicates that the predominant nonlinear mechanism is orientational or conformational in nature.
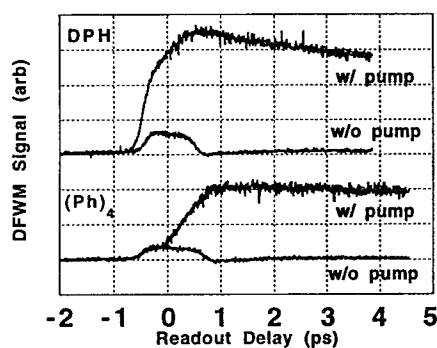
Fig. 1: DFWM signal vs. readout beam delay.
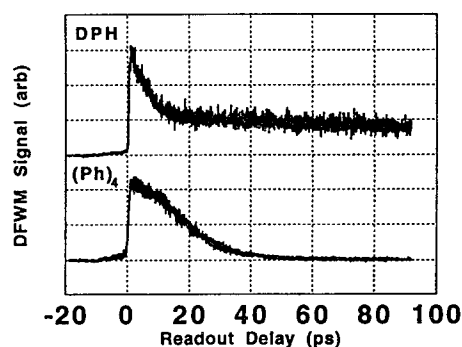
Fig. 2: DFWM signal vs. readout beam delay, with UV pump.

Figure 3 depicts the DFWM dependence on the delay of the pump beam. In these data, the 620 nm beams are set to give the maximum DFWM signal for $(Ph)_4$. The dependence is approximately a single-sided exponential whose time-constant (500 ps) gives the lifetime of the excited-state enhancement. This value equals the singlet-to-triplet transition time reported in Ref. 5 where standard spectroscopic techniques were used to measure the excited state lifetimes. These results suggest that the enhanced DFWM signal for $(Ph)_4$ results from the population in the first excited singlet state.

Fig. 4 shows the increase in the enhancement as a function of the UV pump energy. It is apparent from these results that we are not yet in the saturation regime. This is consistent with the measured transmission spectrum and suggests that a considerably larger DFWM signal could be observed by increasing the pump power or by tuning the pump wavelength.

For device applications, it is critical to ascertain if the enhancement in $\chi^{(3)}$ is associated with an increase in the absorption by the excited-state. We have endeavored to perform pump-probe experiments to detect such excited state absorption at 640 nm. For quaterphenyl, previous reports indicate that the threshold UV flux level for excited state absorption from the lowest

singlet S_1 state is ~ 0.1 J/cm^2.[5, 6] In this study, the UV energy density incident on the samples (~ 1 mJ/cm^2) was significantly lower than this value. Note that the triplet-triplet absorption spectrum of $(Ph)_4$ is also transparent at the DFWM wavelength of 640 nm.[7] The absence of an appreciable excited state absorption implies that the $\chi^{(3)}$ enhancement is primarily due to non-resonant effects. The long-lived mechanisms in evidence in Fig. 2 may therefore be due to solution-based effects such as orientational, librational, or nuclear motions. The index grating formed via such ordering represents a significant portion of the observed response in the case of CS_2 and is believed to result in the observation of a substantial turn-on time for its nonlinearity. A longer turn-on time in comparison to CS_2 might be expected in the case of both DPH and $(Ph)_4$ as they are much larger molecules.
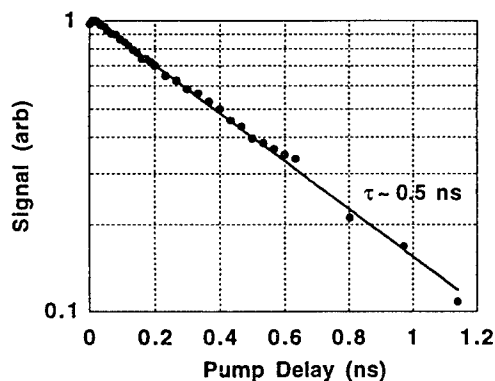
Fig. 3: DFWM signal vs. UV pump delay for $(Ph)_4$. Solid line is a fit to an exponential.
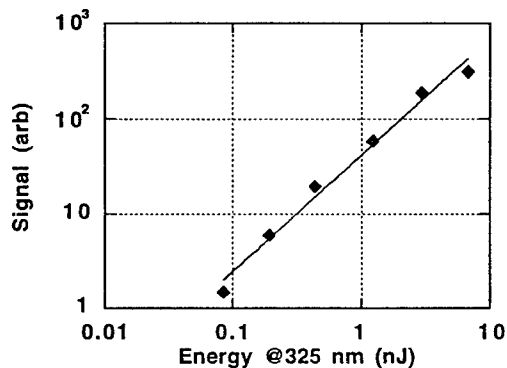
Fig. 4: DFWM signal vs. UV pump energy for $(Ph)_4$.

These results demonstrate that time resolved DFWM technique offers an exceptional method for probing the dynamics of the molecular conformation and orientation after photoexcitation. We have also confirmed the observation large excited-state nonlinear enhancement in DPH of Rodenberger *et al.* and have extended observation of this phenomenon to a new and potentially important class of materials, p-oligophenylenes.

References

1. Q. L. Zhou, J. R. Heflin, K. Y. Wong, O. Zamani-Khamiri and A. F. Garito, Phys. Rev. A **43**, 1673 (1991).
2. J. R. Heflin, D. C. Rodenberger, R. F. Shi, M. Wu, N. Q. Wang, Y. M. Cai and A. F. Garito, Phys. Rev. A **45**, R4233 (1992).
3. D. C. Rodenberger, J. R. Heflin and A. F. Garito, Nature **359**, 309 (1992).
4. H. O. Marcy, M. J. Rosker, L. F. Warren, B. A. Reinhardt, M. Sinclair and C. H. Seeger, J. Chem. Phys. **In Press**, (1994).
5. R. S. Taylor and S. Mihailov, Appl. Phys. B **38**, 131 (1985).
6. P. Cassard, R. S. Taylor, P. B. Corkum and A. J. Alcock, Opt. Commun. **38**, 131 (1981).
7. T. G. Pavlopoulos and P. R. Hammond, J. Amer. Chem. Soc. **96**, (1974).

OBSERVATION OF PARAMETRIC LIGHT SCATTERING

Martti Kauranen, Thierry Verbiest, and André Persoons

Laboratory of Chemical and Biological Dynamics, University of Leuven, Celestijnenlaan 200 D, B-3001 Heverlee, Belgium, Tel. +32-16-201015, Fax. +32-16-201368

Even-order coherent nonlinear optical processes are forbidden, in the electric-dipole approximation, in centrosymmetric material systems such as an isotropic solution. However, orientational fluctuations of noncentrosymmetric molecules can break locally the macroscopic centrosymmetry of such solutions and make incoherent nonlinear scattering processes possible. Second-order light scattering was first observed in 1965 from several liquids and from fused quartz [1]. In these experiments, a single laser beam at frequency ω was incident on the sample and scattered light at the second-harmonic frequency 2ω was detected. Both elastic scattering (hyper-Rayleigh scattering, HRS) at the exact second-harmonic frequency and inelastic scattering (hyper-Raman scattering) with frequency displacements characteristic to the material were observed. More recently, hyper-Rayleigh scattering has gained popularity as a routine technique to determine the first hyperpolarizability β of organic molecules in solution [2].

In this Paper, we present the first experimental observation of a second-order scattering process in which the two incident photons are at different frequencies and sum-frequency radiation is detected [3]. We show that, analogous to HRS, this parametric light-scattering (PLS) process can be used to determine the first hyperpolarizability of organic molecules in solution. We also show that by independent control of the polarizations of the two incident beams and by detecting unpolarized radiation, the process can be used to determine relative values of two independent components of the hyperpolarizability tensor. The independent input polarizations of the two beams provide distinct advantages compared to HRS, which requires the use of depolarized scattered radiation to measure values of individual tensor components [4].

Our experimental setup is shown in Fig. 1. One incident beam is provided by the fundamental (1064 nm) output of an injection seeded Nd:YAG laser (8 ns pulses, 10 Hz). The other incident beam at 954 nm is generated by Raman shifting the frequency doubled output (532 nm) of the Nd:YAG laser. The energy of both incident beams is always less than 1 mJ. The incident laser beams are made counterpropagating and are weakly focussed into a small cell containing an isotropic solution of organic molecules. We take the 954-nm and 1064-nm incident beams to propagate in the negative and positive x directions, respectively. Unpolarized sum-frequency light at 503 nm that is scattered in y direction is collected by a condenser system and is filtered by a low-pass optical filter and an interference filter before detection with a photomultiplier.

For our first set of measurements, both incident beams are polarized in z direction. The intensity of the 1064-nm incident beam is adjusted by means of a half-wave plate. The intensity of the scattered light is of the form [3]

$$I(\omega_1 + \omega_2) = gB^2 I(\omega_1) I(\omega_2) \; , \tag{1}$$

where g is an instrumental factor containing the scattering geometry and local field factors. $I(\omega_1)$ and $I(\omega_2)$ are the intensities of the 954-nm and 1064-nm incident beams, respectively and B is the effective second-order nonlinearity of the solution. In the present experiments, the nonlinearity of the solvent is very small compared to that of the dissolved molecules, and hence B^2 is directly proportional to the number density of dissolved molecules.

In Fig. 2(a), we show the PLS signal as a function of the intensity of the 1064-nm beam for different number densities of *para*-nitroaniline in methanol. The intensity of the 954-nm beam is constant. All curves exhibit the expected linear dependence on the intensity. From the slopes of the linear fits in Fig. 2(a), we determine the quadratic coefficients

$$gB^2 = I(\omega_1 + \omega_2) / I(\omega_1) I(\omega_2) \tag{2}$$
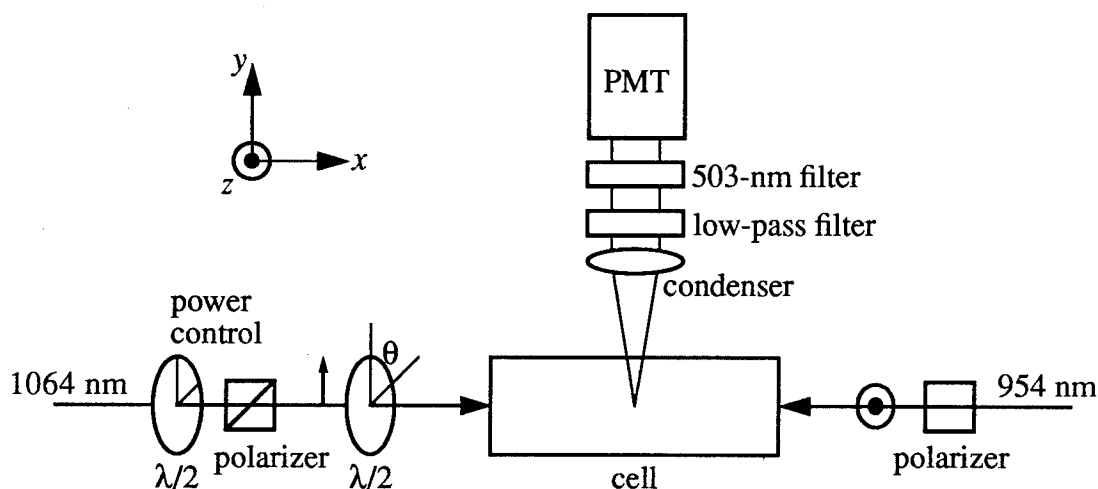
Figure 1. Schematic representation of the experimental setup.

for each number density. The quadratic coefficient has the expected linear dependence on number density as shown in Fig. 2(b). We have repeated a similar set of measurements for *para*-nitroanisol dissolved in methanol. The quadratic coefficient for *para*-nitroanisol is also shown in Fig. 2(b). The slopes of the fitted lines in Fig. 2(b) and the reference value of 34.5×10^{-30} esu [5] for the hyperpolarizability of *para*-nitroaniline yield a value of 12×10^{-30} esu for the hyperpolarizability of *para*-nitroanisol. This value is in perfect agreement with the value that has been measured with the EFISHG technique in chloroform solutions.

We next assume that Kleinman symmetry is approximately valid for *para*-nitroaniline under our experimental conditions. Under this assumption, the two dominant components of the molecular hyperpolarizability tensor are β_{333} and β_{322}. To determine the ratio of these components, we rotate the polarization of the 1064-nm incident beam by a half-wave plate and record the intensity of the (unpolarized) scattered sum-frequency light as a function of the rotation angle of the waveplate. The result is shown in Fig. 3 with a fit to the expected functional form of
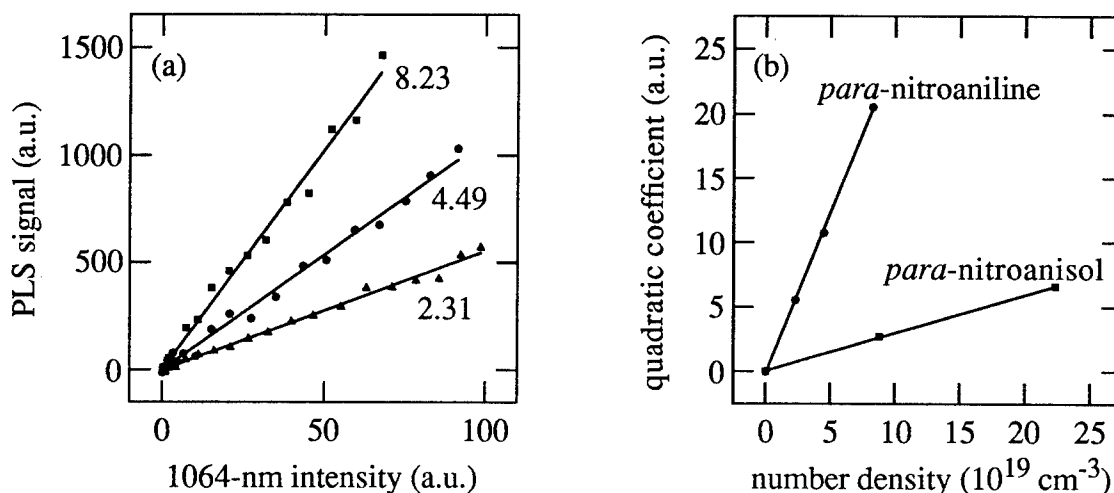
Figure 2. (a) PLS signal as a function of the intensity of the 1064-nm beam for various number densities (in 10^{19} cm^{-3}) of *para*-nitroaniline in methanol. (b) Quadratic coefficient as a function of number density for *para*-nitroaniline and *para*-nitroanisol.
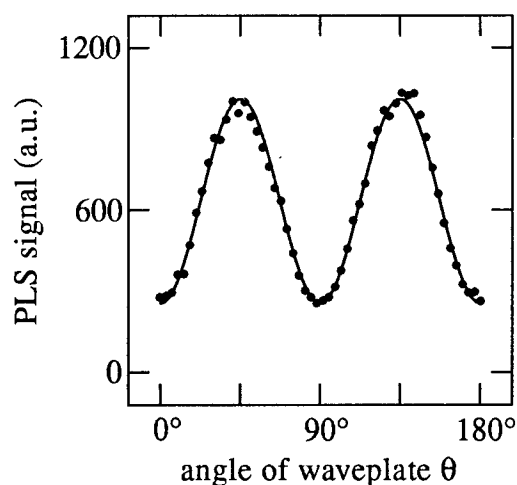
Figure 3. PLS signal as a function of the rotation angle of the half-wave plate that is used to control the polarization of the 1064-nm beam.

$$f(\theta) = a\sin^2 2\theta + b\cos^2 2\theta \ , \tag{3}$$

where θ is the angle of the waveplate measured from y direction. The coefficients a and b are

$$a = 18\beta_{333}^2 + 16\beta_{333}\beta_{322} + 38\beta_{322}^2 \ , \quad b = 4\beta_{333}^2 - 5\beta_{333}\beta_{322} + 17\beta_{322}^2 \ . \tag{4}$$

The fitted values of parameters a (1009.1) and b (253.4) yield a value $\beta_{322}/\beta_{333} \approx -0.06$, in good agreement with the result obtained by measuring depolarized HRS radiation [4].

In conclusion, we have presented the first observations of a parametric light-scattering process in which two incident photons at different frequencies give rise to a scattered photon at the sum frequency through a nonlinear interaction in an isotropic medium. We have shown that this process can be used to determine the first hyperpolarizability β of organic molecules in solution. This new approach can be used to extend HRS measurements to determine values of the hyperpolarizability for arbitrary input frequencies. Independent control of the polarizations of the two incident beams makes it possible to use PLS to determine relative values of two different components of the molecular hyperpolarizability tensor by detecting unpolarized radiation. In such measurements, very high-quality polarizers with their inherent sensitivity to alignment can be used in the collimated input beams to increase the accuracy of the measurement. The insertion losses of polarizers can be easily compensated by increasing the energy of the incident beams. In depolarization measurements of HRS, this compensation is not possible if the input intensities approach damage threshold of the sample and hence the polarizers necessarily reduce the measured signal level. In a more general case, independent polarizations of the incident beams in combination with depolarized scattered radiation can be used to increase the number of tensor components that can be determined by parametric light scattering.

References

1.   R. W. Terhune, P. D. Maker, and C. M. Savage, Phys. Rev. Lett. **14**, 681 (1965).
2.   K. Clays and A. Persoons, Phys. Rev. Lett. **66**, 2980 (1991).
3.   R. Bersohn, Y.-H. Pao, and H. L. Frisch, J. Chem. Phys. **45**, 3184 (1966).
4.   G. J. T. Heesink et al., Phys. Rev. Lett. **71**, 999 (1993).
5.   J. L. Oudar and D. S. Chemla, J. Chem. Phys. **66**, 2664 (1977).

Molecular Design of NLO Active π-Conjugated Compounds

Tatsuo WADA and Hiroyuki SASABE
Frontier Research Program, The Institute of Physical and Chemical Research (RIKEN),
2-1 Hirosawa, Wako, Saitama 351-01, Japan.
Tel: +81-48-462-1111 x6321

Introduction

The intramolecular charge transfer through π-electron conjugation gives large optical non-linearities in the molecular level, *i.e.*, the third-order susceptibility $\chi^{(3)}_{ijkl}(-\omega_4; \omega_1,\omega_2,\omega_3)$ depends on the microscopic third-order polarizability $\gamma_{ijkl}(-\omega_4; \omega_1,\omega_2, \omega_3)$ of constituent molecular unit. We have focused our researches for long on the development of one-dimensional conducting polymers such as polythiophenes, polydiacetylenes and substituted polyphenylacetylenes, and of two-dimensional macrocyclic conjugated compounds such as annulenes and metallophthalocyanine derivatives. In this paper we will discuss the key factors for designing molecular structures and nonlinear optical properties; that is, the dimensionality and symmetry of molecules and/or molecular aggregates.

One Dimensional Systems

In conjugated linear chain structures such as polyenes, π-electrons are delocalized in their motion only in one dimension along the chain axis. Major contribution to γ_{ijkl} is the chain axis component γ_{xxxx} along the chain axis (x-axis), and hence the averaged susceptibility $<\gamma>$ in isotropic media equals to one-fifth of γ_{xxxx}. It has also been found that γ_{xxxx} is more sensitive to the physical length of the chain than to the conformation. Off-resonant $\chi^{(3)}_{1111}(-3\omega; \omega,\omega,\omega)$ determined by the third harmonic generation (THG) is directly related to $<\gamma>$ of the conjugated compound through local field factors f expressed in terms of the refractive indices n_ω and $n_{3\omega}$ as
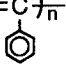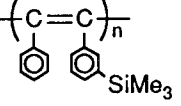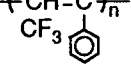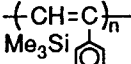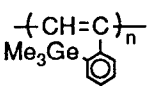
$$\chi^{(3)}_{1111}(-3\omega; \omega, \omega, \omega) = N f_{3\omega} f_\omega f_\omega f_\omega \langle \gamma \rangle (-3\omega; \omega, \omega, \omega), \tag{1}$$

where N is the number of molecules per unit volume.

Unlike polyacetylene, substituted polyacetylenes such as polyphenylacetylene (PPA) possess high molecular weight over 1×10^6, dissolve in various organic solvents, and are considerably thermally stable. The substituted PPAs have alternating double bonds along the main chain and their optical properties can be controlled by introducing bulky groups as a substituent of a phenyl group. We have examined third-order nonlinear optical responses of thin films of various substituted PPAs (Table 1), and applied to nonlinear optical waveguide devices.

The modulation spectra of electroabsorption (EA) were related to the first and second derivatives of unperturbed absorption spectra and scaled quadratically with the applied field. The change of optical absorbance $\Delta\alpha$ under an electric field leads to the change of refractive index Δn through Kramers-Kronig (K-K) transformation:

Table 1. Nonlinear optical properties of substituted polyphenylacetylene thin films.

Polymer		λ_{max} (nm)	$^*\chi^{(3)}$ $(-3\omega;\omega,\omega,\omega)$ (esu)
PPA	$-(CH=C)_n-$	352	5.4×10^{-13}
PDPA	$-(C=C)_n-$ $\quad$ SiMe$_3$	440	8.8×10^{-13}
P(CF$_3$)PA	$-(CH=C)_n-$ CF$_3$	439	3.0×10^{-12}
P(Me$_3$Si)PA	$-(CH=C)_n-$ Me$_3$Si	536	1.7×10^{-11}
P(Me$_3$Ge)PA	$-(CH=C)_n-$ Me$_3$Ge	548	2.6×10^{-11}

* Fused Silica $\chi^{(3)} = 1.4 \times 10^{-14}$ esu at 1907 nm
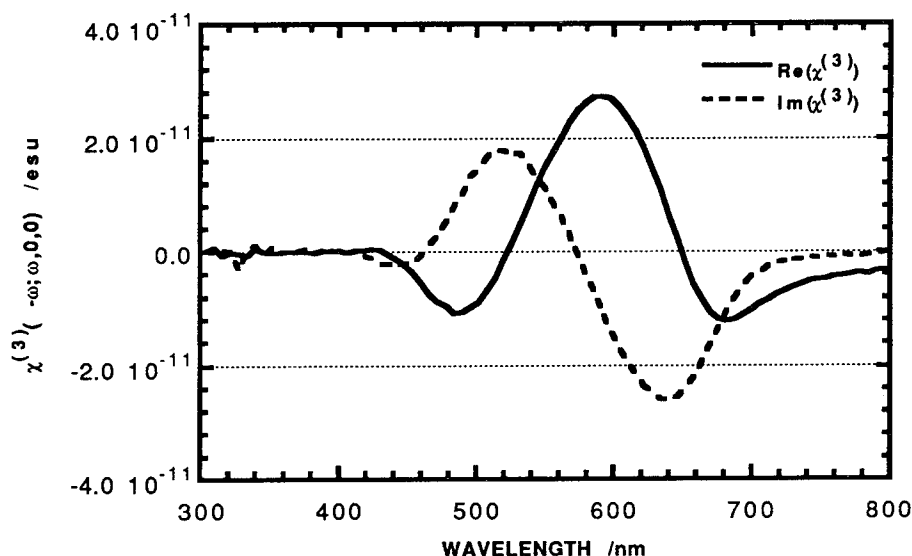
Figure 1 Dispersion of imaginary and real part of $\chi^{(3)}(-\omega;\omega,o,o)$ for P(Me$_3$Ge)PA.

$$\Delta n(\omega) = \frac{c}{\pi} P \int_0^\infty \frac{\Delta\alpha}{\omega'^2 - \omega^2} d\omega', \tag{2}$$

where P denotes the principal value of the integral, and ω and ω' are wavenumbers (cm^{-1}). Since the frequency of external electric field is low and the system can be treated as a steady state, the K-K transformation is applicable to the PPA film. It should be noted that $\Delta\alpha$ is induced by an optically linear process. The complex third-order susceptibility $\chi^{(3)}$ (-$\omega;\omega$, 0,0) in cgs unit can be calculated by

$$\chi^{(3)}(\omega;\omega,0,0) = \frac{n\Delta n - k\Delta k}{2\pi F^2} + i\frac{n\Delta k - k\Delta n}{2\pi F^2} \qquad (3)$$

where F is the external electric field, n and k are respectively the real and imaginary part of complex refractive index, and $k = \lambda\alpha/4\pi$. The dispersion of $\chi^{(3)}$ (-ω;ω,0,0) for P(Me$_3$Ge)PA film is shown in Figure 1. As expected, the EA spectra show the similar shape of the second derivative of the optical absorption spectra. Typical value of $\chi^{(3)}$ (-ω;ω,0,0) for o-substituted PPA was determined to be *ca.* 10^{-11}esu. Remarkable changes in the linear and nonlinear optical properties of PPAs can be achieved by varying the substituents.

Two-Dimensional Systems

In the case of two-dimensional π-conjated systems, the contribution from off-diagonal components of nonlinear polarizability γ_{ijkl} to <γ> can be expected. We have developed novel two-dimensional conjugated systems for second- and third-order nonlinear optics: four types of asymmetrically substituted macrocycles and non-aggregated phthalocyanines, that is, meso-monosubstituted octaethyl metalloporphyrins, β-monosubstituted tetraphenyl metalloporphyrins, mono (*tert*-butyl) vanadyl phthalocyanine, tris (*tert*-butyl) mononitro metallophthalocyanines, and hexadeca (trifluoroethoxy) metallophthalocyanines. We have already suggested the importance of the control of molecular packing in asymmetric vanadyl phthalocyanine in order to enhance $\chi^{(3)}$(-3ω; ω,ω,ω) . No evidence of molecular aggregation was observed in optical absorption and electroabsorption spectra for hexadeca (trifluoroethoxy) metal-free and vanadyl phthalocyanines.

$H_2Pc(t\text{-bu})_3NO_2$:

M=H$_2$, R= —C(CH$_3$)$_2$CH$_3$, X=NO$_2$

$VOPc(t\text{-bu})_3NO_2$:

M=VO, R= —C(CH$_3$)$_2$CH$_3$, X=NO$_2$
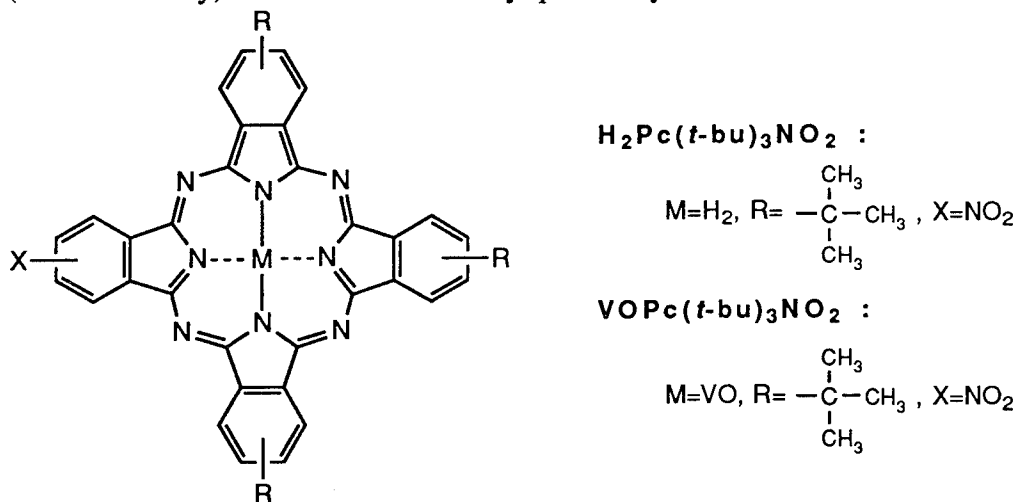
Figure 2 Chemical structures of MPc(t-bu)$_3$NO$_2$.

We performed the crossed-condensation method to obtain the asymmetrically substituted metallophthalocyanines which exhibit excellent solubility. The chemical structures are shown in Figure 2. We examined the second-order nonlinear optical responses of asymmetrically substituted metallophthalocyanine in oriented Z-type Langmuir-Blodgett (LB) films and electric field-induced alignment of molecularly doped polymers by second-harmonic generation (SHG). The one side-coated LB films show similar SHG responses to the poled polymers. No anisotropy in the film plane was detected at a normal incidence.

In conclusion, these one- and two-dimensional π-conjugated systems have a flexibility of molecular design for tuning their nonlinearities in molecular level.

Third-Order Nonlinearities of Dye Molecules and Conjugated Polymers

Christoph Bubeck

Max-Planck-Institute for Polymer Research, Postfach 3148,

D-55021 Mainz, Germany, Tel. (0)6131 379 122

Experimental investigations of the nonlinear optical susceptibilities $\chi^{(3)}$ of several conjugated polymers, oligomers and dye molecules will be presented. They offer the possibility to find characteristic relations between $\chi^{(3)}$ and their chemical structure. Fig. 1 shows typical examples: poly (p - phenylenevinylene) (PPV) and its oligomers (OPV-n), polyphenothiazinobisthiazole (PPT), polyphenylacetylenes (PPA), polythiophenes (PT), oligorylenes (ORy-n) and an oligomeric bridged phthalocyaninato ruthenium complex (OPc). Nonlinear optical spectroscopy can provide additional information on molecular excitation states and their relaxation processes, which is not achievable by linear optical techniques alone.

A survey on recent experiments will be given, aimed to characterize thin films of such organic materials by means of third harmonic generation (THG) and degenerate four wave mixing (DFWM). These experiments are performed with laser wavelengths which are tuned over a large spectral range. Therefore resonance enhancements of the nonlinear optical susceptibilities $\chi^{(3)}(-3\omega;\omega,\omega,\omega)$ and $\chi^{(3)}(-\omega;\omega,\omega,-\omega)$ can be seen clearly. They are induced by single- or multiphoton excitation states. For an accurate evaluation of $\chi^{(3)}$-data, a precise knowledge of the refractive index of the thin films is necessary. It is obtained from a joint application of ellipsometry, prism coupling, Kramers-Kronig analysis and reflection spectroscopy.

General relations between the structure, especially the length L of the conjugated π-electron system and the $\chi^{(3)}$-values can be seen, if $\chi^{(3)}$ is displayed in master plots versus L, λ_{max} (wavelength of the absorption maximum) or $\alpha(\omega)$, which is the absorption coefficient at the laser frequency ω. For one-dimensional systems a scaling law $\chi^{(3)}(-3\omega;\omega,\omega,\omega)/\alpha_{max} \sim \lambda_{max}^{x}$ is found. The experiments indicate, that the exponent x could be much larger as predicted by the theory of Flytzanis et al. In resonant DFWM-experiments it is found that $\chi^{(3)}(-\omega;\omega,\omega,-\omega)$ follows a scaling law $\chi^{(3)} \sim [\alpha(\omega)]^{y}$. Saturable absorption in electronically isolated two-level systems leads to y = 2. With conjugated polymers y = 1 is found in the experiments. This is attributed to phase-space filling effects with excitons. These master plots can be used to evaluate perspectives and limitations of organic $\chi^{(3)}$ materials.

Acknowledgments

References

D. Neher, A. Wolf, C. Bubeck, G. Wegner, "Third Harmonic Generation in Polyphenylacetylene: Exact Determination of Nonlinear Optical Susceptibilities in Ultrathin Films", Chem. Phys. Lett. 163 (1989) 116.

C. Bubeck, A. Grund, A. Kaltbeitzel, D. Neher, A. Mathy, G. Wegner, "Third Order Nonlinear Optical Effects in Conjugated Polymers and Dye Systems" in J. Messier, F. Kajzar, P.N. Prasad (Eds.): Organic Molecules for Nonlinear Optics and Photonics, NATO ASI Series E 194, Kluwer Acad. Publ., Dordrecht, (1991) 335.

C. Bubeck, A. Kaltbeitzel, A. Grund, M. LeClerc, "Resonant Degenerate Four Wave Mixing and Scaling Laws for Saturable Absorption in Thin Films of Conjugated Polymers and Rhodamine 6G", Chem. Phys. 154 (1991) 343.

D. Neher, A. Kaltbeitzel, A. Wolf, C. Bubeck, G. Wegner, "Linear and Nonlinear Optical Properties of Substituted Polyphenylacetylene Thin Films", J. Phys. D: Appl. Phys. 24 (1991) 1193.

A. Grund, A. Kaltbeitzel, A. Mathy, R. Schwarz, C. Bubeck, P. Vermehren, M. Hanack, "Resonant Nonlinear Optical Properties of Spin-Cast Films of Soluble Oligomeric Bridged Phthalocyaninatoruthenium (II) Complexes", J. Phys. Chem. 96 (1992) 7450.

C. Bubeck, "Measurement of Nonlinear Optical Susceptibilities", in G. Zerbi (Ed.): Organic Materials for Photonics - Science and Technology, North-Holland Elsevier, Amsterdam, 1993, p. 215.

C. Bubeck, Nonlinearities of conjugated polymers and dye systems" in V. Degiorgio, C. Flytzanis (Eds.), Nonlinear Optical Materials: Principles and Applications, in press.

A. Kistenmacher, T. Soczka, U. Baier, K. Ueberhofen, C. Bubeck, K. Müllen, "Polyphenothiazinobisthiazole: A novel polymer for third-order nonlinear optics", Acta Polymerica, in press.

A. Mathy, K. Ueberhofen, R. Schenk, H. Gregorius, R. Garay, K. Müllen, C. Bubeck, "Third-harmonic generation spectroscopy of poly(p-phenylenevinylene): A comparison with oligomers and scaling laws for conjugated polymers", submitted.

PPV

OPV-n

PPT

ORy-2

PT

ORy-3

PA

ORy-4

PPA
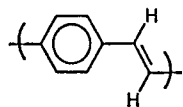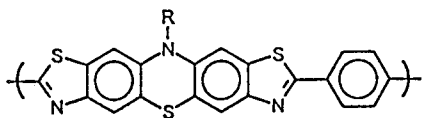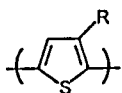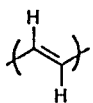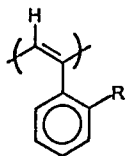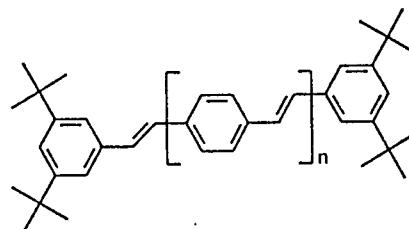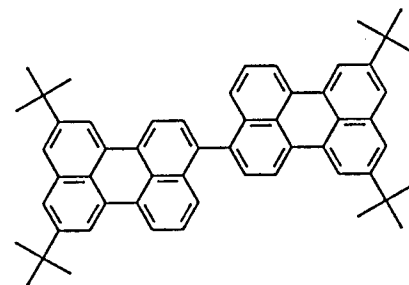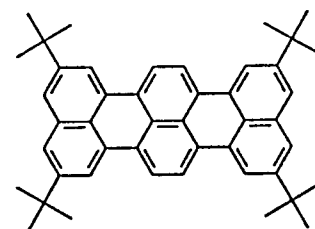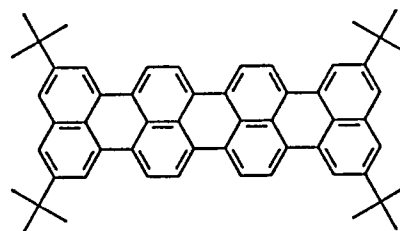
OPc
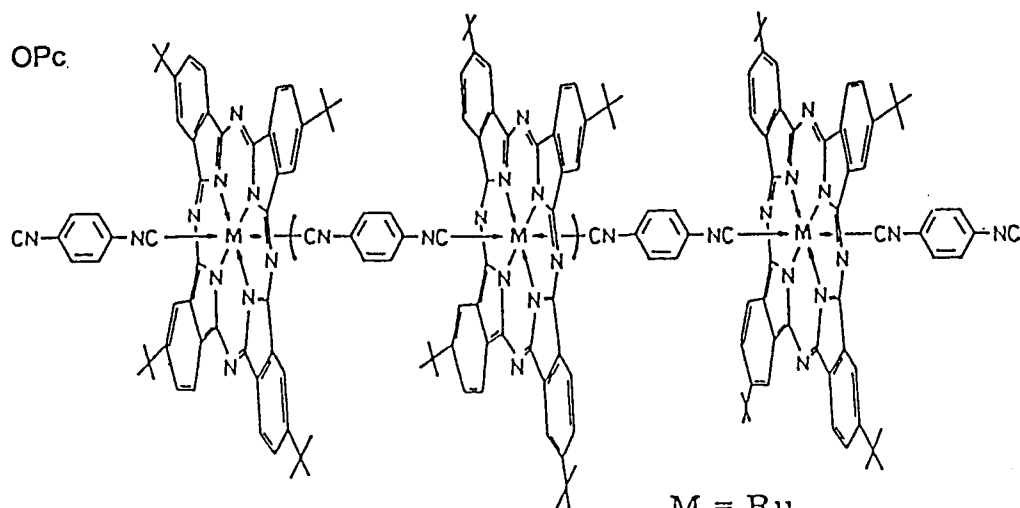
M = Ru

Fig.1:   Chemical structures and abbreviations of some conjugated polymers and oligomers. The substituents represent alkyl chains of various lengths.

23

Nonlinearities of atoms trapped in optical lattices

Gilbert Grynberg

Laboratoire Kastler-Brossel

Department de Physique de l'Ecole Normale Supérieure

24 rue Lhomond, 75231 Paris Cédex 05, FRANCE

(Tel : 33 1 44 32 34 25)

It has been recently shown that atoms can be cooled and trapped in a *three-dimensional (3D) periodic lattice of micron-sized potential wells induced by light* [1] [2].The optical potentials arise from the light-shift of the Zeeman sublevels of the ground state in the optical field created by the superposition of several light beams. To design an optical lattice in which an atom can be efficiently cooled requires first a field geometry appropriate for *Sisyplus cooling* [3] where atoms are optically pumped in the Zeeman sublevel having the lowest energy. Secondly, to obtain long trapping times in the potential wells, it is necessary for the field polarization at the sites of maximum light-shift to be *circular* [4] because the probability that an atom escapes from a well by absorbing a photon having the minority circular polarization is then considerably reduced. These two conditions can be fulfilled by several field configurations and 3D experiments were done with four [1] and six [2] beams however configurations with the minimum number of beams have the considerable advantage to be nonsensitive to the phases of the fields [1] . We present results concerning the transmission and the scattering of a probe beam in these optical lattices. We have observed stimulated Raman and Rayleigh gains as large as 70% for a $1mm^3$ lattice and the occurence of diffraction in the Bragg directions [1]. We discuss the relation between *Bragg diffraction and four-wave mixing.*

Consider a 3D lattice built with N = 4 beams of frequency ω and wavevectors k_i (or a 2D lattice built with N = 3 beams). A probe beam of tunable frequency ω_p and of wavevector k_p excites the vibration modes of an atom in a potential well when $\left|\omega - \omega_p\right| = \Omega_v$ (where Ω_v is an atomic vibration frequency). The probe experiments a stimulated Raman gain when $\omega - \omega_p = \Omega_v$ and absorption when $\omega - \omega_p = -\Omega_v$. In the more general field configuration, three vibration eigenmodes having different eigenfrequencies are observed [5].

We now discuss in which conditions Bragg scattering is observed. It is welknown from solid state text books that Bragg scattering can occur in directions forwhich

$$k_f = k_p + K$$

where $\mathbf{k}_f$ is the wavevector of the scattered photon and $\mathbf{K}$ is a vector of the reciprocal lattice. It is possible to find the reciprocal lattice from the interference pattern created by the beams that generate the optical lattice. However as shown in [1], there is a more elegant way of determining the reciprocal lattice. Condition (1), when multiplied by $\hbar$, can be interpreted as a momentum conservation condition, the change of momentum of the scattered photon being absorbed by the lattice. In the case of optical lattices, *the atoms are bound by light* which means that the change of momentum of the scattered photon should be compensated for by a *redistribution of photons* in the beams creating the lattice. Because, redistribution processes involve absorption in one lattice beam and stimulated emission in another lattice beam, the atomic momentum should change by the quantity

$$\mathbf{P} = \sum_{n=2}^{N} p_n \hbar (\mathbf{k}_1 - \mathbf{k}_n) \tag{2}$$

where the p_n are integers. In a coherent process such as Bragg scattering, the change of momentum should be $\mathbf{0}$ which implies that Bragg scattering occurs in directions such that

$$\mathbf{k}_f - \mathbf{k}_p = \sum_{n=2}^{N} p_n \hbar (\mathbf{k}_1 - \mathbf{k}_n) \tag{3}$$

The comparison with (1) shows that $(\mathbf{k}_1 - \mathbf{k}_2),...,(\mathbf{k}_1 - \mathbf{k}_n)$ are *primitive vectors for the reciprocal lattice*. The simplest Bragg scattering corresponds to the condition $\mathbf{k}_f - \mathbf{k}_p = \mathbf{k}_1 - \mathbf{k}_2$ which is very much like a *phase-matching condition* for a four-wave mixing process.

Figure 1-a shows an experimental observation of the light intensity scattered in the Bragg direction versus $\omega_p - \omega$. The experiment was made in 2D lattice filled with *cesium atoms* and the beam geometry is shown in Fig 1-b. A resonant enhancement of the Bragg scattering is observed for $\omega_p - \omega = \pm\Omega_v$ and $\omega_p - \omega = 0$ (Rayleigh resonance). In this experiment, the peak intensity of the diffracted beam was 2% of the incident intensity.

[1] G. Grynberg, B. Lounis, P. Verkerk, J.-Y. Courtois and C. Salomon, Phy. Rev. Lett.**70**, 2249 (1993).

[2] A. Hemmerich, C. Zimmerman and T.Hänsch, Europhys. Lett.**22**, 89 (1993).

[3] J. Dalibard and C. Cohen-Tannoudji J. Opt. Soc. Am. B**6**, 2023 (1989) ; P. J. Ungar, D.S.Weiss, E. Riis and S. Chu J. Opt. Soc. Am. B**6**, 2058 (1989)

[4] J.-Y. Courtois and G. Grynberg, Phys. Rev. A **46**, 7060 (1992).

[5] P. Verkerk, D. Meacher, A. Coates, J.-Y. Courtois, S. Guibal, B. Lounis, C. Salomon and G. Grynberg, Europhys. Lett.**26**, 171 (1994).
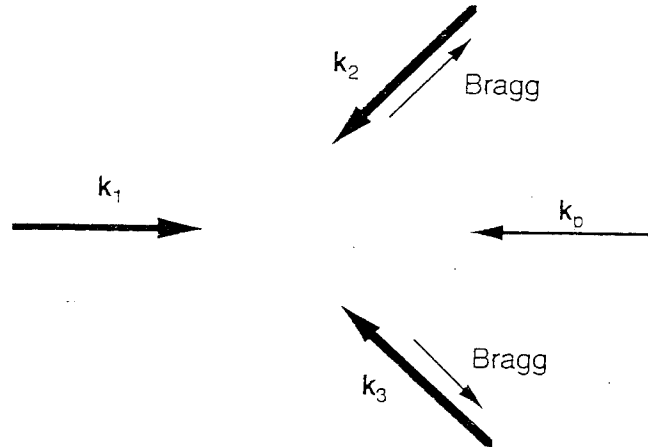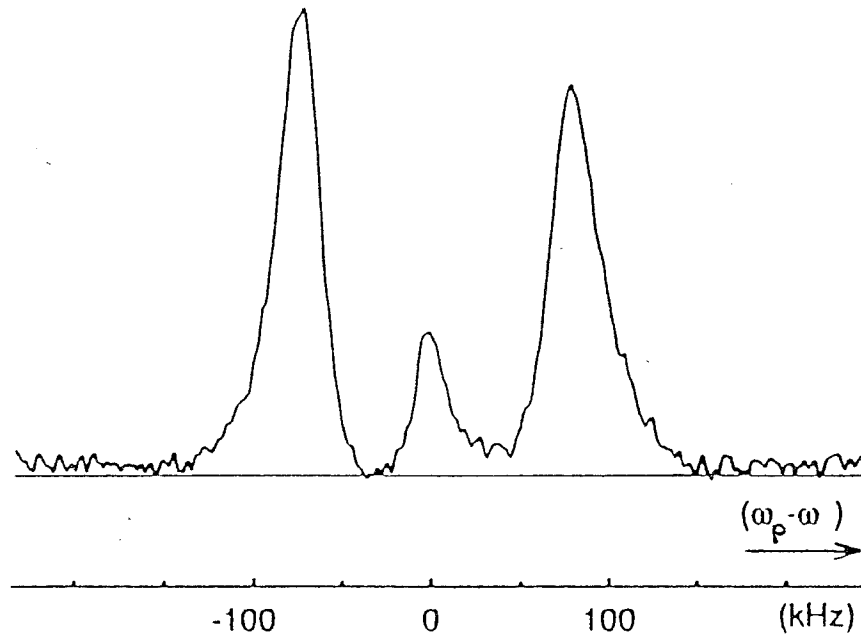
Figure 1 : (a) Intensity of the Bragg scattering versus $\omega_p - \omega$ - (b) Geometry of the incident beam. The typical power is $10mW/cm^2$ for the lattice beam and $0.1mW/cm^2$ for the probe beam.

A New Twist on Light:
Applications of the Optical Vortex Soliton

G. A. Swartzlander, Jr.
Physics Department, Worcester Polytechnic Institute
Worcester, MA 01609-2280

and

C. T. Law
Electrical and Computer Engineering Dept., Johns Hopkins University
Baltimore, Maryland 21218

Summary

An optical vortex appears as a black circular spot surrounded by bright illumination in the transverse cross-section of a light beam. Diffraction rings do not form (as occurs when a plane wave passes a circular object), rather the center of the vortex remains dark. This phenomenon is attributed to the phase of the beam, which twists like a spiral stair-case, along the optical axis. In fact, this field is a well known mode in both waveguide and scattering theory, and is given in cylindrical coordinates by $E(r, \theta, z) = A(r)\exp(\pm i\theta) \exp(i\beta z)$. As will be shown, there are simple methods of producing such linear waves.

In self-defocusing nonlinear refractive media, the refractive index is greatest where the intensity is zero, e. g., in the center of an optical vortex. Nonlinear refraction tends to draw light toward the center of the vortex, however, the phase singularity described above prevents the vortex from filling with light, owing to destructive interference . These two effects, refraction and diffraction, counter-balance one-another, resulting in an "optical vortex soliton" (OVS) [1]. In a Kerr nonlinear medium, the propagation of the scalar field is governed by the (2+1)-D nonlinear Schrodinger equation. This ubiquitous equation also describes superfluid and superconductor phenomena, where stationary vortex phenomena where first discovered [4]. Since 1989 when Coullet, Gil, and Rocca proposed the spontaneous formation of vortices within laser resonators [5], the laser dynamics community has seen an explosion of research on vortices. Before long, single-pass propagation of vortices in nonlinear refractive media was also considered. Several groups, apparently working independently and applying different schools of thought, discovered the OVS phenomenon in the early 1990's. The investigations of Chiao, Deutsch, Garrison and Wright [6] where based on photonic analogies of superfluids. Snyder, Poladian and Mitchell [2] argued that all modes of linear waveguides should have a corresponding "soliton" in some nonlinear medium (quotes are used here because such modes are not necessarily stable [7].) Our work [1] was motivated by a hydrodynamic analogy of the decay of dark soliton stripes under long-period modulations, an effect known as the Kelvin-Helmholtz instability [8]. Using superfluid analogies, McDonald, Syed and Firth described the equations of motion of an

OVS [3]. We will describe application opportunities afforded by the dynamics of single and multiple OVS's.

A single OVS induces a graded optical "fiber" within a bulk nonlinear medium. Although the phase profile prevents the beam from illuminating the dark core, a second weaker (probe) beam with a planar profile may certainly be coupled into the induced waveguide. The guiding properties are determined by the wavelength of the probe beam, the index change induced by the pump, and the size and grade of the waveguide. For a Kerr nonlinear medium, the induced waveguide is characterized by the index profile $\Delta n(1-\tanh(x/w))$, where $\Delta n = n_2 I_0$ is the peak index change, n_2 is the nonlinear refractive coefficient, I_0 is the background intensity of the "pump" beam, and $1/w \approx k\Delta n^{1/2}$.

The OVS corresponds to the second order waveguide mode at cut-off [2]; thus, a band of wavelengths may propagate as single modes. Several application opportunities may be immediately envisioned once we realize that the OVS is actually a variable fiber whose guiding properties may be modulated with light. For example, a cw guided probe beam may be modulated by a pulsed pump beam. Another means of optical control would entail using a powerful (rather than weak) probe beam that tends to erase the induced waveguide; optical bistability may be expected in this case. Perhaps the most intriguing configuration comes from modulating the refractive index locally, e. g., in a region of the waveguide channel -- this may be achieved using a third beam focused on the channel or using electro- or acousto- optical means. Such a three-port device (pump, probe and modulator beam) would function as the optical analog of a field-effect transistor. A schematic of the configuration is shown in Fig. 1. Investigations are underway to determine whether gain can be attained.

The dynamics of two vortices afford opportunities to achieve optical logic operations. When two similar vortices are produced within a single beam, they tend to rotate around one another. Because this motion depends on the presence of both vortices, all-optical logic operations (AND, OR, XOR) are possible by placing detectors in the beam path. Although this process is inherently linear, nonlinear optics may be used to enhance the resolution of the phenomenon. Under linear propagation, the vortex core size expands (owing to diffraction), and will overlap neighboring vortices. Because the rate of revolution of two vortices depends on the square of the separation distance, to minimize the device length it is necessary to have closely spaced vortices that do not diffract, i. e., vortex solitons.

Any distribution of vortices may be positioned with a single laser beam. For example, stationary arrays or ''crystals'' are possible, as well as random distributions that appear turbulent [3]. Between these two extremes is a domain where the vortices are dynamic and well-behaved. This affords opportunities to produce configurable optical interconnections, using OVS's as the waveguides that snake through space to reach a predetermined destination. The underlying physics of all these devices will be described, along with recent experimental and numerical findings.

References

1. G. A. Swartzlander, Jr. and C. T. Law, "Optical vortex-solitons observed in Kerr nonlinear media," Phys. Rev. Lett., **69**, 2503 (1992); G. A. Swartzlander, Jr. and C. T. Law, "The optical vortex soliton," Optics and Photonics News **4**, 10 (1993).

2. A. W. Snyder, L. Poladian, and D. J. Mitchell, "Stable black self-guided beams of circular symmetry in a bulk Kerr medium," Opt. Lett. **17**, 789 (1992).

3. G. S. McDonald, K. S. Syed, and W. J. Firth "Optical vortices in beam propagation through a self-defocussing medium," Opt. Commun. **94**, 469 (1992).

4. L. P. Pitaevskii, "Vortex lines in an imperfect Bose gas," Zh. Eksp. Teor. Fiz. **40**, 646 (1961) [Sov. Phys. JETP **13**, 451 (1961)].

5. P. Coullet, L. Gil, and F. Rocca "Optical Vortices," Opt. Commun. **73**, 403 (1989).

6. R. Y. Chiao, I. H. Deutsch, J. C. Garrison and E. M. Wright, "Serge Akhmanov: a Memorial Volume," H. Walther, ed. (Adam Hilger, Bristol, 1992).

7. C. T. Law and G. A. Swartzlander, Jr., "Polarized optical vortex solitons: Instabilities and dynamics in Kerr nonlinear media," to appear in Chaos, Solitons and Fractals.

8. C. T. Law and G. A. Swartzlander, Jr., "Optical vortex solitons and the stability of dark soliton stripes," Opt. Lett. **18**, 586 (1993); E. A. Kuznetsov and S. K. Turitsyn, "Instability and collapse of solitons in media with defocusing nonlinearity," Zh. Eksp. Teor. Fiz. **94**, 119 (1988) [Sov. Phys. JETP **67**, 1583 (1988)].
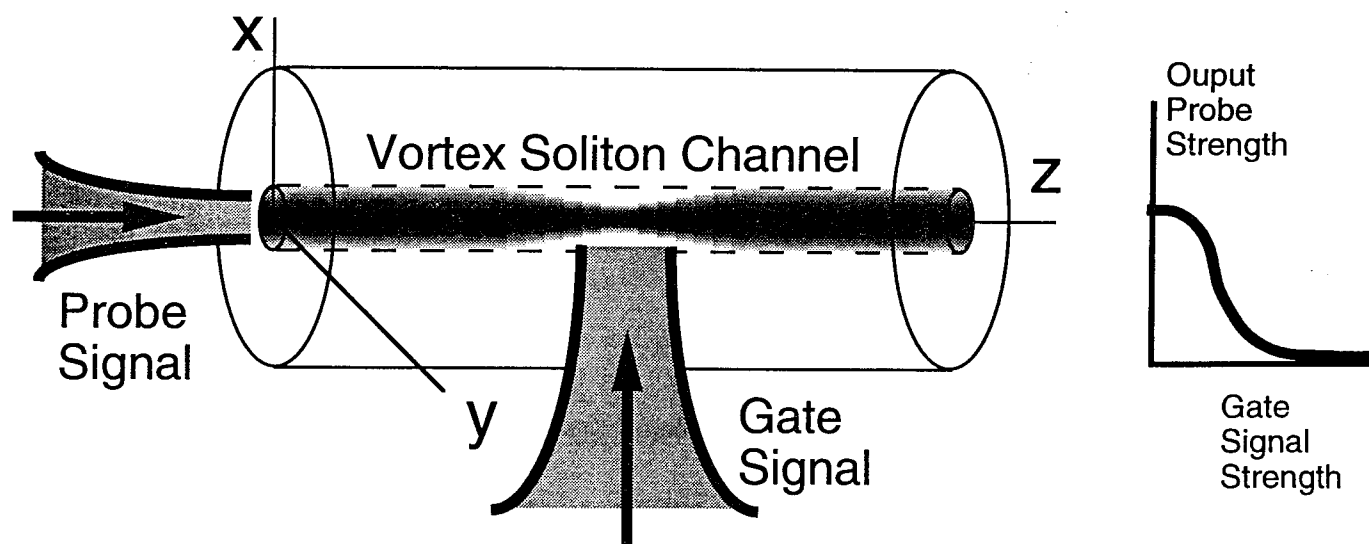
Figure 1. Optical analog of a field-effect transistor. A pump beam (large cylinder) induces an optical vortex soliton which forms a graded-index waveguide channel. A probe beam is coupled into the channel and may be detected at the output of the device. A gate signal perturbs the index profile of the waveguide, causing the probe to decouple from the guide, resulting in a decreased output probe strength.

MB4   Chaos, Period-Doubling and Reverse Bifurcations in an Optically Injected
Semiconductor Laser

V. Kovanis (a), A. Gavrielides (a), T. B. Simpson (b), J. M. Liu (c), and P. M. Alsing (a).
(a) Nonlinear Optics Center, Phillips Laboratory, 3350 Aberdeen Avenue SE, Kirtland AFB, NM 87117-5776,
(b) JAYCOR P.O. Box 85154, San Diego CA 92186-5154,
(c) Department of EE, UCLA, Los Angeles, CA, 90024-159410.

Nonlinear dynamics in optical systems is the subject of considerable current research [1]. An isolated, dc-biased semiconductor laser is sufficiently described by only two rate equations: one for the photon density and another for the carrier density [2]. Consequently, this system cannot exhibit chaotic behavior. In order to induce chaos in such a system, a third degree of freedom is needed. It was predicted that external optical injection can lead to chaos through the period-doubling mechanism [3], and we have recently confirmed that prediction [4].

In this work, we present evidence that the region of chaotic dynamics is bounded as a function of the injection level, and that the laser diode follows a period-doubling route to chaos as the injection level is varied from both above and below the chaotic region. The reverse bifurcation process from chaotic to periodic dynamics with increasing optical injection has not, to the best of our knowledge, been previously reported in laser diodes. Further, we show that dynamic parameters which describe the coupling between the free carriers, gain medium, and oscillating field are strongly modified by the injected field.

To describe the nonlinear optical interaction in a laser diode subject to strong optical injection we employ the single-mode rate-equation model which couples the complex oscillating field with the carrier density [5–7]. In order to perform numerical simulations using the coupled-equation model, we use a set of three real equations in a form which shows explicitly the dependence on specific laser parameters which can be experimentally determined in the weak injection limit [4]:

$$\frac{da}{dt} = \frac{1}{2}\left[\frac{\gamma_c\gamma_n}{\gamma_s\tilde{J}}\tilde{n} - \gamma_p(2a + a^2)\right](1 + a)$$
$$+ \eta a_i \cos\phi + F'/|A_o|, \quad (1)$$

$$\frac{d\phi}{dt} = -\frac{b}{2}\left[\frac{\gamma_c\gamma_n}{\gamma_s\tilde{J}}\tilde{n} - \gamma_p(2a + a^2)\right]$$
$$- \frac{\eta a_i \sin\phi - F''/|A_o|}{1 + a}, \quad (2)$$

$$\frac{d\tilde{n}}{dt} = -\gamma_s\tilde{n} - \gamma_n(1 + a)^2\tilde{n} - \gamma_s\tilde{J}(2a + a^2)$$
$$+ \frac{\gamma_s\gamma_p}{\gamma_c}\tilde{J}(2a + a^2)(1 + a)^2. \quad (3)$$

Here, $a = (|A| - |A_0|)/|A_0|$ and $a_i = |A_i|/|A_0|$, where $|A|$ is the amplitude of the slave laser oscillating field, $|A_0|$ is the free-running, steady-state field amplitude and

$|A_i|$ is the amplitude of the injection field. ϕ is the phase difference between A and A_i. $\tilde{n} = (N - N_0)/N_0$, where N is the carrier density and N_0 is the steady-state carrier density of the free-running laser. b is the linewidth enhancement factor and γ_c, γ_n, γ_p, and γ_s are the photon decay rate, stimulated emission rate, gain saturation rate, and spontaneous carrier decay rate, respectively [6,8]. $\tilde{J} = (J/ed - \gamma_s N_0)/\gamma_s N_0$, where J/ed is the carrier density injection rate. F' and F'' are Langevin source terms for spontaneous emission noise injected into the laser mode [2,7]. All input parameters required to numerically solve the set of coupled differential equations for a, ϕ and $\tilde{n}$ can be determined experimentally [6,8].
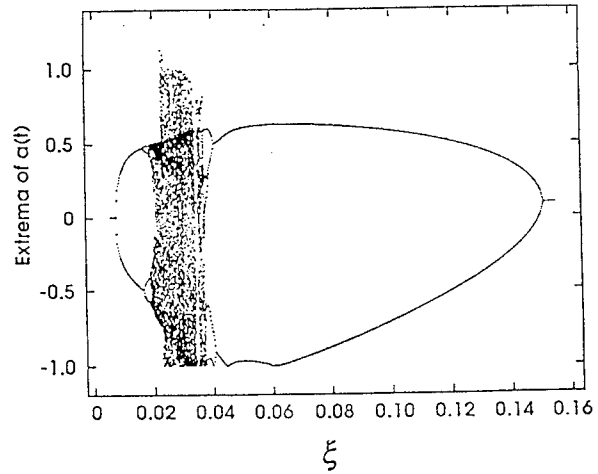
Figure 1. Numerically obtained bifurcation diagram of the extrema of the normalized optical field amplitude, $a(t)$, versus the normalized injection level, ξ. Injection is at the free-running frequency of the slave laser.

The lasers used in our investigation were nearly single-mode GaAs/AlGaAs quantum well lasers operating at 827.6 nm. They have a Fabry-Perot cavity of 500 μm in length, with both sides naturally cleaved. Both the master and slave lasers were temperature and current

stabilized. The frequency of the master laser was tuned to the free-running frequency of the slave laser to within 100 MHz. The output of the master laser was injected directly into the slave laser with careful alignment to have good coupling into the laser mode. Isolators were used to make sure that no light was injected into the master laser. The optical spectrum of the output of the slave laser was monitored with a Newport SR-240C scanning Fabry-Perot which has a free spectral range of 2 THz and a finesse of greater than 50000.

Figure 1 depicts the numerically obtained bifurcation diagram of the values of the extrema of the electric field amplitude versus the injection parameter $\xi = (\eta A_i)/(\gamma_c A_0)$. The normalized injected power is proportional to ξ^2. As the injection level is increased, the laser follows a period-doubling bifurcation route to chaos and then a similar, but reversed, bifurcation route out of the chaotic region.

The coupled equations are numerically integrated, and the resulting time series are Fourier transformed, for various injection levels using noise and dynamic parameters of the laser independently determined by the four-wave mixing experiment [7,8]. Two sets of calculated optical spectra were obtained at injection levels similar to the corresponding experimental spectra shown in Fig. 2(a) and 2(b). The spectra in Figs. 2(c) and 2(d) include a spontaneous emission noise source. The positions of the computed peaks appear at the same frequencies as the corresponding experimental peaks. The relative strength of the computed peaks is consistent with the experimentally obtained spectra when noise is present, though there is some discrepancy in the details of the different peaks. The generation of the period-doubling features happens at approximately the same injection level as experimentally observed.
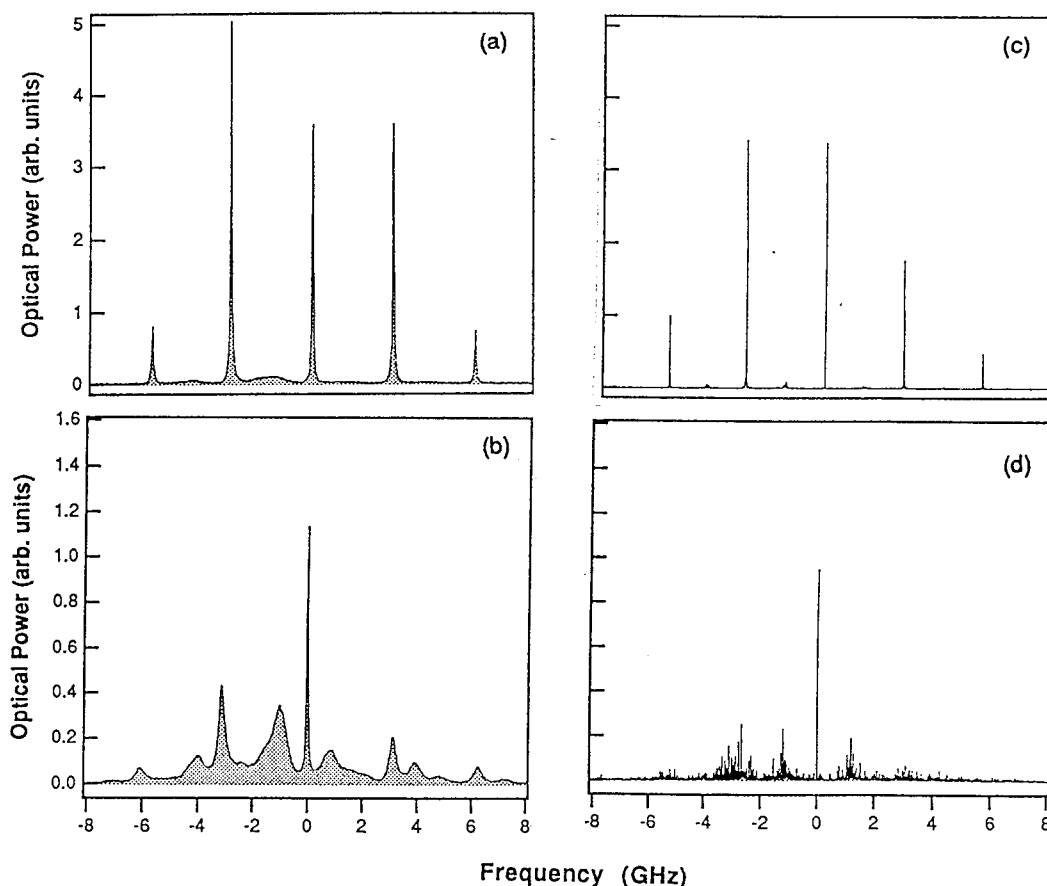
Figure 2. Optical spectra of a semiconductor laser under optical injection at two levels in a period-doubling into chaos. (a), and (b) are experimentally measured spectra and (c), and (d) are calculated spectra with noise sources present. The parameters used in this calculation were experimentally determined using the four-wave mixing techique.

In Figure 3 we observe that the relaxation oscillation frequency changes as the injected field is increased in the strong injection regime. Figure 3 compares the experimentally measured oscillation frequencies with the frequencies derived by a linear stability analysis of the coupled equation model. Over the range where the relaxation frequency more than doubles, the average optical

power circulating within the diode cavity and the average carrier density have changed by only a few persent. The good agreement between the observed experimental data and the coupled equation model shows that the fixed parameters on which it is based, the gain of the laser diode, tha cavityu and the spontaneous carrier relaxation rates, and tha linewidth enhanhancement factor, are not strongly influenced by the optical injection. However, the dynamics response of the diode is clearly modified.

It was also found that minor changes in the linewidth enhancement factor can induce large changes in the calculated bifurcation diagram and optical spectra. The numerical results discussed above were obtained with a linewidth enhancement factor of $b = 3.47$, which is well within the range of uncertainty of the value determined by the four-wave mixing experiment [6,8]. We have found that the laser would not develop into a chaotic state if $b \lesssim 3.1$. Even with noise, there is a major qualitative defference between the spectra of a diode which has only undergone period doubling and one that has entered a chaotic region.

dicates that the high frequency dynamics of the system is not dominated by the presence of the side modes for these experimental conditions.

In conclusion, we have observed a reverse bifurcation from chaotic to periodic dynamics in a semiconductor laser subject to strong optical injection at its free-running frequency. Spontaneous emission noise effects obscure specific spectral features in the reverse period-doubling region, but by measuring the dynamic parameters of the laser we have shown that the coupled complex-field and carrier density model accounts for the observed spectra. We have also observed that that key dynamic prameters describing the photon-carrier coupling in the coupled complex-field and carrier density model are strongly modified by the injecting field as predicted by a linearized analysis of the coupled differential equations.

[1] See, for example, **Nonlinear Dynamics in Optical Systems Technical Digest, 1992** (Optical Society of America, Washington, D.C., 1992) vol. 16.
[2] See, for example, G. P. Agrawal and N. K. Dutta, **Long-Wavelength Semiconductor Lasers**, (Van Nostrand Reinhold, New York, 1986) Chap. 6.
[3] J. Sacher, D.Baums, P. Panknin, W. Elsässer, and E. O. Göbel, Phys. Rev. A. **45**, 1893 (1992).
[4] T.B. Simpson, J.M. Liu, A. Gavrielides, V. Kovanis, and P.M. Alsing, submitted to Appl. Phys. Lett.
[5] T. B. Simpson and J. M. Liu, J. Appl. Phys. **73**, 2587 (1993).
[6] J. M. Liu and T. B. Simpson, "Four wave mixing and Optical Modulation in a Semiconductor Laser" to appear in IEEE J. Quantum Electron.
[7] T. B. Simpson and J. M. Liu, submitted to Phys. Rev. Lett.
[8] J. M. Liu and T. B. Simpson, IEEE Photonics Technol. Lett. **4**, 380 (1993).

Figure 3. Calculated and experimentally measured resonance osillation frequencies as a function of the normalized amplitude of the injection field.

In the theoretical results discussed above, the effect of side modes was not included. The single-mode model used here cannot, of course, account for the partition of power to the side modes and further work is needed to quantify the effect of the side modes. The good agreement between the spectra calculated from the single-mode model with noise and the experimental data in-

Quasi-phasematched optical frequency conversion in LiNbO3 waveguides

M. L. Bortz

E. L. Ginzton Laboratory

Stanford University

Stanford, California 94305

Quasi-phasematched optical frequency conversion in ferroelectric waveguides has evolved in the past several years from the initial laboratory demonstration into a nearly commercial technology. Advances in periodic poling of ferroelectric materials for quasi-phasematching(QPM), characterization of waveguide fabrication processes for modal confinement, and high power single longitudinal and transverse mode laser diodes have resulted in the demonstration of cw single pass QPM-SHG conversion efficiencies exceeding 10 %.[1] These same advances have resulted in the demonstration of other second order nonlinear optical interactions, including the generation of 2-3 μm radiation through QPM difference frequency mixing and QPM optical parametric oscillation near 1.5 μm. This presentation will review quasi-phasematched optical frequency conversion in LiNbO3 waveguides and discuss several different waveguide frequency conversion devices.

The motivation for developing waveguide frequency conversion devices stems from the 10^2-10^3 fold efficiency enhancements over bulk interactions due to modal confinement. For example, the theoretical, single pass, birefringently phasematched SHG efficiency in a LiNbO3 waveguide can exceed 100 %/W-cm^2; for a 1 cm long interaction length, 100 mW of fundamental radiation would generate 10 mW of second harmonic radiation. This enhancement was known for a long time, but devices suffered from problems arising from the use of birefringent phasematching. A technique to circumvent birefringent phasematching was invented by Bloembergen in 1962,[2] but but not implemented until recently. Termed quasi-phasematching, this approach involves a periodic modulation of the nonlinear susceptibility of the material, resulting in a periodic modulation of the nonlinear polarization. A spatial harmonic of the nonlinear polarization may be chosen to match that of the freely propagating field, resulting in a signal that grows quadratically with distance, similar to conventional phasematching. Periodic modulation of the sign of the nonlinear coefficient yields the highest conversion efficiency and can be achieved in LiNbO3 through ferroelectric domain inversion. QPM has emerged as the most versatile method to achieve phasematching. The real utility of QPM is that any interaction may be phasematched at room temperature, and the fields may be polarized in the same direction to allow use of the large d_{33} nonlinear coefficient in LiNbO3. Theoretical waveguide QPM-SHG efficiencies can exceed 2000 %/W-cm^2. Reference 3 contains a detailed analysis of QPM.

There are several important issues in the design of waveguide frequency conversion devices. Devices are usually formed by fabricating a ferroelectric domain inversion grating for QPM, followed by channel waveguide fabrication. While the QPM grating period can readily be controlled, a priori knowledge of the dispersion in the phase velocities of the waveguide modes at each wavelength may be unavailable, making prediction of the phasematching wavelength difficult. The efficiency of a waveguide interaction is given by the cross-sectional spatial overlap integral between the waveguide modes, the relevant Fourier component of the ferroelectric domain grating used for quasi-phasematching, and the nonlinear coefficient in the waveguide. There are several techniques based on periodic dopant diffusion near the Curie temperature that result in ferroelectric domain inversion in LiNbO3. These methods generally yield domain gratings that have depths about 1/3 of the period, with a duty cycle that varies with depth. The overlap between the domain grating and the waveguide modes couples the two separate material processing steps and complicates device design.

The widest range of devices, and the highest normalized conversion efficiency devices for blue light generation, have been obtained in LiNbO3 using titanium diffusion for periodic ferroelectric domain inversion[4] and the annealed proton exchange (APE) technique for waveguide fabrication. Development of models for the linear[5] and nonlinear[6] optical properties of APE-LiNbO3 waveguides combined with studies of the domain grating for different processing conditions have allowed us to fabricate and optimize a variety of frequency conversion devices. Figure 1

shows the theoretical waveguide modes, the Fourier coefficient of the domain grating used for QPM, and the nonlinear coefficient vs. depth for a SHG device with the second harmonic in either the TM_{00} and TM_{01} transverse mode. Evaluation of the spatial overlap integrals are very helpful in designing devices with optimized efficiencies, and knowledge of the effective mode indices is useful for accurate prediction of the phasematching wavelength. For example, we recently demonstrated a QPM-SHG device that doubled 976 nm radiation with an efficiency exceeding 200 %/W, the highest values to date for waveguide QPM-SHG.[7]
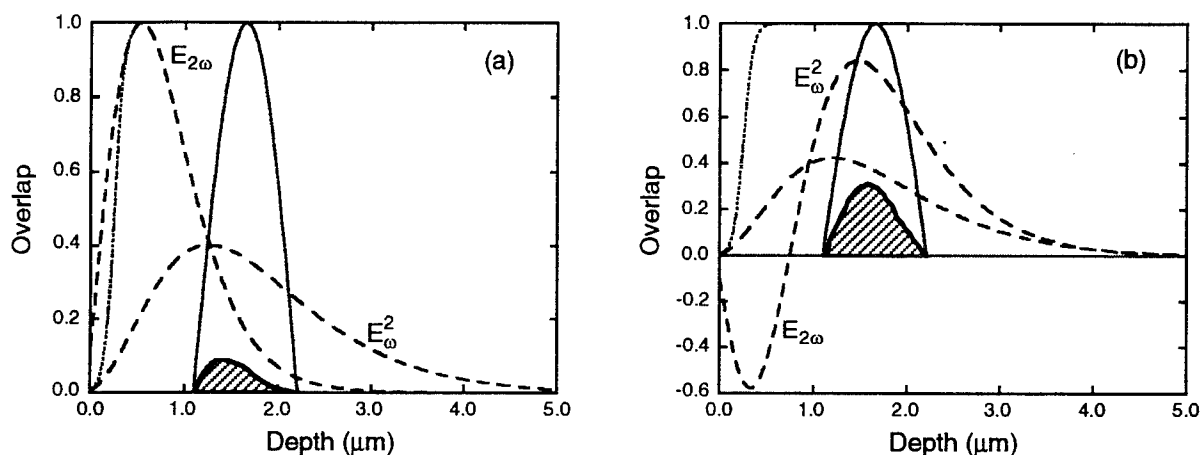
Figure 1. Waveguide modes (dashed lines), Fourier coefficient of the domain grating (solid lines), the nonlinear coefficient (dotted lines), and product of these terms (hatched area) vs. depth for a QPM-SHG device with the second harmonic in either the a) TM_{00} and b) TM_{01} transverse mode.

Quasi-phasematching offers new opportunities for controlling the tuning characteristics of nonlinear optical interactions. The wavelength or temperature tuning curve is determined by the square of the magnitude of the Fourier transform of the axial distribution of the nonlinear coefficient; QPM with a uniform grating shifts the $sinc^2$ tuning curve away from $\Delta k = 0$ but doesn't alter its shape. Perturbations in the period, duty cycle, or phase of an ideal QPM grating can be used to engineer a desired phasematching response. Since shortening the length of a uniform grating results in a linear increase in bandwidth but a quadratic reduction in peak efficiency, a useful tuning curve is one that yields a better trade-off between bandwidth and peak efficiency. We recently demonstrated a QPM-SHG device with a linear trade-off by imposing aperiodic phase reversals on an otherwise ideal QPM grating.[8] Figure 2 shows the experimental and theoretical results for a SHG device using uniform and phase-reversed QPM gratings. The aperiodic phase reversal sequence used was based on a 13-bit Barker code. The bandwidth of this interaction was increased by an order of magnitude over the uniform interaction, with an accompanying linear efficiency reduction.

Quasi-phasematched waveguide frequency conversion is not limited to SHG; several different types of parametric interactions have recently been demonstrated in $LiNbO_3$ waveguides. We demonstrated difference frequency generation (DFG) of near IR diode laser wavelengths to generate 2.1 μm[9] and 2.6-3.1 μm[10] radiation, the longest wavelengths generated to date in $LiNbO_3$ waveguides. Idler powers of about 5 μW were measured, suitable for spectroscopic investigations of molecular species. We also demonstrated nearly degenerate DFG at 1.5 μm for potential application as an all-optical channel shifter, an important device in wavelength division multiplexed communication systems.[11] Wavelength conversion from a 1.564 μm signal to a 1.559 μm idler with an insertion loss due to the frequency conversion process of -17.8 dB was achieved, the best to date using $\chi^{(2)}$ for this application. With bandwidths exceeding 100 nm, these devices may be useful for broadband wavelength conversion. The waveguide and domain inversion models accurately predicted the performance of these parametric devices. Optimization similar to that performed for SHG devices indicate that idler powers exceeding 1 mW at 3.0 μm and wavelength conversion with a -3 dB loss at 1.5 μm should be possible with $\approx$ 100 mW laser diode pump sources.

The 1.5 μm parametric devices described above also served as the first step towards the demonstration of QPM-optical parametric amplification and QPM-optical parametric oscillation (OPO).[12] We measured a parametric

gain of $e^{0.96}$ = 2.6 with 5.5 W of peak pump power exiting the 1 cm long waveguide, corresponding to an efficiency of 21 %/W. A symmetric OPO cavity was formed by affixing thin mirrors to the waveguide endfaces with a fluorinert liquid. The mirrors had a 90 % reflectivity band extending from 1.4-1.7 μm. At 1.55 μm, the independently measured waveguide propagation losses 9 %/cm and the roundtrip OPO cavity losses were 35 %. The measured cavity loss and observed parametric gain yield a predicted singly resonant oscillator (SRO) threshold about 2.4 W. We observed parametric oscillation with peak pump powers exceeding 4.5 W coupled into the wavguide. Figure 3 shows the tuning data for this device for several nm of pump wavelength tuning. This interaction in LiNbO$_3$ waveguides could prove useful for generating rapidly tunable radiation over hundreds of nm between 1.2 - 1.8 μm using a near-IR laser diode. Overlap integral calculations indicate that a factor of 4 increase in the parametric gain can be achieved by optimized Ti-diffusion and APE-waveguide fabrication receipes. Along with a factor of 2 reduction in the waveguide propagation losses and optimized output coupling, singly resonant QPM-OPO thresholds below 100 mW should be possible in LiNbO$_3$ waveguides, suggesting cw diode pumping.

We have demonstrated a variety of quasi-phasematched frequency conversion devices in LiNbO$_3$ waveguides. Development of models describing the material fabrication processes used for domain inversion and waveguide fabrication allow rapid device demonstration and optimization. More sophisticated quasi-phasematched optical frequency conversion devices will probably be demonstrated in the near future.
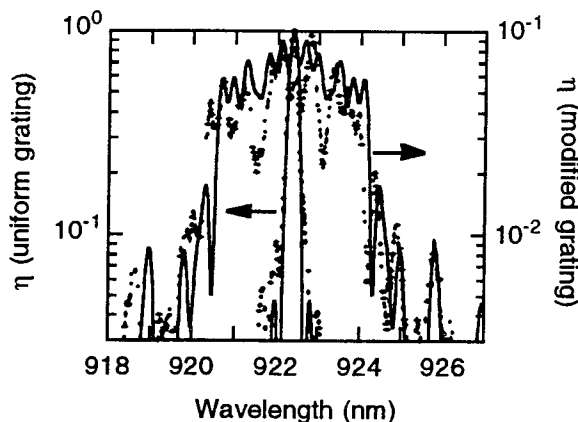
Figure 2. Theoretical and experimental SHG tuning curves from waveguides with uniform and phase reversed gratings.
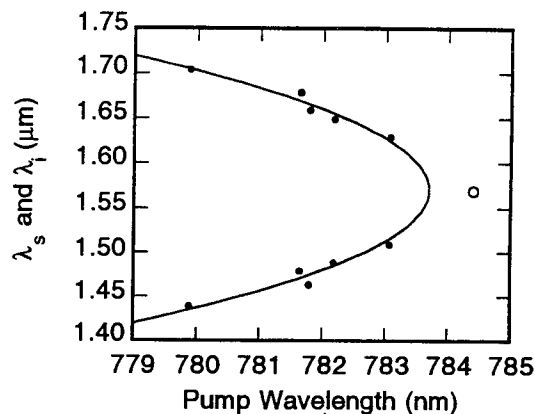
Figure 3. Signal (λ_s) and idler (λ_i) wavelength vs. pump wavelength for a LiNbO$_3$ waveguide OPO. The line is a parabolic fit to the data.

1   K. Yamamoto, K. Mizuuchi, Y. Kitaoka, and M. Kato, Appl. Phys. Lett., 62, 2599 (1993).
2   J. A. Armstrong, N. Bloembergen, J. Ducuing, and P. S. Pershan, Phys. Rev., 127, 1918 (1962).
3   M. M. Fejer, G. A. Magel, D. H. Jundt, and R. L. Byer, IEEE J. Quantum. Electron., 28, 2631 (1992).
4   E. J. Lim, M. M. Fejer, R. L. Byer, and W. J. Kozlovsky, Electron. Lett., 25, 731 (1989).
5   M. L. Bortz and M. M. Fejer, Opt. Lett., 6, 1844 (1991).
6   M. L. Bortz, L. A. Eyres, and M. M. Fejer, Appl. Phys. Lett., 61, 2263 (1993).
7   M. L. Bortz, S. J. Field, M. M. Fejer, D. W. Nam, R. G. Waarts, and D. F. Welch, To be published in IEEE J. Quantum. Electron.
8   M. L. Bortz, M. Fujimura, and M. M. Fejer, Electron. Lett., 30, 34 (1994).
9   E. J. Lim, H. M. Hertz, M. L. Bortz, and M. M. Fejer, Appl. Phys. Lett., 59, 2207 (1991).
10 S. Sanders, D. W. Nam, R. J. Lang, M. L. Bortz, M.M. Fejer, Conference on Lasers and Electro-Optics, 1994, paper CThD4.
11 M. L. Bortz, D. Serkland, and M. M. Fejer, Conference on Lasers and Electro-Optics, 1994, paper CThD6.
12 M. L. Bortz, M. A. Arbore, and M. M. Fejer, Conference on Lasers and Electro-Optics, 1994, paper CPD13.

Second-Order Cascaded Nonlinearity in Lithium Niobate Channel Waveguides

R. Schiek, D.Y. Kim, M.L. Sundheimer, G.I. Stegeman
CREOL, University of Central Florida, 12424 Research Parkway
Orlando, FL 32826, USA

The large nonlinear phase shifts produced by the cascaded second-order $\chi^{(2)} : \chi^{(2)}$ nonlinearity [1] make this process interesting for fast all-optical data processing. Due to the well-known advantages of waveguiding for nonlinear optics, cascading is most efficiently implemented in optical waveguide structures. In fact the first observations of cascading in waveguides by spectral broadening [2] and interferometric intensity-dependent phase shift measurements [3] have been reported. Here we describe a systematic interferometric investigation of the influence of the wavevector-mismatch on cascading. Titanium indiffused $LiNbO_3$ waveguides are used because their superiour optical quality and the detailed knowledge of their fabrication and characterization make them promising candidates for the first application of cascading in all-optical data processing.

We investigated several $47mm$ long channel waveguides with propagation along the X-axis of a Y-cut crystal. They were produced by indiffusion of $43nm$ thick Ti-stripes of different widths varying between $4\mu m$ and $25\mu m$ at a temperature of $1060°C$ during a time of 9 hours. The resulting waveguides have relatively large effective areas ($20 \sim 125\mu m^2$) and small core index enhancements ($0.001 \sim 0.004$) yielding low loss waveguides ($0.03 \sim 0.4dB/cm$). The waveguides are characterized by measuring the number of guided modes and their intensity profiles at the Nd:YAG-wavelength $\lambda = 1.32\mu m$ and the second harmonic $\lambda = 0.66\mu m$. Theoretical modelling is based on graded index profiles which are dependent on wavelength and polarization and which are determined by the indiffused Ti-concentration profile [4]. The agreement between the experimental and the theoretical waveguide characterization guarantees that the theory is comprehensive enough to be an essential tool for adjusting and optimizing the conditions for cascading.

SHG is phase-matched in the channels by coupling fundamental TM-modes with a wavelength of $\lambda = 1.32\mu m$ to second harmonic TE-modes. The following results were obtained with a single mode waveguide at the fundamental resulting from indiffusion of a Ti-stripe with $10\mu m$ width. The temperature-dependent Sellmeier equations yield a predicted phase-matching temperature of $T_{PM} = 359.42°C$ for optimizing the coupling between the fundamental TM_{00} and the second harmonic TE_{00} mode. In order to tune the wavevector-

mismatch around phase-matching the crystal is placed in an oven with temperature controlled to a stability of $30 mK$. The measured spectrum of the SHG shows maximum conversion at a temperature of $339.9°C$. An overestimate of the birefringence, predicted by the Sellmeier Equations used, explains the discrepancy of $19.5K$. The serious asymmetry in the spectrum is well explained by the nonuniform temperature profile in the oven. A flat profile in the center of the oven provides phase-matching only over a distance of $\approx 20mm$ in the waveguide center. The temperature falls toward the edges of the oven. Taking into account the resulting change of the wavevector-mismatch along the waveguide, we calculate a spectrum in good agreement to the observed spectrum. The calculated spectrum in Fig. 1 is corrected for the T_{PM} discrepancy. The increased bandwith of the measured resonances indicate that the temperature profile which has been used in the calculations yields an overestimate of the effective phase-matching length.
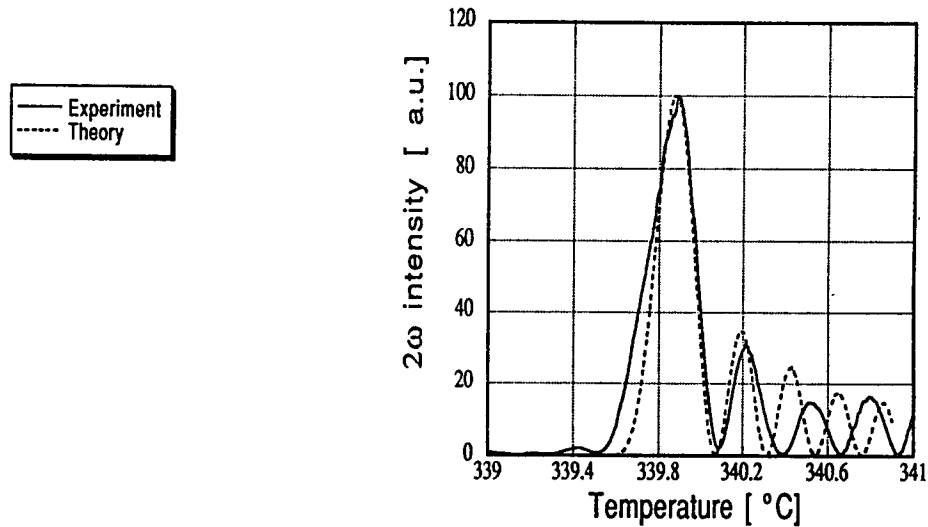
Figure 1: Temperature dependence of second harmonic generation

With the interferometer described in detail elsewhere [5], we observed intensity-dependent phase shifts of the fundamental with opposite sign on either side of the phase-matching temperature (see Fig. 2). Again, we find an asymmetry in the results around the phase-matching temperature. It is worth noting that this is not a drawback! In fact such a variable wavevector-mismatch can be a great advantage: an appropriate wavevector-mismatch distribution can be used to tailor and optimize the effective nonlinearity for bandwidth and throughput. In our example the cascading is improved by having larger phase-shifts at lower temperatures where damping of the fundamental due to conversion to the second harmonic is minimized.

The observed nonlinear phase shifts and the good agreement between measurement and simulation confirms the usefulness of the $LiNbO_3$ material system and that the model can

be used to design devices for a first demonstation of all-optical data processing based on cascading.

We thank Dr. W. Sohler from the University-GH-Paderborn for providing the $Ti : LiNbO_3$-waveguides and the crystal oven.
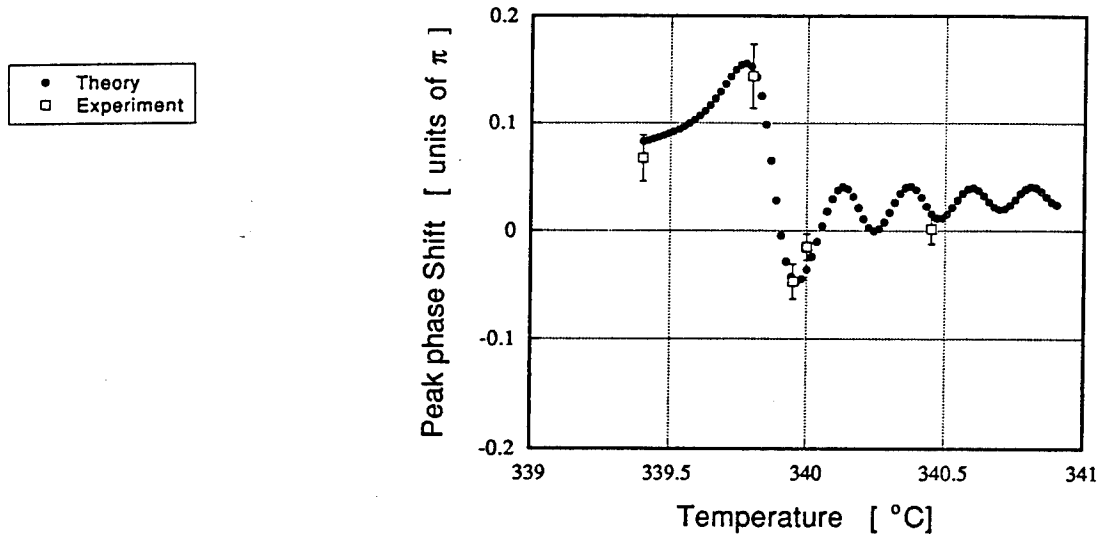
Figure 2: Nonlinear phase shift (Fundamental peak power: $P_{peak} = 10W$, SHG-efficiency: $E_{peak} = 40\%$)

References

[1] G.I. Stegeman, M. Sheik-Bahae, E. Van Stryland, G. Assanto: Opt. Lett., Vol. 18, p. 13 (1993).

[2] M.L. Sundheimer, C. Bosshard, E. Van Stryland, G.I. Stegeman: Opt. Lett., Vol. 18, p. 1397 (1993).

[3] D.Y. Kim, W.E. Torruellas, J. Kang, C. Bosshard, G.I. Stegeman, P. Vidakovic, J. Zyss, W.E. Moerner, R. Twieg, G. Bjorklund: Opt. Lett., submitted.

[4] E. Strake, G.P. Bava, I. Montrosset: J. Lightwave Technology, Vol. 6, p.1126 (1988).

[5] K.B. Rochford, R. Zanoni, G.I. Stegeman, W. Krug, E. Miao, M.W. Beranek: IEEE J. Quant. Electron., Vol. 28, p. 2044 (1992).

Application of injection-locked high power diode laser arrays as pump source for efficient green or blue Nd:YAB lasers and cw KTP optical parametric oscillators

R. Knappe, J. Bartschke, C. Becher, B. Beier, M. Scheidt, K.-J. Boller
and R. Wallenstein

Universität Kaiserslautern
Fachbereich Physik
67653 Kaiserslautern, Germany

Injection-locking of high power diode laser arrays[1] is a powerful means to improve the spectral and spatial quality of high power diode lasers. In our experiments the 45mW output of a single stripe diode laser (SDL 5422) was focussed, for example, into a 20 stripe 1W diode laser array (Siemens 480401). The substantial improvement in beam quality is shown in Fig. 1. The injection-locked array emits about 80% of the 800mW output power of the free running array in a nearly diffraction limited beam. While, free running, the diode laser array is highly multi-mode with a spectral width of 2-3nm, the injection-locked radiation is single-mode with a spectral width of less than 20MHz. Injection-locking thus improved the spatial power density by a factor of 50 and the spectral power density by 5 to 6 orders of magnitude.
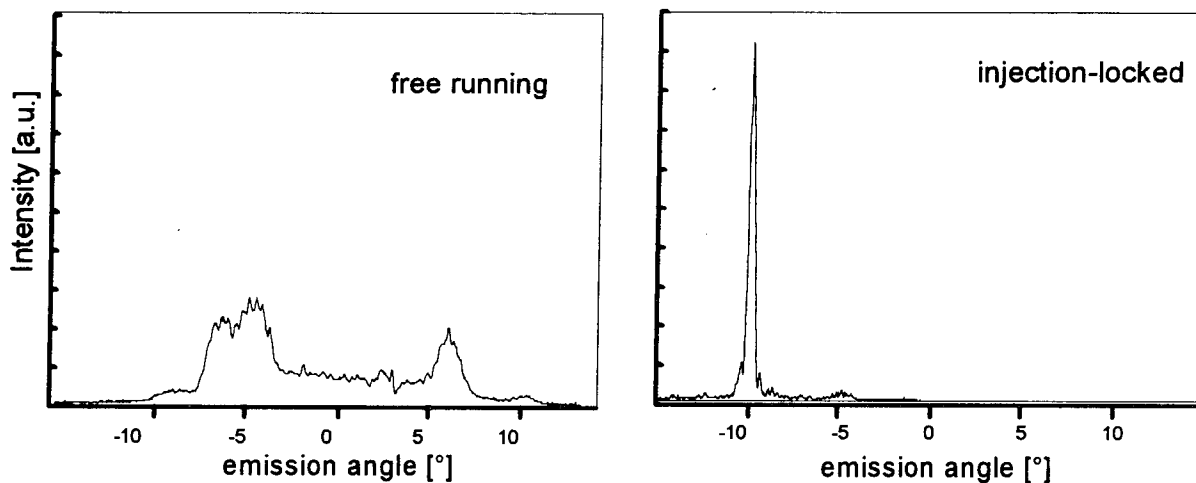
Fig. 1: Far field of a 20-stripe diode laser A: without injection-locking and B: with injection-locking.

Injection-locked diode laser arrays are of advantage for many applications, like nonlinear frequency conversation [2], or pumping of solid state lasers with small mode volumes.

An example of such laser is the self frequency doubling Nd:YAB laser [3]. For optimum efficiency, the TEM_{00} beam waist should be about $25\mu m$. For TEM_{00}-mode operation, the pumped crystal volume should not exceed the volume of the laser mode.

The importance of a small pump focus is seen from Fig. 2.A. The efficiency increases considerably with smaller emitter size of the pump laser. Best results are expected for TEM_{00} pump radiation. Fig.2.B shows the output of a Nd:YAB laser, endpumped by an injection-locked diode laser array, vs pump power. With 500mW at 807nm the power of the 531nm output is close to 50mW. For comparision, the same Nd:YAB laser was pumped with a TEM_{00} mode Ti:Sapphire laser. As seen in Fig. 2.B, the output is identical to the one measured with the injection-locked array.
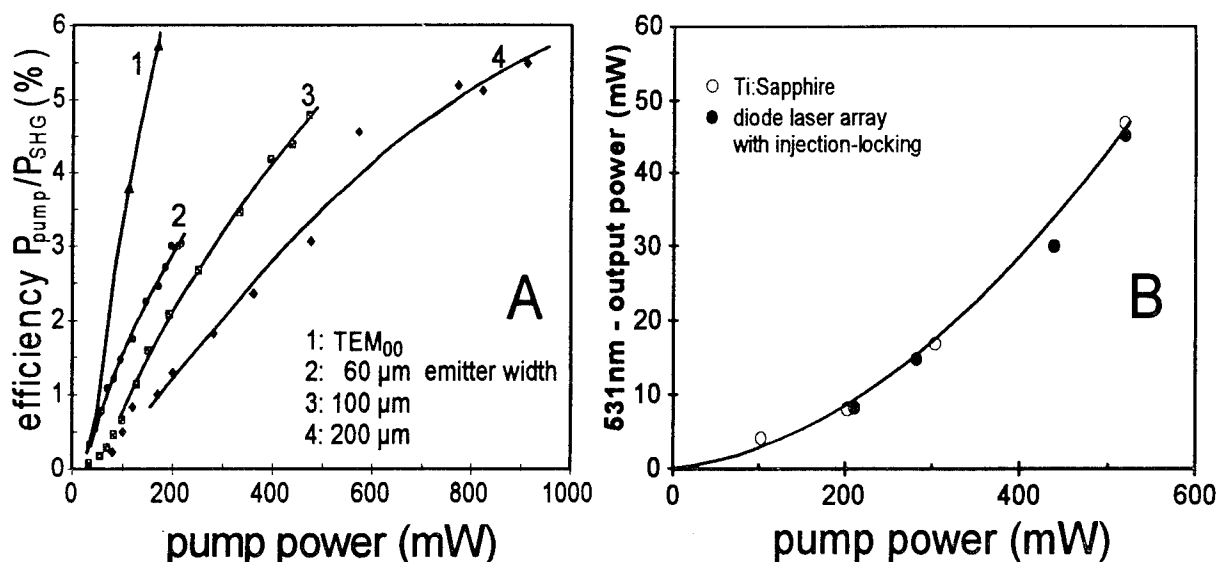
Fig. 2: A: Efficiency of self frequency doubling Nd:YAB lasers pumped by diode laser arrays with different emitter sizes or the TEM_{00} output of a Ti:Sapphire laser
B: 531nm TEM_{00} output of a Nd:YAB laser pumped by an injection-locked diode laser array (dark cirkles) or the TEM_{00} output of a Ti:Sapphire laser (open circles)

The Nd:YAB laser's visible efficiency increases with laser- and thus with pump power. With 2.2W from the Ti:Sapphire laser, the Nd:YAB laser emitted more than 450mW of single mode 531nm radiation. This corresponds to an optical (807nm to 531nm) conversion efficiency of more than 20 percent! The same efficiency and output power will be obtained with multi-Watt injection-locked diode laser arrays which are at present under investigation.

The injection-locked array radiation is also of advantage as pump source for single frequency self frequency doubling Nd:YAB microchip lasers.

With appropriate orientation the Nd:YAB crystal generates also the sumfrequency of the fundamental 1062nm laser radiation and the coherent pump light. In this way up to 6mW of blue radiation were generated in the wavelength range of 452 - 466nm. The continuous tunability is achieved by changing the wavelength of the pump light.

Blue light is also obtained by self frequency doubling in a quasi three-level Nd:YAB laser. Angle tuning of the 1.9mm long Nd:YAB crystal (cut at 34.5°) generated blue light at 454.5nm, 454.9nm and 455nm.

Besides Nd:YAB the new laser crystal Nd:LaSc$_3$(BO$_3$)$_4$ could be another efficient self frequency doubling laser material, if grown in the noncentric trigonal space group R32. So far only crystals grown in the centrosymmetric space group C2/m are available. The advantages properties of this laser material is demonstrated by a 0.22mm thick 25% Nd-doped LaSc$_3$(BO$_3$)$_4$ microchip laser which generated up to 180mW of single-frequency radiation if pumped by 450mW of injection-locked diode laser radiation[4].

Besides for laser pumping injection-locked diode laser arrays should be compact pump sources for cw optical parametric oscillators. For this purpose we investigate the cw operation of a tunable noncritically phasematched KTP-OPO with a 12mm long KTP-crystal (XY-cut) placed in a linear cavity, resonant either for the signal- and idler wave or the signal- and pump radiation. The OPO is pumped at present by a cw single-mode Ti:Sapphire laser. Because of the tunability of this pump source (710 - 980nm) signal- and idler waves are tunable in the range of 1.05 - 1.3μm and 2.2 - 3.1μm respectively. The collinear pumping maintains the required perfect alignment.

In first experiments, the doubly resonant OPOs were operated at pump wavelengths of 715 - 820nm which corresponds to 1.05 - 1.17μm and 2.25 - 2.75μm of the signal- and idler radiation. Although the losses in the OPO cavity are not yet minimized, the threshold was as low as 150mW. With a pump power of 2W the total output power exceeded 80mW.

A detailed characterization of this OPO system and its spectral properties will be presented, including investigations which use the radiation of an injection-locked 1W, 764nm diode laser array as pump source.

References

1. L.Y. Pang, E.S. Kintzner and J.G. Fujimoto, Opt. Lett. **15**, 728 (1990) and ref. therein
2. M.K. Chun, L. Goldberg and J.F. Weller, Appl. Phys. Lett. **53**, 1170 (1988)
3. I. Schütz, I. Freitag and R. Wallenstein, Opt. Commun. **27**, 221 (1990) and ref. therein
4. B. Beier, J.-P. Meyn, R. Knappe, K.-J. Boller, G. Huber and R. Wallenstein, Appl. Phys. B (in press)

Single-mode optical parametric oscillator system of BBO and KNbO₃ tunable from the visible (0.42μm) to the infrared (4μm)

Single-mode optical parametric oscillator system of BBO and $KNbO_3$ tunable
from the visible (0.42μm) to the infrared (4μm)

A. Fix, R. Urschel, G. Goeritz, D. Wildt, A. Borsutzky, and R. Wallenstein

Fachbereich Physik
Universität Kaiserslautern
67663 Kaiserslautern, Germany

As has been demonstrated in previous investigations[1,2] Nd:YAG laser-pumped optical parametric oscillators (OPO) of beta-barium borate (BBO) are powerful all-solid-state sources of coherent radiation with a large tuning range (300-3000nm), high internal conversion efficiency (60-70%), and high output energies (100-200mJ). Narrowband operation was achieved by injection seeding with low power monochromatic radiation[3].

In the present OPO-system the seed radiation is generated by a BBO-OPO with a wide mode spacing (of about 1cm⁻¹). This OPO - with a 2.5-mm-long BBO crystal in a 3.6-mm-long flat-flat mirror resonator - is pumped by an injection seeded frequency tripled Q-switched Nd:YAG laser. Despite the short crystal the OPO efficiency exceeds 25% at a 355nm pump pulse energy of 30mJ (3 times above threshold).
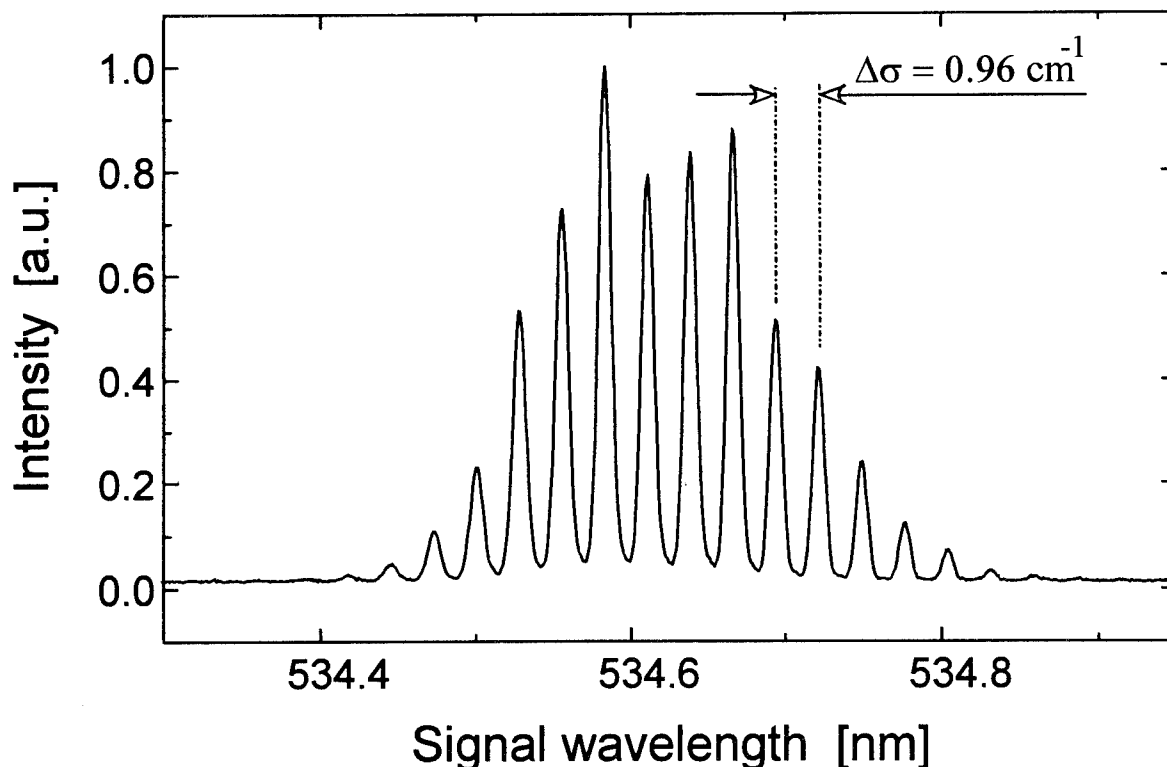
Fig.1 Averaged mode spectrum of the short-cavity BBO-OPO oscillator.

The OPO signal wave mode spectrum is shown in Fig. 1 recorded with a 1m spectrometer and a 1728-element photodiode-array providing a spectral resolution of $0.25cm^{-1}$. The width of the spectral mode distribution is determined by the gain bandwidth. The pulse-to-pulse energy of the individual OPO modes varies considerably. The pulse energy distribution in an individual mode is close to an exponential function. The mode energy cross correlation coefficient for different modes indicates that mode coupling is almost negligible.

Because of the wide mode spacing a single mode is easily separated by a spectral filter like a Fabry-Perot (FSR $25cm^{-1}$, Finesse > 30). The width of the mode transmitted by the Fabry-Perot is less than $0.03cm^{-1}$. The wavelength is tuned by synchronous piezoelectric tuning of the length of the OPO cavity and of the mode-selecting Fabry-Perot.

The radiation of the selected single mode (with pulse powers of 10-100μJ) is used to seed a 355-nm-pumped high power BBO-OPO (consisting of a flat-flat mirror cavity and a 12-mm-long BBO crystal). With a pump power of 70mJ the energy of the single-mode output (Fig. 2) exceeds 10mJ.
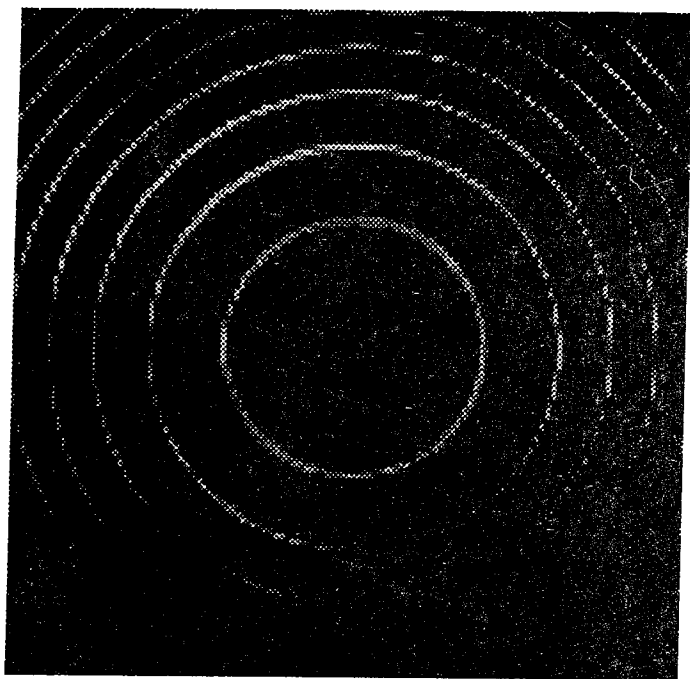
Fig. 2 Fabry-Perot ring pattern of the seeded single-mode BBO-OPO (FSR $25cm^{-1}$, Finesse < 30).

For BBO the infrared transparency limit restricts high power OPO operation to wavelengths shorter than 2.3μm. For the generation of infrared radiation at longer wavelengths the OPO crystals of choice are KTP or $KNbO_3$ (KNB). While transparency range and damage threshold of these crystals are similar, the effective nonlinear coefficient of KNB is about three times as high as the one of KTP.

In our investigations a KNB-OPO was pumped by pulsed 1.06μm Nd:YAG radiation. The OPO consisted of a 7.8-mm-long crystal (type I, $\theta = 41°$, $\Phi = 0°$) placed in a 12-mm-long flat-flat mirror cavity resonant for the signal wave. The energy density at threshold was about $0.48Jcm^{-2}$ and $0.58Jcm^{-2}$ for 1% and 10% output coupling, respectively. These thresholds are about 3 times higher than expected from theory[4]. This may indicate that the value of the effective nonlinearity quoted in the literature is too large.

The OPO wavelengths measured and calculated[5] as function of the phase-matching angle are shown in Fig. 3. As seen in this figure signal and idler wave are tunable in the range of 1.45-2.01μm and 2.27-4.0μm, respectively, using two sets of mirrors. With appropriate mirrors the tuning range could be extended to 1.4 - 4.5μm.
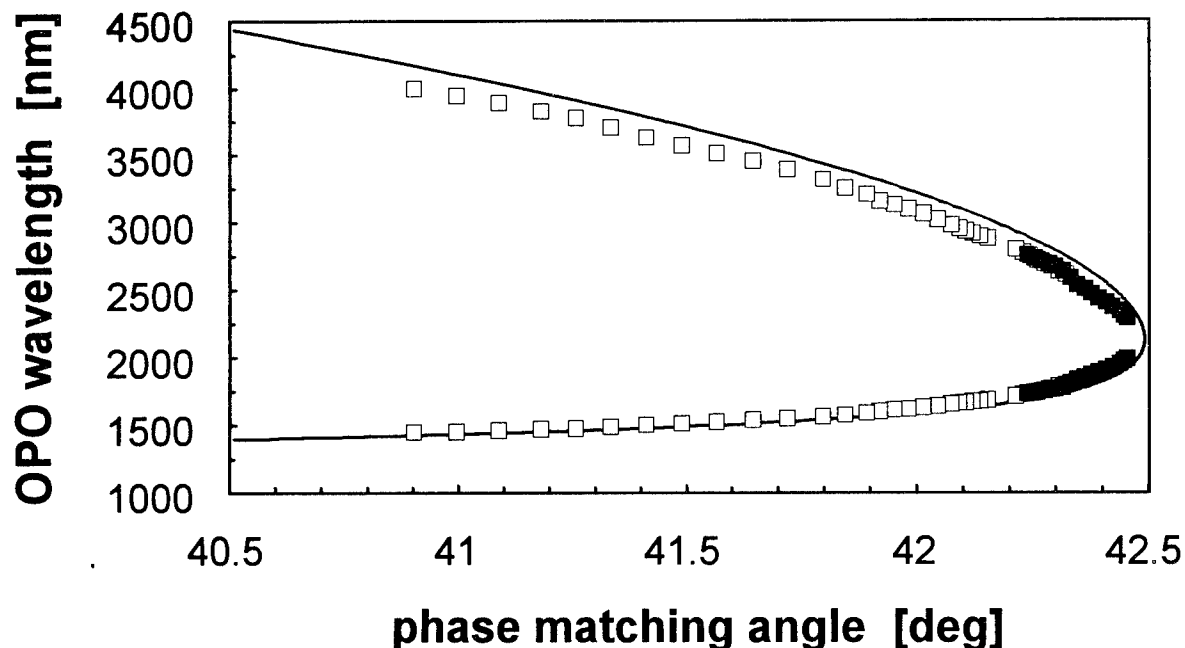
Fig. 3   Measured and calculated wavelengths of the signal and idler radiation of the 1.064-μm-pumped KNB-OPO.

At pump energies of two times above threshold (82mJ in a pump beam with 3mm in diameter) and a 10% output coupler the OPO efficiency is about 14%. This corresponds to pulse energies exceeding 5mJ at both the signal and idler wavelength. The OPO bandwidth increases with the signal wavelength from less than 5nm at λ_s < 1.7μm to 15-30nm at λ_s > 1.8μm. Narrowband single-mode operation was achieved by injection seeding with infrared idler radiation of the single-mode BBO-OPO. In this way the KNB-OPO is a powerful source of tunable narrowband infrared radiation.

References

1.   A. Fix, T. Schröder, and R. Wallenstein, Laser Optoelectron. **23**, 106 (1991) and references therein.
2.   C.L. Tang, W.R. Bosenberg, T. Ukachi, R.J. Lane, and L.K. Cheng, Proc. IEEE **80**, 365 (1992).
3.   J.G. Haub, M.J. Johnson, B.J. Orr, R. Wallenstein, Appl. Phys. Lett. **58**, 1718 (1991) and references therein.
4.   S.J. Brosnan, R.L. Byer, IEEE J. QE-**15**, 415 (1979).
5.   B. Zysset, I. Biaggio, P. Günter, J. Opt. Soc. Am. B **9**, 380 (1992).

Second-Harmonic Controlled All-Optical Modulation by Cascading

D.J. Hagan, M. Sheik-Bahae, Z. Wang, G. Stegeman
W. E. Toruellas and E.W. Van Stryland

Center for Research and Education in Optics and Lasers
(CREOL)
University of Central Florida
Orlando, FL 32816

G. Assanto
Department of Electronic Engineering, III University of Rome
Via Eudossiana 18, 00184 Rome, Italy

One of the key features of electronics is that the complex amplitude, including phase, can be preserved, modulated, amplified and recovered electronically during signal processing. Since the first work on optical bistability, the nonlinear optics community has been trying to develop such transistor operations for optical beams by using an intensity-dependent refractive index.[1] This has placed emphasis on using intensity as a control variable, omitting the opportunity for utilizing the optical phase. A totally different approach is to use second-order nonlinear processes such as second-harmonic generation (SHG) or parametric generation. These interactions are **coherent**, therefore, both amplitude *and* phase of the fundamental and second harmonic (when the SHG process is seeded) determine the output signal. As an initial step, nonlinear phase shifts (both + and -) in the fundamental beam have been recently demonstrated by using the Z-scan in bulk SHG-active media[2] and by self-phase modulation[3] in quasi-phasematched waveguide media, all in agreement with theoretical predictions. Figure 1 shows the phase shift as a function of detuning from phase match for a crystal of $KNbO_3$. This cascaded second-order nonlinearity provides an alternative to conventional nonlinear refractive (n_2) materials for all-optical switching application, and it circumvents the problems of obtaining large n_2 combined with low loss as there is no irreversible loss in the $\chi^{(2)}$ process, i.e., the interaction can be terminated when all the light has been reconverted to the fundamental by proper choice of crystal length. These phase shifts depend on the phase mismatch Δk so that by controlling Δk, we may 'tune' the nonlinearity to a desired application. For example, a positive Δk results in a negative phase shift and vice-versa.[2] Physically, these phase shifts do not result from induced changes in refractive index, but arise from energy exchange, and subsequent propagation at different phase velocities, between the fundamental (ω) and second-harmonic (2ω) waves. If there is no input at the second harmonic and $\Delta k=0$, energy is always transferred from ω to 2ω. It is well known that for $\Delta k \neq 0$, the direction of energy transfer is reversed upon propagating a distance of one coherence length (ℓ_c) and the energy is completely converted back to the fundamental after a disance $2\ell_c$. Due to the phase mismatch, the phase of the downconverted light is shifted with respect to the original (unconverted) wave and hence the fundamental experiences an irradiance dependent phase shift. Because the process of nonlinear phase shifting involves upconversion followed by downconversion, it is referred to as a 'cascaded $\chi^{(2)}:\chi^{(2)}$ process'. It has been shown theoretically that such nonlinear phase shifts may be applied to nonlinear Mach-Zehnder and directional coupler switching devices.[4] Furthermore, numerical studies show that if a weak SHG beam is also input, both the amplitude and phase of the fundamental output can be controlled with the phase and/or amplitude of the seed,[5] leading to new applications to switching devices, including small signal gain and transistor action[6,7]
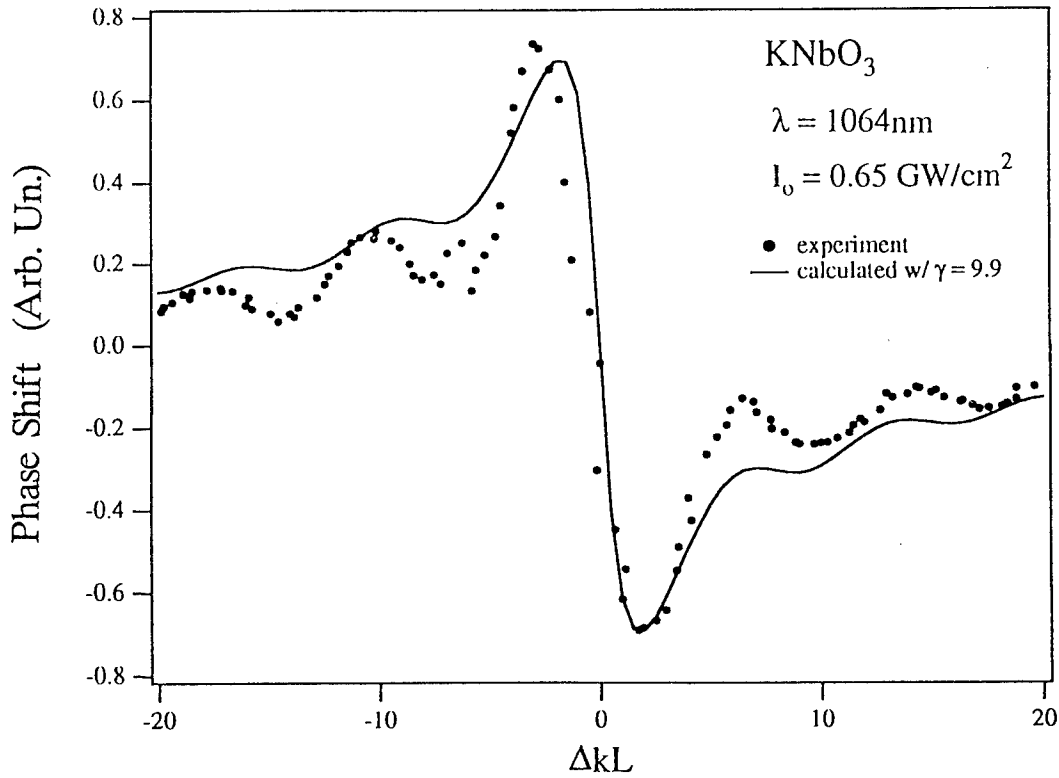
Figure 1. Phase shift versus phase mismatch, ΔkL, in a 0.5 cm thick sample of $KNbO_3$ along with theory.

Here, we consider this arrangement where the coherence of the second-order interaction is utilized. We introduce an input second-harmonic wave which has a well defined phase with respect to the fundamental, $\Delta\phi$, at the input . We refer to this second-harmonic input as the 'seed' or control pulse. We show that under certain conditions, even a very weak seed can strongly modulate the transmitted fundamental irradiance. For $\Delta k=0$, the phase of the emerging second harmonic is $\pi/2$ with respect to the fundamental. Hence the application of a weak seed with $\Delta\phi=\pi/2$ will have minimal effect on the output of the system. However if $\Delta\phi$ is 0 or π, the irradiances of the transmitted waves may be strongly modulated. Hence, either phase or amplitude modulation (PM or AM) of the seed results in a strong amplitude modulation of the fundamental. The AM-AM transfer with gain between the two frequencies is analagous to transistor action (although the control beam is at a different frequency). For $\Delta k \neq 0$, we find that the differential gain may be larger than for $\Delta k=0$. Plane wave calculations show that 100% modulation may be obtained, but spatial and temporal variation of practical optical inputs results in less ideal switching characteristics.

A 1 mm thick sample of KTP, oriented for type II phasematching for SHG at $\lambda=1.06\mu m$ is used to experimentally demonstrate modulation of the fundamental by a weak seed. Using a Q-switched and modelocked, 20 ps FWHM Nd:YAG laser pulse, a thin type I phase-matched KDP crystal was used to produce the second harmonic seed. Control of $\Delta\phi$ is accomplished by passing the collinear seed and unconverted 1.06 μm pulses through a cell containing N_2 gas. By varying the pressure, we exploit the dispersion of the gas to produce a precise variation of $\Delta\phi$. The output of this cell is then weakly focused into the KTP crystal. We either monitor the energy transmittance of the pulse, or by imaging and using a small aperture, we eliminate spatial integration effects and observe the transmitted on-axis fluence of the fundamental.

In Fig. 2(a) we show the experimental variation of on-axis fluence transmittance, T_F, as a function of peak on-axis irradiance with $\Delta kL = 1.1$ radians, for cases of $\Delta\phi = 0$ and $\Delta\phi = \pi$. In this experiment, the seed fraction is continually varying since the efficiency of the seed generation process increases with laser output.
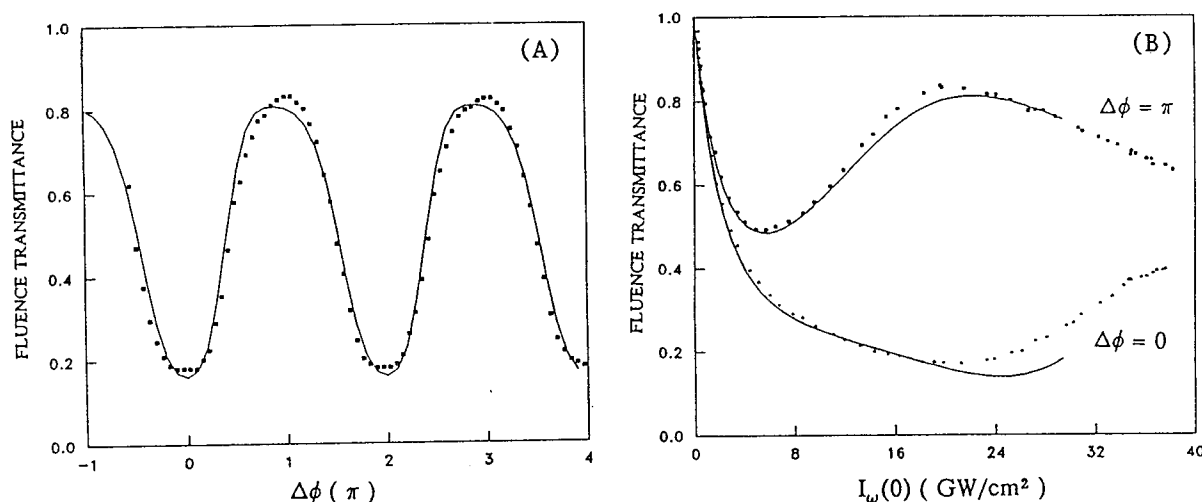
Figure 2: (a) On-axis transmitted fluence as a function of input 1.06 μm irradiance with a weak second-harmonic seed. (b) the transmitted fluence versus $\Delta\phi$ at an input irradiance of 20 GW/cm². The solid lines in (a) and (b) are theoretical calculations from the harmonic generation equations.

As seen in Fig. 2(b) the input irradiance can be chosen to give a modulation with phase (or amplitude) of up to 4:1 agreeing with the calculations obtained from the standard harmonic generation equations including temporal integration over the time varying pulse. At this irradiance the seed energy is $\simeq 1\%$ of the fundamental energy ($\simeq 2.8\%$ of the fundamental peak irradiance). Similar experiments have begun on a crystalline sample of the organic material DAN which has a d_{eff} approximately 10 times that of KTP.[8]

The results presented here give a demonstration of the potential of all-optical switching using $\chi^{(2)}$ nonlinearities. The switching irradiance scales as $[\chi^{(2)}]^{-2}$, so that new organic crystals with $\chi^{(2)}$ more than ten times that of KTP will significantly reduce switching irradiances. In addition, waveguide geometries will lead to further reductions in the switching energy.

We wish to thank W.E. Moerner, R. Tweig and G. Bjorklund for supplying the DAN crystal.

REFERENCES
[1] H. M. Gibbs, "Optical Bistability: Controlling Light by Light", (Academic, New York, 1985)
[2] R. DeSalvo, *et al.*, Opt. Lett. **17**, 28 (1992)
[3] M. Sundheimer, *et al.*, Opt. Lett. **18**, 1397 (1993)
[4] G. Assanto, *et al.*, Appl. Phys. Lett. **62**, 1323 (1993)
[5] J.A. Armstrong, *et al.*, Phys. Rev., **127**, 1918 (1962)
[6] G. Assanto, *et al.*, IEEE J. Quantum Electron, To be published.
[7] P. St. J. Russell, Electronics Letters, **29**, 1228 (1993)
[8] J.-C. Baumbert, *et al.*, Appl. Phys. Lett. **51**, 1484 (1987)

Intracavity and extracavity sum-frequency generation between pump and signal waves of an optical parametric oscillator

E. C. Cheung, Karl Koch, and Gerald T. Moore*

Nonlinear Optics Center, Phillips Laboratory
3550 Aberdeen Avenue SE, Kirtland AFB, NM 87117-5776

SUMMARY.

Sum-frequency generation (SFG) between the pump and the signal waves of an optical parametric oscillator (OPO) is a promising efficient means of generating widely wavelength-tunable radiation of shorter wavelengths [1]. Shortly after the advent of OPO's, intracavity SFG and second-harmonic generation in OPO's were investigated both theoretically and experimentally [2,3]. However, the spectral quality and the stability of their outputs were poor because the nonlinear materials and the lasers then available required the use of doubly resonant OPO's. Recently, intracavity second-harmonic generation in a Ti:sapphire-laser-pumped femtosecond, singly resonant OPO was demonstrated, yielding nearly transform-limited pulses at greater than 10% overall conversion efficiency [4]. In this paper, we report SFG between the pump and the signal waves of a singly resonant $AgGaS_2$ OPO, synchronously pumped by 100-psec pulses from a conventional CW actively mode-locked Nd:YAG laser.

We have investigated both intracavity SFG and extracavity SFG between the resonant signal beam and the residual pump beam that is not converted in the parametric generation process. For intracavity SFG, the pump beam can be incident first either on the SFG crystal or the OPO crystal. We refer to these two orderings for intracavity SFG as the SFG→OPO and the OPO→SFG configurations, respectively. It is theoretically shown in Ref. [1] that the SFG→OPO configuration is more favorable than the OPO→SFG configuration in terms of the stability of the output, the conversion efficiency over a large range of pump powers, and the power loading on the OPO crystal.

Schematic diagrams of the three configurations for SFG are shown in Fig. 1. The three experiments are based on a $AgGaS_2$ singly resonant OPO that is reported in Ref [5]. The average pump power incident on the OPO was reduced from 20 W to 625 mW by passing the pump beam through a low-duty-cycle chopper. In the experiments described in this paper, the OPO consists of a single 10-cm long $AgGaS_2$ crystal, placed at near normal incidence with respect to the pump beam. We use for SFG a single 8.5-mm long KTP crystal, cut for type-II phase matching with $\theta = 79°$ and $\phi = 0°$. The pump beam at 1.064 μm and the sum-frequency beam near 589 nm are ordinary waves, and the signal beam near 1.319 μm is extraordinary.

For extracavity SFG, we use an output coupler of 4% transmission at 1.319 μm and 93% transmission at 1.064μ. The pump and the signal beams are focused by a 10-cm focal
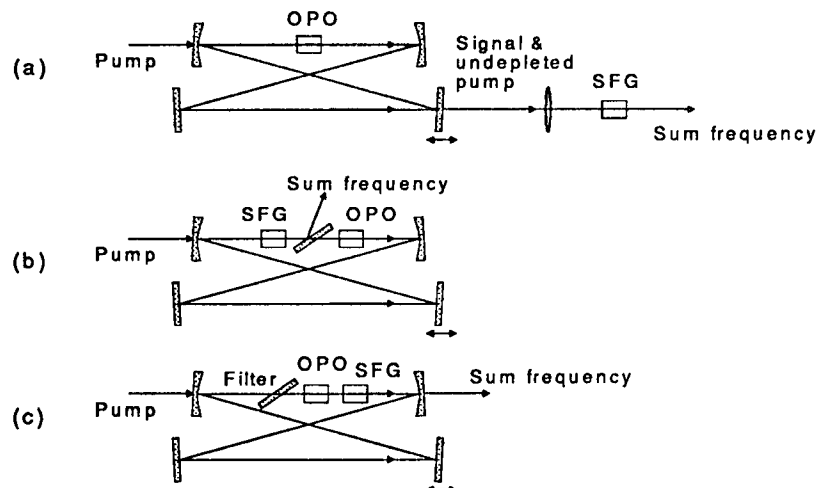
Figure 1: Schematic diagrams of experimental setups. (a) External SFG, (b) intracavity SFG→OPO configuration, and (c) intracavity OPO→SFG configuration.
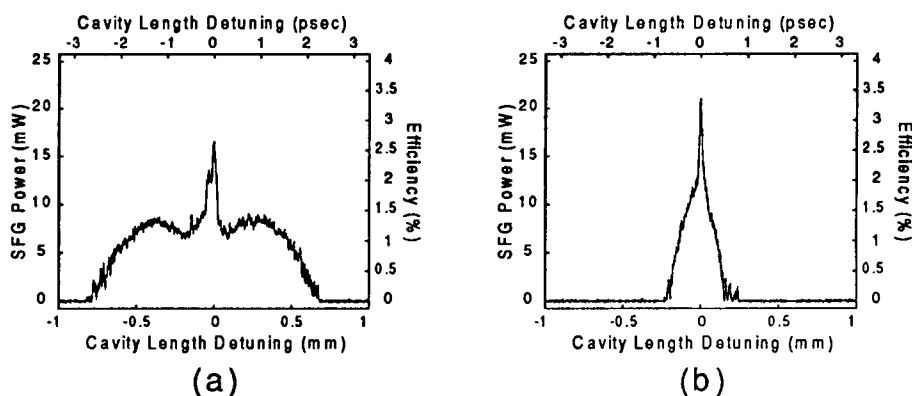
Figure 2: Cavity length detuning characteristics of extracavity SFG when the OPO cavity is aligned to maximize the power of (a) the signal from the OPO, and (b) the sum frequency.

length lens to spot sizes of approximately 44 and 55 μm, respectively, at the KTP crystal. The results are shown in Fig. 2. Figure 2(a) shows the SFG power as the round-trip length of the OPO cavity is varied while the OPO is aligned to optimize for the OPO signal output. However, the OPO aligned in this manner does not yield the maximum SFG conversion because the pump pulses are substantially depleted and the birefringence of the AgGaS$_2$ crystal causes spatial walkoff between the pump and the signal beams. Better SFG conversion efficiency can be achieved by having a better balance between the pump and the signal powers and a better spatial beam overlap between the pump and signal. By aligning the OPO cavity to maximize the SFG power rather than the OPO signal output, higher conversion efficiency is obtained as shown in Fig. 2(b).

For intracavity SFG, the output coupler is replaced by a high reflector at 1.319 μm. Because AgGaS$_2$ crystals absorb 589-nm radiation, we place a color filter (uncoated RG695 glass) in front of the AgGaS$_2$ crystal to filter out the sum-frequency radiation in the
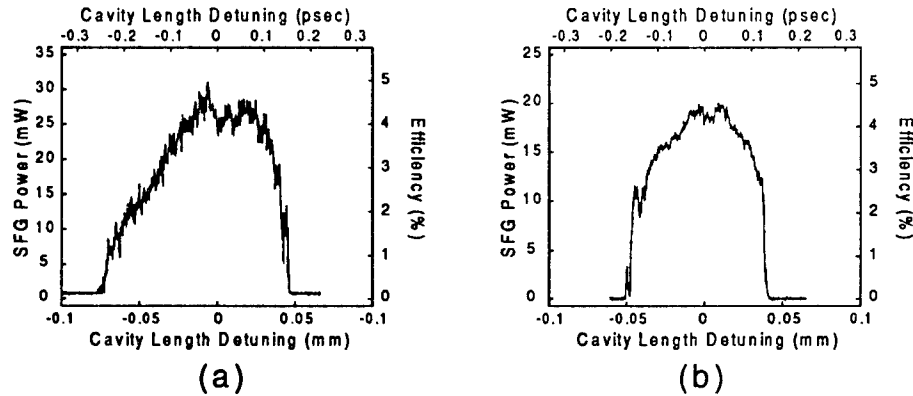
Figure 3: Cavity-length detuning characteristics of intracavity SFG with the crystals arranged in (a) the SFG→OPO configuration and (b) the OPO→SFG configuration.

SFG→OPO configuration. The color filter is placed at Brewster angle, and the measured transmissions for the signal and the pump beams are 100% and 70%, respectively. The color filter also reflects 20% of the sum-frequency radiation. To better compare the two intracavity configurations, we also place the color filter in front of the $AgGaS_2$ in the OPO→SFG configuration.

The results of the intracavity experiments are shown in Fig. 3. In both configurations, the cavity is aligned for maximum SFG power. The conversion efficiency is calculated with the incident pump power at the $AgGaS_2$ crystal and at the KTP crystal for the SFG→OPO and the OPO→SFG configurations, respectively. Overall conversion efficiencies of slightly less than 5% are achieved in both configurations. In the OPO→SFG configuration, the color filter, which was used only for the purpose of comparison, can be removed to increase the incident pump power. With the incident pump power at 625 mW in the OPO→SFG configuration, we observe conversion efficiencies as high at 10%, which corresponds to a SFG power of 62.5 mW at 589 nm.

*G. T. Moore is also at the Center for Advanced Studies, University of New Mexico, Albuquerque, NM 87131.

References.

1. Gerald T. Moore and Karl Koch, IEEE J. Quantum Electron. **29**, 2334 (1993).
2. Paul P. Bey and Chung L. Tang, IEEE J. Quantum Electron. **QE-8**, 361 (1972).
3. A. J. Campillo, IEEE J. Quantum Electron. **QE-8**, 914 (1972).
4. R. J. Ellingson and C. L. Tang, Opt. Lett. **18**, 438 (1993).
5. E. C. Cheung, Karl Koch, and Gerald T. Moore, "Silver thiogallate, singly resonant optical parametric oscillator pumped by a continuous-wave mode-locked Nd:YAG laser". Submitted to Opt. Lett.

BESSELFUNCTION MODES, SYMMETRY BREAKING AND PHASE TRANSITIONS IN DIFFRACTIVE OPTICAL PATTERN FORMATION PROCESSES

R. Macdonald and H. Danlewski
Optisches Institut Technische Universität Berlin
Strasse des 17. Juni 135, D-10623 Berlin, Germany
E-Mail: MAC0432@MOEBIUS.PHYSIK.TU-BERLIN.DE
Tel: ++49-30-314 23636 , Fax: ++49-30-314 26888

Summary

Complex transverse effects in nonlinear optics like spontaneous pattern formation and nonlinear dynamic phenomena have attracted increasing research activities during the recent years [1]. Beside being of fundamental interest, the understanding of these effects is important for many applications where optical nonlinearities shall be used with any kind of optical feedback. Nonlinear dynamics and pattern formation may inherently appear e.g. in devices like optically bistable filters [2] or lasers [3] leading to complex spatial and temporal behaviour. Pattern formation and self-organization is also discussed to be important in future applications like optical pattern recognition [4], associative memory [5], optical information storages [6] and adaptive optics [7].

In order to understand features of pattern formation processes in more complex systems, one needs to deal with simpler systems first. Recently [8, 9], a rather elementary arrangement, consisting of a thin Kerr-slice in front of a single feedback mirror was shown to exhibit diffractive spatial instabilities and spontaneous two-dimensional pattern formation using nematic liquid crystals as nonlinear optical media (Fig.1). In the present contribution it is shown that the predicted [10, 11] hexagons may only appear with plane input waves but are generally not observed in experiments with laser beams of finite diameter. It is shown that the observed patterns for axially symmetric input intensity profiles using cylindrical transverse coordinates ρ and φ can be described analytically [12] by superposition of Besselfunction spatial modes as

$$\overline{n} = \sum_m \overline{n}_m(q, t) \cos\{-m\varphi\} J_m(q\rho) \qquad \text{for } 0 \leq \rho \leq w_o \qquad (1)$$

where $\overline{n}$ is the refractive index modulation, w_o the input beam radius and J_m a Besselfunction of first kind and integer order m. Examples of observed patterns compared with modes eqn. 1 are displayed in Fig. 2.
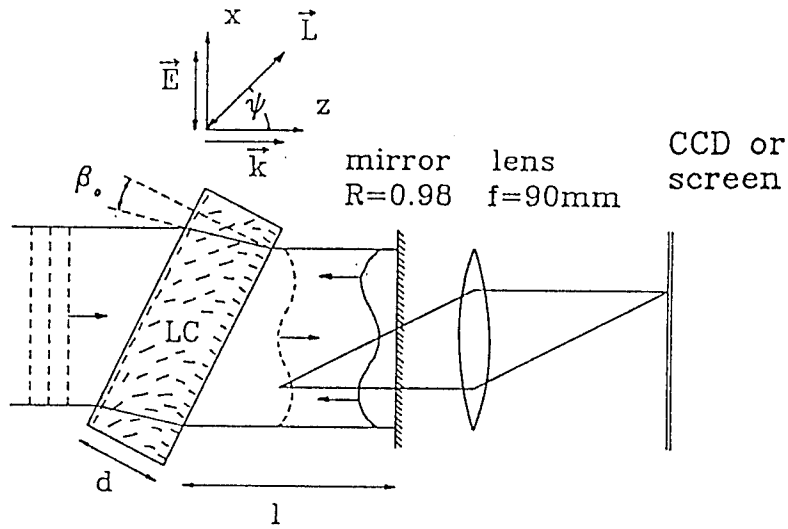
Fig.1: Scheme of the feedback-mirror experiment. The nonlinear liquid crystal film (LC) is placed in front of a high reflectivity mirror and illuminated with a linear polarized cw laser beam. The pattern formation is observed by imaging the transverse near field distribution with a lens on a CCD camera or a screen.

$I = 11\ W/cm^2,\ l = 17cm$ $I = 28\ W/cm^2,\ l = 20cm$ $I = 30\ W/cm^2,\ l = 17cm$ $I = 19\ W/cm^2,\ l = 11cm$

$J_0(q\rho)$ $J_3(q\rho)\cos(3\varphi)$ $J_0(q\rho)+J_5(q\rho)\cos(5\varphi)$ $J_0(q\rho)+J_6(q\rho)\cos(6\varphi)$
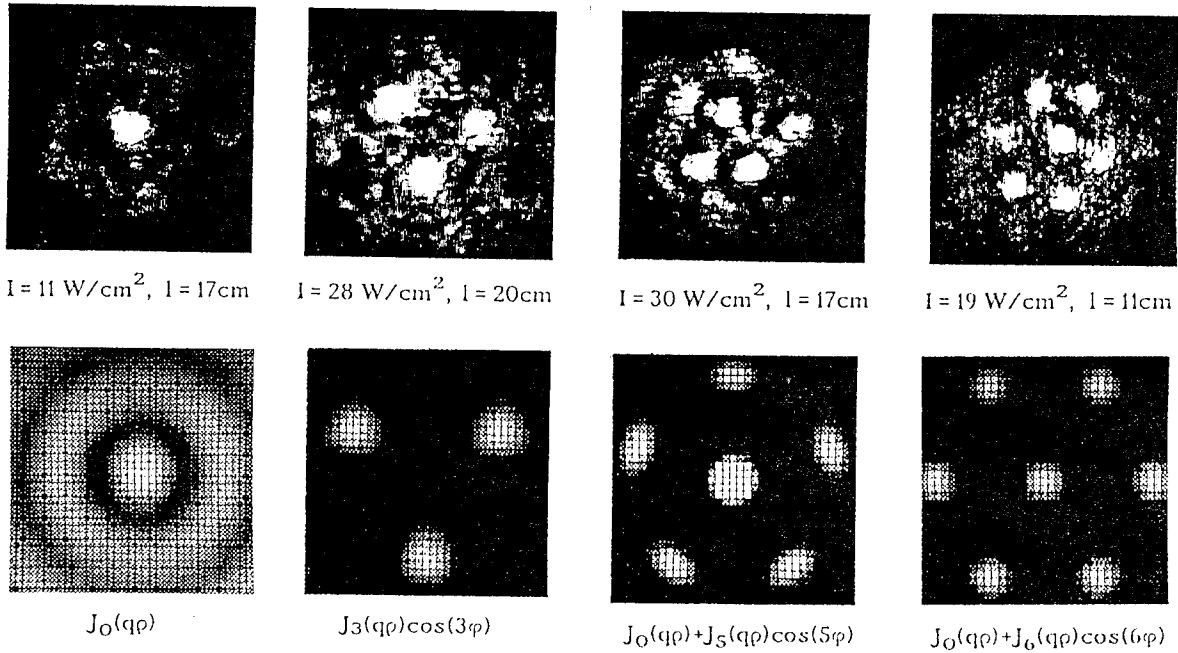
Fig.2: Examples of patterns obtained with the feedback-arrangement and comparision with calculated Besselfunction modes, cf. eqn.1.

For modes $m > 0$ the observed patterns exhibit symmetry breaking from the O_2 space group of the input intensity profile into reduced subgroups D_m. If, however, $m = 0$, the patterns consist of concentric rings showing no symmetry breaking at all. Furthermore, the observed patterns are discussed in terms of phase transitions. Performing a nonlinear analysis of the generalized Landau-Ginzburg equation describing the system, it is shown that the investigated pattern formation can be described by second order phase transitions if $m > 0$ but is of first order for $m = 0$. Consequently, bistability and hysteresis can be expected in the latter case, which has been experimentally verified using photo-thermal nonlinearities in these experiments for the first time.

Our experimental results and analytical description of the patterns will be discussed and compared with numerical simulations [13] of an arbitrary Kerr-slice in front of a feedback mirror considering gaussian input beams, and with more specific simulations of a liquid crystal film in the investigated arrangement which have been performed very recently [14].

Acknowledgements

References

1   N.B. Abraham, W.J. Firth; *J.Opt.Soc.Am B* **7**, p.948 (1990)
2   M. Kreuzer, W. Balzer, T. Tschudi; *Appl. Optics* **29,** p.579 (1990)
3   L.A. Lugiato et al.; *J.Opt.Soc.Am. B* **7**, p.1019 (1990)
4   H. Haken, in *Pattern Formation by Dynamical Systems and Pattern Recognition* edited by H. Haken, Springer Series in Synergetics **5** (Springer Berlin 1979)
5   T. Kohonen, *Selforganisation and Associative Memory*; Springer Series in Information Sciences **8**, (Springer Berlin 1989)
6   G.S. McDonald, W.J. Firth; *J.Opt.Soc.Am B* **7**, p.1328 (1990)
7   W.J. Firth, M.A. Vorontsov; *J.Mod.Optics* **40**, p.1841 (1993)
8   R. Macdonald, H.J. Eichler; *Opt.Commun.* **89**, .289 (1992)
9   M. Tamburrini, M. Bonavita, S. Wabnitz, E. Santamato; *Opt.Lett.* **18**, p.855 (1993)
10   G.D'Alessandro, W.J. Firth; *Phys.Rev.Lett.* **66**, p.2597 (1991)
11   G.D'Alessandro, W.J. Firth; *Phys.Rev.A* **46**, p.537 (1991)
12   R. Macdonald, H. Danlewski; *Mol.Cryst.Liq.Cryst.* (to appear 1994)
13   F. Papoff, G.D'Alessandro, G.-L. Oppo; *Phys.Rev.A* **48**, p.634 (1993)
14   A. Kilian, L. Bennett; (presentation on this conference)

THE VECTOR SOLITON ASSOCIATED WITH POLARIZATION MODULATIONAL INSTABILITY IN THE NORMAL DISPERSION REGIME

M. Haelterman
Université Libre de Bruxelles, Optique Nonlinéaire Théorique,
Campus Plaine, CP 231, B-1050 Bruxelles, Belgium
tel: +32 2 650 5819; fax: +32 2 650 5824; e-mail: mhaelter@ulb.ac.be

A. P. Sheppard
Optical Sciences Centre, Australian National University, Canberra, Australia
tel: +61 6 249 4061; fax: +61 6 249 5184; e-mail: aps124@rsphy1.anu.edu.au

When accounting for the polarization of the electromagnetic field, light propagation in isotropic Kerr materials is described by two incoherently coupled nonlinear Schrödinger (NLS) equations [1]. It is known since the early study of Berkhoer and Zakharov that incoherent coupling between two NLS equations leads to an extension of the frequency domain of modulational instability (MI) to the normal dispersion regime [1]. The physical mechanism behind incoherent coupling is cross-phase modulation (XPM) which refers, in this case, to each polarization component modulating the phase of the other. It was shown, in the context of fiber optics, that MI with normal dispersion can also occur through XPM between waves of different frequencies [2]. The author of this latter work foresaw the fundamental importance of this phenomenon when he conjectured that a soliton must exist that is associated with MI in the normal dispersion regime in the same way as the bright NLS soliton is associated with MI of the scalar NLS equation in anomalous dispersion. The aim of our analysis is to confirm the existence and describe the features of this fundamental soliton.

In dimensionless units the evolution of the circular polarization components of light propagating in a normally dispersive Kerr medium is ruled by the incoherently coupled NLS equations [1]

$$i\partial_z E_\pm - \partial_{tt}E_\pm + |E_\pm|^2 E_\pm + \sigma |E_\mp|^2 E_\pm = 0 \tag{1}$$

where $E_\pm$ are the counterrotating polarization components, z is the coordinate along the propagation axis, t is the time in the Gallilean reference frame travelling at the group velocity of the waves, and σ is the XPM coefficient related to the nonlinear susceptibility tensor of the material. From a standard linear stability analysis it was shown in ref.[1] that the linearly polarized continuous wave (cw) solution of this equation, i.e., $E_+ = E_- = E_o\exp[(1+\sigma)i|E_o|^2z]$, is modulationally unstable. A more thorough analysis of the problem [3] indicates that modulational instability of this linearly polarized wave induces the growth of periodic perturbations of opposite sign in the two circular polarization components. As a consequence, one may expect that, up to the nonlinear stage of the modulation, the envelopes of the two circularly polarized fields exhibit two identical but π out-of-phase periodic structures. Since this instability involves a change of the state of polarization of the field, it is called polarization modulational instability (PMI).

In order to study the dynamics of the periodic solutions associated with PMI of eq.(1), we introduce the truncated three-wave model of ref.[4]. This model is based on the Fourier mode truncation of the π out-of-phase periodic structures of both field components:

$$E_\pm(z,t) = E_0(z) \pm \sqrt{2}E_1(z)\cos(\Omega t) \tag{2}$$

where Ω is the frequency of the temporal patterns. Introducing the powers P_0, P_1 and the phases ϕ_0 and ϕ_1 of the pump and sideband waves through the relations $E_0 = (P_0)^{1/2}\exp(i\phi_0)$ and $E_1 = (P_1)^{1/2}\exp(i\phi_1)$, the model reduces to a set of coupled ode's for the real variables $\eta = P_1/P$ and $\phi = \phi_0 - \phi_1$, where P is the total power $P = |E_0|^2 + |E_1|^2$. Simple algebra shows that the variables are in fact conjugated through the Hamiltonian

$$H(\eta,\phi) = (\Omega^2/P - \sigma + 1) + (5\sigma - 3)\eta^2/4 - (\sigma - 1)(1-\eta)\eta\cos^2\phi \qquad (3)$$

A simple glance at the contour lines of $H(\eta,\phi)$ allows us therefore to characterize the dynamics of the periodic solutions of eq.(1). These contour lines are shown in fig.1 in polar coordinates (η,ϕ) for which the origin represent the linearly polarized cw solution. PMI of this solution corresponds naturally to the presence at the origin of a hyperbolic unstable fixed point. The associated homoclinic orbit surrounds two stable elliptic fixed points which reveal the existence of stationary periodic solutions to eq.(1). These stationary periodic solutions are the equivalent of the so-called cnoidal waves of the scalar NLS equation.

In the case of the scalar NLS equation the link between modulational instability and the bright soliton can be simply seen by verifying that the cnoidal waves tend to the sech-envelope soliton as their period tends to infinity (see ref.[5] for a detailed analysis). Here, to identify the soliton associated with PMI we have therefore to study the stationary periodic solutions as their period tends to infinity, i.e., for $\Omega \to 0$. Such a study cannot be performed by means of the Hamiltonian model which is only valid for frequencies close to the optimal frequency of PMI. However, the information brought by this simplified model (namely the stationary periodic solutions have the form $E_+ = u(t)\exp(i\beta z)$, $E_- = v(t)\exp(i\beta z)$ where $u(t)$ and $v(t)$ are two real identical but π out-of-phase periodic functions) allow us to calculate the stationary periodic solutions numerically from the full dynamical model eq.(1) in a very easy way. Fig.2 shows the envelopes $u(t)$ and $v(t)$ of these solutions for different values of the frequency Ω. We see that as Ω decreases, the envelopes acquire higher harmonics corresponding to the appearance of domains of constant polarization separated by localized structures in which the polarization of the field switches from one circular polarization to the other. Fig.3 shows the envelopes obtained in the limit $\Omega \to 0$. We see that they take the form of two symmetric semi-infinite kink waves. The localized structure they form appears then as a solitary wave exactly as the sech-envelope soliton constitutes the limiting state of the cnoidal waves of the scalar NLS equation. As a consequence, this new solitary wave must be seen as being the soliton associated with polarization modulational instability. We have checked the stability of the vector soliton by numerical simulation of the full dynamical model eq.(1). As illustrated in fig.4 which shows the collision between a gray NLS soliton and the vector soliton, we verified a robust soliton-like nature of this new fundamental nonlinear wave.

References

[1] A. L. Berkhoer and V. E. Zakharov, Sov. Phys. JETP **31**, 486 (1970).
[2] G. P. Agrawal, Phys. Rev. Lett. **59**, 880 (1987).
[3] M. Haelterman and A. P. Sheppard, Phys. Rev. E (in press, accepted December 1993).
[4] S. Trillo and S. Wabnitz, Phys. Lett. **A159**, 252 (1991).
[5] N. N. Akhmediev, V. M. Eleonskii, and N. E. Kulagin, Theor. Math. Phys. **72**, 809 (1987)
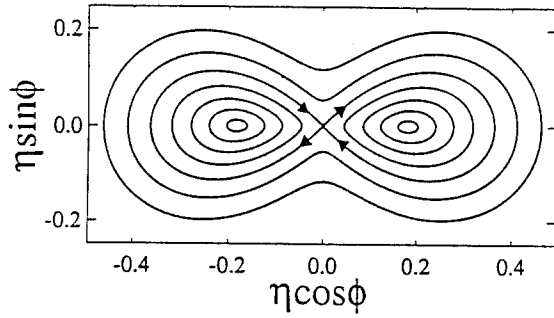
Fig.1: Phase portrait of the dynamics of the periodic solutionsof eq.(1) as obtained from the truncated Hamiltonian system. The homoclinic orbit reveals the existence of stable elliptic points representing the stationary periodic solutions of eq.(1).
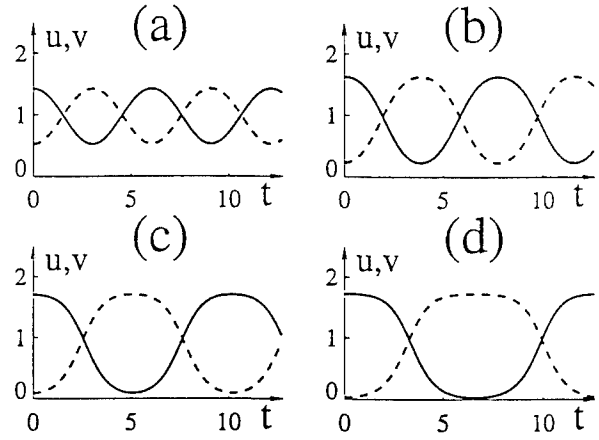
Fig.2: Envelopes of the stationary periodic solutions obtained from numerical integration of eq.(1). (a) Ω = 1, (b) Ω = 0.8, (c) Ω = 0.6, (d) Ω = 0.5. We observe the formation of localized structures as Ω tends to zero.
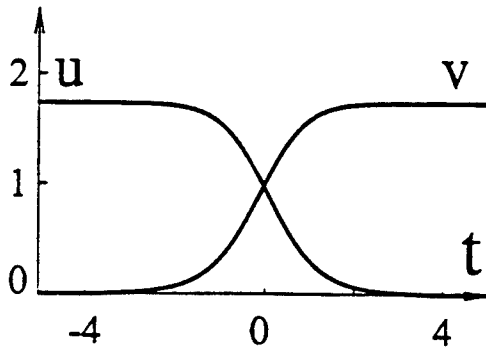
Fig.3: Envelopes of the stationary periodic solutions obtained in the limit Ω = 0, i.e., envelopes of the vector soliton associated with PMI.
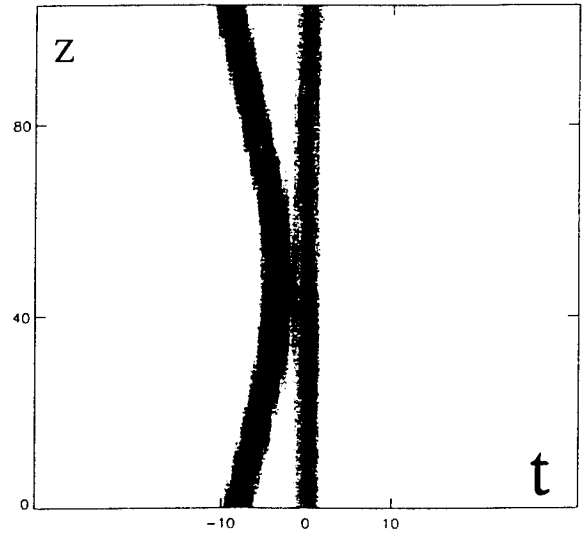
Fig.4: Numerical simulation showing the collision of the vector soliton and a gray NLS soliton inscribed onto the constant background of uniform circular polarization. We see that the gray NLS soliton simply bounces back on the vector soliton which remains totaly unchanged.

56

Stable Four-Dimensional Solitons in Graded-Index Materials with Kerr Nonlinearity

Yinchieh Lai and Chih-Hung Chien

Institute of Electro-Optical Engineering, National Chiao-Tung University

Hsinchu, Taiwan, R.O.C.

Tel:886-35-712121 ex 4277   Fax:886-35-716631   E-mail: yclai@cc.nctu.edu.tw

Jyhpyng Wang

Institute of Atomic and Molecular Sciences, Academia Sinica

and Department of Electrical Engineering, National Taiwan University

Taipei, Taiwan, R.O.C.

Optical Kerr nonlinearity can give rise to interesting soliton phenomena. Spatially, the combined effects of Kerr nonlinearity with diffraction produces spatial solitons. Temporally, the combined effects of Kerr nonlinearity with group velocity dispersion produces temporal solitons. In homogeneous media with cubic instantaneous Kerr nonlinearity, solitons in more than two dimensions are not stable. Recently it was found that there exist stable 3D soliton solutions in graded-index (GRIN) materials as long as the optical power is less than a critical power[1]. The graded-index seems to help stabilize the soliton solution. This strongly suggests that stable four dimensional (3D space + 1D time) solitons may also exist in GRIN materials. In the present paper, by using a variational approach, we have investigated the propagation of a 4D optical pulses through graded-index materials with Kerr nonlinearity. We find that stable 4D solitons can exist as long as the dispersion is negative and as long as the pulse energy is less than a critical energy.

A GRIN material is a material with a parabolic refractive index.

$$n(x,y,z) = n_o(\omega)[1 - \frac{G(\omega)}{2}(x^2 + y^2)] \tag{1}$$

The propagation of an optical pulse on the axis of a GRIN waveguide is described by the following usually used paraxial wave equation in the time domain.

$$j\frac{\partial u}{\partial z} = \alpha_o(\frac{\partial^2 u}{\partial x^2} + \frac{\partial^2 u}{\partial y^2}) - \frac{D}{2}\frac{\partial^2 u}{\partial t^2} - \beta(x^2 + y^2)u + K|u|^2 u \tag{2}$$

Here $u(x,y,z,t)$ is the pulse envelope in the time domain. If the carrier frequency of the pulse is ω_o and the propagation constant in the center of the GRIN material is $k(\omega) = n_o(\omega)\omega/c$, then the coefficients in eq.(2) are given by $\alpha_o = 1/[2\ k(\omega_o)]$, $D = k''(\omega_o)$, $\beta = k(\omega_o)G(\omega_o)/2$ and $K = \frac{k(\omega_o)n_2}{n_o(\omega_o)}$. Here n_2 is the nonlinear coefficient of the refractive index.

By using the standard variational approach based on the Ritz optimization procedure[2] and by assuming that the pulse can be well described by the following solution ansatz :

$$u(x,y,z,t) = A(z)\exp[j\theta(z)]F[\frac{x}{w(z)}]F[\frac{y}{w(z)}]F[\frac{t}{w_t(z)}]\exp[j\frac{p(z)}{2}(x^2+y^2)+j\frac{p_t(z)}{2}t^2] \tag{3}$$

we obtain the following evolution equations for the four pulse parameters.

$$\frac{dw}{dz} = -2\alpha_o pw \tag{4}$$

$$\frac{dp}{dz} = 2\alpha_o[p^2 - c_1\frac{1}{w^4}] + 2\beta + c_2\frac{KE_o}{w^4 w_t} \tag{5}$$

$$\frac{dw_t}{dz} = Dp_t w_t \tag{6}$$

$$\frac{dp_t}{dz} = -D[p_t^2 - c_1\frac{1}{w_t^4}] + c_2\frac{KE_o}{w^2 w_t^3} \tag{7}$$

Here the two coefficients c_1 and c_2 are two constants that depend on the pulseshape function F. For a gaussian pulseshape $[F(x) = \exp(-x^2/2)]$, $c_1 = 1$ and $c_2 = 1/(4\sqrt{2})$. $E_o = A^2 w^2 w_t$ is a measure of the pulse energy. Its relation to the real pulse energy also depends on the pulseshape function F. For the same gaussian pulseshape, the real pulse energy E_p is given by $E_p = \pi^{3/2} E_o$.

We find that eqs.(4-7) have stationary soliton solutions as long as the dispersion parameter D is negative and E_o is not too large.

$$0 \le E_o \le \sqrt{\frac{4c_1^{5/2}}{3^{3/2}c_2^2} \frac{|D|\alpha_o^{3/2}}{\sqrt{\beta}K^2}} \tag{8}$$

The stationary beam width and pulse duration are plotted in Figure 1 and 2 in normalized units. The normalization units we use are : (1) spatial width : $w_n = (c_1\alpha_o/\beta)^{1/4}$ (2) pulse duration : $w_{tn} = [c_1|D|^2/(4\alpha_o\beta)]^{1/4}$ (3) energy : $E_{on} = \sqrt{(c_1^{5/2}|D|\alpha_o^{3/2})/(8c_2^2\sqrt{\beta}K^2)}$. After performing the stability analysis, we find that one branch of the solution is stable while the other one is unstable. This has been labeled in Figure 1 and 2, too.

As a numerical example, for a typical GRIN lens (W-2.0 from NSG America Inc.), at the 620 nm wavelength, $G_o = 9.3 \times 10^4 \ m^{-2}$, $\beta = 7.5 \times 10^{11} \ m^{-3}$, $\alpha_0 = 3.1 \times 10^{-8} \ m$. If $n_2 = 3.2 \times 10^{-20} \ m^2/W$, then $K = 3.2 \times 10^{-13} \ m/W$. These are the typical magnitudes of the parameters for commercially available GRIN materials. However, at this wavelength the dispersion of this material is positive with $D = 1.4 \times 10^{-25} \ sec^2/m$. Since there is no (bright) soliton solution when the dispersion is positive, it may seem that one needs to try other materials or other wavelengths. Fortunately the situation is not so bad. It has been shown recently by one of the authors (J. Wang) and his students that by off-axially propagating the optical pulse in a helix trajectory, the net dispersion can be made negative[3]. Negative dispersion up to hundreds of square femtoseconds can be generated by a 1 cm long commercial GRIN materials. They also proposed to generate optical solitons at a wide range of wavelengths by taking advantage of this phenomenon[4]. We have generalized our variational approach to treat off-axial pulse propagation problems[5]. We find that if the pulse propagates in a helix trajectory with the offset distance remaining constant and if the beamwidth is much smaller than the

offset distance, then eqs.(4-7) are still correct except that the dispersion parameter D has a new value. If we assume $D = -5 \times 10^{-26} sec^2/m$ and the pulseshape is gaussian, for 4-D solitons to exist, E_o has to be less than 8.7 nJ. That is, the pulse energy $E_p = \pi^{3/2} E_o$ has to be less than $48 nJ$. If we choose $E_o = 1$ nJ, then the soliton beam width is $w = 14$ μm and the soliton duration is $w_t = 180$ fs. From the numbers given above, it can be seen that there should be no big difficulty in generating such solitons in today's laser labs. We believe this may be the simplest method to generate solitons at a wide range of wavelengths.

In our variational formulation, the biggest approximation is the solution ansatz eq.(3). In eq.(3), the beamwidth is assumed to be the same across the whole pulse. We think this is a good assumption for solitons if they exist. Intuitively, for solitons the self focusing, diffraction, selfphase modulation and dispersion effects should be in balance to produce a nice pulse and thus the solution ansatz eq.(3) should be good enough. To make further investigation, we are currently using a more general solution ansatz to study the same problem. The results will be presented in the conference, too.

References

1. M. Karlsson, D. Anderson, and M. Desaix, Opt. Lett. **17**, 22-24(1992).

2. D. Anderson, Phys. Rev. A **15**, 3135-3145 (1983).

3. A.C. Tien, R. Chang, and J. Wang, Opt. Lett. **17**, 1177-1179 (1992).

4. R. Chang, and J. Wang, Opt. Lett. **18**, 266-268 (1993).

5. C.-H. Chien, Y. Lai and J. Wang, "Off-axial pulse propagation in graded-index waveguides with Kerr nonlinearity – a variational approach", to be submitted to J. Opt. Soc. Am. B.
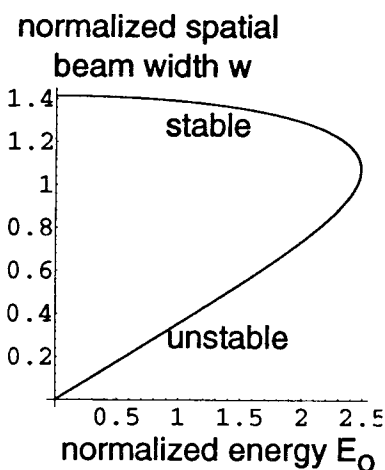
Figure 1
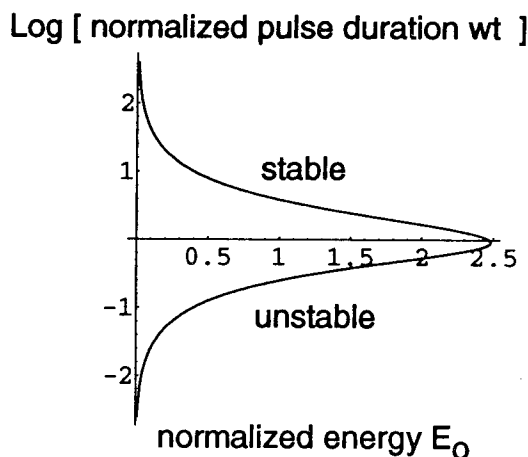
Figure 2

Self-organization of the Photorefractive Scattering in $KNbO_3$ in a Hexagonal Spot Array

P.P. Banerjee and H-L. Yu
Department of Electrical and Computer Engineering
University of Alabama in Huntsville, Huntsville AL 35899
ph: (205) 895 6215 ext. 416

N. Kukhtarev
Physics Department
Alabama A&M University, Normal AL 35762

1. Introduction

Potassium niobate ($KNbO_3$) is an attractive choice as a photorefractive material for dynamic holography because of its large electrooptic coefficient and high photosensitivity. The physical mechanism behind hologram storage and retrieval has been recently extensively studied [1,2].

In this paper we describe a new nonlinear phenomenon observed during scattering of a single Ar laser beam in a photorefractive $KNbO_3$:Fe crsytal. A vertically polarized laser beam (see Fig. 1) initially scatters in a cone angle $V \approx 2$ degrees behind the crystal, and later rearranges in a hexagonal spot array: the transmitted beam is surrounded by six spots lying on the scattering cone. These six spots may rotate about the center, and the rotation speed and the intensity ratio of the peripheral spots to the central spot are dependent on the intensity and diameter of the incident beam.

This remarkable self-organization of the scattering cone into a hexagonal spot array may be explained by a holographic intermode scattering [3] which develops in two stages. In the first stage, scattered light is rearranged into a cone due to intermode scattering, forming the first generation of gratings. At the second stage, waves scattered in the cone write new holographic gratings (second generation gratings), and those amongst them that have holographic grating vectors equal to the strongest gratings from the first generation gartings are enhanced. This holographic self-organization model explains the appearance of hexagonal spot structure around the transmitted beam.

2. Experimental Results

The experimental setup is shown in Fig. 1. An Ar laser ($\lambda=514$ nm) with vertical polarization and with initial beam diameter of 1mm is reduced to a beam diameter of 0.5 mm using a confocal L_1-L_2 lens combination, and illuminates a $KNbO_3$:Fe crystal of dimensions $5 \times 5 \times 5$ mm^3. When the laser beam is exactly normal to the incident surface, the far-field pattern comprises a strong central spot with a peripheral ring (which appears instantaneously), which

thereafter, evolves into six symmetrically spaced spots on the ring, as shown in Fig.2. The angle of divergence of the peripheral cone is approximately 2 degrees. The time taken to form the spots is in the order of a few seconds for an incident power of 7.5 mW. Both the central spot as well as the peripheral spots are predominantly vertically polarized. The intensity ratio of each peripheral spot to the central spot is about 7%. If the incident angle is slightly off-normal (≈ 0.5 degrees), the six spots are observed to have unequal intensities, and the entire pattern rotates. The rotation speed depends on the incident beam intensity: for instance, it is 55 degrees per minute when the incident power is 7.5 mW.

When the illuminating beam diameter is changed to 1 mm, the intensity ratio of each perpheral spot to the central spot is reduced to about 1%. With an incident power of 7.5 mW, the rotation speed decreases to 4.5 degrees per minute. With increased power (viz. 15 mW), the rotation speed increase to 11 degrees per minute.

3. Discussion

This unusual phenomenon of self-organization of the scattered light in a hexagonal spot pattern may be explained by competitive supporting interactions between two generations of photorefractive gratings. The small angle of cone scattering (approximately 2 degrees) may be due to the confinement of scattering near the optical axis and the optical ray axis. For principal values of refractive indices in $KNbO_3$ at 0.514 microns [4] $n_x=2.3337$, $n_y=2.3951$ and $n_z=2.2121$, we obtain in the z-y plane, the angle of the optical axis (w.r.t. z-axis) is 33.8 degrees, and for the ray axis, the angle is 35.96 degrees [5], which implies an angle difference of 2.2 degrees. This value is close to the observed scattering cone angle, and gives us good hints to detailed calculations of observed phenomenon, which is now in progress.

References

[1] G. Montemezzani and P. Gunter, J. Opt. Soc. Amer. B **7** 2323 (1990).
[2] G. Montemezzani, M. Zgonik and P. Gunter, J. Opt. Soc. Amer. B **10** 171 (1993).
[3] N.V. Kukhtarev, E. Kratzig, H.C. Kulich, R.A. Rupp and J. Albers, Appl. Phys. B **35** 17 (1984).
[4] B. Zysset, I. Biaggio and P. Gunter, J. Opt. Soc. Amer. B **9** 380 (1992).
[5] M. Born and E. Wolf, Principles of Optics, Macmillan, NY (1964).
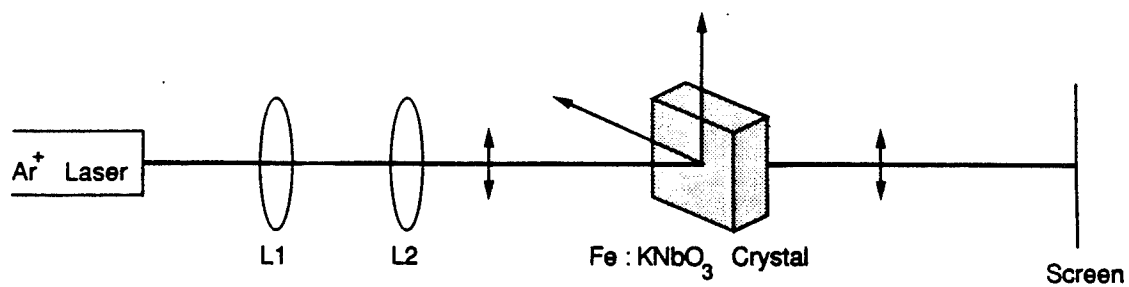
Fig. 1 Experimental setup.

Fig. 2 Far-field pattern showing central spot and hexagonal spot array.

Polarization patterns in a passive ring-cavity

J. B. Geddes and J. V. Moloney
Arizona Center for Mathematical Sciences
Department of Mathematics
University of Arizona
Tucson, AZ 85721 USA
Telephone: (602) 621 8129
Fax: (602) 621 1510

E. M. Wright
Optical Sciences Center
University of Arizona
Tucson, AZ 85721 USA

W. J. Firth
Department of Physics and Applied Physics
University of Strathclyde
Glasgow, G4 0NG Scotland

A ring-cavity system, filled with an isotropic nonlinear medium and driven by a linearly polarized coherent input field, has been the subject of intense study over the last decade. This system can show a number of non-equilibrium phase transitions, including optical bistability (OB) [1], and transverse pattern formation [2–5]. In particular, a mean field OB model [4] was found to give rise to hexagonal patterns, at least for a self-focusing medium. This mean-field model was shown to represent a special case of a more general infinite dimensional map describing transverse coherent structures in optical bistability [3]. A self-defocusing medium has not been studied in great detail for the reason that the parameter regime in which transverse pattern formation occurs coincides with the bistable regime: The instability responsible for pattern formation then simply serves to drive the system from the unstable lower branch to the stable upper branch. This conclusion, however, is based on the assumption that the internal field in the nonlinear ring-cavity preserves its polarization state as that of the input field. Here we extend the mean field model to include polarization effects. This extension leads to a polarization instability which can occur without accompanying OB for a defocusing medium. We find that there are in fact two pattern forming modes, one of which preserves the state of polarization of the field (symmetric mode) while the other does not (asymmetric mode). The symmetric mode, which dominates in a self-focusing medium, gives rise to hexagonal patterns while the asymmetric mode, which prohibits the formation of transcritical hexagons, may be isolated in a self-defocusing medium. In this case we find that rolls dominate close to the instability threshold, while further from equilibrium we observe a variety of structures including disclinations, dislocations and roman-arches.

Our basic model consists of a nonlinear ring-cavity which is filled with an isotropic nonlinear Kerr medium and driven by a linearly polarized input field. We may generalize the mean-field model [2] by allowing for the vector nature of the field, in which case the

evolution equation for the electric field becomes

$$\frac{\partial \mathbf{E}}{\partial t} = -(1 + i\eta\theta)\mathbf{E} + \mathbf{E_I} + ia\nabla^2\mathbf{E} + i\eta(A(\mathbf{E}.\mathbf{E}^*)\mathbf{E} + \frac{B}{2}(\mathbf{E}.\mathbf{E})\mathbf{E}^*)$$

where $\mathbf{E} = \mathrm{col}(\mathcal{E}_x, \mathcal{E}_y)$ is the (scaled) vector electric field envelope, $\mathbf{E_I}$ is the input field, $\eta = +1(-1)$ indicates self-focusing (self-defocusing), θ is the cavity detuning parameter, ∇^2 is the transverse Laplacian and $'a'$ measures the relative strength of transverse diffraction. The scaling employed is identical to those in references [2,4]. Note that $A + B/2 = 1$ and for the Kerr effect in liquids $A = 1/4, B = 3/2$ while $A = 1, B = 0$ for an electrostrictive nonlinearity. The mean field model [2] is recovered in the limit of a linearly polarized field, e.g. $\mathbf{E} = \mathbf{x}\mathcal{E}$, for arbitrary A and B. Their work, however, gives no indication of whether these linearly polarized solutions are stable.

These equations admit both symmetric and asymmetric stationary plane-wave solutions. The symmetric solutions give rise to vector fields with the same linear polarization state as the input field. This corresponds to the scalar case previously discussed in references [2,4]. Asymmetric solutions were previously discussed [6] in the context of OB in a symmetrically pumped ring resonator. In that case the symmetry was with respect to the propagation direction around the ring cavity, whereas here the asymmetry is with respect to the two circular polarizations.

Linear stability analysis of the symmetric stationary plane-wave solutions reveals two distinct forms of instability – symmetric and asymmetric instability. In the former case, the perturbations to the plane-wave solutions are in phase, so the field remains linearly polarized even though the underlying (symmetric) solution is unstable. The symmetry between the two circular polarization states is therefore preserved, and the vector field maintains the same linear polarization as the input field. This case is identical to that previously described in references [2,4], that is, the scalar case.

In the latter case, i.e., that of asymmetric instability, the perturbations are π out of phase. This is a polarization instability which produces a symmetry breaking between the two circular polarizations, and causes the vector field to evolve away from the linear polarization state of the input field.

We will report on the consequences of the existence of these two distinct pattern forming modes. Why distinct? Hexagonal patterns are generically preferred in the absence of further symmetries [7], such as an inversion symmetry. The symmetric instability gives rise to a mode which does not have this symmetry and we therefore expect, in general, that (transcritical) hexagon will dominate. This was confirmed in the scalar case [4,5], where the instability is to the symmetric mode.

The asymmetric instability, on the other hand, yields a mode which possesses the inversion symmetry. In general we do not expect hexagons in this case and we have begun to consider which planforms are permissible. If we operate close to the bifurcation point then we can completely isolate the asymmetric mode in a self-defocusing medium when $\theta < 2$. We have run numerical simulations on our model equations on a periodic domain for a variety of parameter values, and in Figure 1 we show the results for B=2 (A=0), $\theta = 1$. Figure 1(a) shows the stationary solution that prevails at 50 % above threshold, and it exhibits several interesting features. The underlying structure consists of rolls, and we see several dislocations, a disclination at the top and a roman arch. The next five images depict the

temporal evolution of Figure 1(a) when we decrease the pump to 10 % above threshold. The disclination and the roman arch are unstable and the final state, once the remaining dislocations glide across rolls and annihilate, is a set of straight parallel rolls.

(a) (b) (c)

(d) (e) (f)
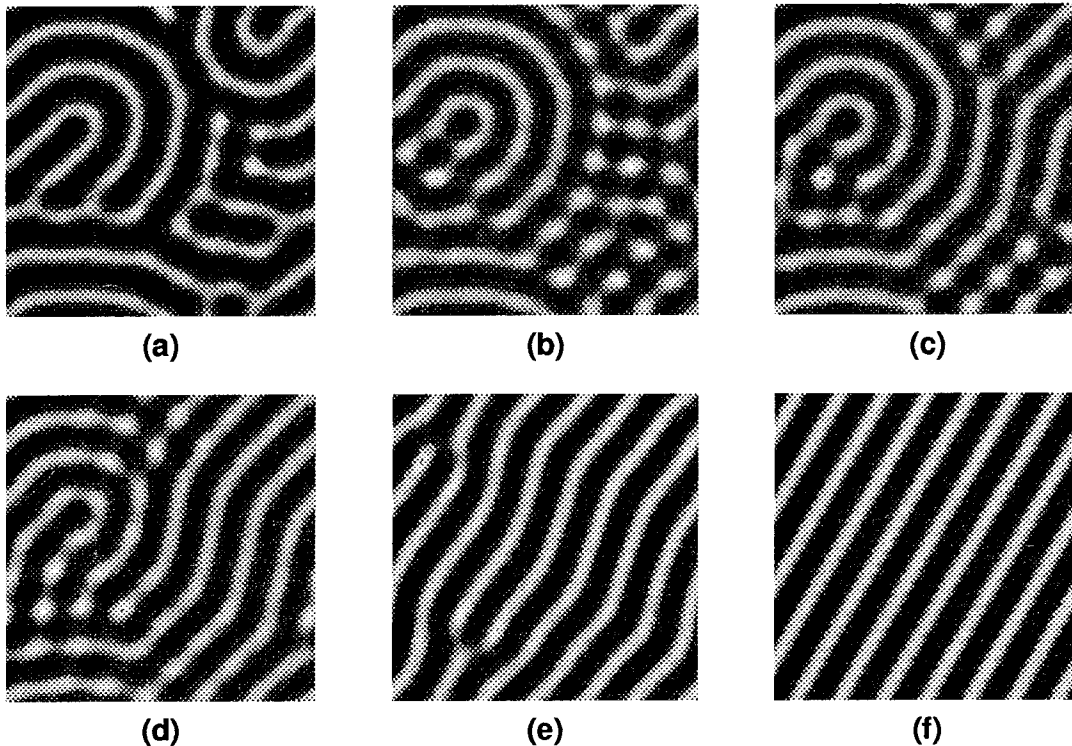
[1] H. M. Gibbs, *Controlling light with light*, (Academic press, Orlando, 1985).

[2] L. A. Lugiato and R. Lefever, Spatial dissipative structures in passive optical systems, *Phys. Rev. Lett.* **58**, 2209-2211 (1987).

[3] A. Quarzeddini, H. Adachihara and J. V. Moloney, Spontaneous spatial symmetry breaking in passive nonlinear optical feedback systems, *Phys. Rev. A* **38**, 2005-2010 (1988).

[4] W. J. Firth, A. J. Scroggie, G. S. McDonald and L. A. Lugiato, Hexagonal patterns in optical bistability, *Phys. Rev. A* **46**, R3609-R3612 (1992).

[5] M. Tlidi, M. Georgiou and P. Mandel, Transverse patterns in nascent optical bistability, *Phys. Rev. A* **48**, 4605-4609 (1993).

[6] A. E. Kaplan and P. Meystre, Directionally asymmetrical bistability in a symmetrically pumped nonlinear ring interferometer, *Opt. Commun.* **40**, 229-232 (1982).

[7] J. B Geddes, R. A. Indik, J. V. Moloney and W. J. Firth, Hexagons and squares in a passive nonlinear optical system, Submitted to *Phys. Rev. A* (1993).

Pattern Dynamics in Large Aspect Ratio Lasers

Q. Feng, J. Lega, J.V. Moloney and A.C. Newell

Arizona Center for Mathematical Sciences

Department of Mathematics

University of Arizona

Tucson, Az. 85721

Telephone: (602)-621-6755

Fax: (602)-621-1510

Recent experiments [1] have established that exotic transverse patterns such as defects, squares etc, can emerge across the aperture of a large Fresnel number laser. A key theoretical observation, for example, is that the Maxwell-Bloch equations describing wide aperture homogeneously [2], inhomogeneously broadened lasers or, the many-body Maxwell-Semiconductor Bloch equations describing a broad area semiconductor laser, are isomorphic to a certain class of universal order parameter equations describing patterns in general. The latter equations are universal in the sense that they describe patterns (convection rolls, squares, hexagons etc), and their defects in diverse physical systems such as fluids, liquid crystals, magnetisation phenomena near a critical point (for example a Lifshitz point). The basic mathematical form of the order parameter equations remains fixed with the physics of the relevant process contained in their coefficients. Quantitative information on the scaling laws determining characteristic space and time scales are reflected in how the physical parameters are combined in these coefficients. Such scaling behavior is by no means evident in the original physical model equations.

Of what relevance are such equations to laser physics? First of all, they remove a spurious non-physical instability associated with standard adiabatic elimination of the polarization variable in the Maxwell-Bloch equations when diffraction is added [3]. These instabilities mimic grid oscillations

and are often mistakenly identified with unstable numerical schemes. Secondly, the analysis of such equations tells us which transverse patterns (modes) are selected near threshold and whether these are stable to further sideband instabilities. Thirdly the stability of a particular pattern (shape of a mode in the transverse dimension) can be inferred analytically from the study of a phase evolution equation associated to that particular pattern. The combination of original physical model, order parameter equation and phase equation provides a unique self-consistency check of the theory.

The Maxwell-Bloch laser equations for a transversely extended single longitudinal mode laser are given by:

$$
\begin{aligned}
e_t &+ ia\nabla^2 e = -\sigma e + \sigma p \\
p_t &+ (1 + i\Omega)p = (r - n)e \\
n_t &+ bn = \frac{1}{2}(e^*p + p^*e)
\end{aligned}
\tag{1}
$$

where time is scaled to the polarizationdephasing rate γ_1, $\sigma = \frac{\kappa}{\gamma_1}$, $b = \frac{\gamma_2}{\gamma_1}$ and $\Omega = (\omega_{12} - \omega)/\gamma_1$.

Complex order parameter equations for class C lasers ($\gamma_1 \approx \gamma_2 \approx \kappa$) where γ_2 is the inversion decay rate and κ the cavity damping rate, belong to the Lorenz-like class of systems and have been studied in some detail [4,5]. Near-field transverse traveling wave solutions, which are the only known exact finite amplitude solutions to the Maxwell-Bloch equations given below, tend to be robust in large ranges of physical parameter space. When the detuning of the laser from the gain peak is finite and negative ($\Omega < 0$) the near threshold pattern dynamics is described by the Complex Ginzburg-Landau order parameter equation [4]. The transversely homogeneous state of the laser tends to be stable but defects (complex zeroes of the field) can arise from noisy initial conditions and these tend to persist and show complex spatio-temporal behavior. For positive detuning ($\Omega > 0$), two coupled order parameter equations, called Complex Newell-Whitehead-Segel (CNWS), appear as the natural description of near-threshold patterns representing counterpropagating traveling waves in the transverse x-y plane [5]. The presence of one traveling wave tends to depress the other traveling in the opposite direction and the far-field output of the laser tends to appear as a single off-axis lobe.

We will discuss a novel out-of-phase (by $\frac{\pi}{2}$) oscillating standing wave pattern which appears as a stable output of the laser near threshold. This pattern when time-averaged (to allow for an integrating detector) appears as a stationary square lattice bearing a remarkable similarity to the recent experimental observations in a high Fresnel number CO_2 laser. We also predict the existence of complex spatio-temporal pattern evolutions which, when time integrated, appear stationary and rather regular. The geometry of the external pump can profoundly influence the nature and relative disposition of near-field patterns. Figure 1 shows a sequence of frames of the near-field intensities of square and circular geometry wide aperture two-level laser. Each of these pictures are stationary in intensity but show dynamic traveling wave and spiral-like patterns in the real and imaginary parts of the complex field. The boundary conditions in the square pictures are periodic and in the circular pictures the region outside the pattern is absorbing. With reflecting boundary conditions, one can observe complex spatiotemporal dynamics in the near-field intensity but the time averaged dynamics appear stationary.

We will show that near the peak of the gain curve, the pattern dynamics is described by a Complex Swift-Hohenberg equation (CSH). The real order parameter version of this equation was originally derived in the context of hydrodynamic fluctuations at a convective instability and is also relevant to the study of a phase transition near a "Lifshitz point" for example, in alloys. Using singular perturbation methods and multiple scales (time and space) analysis we obtain the following CSH equation for a two-level laser:

$$(\sigma + 1)\frac{\partial \psi}{\partial t} = \sigma(r - 1)\psi - \frac{\sigma}{(1 + \sigma)^2}(\Omega + a\nabla^2)^2\psi + ia\nabla^2\psi - \frac{\sigma}{b}|\psi|^2\psi \qquad (2)$$

where ψ is the complex order parameter. We will also demonstrate that for a Class B laser, the single order parameter equation description is invalid. We obtain instead a generalized rate equation description which captures the correct physics and consequently does not suffer from the spurious instability mentioned above.
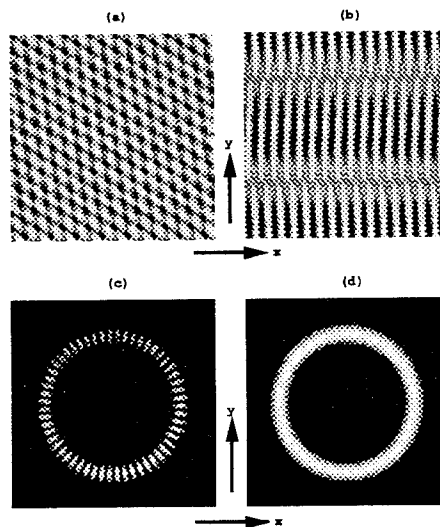
Figure 1 (a) Square like lattice observed in the near-field intensity of a wide aperture laser. (b) Zippper states, (c) annular standing wave in a dylindrically pumped laser and (d) annular emission in the same geometry as (c).

References

[1] F.T. Arecchi, G. Giacomelli, P.L. Ramazza and S. Residori, Phys. Rev. Lett., **65** 2531 (1990); D. Dangoisse, D. Hennequin, C. Lepers, E. Louvergneaux and P. Glorieux, Phys. Rev. A, **46** (1992).

[2] A.C. Newell and J.V. Moloney, "Nonlinear Optics", (Addison-Wesley, Reading, Massachussets) 1992.

[3] P.K. Jakobsen, J.V. Moloney, A.C. Newell and R. Indik, Phys. Rev. A., **45** 8129 (1992)

[4] J. Lega, P.K. Jakobsen, J.V. Moloney and A.C. Newell, Phys. Rev. A, "Nonlinear transverse modes of large aspect ratio lasers: II Pattern analysis near and beyond threshold", (in press) 1994.

Numerical simulations of composite grating dynamics

in photorefractive crystal

Hironori Sasaki, Jian Ma, Yeshaiahu Fainman and Sing H. Lee
Department of Electrical and Computer Engineering
University of California, San Diego, La Jolla, CA 92093
(619)534-2413

Photorefractive crystals have promising applications in storage for parallel information processing due to their large storage capacity, fast access time and read / write / erase capabilities. The dynamics of a composite grating[1] which consists of an original grating and a newly superimposed grating with arbitrary relative phase shift has been investigated for reconfigurable optical interconnection[2], updating interconnection weights in neural networks[3] and fast update in photorefractive memories.[4] However, previous research[5] neglects beam coupling effects such as nonuniform distribution of the space charge field along the crystal depth and fringe bending phenomena. In this summary of presentation, the effects of beam coupling on the dynamics of a composite grating is investigated by numerical simulations.

The dynamics of a composite grating is derived by solving a combination of coupled wave equations and photorefractive material equations.[6,7] The behavior of the beam coupling can be described by the following coupled wave equations,

$$
\begin{cases}
\dfrac{\partial S_1}{\partial z} = i\,\Gamma\, E_{sc}\, S_2 \\
\dfrac{\partial S_2}{\partial z} = i\,\Gamma\, E_{sc}^{*}\, S_1
\end{cases}
\tag{1}
$$

where S_1 and S_2 are complex amplitudes of the two writing beams, Γ is the coupling coefficient, E_{sc} is the complex amplitude of the space charge field, z denotes the coordinate in the direction of photorefractive crystal thickness. Assuming first order perturbation, the dynamics of a space charge field E_{sc} is obtained from material equations[8] and is given by

$$
\frac{\partial}{\partial t_N}\frac{E_{sc}}{E_q} + A\,\frac{E_{sc}}{E_q} = B\,\frac{S_1 S_2^{*}}{I_0},
\tag{2}
$$

where I_0 is the sum of the two writing beam intensities, E_q is the limiting space charge field, $t_N = t / \tau$ is the time normalized with respect to the dielectric relaxation time τ, and A and B are constants determined by materials as well as recording conditions.

Eqs. (1) and (2) are numerically solved using the following assumptions: photorefractive crystal is SBN, the grating period is 1 μm, two writing beams have extraordinary polarization. Material parameters are taken from the literatures.[9,10] Two different cases are considered: crystal thickness is 3 mm with no external electric field, and 1 mm with dc external electric field of 8 kV/ cm applied along the crystal optic axis. The first case (with no electric field) includes only the effect of the nonuniform distribution of the space charge field due to beam coupling, and the

selective erasure is realized by applying the phase shift of 180°. The second case (with electric field) includes both nonuniform distribution of the space charge field and the fringe bending effect. Figs. 1(a) and 1(b) show the time evolution of the diffraction efficiency of the composite grating for recording with and without electric field. First, the original grating was recorded for a certain period of time, then various relative phase shifts were introduced in one of the two writing beams at $t_N = 2.0$ for Fig. 1(a) and $t_N = 0.5$ for Fig. 1(b). Phase shift ψ was determined so that the diffraction efficiency reaches the minimum value during the erasure process: $\psi = 180°$ for the case with no electric field and $\psi = 285°$ for the case with the dc electric field of 8 kV/cm. Both cases show reasonably large decrease in diffraction efficiency. Figs. 2(a) and 2(b) show the normalized amplitude of the space charge field $|E_{sc}| / E_q$ as a function of crystal depth z at various times after the phase shift was introduced. Fig. 2(a) shows that the original grating in the deeper region of the crystal is erased faster by the superimposed one than that in the shallower region because the initial space charge field distribution is nonuniform due to beam coupling. Fig. 2(b) shows that the original grating is completely erased only at the center of the crystal. Since the fringe bending results in dramatic phase change between the interference pattern and the space charge field, simply applying a constant phase shift does not lead to the effective erasure of the original grating over the entire crystal thickness. Both Figs. 2(a) and 2(b) indicate that there remains residual grating when the overall grating diffraction efficiency reaches zero. This contradiction between the zero diffraction efficiency and the residual grating is clearly explained in Figs. 3(a) and 3(b). Figs. 3(a) and 3(b) show the integrated diffraction efficiency as a function of crystal depth z at various times. Since the phase of the composite grating varies depending on the crystal depth z, the diffracted beams from the shallower region and the deeper region of the crystal destructively interfere and result in smaller integrated diffraction efficiency at the output surface of the crystal.

The dynamics of the composite grating is investigated using numerical calculations including the effects of beam coupling. Both nonuniform distribution of the space charge field and the fringe bending result in the residual grating after the erasure process. Simple analytical solutions which neglect beam coupling effects will be compared with the simulation results in terms of memory applications at the presentation.

References

1. J. P. Huignard, J. P. Herriau and F. Micheron, Ferroelectrics **11**, 393 - 396 (1976).
2. A. Marrakchi, Opt. Lett. **14**, 326 - 328 (1989).
3. J. H. Hong, S. Campbell and P. Yeh, Appl. Opt. **29**, 3019 - 3025 (1990).
4. H. Sasaki, J. Ma, Y. Fainman, S. H. Lee and Y. Taketomi, Opt. Lett. **17**, 1468 - 1470 (1992).
5. H. Sasaki, J. Ma, Y. Fainman and S. H. Lee, *Nonlinear Optics; Materials, Fundamentals, and Applications Technical Digest* **18**, 88 - 90 (1992).
6. N. Kukhtarev, V. Markov and S. Odulov, Opt. Commun. **23**, 338 - 343 (1977).
7. J. M. Heaton and L. Solymar, Optica Acta **32**, 397 - 408 (1985).
8. N. V. Kukhtarev, Sov. Tech. Phys. Lett. **2**, 438 - 440 (1976).
9. J. Ma, J. E. Ford, Y. Taketomi and S. H. Lee, Opt. Lett. **16**, 270 - 272 (1991).
10. J. E. Ford, J. Ma, Y. Fainman, S. H. Lee, Y. Taketomi, D. Bize and R. R. Neurgaonkar, J. Opt. Soc. Am. A **9**, 1183 - 1192 (1992).
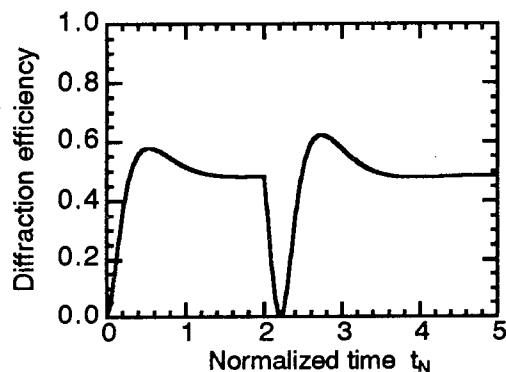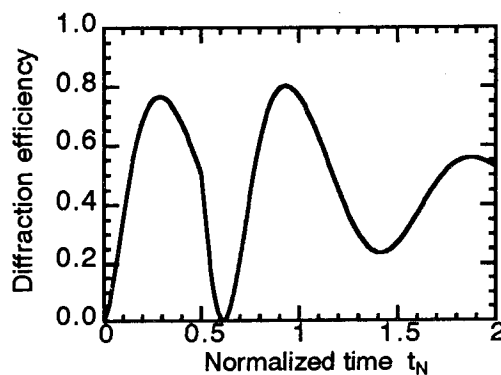
(a)   (b)

Figure 1. Time evolution of the diffraction efficiency of the composite grating with (a) no electric field and (b) dc electric field of 8 kV/cm along the optic axis.
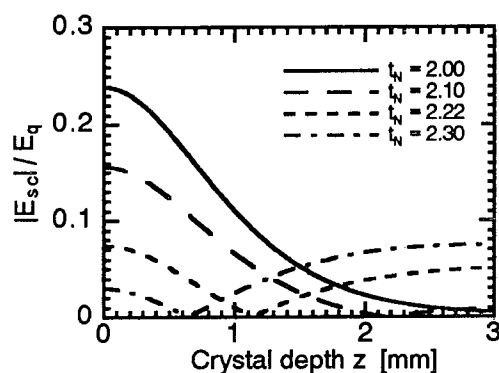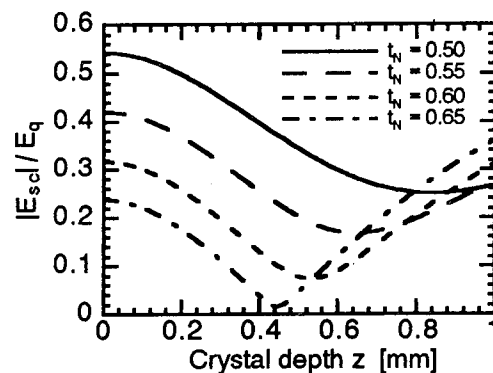
(a)   (b)

Figure 2. Normalized space charge field $|E_{sc}|$ / E_q as a function of crystal depth z with (a) no electric field and (b) dc electric field of 8 kV/cm along the optic axis.
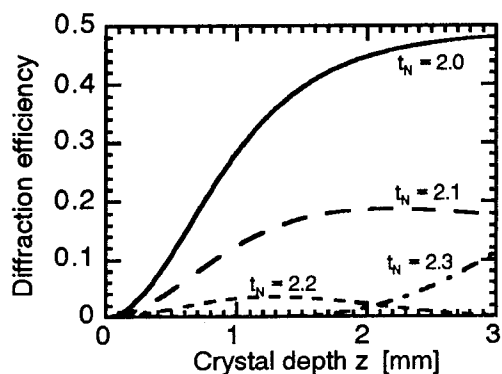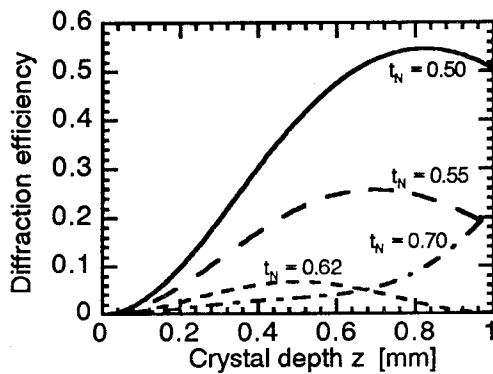
(a)   (b)

Figure 3. Integrated diffraction efficiency of the composite grating as a function of crystal depth z with (a) no electric field and (b) dc electric field of 8 kV/cm along the optic axis.

MP8

Controlling Unstable Periodic Orbits in a Nonlinear Optical System: the Ikeda Map

P. M. Alsing, A. Gavrielides, and V. Kovanis

Nonlinear Optics Center, Phillips Laboratory, 3350 Aberdeen Avenue SE, Kirtland AFB, NM 87117-5776

SUMMARY

With the publication of the seminal paper by Ott, Grebogi and Yorke (OGY) [1] the concept of *controlling* chaos has become part of the lexicon of physicists and engineers dealing with chaotic nonlinear dynamical systems. The authors showed that by using small, judiciously applied perturbations the unstable periodic orbits, which are dense in a chaotic attractor, could be stabilized. The strength of their approach lies in the absence of the necessity for any *a priori* analytical model of the chaotic system in order to affect the control. The information required to construct the controlling perturbations can be extracted from experimental time series obtained from the unperturbed system. Since the publication of [1], the OGY controlling algorithm, and numerous variations upon its central concepts, have been implemented numerically and experimentally in a host of nonlinear dynamical systems ranging from lasers and electronic circuits to chemical and biological systems. For excellent review articles see [2] and the references therein.

In this paper we wish to discuss the application of the OGY scheme and some of its variants to the Ikeda-Hammel-Jones-Maloney map given by [3]

$$z_{n+1} = p_0 + R z_n exp \left[i\phi - i\frac{\alpha}{1+ \mid z_n \mid^2} \right]. \quad (1)$$

The Ikeda map can be envisioned as arising from a string of light pulses of intracavity amplitude E_n impinging on a partially transmittig mirror M_1 of a ring cavity with a nonlinear dispersive medium, as depicted in Fig. 1. Here we assume the time interval between the pulses is adjusted to the round-trip travel time in the ring cavity. This form of the map assumes that saturable absorption has been ignored and that the dimensionless detuning of the laser two-level-atom $\Delta \gg 1$ [$\Delta = (\omega - \omega_{ab})/\gamma_\perp$], but not so large that we are in the Kerr limit. In addition, the usual assumption has been made that the response of the nonlinear medium in the cavity is much faster than the cavity round trip time. The various parameters of the Ikeda map are defined as follows:

$$p_0 = \sqrt{T}\frac{E_{in}}{\Delta}, \qquad \phi = kL,$$

$$\alpha = \frac{\alpha_0 L}{2\Delta}, \qquad z_n = \frac{E_n}{\Delta},$$

where p_0 is the dimensionless input amplitude, $T = 1 - R$ is the input and output mirror intenstiy transmission function, ϕ is the laser empty-cavity detuning, $\alpha_0 L$ is the linear absorption per pass, and z_n is the dimensionless intracavity complex field amplitude. The map is area

contracting, i.e. $det J = R^2 = \lambda_1\lambda_2 < 1$, where λ_1 and λ_2 are the the eigenvalues of the Jacobian J of the map.

The Ikeda map demonstrates a richness of nonlinear phenomena such as bistability, hysteresis, period doubling bifurcations and chaos. Recently, van der Mark *et al.* [4] have conducted experiments using a single-mode glass fiber as the nonlinear dispersive medium and 10 ps laser pulses in a ring cavity to investigate the influence of group velocity dispersion and pulse shape in the map.
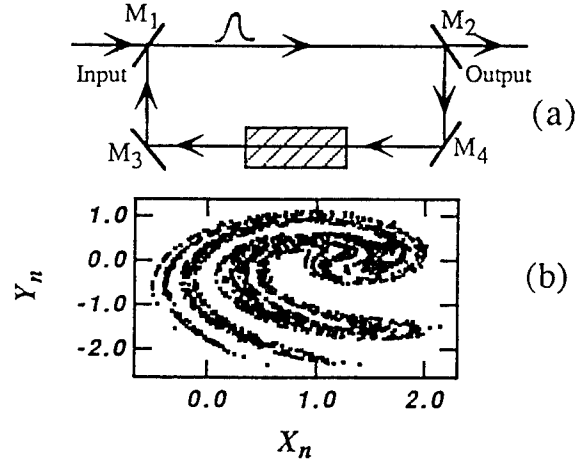
Fig. 1: (a) Ikeda map viewed as a sequence of pulses entering a ring cavity with a nonlinear dispersive medium through a partially tranmitting mirror M_1; (b) the chaotic attractor for the Ikeda map Eq. (1), ($z_n = x_n + iy_n$) with parameter values $p_0 = 1.25$, $R = 0.9$, $\phi = 0$ and $\alpha = 7.0$.

For the parameter values $p_0 = 1.25$, $R = 0.9$, $\phi = 0$ and $\alpha = 7.0$ the Ikeda map is chaotic. We wish to apply the OGY algorithm to control the unstable periodic orbit buried inside the attractor. Before we begin, we first recall the derivation of the OGY formula for a general chaotic nonlinear dynamical system.

Let ξ_n be a vector of the phase space variables of some dynamical system at the crossing of some surface of section through which the trajectories pass. There exits a Poincaré map F, depending on some control parameter p, which relates the values of successive iterative crossings via $\xi_{n+1} = F(\xi_n, p)$. In their original paper, Ott, Grebogi and Yorke [1] derived a formula for the perturbations necessary to control the unstable periodic orbits

$$\delta p_n = \frac{\lambda_u}{\lambda_u - 1} \frac{f_u \cdot (\xi_n - \xi_F(p_0))}{f_u \cdot g}. \quad (2)$$

Here, λ_u is the eigenvalue of the unstable contravariant eigenvector f_u of the local mapping $D_\xi F(\xi_F, p_0)$, eval-

72

uated at the fixed point $\boldsymbol{\xi}_F$, of $\boldsymbol{F}$, and $\boldsymbol{g} \equiv \boldsymbol{D}_p \boldsymbol{F}(\boldsymbol{\xi}_F, p_0)$ the shift of the fixed point due to a change in the control parameter. The OGY formula is derived by requiring that upon application of the perturbation, the next iterate of the mapping falls on the stable manifold of the fixed point. If this is the case, then successive iterates of the mapping will be attracted to the fixed point, and a period one orbit will have been extracted from the chaotic attractor. Equation (1) is derived for a local mapping with one unstable eigenvalue ($|\lambda_u| > 1$), which is applicable to the Ikeda map.

For the parameter values used, the Ikeda map has an unstable fixed point at $(x_F, y_F) = (0.6723, 0.4132)$. To measure $\boldsymbol{g}$, the change in the fixed point as we vary the dimensionless input p_0, we could observe the Ikeda map at an input value of $p_0 + \delta p$, measure the new fixed point and approximate $\boldsymbol{g} \approx \{[x_F(p_0 + \delta p) - x_F(p_0)]/\delta p, [y_F(p_0 + \delta p) - y_F(p_0)]/\delta p\}$. A strict application of the OGY formula would imply a measurement of the real and imaginary parts of the electric field amplitude z_n, which constitutes the 2 dimensional phase space. Figure 2 shows a numerical implimentation of Eq. (2) where the control is turned on at some arbitrary iterate $n = 0$ after the system has been running for some time such that all subsequent points are on the attractor.
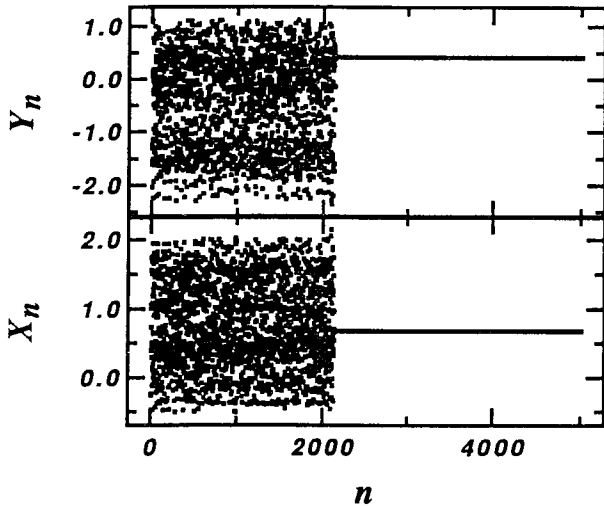
Fig. 2: A straight forward implementation of Eq. (2) showing the stabilization of the unstable period 1 orbit of the Ikeda map located at $(x_F, y_F) = (0.6723, 0.4132)$.

The Ikeda map is an example of a nonlinear differential-delay dynamical system for which a map can be derived. Recently Gavrielides *et al.* [5] have demonstrated that by using the OGY algorithm, unstable orbits of up to period eight can be controlled in the Lang-Kobayashi system. This system is described by a set of three nonlinear differential-delay equations describing chaos in a semiconductor laser subject to a small amount of optical feedback from an external mirror.

In an actual experiment, the detection of the real and imaginary parts of the electric field is not practical. A

more accessible experimental variable is the intensity $I_n = \boldsymbol{H}(z_n) \equiv |z_n|^2 = x_n^2 + y_n^2$. However, the intensity poses a problem for the OGY formula since Eq. (1) has assumed that $\boldsymbol{\xi}_n$ is the state of the system defined by the full set of phase space variables, for which single scalar time series I_n is clearly not. Dressler and Nitsche [6] addressed this problem by considering the modification of the OGY formula when a *delay coordinate vector* $\boldsymbol{X}(t) = \{x(t), x(t - \tau), \ldots, x(t - (M-1)\tau)\}$, constructed from a single scalar time series $x(t)$, is used to reconstruct the attractor. The mapping from the full set of phase space variables to the delay coordinates introduces a dependence of the Poincaré map $\boldsymbol{F}$ on p_{n-1} in addition to the normal dependence on p_n. For the case of the Ikeda map we can consider a vector $\boldsymbol{\xi}_n \equiv \{I_n, I_{n-1}, \ldots, I_{n-(M-1)}\}$, where I_n is the value of the intensity at the nth peak ($\dot{I}(t) = 0, \ddot{I}(t) < 0$). In this case we do not have a delay coordinate embedding, but the mapping $\boldsymbol{H}$ induces a similar additional dependence of $\boldsymbol{F}$ on δp_{n-1}, i.e. $\boldsymbol{\xi}_{n+1} = \boldsymbol{F}(\boldsymbol{\xi}_n, p_{n-1}, p_n)$. Therefore, a perturbation formula can be derived in exact analogy with that of Dressler and Nitsche by requiring that $\boldsymbol{f}_u \cdot \delta \boldsymbol{\xi}_{n+2} = 0$ and $\delta p_{n+1} = 0$ yielding [6]

$$\delta p_n = -\lambda_u \left(\frac{\lambda_u}{\lambda_u \boldsymbol{f}_u \cdot \boldsymbol{u} + \boldsymbol{f}_u \cdot \boldsymbol{v}} \boldsymbol{f}_u \cdot \delta \boldsymbol{\xi}_n \right.$$
$$\left. + \frac{\boldsymbol{f}_u \cdot \boldsymbol{v}}{\lambda_u \boldsymbol{f}_u \cdot \boldsymbol{u} + \boldsymbol{f}_u \cdot \boldsymbol{v}} \delta p_{n-1} \right), \qquad (3)$$

with $\boldsymbol{u} \equiv \boldsymbol{D}_{p_n} \boldsymbol{F}$ and $\boldsymbol{v} \equiv \boldsymbol{D}_{p_{n-1}} \boldsymbol{F}$ evaluated at the fixed point $\boldsymbol{\xi}_F(p_0)$ and $p_n = p_{n-1} = p_0$. Equation (3) is in fact the controlling perturbation formula for the simplest case of projecting down from a general N-dimensional phase space state vector (here $N = 2$) to a single scalar variable. This projection produces a dependence of δp_n on the history of the $N - 1$ previous values of the perturbations [7]. Figure 3 shows the stabilization of the intensity unstable periodic orbit at the fixed point $I_F = x_F^2 + y_F^2$.
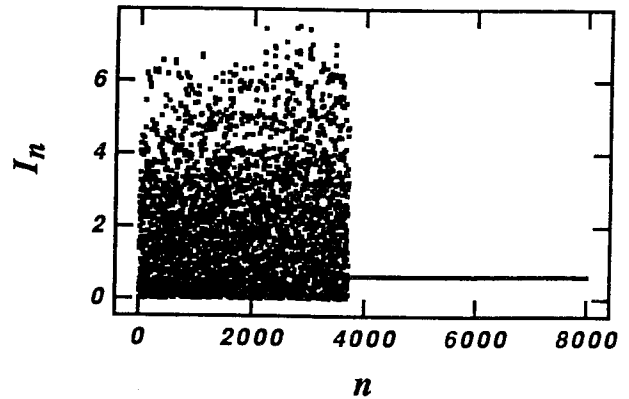
Fig. 3: Stabilization of the Ikeda map from measurements of the intensity peaks I_n, via Eq. (3). Here $\delta \boldsymbol{\xi}_n = (I_n - I_F, I_{n-1} - I_F)$ where $I_F = x_F^2 + y_F^2$ and $(x_F, y_F) = (0.6723, 0.4132)$.

Notice that the above OGY perturbation formulas use

data $\delta\xi_n$ measured at the nth peak to control the $n+1$ peak. Depending upon the apparatus used in an experiment, one may be concerned about the time involved in the process of detecting the peak of the intensity, calculating the controlling perturbation and then implementing it. For example, in the experiment by van der Mark *et al.* [4], the cavity round-trip time was 48ns. To tackle such situations, Alsing *et al.* [8] have developed an OGY-based controlling scheme which utilizes data measured at the $n-k$ peak to control the $n+1$ peak. They call this method *prior iterate control* (PIC). The PIC formula corresponding to the Dressler and Nitsche formula Eq. (3) is

$$\delta p_n^{(1)} = -\lambda_u \left[\lambda_u \left(\frac{\lambda_u}{\lambda_u f_u \cdot u + f_u \cdot v} f_u \cdot \delta\xi_{n-1} \right. \right.$$
$$\left. \left. + \frac{f_u \cdot v}{\lambda_u f_u \cdot u + f_u \cdot v} \delta p_{n-2}^{(1)} \right) + \delta p_{n-1}^{(1)} \right] \quad (4)$$

where the superscript (1) on δp's denote the use of data measured one iterate back to affect the control. An application of Eq. (4) to the Ikeda map yields a plot of I_n versus n similar to Fig 3. For one iterate back, the transient time preceeding the time to control is essentially the same as for Eq. (3).

Note that the first two terms of Eq. (4) are just the negative of the Dressler Nistsche formula Eq. (3) with the change of indices from $n \to n-1$. When $\delta p_n = 0$, the terms inside the square brackets simply reproduce the Dressler Nitsche formula one iterate back. Therefore, instead of using the data $\{\delta\xi_n, \delta p_{n-1}\}$ to control the nth peak, the PIC formula Eq. (4) uses the information $\{\delta\xi_{n-1}, \delta p_{n-2}, \delta p_{n-1}\}$, one iterate back, to accomplish the same task. The extra factor of λ_u out front has the implication that the control region for the PIC formula is $|\lambda_u|$ times smaller than the corresponding region when Eq. (3) is used. This point is discussed more fully in [8].

The general form of PIC perturbation formula using data measured k iterations back is

$$\delta p_n^{(k)} = \lambda_u \left[-\delta p_{n-1}^{(k)} + \lambda_u \left[-\delta p_{n-2}^{(k)} + \lambda_u \left[\dots \right. \right. \right.$$
$$\left. \left. \left. + \lambda_u \left[-\delta p_{n-k}^{(k)} + \delta p_{n-k}^{(OGY)} \right] \right] \dots \right] \quad (5)$$

where $\delta p_{n-k}^{(OGY)}$ denotes an OGY controlling formula [e.g. Eq. (2) or Eq. (3)] with the index on $\delta\xi_n$ shifted to $n-k$. We can view Eq. (5) as follows. At the nth iterate we measure the signal difference $\delta\xi_n$ and apply the perturbation $\delta p_n^{(k)}$ which has been calculated using the signal difference $\delta\xi_{n-k}$. By shifting the indices of Eq. (4) from $n \to \{n+1, n+2, \dots, n+k\}$, we have all the necessary information to calculate $\{\delta p_{n+1}^{(k)}, \delta p_{n+2}^{(k)}, \dots, \delta p_{n+k}^{(k)}\}$ at the nth iterate. By keeping a history of the $\delta\xi_n$ and $\delta p_n^{(k)}$ used, we can always maintain a difference of k iterations between the time at which we compute the perturbation and the time when we need to apply it.

As a final implementation of an OGY-based controlling algorithm we note that Alsing *et al.* [9] have demonstrated numerically that a feed-forward backpropagating neural network can be trained to control unstable periodic orbits for a variety controlling perturbation formulas. It has been shown by a number of authors [10] that neural networks can be useful in extracting chaotic attractors from noisy data. The thrust of [9] was to show that the neural network need only be trained about the fixed point of the attractor and the necessary information could be extracted soley from experimental data obtained from the unperturbed system.

When training is performed with the above OGY-based formulas in which δp_n depends on δp_{n-1} the neural network is implicitly learning the chaotic map locally about the fixed point. Even though the neural network is trained on the unperturbed system, in which case the fixed point is at $\xi_F(p_0)$, it is still able to control the unstable periodic orbit in the presence of a iterate dependent fixed point $\xi_F(p_n)$ where $p_n = p_0 + \delta p_n$. This is a manifestation of the robustness exhibited by the OGY algorithm in its tolerance of small amounts of noise in the controlling perturbation.

[1] E. Ott, C. Grebogi, and J. A. Yorke, Phys. Rev. Lett. **64**, 1196 (1990).

[2] T. Shinbrot, E. Ott, C. Grebogi, and J. Yorke, Nature **363**, 411 (1993); T. Shinbrot, Nonlinear Science Today **3**, 1 (1993).

[3] K. Ikeda, Opt. Comm. **30**, 257 (1979); S.M. Hammel, C.K.R.T. Jones, and J.V. Maloney, J. Opt. Soc. Am. B **2**, 552 (1985); F.M. Mitschke, Invited Talk, 2nd Exp. Chaos Conf., Arlington, VA (October 1993).

[4] M.B. van der Mark, J.M. Schins, and A. Lagendijk, Opt. Comm. **98**, 120 (1993).

[5] A. Gavrielides, V. Kovanis, and P.M. Alsing, Chaos in Optics, R. Roy, Ed., Proc. SPIE **2039**, 250 (1993); A. Gavrielides and V. Kovanis, Phys. Rev. E (in press).

[6] U. Dressler and G. Nitsche, Phy. Rev. Lett. **68**, 1 (1992).

[7] D. Auerbach, E. Ott, C. Grebogi, and J. A. Yorke, Phys. Rev. Lett. **69**, 3479 (1992).

[8] P.M. Alsing, A. Gavrielides, and V. Kovanis, Chaos and Nonlinear Dynamics: Methods and Commercialization, H.S. Wisniewski, Editor, Proc. SPIE **2037** 126 (1993); Phys. Rev. E **49**, 1225 (1994).

[9] P.M. Alsing, A. Gavrielides, and V. Kovanis, "History dependent control of unstable periodic orbits," submitted to Phys. Rev. E (1994).

[10] A. Lapedes and R. Farber, Tech report LAUR-87-2662, Los Alamos National Laboratory (1987); A.M. Albano, A. Passamante, T. Hediger and M.E. Farrell, *Physica D* **58**, 1 (1992).

SPONTANEOUS PATTERN FORMATION IN AN ABSORPTIVE SYSTEM

W. J. Firth and A. J. Scroggie
Department of Physics and Applied Physics
John Anderson Building
107 Rottenrow
Glasgow, G4 0NG, UK
Telephone No. (UK) 41 552 4400

We present analytical and numerical results indicating pattern formation in a purely absorptive medium, namely a resonantly-excited two-level system in a ring cavity. Pattern formation occurs when the cavity is mistuned such that the optical wavelength exceeds that of the nearby cavity mode. But then off-axis or "tilted" waves can exactly fit the cavity, and this determines the dominant transverse wave vector of the pattern. This is a geometrical, linear, and very general mechanism found also in lasers [1] and recently in OPO's [2].

We use the mean-field ring cavity model described by the Maxwell-Bloch equations [3–5]. In terms of deviations from the steady state values:

$$x = x_s(1 + A); \quad p = p_s(1 + P); \quad f = f_s(1 + F) \tag{1}$$

the Maxwell-Bloch equations are exactly equivalent to:

$$\dot{A} = \kappa \left[-A(1 + i\theta) - \frac{2C(1 - i\Delta)}{1 + \Delta^2 + I} P + ia\nabla^2 A \right] \tag{2}$$

$$\dot{P} = \gamma_\perp (1 + i\Delta) [A + F - P + AF] \tag{3}$$

$$\dot{F} = -\gamma_\parallel \left[F + I Re \left(\frac{P^* + A + P^* A}{1 - i\Delta} \right) \right] \tag{4}$$

where $I = |x_s|^2$, and the other symbols have their usual meanings [4]. There is a pattern-forming instability with $K = K_c$ where

$$\theta + aK_c^2 = 0 ; \quad \theta < 0 \tag{5}$$

This is precisely the condition under which the tilt of the perturbation wave cancels the cavity mistuning. For $\Delta \neq 0$, the medium contribute to the cavity tuning and complicates the interpretation of K_c.

We have performed perturbative nonlinear analysis of (2, 3, 4), and obtain amplitude equations with a diffusive spatial coupling. The system is well-behaved around $\Delta = 0$ for finite, negative θ. A quadratic coupling characteristic of hexagon formation is found [6]. Unusually for an optical system, it may be of either sign, or indeed zero, implying that both positive and negative hexagons, and also rolls, should exist as stable patterns for appropriate parameter values.

We have developed numerical codes to simulate the system on a square grid with periodic boundary conditions. We concentrate on the case $\Delta = 0$ and $\theta = -1$. Selecting a value of C greater than 4 and increasing I across the instability region, we observe a transition in the stable pattern which forms from noise: "hexagonal spot patterns" (H^+) for $I < 3$; rolls for $I \simeq 3$; "honeycomb (H^-) for $I > 3$ (see Figure 1). Near basin boundaries, domains of different patterns typically form from noise, then one pattern invades the other, eventually winning (see Figure 2).

Results for the case $\Delta \neq 0$ are broadly similar to those described for $\Delta = 0$, and relevant analysis and simulations will be presented. Extension of these models to describe real alkali vapours [7], by inclusion of polarisation and optical pumping dynamics, will be described.

References

[1] P. K. Jakobsen, J. V. Moloney, A. C. Newell and R. Indik, Phys.Rev.A **45**, 8129–8137 (1992)

[2] G.-L. Oppo, M. Brambilla and L. A. Lugiato, Phys.Rev.A (in press)

[3] L. A. Lugiato and R. Lefever, Phys.Rev.Lett. **58**, 2209 (1987)

[4] L. A. Lugiato and C. Oldano, Phys.Rev. A **37**, 3896 (1988)

[5] P. Mandel, M. Georgiou and T. Erneux, Phys.Rev. A **47** 4277 (1993)

[6] W. J. Firth, A. J. Scroggie, G. S. McDonald and L. A. Lugiato, Phys.Rev. A **46**, R3609 (1992)

[7] A. Petrossian, M. Pinard, A. Maitre, J. Y. Courtois and G. Grynberg, Europhys.Lett. **18**, 689 (1992)

(a)   (b)   (c)
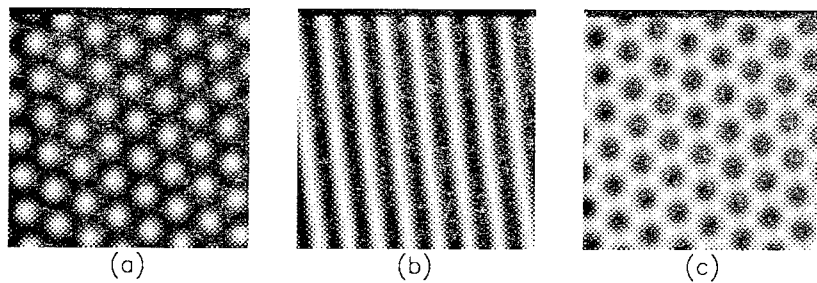
Figure 1: Example of the change in the stable pattern observed as I is varied at a fixed value of $C(= 4.4)$. (a) H^+ for $I = 2.9$ (b) rolls for $I = 3.3$ (c) H^- for $I = 4.5$. $\Delta = 0$, $\theta = -1$.

(a)   (b)   (c)
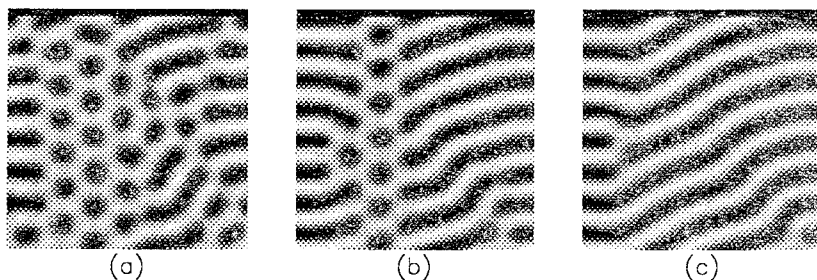
Figure 2: Time sequence showing roll–H^- competition with rolls winning. The figures show the real part of the field at (a) t=240, (b) t=400, (c) t=560 cavity lifetimes. $\Delta = 0$, $\theta = -1$, $I = 5.5$, $C = 5$. The defects in the roll pattern persist with no perceptible change until the end of the simulation (t=3600 cavity lifetimes).

TIME-RESOLVED DFWM SPECTROSCOPY OF FULLERENE IN TOLUENE AND GLASS

Huimin Liu and Weiyi Jia

Department of Physics, University of Puerto Rico, Mayaguez,
PR 00681, U.S.A. Tel: (809)-265-3844

Recently, the interest in the nonlinear optical properties of C_{60} and C_{70} have resulted in a great number of experiments[1-3]. These experiments focus on the third order susceptibility of these material using a variety of techniques. In these experiments , emphasis was placed on the determination of the third order nonlinear susceptibility $\chi^{(3)}$. The large variations in the measurements have caused a number of discussions[2,3]. In order to to understand the reason causing the discrepancies in numerical determination of $\chi^{(3)}$ we use time-resolved DFWM spectroscopy to show that three signal components appeared with time evolution, which obscured the intrinsic signal associated with the measurement of $\chi^{(3)}$. Furthermore, attempt to add fullerene into a laser glass host was made. To compare the DFWM spectroscopy of fullerene in toluene with that of fullerene in glass shows that fullerene does exist in glass matrix after melting at high temperature.

Single 20 ps pulse from a Nd:YAG laser operating at $\lambda = 532$ nm was used in the conventional backward propagating degenerate four-wave mixing geometry[4]. The purified C_{60} and C_{70} powder samples were provided by Dr. D.R. Huffman. Fullerene-doped inorganic fluorophosphate glass was prepared by using a special device to isolate from the atmosphere and melted at high temperature. The obtained glass sample is transparent and the electronmicroscopy analysis shows that fullerene is dissolved homogeneously in glass matrix.

The observed ps-DFWM spectrum is categorized into three probe delay time regions as shown in the figure: a sharp scattering peak at zero delay with a FWHM equal to the autocorrelation of the three pulses, a small decaying transient signal which lasts a couple of hundred picoseconds and is then obscured by the third intense, periodic signal. The left side of the figure shows the time dependence of the absolute diffraction efficiency for 0.4g/ℓ C_{60}-toluene solution along with that of pure toluene. It is seen that the intensity of each signal component is dependent on the sample. In particular, the absolute scattered probe-signal intensity of the peak at zero delay (coherence peak) decreases with addition of C_{60} to toluene. Conversely, the maximum of the periodic signal undergoes a anomalously large increase due to the presence of C_{60} and C_{70}. Therefore, while the coherence peak is the dominant scattering mechanism in toluene with an intensity ratio of I(coherence)/I(periodic) ~ 20, the periodic peak is the dominant mechanism in C_{60}-toluene samples with a ratio of I(periodic)/I(coherence) ~ 20. The coherent peak is associated with the third order susceptibility $\chi^{(3)}$ of the material, and the periodic oscillation signal originates from laser-induced-phonon-spectroscopy(LIPS)[5]. The inset in the figure shows a
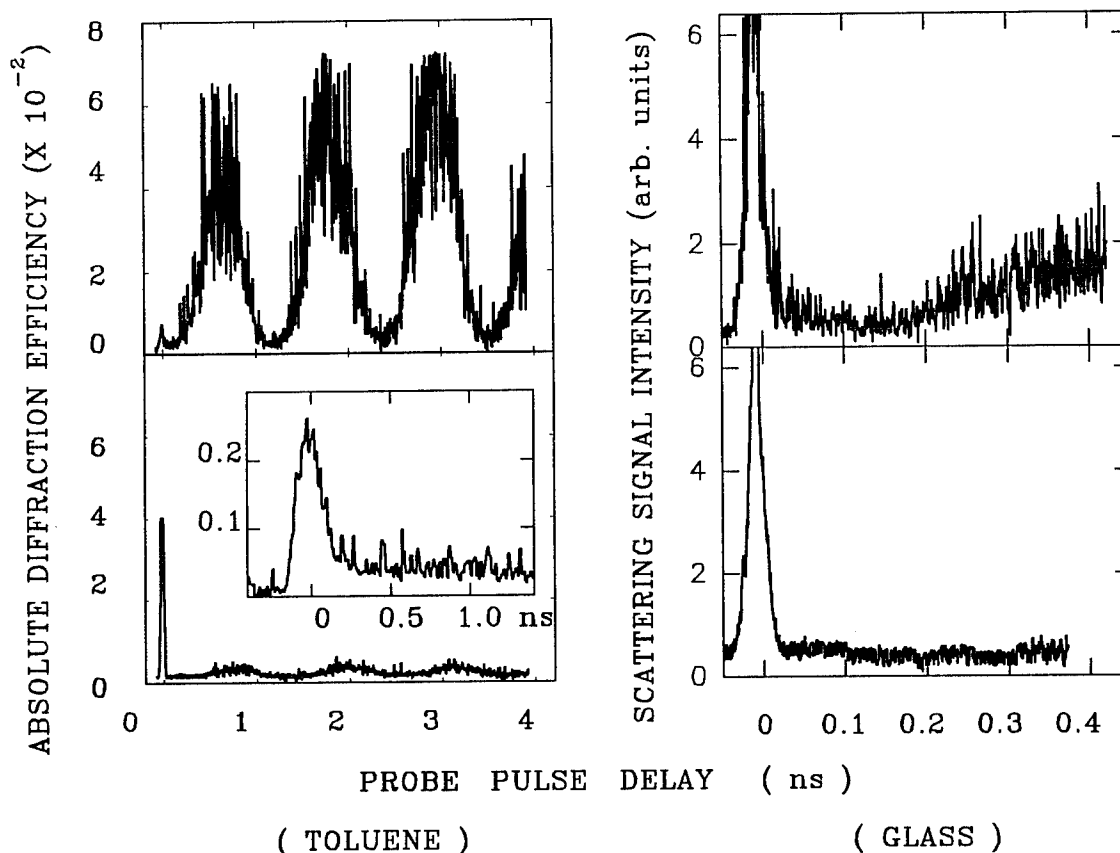
FIGURE. Time—resolved DFWM spectra of fullerene in toluene(Top—left) and fluorophosphate glass(Top—right). The lower traces represent the DFWM spectra of undoped toluene solvent and glass. The experiments were conducted at pump beam crossing angle of 21.1° for the left and 8.1° for the right. The inset(on the left) shows the expansion of coherent peak at zero delay, representing the population grating.

population grating signal which is immediately following the coherence peak and only observable in the fullerene doped toluene or glass. The population grating is produced by optical excitation from singlet S_0 state of fullerene to excited S_1 state followed by a rapid relaxation to triplet T_1 state.

The right side of the figure represents the spectrum of fullerene-doped fluorophosphate glass. The intensity ratio of I(periodic)/I(coherent) was measured to be ~0.8, much smaller than that of fullerene-doped toluene. The reason for less intense LIPS signal in glass is due to much smaller concentration of fullerene, which has so far been achieved. The population grating signal was also observed in glass. The decay rate of the signal is ~10^6/s, much larger than ~10^4/s for C_{60}-toluene[6], reflecting a stronger lattice relaxation existing in glass matrix.

Changes in the refractive index at zero delay can be divided as those arising from toluene and those due to fullerene. These coefficients are related to $\chi^{(3)}$ and the values estimated through comparison with scattering from CS_2. $\chi^{(3)}$ for pure toluene was found to be 3.7×10^{-14}(esu). Since the coherence peak is reduced in the fullerene solutions, it can be concluded that the contributions due to dopants are opposite in sign to those due to the solvent. This is consistent with previous studies in these materials[7]. Numerical estimations of dopant contributions are further complicated by inclusion of scattering due to absorption changes. Such changes may arise in these samples since addition of dopants increases absorption at 532 nm[7].

The signal, at longer delays, due to LIPS has two main characteristics. Firstly, the LIPS signal in fullerene-toluene is at least an order of magnitude greater than the LIPS signal due to pure toluene. Secondly, the ratio of scattered signal due to $\chi^{(3)}$ to LIPS undergoes two orders of magnitude decrease due to presence of fullerene dopants. This reduction was found to be even larger from C_{60} to C_{70} doped toluene samples. It originates from (i) increase in the LIPS signal due to C_{60} or C_{70}, (ii) the decrease in the coherence peak due to presence of oppositely contributing factors.

To summarize, addition of C_{60} to solvent and glass matrix increases the LIPS signal by at least an order of magnitude while decreasing the coherence peak by a factor of 3.4 in C_{60}-toluene, and a factor of 5.3 in C_{70}-toluene. Such an effect may result in erroneous calculations of $\chi^{(3)}$ which are based on comparison of the coherence peak with a standard of CS_2.

REFERENCES:
1. W.J.Blau, H.J.Byrne, D.J.Cardin, T.J.Dennis, J.P.Hare, H.W.Kroto, R.Taylor and D.R.M.Walton, Phys.Rev.Let., **67**, 1423(1991).
2. Z.H.Kafafi et al, Chem.Phys.Let., **188**, 492(1992).Phys.Rev.Lett., **68**, 2705(1992).
3. Y.Wang and L.T.Cheng, J.Phys.Chem. **96**, 1530 (1992).
4. H.Liu, R.C.Powell, L.A.Boatner, J.Appl.Phys., **70**, 20(1991).
5. M.D.Fayer, IEEE J.Quantum Electrn., **QE-22**, 1437(1986).
6. M.Lee et al., Chem.Phys.Lett., **196**, 325(1992).
7. Z.Zhang, D.Wang, P.Ye, Y.Li, P.Wu and D.Zhu, Optics Letters, **17**, 973(1992).

SENSITIVE DETECTION OF BIOMOLECULAR CHIRALITY BY NONLINEAR OPTICAL ACTIVITY

Thierry Verbiest, Martti Kauranen, and André Persoons

Laboratory of Chemical and Biological Dynamics, University of Leuven, Celestijnenlaan 200 D, B-3001 Heverlee, Belgium, Tel. +32-16-201015, Fax. +32-16-201368

Chiral molecules interact differently with left- and right-hand circularly-polarized light. This optical activity provides the basis for several linear optical techniques that can be used to detect molecular chirality. Optical-activity effects arise from contributions of magnetic-dipole transitions, in addition to the usual electric-dipole transitions, to the linear optical properties of chiral media [1]. Due to their helical structure, chiral molecules possess magnetic transition moments that are much larger than those of achiral (e.g., atomic) media.

Circular-difference effects have been predicted to occur also in nonlinear optical processes. Such effects were recently observed in second-harmonic generation from chiral molecules adsorbed at an air/water interface [2]. However, no conclusive evidence was provided as to which of the several proposed mechanisms would be responsible for the observed effects. We have studied nonlinear optical activity in second-harmonic generation from Langmuir-Blodgett monolayers of a synthetic chiral polymers. All observed effects are explained by a model that includes the contributions of both electric and magnetic dipole transitions to the second-order nonlinearity of the chiral surface. In this Paper, we use samples of bacteriorhodopsin as an example to show that such nonlinear optical activity can be used as a sensitive probe of chiral environment of biological material.

To include the contributions of magnetic-dipole transitions to the second-order nonlinearity of the chiral surface, we take the nonlinear polarization of the surface to be

$$P_i(2\omega) = \sum_{j,k} [\chi_{ijk}^{eee} E_j(\omega) E_k(\omega) + \chi_{ijk}^{eem} E_j(\omega) B_k(\omega)] \quad . \tag{1}$$

Similarly, the nonlinear magnetization of the surface is

$$M_i(2\omega) = \sum_{jk} \chi_{ijk}^{mee} E_j(\omega) E_k(\omega) \quad . \tag{2}$$

In Eqs. (1) and (2), $E(\omega)$ and $B(\omega)$ are the electric field and the magnetic induction field at the fundamental frequency, respectively. The subscripts i, j, and k refer to Cartesian coordinates and the superscripts e and m refer to electric and magnetic dipole interactions between the molecules and the light field, respectively. Thus, χ^{eee} is the usual second-order nonlinear susceptibility, which depends only on electric-dipole transitions, and χ^{eem} and χ^{mee} are susceptibilities that account for magnetic-dipole contributions to the nonlinearity [3]. For real molecular wavefunctions and for off-resonant excitation, the components of χ^{eee} are real and the components of χ^{eem} and χ^{mee} are imaginary. Furthermore, even under resonant conditions, this 90° phase difference between the electric and magnetic contributions is approximately preserved.

The chiral surface consists of a collection of electric and magnetic dipoles that radiate at the second-harmonic frequency. By averaging the dipoles over dimensions larger than molecules but smaller than wavelength, the effective oscillating dipole moments are proportional to the nonlinear polarization and magnetization given by Eqs. (1) and (2). In the far field, the electric component of the second-harmonic field that is radiated by the oscillating dipoles is

$$E(2\omega) \sim [n \times P(2\omega)] \times n - n \times M(2\omega) \quad , \tag{3}$$

where n is the direction of observation. The finite size of the fundamental beam provides a phase-matching condition in the plane of the surface. However, the sub-wavelength thickness
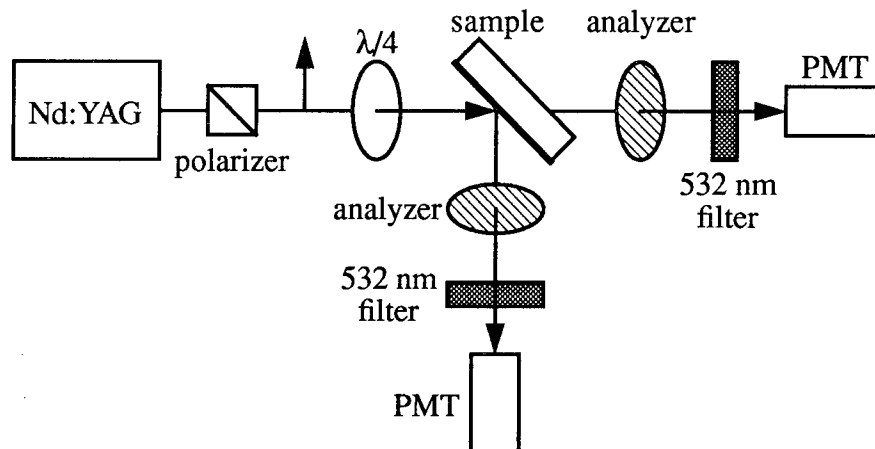
Figure 1. Schematic representation of the experimental setup.

of the surface allows second-harmonic light from elementary dipoles to be coherently added in the transmitted and reflected directions.

The nonlinear polarization and magnetization of the surface and the amplitudes of the reflected and transmitted second-harmonic fields can be directly calculated by using Eqs. (1)-(3) and the tensor components of χ^{eee}, χ^{eem}, and χ^{mee} that are compatible with the symmetry of the surface. The circular-difference response of the process then arises from interference between the electric (real) and magnetic (imaginary) contributions to the nonlinearity.

Our experimental setup is schematically shown in Fig. 1. We illuminate the chiral surface with the intense (~100 MW/cm^2) beam of an injection seeded Nd:YAG laser (1064 nm, ~10 ns pulse length, 10 Hz repetition rate). The polarization of the incident beam is varied from linear to left- and right-hand circular by means of a half-wave plate. The sample is oriented at ~45° angle of incidence with respect to the fundamental beam and the initial linear polarization of the beam is p-polarized with respect to the sample. The waveplate is rotated through an angle of 360° and the intensity of the s- and p-polarized components of the second-harmonic field is recorded in transmission and in reflection.

To assess the sensitivity of nonlinear optical activity in detecting chirality of biological material, we use bacteriorhodopsin as an example. We have observed nonlinear optical activity from all bacteriorhodopsin samples that were prepared, independent of the sample preparation. For a typical sample, a drop of bacteriorhodopsin in water is placed between two glass substrates. A typical experimental result is shown in Fig. 2(a). A theoretical fit to the experimental results based on our model is shown in Fig. 2(b). The efficiency of second-harmonic generation from the sample is seen to be strongly dependent on the helicity of the incident light.

It is interesting to compare these results to those obtained by linear circular dichroism from samples of bacteriorhodopsin [4]. We express the relative magnitude of the circular-difference effect as

$$\Delta I / I \ = \ 2 \, (I_{\text{left}} - I_{\text{right}}) / (I_{\text{left}} + I_{\text{right}}) \ , \tag{4}$$

where I is the intensity of the detected second-harmonic light and the subscripts refer to the helicity of the fundamental beam. For our bacteriorhodopsin samples, $\Delta I / I$ ranges from ~5% up to ~100%, depending on the polarization of the detected second-harmonic light. Linear circular-dichroism spectra of bacteriorhodopsin, on the other hand, typically show a relative circular-difference effect of $\Delta \varepsilon / \varepsilon = 0.1\%$, where ε is the (linear) molar extinction coefficient. Hence, the nonlinear circular-difference signal is up to three orders of magnitude higher than the linear. Furthermore, we typically used an amount of bacteriorhodopsin (10^{-11} moles) that is
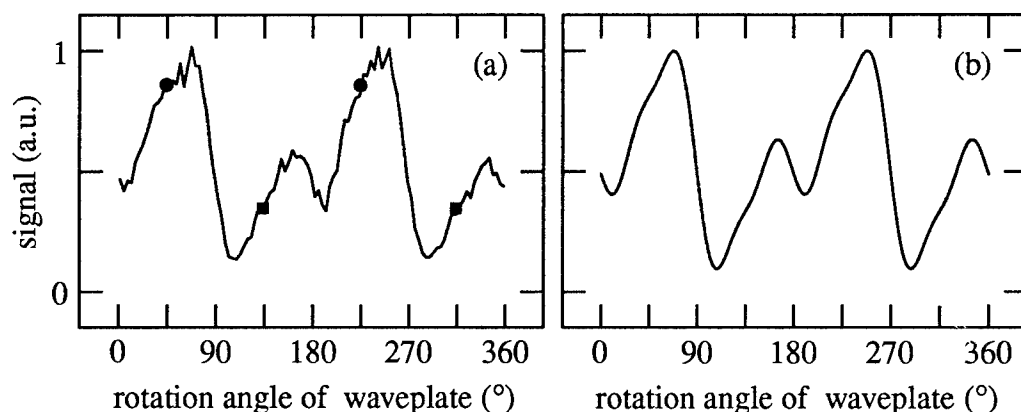
Figure 2. Experimental (a) and theoretical (b) results for the intensity of the *s*-polarized component of the second-harmonic field that is generated in the transmitted direction from bacteriorhodopsin. The plots are shown as functions of the rotation angle of the quarter-wave plate that was used to control the state of polarization of the fundamental beam. The linear polarization (0°, 90°, 180°, and 360°) corresponds to a *p*-polarized fundamental field with respect to the sample. The intensities of the second-harmonic field for the two circular polarizations (45°, 135°, 225°, and 315°) of the fundamental field are indicated by the circles and the squares.

three orders of magnitude less than that used in linear measurements. We believe that the amount of material can be further reduced in future refinements of our experiments. This high sensitivity makes this nonlinear approach a potential tool for analytical (bio)chemistry to detect chirality from small amounts of molecules.

Other advantages of nonlinear optical activity are related to properties of second-harmonic generation. Linear optical-activity effects in isotropic solution depend only on transitions from the ground state to the excited states of the molecules through $\mu \cdot \mathbf{m}$, where μ and $\mathbf{m}$ are the electric and magnetic dipole moments, respectively [1]. Hence, structural chirality of a molecule does not necessarily give rise to strong linear optical activity. Nonlinear optical activity depends also on transitions between different excited states. Furthermore, a large number of tensor components of second-order susceptibilities are allowed by the symmetry of chiral surfaces. Hence, nonlinear optical activity can be used to probe molecular properties linked to chirality on a more fundamental level than the linear techniques. Chiral molecules with low linear optical activity could therefore give rise to an easily measurable nonlinear optical activity. Also, nonlinear optical activity considered here is a surface-specific process provided that the media on the two sides of the surface are isotropic. This feature could be important in surface chemistry and cell biology because the nonlinear approach makes the chiral environment of biological membranes and interfaces accessible to measurement.

References

1.   E. U. Condon, Rev. Mod. Phys. **9**, 432 (1937).
2.   T. Petralli-Mallow *et al.*, J. Phys. Chem. **97**, 1383 (1993).
3.   P. S. Pershan, Phys. Rev. **130**, 919 (1963).
4.   B. Becher and J. Y. Cassim, Biophys. J. **16**, 1183 (1976).

Giant static dipole moment and polarizability in highly oriented J-aggregates

Kazuhiko Misawa and Takayoshi Kobayashi

Department of Physics, Faculty of Science, University of Tokyo,
7-3-1 Hongo, Bunkyo-ku, Tokyo 113, Japan
phone 81-3-3812-2111 ext.4228, fax 81-3-3818-7812

J-aggregates of cyanine dyes show a sharp absorption peak, called J-band, below the transition band of monomers [1, 2]. The band is due to the transition of excitons delocalized over an aggregate by intermolecular dipole interaction. A simple model of N identical molecules aligned in a one-dimensional chain has been proposed to explain the optical spectrum of the J-aggregates [3-6].

In the present paper, we report extremely large change in a static dipole moment and polarizability observed in oriented J-aggregates of 1,1'-diethyl-2,2'-quinocyanine bromide [pseudoisocyanine bromide (PIC-Br)] by electro-modulation spectroscopy. Recently, we have developed a new method, named "vertical spin-coating", to prepare highly oriented J-aggregates dispersed in polymer films [7, 8]. The solid-state oriented films prepared by the vertical spin-coating enabled us to measure the polarization dependence of the electro-absorption spectra for the first time. The electro-absorption spectra due to the Kerr effects were measured in all the four parallel and perpendicular configurations of both the polarization and static electric field with respect to the oriented axis.

The absorbance change due to the Kerr effect is given by

$$\Delta A_{\mathrm{Kerr}} = \frac{1}{2}\frac{\partial^2 A}{\partial E^2}(\Delta\mu\cdot\mathbf{F})^2 - \frac{1}{2}\frac{\partial A}{\partial E}\,\mathbf{F}{:}\Delta\alpha{:}\mathbf{F} \quad , \tag{2}$$

where $\Delta\mu, \Delta\alpha, \mathbf{F}, A, E$ are the static dipole change, the change in the linear polarizability, the applied electric field, the linear absorbance, and the photon energy, respectively.

Charge separation between the cationic dye molecules and anions is much larger than charge transfer among dye molecules to form the static dipole moment. The former should more likely cause the static dipole moment, and the static dipole change is due to the displacement of the anions. Since the motion of the anions is not instantaneous as electronic response, it results in some phase retardation,ϕ , of the response to the applied field.

The polarizability change is considered to be mainly due to π electrons in the J-aggregate. The response of the contribution from the polarizability is instanteneous.

Static dipole changes were determined corresponding to the four different configurations as shown in Fig. 1. These are larger than the static dipole change reported for polar organic molecules used in studies of the optical nonlinearities [9]. We recently conclude the size of the aggregates to be in the range from 20 to 100 [10]. Change in a static dipole moment in each molecular unit is no more than 1 debye.

Although the linear dichroism is remarkable, the static dipole change showed no large difference between the parallel and perpendicualr applied fields. Almost isotropic response of the EO effect in the oriented J-aggregates suggests that the displacement of the anions is most probable.

On the contrary, the polarizability change is dominant with the external field applied parallel to the chain axis, as shown in Fig. 2. The transient dipole moment of the one-dimensional excitons in the oriented J-aggregates is also in the same direction as the axis. This anisotropy in the polarizability change is interpreted in relation with delocalized excitons along the one-dimensional chain of J-aggregates.

The polarizability change obtained here is about 100 times larger than that of DMANS [9]. The enhancement is due to the delocalization of the excitons, and this factor means the average number of the constituent molecules in an aggregate. It is consitent with the aggregate size reported previously [10].

References

[1] E.E. Jelly, Nature **138**, (1936) 1009.

[2] G. Scheibe, Angew. Chem. **49**, (1936) 563.

[3] P.O.J. Scherer and S.F. Fischer, Chem. Phys. **86**, (1984) 269.

[4] E.W. Knapp, Chem. Phys. **85**, (1984) 73.

[5] G. Juzeliunas, Z. Phys. D **8**, (1988) 379.

[6] F.C. Spano and S. Mukamel, J. Chem. Phys. **91**, (1989) 7988.

[7] K. Misawa, H. Ono, K. Minoshima, and T. Kobayashi, Appl. Phys. Lett. **63**, (1993) 577.

[8] K. Misawa, H. Ono, K. Minoshima, and T. Kobayashi, J. Lumin., in press.

[9] H. Kuhn and A. Schweig, Chem. Phys. Lett. **1**, (1967) 255.

[10] K. Minoshima, M. Taiji, K. Misawa, and T. Kobayashi, Chem. Phys. Lett., in press.
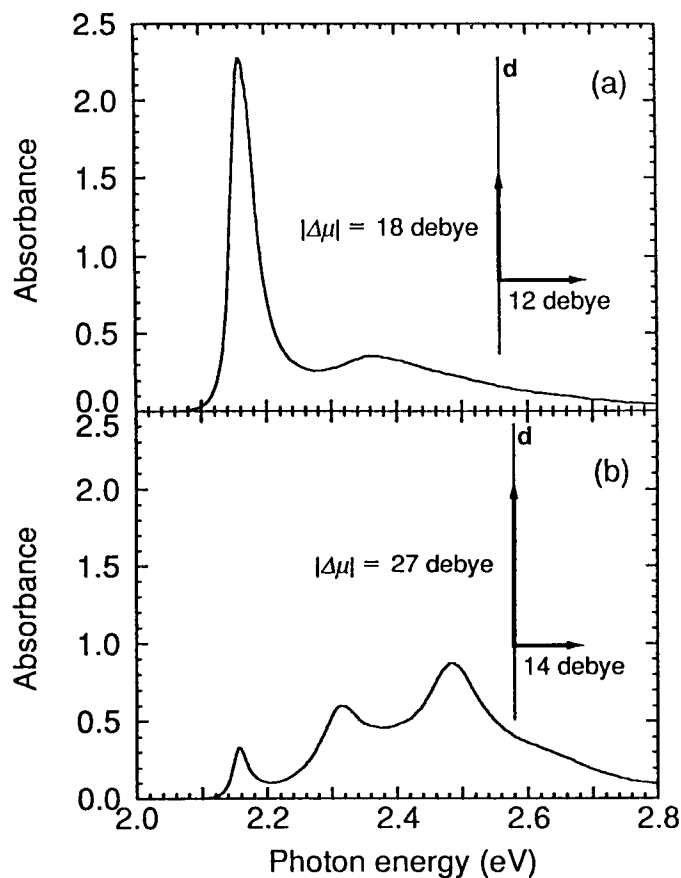
Fig. 1: Change in static dipole moments determined from the electro-absorption spectra of the broadening components. Linear absorption spectra for (a) parallel and (b) perpendicular polarizations are also shown.
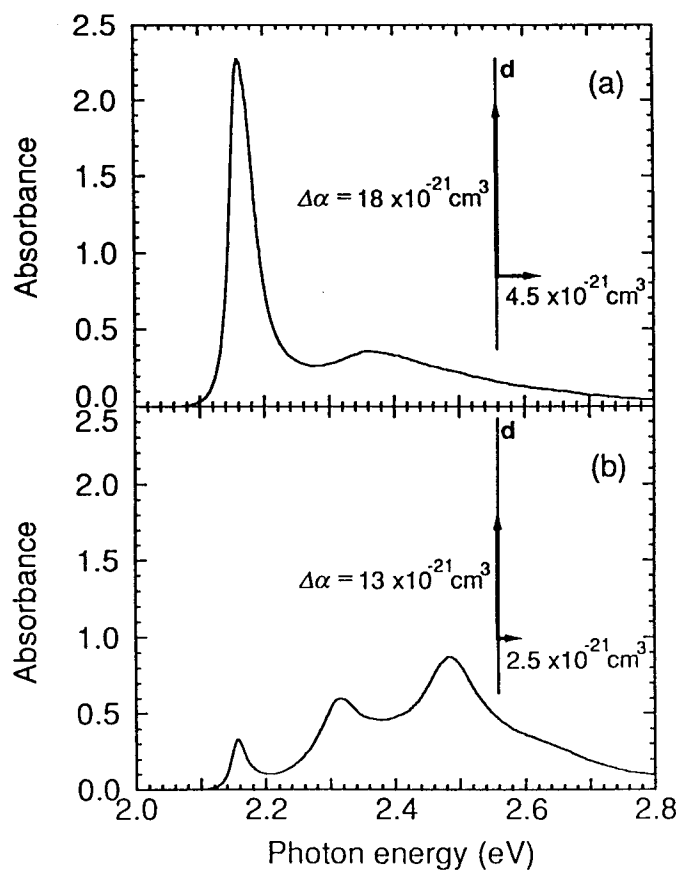
Fig. 2: Change in polarizability determined from the electro-absorption spectra of the shift components.

Polymeric Guest-Host System for Nonlinear Optical Fibre

G.D. Peng, A.Latif, P.L. Chu, R.A. Chaplin
University of South Wales, Kensington, U.K.

The application of organic materials for nonlinear optical processes, such optical modulation and all-optical switching, has been gaining considerable interest in recent years [1]. Organic polymer materials do provide very good synthetic and processing options that are not available with single crystal or multiple quantum well MQW classes of NLO materials and, importantly, they have considerable higher nonlinearity than the usual optical fibre material, viz. silica.

The study of organic polymers for NLO optical fibre devices are still at the very beginning stage. Previously, organic polymer fibres with dye-doped cores have been reported [2]. There poly(methyl methacrylate) (PMMA) has been used as the base materials while several dyes which possess large third order nonlinear optical susceptibility are used as the core dopants. Another report presents a picosecond fibre optical switch achieved from a capillary glass fibre with liquid organic core [3]. However, better core-doping organic compounds with low loss, high nonlinearity and fast response are still to be pursued. We started to study organic polymer materials for high nonlinear fibre recently. Our attention is focussed on polymer fibre doped with conjugated organic polymers which have been shown to have very large non-resonance third-order nonlinearities.

We start with acrylic monomers: methyl methacrylate (MMA) and ethyl methacrylate (EMA), as the base materials. These materials have low refractive indices (in the range of 1.41~1.42). After polymerisation, their indices increase due to the volume reduction during liquid-to-solid phase transition. Polymerised materials: PMMA, PEMA, or poly(MMA-EMA) gives indices in the range of 1.478 ~ 1.482, varying with polymerisation conditions. Obviously, these indices match well with silica fibres. In fact, using another similar monomer (trifluoro-ethylmethacrylate -TFEMA) [4], we can produce copolymers with lower refractive indices. In one of our experiments, copolymerisation of EMA (67%wt) and TFEMA (33%wt) produced good polymers with index 1.4636. Even lower index is possible with larger percentage of TFEMA.

Concerning the core materials, there are several conditions to be satisfied before a desirable organic fibres can be made. Firstly, we require that highly nonlinear organic compounds be uniformly dissolved in the monomers. Normally, to enhance significantly the nonlinearity, we need to dope as much nonlinear organic materials as possible. Secondly, the doped materials should be fabricated with a slightly elevated refractive such that light could be confined to regions of high third order nonlinear-optical susceptibility. Thirdly, the polymer core and cladding should have their thermal properties enabling fibre drawing. Also mismatch of thermal properties between core and cladding should be kept low since it could introduce internal stresses to fibre during drawing. Finally, it is essential to assure a smooth core-cladding boundary to avoid significant scattering.

We have tested different polymerisation conditions and different combinations of organic materials. Different rod polymer or copolymer samples of PMMA, PEMA, poly(MMA-EMA), poly(EMA-TFEMA) and poly(MMA-EMA-TFEMA) have been fabricated and their refractive indices and losses have been measured. Both PMMA and PEMA have optical transmission windows at 1300nm and 1550nm and that PEMA have lower losses that PEMA in the windows.

For the loss of PMMA, we are able to compare with reported results in Refs. [2] and [5], and find agreeable results (their material loss at 1300nm ranges from 0.2 to 0.6 dB/cm).

We have selected a conjugated biochemical - β-carotene, as our first trial dopant. β-carotene is known to be a typical conjugate organic material which has the Kerr coefficient, n2, as high as 1.4×10^{-16} m^2/W (about 5000 times that of silica). We have experimented to incorporate β-carotene into PMMA, PEMA or PMMA/PEMA). Good and uniform polymer and copolymer rods doped with β-carotene have been successfully fabricated. The loss spectrum of a PMMA doped with 4.4%wt β-carotene is shown Fig.1. We could find that the loss at 1300nm and 1550nm are increased to 1dB/cm and 1.5dB/cm respectively. The percentage concentration of the highly nonlinear organic dopant is directly related to the enhancement of the fibre nonlinearity. However, we find that β-carotene concentration will be saturated at about 5% by weight in MMA, EMA or both of them as solvents. We note that the incorporation of β-carotene to polymers does not change much their thermal properties and that the thermal properties of polymers mainly depend on the base materials used. Evidently PEMA has lower transition

absorption (1/cm)

wavelength (nm)

Fig.1 Absorption spectrum of a sample of PMMA doped with β–carotene (4.4% wt).

temperature than that of PMMA. Therefore for PMMA/PEMA copolymers, the higher percentage of EMA the lower transition temperature. We use benzoyl peroxide or laurel peroxide as initiator. Different levels of initiators, ranging from 0.005 ~ 2 %wt, have been experimented. From the experiment, it is found that higher initiator level will result in slightly lower transition temperature. This may imply that lower molecular weight be obtained with higher initiator level, as we would expect. The refractive index of β-carotene is about 1.53. Doping a few percents of β-carotene into PMMA/PEMA copolymer elevates the refractive index by a fraction of one percent. For the sample shown in Fig.1 where β-carotene dosage is 4.4%wt, the resulted index is 1.486, a raise of 0.003 from the corresponding sample without β-carotene.

We have tried two methods to make a polymer fibre preform. In the first method, a small doped polymer rod (2.5mm) is fully polymerised. The rod is then put and fastened in the centre of a glass tube (inside diameter 24mm). Now partially polymerised cladding materials is filled into the tube and it is put into oven for the cladding polymerisation. Unfortunately, this method failed to produce any good fibre preform up to now. The main difficulty is how to control properly the pre-polymerisation of cladding materials. The core rod will dissolve quickly, if cladding materials is only lightly pre-polymerised. However, enormous air bubbles would come out if the cladding materials is over pre-polymerised.

In the second method, we put a small teflon rod in the tube and fill it with cladding materials. Thus we begin with cladding polymerisation. After removing the teflon rod, we fill with core monomers as well as dissolved dopant and do core polymerisation. Uniform preforms free from air bubbles have been fabricated with this method. The polymerisation usually takes from 3 to 6 days. This time scale is significantly fast than the method used in Ref.[2] where polymerisation of core takes over one month to avoid air bubbles. In Fig.2, we show the refractive index profile of a β-carotene doped preform we fabricated. Here the core to cladding index difference is about 0.005 which is appropriate for weakly-guiding fully polymer optical fibres.

n-1.46
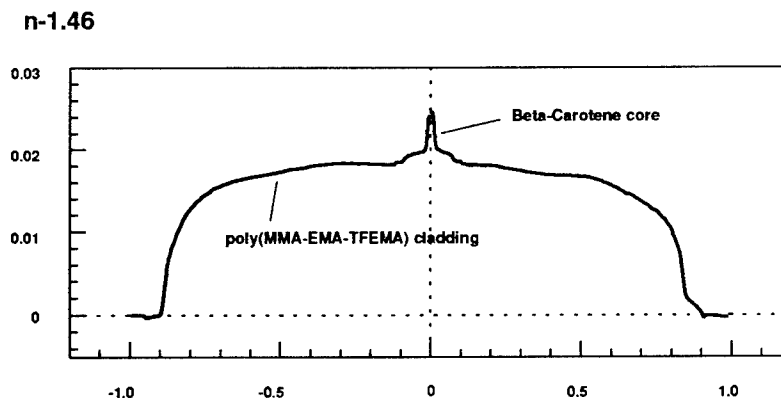
Fig.2 The refractive index profile of one polymer fibre preform we fabricated.
The preform has a poly(MMA38.3%-EMA48.7%-TFEMA13%) cladding
and a poly (MMA44%-EMA56%) core doped with 4.4%wt β-carotene.

In summary, preliminary experimental study on nonlinear organic polymer fibre is carried out by characterising material losses, refractive indices, and thermal and mechanical properties of several organic polymers, e.g. poly(MMA-EMA) and poly(MMA-EMA-TFEMA), and a highly nonlinear organic compound (β-carotene). The polymerisation or copolymerisation conditions have been investigated and low loss samples for either core or cladding have been fabricated. Further, we have fabricated uniform PMMA/PEMA fibre preforms doped with β-carotene. The work is being continued to investigate other high nonlinearity organic compounds and to fabricate nonlinear polymer fibres, upon the completion of a fibre drawing setup.

References:

[1] D. R. Ulrich, "Overview: nonlinear optical organics and devices", Optical Materials for nonlinear optics, D.B. Hann (ed.), (Royal Society of Chemistry, London), pp.241-274, 1989

[2] M. G. Kuzyk, U. C. Paek and C. W. Dirk, "Guest-host polymer fibres for nonlinear optics", Appl. Phys. Lett. 59(8), 902-904, 1991

[3] H. Kanbara, M. Asobe, K. Kubodera, T. Kaino and T. Kurihara, "All-optical picosecond switch using organic single-mode fibre waveguide", Appl. Phys. Lett. 61(19), 2290-2292, 1992

[4] D. Bosc and C. Toinen, "Fully polymer single-mode optical fiber", IEEE Photo. Tech. Lett. 4(7), 749-751, 1992

[5] T. Kaino, "Low loss plastic optical fibres", Japan J. Appl. Phys. 24, 1661, 1985

Thermally induced stress relaxation of silicon dioxide on vicinal Si(111) studied with surface nonlinear-optical techniques

G. Lüpke, F. Wolter, U. Emmerichs, C. Meyer, and H. Kurz
Institute of Semiconductor Electronics II,
Rheinisch-Westfälische Technische Hochschule, 52056 Aachen, Germany

T. Yasuda, and G. Lucovsky
Departments of Physics, North Carolina State University,
Raleigh, NC 27695-8202, USA

C.H. Bjorkman
Research Center for Integrated Systems,
Hiroshima University, 1.4-2 Kagamiyama,Higashi-Hiroshima 724, Japan

Summary

We report on optical second–harmonic (SH) and sum–frequency (SF) measurements from vicinal Si(111)–interfaces covered with a thermally grown oxide film and subjected to different annealing temperatures. We observed that the azimuthal anisotropy in the nonlinear optical response from the Si/SiO_2 interface changes after rapid thermal annealing (RTA) [1]. The RTA step allows relaxation of strain in the oxide film and at the Si/SiO_2 interface. The SH and SF photon energies of 3.1 eV and 3.5 eV are close to the recently observed strong resonance at 3.3 eV which arises from the presence of strained bonds at the Si/SiO_2 interface [2]. We suggest that the change of the step-induced onefold symmetry indicates the relaxation of atomic bondings at the steps of the interface. The relaxation mechanism can be well described by the viscous flow model [3].

In our experiments Si(111) wafers with off–axis orientation of $5° \pm 0.5°$ in the [11$\bar{2}$] direction were studied. On these surfaces an oxide (30 nm) was grown in a dry oxygen ambient at a temperature of 850° C [1]. Some of the samples were subjected to RTA (900°–1100° C for 100 s) in a dry argon atmosphere but containing enough oxygen to prevent reduction of the oxide [1]. For SH generation we used a mode-locked Ti:sapphire laser operating at a wavelength of 780 nm (1.55 eV), generating a train of 100 fs pulses at 78 MHz with an average power of 0.4 W. For SF generation we mixed the fundamental (1053 nm) and the frequency-doubled 40 ps laser pulses of a Nd:YLF regenerative amplifier. In our experiments we used the *ps* (*p* in, *s* out) and *sp* polarization configurations, where the reflected SH and SF signal were measured as a function of sample azimuthal orientation. Using a truncated Fourier expansion to fit the azimuthal dependence of the reflected SH and SF field we have deduced the complex Fourier coefficients c_m for various rapid thermally annealed Si/SiO_2 interfaces [4]. The
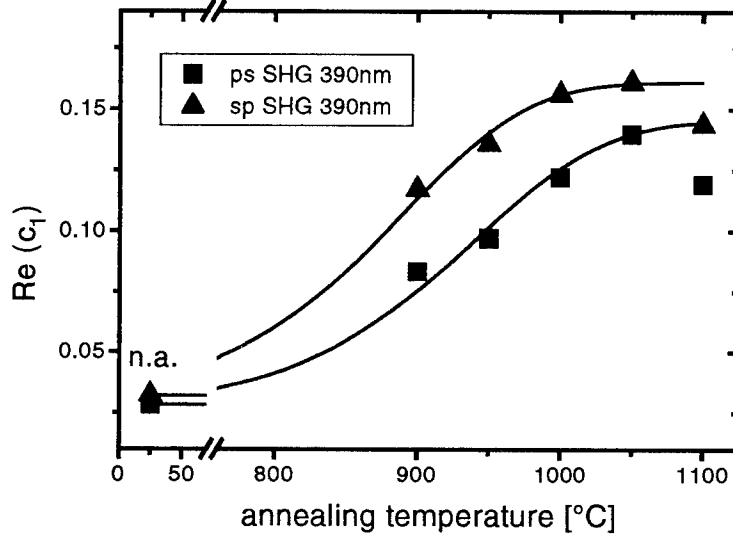
Figure 1: c_1 after thermal annealing as a function of annealing temperature. The solid curves are best fits using Eq. (1).

onefold coefficient c_1 is indicative of intrinsic C_{1v} symmetry arising from steps, whereas c_3 is generated over the entire terrace [4]. Within the experimental error the c_3 remain constant after RTA, therefore we have normalized c_1 to c_3.

Figure 1 shows $Re(c_1)$ obtained from SH measurements for various annealing temperatures. The experimental results shown in Fig. 1 are well described by the stretched exponential relaxation model (see Ref. [3]) as

$$c_1(T) - c_1(f.r.) = (c_1(n.a.) - c_1(f.r.)) \exp\left\{ -\left(\frac{t_a}{\tau(T)}\right)^\alpha \right\} \qquad (1)$$

where $c_1(n.a.)$ and $c_1(f.r.)$ are the values of the non-annealed oxide and the oxide fully relaxed, and the annealing time t_a is 100 sec in all RTA. The parameter α is a measure of the coupling to cooperativity, and the best fitted values for α are about 0.32 which is in agreement with $\alpha = 0.3$ obtained from ellipsometry measurements on Suprasil W silica glass [3]. The relaxation time for the oxide density is expressed as $\tau(T) = \tau_0 \exp(E_a/k_b T)$ where $\tau_0 = 2 \times 10^{-20} sec$ and $E_a = 5.1 eV$.

In Fig. 2 are plotted the variation of $\log \tau$ vs $10^3/T$ for various polarization combinations of SH and SF generation. Indeed τ has an activated behavior with temperature. The comparison with viscosity variation vs temperature found for thermally grown dry oxides and fused silica yields a remarkable good agreement for the activation energy which is about 5 eV [3]. However the SiO_2 structure is quite flexible indicating, that the stress relaxation of atomic bondings at the
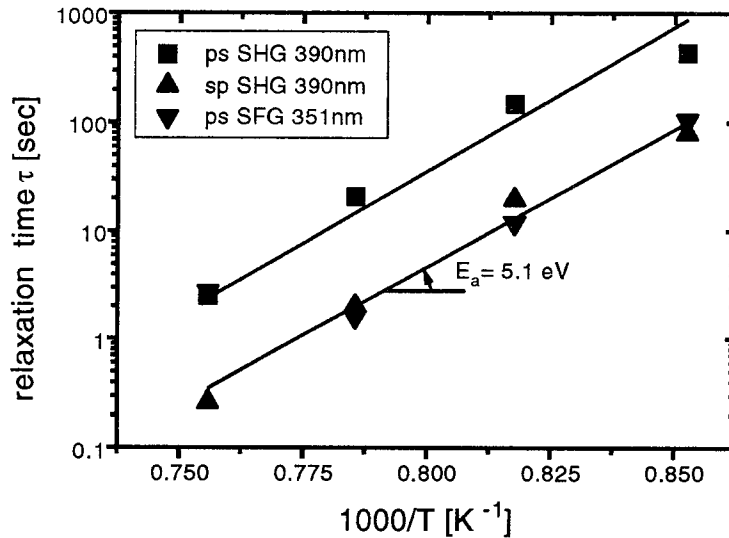
Figure 2: Relaxation time τ as a function of reverse temperature $10^3/T$.

steps requires breaking bonds in agreement with the viscous flow model [3]. The relaxation time at $900°C$ is 160 sec, while at $1050°C$ τ is only 1 sec. Therefore, the RTA process below $900°C$ relaxes the bondings at the steps only a little, whereas the relaxation is complete after RTA above $1050°C$. In the actual oxidation process around $850°C$, the thermal relaxation significantly influences the oxidation rate because the relaxation time (25 min at $850°C$) is less than the actual processing time (150 min).

References

[1] C.H. Bjorkman, T. Yasuda, C.E. Shearon, Jr., Y. Ma, G. Lucovsky, U. Emmerichs, C. Meyer, K. Leo, and H. Kurz, J. Vac. Sci. Technol. B **11**, 1521 (1993).

[2] W. Daum, H.J. Krause, U. Reichel, and H. Ibach, Phys. Rev. Lett. **71**, 1234 (1993).

[3] K. Taniguchi, M. Tanaka, C. Hamaguchi, and K. Imai, J. Appl. Phys. **67**, 2195 (1990), and references therein.

[4] G. Lüpke, D.J. Bottomley, and H.M. van Driel, J. Opt. Soc. Am. B **11**, 33 (1994).

DYNAMICS OF POLARITON SOLITONS IN SEMICONDUCTORS: FORMATION, PROPAGATION, AND INTERACTION

<u>Irina B. Talanina</u>, and Michael A. Collins

Research School of Chemistry, Australian National University, Canberra, ACT 0200, Australia
Phone: (61) 6 249 3773; Fax: (61) 6 249 0750

Vladimir M. Agranovich

Institute of Spectroscopy, Russian Academy of Sciences, 142092 Troitsk, Moscow Region, Russia. Phone: (7) 095 334 0224

The concept of polariton solitons, which has recently emerged in semiconductor optics, describes a new aspect of light-matter interaction processes. The physical cause which leads to polariton soliton formation is an exact balance between the dispersive spreading of a polariton pulse and third-order nonlinear effects; as a result, the polariton wave packet propagates through a crystal without changing its shape. The formation of steady-state polariton pulses is not only of fundamental interest as a phenomenon not encountered in conventional linear optics of semiconductors, it may also prove useful for applications in all-optical devices.

We consider formation of bright and dark polariton solitons in semiconductor crystals and show that these solitons have some properties which are different from the properties of the solitons in optical fibers.

To describe optical pulse propagation in a semiconductor crystal in the spectral region of an exciton resonance, we use a new approach described in Ref. 1. In this approach, the nonlinear material equation which relates the induced excitonic polarization, $P(z,t)$, and the electric field of the light, $E(z,t)$, (propagating along the z axis) in a nongyrotropic cubic Kerr-type crystal can be written as

$$\left\{ \frac{\partial^2}{\partial t^2} + \gamma \frac{\partial}{\partial t} + \omega_T^2 - \frac{\hbar \omega_T}{\mu} \frac{\partial^2}{\partial z^2} \right\} P(z,t) + \chi_0 \left| P(z,t) \right|^2 P(z,t) = \alpha E(z,t), \tag{1}$$

where $\alpha = \varepsilon_0 (\omega_L^2 - \omega_T^2)/4\pi$, ε_0 is the background dielectric constant of the medium, ω_L and ω_T are the frequencies of longitudinal and transverse excitons, respectively, μ is the exciton effective mass, γ is the damping constant, and χ_0 is a nonlinear coefficient ($\chi_0 > 0$).

Eq. (1) together with the wave equation for the propagation of a plane wave packet in an isotropic dispersive medium

$$\frac{\partial^2 E(z,t)}{\partial z^2} - \frac{\varepsilon_0}{c^2} \frac{\partial^2 E(z,t)}{\partial t^2} = \frac{4\pi}{c^2} \frac{\partial^2 P(z,t)}{\partial t^2} \tag{2}$$

gives the complete system of equations describing the dispersive and nonlinear properties of a solid in the frequency range investigated.

We seek a solution of the system of equations (1)-(2) in the form

$$P(z,t) = \tilde{P}(z,t)\exp\left[i(Qz - \Omega t)\right],$$

(3)

where Ω is a carrier frequency, $Q(\Omega)$ is determined by the dispersion low of the polaritons, and the amplitude is a slowly varying envelope function.

In the moving coordinate system ($x = z$, $\eta = t - z/U$), we finally obtain the perturbed Nonlinear Schrödinger Equation for the envelope function

$$i\frac{\partial \tilde{P}}{\partial \xi} - \frac{1}{2}k''\frac{\partial^2 \tilde{P}}{\partial \eta^2} + O(\xi,\eta) + \chi_0\left|\tilde{P}\right|^2 \tilde{P} = 0,$$

(4)

where U and k'' characterize the group velocity and the group dispersion of a polariton, respectively, and $O(\xi,\eta)$ is a Hamiltonian perturbation.[1]

In anomalous dispersion regime, Eq. (4) has a bright soliton solution

$$\tilde{P}(\xi,\eta) = \varphi_0 \mathrm{sech}(\eta/\tau)\exp\left[i(\nu\xi + \beta\eta)\right],$$

(5)

where the relations between the soliton parameters are given in Ref. 1. Eq. (4) has also a dark soliton solution in normal dispersion regime.

Analyzing the properties of the polariton solitons, we show that these solitons: a) have a restriction on the soliton duration to be larger than a certain critical value; b) are wave number and frequency downshifted from the corresponding small amplitude polaritons.

Numerical calculations have been performed to determine the critical value of the soliton duration as a function of photon energy and the values of the wave number and frequency downshifts as a function of the soliton duration for CuCl, CdS, and GaAs crystals.

The influence of damping on propagation dynamics of bright polariton solitons has been examined, and the conditions for observations of these solitons in semiconductor crystals have been discussed.

We also consider a nonlinear resonant interaction between two different polariton waves in spectral region near an exciton resonance. At frequencies above ω_L, where spatial dispersion leads to the existence of an additional polariton wave, two different excitations propagate through a crystal at the same frequency - the upper branch polariton, UP, and the lower branch polariton, LP. In the presence of Kerr nonlinearity, the interaction between UP and LP, which are generated simultaneously by an initial laser pulse, can lead to coupled propagation of UP and LP wave packets through the crystal. We show that UP wave packet can form a soliton and provide a "potential" within which the LP is trapped.[2] Numerical calculations for CuCl and CdS have been performed to examine the conditions under which this trapping effect can take place.

1.   I.B. Talanina, M.A. Collins, and V.M. Agranovich, Polariton solitons in semiconductors, *Solid State Commun.* **88**, 541 (1993).
2.   I.B. Talanina, M.A. Collins, and V.M. Agranovich, Polariton trapping by a soliton near an excitonic resonance, *Phys. Rev. B* **49**, 1517 (1994).

Fabrication of Highly Perfect Single Crystals and Nonlinear Optical Properties of Organic Material, 3-Methyl-4-methoxy-4'-nitrostilbene (MMONS)

Choon Sup Yoon
Korea Advanced Institute of Science and Technology
Department of Physics, KAIST, Daeduck Science Town, Taejon, Korea
Tel. +82-42-869-2532

Hyung-ki Hong
Korea Advanced Institute of Science and Technology
Department of Physics, KAIST, Daeduck Science Town, Taejon, Korea
Tel. +82-42-869-2572

Min Young Lee
Ewha Women's University
Dept. of Chemistry, Ewha Women's Univ., Seodaemungu, Seoul, Korea
Tel. +82-2-360-2383

Kwang Sup Lee
Hannam University
Dept. of Macromolecular Science, Hannam Univ., Daeduckgu, Taejon, Korea
Tel. +82-42-629-7394

3-Methyl-4-methoxy-4'-nitrostilbene (MMONS) exhibits one of the largest powder second harmonic signals (1250 × urea)[1] and thus has a great potential in frequency doubling and parametric conversion. The crystal possesses highly polar structure which leads to the abnormal growth behavior in the polar c-direction. The single crystals of a size $40 \times 35 \times 30$ mm^3 and of an excellent quality could be grown from methyl ethyl ketone solution by controlled solvent evaporation (Fig.1).

Refractive indices were measured by using Brewster angle method[2] at the wavelengths of 1.064 μm , 0.632 μm and 0.532 μm. Phase matching angles for the second harmonic generation were determined from the refractive index data (Fig.2) and it was found that the type I and type II phase matchings are possible. The measured phase matching directions agree to within 0.3° of those calculated from the Sellmeier equations. The walk off angle for the type II phase matching is rather large and varies from 7 to 12° , depending on the polar and azimuthal angles. However the walk off angle for the type I can be as small as 0.57° for $\theta = 14.08°$ and $\phi = 5.0°$.

The effective nonlinear optical coefficient was measured relative to LiNbO$_3$ by using Maker fringe method and d$_{eff}$ = 67 pm/V. The laser damage thresholds are observed to be greater than 1 GW/cm^2 at 1.06 μm where the type I phase matching occurs. The full width at half maximum of the phase matching peaks is about 0.5°.

94
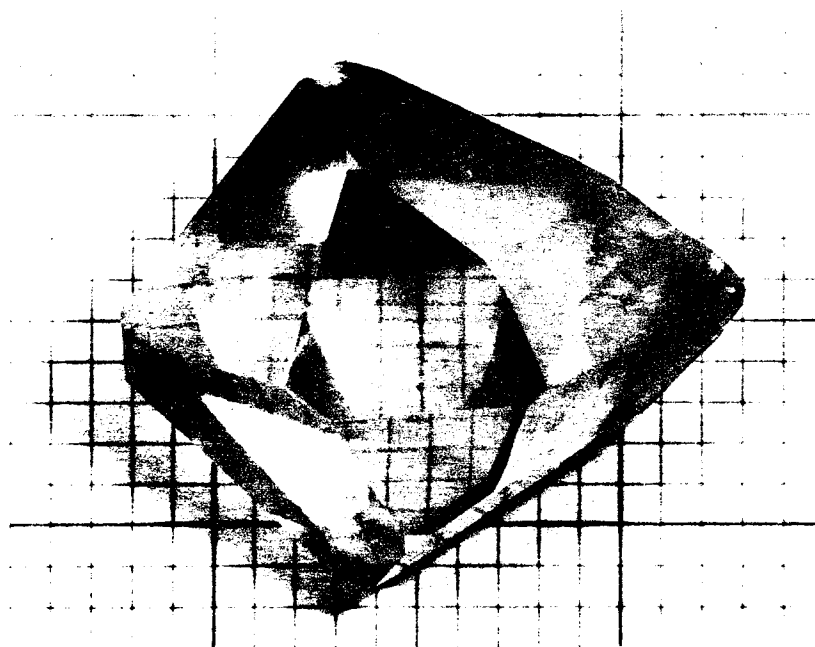
Fig.1. MMONS crystal grown from solution by solvent evaporation.
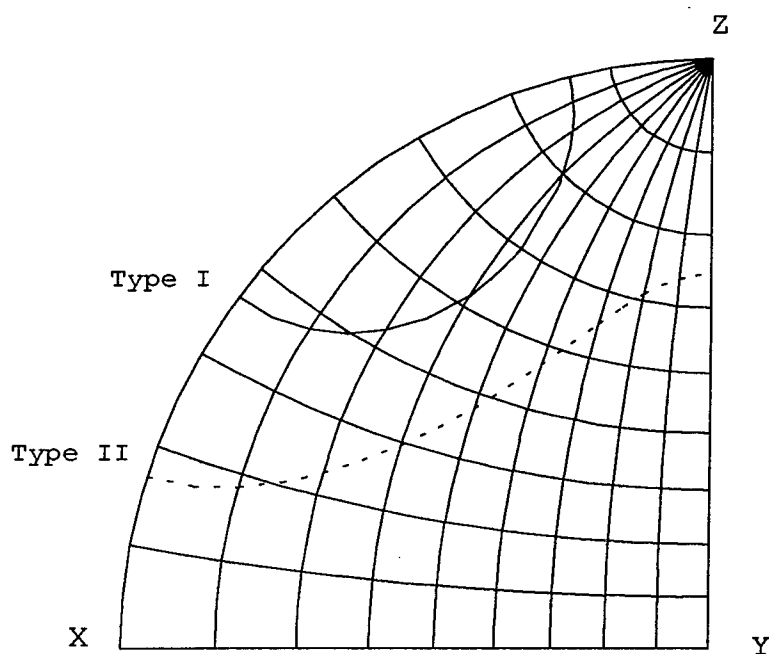
Fig.2. Loci for the second harmonic generation at 1.06 μm.

References

(1) W.Tam, B.Guerin, J.C.Calabrese and S.H.Stevenson, *Chem.Phys.Lett.*, **154**, 93(1989).
(2) C.H.Grossman and A.F.Garito, *Mol.Cryst.Liq.Cryst.*, **168**, 255(1989)

Mutually-Pumped Phase Conjugation
in Photorefractive Crystals with Partially Coherent Beams

Q. Byron He, and H.K. Liu
Jet Propulsion Laboratory
California Institute of Technology
4800 Oak Grove Dr.
Pasadena, CA 91109
Tel (818) 354-1739, Fax (818) 393-5013

P. Yeh
University of California, Santa Barbara
Santa Barbara, CA 93106

S. C. De La Cruz, and J. Feinberg
University of Southern California
Los Angeles, CA 90089-0484

Summary

A mutually-pumped phase conjugator takes two input beams and transforms each into the phase-conjugate replica of the other [1]. The two input beams need not be coherent with each other. These conjugators may prove useful for optical communication, laser phase-locking, optical interconnection, and optical computing [2]. It has been experimentally observed that making the two input beams mutually coherent changes the performance of some mutually-pumped conjugators, but not of others [3]. Here we present experimental results and theoretical calculations on the performance of various mutually-pumped phase conjugators that use photorefractive crystals. Our theory includes the usual transmission grating but also includes a reflection grating [4] and backscattering gratings inside the photorefractive crystal. In addition, we allow depletion and absorption of all of the beams. For simplicity, however, we do limit ourselves to the case of one interaction region. We assume that charge transport is dominated by diffusion, so that all of the coupling constants are real. Figure 1 shows two input plane waves have amplitudes A_2 and A_4, respectively. These two waves have a mutual coherence of v $(0 \leq v \leq 1)$. As long as the these two input waves are at least partially coherent ($v \neq 0$), then in addition to the transmission grating $A_1 A_4^* + A_2^* A_3$, there is a reflection grating $A_1 A_3^* + A_2^* A_4$, and backscattering gratings $A_1 A_2^*$, and $A_3 A_4^*$ present in the crystal. The nonlinear coupled wave equations are then:

$$\frac{dA_1}{dz} = \gamma_t \frac{A_1 A_4^* + A_2^* A_3}{I_0} A_4 + v \left[\gamma_r \frac{A_1 A_3^* + A_2^* A_4}{I_0} A_3 + \gamma_{backscatter} \frac{A_1 A_2^*}{I_0} A_2 \right] - \alpha A_1$$

$$\frac{dA_2^*}{dz} = \gamma_t \frac{A_1 A_4^* + A_2^* A_3}{I_0} A_3^* + v \left[\gamma_r \frac{A_1 A_3^* + A_2^* A_4}{I_0} A_4^* + \gamma_{backscatter} \frac{A_1 A_2^*}{I_0} A_1^* \right] + \alpha A_2^*$$

$$\frac{dA_3}{dz} = -\gamma_t \frac{A_1 A_4^* + A_2^* A_3}{I_0} A_2 + v \left[\gamma_r \frac{A_1^* A_3 + A_2 A_4^*}{I_0} A_1 - \gamma_{backscatter-prime} \frac{A_3 A_4^*}{I_0} A_4 \right] + \alpha A_3$$

$$\frac{dA_4^*}{dz} = -\gamma_t \frac{A_1 A_4^* + A_2^* A_3}{I_0} A_1^* + v \left[\gamma_r \frac{A_1^* A_3 + A_2 A_4^*}{I_0} A_2^* - \gamma_{backscatter-prime} \frac{A_3 A_4^*}{I_0} A_3 \right] - \alpha A_4^*$$

with the boundary conditions

$$A_1(0) = A_3(L) = 0, \quad \text{and} \quad \frac{|A_4(0)|^2}{|A_2(L)|^2} = q,$$

where $I_0 = |A_1|^2 + |A_2|^2 + |A_3|^2 + |A_4|^2$ is the total intensity of the beams, γ_t, γ_r, $\gamma_{backscatter}$, and $\gamma_{backscatter-prime}$ are the photorefractive coupling coefficients for the transmission grating, the reflection grating, and the two backscattering gratings, respectively, q is the intensity ratio of the pump beams, L is the interaction length, and α is the bulk amplitude absorption coefficient of crystal. When the two input beams are mutually incoherent ($v = 0$), these coupled-wave equations reduce to the conventional equations having only a transmission grating [5].

We solve the coupled-wave equations numerically and investigate the transmission of the device as a function of the mutual coherence of the two input beams. Two transmissions are defined by the ratio of the phase-conjugate power to the pump power, i.e.,

$T_{left-to-right} = \dfrac{|A_1(L)|^2}{|A_4(0)|^2}$ for the left-to-right transmission, and $T_{right-to-left} = \dfrac{|A_3(0)|^2}{|A_2(L)|^2}$ for the right-to-left transmission. For a mutually-pumped phase conjugator having only a transmission grating, these two transmissions are equal [5]; however, in the presence of additional gratings, these two transmissions are no longer the same. Depending on the sign and the magnitude of the backscattering grating coupling strengths, the performance of mutually-pumped phase conjugators can be significantly enhanced or reduced when the two input beams become mutually coherent. We also performed experiments to verify our theoretical model. We carefully vibrate a mirror to vary the mutual coherence of the two input beams. For example, Fig. 2 shows the measured transmissions $T_{left-to-right}$ and $T_{right-to-left}$ versus the mutual coherence of the two input beams in a BaTiO3 crystal acting as a British conjugator [6]. The solid and dashed lines are our theoretical fits using lots of free parameters.

In conclusion, we have investigated the performance of mutually-pumped phase conjugators where the two input beams are partially coherent. For some conjugator geometries our experimental results are in good agreement with our calculations. This study shows that reflection and backscattering gratings have different effects on the performance of different mutually-pumped phase conjugators. This work at UCSB and USC was supported by the Air Force Office of Scientific Research.

References

[1]   S. Weiss, S. Sternklar, and B. Fischer, Opt. Lett. 12, 114 (1987).
[2]   See, for example, P. Yeh, Introduction to Photorefractive Nonlinear Optics, (Wiley, 1993).
[3]   M. T. Gruneisen, E. D. Seeberger, J. F. Mileski, and K. Koch, Opt. Lett. 16, 596 (1991) and S.-C. De La Cruz, S. MacCormack, and J. Feinberg, Tech. Digest of CLEO'93, 532 (1993).
[4]   W. Krolikowiski, and M. R. Belic, Opt. Lett.,13, 149 (1988).
[5]   M. Cronin-Golomb, B. Fischer, J. O. White, and A. Yariv, IEEE J. Quantum Electron. QE-20, 12 (1984) and Q. C. He, IEEE J. Quantum Electron. QE-24, 2507 (1988).
[6]   A. M. Smout, and R. W. Eason, Opt. Lett.,12, 498 (1987).
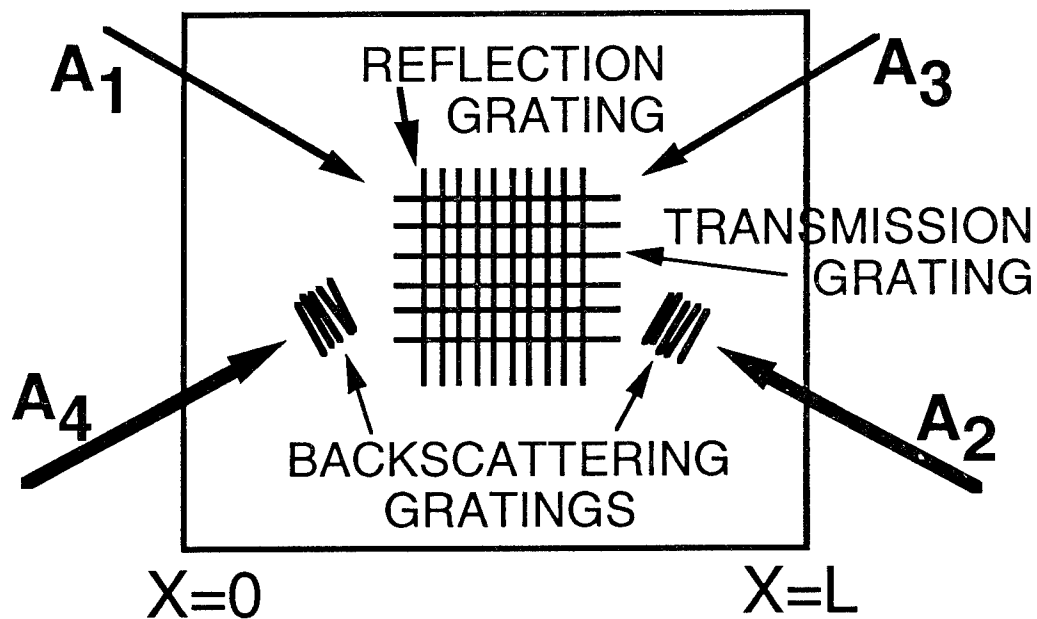
Fig. 1 Schematic diagram of a photorefractive mutually-pumped phase conjugator. The various gratings are here shown displaced for clarity.
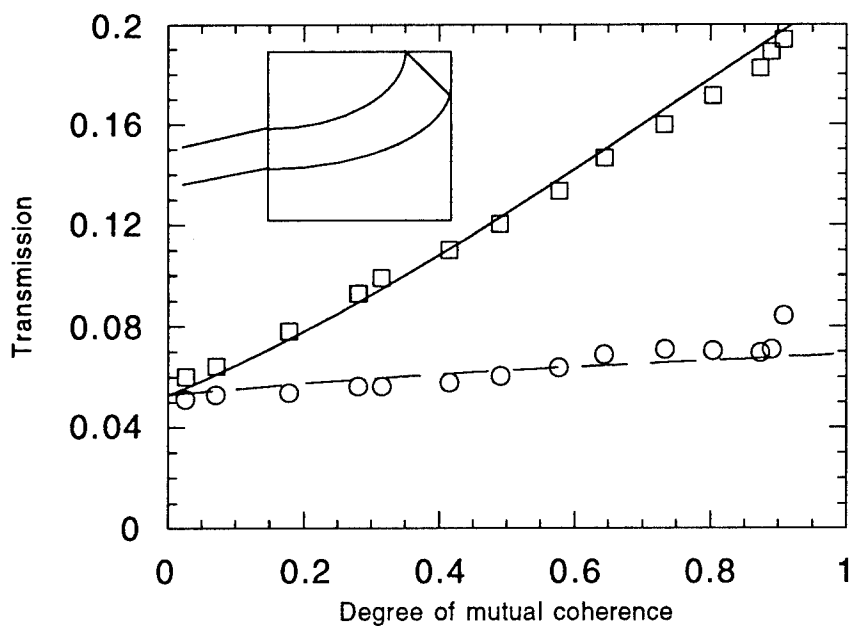
Fig. 2 The two transmissions as a function of degree of mutual coherence for photorefractive "British" mutually-pumped phase conjugator. The points are experimental measurements. The lines are fits from the theoretical model.

Nonlinear Optical Properties and Holographic Recording Performance of Methyl Orange
Doped Polymer Films

Janine V. Reardon, Earlie Oliver, and Don A. Gregory, Department of Physics
University of Alabama in Huntsville, Huntsville, AL 35899, TEL: (205) 895-6276 ext 314
Joseph K. McDonald and Teresa C. Atkins, U. S. Army Missile Command,
AMSMI-RD-WS-CM, Redstone Arsenal, AL 35898-5248, TEL: (205) 876-1993

SUMMARY

Organic dyes show great potential in the field of nonlinear optics due to their high phase conjugate reflectivities. The large effective third-order nonlinear coefficients they possess are a result of saturable absorption and the long lifetime of their transient states.[1,2] Aromatic azo compounds have been the focus of much attention in recent years in the fields of holographic storage and information processing.[3-6] Azo dyes are attractive because of their low cost and many of them are water soluble, making the preparation of samples simple and inexpensive. Also, the molecular designs of these materials can be optically altered to produce optimal results.[3] Possible applications for azo dyes include image processing, interferometry, signal processing, optical switches and other devices, and recording materials for holography, nonlinear optics, and optical waveguides.[4,6-11]

One of the contributing factors to the nonlinear properties of organic dyes is the trans $\leftrightarrow$ cis photoisomerization which occurs in the molecules. Optical excitement induces rearrangement or rotation around the central N=N bond.[3,12] This conformational change induces reversible anisotropic changes in both the absorption and refractive index of materials which have been doped with these molecules. Information can be written to and erased from these materials with polarized optical fields.

Since the azo dyes must be allowed to photoisomerize, a polymer matrix has to be chosen that will allow the reorientation of the molecules through photostimulation.[12] Both liquid and solid matrices can be used, but liquid solutions require high-intensity light pulses, their time of memory is very short, and the interference pattern is unstable.[5] Solid materials, on the other hand, provide a strong nonlinear response when orientational gratings are formed. These gratings also offer better signal-to-noise ratios.[2,13] The properties of these dyes also depend on the matrix material. The effects of matrix and pH on the phase conjugate signal and holographic recording have been studied for methyl orange.

The azo dyes used in this experiment were purchased from Aldrich Chemical Company and were prepared in various solutions such as water, ethanol, polyvinyl alcohol (PVA), PMMA, and epoxy. Some of the solutions were spin-coated onto or pressed between glass plates to observe any differences between the signals from liquid and solid matrices. A Cary model 2300 UV-VIS-NIR spectrophotometer was used to take the absorption spectra of the samples.

The DFWM experimental setup shown in Figure 1 was the standard scheme for optical phase conjugation. A Lambda Physik EMG 102 MSC excimer laser operating at 308 nm using xenon chloride was used to pump a Lambda Physik FL 2002 dye laser. The wavelength on the dye laser was set at 480 nm because of the resonance enhanced strong phase conjugate signals obtained from the samples at this wavelength.

Holograms were written in the samples using the 514 nm line of a Spectra Physics Argon Ion laser. A HeNe laser was used to reconstruct the hologram because of the low absorption of the dye at this wavelength. The experimental system is shown in Figure 2. Both intensity and polarization gratings were written to the material using parallel and perpendicular polarized object and reference beams, respectively. The angle at which the reconstruction beam reflected off mirror M4 satisfied the Bragg diffraction equation for a thick grating with a fringe spacing, $d = (\lambda/2\sin\Theta)$, where $\lambda = 514$ nm and Θ is the angle between the reference and the object beams.
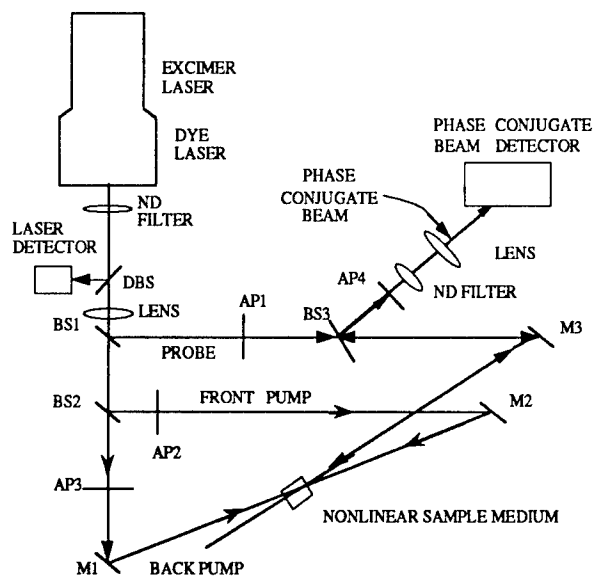
Figure 1: Degenerate four wave mixing setup
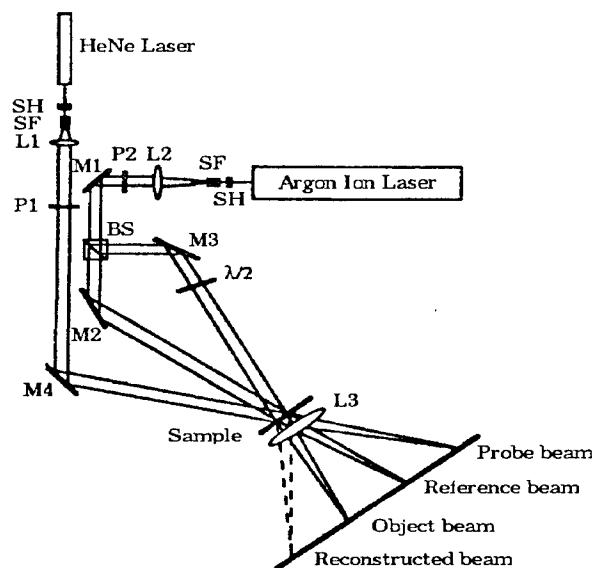
Figure 2: Holographic setup

The phase conjugate signal of methyl orange in different matrices has been measured. A large signal was observed in all of the samples. A normal dependence of the phase conjugate signal to the laser input intensity was obtained (see Figure 3). No significant enhancement of any matrix relative to the other matrices was observed, implying that for this azo dye, the choice of matrix has little effect on its signal. pH has a significant effect on the color of methyl orange (see Figure 4) but no differences were observed in the phase conjugate signal of samples that were acidic or basic.

Methyl orange doped in PVA and epoxy were used to study the effects of matrix on holographic recording. In a low pH media no holograpic response was observed from the methyl orange in either film. In neutral to basic media, grating growth, decay and erasure times for the epoxy films were found to be much slower than the PVA films. The highest resolution was obtained with the PVA films. These results were anticipated due to the relative rigidity of the materials. The resolution of the PVA films is comparable to that of silver halide film. Both the PVA and the epoxy based films have extremely slow response times when compared to silver halide and photopolymer films. Diffraction efficiencies for polarization gratings were found to exceed the diffraction efficiencies for intensity gratings in both PVA and epoxy systems, in agreement with other research published.[14] The maximum diffraction efficiency observed in the PVA films was higher compared to the epoxy film although very weak compared to silver halide. Decay times for information written to the films are on the order of hours in the epoxy films, much longer than the several minutes decay time of the PVA films. The damage threshold of
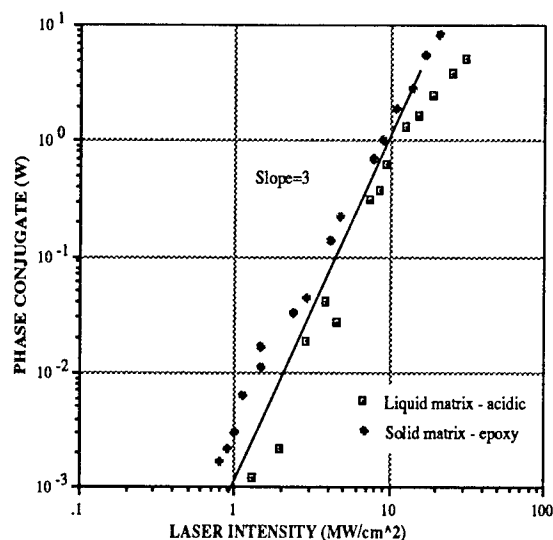
Figure 3. DFWM of Methyl
Orange
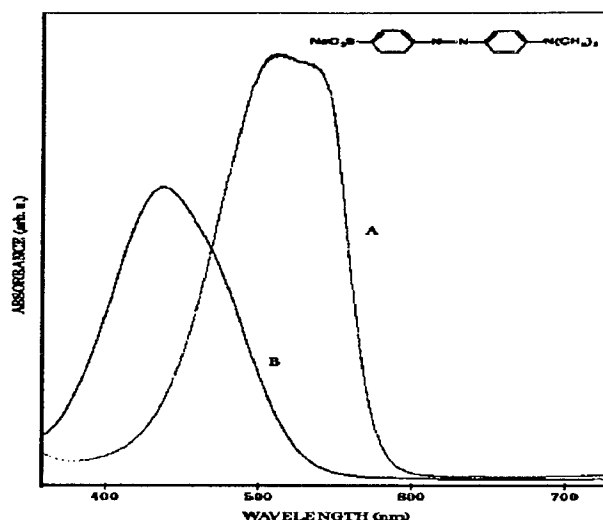
Figure 4. Absorption spectra of Methyl
Orange in **A**) acidic and **B**) basic solution

the epoxy film was found to be higher than the PVA film. Since PVA is water soluble, humidity was found to damage the surface of the film and affect the storage time.

In conclusion, solid and liquid matrices and changing pH of methyl orange showed no significant difference in the DFWM results. Holographic recording in methyl orange doped films was observed only in the basic form of the azo dye. The increased damage threshold and decreased humidity sensitivity however, make the epoxy films much more attractive for practical applications even with the increased write/erase cycle time over the PVA films.

REFERENCES

1. K.P.B Moosad, T.M. Abdul Rasheed, and V.P.N.Nampoori, Opt. Eng., **29**(1), 47-51 (1990).
2. I.V. Tomov, B. VanWonterghem, A.S. Dvornikov, T.E. Dutton, and P.M. Rentzepis, J. Opt. Soc. Am., B **8**(7), 1477-1482 (1991).
3. J.J.A. Couture and R.A. Lessard, Appl. Opt., **27**(16), 3368-3374 (1988).
4. R.A. Lessard, C. Malouin, R. Changkakoti, and G. Manivannan, Opt. Eng., **32**(4), 665-670 (1993).
5. T. Todorov, L. Nikolova, N. Tomova, and V. Dragostinova, IEEE J. Quant. Elect., QE-**22**(8), 1262-1266 (1986).
6. L. Nikolava, K. Stoyanova, and T. Todorov, Opt. Comm., **64**(1), 75-80 (1987).
7. W.M. Dennis, W. Blau, and D.J. Bradley, Opt. Eng., **25**(4), 538-540 (1986).
8. H. Fujiwara and K. Nakagawa, Opt. Comm., **55**(6), 386-389 (1985).
9. H. Fujiwara and K Nakagawa, Opt. Comm., **66**(5,6), 307-310 (1988).
10. .S.A. Jenekhe, S.K. Lo, and S.R. Flom, Appl. Phys. Lett., **54**(25), 2524-2525 (1989).
11. Y. Silberberg and I. Bar-Joseph, IEEE J. Quant. Elect., QE-**17**(9), 1967-1970 (1981).
12. E. Mohajerani, E. Whale, and G.R. Mitchell, Opt. Comm., **92**(4,5,6), 403-409 (1992).
13. I.V. Tomov, T.E. Dutton, B. VanWonterghem, and P.M. Retzepis, J. Appl. Phys., **70**(1), 36-40 (1991).
14. T. Todorov, L. Nikolova, and N. Tomova, Appl. Opt.,**23**(24), 4588-4591 (1984).

Nonlinear Optical Properties of Conjugated Oligomers : A Simple Model for Length Dependence and Conformation

Y. Verbandt, H. Thienpont, I. Veretennicoff,

Applied Physics Department, Vrije Universiteit Brussel, Pleinlaan 2, B-1050 Brussel, Belgium, tel. 32-2-641.36.13, fax. 32-2-641.34.50, Internet yverband@vub.ac.be,

P. Geerlings,

Chemistry Department, Vrije Universiteit Brussel, Pleinlaan 2, B-1050 Brussel, Belgium,

and

G. L. J. A. Rikken

Philips Research Laboratories, P. O. Box 80000, NL-5600 JA Eindhoven, The Netherlands.

The delocalisation of the π electrons along the backbone of one-dimensionally conjugated molecules gives rise to large electrical polarizabilities. Therefore, a large nonlinear response can be expected in these systems. A major technological advantage of organic materials for photonics applications is that these molecules are relatively easily processable into thin films on various substrates. Because the solubility of these centrosymmetric molecules decreases drastically with length, an accurate estimation of the saturation length (i. e. the number of repeat units at which the length dependence of the optical response becomes linear) yields valuable information. Thienpont *et al.*[1] report experiments where a saturation of the optical nonlinearity for the oligothiophenes is observed. In present contribution, we show that the coupling between the repeat units in the chain determines the length dependence of the optical properties, without having to introduce any anharmonicity of the constituents. Furthermore, we present quantitative results on the effects of conformation. Therefore, this contribution can be seen as both a simplification and an extension of previous work[2].

We propose to model the oligomeric series by a periodic succession of *harmonic* oscillators (Eq. 1), truncated at a distance l_d, i. e. monomer delocalisation length (Fig. 1).

$$V(x) = \frac{1}{2}m\omega_0^2 x^2 \quad \text{for} \quad -\frac{l_d}{2} \le x \le \frac{l_d}{2} \tag{1}$$

If we associate two electrons with each repeat unit of the oligomer and apply a static electric field, we obtain, as outlined in Ref. 2, the optical band gap E_g, the polarizability α and the second hyperpolarizability γ. The two parameters in this model are the resonance pulsation of the monomer harmonic oscillator ω_0 and the delocalisation length l_d. Fig. 2 displays the calculated second hyperpolarizability γ as a function of the number of repeat units N, together with the available experimental data[1,3] and recently published detailed quantum-chemical calculations[4] for the thiophene oligomeric series. The experimental values are reduced to their static limit using the well-known dispersion relations for a two-level system and the parameters are obtained from the experimental band gaps of the monomer and dimer. The

calculated band gap and linear polarizability show a very similar behaviour to the ones we presented in Ref. 2, but we stress that there the results were obtained with a model for which the monomer potential is anharmonic. Here however, the saturation of the optical properties is obtained by a model potential, where the individual constituents do *not* possess a nonlinear response. On visual inspection of Fig. 2, it can also be noted that the extrapolation of the calculations to N=1 provides a rather good estimate of the experimental monomer hyperpolarizability γ.
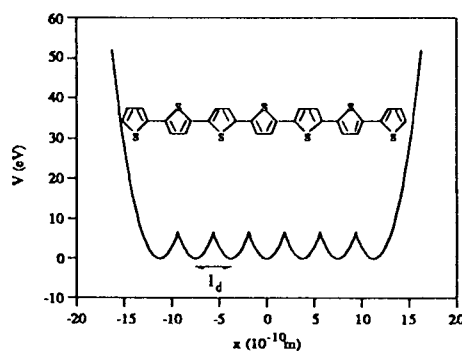
Fig. 1 : Potential energy profile for the thiophenen oligomer of 7 repeat units as a function of the coordinate along the molecule backbone x.
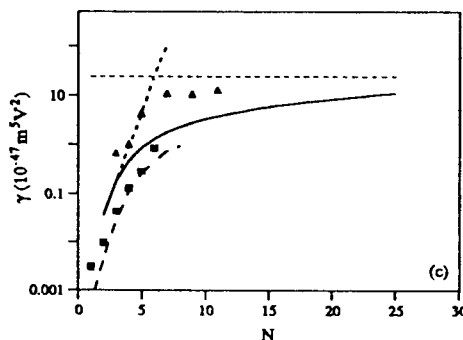
Fig. 2 : Second hyperpolarizability γ ($10^{-47}m^5V^{-2}$) vs. number of repeat units N for thiophene oligomers (our calculations (plain line); ab initio calculations by Beljonne et al.[4] (long dashes); experimental values : Thienpont et al.[1] (triangles), Zhao et al.[3] (squares)). The dashed lines indicate the short-chain and long-chain length dependencies.

In order to study the effect of conformation, we calculate the optical band gap E_g as a function of the monomer delocalisation length l_d for the biphenyl molecule, using the parameter value for ω_0 determined from the band gap of benzene[5]. As the dihedral angle θ between the two phenyl rings increases, the overlap between the p_z orbitals of the two carbon atoms on either side of the bond will decrease, resulting in an increased bond length and hence an inhibition of the tunneling. This is modeled by an increase of the potential barrier between the two consecutive wells. By increasing the spacing between the monomer potential wells l_d and relating this spacing to the overlap of the p_z orbitals following Eq. 2, we obtain the dependence of the optical band gap on the dihedral angle θ (Fig. 3).

103

$$S(r,0°) = S(r_0,0°).\cos\theta \qquad\qquad (2)$$

Here, S stands for the π-π overlap integral between two carbon atoms, calculated on Slater type orbitals with an orbital exponent[6] of 1.625 and r_0 for the bond length r (defined in inset of Fig. 3) at θ=0°. The experimental points also shown in Fig. 3 are the mean values of the data compiled from numerous sources for biphenyl in the crystalline and gas phase and in different solutions in nonpolar solvents. The flags indicate the range of measurements found in the literature.
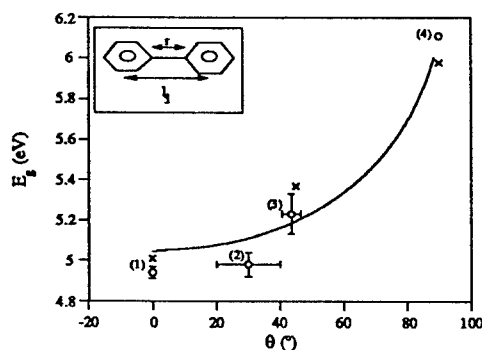
Fig. 3 : Optical bandgap Eg (eV) vs. dihedral angle θ (°) for biphenyl. Our calculations (plain line); Pariser-Parr-Pople calculations[7] (crosses); experimental values (circles) : (1) solid state, (2) liquid phase, (3) gas phase, (4) the value for benzene[5]. Inset : molecular structure and parameter definition.

In conclusion, we have shown that resonant tunneling phenomena *alone* can account for the length dependence of the optical properties of conjugated systems, in good agreement with the experiments of Thienpont *et al.*[1]. In addition, we have quantitatively studied the effect of a twist in the conjugated chain by using a very simple relationship between the spacing of the minima in the potential profile and the dihedral angle between the tilted p_z orbitals. The results on the biphenyl molecule are in good agreement with the experimental data. The very simple parametrisation of the model makes it a powerful tool for the estimation of the optimum length of newly designed conjugated molecules. In fact, the optical band gap of the monomer and its geometry are sufficient to predict the oligomer length at which the optical properties level off. Hence, the physical lower limits of ω_0 and l_d will determine the maximum molecular nonlinear response obtainable in these conjugated systems. Therefore, one should focus on the ordering of the molecules into a proper macroscopic sample to obtain organic materials suitable for ultrafast optical switching.

[1]H. Thienpont, G. L. J. A. Rikken, E. W. Meijer, W. ten Hoeve, and H. Wynberg, Phys. Rev. Lett. 65, 2141 (1990).
[2]Y. Verbandt, H. Thienpont, I. Veretennicoff, and G. L. J. A. Rikken, Phys. Rev. B 48, 8651 (1993).
[3]M. Zhao, B. P. Singh, and P. N. Prasad, J. Chem. Phys. 89, 5535 (1988).
[4]D. Beljonne, Z. Shuai, and J. L. Brédas, J. Chem. Phys. 98, 8819 (1993).
[5]R. S. Mulliken, C. A. Rieke, D. Orloff, and H. Orloff, J. Chem. Phys. 17, 1248 (1949).
[6]R. Grinter, Mol. Phys. 11, 7 (1966).
[7]M. Zhao, M. Samoc, B. P. Singh, and P. N. Prasad, J. Phys. Chem. 93, 7916 (1989).

Investigation of the nonlinear optical properties of quantum confined InP deposited in porous glass

M.D. Dvorak*, D.G. Hendershot, and B.L. Justus
*ONT/ASEE Postdoctoral Fellow
Naval Research Laboratory, Code 5610, Washington DC 20375-5338
202-767-9483

There has been much recent interest in the optical properties of semiconductor microcrystals which are of sufficiently small size that quantum size effects become important [1-4]. The deep potential well in these systems provides strong confinement of the carriers, profoundly altering the observed linear and nonlinear optical properties. The ability to control the strength of this confinement, and consequently the optical properties of the material, by using different microcrystal sizes provides a rich field of study and has the potential to provide materials for photonic device applications.

One method used in the fabrication of such structures is to grow the semiconductor in a glass matrix, and glasses doped with II-VI and I-VII materials have been investigated [5-9]. These fabrication techniques are not as well suited, however, to III-V and IV-IV semiconductors. An alternative is to grow these materials in the voids present in a porous glass such as Corning Vycor glass. In this work we report studies of the optical properties of InP microcrystals deposited in Vycor.

The Z-scan [10-12], in which the sample under study is moved along the direction of propagation of a focused beam, has been employed to study these systems. This experimental technique allows measurement of the bound electronic nonlinear refractive index γ, the refractive index change per unit photoexcited charge carrier density σ_r, and the two photon absorption coefficient β. In [9] a Q-switched/mode-locked Nd:YAG laser providing 100psec duration pulses at 1064nm was used to study 40Å radius GaAs microcrystals. These experiments found $\gamma=-5.6\times10^{-12}$cm2/W, $\sigma_r=-8.5\times10^{-21}$cm3, and $\beta=30$cm/GW. The importance of the quantum confinement to these results becomes clear when one considers that the GaAs represented, by volume, only about 1% of the the sample.

Here, we report results of Z-scans with 150Å InP microcrystals deposited in Vycor. This work employed a Q-switched/mode-locked Nd:YAG laser which pumped a Ti:sapphire laser. The system was operated at 850nm and provided pulses of 8nsec duration. These studies have determined γ to be negative in these materials at this wavelength, with $|\gamma|<1.3\times10^{-12}$cm2/W. The results also indicate significant nonlinear

absorption which could not be attributed to a single loss mechanism. Given the relatively long pulse duration, excited-state absorption is a reasonable explanation for this nonlinear loss. It was not possible, therefore, to extract β from these measurements.

In other work with 150Å InP microcrystals, a pulse plucker was used in conjunction with the Q-switched/mode-locked Nd:YAG laser to provide single 100psec duration pulses at a repetition rate of 1kHz. Figure 1 shows the result from one Z-scan. The peak incident intensity in this case was 1.8GW/cm^2 and the aperture size [10-12] was S=0.64. This data clearly indicates that the bound electronic nonlinear refractive index is negative in this system, and we find $\gamma=-0.4\times10^{-12}$cm^2/W for this incident irradiance. Unlike the previous set of studies, however, nonlinear absorption was negligible, which we attribute to the difference in pulse duration between the two sets of measurements. The absence of significant nonlinear absorption can be inferred from Figure 1 by the good agreement between the values of (the peak transmittance-1) and (1-the minimum transmittance) [11,12]. The absence of nonlinear absorption was further confirmed by open aperture Z-scans. In both InP studies the concentration in the glass was only about 3% by volume, again indicating the strong influence of the quantum confinement on the optical properties of these systems. Pump/probe experiments have also been performed to study the temporal characteristics of the optical nonlinearities. This work was performed by placing the sample at, for example, the transmittance maximum and observing the temporal decay of the signal with a probe beam.

In conclusion, we report results of Z-scan experiments with InP microcrystals deposited in Vycor. The data indicates that the quantum confinement provided by the microcrystals produces a significant nonlinear refractive index. It is also shown that, for a short pulse duration (100psec), nonlinear absorption is negligible at 1064nm. Further, the temporal characteristics of the optical nonlinearities have also been investigated.
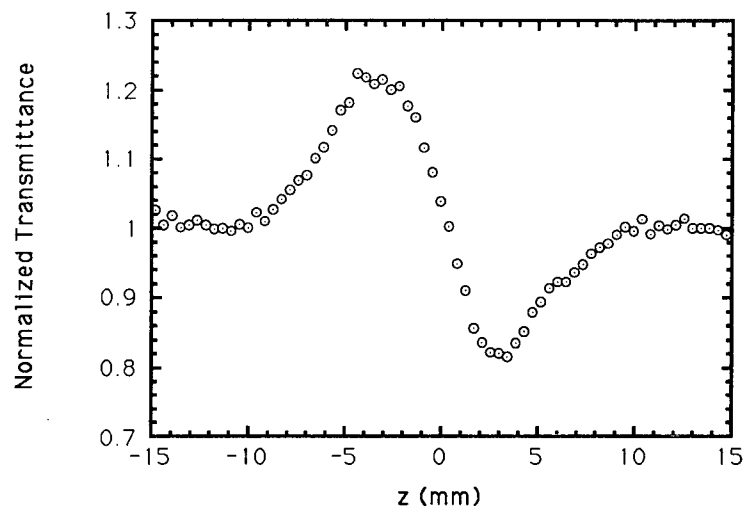
FIGURE 1: Closed aperture Z-scan data (S=0.64) for a 400 micron thick Vycor glass sample with 150Å radius InP microcrystals. The peak incident intensity was 1.8GW/cm^2 and the laser wavelength was 1064nm.

References:
1. S. Schmitt-Rink, D. A. B. Miller, and D. S. Chemla, Phys. Rev. B **35**, 8113 (1987).
2. E. Hanamura, Phys. Rev. B **37**, 1273 (1988).
3. L. Banyai, Y. Z. Hu, M. Lindberg, and S. W. Koch, Phys. Rev. B **38**, 8142 (1988).
4. Y. Wang, Acc. Chem. Res. **24**, 133 (1991).
5. N. Peyghambarian, B. Fluegel, D. Hulin, A. Migus, M. Joffre, A. Antonetti, S. W. Koch, and M. Lindberg, IEEE J. Quant. Electron. **25**, 2516 (1989).
6. P. Horan and W. Blau, J. Opt. Soc. Am. B **7**, 304 (1990).
7. S. H. Park, R. A. Morgan, Y. Z. Hu, M. Lindberg, S. W. Koch, and N. Peyghambarian, J. Opt. Soc. Am. B **7**, 2097 (1990).
8. B. L. Justus, M. E. Seaver, J. A. Ruller, and A. J. Campillo, Appl. Phys. Lett. **57**, 1381 (1990).
9. B. L. Justus, R. J. Tonucci, and A. D. Berry, Appl. Phys. Lett. **61**, 3151 (1992).
10. M. S. Bahae, A. A. Said, and E. W. Van Stryland, Opt. Lett. **14**, 955 (1989).
11. M. S. Bahae, A. A. Said, T. H. Wei, D. J. Hagan, and E. W. Van Stryland, IEEE J. Quant. Electron. **26**, 760 (1990).
12. A. A. Said, M. S. Bahae, D. J. Hagan, T. H. Wei, J. Wang, J. Young, and E. W. Van Stryland, J. Opt. Soc. Am. B **9**, 405 (1992).

SOLITONS IN MULTICORE NONLINEAR WAVEGUIDE ARRAYS

A. V. Buryak   and   N. N. Akhmediev
Optical Sciences Centre, Institute of Advanced Studies,
Australian National University,
Canberra, A.C.T. 2601, Australia
phone: 61-6-2490191

Physical phenomena in arrays of multiple nonlinear waveguides or fibres have attracted much attention in recent years [1-4].

In these works, the input radiation usually has been assumed to be a continuous wave. However, in real devices CW excitation has two major problems. Firstly, CW is known to be modulationally unstable at powers close to the threshold switching powers. Secondly, only short pulses (preferably solitons) rather than quasi CW-signals can be used for ultrafast all-optical switching. In this paper we start to investigate solitary wave propagation in multi-core nonlinear fibre arrays of circular symmetry. We find new classes of stationary solitary wave solutions for this type of array. We also investigate the structure of these new soliton solutions and the parameter regions where they exist. It is shown that the bifurcation phenomenon, which was recently found for the case of the two-core nonlinear coupler [5], has a universal character and can be observed for every number n of cores in a multi-core nonlinear fibre array of circular symmetry.

The propagation of pulses in an array of n coupled nonlinear fibres of circular symmetry (the geometry of a sample fibre array is shown in the Fig.1, $n \geq 3$) can be described in terms of n linearly coupled nonlinear Schrödinger equations (NLSE) [4]. In normalised form, this set of NLSE's is given by:

$$i\frac{\partial U_1}{\partial \xi} + \frac{1}{2}\frac{\partial^2 U_1}{\partial \tau^2} + |U_1|^2 U_1 + K(U_n + U_2) = 0$$

$$i\frac{\partial U_2}{\partial \xi} + \frac{1}{2}\frac{\partial^2 U_2}{\partial \tau^2} + |U_2|^2 U_2 + K(U_1 + U_3) = 0$$

$$\cdots \cdots$$

$$\qquad\qquad\qquad\qquad\qquad\qquad\qquad (1)$$

$$i\frac{\partial U_n}{\partial \xi} + \frac{1}{2}\frac{\partial^2 U_n}{\partial \tau^2} + |U_n|^2 U_n + K(U_{n-1} + U_1) = 0$$

All variables are dimensionless and normalised. We consider K to be the only material constant of the problem and assume that K > 0.

Using substitutions :

$$U_i(\xi, \tau) = u_i(\tau, q') e^{iq'\xi} \qquad\qquad\qquad (2)$$

$$u_i = \sqrt{K}\, f_i, \quad \tau = t/\sqrt{K}, \qquad q' = qK \qquad\qquad (3)$$

where i is the index of a core (n is the number of the cores), we obtain:

$$\frac{1}{2}\frac{d^2 f_1}{dt^2} - qf_1 + f_1^3 + (f_n + f_2) = 0$$

$$\frac{1}{2}\frac{d^2 f_2}{dt^2} - qf_2 + f_2^3 + (f_1 + f_3) = 0$$

$$. \quad . \quad . \quad .$$

$$\frac{1}{2}\frac{d^2 f_n}{dt^2} - qf_n + f_n^3 + (f_{n-1} + f_1) = 0$$

(4)

which has now only one combined parameter $q = q^*/K$. This combined parameter is the only parameter of the problem.

Eqs. (4) are invariant with respect to four major symmetry transformations. They are the following:

(a) rotation symmetry $(f_i \rightarrow f_{i+1}$, for $1 \leq i \leq (n - 1)$ and $f_n \rightarrow f_1$),

(b) mirror symmetry $(f_1 \rightarrow f_1$ and $f_{1+i} \rightarrow f_{n+1-i}$ for $1 \leq i \leq (n - 1))$,

(c) sign inversion symmetry $(f_i \rightarrow -f_i$, for $1 \leq i \leq n)$,

(d) time reversal symmetry $(f_i(t) \rightarrow f_i(-t)$ for $1 \leq i \leq n)$.

The internal symmetries of the system (4) result in the existence of a solution, which exists for every value of n ($n \geq 3$) This is the fully symmetric solution:

$$f_i = \sqrt{2(q-2)} \, \text{sech} \, [\sqrt{2(q-2)} \, t] \, ,$$

(5)

for all i values ($1 \leq i \leq n$). Using the approach of [5] we can find the positions of the points where asymmetric solutions bifurcate from the solution which has identical pulses in each core:

$$q_{j-1}^{(n)} = \frac{8 - 2\cos(2\pi(j-1)/n)}{3}$$

(6)

Eqs.(6) determine the location of the bifurcation points. (Superscript n and subscript $(j-1)$ (where $2 \geq j \geq n$) denote the number of the cores and the number of the bifurcation respectively.)

The convenient way to classify soliton solutions is by the construction of the energy-dispersion diagram [5, 6]. The energy of a stationary soliton solution is defined by:

$$Q(q) = \int_{-\infty}^{\infty} \sum_{i=1}^{n} |U_i|^2 d\tau = \int_{-\infty}^{\infty} \sum_{i=1}^{n} u_i^2 \, d\tau = K^{1/2} \int_{-\infty}^{\infty} \sum_{i=1}^{n} f_i^2 \, dt = K^{1/2} \int_{-\infty}^{\infty} \sum_{i=1}^{n} x_i^2 \, dt$$

(7)

On this diagram, a bifurcation point can be explicitly seen as the point where a curve which corresponds to the solution of one type splits off from a curve which corresponds to another type of solution.

Since in any switching phenomena, nonlinear modes with the lowest energy are initially excited, we have carried out a full numerical investigation only for the asymmetric solutions of the lowest order. The energy-dispersion bifurcation diagrams for the cases n = 3, 4, 5 are shown in Fig 1 (a, b, c respectively). Only the curves for the fully

symmetric and the lowest order asymmetric soliton solutions are shown. The curve of parabolic shape corresponds to the symmetric state (S-curve). The curves for asymmetric states of the lowest order split off from it at the bifurcation point M_1. We also show the position of all other bifurcation points whenever they exist for a given n.
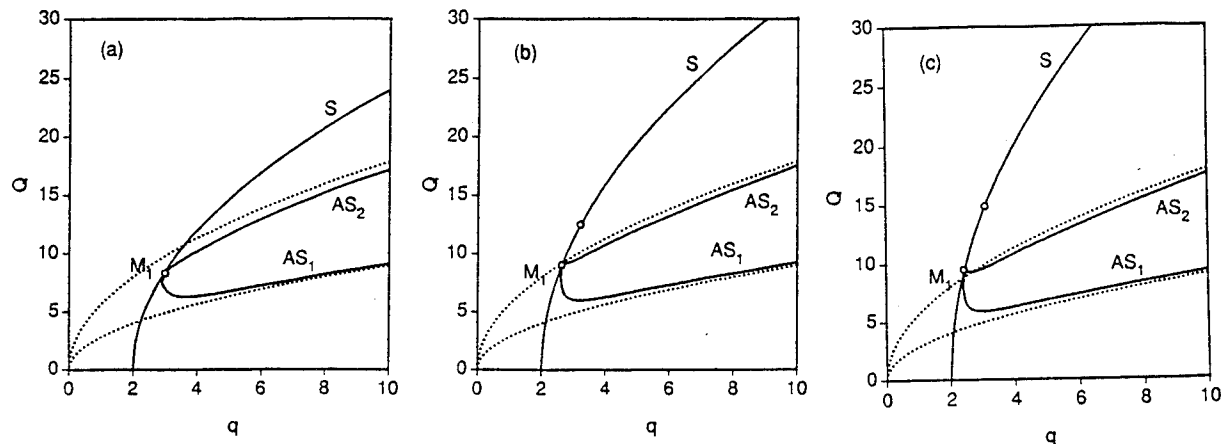
The numerical results obtained for the cases $n = 3$, 4 and 5 show that the number and positions of the points of bifurcation are in accord with formula (6).

In conclusion, we have investigated the problem of stationary pulse propagation in circular arrays of n coupled nonlinear fibres. At low energies, the stationary pulses can only propagate in the array if their field envelopes have identical forms and amplitudes in all fibres. Increasing the energy above the energy of the first bifurcation gives the possibility of a redistribution of energy among the cores, so that the energy becomes concentrated in a few cores. Further increase in the total energy leads to a concentration of the energy in a single core.

REFERENCES

1. D. J. Mitchell, A. W. Snyder, Y. Chen, 'Nonlinear Triple Core Couplers', Electronics Letters, **26**, 1164-1165, (1990);

2. D. N. Christodoulides, R. I. Joseph, 'Vector Solitons in Birefringent Fibres', Optics Letters, **13**, 794-796, (1988).

3. C. Schmidt-Hattenberger, U. Trutschel, and F. Lederer, 'Nonlinear Switching in Multiple-Core Couplers', Optics Letters, **16**, 294-296, (1991).

4. J. M. Soto-Crespo, E. M. Wright, 'All-Optical Switching of Solitons in Two and Three-Core Nonlinear Fiber Couplers', J. Phys. **70**, 7240-7243, (1991).

5. N. N. Akhmediev, A. Ankiewicz, 'Novel Soliton States and Bifurcation Phenomena in Nonlinear Fiber Couplers', Phys. Rev. Letters, **70**, 2395-2398, (1993).

6. J. M. Soto-Crespo, N. N. Akhmediev, 'Stability of the Soliton States in a Nonlinear Fiber Coupler', Phys.Rev.E, 1993 (in press)

THIRD ORDER OPTICAL NON-LINEARITY OF POLY(P-PHENYLENEVINYLENE) AT 800nm

B. Luther-Davies, M. Samoc, A. Samoc, M. Woodruff

Laser Physics Centre

Research School of Physical Sciences and Engineering

The Australian National University

Canberra ACT 0200

Telephone (61) 62 494244

Poly(p-phenylenevinylene) (PPV) is a conjugated polymer known for its interesting optical and electrical properties. In particular large values of its third order optical non-linearity have been reported at wavelengths close to its single photon absorption edge[1]. Of special interest is the fact that PPV is processible in the form of a soluble precursor which can be dissolved in water and mixed with media such as sol-gel glasses to obtain organic/inorganic composites of good optical quality useful for waveguide fabrication.

The crucial point in determining the application of the material in photonics is however, the ratio of the real to imaginary parts of the non-linear susceptibility[2] as well as the sign of the real part. These determine the kind of phenomena that can be observed using the material, and if sufficient non-linear phase accumulation can occur for a given application before multi-photon absorption attenuates the non-linear waves.

Between its single and two-photon absorption edges PPV is expected to have a defocussing non-linearity and although measurements of the magnitude of χ_3 around 600nm have been reported the sign has not yet been determined. A defocussing non-linearity is required for the excitation of dark spatial solitons which are predicted to be relatively insensitive to two-photon absorption[3] in photonic applications. It is thus of interest to determine the non-linear properties of PPV within its transmission band.

We, therefore, report here measurements of the sign and magnitude of the third order non-linearity, and the magnitude of the two photon absorption coefficient using 125fs pulses from an amplified mode-locked Ti:sapphire laser. We also demonstrate that the non-linear index change saturates at $\Delta n \approx 10^{-2}$, with saturation accompanied by the appearance of a long lived component in the transient grating generated within the material associated with excited state absorption.

Single pulses extracted from the pulse train from a Coherent MIRA fs Ti:sapphire laser were amplified to a maximum energy of 1mJ using a standing wave Ti:sapphire regenerative amplifier pumped at 30Hz by a frequency doubled Quantaray

GCR-130-30 Nd:YAG laser. After recompression the pulse duration was measured to be 125±5fs. The amplified beam was split into three and configured in the BOXCARS geometry for time resolved forward DFWM measurements of the optical non-linearity. The beams were loosely focussed to ≈300μm diameter onto 3-4μm thick PPV samples on glass microscope slides as substrates. The PPV films were fabricated from a precursor with a tetrahydrothiophene leaving group synthesized according to [4] and their thickness determined from the waveguide modes using a METRICON prism coupler. By measuring the non-linearity as a function of laser intensity it was possible to determine its saturation properties. Fused silica was used as a reference material to obtain the magnitude of the non-linearities from the DFWM signals.

Typical data from these experiments are shown in figure 1 which illustrates the presence of two contributions to the transient grating formed in PPV: one a fast component limited only by the pulsewidth of the laser and corresponding to an $n_2 \approx 7.5 \pm 0.5 \ 10^{-13} cm^2/W$; and the second an intensity dependent tail attributed to the onset of excited state absorption.

In other experiments single beam power dependent transmission measurements and two-beam pump-probe measurements allowed the two photon absorption coefficient to be determined as $\beta \approx 1.1 \ 10^{-8} cm/W$, whilst the eclipsing z-scan[5] technique was used to determine the sign of the non-linearity as negative.

The consequences of these results for the application of PPV in photonics will be discussed.

REFERENCES

[1] see e.g. B.P Singh, P.N. Prasad, F.E. Karasz, Polymer **29**, 1940 (1988); Y. Pang, M. Samoc, P.N. Prasad, J. Chem. Phys. **94**, 5282 (1991); J. Swiatkiewicz, P.N. Prasad, F.E. Karasz, J. Appl. Phys. **74**, 525 (1993); D. McBranch, M.Sinclair, A.J.Heeger, Synthetic metals, 29, E85 (1989);C. Bubeck, A. Kaltbeitzel, A. Grund and M. LeClerc, Chem.Phys. 154 343 (1991).

[2] See e.g. G.I. Stegeman, in *Contemporary Nonlinear Optics*, Academic Press, 1, (1992).

[3] X. Yang, Y Kishvar, B. Luther-Davies, to be published.

[4] D.R. Gagnon, J.D Capistran, F.E. Karasz, R.W. Lenz, S. Antoun, Polymer **28**, 567 (1987)

[5] T. Xia, D.J. Hagan, M. Sheik-Bahae, E.W. Van Stryland, to be published.
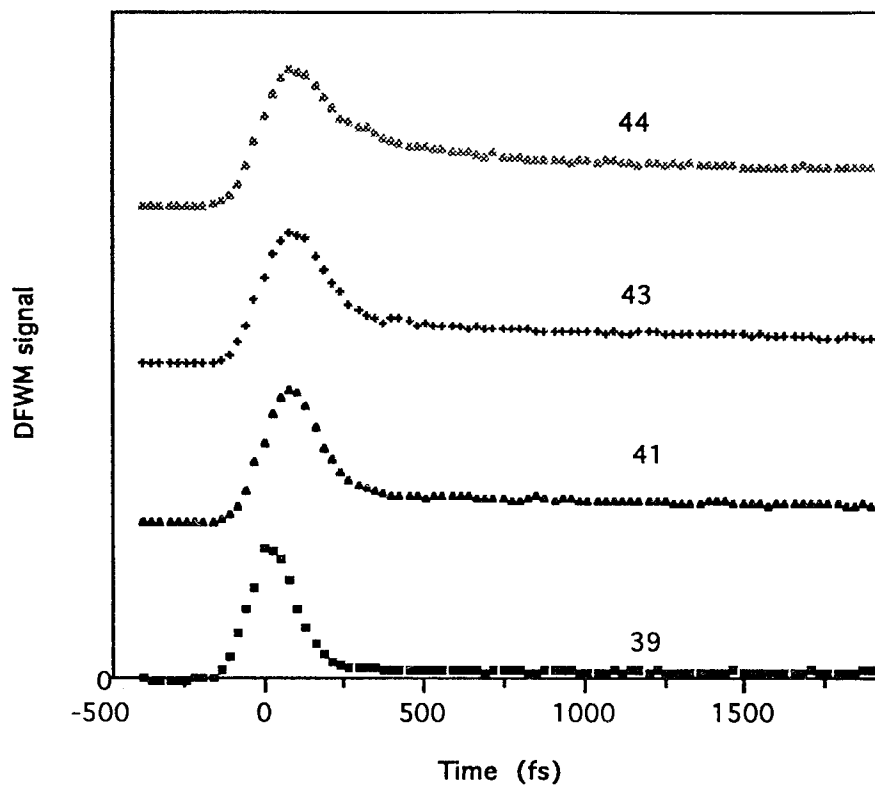
Fig.1 DFWM scans for a 3μm thick PPV film on glass substrate obtained at the following intensities:1.3GW/cm^2 (39); 32GW/cm^2 (41); 57 GW/cm^2 (43); 80GW/cm^2 (44).

Two-photon absorption in π-conjugated polymers due to biexcitonic states

V.A.Shakin

Photodynamics Center, RIKEN, Nagamachi Koeji 19-1399, Aoba-ku, Sendai 980, Japan
Tel. 81-22 228 2012

Shuji Abe

Electrotechnical Laboratories, Umezono 1-1-4, Tsukuba 305, Japan. Tel. 81-298 58 5370

Today conjugated polymers are among the most promising nonlinear materials. The configuration interaction (CI) method utilizing Pariser-Parr-Pople (PPP) model has proved to be very efficient for the calculation of the nonlinear optical properties of organic molecules. Until now such calculations in the case of conjugated polymers were restricted to either very small systems (about dozen sites) or only one-electron excited states taken into account (S-CI). However, S-CI approximation is usually insufficient to describe properly nonlinear effects, and inclusion of double excited states is inevitable. Here we are interested in the properties of bulk polymer solids, so that, using cyclic boundary condition, we can treat relatively long chains in the CI calculation with all single and double excitations taken into consideration (SD-CI).

The third order susceptibility, $\chi^{(3)}(\omega;\omega,-\omega,\omega)$, is calculated in the SD-CI approximation using PPP hamiltonian [1] for polymer rings of $N=2M$ sites (we present here the results for $N=40$) with the same number of electrons interacting with each other through the Pople potential $V_{nm}=Va/r_{nm}$, where r_{nm} is the distance between the sites n and m, and a is the average site spacing. The polymer ring is supposed to be dimerized with the transfer energy modulation δt. All energy-like quantities are presented here in units of transfer energy t (typical value is about 2eV). On-site interaction energy is taken $U=2V=2t$.
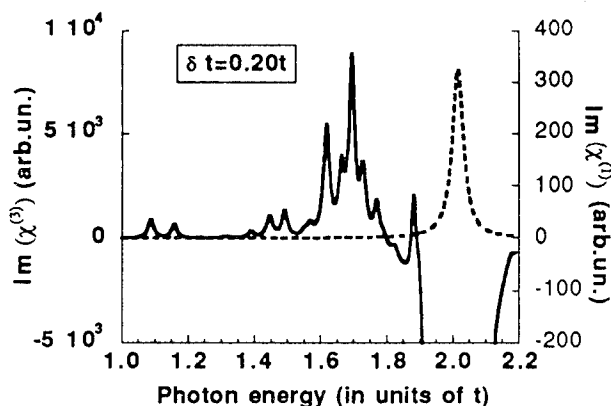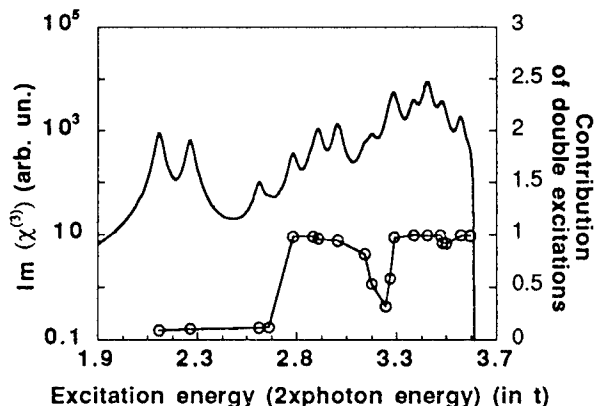
Fig.1   Fig.2

Fig.1 shows a typical spectrum of the imaginary part of $\chi^{(3)}(\omega;\omega,-\omega,\omega)$ (solid line). The damping is introduced phenomenologically and has a relatively small value (0.02t) to resolve resonance peaks. In the region of the two-photon absorption one can clearly see two groups of peaks. The smaller group represents the peaks which usually appear in the S-CI approximation [1], while the large broad group of peaks near the excitonic linear absorption resonance is an essential feature of SD-CI calculations. This becomes obvious if we analyze a contribution of the double excitations to the resonant states in the region of the two-photon absorption (Fig.2). The contribution of double excitations we define here as a sum of the squares of modular of the expansion coefficients related with wave functions of Hartree-Fock double excited states in the

series, which represents an eigenfunction of the PPP hamiltonian. The positions of its eigenvalues are marked in Fig.2 by circles. It should be noted here that the absolute values of the resonant energies should be corrected to the lower magnitudes, because in the case of long polymers a neglecting of higher order excitations (triple and so on) leads to the overestimation of the resultant excitation energies. But as for the relative position of the eigenstates of the PPP hamiltonian, it can be satisfactory described in the SD-CI approximation, the exception being the pair of the lowest one-photon and two-photon excited states [2].

In the present work we have also investigated the dependence of the two-photon absorption spectrum upon some parameters of conjugated polymers. Figures 3(a) and 3(b) differ only by the value of the transfer energy modulation δt. It is clear that polymers with weaker dimerization are more favorable for getting strong two-photon absorption.
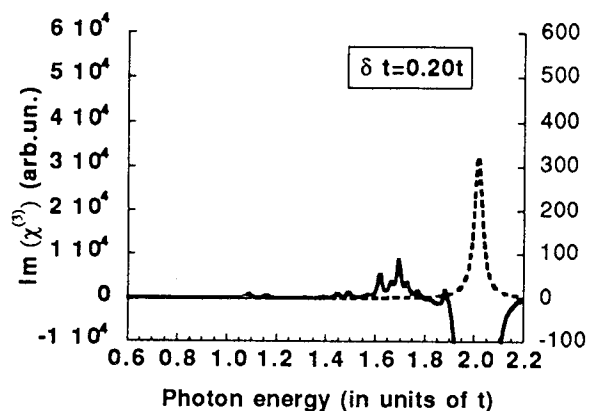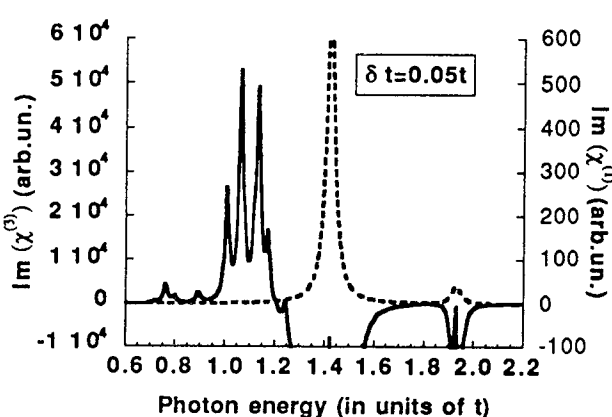
Fig.3(a)   Fig.3(b)

Two-photon absorption spectrum demonstrates also a strong dependence upon the strength of the electron-electron interaction (Fig. 4(a) and 4(b) for $\delta t=0.1t$). Two times increase in the interaction strength has forced us to use logarithmic scale to show the difference. So, we may conclude that conjugated polymers with strongly correlated electrons are poor candidates for systems with a large optical nonlinearity.
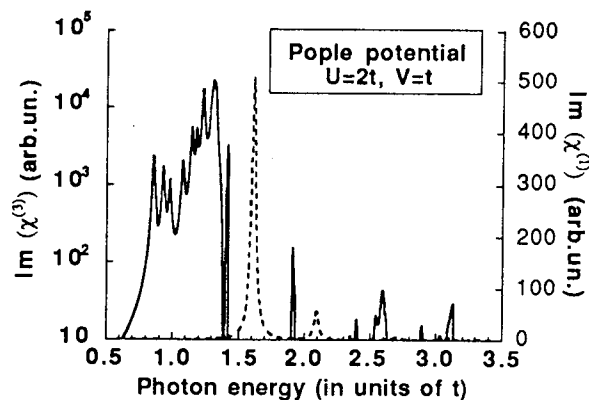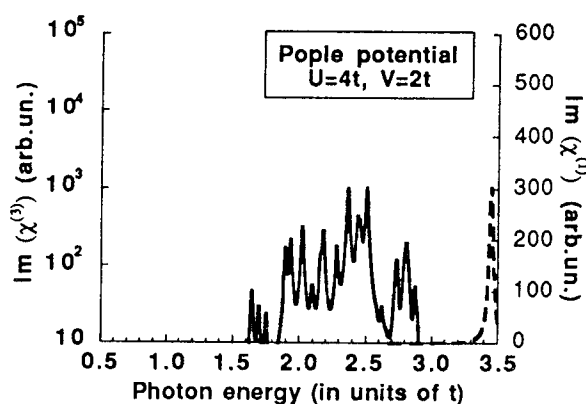
Fig.4(a)   Fig.4(b)

References
1. S.Abe, M.Schreiber, W.P.Su and J.Yu, Phys.Rev. B **45**, 9432 (1992)
2. P.Tavan and K.Schulten, J.Chem.Phys. **70**, 5407 (1979)

THIRD-ORDER SUSCEPTIBILITY OF NEW MACROCYCLIC CONJUGATED SYSTEMS

Qihuang Gong, Shao-chen Yang and Xingyu Gao
Department of Physics, Mesoscopic Physics Lab., Peking University,
Beijing 100871, China
Tel. 01-2501738, Fax. 01-2501615

Wenfang Sun Shiming Dong and Duoyuan Wang
Institute of Photographic Chemistry, Beijing 100101, China

Recently, there is a rapidly growth of interest in two-dimensional π-electron organic materials due to their large third-order nonlinear optical effects, thermal and physical stabilities and film forming property. A considerable amount of investigations on porphyrin[1,2] and phthalocyanines[3] has been accumulated. In this paper, the nonlinearity of a new kind of macrocyclic metal-coordinated complex and their derivates was reported.

The new metal-coordinated molecules are asymmetric tripyrrane-containing 22 π-electrons aromatic macrocyclic cadmium (2+) complex (I) and gadolinium (3+) complex (II). The chemical structures of the molecules are shown in Fig. 1. Both the complexes were synthesized by an improved procedure, in which the acid-catalyzed 1:1 shiff base condensation of 0-phenylenediamine with diformyltripyrrane were used and sequentially oxidized to form the methine bridged 22 π-electrons aromatic macrocyclic \metal complexes in high yields by treating with corresponding chloride in the presence of air [4]. To investigate the affect of the charge transfer within the molecule on the nonlinearity, a series of electron accepting groups, such as $-NO_2$, $-CO_2Na$ and $-Cl$, were incorporated to the pyrolane.

I   II
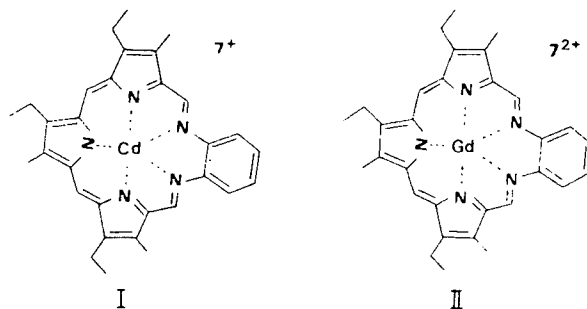
Fig. 1 Chemical Structure of two complexes

All the complexes and their derivates were studied with degenerate four wave

mixing (DFWM) in solution state. The solvant is methanol. The experimental arrangement was a standard phase conjugate DFWM, similar to our previous report[5]. 5 nanosecond pulses at 1064nm from a Q-switched YAG laser was used. The spectroscopic analysis indicated that there is no absorption in the region of 1064nm. The value of $\chi^{(3)}$ for the solutions were measured by using CS_2 as a reference. Both xxxx and xyyx components of $\chi^{(3)}$ were measured by changing the probe beam polarization with a $\lambda/4$ waveplate. The ratio of xxxx component to xyyx component for the samples was determined to be 3:1 within the measurement error. This excludes the contribution from the thermal effect. With the magnitude of $\chi^{(3)}$ measured for the solutions at a certain concentration, the value of third-order hyperpolarizability of the molecules were obtained with the relation[6] of $\chi^{(3)}=NL^4\gamma$. Where, N is the number density and $L^4 =[(n^2+2)/3]^4$ the local field correction term, n is the refractive index for the solution. The results are shown in table I.

TABLE I   The third-order hyperpolarizability of complexes and derivates

Sample	γ_{xxxx} (10^{-31}esu)	Harmitt constant
Gd^{7++}:Cycle	1.2	/
Gd^{7+}:Cycle	1.0	/
Gd^{7+}:Cycle-CO_2Na	1.0	0
Gd^{7+}:Cycle-Cl	1.15	0.23
Gd^{7+}:Cycle-NO_2	1.47	0.78

It is clearly that the nonlinearity of the molecules is enhanced by incorporated an electron accepting group. The magnitude of of γ is linearly increased with the increment of Harmitt constant. This is of great importance for synthesising new macrocylic π-conjugated molecules.

Reference
[1] R.A. Norwood and J.R. Sounik, Appl. Phys. Lett. 60 (1991) 295
[2] D.V.G.L.N. Rao and F.J. Aranda, Appl. Phys. Lett. 58 (1991) 1241
[3] J.S. Shirk etal. International J. Nonlinear Optical Physics, 1 (1992) 699
[4] Wenfang Sun etal. Chinese Chem. Lett. 4 (1993) 225
[5] Q. Gong etal. Appl. Phys. Lett. 59 (1991) 381
[6] M.D. Levenson and N. Bloembergen, J. Chem. Phys. 60 (1974) 1323

Nonlinear Raman Processes in Polydiacetylenes

Takayoshi Kobayashi[1], Masayuki Yoshizawa[2], and Yasuhiro Hattori[3]

[1]Department of Physics, Faculty of Science, University of Tokyo,
Hongo 7-3-1, Bunkyo-ku, Tokyo 113, Japan
  Phone +(81)-3-3812-2111 ext 4227
  FAX +(81)-3-3818-7812
[2]Department of Physics, Faculty of Science, Tohoku University, Aramaki,
Aoba-ku, Sendai-shi 980, Japan
  Phone +(81)-22-222-1800 ext 3274
  FAX +(81)-22-225-1891
[3]New Chemistry R&D Laboratories, Sumitomo Electric Industries,
Shimaya 1-1-3, Konohana-ku, Osaka-shi 554, Japan

In the present paper we have developed a Raman gain spectroscopy with femtosecond resolution. The advantage of the method is as follows. (1) The method is not suffered from disturbance by fluorescence. (2) The interference of signal with nonresonant background does not appear. This is extremely advantageous to the time-resolved CARS spectroscopy. We have applied this new method to the excitons in polydiacetylene (PDA) with only 1.5 ps lifetime. This offers the vibrational spectrum with the highest time resolution.

Conjugated polymers have attracted much attention because of their unique properties as model compounds of one-dimensional electronic systems. Conjugated polymers have localized excited states with geometrical relaxation. We have investigated self-trapped exciton (STE) in polydiacetylene (PDA) using femtosecond spectroscopy [1-6]. The formation process of STE from free-exciton (FE) has been observed as a spectral change of photoinduced absorption with a time constant of about 150 fs [4]. Transient fluorescence from FE in PDA observed by probe saturation spectroscopy (PSS) has a peak at 1.9 eV and decays with the formation of the STE [6].

Time-resolved resonance Raman spectroscopy has been recognized as a powerful method for studying structures of transient species and electronic excited states. Terai et al. have calculated phonon modes of localized excited states in $(CH)_x$ and predicted that solitons and polarons can be distinguished by Raman spectroscopy [7]. However, only a few time-resolved Raman experiments have been performed in conjugated polymers because of the difficulty due to very short lifetime of the excited states [8,9]. However, the observed signals are due to the depletion of the ground state. New phonon modes of excited states in conjugated polymers have not been observed by transient Raman spectroscopy.

The femtosecond Raman gain spectroscopy was performed using three pulses of femtosecond durations as shown in Fig. 1. The 1.97-eV femtosecond pulse was generated by a colliding-pulse mode-locked dye laser and amplified by a four-stage dye amplifier [1]. The duration and energy of the amplified pulse were 100 fs and $200\mu J$, respectively. The amplified pulse was split into three beams. The first beam (pump-1) generated excited states in PDA. A part of white continuum generated from the second one was amplified by a two-stage dye amplifier. The amplified pulse has the center photon energy of 1.78 eV and the duration of 200 fs and was used for the pump pulse of the Raman gain spectroscopy (pump-2). The probe pulse was white continuum generated from the last beam. Using this technique the time dependence and spectra of

photoinduced absorption, bleaching, stimulated emission, and Raman gain were observed at the same time. The Raman gain signal was distinguished using the time dependence and sharp structure. Polarizations of the three beams were parallel to oriented polymer chains of PDA-3BCMU deposited on a KCl crystal [5]. All the experiment was done at room temperature.

Figure 2 shows Raman gain spectra obtained using the 1.78-eV pulse at several delay times after the 1.97-eV photo-excitation. At -0.5 ps, two Raman

Fig.1 Time-resolved Raman gain spectroscopy.

gain peaks are observed at 1440 and 2060 cm^{-1}. They are assigned to the stretching vibrations of the C=C and C≡C bonds in the acetylene-like structure of the ground state. The spectrum at 0.0 ps has broad signal below the 1440 cm^{-1} Raman peak down to 1000 cm^{-1}. At delay time longer than 0.2 ps the Raman signal has a clear peak at 1200 cm^{-1}. The spectral change of the Raman signal around 1200 cm^{-1} is reproducible and is observed also in PDA-C_4UC_4. The width of the 2060 cm^{-1} Raman signal becomes slightly broader after the photoexcitation, but no new Raman peak is observed around 2000 cm^{-1}.

Figure 3 shows the transient Raman gain change at 1200 and 1440 cm^{-1}. The negative change at 1440 cm^{-1} is explained by the depletion of the ground state due to the formation of STE. The time dependence is consistent with the decay kinetics of the STE. The signal appears slightly slower than the 1.97-eV pump pulse and decays within several picoseconds. The solid curve is the
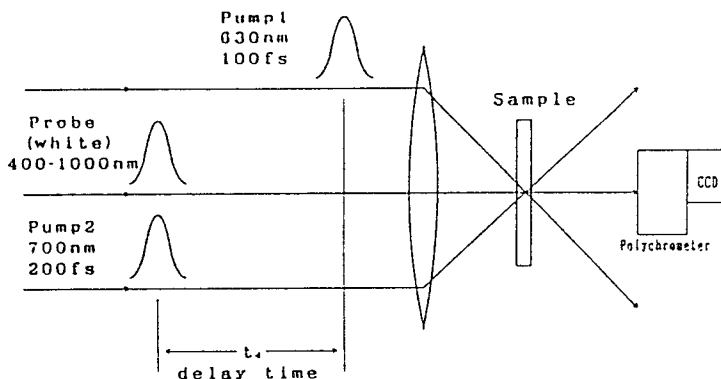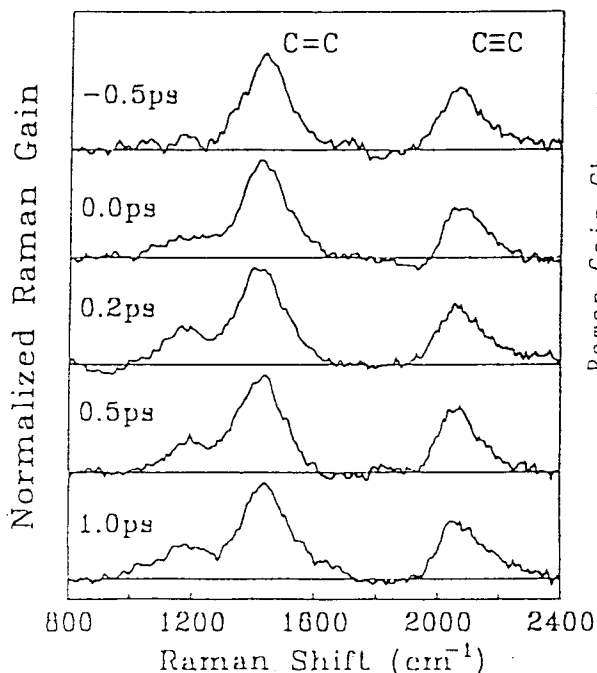
Fig. 2. Normalized resonance Raman gain spectra at several delay times after the 1.97-eV photoexcitation.
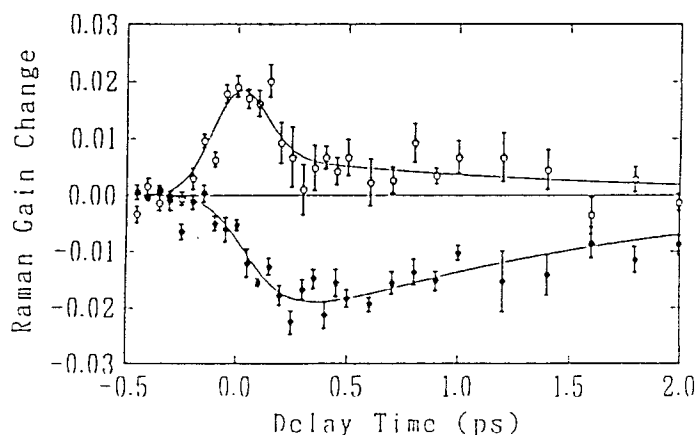
Fig. 3. Transient Raman gain changes at 1200 cm^{-1} (open circles) and 1440 cm^{-1} (closed circles) after the 1.97 eV photoexcitation. The solid curves are the best fitted curves with time constants of 150 fs and 1.5 ps. The resolution time is 300 fs.

119

best fitted curve using time constants of 150 fs and 1.5 ps. The change at 2060 cm^{-1} is also negative and has similar time dependence with the 1440-cm^{-1} signal. The time dependence of the Raman signal at 1200 cm^{-1} has two components. The long-life component decays within several picoseconds and is assigned to the STE. The short-life component has time constant shorter than the present resolution time of 300 fs and is probably due to the nonthermal STE, because the 1.78-eV pulse can be resonant with the transition between the nonthermal STE and the ground state.

The theoretical calculation has predicted that the localized excitations in trans-$(CH)_x$ have several Raman active phonon modes [7]. The expected signal is the reduction of the stretching vibration modes and new Raman lines at lower frequencies than the stretching modes. The Raman signal observed in PDA is similar to this feature. However, the phonon modes of the STE in PDA have not been investigated. Here, the observed Raman frequency is compared with stretching modes of center bonds in unsaturated hydrocarbons with four carbon atoms, i.e. repeat units of PDA [10]. The formation of the STE in PDA is expected to be the geometrical relaxation from the acetylene-like structure $(=CR-C \equiv C-CR=)_x$ to the butatriene-like structure $(-CR=C=C=CR-)_x$. The C=C bond in trans-butene-2 $(CH_3-CH=CH-CH_3)$ has a stretching mode with 1675 cm^{-1}, while the frequency of the C-C bond in trans-1,3-butadiene $(CH_2=CH-CH=CH_2)$ is 1202 cm^{-1}. Therefore, the 1200 cm^{-1} Raman peak can be assigned to the C-C bond in the butatriene-like structure. However, Raman signal due to the C=C bond in the butatriene-like structure cannot be observed in this study. It can be explained by close frequencies of the stretching modes of the center C=C bond in butatriene $(CH_2=C=C=CH_2)$ and the C≡C bond in dimetylacetylene $(CH_3-C \equiv C-CH_3)$, 2079 and 2235 cm^{-1}, respectively. The expected new Raman signal near the 2060 cm^{-1} peak cannot be resolved in this study because of the broad pump spectrum.

In conclusion, we developed a new timr resolved Raman spectroscopy and the new Raman peak due to self-trapped exciton in PDA has been observed at 1200 cm^{-1} for the first time by the femtosecond time-resolved Raman gain spectroscopy. The observed Raman signals indicate the butatriene-like structure due to the formation of the STE after the geometrical relaxation from the acetylene-like structure in the FE state.

References

[1] M. Yoshizawa, M. Taiji, and T. Kobayashi, IEEE J. Quantum Electron. **QE-25**, 2532 (1989).
[2] T. Kobayashi, M. Yoshizawa, M. Hasegawa, and M. Taiji, J. Opt. Soc. Am. **B7**, 1558 (1990).
[3] M. Yoshizawa, A. Yasuda, and T. Kobayashi, Appl. Phys. **B53**, 296 (1991).
[4] M. Yoshizawa, K. Nishiyama, M. Fujihira, and T. Kobayashi, Chem. Phys. Lett. **270**, 461 (1993).
[5] M. Yoshizawa, Y. Hattori, and T. Kobayashi, Phys. Rev. B47, 3882 (1993).
[6] A. Yasuda, M. Yoshizawa, and T. Kobayashi, Chem. Phys. Lett. **209**, 281 (1993).
[7] A. Terai, Y. Ono, and Y. Wada, J. Phys. Soc. Jpn. **58**, 3798 (1989).
[8] L. X. Zheng, R. E. Benner, Z. V. Vardeny, and G. L. Baker, Synth. Metals **49**, 313 (1992).
[9] G. Lanzani, L. X. Zheng, G. Figari, R. E. Benner, and Z. V. Vardeny, Phys. Rev. Lett. **68**, 3104 (1992).
[10] L. M. Sverdlov, M. A. Kovner, and E. P. Krainov, Vibrational Spectra of Polyatomic Molecules, (John Wiley & Sons, New York, Toronto, 1970), pp.282-323.

Ultrafast Nonlinear Processes in One-Dimensional J-aggregates

Takayoshi Kobayashi, Kaoru Minoshima[1], Makoto Taiji[2], and Kazuhiko Misawa

Department of Physics, Faculty of Science, University of Tokyo,
7-3-1 Hongo, Bunkyo-ku, Tokyo 113, Japan
Phone 81-3-3812-2111 ext. 4227, Fax 81-3-3818-7812

[1]*Quantum Metrology Department, National Research Laboratory of Metrology,*
1-1-4 Umezono, Tsukuba, Ibaraki 305, Japan
[2]*College of Arts and Sciences, University of Tokyo,*
3-8-1 Komaba, Meguro, Tokyo 153, Japan

Summary

J-aggregates of cyanine dyes[1,2] are attracting interest of many scientists from a spectroscopic viewpoint, because they are expected to show the crossover between the macroscopic properties of bulk materials and microscopic ones of isolated molecules.

The mechanism of the femtosecond nonlinear response of excitons has not yet been studied on the basis of the one-dimensional Frenkel-exciton model. Recently, the transition from a 1-exciton state to a 2-exciton state was observed in ethyleneglycol/water-glass (EGWG) by femtosecond[3,4] and picosecond[5] pump-probe spectroscopies. The present paper describes the first observation of femtosecond many exciton states in one-dimensional J-aggregates of 1,1'-diethyl-2,2'-quinocyanine bromide [pseudoisocyanine bromide (PIC-Br)] in EGWG at low temperatures. The decay time of the many-exciton state was determined to be 200 fs.

Time-resolved difference absorption spectra of J-aggregates in EGWG were measured in the whole spectral region covering the J-band at 2.18 eV. The pump light resonant on the J-band is amplified white continuum with a 300-fs pulse dulation. All the experiments were performed at 20 K. The excitation power density at 2.18 eV was changed in the range between 0.98 GW/cm^2 and 0.15 GW/cm^2.

To analyze the complicated temporal behavior of the transient difference absorption spectra and to extract the characteristic spectral change, the time dependence of the absorbance change was fitted with a few exponential functions. To describe the absorbance change in the whole spectral region by the same functions, at least three exponential functions with the characteristic time constants of 200 fs (Γ_1^{-1}), 1.5 ps (Γ_2^{-1}), and 20 ps (Γ_3^{-1}) were needed, besides an instantaneously responding component and a long-life component ($\gg$ 100 ps).

There are various models which can explain the observed temporal behavior characterized by the above three time constants. Here we adopted one of the simplest models, such that the system relaxes sequentially via three excited states $|i\rangle$ ($i = 1, 2, 3$) with each relaxation rate of Γ_i . Here the absorption spectra per unit population density in the three states are defined as A_i ($i = 1, 2, 3$), and stationary absorption spectra per unit population is defined as A_0. The difference spectra ΔA_i ($= A_i - 2A_0$) multiplied by the excitation population density ρ are shown in Fig. 1 in the case of the highest excitation power density. The derivative shape with induced absorption at the higher energy of the bleaching appears just after excitation, and the zero-crossing point shifted red within 200 fs. Finally the signs of the absorbance changes at the longer and shorter wavelengths are reversed in 1.5 ps.

Figure 2-(1) shows the effect of excitation density on the shape of the ΔA_1 spectrum. In the case of the high intensity excitation, the relative intensity of the peak absorbance change is substantially suppressed and the tail appears in the high energy side of the peak.

In the case of the low-power excitation, the transition from the 1- to 2-exciton state is dominant. When the excitation power is increased, the transitions from the n- to (n+1)-exciton state with larger n than 2 start to contribute to the difference absorption spectra. Because the transitions from the $n(\geq 2)$-exciton states have higher energies than that from the 1-exciton, the peak position of the induced absorption spectrum shifted blue with a tail on the higher energy side of the spectra in the case of higher density excitation. The absorbance change represented by the ΔA_1 is due to the $n(\geq 2)$-exciton states, which are concluded to be dominated by the 2-exciton state from the the estimated exciton density. A typical decay time of the many-exciton states is about 200 fs.

Figure 2-(2) shows the intensity dependence of ΔA_2. In comparison with Fig. 2-(1), the higher energy side of the induced absorption of the high-power excitation disappears, resulting in a spectral shape similar to that of the lower excitation. Since the higher n-exciton states decay much faster than the 1-exciton states, ΔA_2 is mainly due to the transition from the 1- to 2-exciton state. As a result, the induced absorption from the 1- to 2-exciton state is increased and the zero-crossing point shifts to the lower probe photon energy.

In conclusion, we observed the transitions from n-exciton states to (n+1)-exciton states ($n \geq 1$) of one-dimensional J-aggregates by femtosecond pump-probe spectroscopy and found the decay time of the $n(\geq 2)$-exciton states to be 200 fs.
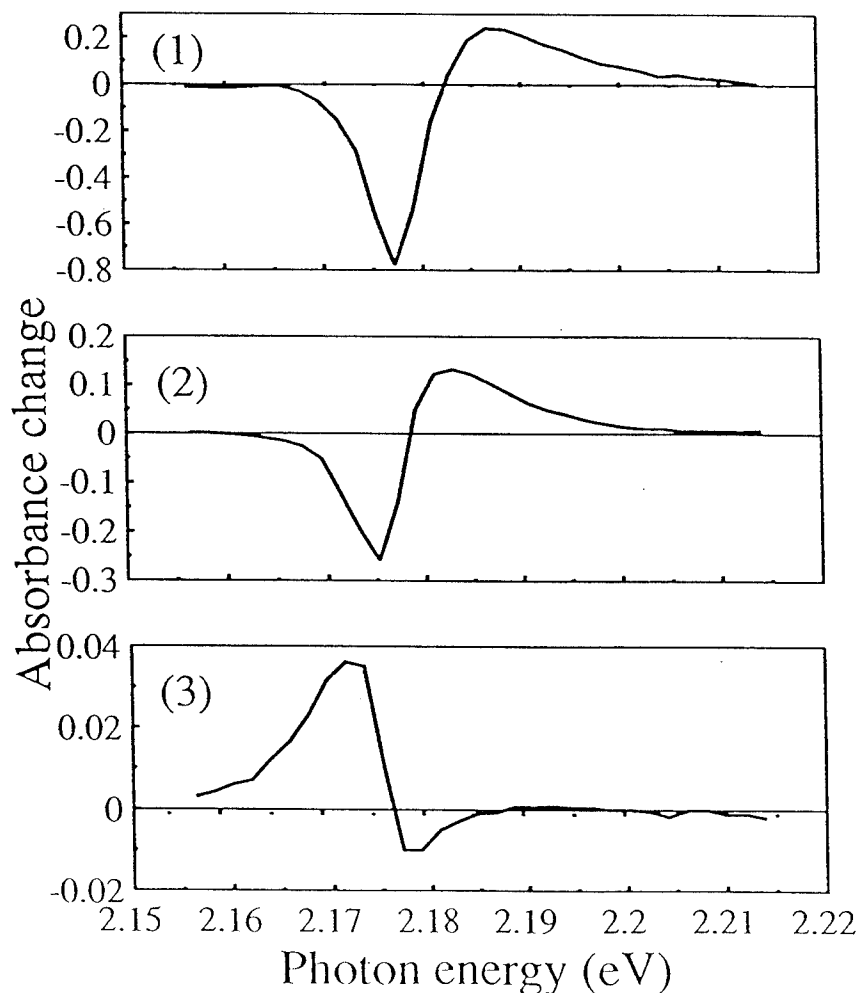
Fig. 1: Difference absorption spectra,(1) $\rho \Delta A_1$, (2) $\rho \Delta A_2$, and (3) $\rho \Delta A_3$, with the highest excitation power density.
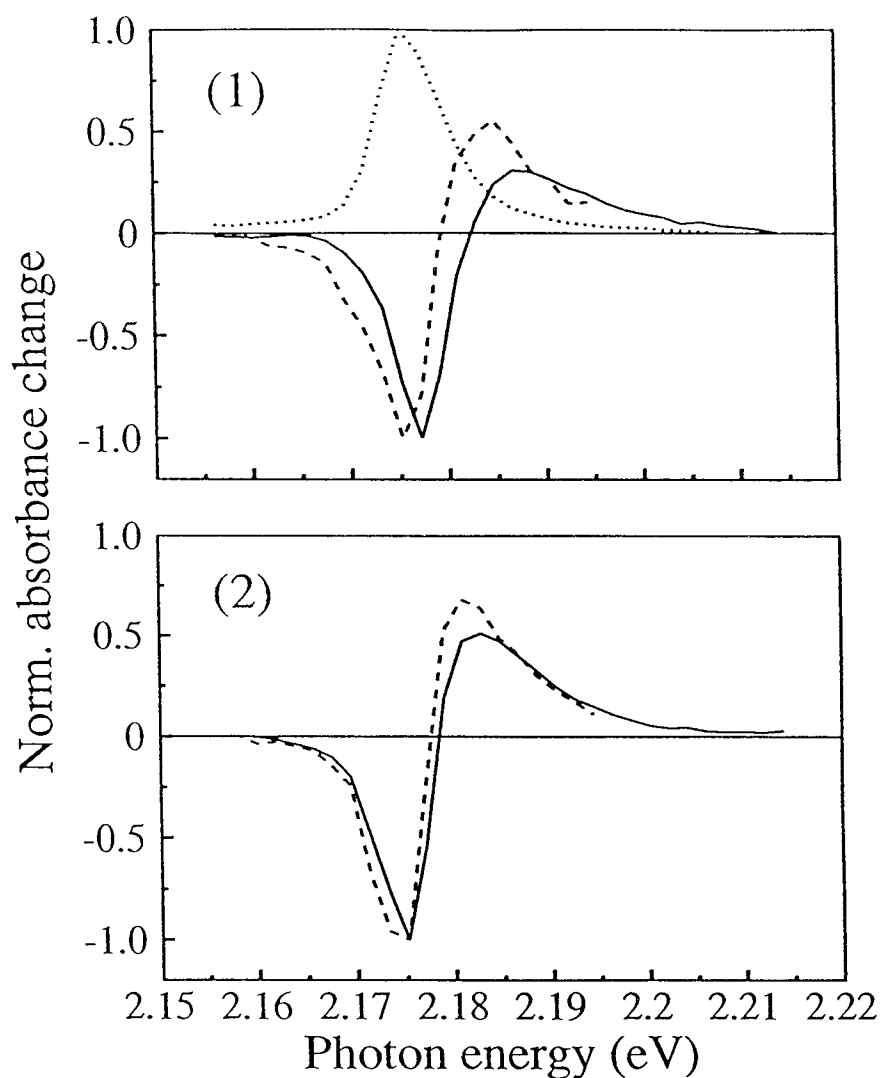
Fig. 2: The pump intensity dependence of (1) ΔA_1 and (2) ΔA_2. Solid and broken lines are obtained by high (0.98 GW/cm^2) and low (0.15 GW/cm^2) excitation power density, respectively. Dotted line shows the stationary absorption spectrum.

References

[1]E.E. Jelly, Nature **138**, 1009 (1936).

[2]G. Scheibe, Angew. Chem. **49**, 563 (1936).

[3]K. Minoshima, M. Taiji, and T. Kobayashi, *Quantum Electronics Laser Science, 1993 Technical Digest Series Vol.12,* Optical Society of America, Washington, DC, 1993, pp. 245.

[4]K. Minoshima, M. Taiji, K. Misawa, and T. Kobayashi, Chem. Phys. Lett., in press.

[5]H. Fidder, J. Knoester, and D.A. Wiersma, J. Chem. Phys. **98**, 6564 (1993).

Quadratically Enhanced Second Harmonic Generation from Interleaved Langmuir-Blodgett Multilayers

Shihong MA, Kui HAN, Xingze LU, Gongming WANG, Wencheng WANG, Zhiming ZHANG
Fudan-T.D. Lee Physics Laboratory, Laboratory of Laser Physics & Optics, Fudan University, Shanghai 200433, China
Tel: 0086-21-5492222 Ext 2374, Fax: 0086-21-5493232
Zhongqi YAO
Lanzhou Institute of Chemistry and Physics, Academia Sinica, Lanzhou 730000, China

In this paper we report a new type of two-legged amphiphilic molecule spacers 1,10-bistearyl--4,6,13,15--tetraene--18--nitrogencrown--6 (NC), the principle being that the single leg of the optical nonlinear hemicyanine derivative (HD) (E-N-docosyl-4-(2-(4-diethylaminophenyl)ethenyl)pyridinium bromide (DAEP)) dye might insert in the spacer molecules thus fasten the interleaved LB multilayers, and improve the degree of order & structural stability. Quadratic SH intensity enhancement has been achieved up to 114 layer (57 bilayers) in the above mentioned LB multilayers.

The chemical structure of the amphiphilic hemicyanine derivative dye and two-legged spacer material used in this work are shown in Figure 1.

The interleaved multilayers were deposited on hydrophilically treated glass slides at a constant pressure of 30mNm^{-1} HD was deposited on the first upstroke at a rate of 3mm/min while NC on the following downstroke at 2mm/min, the process was repeated up to 114 layers (57 bilayers).

SHG measurements were carried out using a set-up (seeing reference[2]). By SHG measurement, we found that the molecular hyperpolarizability β of NC was less than 10^{-30} esu which was much smaller than that of HD (10^{-28} esu), therefore the direct contribution of NC to $\chi^{(2)}$ of the interleaved multilayers could be safely excluded.

The SH light intensity is given by :

$$I_{2\omega} = \frac{2\omega^2 d_{eff}^2 l^2}{c^3 \varepsilon_0 n_1^2 (n_2)} (I_\omega)^2 sinc^2 (\frac{\Delta kl}{2})$$

According to equation (1), measured SH intensity should increase quadratically with l, or number of bilayers, if the molecules in the multilayer form a perfectly aligned array. Thus a quadratic dependence of SH intensity with bilayer number could be consider as a criterion for perfect degree of order in LB multilayers. Here we deposited up to fifty-seven bilayers of HD interleaved with NC maintaining a transfer ratio of 1±0.08 which was much better than pure HD Y-type multilayers in the same conditions. Our measured data of square root of the SH intensity vs. bilayer number of HD interleaved with two-legged NC are shown in Figure 2. The results indicate that SHG intensity increase quadratically with increasing bilayer number of up to 57 bilayers which was considerably higher than the upper limit of bilayer number (~20) when fatty acid was adopted as a spacer in the same condition[3] Both perfect transfer ratio and quadratic dependence showed that NC played a good role of spacer which improved degree of order and enhanced SHG intensity of LB multilayers.

Those promising features could be due to insertion of the docosyl tail of the HD dye between the open dioctadecanoyl legs of NC. A preliminary evidence for it has been provided by Small-angle X-ray Diffraction. Assuming the two approximately identical densities did not change too much after molecules were deposited to glass substrates, we infer that the above mentioned fastening happened between two species at a ratio 1:1.

A non-centrosymmetric LB multilayer structure has been fabricated by interleaving an optically active component (HD) with an inert spacer (NC) having an appropriate molecular geometry to fasten the bilayer. The NC molecule has attractive features as an spacer in fabrication of LB multilayers made from many optically nonlinear materials with

hydrophobic long tails. Quadratic SHG dependence has been realized in such multilayer systems.

Reference
1. P. N. Prasad and D. J. Williams, "Introduction to Nonlinear Optical effects in molecules and polymers", Wiley-Interscience, New York (1991)
2. L. Y. Liu, H. Xiao, J. B. Zheng, W. C. Wang, L. X. Xu, F. G. Tao and J. C. Hu, *Chinese Phys.*, 11 (1991) 679-683
3. L. M. Hayden, B. L. Anderson, J. Y. S. Lam, B. G. Higgins, P. Stoeve and S. T. Kowel, *Thin Solid Films*, 160 (1988) 379-388
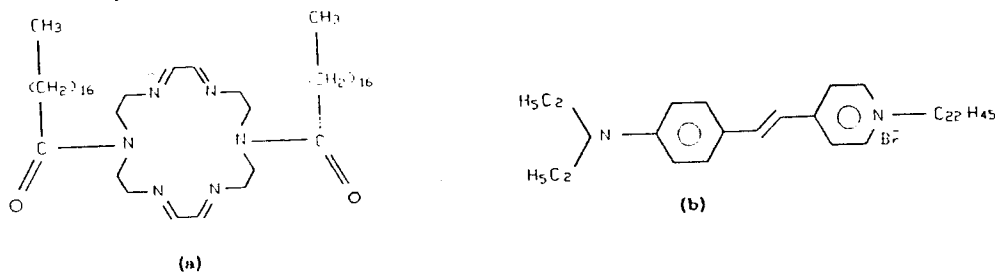
Figure 1. Molecular structure of (a) 1,10-bistearyl--4,6,13,15--tetraene--18--nitrogencrown--6, (NC); (b) E-N-docosyl-4-(2-(4-diethylaminophenyl)ethenyl)pyridinium bromide, (HD)
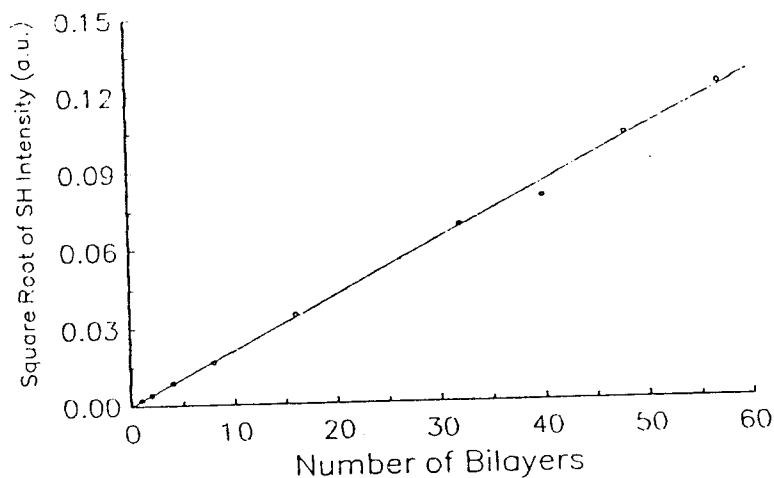
Figure 2. Square root of the second harmonic intensity versus bilayer number for interleaved Y-type LB multilayers

Nonlinear Optical Properties and Poling Dynamics of a Side-ChainPolyimide/Disperse-Red Dye Film: *In Situ* Optical Second-Harmonic Generation Study

J.Y. Huang, C.L. Liao, C.J. Chang, W.T. Whang

Chiao Tung University, Tiawan, R.O.C.

Nonlinear optical (NLO) polymers are advantageous over inorganic crystalline materials in several aspects[1] and have found interesting applications such as modulators, switches, and more recently as photorefractive devices. However, the second-order NLO response of the materials, which is created by an electric poling process, decays as time lapses. For the use of an electro-optic device, it is highly desirable to keep the NLO response in an infinitely long period. But for the photorefractive applications, a fast response of the orientational distribution of NLO molecules to an electric field is more important.[2] For both cases, the orientational distribution and its response to an electric field convey valuable information of the polymeric materials. In this report, we will show that probing the orientational distribution of NLO molecules during the poling process provides insight of the thermal stability of NLO response and the underlying interaction between the polymer and NLO molecules.

Two types of aromatic polyimide films, poly(pyromelliticdianhydride)-DR 19 (abbreviated as PMDA-DR 19, $T_g \sim 110^\circ$C) and poly(pyromelliticdianhydride)-4,4'-diaminodiphenyl ether-DR 1 (abbreviated as POA-DR 1, $T_g \sim 165^\circ$C), were used in this study. During the poling, we measured the second-harmonic (SH) signal, temperature, and electric field across the film simultaneously. Fig. 1 shows the results of the SH measurement, $I_{p \to p}$, as a function of the film temperature. The averaged polar angle of NLO molecules can be deduced from the ratio of $I_{p \to p}$ and $I_{s \to p}$ and the result is depicted in Fig. 2 for PMDA-DR 19. The polar angle was found to change irregularly as the film was heated (see the open symbols in Fig. 2). It was attributed to the appearance of randomly distributed potential wells inside a fresh prepared polymer. After the polymer was kept at the poling temperature for a sufficiently long period and then was cooled down to room temperature, the polar angle of the DR 19 molecules varied smoothly with the temperature (filled squares). It is interesting to note that the polar angle levels off to a constant when the temperature decreases below the glass transition point, which clearly indicates that the result be caused by the global motion of polymer chains. Similar phenomena were observed for POA-DR 1.

The NLO response and thermal stability of the polymers critically depend on the duration of the highest poling temperature. An IR absorption measurement indicates that chemical reactions between functional groups on the polymer chains occur, which reduce the cavity volume around the NLO molecules and thus improve the thermal stability. By using the information of poling dynamics, an optimum poling procedure was devised. Above T_g, the temperature variation of $I_{p \to p}$ measured with a long poling film closely matches with the calculated result from a simple free rotor model which the thermal fluctuation and the alignment strength of the poling field are taken into account (see the dashed curves in Fig. 3). The agreement is less satisfactory for the sample with a shorter poling time since the chain motion in the short poling film is significantly larger than the long poling sample. The large discrepancy below T_g originates from the interaction between the polymeric matrix and NLO molecules, which is not taken into accounted in this simple model. We also added epoxy into PMDA-DR 19 to control the glass transition temperature and then investigated the kinetics of the thermal decay of NLO response. The kinetic parameters deduced were found to correlate well with the poling dynamics.

References

1. G. T. Boyd, *Polymers for Nonlinear Optics*, in *Polymers for Electronic and Photonic Applications*, ed. C. P. Wong, pp. 467-506, Academic Press, Inc. (San Diego, 1993).
2. W. E. Moerner *et al.*, J. Opt. Soc. Am. B, Dec. 1993.

Figure Captions

Fig. 1 The second-harmonic (SH) intensity, $I_{p \to p}(2\omega)$, is plotted as a function of the temperature of PMDA-DR 19 during the corona poling. The heating data are indicated by open squares and the cooling by filled symbols.

Fig. 2 The polar angle of the NLO dye molecules in PMDA-DR 19 during the heating (open symbols) or cooling (filled squares) process of the corona poling.

Fig. 3 $I_{p \to p}(2\omega)$ versus the temperature of PMDA-DR 19 at the cooling process of the corona poling. The film was kept at the poling temperature for 30 minutes (bottom) or 120 minutes (up). The dashed lines are the theoretical curves calculated from a simple free rotor model.
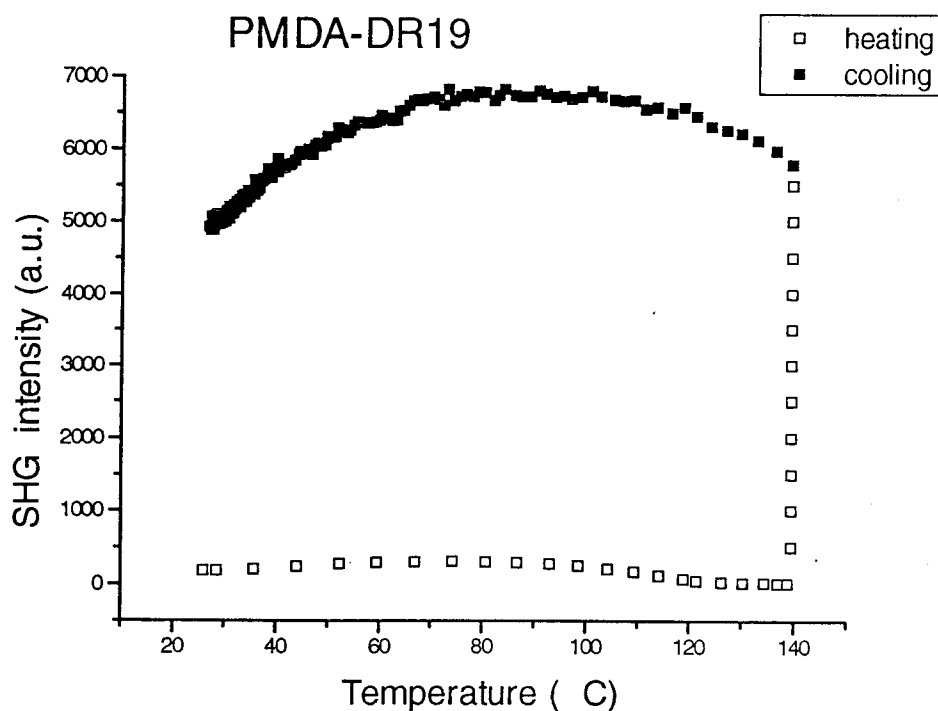
Fig. 1
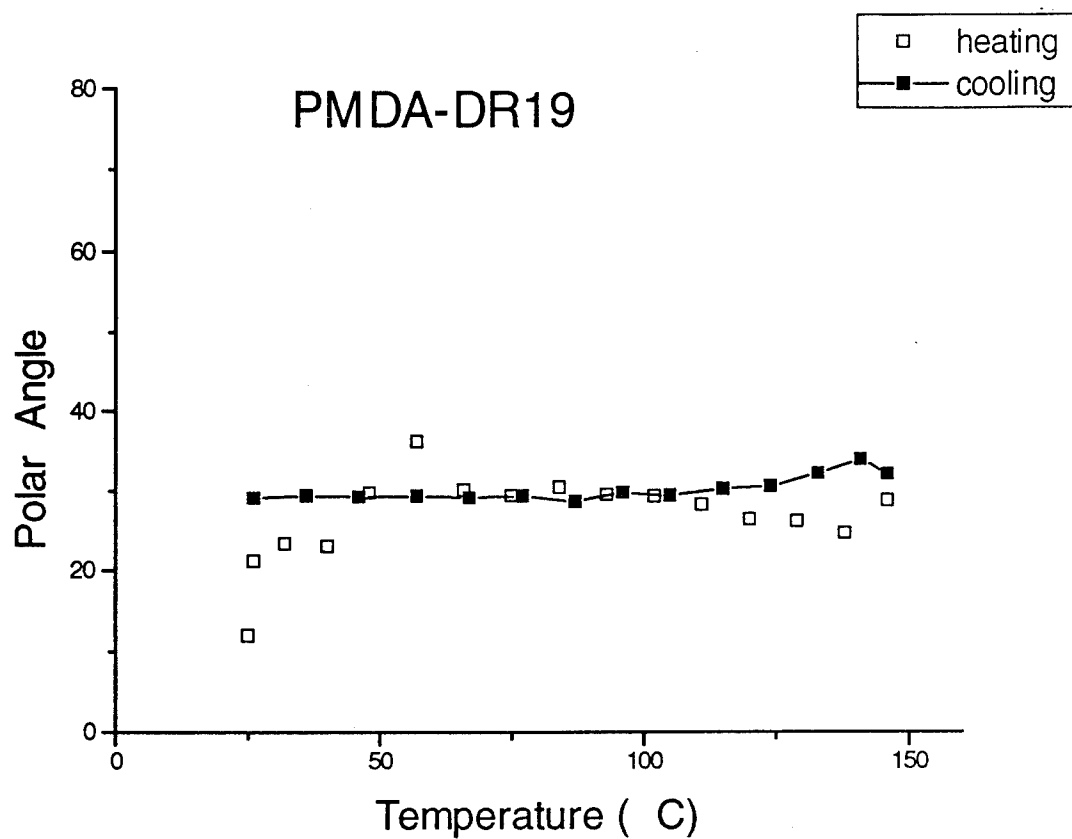
Fig. 2
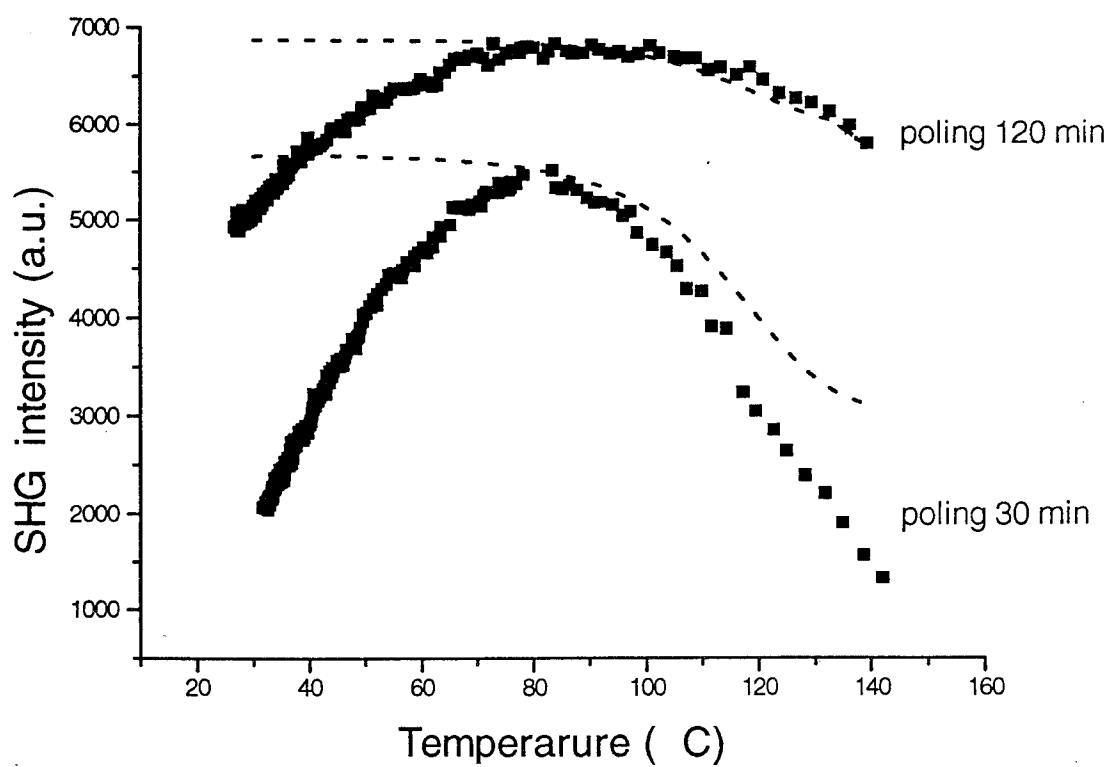
Nonlinear Optical Studies of the Molecular Structure in CH₃OH/H₂O and CH₃CN/H₂O Binary Liquid Mixtures

J.Y. Huang, M.H. Wu, *Chiao Tung University, Tiawan, R.O.C.*; Y.R. Shen, *University of California, Berkeley, CA*

Hydrogen bonding liquids, such as methanol and water, exhibit peculiar thermodynamic behaviors. These liquids as well as the binary mixtures are important solvents and relevant to many chemical and biochemical processes appeared in our daily living. Unfortunately, our understanding of these liquid systems are rather poor owing to the lack of suitable techniques with which the molecular structure can be probed. In the past, the structural information of liquids was obtained indirectly by the measurements of thermodynamic quantities. We will show in this report that important structural information of liquids can be deduced by use of third-harmonic generation (THG) and infrared-visible sum-frequency generation (IVSFG).

Fig. 1 shows the measured THG susceptibility (χ_M) of CH₃OH/H₂O versus the mole fraction of methanol (c_M). The THG susceptibility, which has been normalized with that of fused silica, exhibits a nonlinear dependence on c_M. Since χ_M can be expressed in terms of the THG susceptibility of water (χ_W) and methanol (χ_M) as

$$\chi_T(c_M) = c_M \chi_m + (1 - c_M)\chi_w \qquad (1)$$

thus the nonlinear behavior of χ_T on c_M indicates that both χ_M and χ_W be concentration dependent. Considering that the correlation length of liquid molecules in CH₃OH/H₂O is much shorter than the excited area, the observed concentration dependence must be caused by the different strength of hydrogen bonding experienced by the liquid molecules as they are mixed. A simple molecular model based on the hydrogen bonding strength will be proposed to explain the features observed in the measured THG susceptibility. By applying IVSFG to the liquid surface, the orientational order of methanol molecules at the liquid/vapor interface was found to increase as the surface methanol molecules were hydrated. Similar IVSFG results were also reported by Laubereau *et al.*[1] previously.

We also studied CH₃CN/H₂O with THG technique (see Fig. 2). Different behavior from that of CH₃OH/H₂O was observed. Within our experimental accuracy, χ_T of the CH₃CN/H₂O mixture was found to linearly depend on the mole fraction of acetonitrile (c_A) when $c_A > 0.3$. But abrupt change was observed at $c_A \sim 0.3$. This change can be attributed to a phase separation of the binary solution into acetonitrile rich and water rich regions[2] when there is a significant amount of acetonitrile in the solution. By applying IVSFG to the liquid/vapor interface of CH₃CN/H₂O, Eisenthal *et al.*[3] observed sudden structural change at the liquid/vapor interface at $c_A \sim 0.07$. The asymmetric interaction experienced by the surface acetonitrile molecules is considered to be the major cause of the less acetonitrile molecules being needed for the structural change at the liquid/vapor interface.

References

1. K. Wolfrum, H. Graener, and A. Laubereau, Chem. Phys. Lett. 213, 41 (1993).
2. D. A. Armitage, M. J. Blandamer, M. J. Foster, N. J. Hidden, K. W. Morcom, M. C. R. Symons, and M. J. Wootten, Trans. Faraday Soc. 64, 11193 (1968).
3. D. Zhang, J. H. Gutow, Eisenthal, and T. F. Heinz, J. Chem. Phys. 98, 5099 (1993).

Figure Captions

Fig. 1 Measured THG susceptibility of methanol/water mixture as a function of the mole fraction of methanol. The data of THG susceptibility are normalized with that of fused silica glass.

Fig. 2 Enhancement of the orientational order of methanol molecules at the liquid/vapor interface of CH_3OH/H_2O versus the mole fraction of methanol. The curve is deduced from the fit of the measured IVSFG susceptibility of the symmetric stretch of the methyl group ($v \sim 2830$ cm^{-1}) to a theoretical formula for the effective surface susceptibility.

Fig. 3 Measured THG susceptibility of acetonitrile/water mixture as a function of the mole fraction of acetonitrile. The THG susceptibility data are normalized with that of fused silica glass.
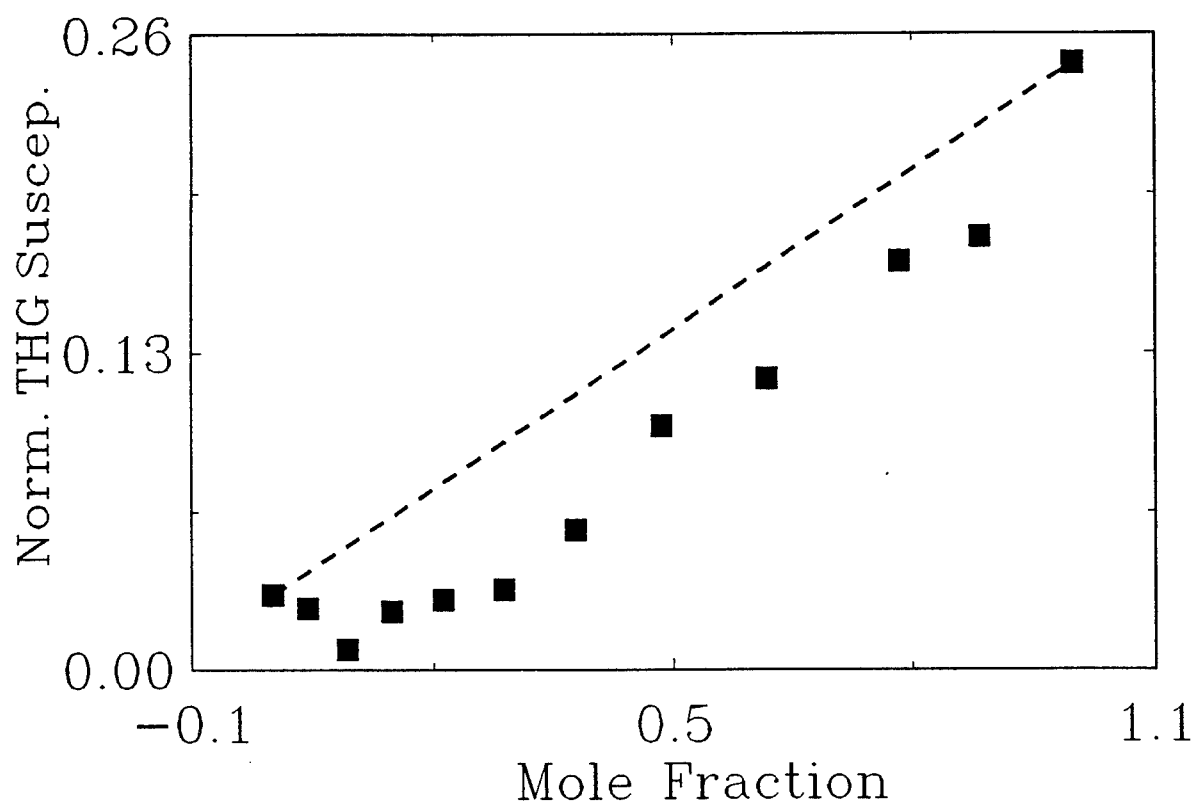
Fig. 1
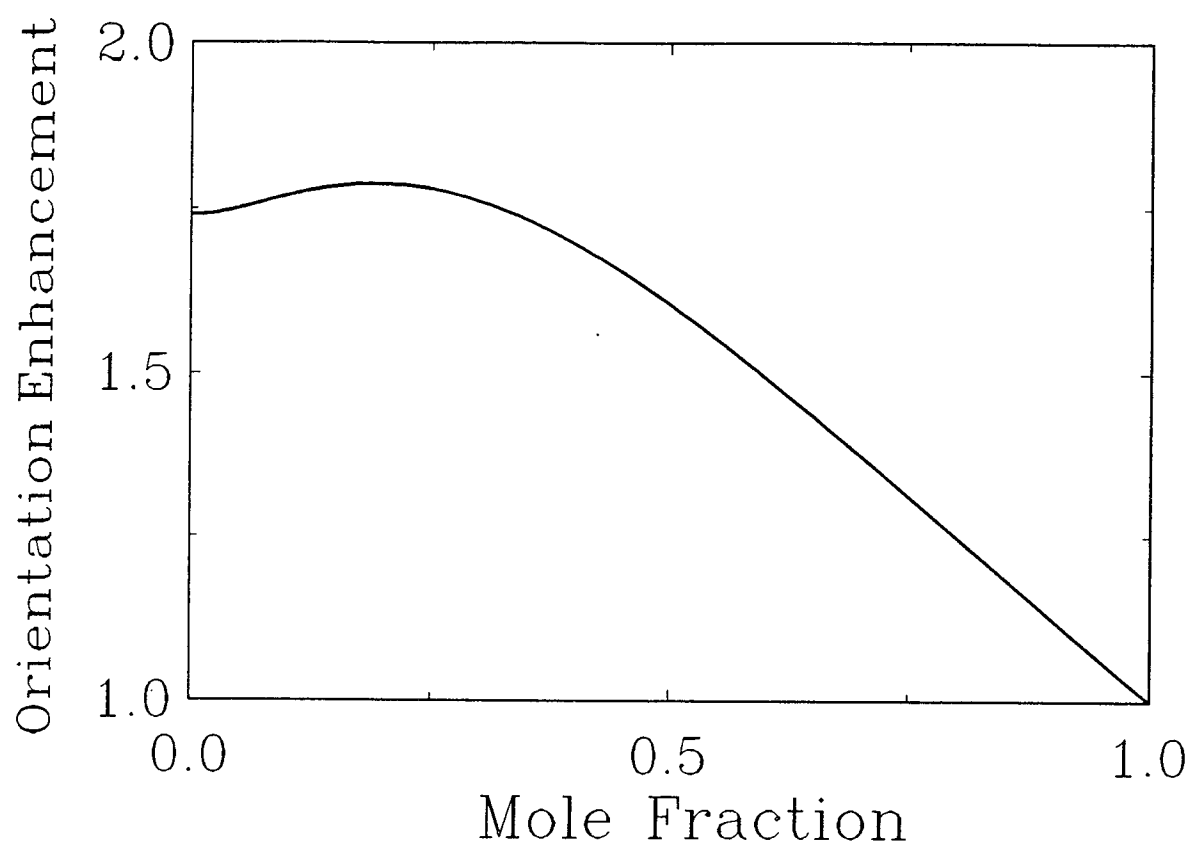
Fig. 2
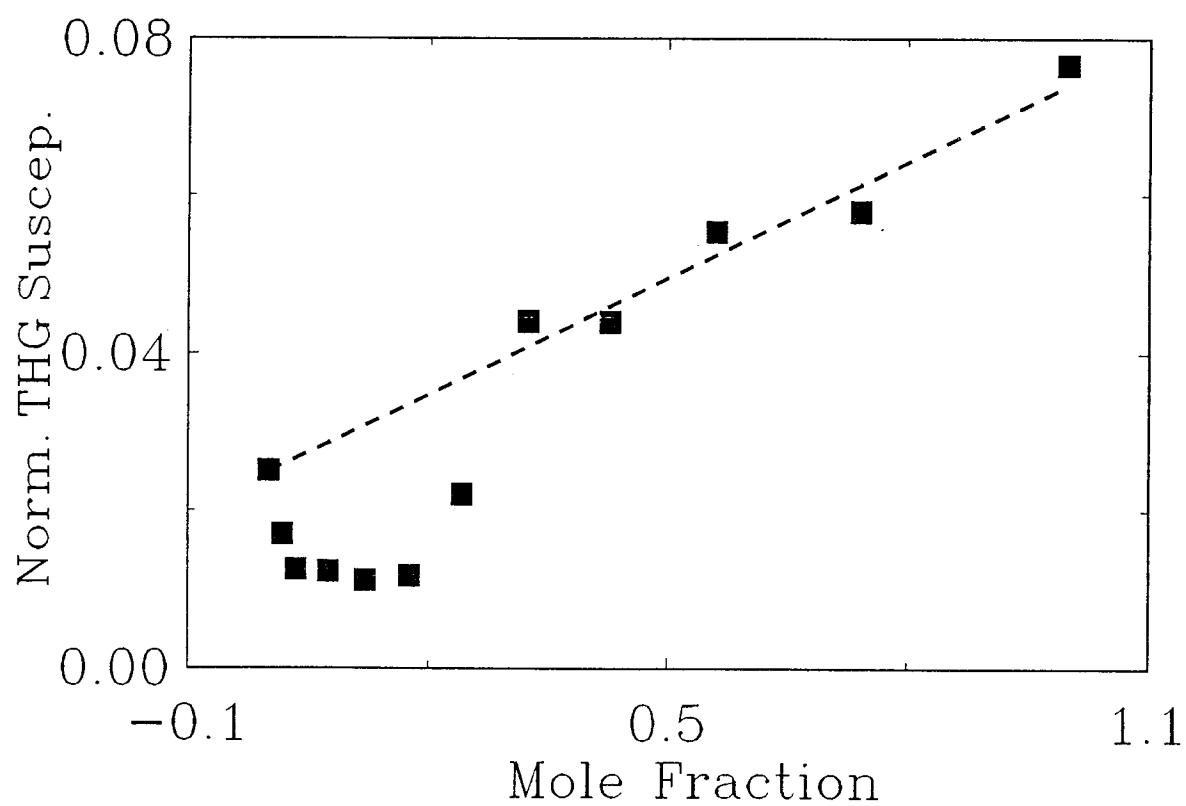
Monday Papers Not Available

MB2   Quantum Teleportation and Quantum Computation

MC4   Total Internal Reflection Resonators for Nonlinear Optics

MP12   Monolayer Surface Freezing of Normal Alkanes Studied by Sum-Frequency Generation

TUESDAY, JULY 26

TUA: Quantum Wells and Semiconductors

TUB: Ultrafast Spectroscopy

TUC: Ultrashort Pulse Sources and
High Intensity Phenomena

TUP: Poster Session II

Piezoelectric Optical Nonlinearities in Strained [111] InGaAs-GaAs Multiple Quantum Well p-i-n Structures

Arthur L. Smirl, X. R. Huang, D. R. Harken, A. N. Cartwright and D. S. McCallum
Center for Laser Science and Engineering, 100 IATL, University of Iowa, Iowa City, IA 52242
Tel. (319) 335 3460
and
J. L. Sánchez-Rojas, A. Sacedón, F. González-Sanz, E. Calleja and E. Muñoz
Dpto. Ing. Electrónica, ETSI Telecomunicación, Univ. Politécnica de Madrid, Ciudad Universitaria,
28040-Madrid, Spain.
Tel. 34.1.336 73 21

Strained multiple quantum well (MQW) structures composed of zincblende materials grown on substrates oriented in directions other than [100] are attractive for a number of novel nonlinear optical and electronic device applications because of the presence of large piezoelectric fields along the growth directions. For example, strain-induced piezoelectric fields in such structures have been exploited to produce self-electro-optic effect devices (SEEDs) that exhibit a blue shift with applied voltage and that consequently have a lower switching voltage.[1] In addition, improved performance has been predicted for piezoelectric electronic devices such as HEMTs.[2] Full exploitation of strained piezoelectric MQWs, however, depends on a more thorough understanding of the band structure, carrier dynamics, and nonlinear optical processes in these materials. Thus far, the existence[3] and screening[4] of these piezoelectric fields have been demonstrated, and the steady-state nonlinear optical response of piezoelectric MQWs has been shown[5,6] to be an order of magnitude larger than that measured in similar structures grown in the [100] direction. Most recently,[6] by comparing the transient and steady-state differential transmission spectra, we have demonstrated that the larger steady-state response for [111]-oriented MQWs is caused by carrier accumulation over the longer (density-dependent) lifetime for such a sample and that it is not the result of a larger nonlinear optical cross section.

Here, we provide the first temporal and spectral resolution of the optical nonlinearities associated with the screening of the built-in fields in p-i(MQW)-n structures. Moreover, we demonstrate that the nature and magnitude of the nonlinear optical response and the carrier dynamics in such structures depend critically on the band structure and that simple changes in the band structure can make dramatic changes in both. We do this by embedding strained [111]-oriented InGaAs-GaAs MQWs in the intrinsic region of a p-i-n structure such that the p-i-n field opposes the piezoelectic field. We then show that, by simply doubling the barrier thickness in one of two otherwise identical p-i(MQW)-n structures, we can transform the nonlinear response associated with a blue shift into one associated with a red shift.

The distinctly different band structures of the two samples are shown schematically in the inset Figs. 1a and 2a. In addition, detail of a single period of each QW structure is provided in inset Figs. 1b and 2b. Each sample contains ten 10-nm-wide $In_{0.15}Ga_{0.85}As$ quantum wells that are separated by GaAs barriers. In one sample (#279) the barriers are 15 nm wide, whereas in the other sample (#280) the barriers are 30 nm wide. In each sample, the QWs are clad on both sides by undoped GaAs spacer layers with thicknesses chosen to make the total thickness of each intrinsic region 570 nm. Both samples were grown on n+ doped [111]B-oriented substrates. Finally, a 300-nm-thick p+ GaAs cap layer was grown to complete the p-i-n structure. The n+ and p+ doping concentration was sufficiently large (>2 x 10^{18} cm^{-3}) to allow a built-in potential of ~1.4 V to form between the doped regions in each sample without completely depleting the doped regions. The samples did not have electrodes applied and were not connected to any external potential. The piezoelectric field in the wells was estimated to be ~215 kV/cm. Because of the orientation of the substrate and the locations of the doped regions, the piezoelectric field points in the opposite direction to the built-in p-i-n electric field. The design of sample #279 is such that the accumulated decrease in potential over the entire MQW region due to the piezoelectric field is greater than the accumulated increase due to the p-i-n field. As a result, the net potential change is negative over the MQW region, resulting in a local potential minimum for electrons at the end of the MQW region nearer the

p+ region and a local potential minimum for holes at the end of the MQW region nearer the n+ region. By contrast, in sample #280, the barriers widths are increased to ensure the opposite conditions. That is, the design is such that the accumulated decrease in potential associated with the piezoelectric field is approximately equal to, but slightly less than, the accumulated increase due to the p-i-n. In the latter case, the average potential in the MQW region is approximately flat and there is no local minimum in the average potential for the electrons or holes immediately adjacent to the MQW region. Finally, as a reference, a third sample was grown with the same structure as sample #280 except that it was grown on a [100]-oriented substrate. This sample (#280R) contains no piezoelectric field.
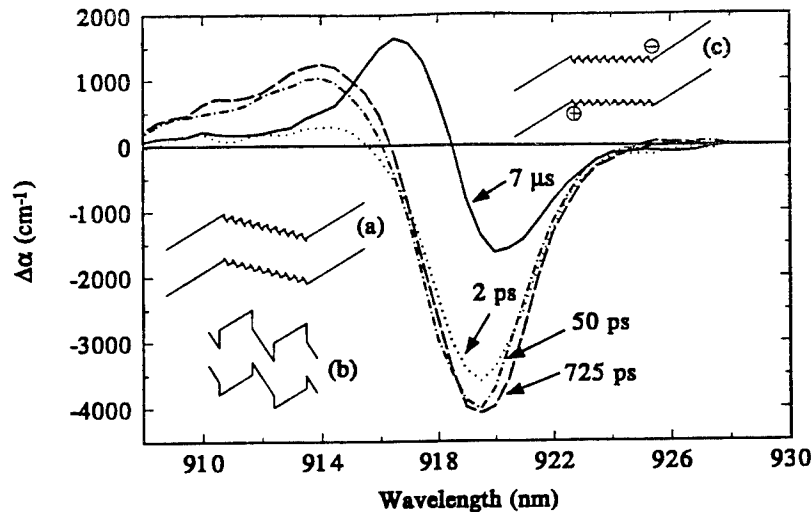
Fig. 1   Absorption coefficient change, Δα, of p-i-n 279 plotted as a function of wavelength for selected probe delays at a pump fluence of 3 μJ/cm². The insets show the bandstructures of (a) the unexcited sample, (b) a single quantum well period and (c) the sample after photoexcitation.

The changes in absorption coefficient for each of these three samples was measured as a function of time, of wavelength, and of excitation level using a tunable, cavity-dumped CW modelocked dye laser that produced pulses of 3.2 ps (FWHM) at a 147 kHz repetition rate (~7 μs between pulses). The absorption changes were extracted from differential transmission measurements, in which a weak probe beam was used to measure the change in transmission induced by a pump beam.

Several representative spectra for sample #279 are shown in Fig 1 for selected time delays between pump and probe pulses. (The sample temperature was 80 K for all data to be discussed here.) Several features are of note. First, we comment that the curve labeled 7 μs was obtained by acquiring the Δα spectrum with the probe arranged to arrive 50 ps before the pump, which corresponds to 7 μs after the previous pump pulse. This Δα spectrum is indicative of a blue-shifted exciton, and it represents the accumulated (quasi-steady-state) change induced by the previous pump pulses. This accumulated background (or bias) must be taken into account when performing line shape analyses on the remaining spectra. When this is done, the other spectra (as well as those not shown) are consistent with the following: Immediately following the pump (2 ps), the Δα spectrum consists of a small positive lobe followed by a large negative lobe, consistent with a bleaching of the already blue-shifted excitons as carriers are photogenerated in the wells. The bleaching component then gradually decays as carriers escape from the wells and drift to screen the electric field experienced by the quantum wells or as they eventually recombine. As depicted in the inset Fig. 1c, the photogenerated carriers accumulate in the local potential minima at the ends of the MQW regions until this region is on the average flat. The carriers in this location screen the

MQWs, but not the undoped intrinsic layers, thereby reducing the electric field experienced by each QW and causing a blue shift of the exciton. These spatially-separated carriers recombine non-exponentially on very long time scales, as evidenced by the remaining absorbance change at 7 µs.

Similar results for sample #280 are shown in Fig. 2. The interpretations and the carrier dynamics are similar to those discussed in conjunction with Fig. 1 with the following significant exceptions: In sample #280, photoexcitation produces a definite red shift, in direct contrast to the blue shift observed in #279. As the electrons and holes escape the wells, they drift to the doped regions as depicted in the inset Fig. 2c. Consequently, by comparison to Fig. 1c, these carriers screen both the MQWs and the undoped intrinsic layers, increasing the electric field experienced by the QWs and causing a redshift of the exciton. Finally, notice that the peak nonlinear response arising from screening in this sample is half that of the previous sample.
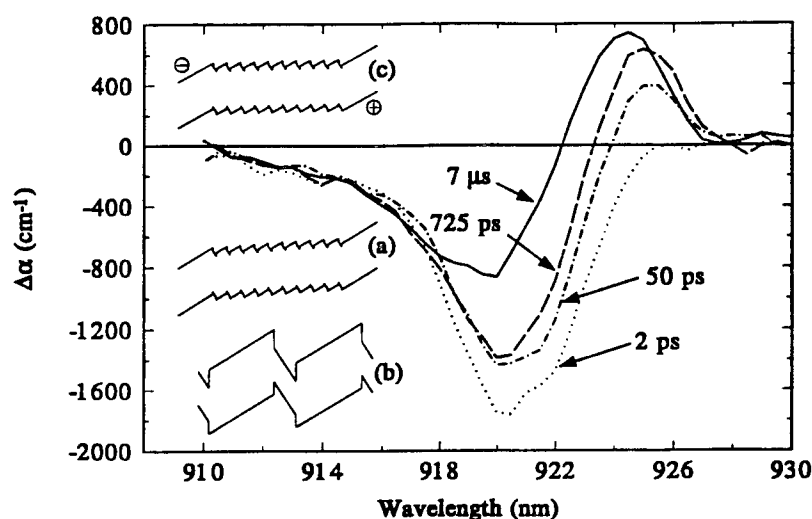
Fig. 2   Absorption coefficient change, $\Delta\alpha$, of p-i-n 280 plotted as a function of wavelength for selected probe delays at a pump fluence of 3 µJ/cm^2. The insets show the bandstructures of (a) the unexcited sample, (b) a single quantum well period and (c) the sample after photoexcitation.

Detailed line shape analyses confirm that our results are consistent with the above qualitative interpretation and are consistent with the band structure assumed here. We emphasize that a simple doubling of the barrier width in one of two otherwise identical samples with opposing built-in fields converted a blue shift to a red shift, changed the location where the carriers tend to accumulate, and modified the magnitude of the response. This example illustrates the flexibility in tailoring the nonlinear optical response of such structures.

1.   K. W. Goossen, E. A. Caridi, T. Y. Chang, J. B. Stark, D. A. B. Miller, and R. A. Morgan, Appl. Phys. Lett. 56, 715 (1990).
2.   J. L. Sánchez-Rojas and E. Muñoz, Proc. IEEE/Cornell Conference an Advanced Concepts in High Speed Semiconductor Devices and Circuits, p. 431 (1993).
3.   E. A. Caridi, T. Y. Chang, K. W. Goossen, and L. F. Eastman, Appl. Phys. Lett. 56, 659 (1990).
4.   T. S. Moise, L. J. Guido, R. C. Barker, J. O. White, and A. R. Kost, Appl. Phys. Lett. 60, 2637 (1992).
5.   I. Sela, D. E. Watkins, B. K. Laurich, D. L. Smith, S. Subbana, and H. Kroemer, Appl. Phys. Lett. 58, 684 (1991).
6.   A. N. Cartwright, D. S. McCallum, T. F. Boggess, A. L. Smirl, T. S. Moise, L. J. Guido, R. C. Barker, and B. S. Wherrett, J. Appl. Phys. 73, 7767 (1993).

A Novel Optical Nonlinearity in a Semiconductor Gain Medium and its Applications to Wavelength Filtering

Serge Dubovitsky, William H. Steier, Atul Mathur and P.D. Dapkus

Center for Photonic Technology
Department of Electrical Engineering, m/s 0483
University of Southern California
Los Angeles, CA 90089-0483
(213)740-4412

We report here on a novel NLO material and a new approach to an implementation of tunable, very narrow band, wavelength filtering and wavelength recognition based on the time response of an optical nonlinearity. The approach makes possible some important new optical devices for wavelength division multiplexing and is based on a new optical nonlinearity: a optically induced birefringence sensitive to the intensity <u>and</u> polarization of the optical signal.

The proposed wavelength filtering can best be understood by considering a four-wave mixing(FWM) interaction in an NLO medium with a finite time response, τ. The configuration is shown in Fig. 1. An input composed of several optical wavelengths, or equivalently frequencies $\omega_1...\omega_j...\omega_N$, interacts with two local pump beams at frequency ω_p, E_p and E'_p. An NLO grating is written by E_j and E_p and the FWM interaction deflects pump E'_p into the output port only if the frequency ω_j, such that $\omega_j - \omega_p < 1/\tau$, is present in the input. The deflected beam, E_0 is frequency shifted into ω_j and contains any modulation which might be on the input E_j. The FWM interaction thus filters from the input a band of wavelengths centered around λ_p. The filter bandwidth, $\Delta\omega = 1/\tau$, is determined by the time response of the nonlinear optical medium used to affect the nonlinear interaction. In the conventional FWM configuration, the input, pumps, and the deflected output propagate in different directions and therefore the various beams are easily isolated on the basis of their direction of propagation.
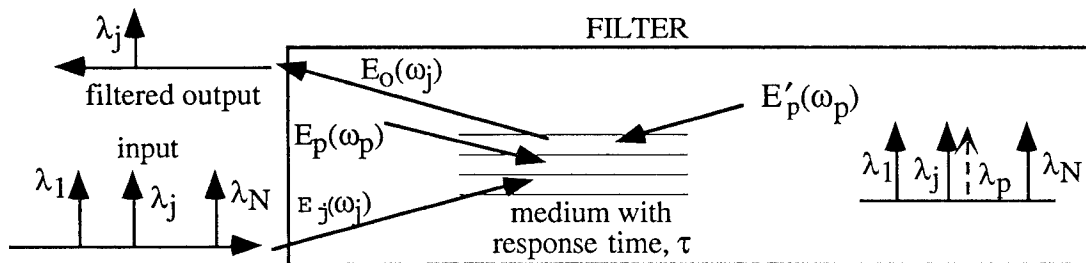
Fig. 1. Wavelength filtering based on a FWM interaction.

For the implementation of a wavelength filter suitable for practical applications there are significant advantages in using an integrated optics approach because of the increased optical intensities, large interaction lengths, and ease of integration into optical systems. A desirable filter would also have a bandwidth in the gigahertzs ($\Delta\lambda \sim 0.1$ Å) range and hence would require a NLO medium with a time response in the sub-nanosecond range. The integrated optics implementation implies a collinear interaction in a waveguide and therefore does not allow the separation of the beams by direction of propagation, as is done in a typical FWM configuration.

To isolate the desired output, E_o, from the pump, E'_p, in a collinear configuration we propose to use a medium with nonlinear birefringence sensitive to the intensity <u>and</u> polarization of the optical signals, i.e. <u>nonlinear polarization-dependent birefringence</u>. In this medium the TM intensity would change the TM index more than it would change the TE index and vice versa. In such a medium, shown in Fig. 2 the interfering copropagating pump, E_p, and the signal, E_j, produce a total polarization vector rotating at $\Omega = \omega_p - \omega_j$. This produces a waveplate oscillating at Ω, which is somewhat analogous to the grating in Fig. 1. The counterpropagating pump, E'_p, reads the waveplate and as a result, in addition to the usual frequency shift, this medium rotates the polarization of the counterpropagating pump, E'_p. The angular deflection of Fig. 1 is replaced by the rotation of polarization in Fig. 2. The rotation of polarization in a collinear configuration allows one to separate the generated output, E_o, from the pump based on polarization.

Fig 2 . Wavelength filtering in a collinear configuration. The generated sidebands, E_o, of the pump E'_p are separated from the pump E'_p on the basis of polarization.

To implement the above concept one requires a medium with the appropriate response time and nonlinear polarization-dependent birefringence. We have therefore investigated this NLO effect in a novel semiconductor gain medium based on strained quantum wells. In general, the semiconductor gain medium has an ideal response time for filtering (~0.2ns), which leads to 0.3 Å bandwidth, and has been demonstrated as a very efficient FWM medium[1]. The nonlinear effect is the gain saturation which in semiconductors also produces an index change due to a linewidth enhancement factor.

The particular medium has recently been demonstrated[2] and used to implement two polarization lasers[2] and polarization insensitive amplifiers[3]. The gain medium consists of compressive and tensile strain quantum wells(T/C QW) and can be thought of as two separate but inter-dependent sources of optical gain. The compressively strained wells, with the heavy holes occupying the lowest energy level in the valence band, serve as the main source of TE gain. The tensile strain wells, where the light holes are in the lowest valence level, split their gain as 3/4 TM and 1/4 TE and therefore provide the sole source of TM gain. The interaction of light holes with both polarizations determines the minimum possible coupling between the sources of TE and TM gains, whereas the coupling of carrier densities in the different wells[4] determines the actual amount of cross-coupling between the gains. The coupling of the carrier densities in the wells occurs due to a finite carrier escape rate from the wells. The polarization resolved gain saturation properties of the medium have been analyzed[4] and tailored for an implementation of a wavelength converter[5, 6]. The effective nonlinear polarization-dependent

birefringence of the medium results from differential saturation of the two gains and therefore depends on the cross-coupling. Low cross-coupling results in high birefringence. The amount of cross-coupling depends on placement, structure and operating condition of the quantum wells in the amplifier and therefore can be somewhat tailored for a given application.

We have experimentally investigated and demonstrated the NLO waveplate due to nonlinear polarization-dependent birefringence in an InGaAsP T/C QW amplifier at 1.319 μm as shown in Fig. 3. The input beam is a linearly polarized beam at 10° off the TM axis and is intensity modulated at frequency f. The large TM component preferentially saturates the TM gain and changes the TM index due to the polarization sensitive saturation. This creates a waveplate oscillating at f which is read by the intensity modulated input. The output contains a component polarized at 90° and modulated at $2f$. This component is the product of the input beam modulated at f, and the medium birefringence, which is also modulated at f. The amplitude of the orthogonal component at $2f$ is a measure of the NLO waveplate. We have observed the intensity induced waveplate and measured up to 1.45 radians of birefringence when optical resonance effects in the amplifier enhanced the effect. The measurements demonstrate this new NLO effect and the analysis shows how the effect can be increased by designing the amplifying medium to further isolate the TM and TE gain saturation.
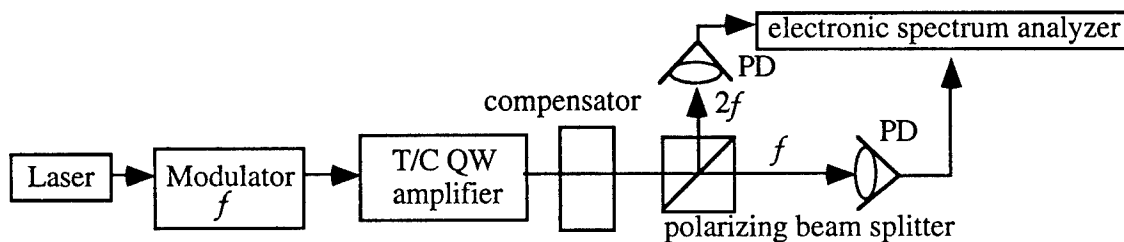
Fig. 3. Schematic of the experimental setup used to measure the nonlinear polarization-dependent birefringence

References

1. T. Mukai and T. Saitoh, "Detuning characteristics and conversion efficiency of nearly degenerate four-wave mixing in a 1.5-um traveling-wave semiconductor laser amplifier", *IEEE J. Quantum Electron.*, vol.26, no.5, pp.865-875,, 1990.
2. A. Mathur and P. D. Dapkus, "Polarization insensitive strained quantum well gain medium for lasers and optical amplifiers", *Appl. Phys. Lett.*, vol.61, no.24, pp.2845-2847, 1992.
3. L. F. Tiemeijer, P. J. A. Thijs, T. van Dongen, R. W. M. Slootweg, J. M. M. van der Heijden, J. J. M. Binsma and M. P. C. M. Krijn, "Polarization insensitive multiple quantum well laser amplifiers for the 1300 nm window", *Appl. Phys. Lett.*, vol.62, no.8, pp.826-828, 1993.
4. S. Dubovitsky, W. H. Steier, A. Mathur and P. D. Dapkus, "Gain saturation properties of a semiconductor gain medium with tensile and compressive strain quantum wells", *to appear in the Special Issue of IEEE J. Quantum Electron. on Strained-Layer Optoelectronic Materials and Devices.*, February, 1994.
5. S. Dubovitsky, A. Mathur, W. H. Steier and P. D. Dapkus, "Gain saturation properties of a polarization insensitive semiconductor amplifier implemented with tensile and compressive strain quantum wells", *to appear in the IEEE Photon. Technol. Lett.*, vol.6, no.2, 1994.
6. S. Dubovitsky, P. D. Dapkus, A. Mathur and W. H. Steier, "Wavelength conversion in a quantum well polarization insensitive amplifier", *submitted to IEEE Photon. Technol. Lett.*, 1994.

Four-Wave Mixing in Semiconductor Traveling-wave Amplifiers for Efficient, Broadband, Wavelength Conversion up to 65 nm

Kerry J. Vahala, Jianhui Zhou, Namkyoo Park
Department of Applied Physics, Mail Stop 128-95
California Institute of Technology, Pasadena, California 91125

Michael A. Newkirk, and Barry I. Miller
AT&T Bell Laboratories, Holmdel, New Jersey 07733

Wavelength conversion is recognized as an important function in future fiber networks employing wavelength division multiplexing. We have recently demonstrated broad-band wavelength conversion over spans as large as 27 nm [1, 2]. Our approach uses ultra-fast four-wave mixing dynamics associated with intraband relaxation mechanisms in semiconductor traveling-wave amplifiers (TWA's). In this paper we present new results showing conversion over wavelength spans as large as 65 nm. This surpasses the previous record by over a factor of two. Of equal importance, we also verify experimentally our previous theoretical prediction that wavelength conversion efficiency varies as the cube of TWA single pass gain.

In the course of our previous work [2], we have shown that the theoretical efficiency, η, of this process can be expressed by the simple relation:

$$\eta = 3G + 2P + R(\Delta\lambda)$$

where η is the ratio in dB of the converted signal output power to the signal input power and G is the single pass TWA optical gain. A crucial point is the presence of $3G$ in this expression - *essentially, the wavelength converter uses the available TWA optical gain three times*. We verified this expression using an experimental setup similar to that described in [2]. Tunable, single-frequency, erbium fiber ring lasers were used as pump and signal sources and TWA devices used contained tensile-strained mutli-quantum well active layers described in [3]. Figure 1 shows conversion efficiency data plotted versus single-pass saturated optical gain. The pump power was -5.2 dBm and the signal power was -11.3 dBm. The measured slope of 3.18 confirms the cubic dependence of efficiency on single pass gain.
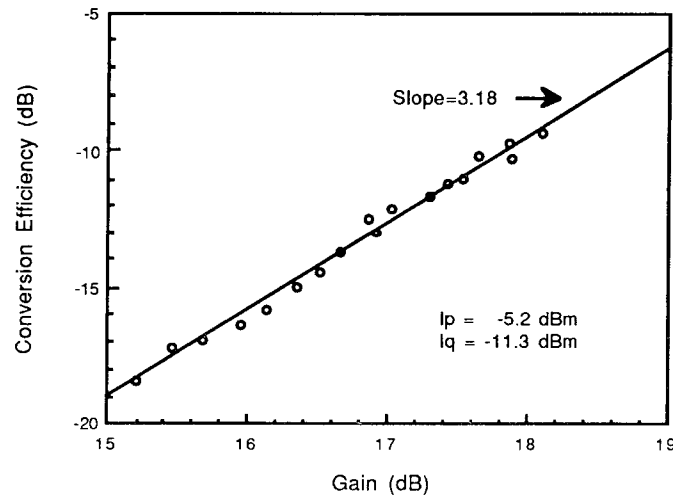
Figure 1: Measured conversion efficiency versus saturated single-pass TWA optical gain, showing cubic dependence of efficiency on gain.

Other parameters appearing in the above equation include the input optical pump-wave power P (expressed in dBm), and a quantity we call the relative efficiency function, $R(\Delta\lambda)$. The relative efficiency function contains information on the intraband dynamics responsible for wide-band four-wave mixing. By using a tandem geometry amplifier (i.e., two low gain amplifiers in series, separated by an optical isolator), it was possible to measure $R(\Delta\lambda)$ for wavelength shifts as large as 65 nm. Data for positive and negative wavelength shifts are presented in figure 2. It is important to note that figure 2 is *not* the actual conversion efficiency, η, which is a vastly larger number, because of its dependence on amplifier gain, G (in dB), and pump power, P (in dBm). Once, however, $R(\Delta\lambda)$ is measured, the requirements on these other quantities for specific conversion efficiencies are known. Based on the above data, figure 3 shows the TWA single-pass gain required for lossless wavelength conversion versus the desired wavelength shift. The four-wave mixing pump power assumed in this calculation is a modest -9 dBm. Because of the cubic gain dependence verified here, it can be seen that 100% efficiency is attainable for wavelength shifts as large as 65 nm with optical gains in the range of 30 dB.
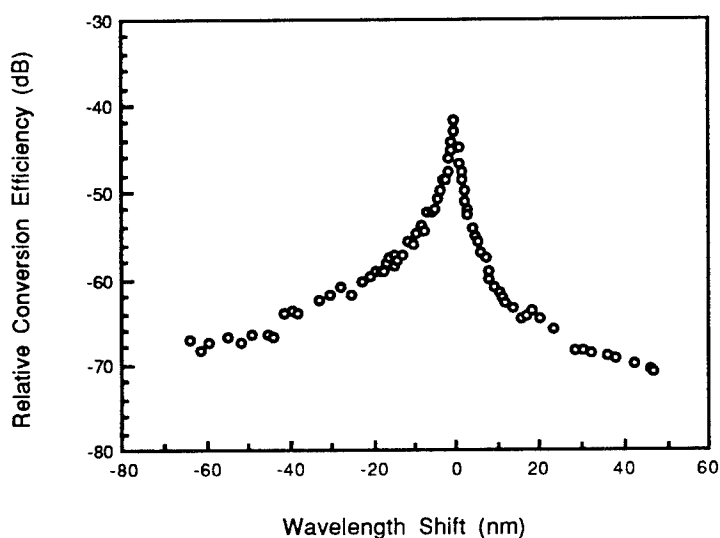
Figure 2: Measured relative conversion efficiency function,$R(\Delta\lambda)$, versus wavelength shift. Note:$R(\Delta\lambda)$ is not the actual conversion efficiency (see equation in paper).
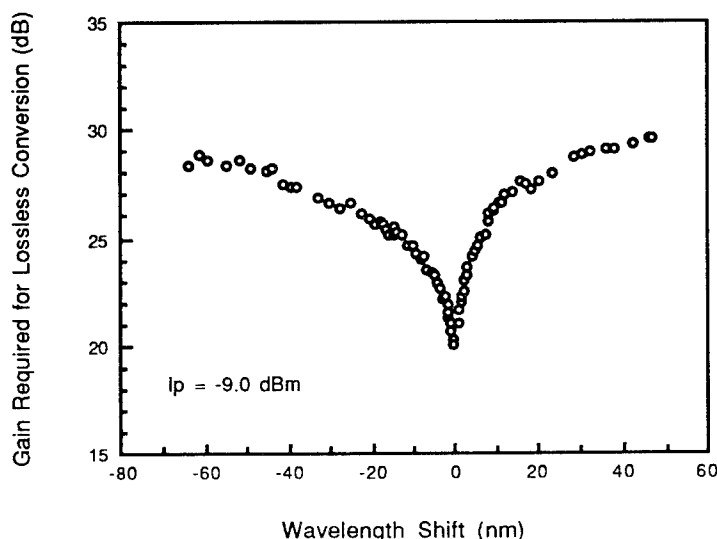
Figure 3: Single pass TWA optical gain required for lossless wavelength conversion.

Due to the limited single pass optical gain of the tandem converter tested here (18.9 dB), lower efficiencies were observed. Figure 4 shows the measured efficiency versus wavelength down-shift for a pump power of -7.0 dBm. Despite the reduced gain, significant wavelength shifts with high efficiency are possible (e.g., -12 dB for 10 nm of shift). These values are already sufficient for certain system applications.
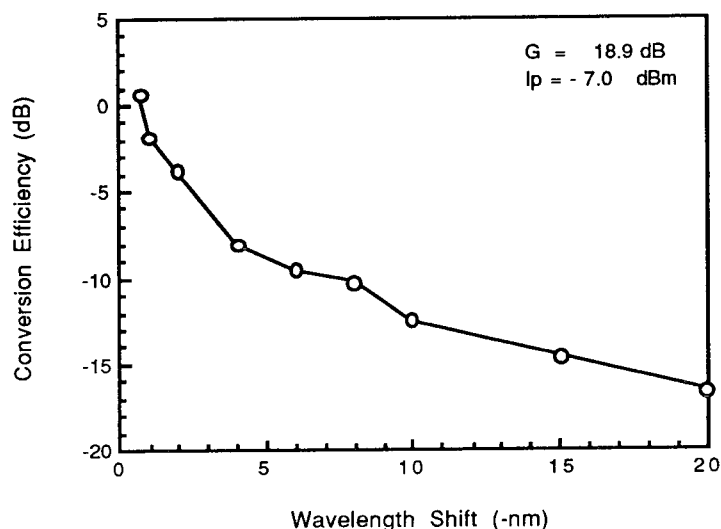
Figure 4: Measured wavelength conversion efficiency versus wavelength downshift for a pump power of -7.0 dBm.

References

[1] J. Zhou, N. Park, J. W. Dawson, K. J. Vahala, M. A. Newkirk, and B. I. Miller, *LEOS'93*, paper OS3.2.

[2] J. Zhou, N. Park, J. W. Dawson, K. J. Vahala, M. A. Newkirk, and B. I. Miller, *IEEE Photon. Tech. Lett.*, **6**, (1994). (to be published in the January issue).

[3] M. A. Newkirk, B. I. Miller, U. Koren, M. G. Young, M. Chen, R. M. Jopson, and C. A. Burrus, *IEEE Photon. Tech. Lett.*, **4**, 406 (1993).

Dynamics of Instantaneous Frequency and Amplitude of Coherent Wave Mixing in Quantum Confined Semiconductor Structures

Daniel S. Chemla

Department of Physics, University of California at Berkeley

Materials Sciences Divisions, Lawrence Berkeley Laboratory

In the last fifteen years, quantum confined semiconductor structures (QCSS) have attracted much attention because of their novel properties and their potential for electronic and photonic applications [1]. Electronic and optical properties of QCSS are dominated by the combined effects of quantum statistics and Coulomb interaction Their response to electromagnetic excitations is determined by a polarization which possesses **a time dependent amplitude and phase**. Although the phase is a very sensitive probe of microscopic scattering and collision mechanisms, most of ultrafast spectroscopy of heterostructures has concentrated on measuring the amplitude only [2].
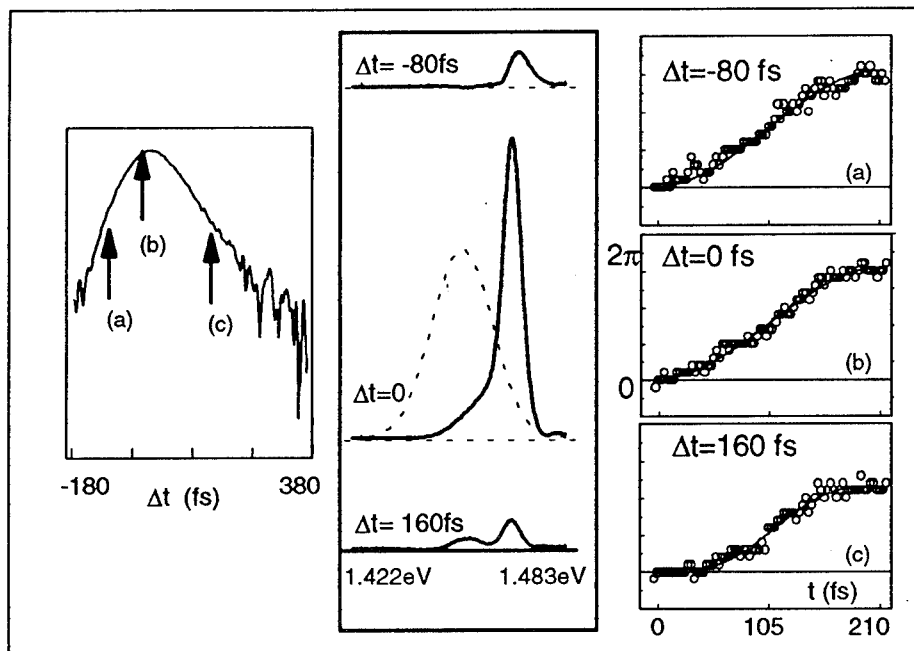
Figure 1: Left, CWM time integrated intensity vs Δt. Center CWM power spectra for the 3 Δt marked by the arrows. Right, dynamics of the phase (relative to the Laser) within the ultrashort pulse emission for the same 3 Δt.

Using a combination of time-resolved, frequency-resolved, and interferometric correlation techniques we have recently investigated the phase and amplitude of coherent wave mixing (CWM) emission from quantum well structures excited by two ultrashort pulses [3]. For excitation near the absorption edge, we have observed ultrafast nonlinear phase dynamics that are very sensitive to the two times involved in the experiment Δt, the time delay between the exciting pulses and, t, the absolute time within one pulsed emission. The left part of Figure 1 shows the usually measured time integrated CWM signal vs Δt for a configuration where only the lowest resonance is excited. In the center part of the figure the CWM power spectra, for the three Δt indicated by arrows, clearly demonstrates that the frequency content of the signal depends strongly on the time delay Δt. Furthermore, as shown in the right side of the figure, the phase difference between the signal and a reference laser, $\Delta \phi$, exhibits, within each ultrashort pulse, a nonlinear dynamics vs t, which also depends on Δt [3].

When two resonances are simultaneously excited we observe quantum beats whose dynamics can be extremely fast just above the fundamental limit, $\Delta \omega \Delta t \sim 1$. As shown in Figure 2a, for the case of two resonances 15meV apart, $\Delta \phi$ exhibits an abrupt π-shift at the beat. Figure 2b compares the
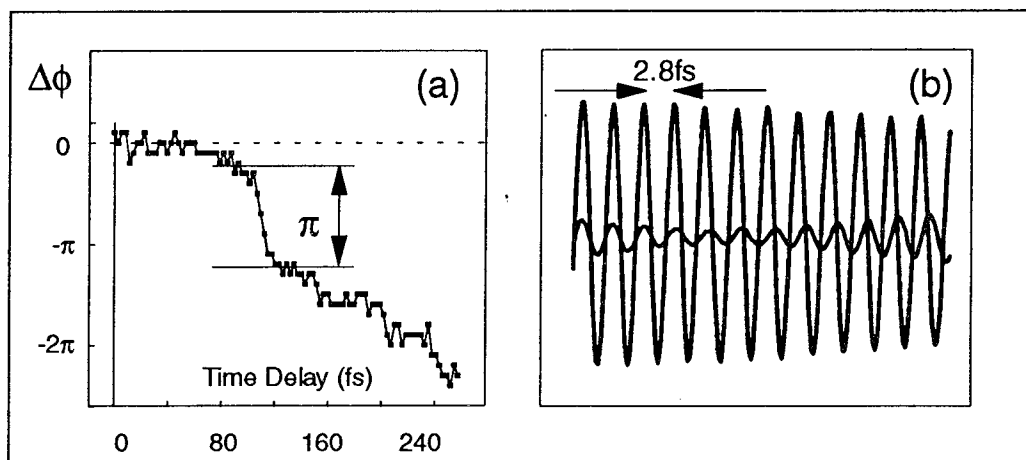
Figure 2: (a) Evolution of the phase difference between the CWM emission and the reference laser, (b) details of the interferometric auto-correlation fringes at the center and close to the first node of the trace.

interferometric fringes at the beginning of the emission and close to the beat, showing that this shift is completed in 12 fringes or 50fs and, therefore, corresponds to $\Delta\omega\Delta t \sim 1.4$.
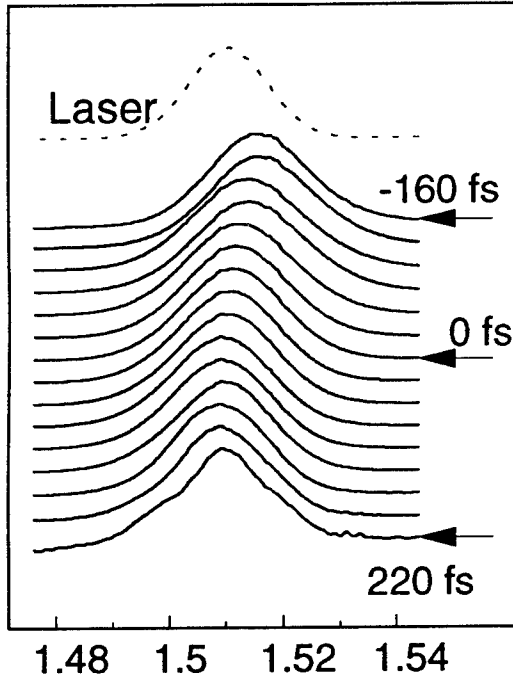
Figure 3: Spectrogram of the CWM for excitation in the continuum of quasi free e-h pairs.

For excitation in the two-dimensional continuum of quasi-free e-h states, 44mev above the lowest exciton state, the dephasing time is of the order of a few tens of fs [4]. When the pulse duration exceeds T_2, the dephasing time, the time integrated CWM provides no interesting information. In contrast the temporal evolution of the CWM power spectra gives directly the spectrogram [2] and is a direct visualization of the phase dynamics of the emission.

As shown in Figure 3, we observe as a function of Δt a clear dynamical shift of the power spectrum relative to that of the laser spectrum. We attribute this effect to the dynamics of the non-equilibrium e-h Fermi-sea created by the intense pulse [5]. This "*blue shifted*" emission is the counterpart of the "*red shifted*" spectral hole burning observed in pump-probe experiments [6]. This effect corresponds for non-equilibrium distributions to the well known Fermi-edge singularity of equilibrium distributions.

Elaborate numerical simulations based on the semiconductor Bloch equations [7] account for the general features of the experiments. They fail, however, to reproduce important aspects of the data which we track back to the statistical treatment of screening and Lorentzian description of dephasing. These experiments challenge the present theoretical description of semiconductors and reveal a need for refinements in the treatment of microscopic processes in non-Markovian theory. On an ultrashort time scale

the microscopic effects of laser induced non-equilibrium populations cannot be described by statistical or mean-field approaches. The parameters of the materials, effective masses, resonance energies, transition amplitudes, etc., all experience an ultrafast time dependent renormalization [8]. General and consistent descriptions of Coulomb scattering and phonon collisions have been proposed [9,10], but they have not yet been applied to complicated nonlinear optical experiments such as those described in this lecture.

References

[1] S. Schmitt-Rink, D.S. Chemla, D.A.B. Miller, Adv. Phys., **38**, 89 (1989),

[2] See, however, J. Paye, IEEE Journ. Quant. Elect. 28, 2262 (1992), and D.J. Kane, R. Trebino, IEEE Journ. Quantum Elect., **29**, 571, (1993)

[3] J.-Y. Bigot, M.-A. Mycek, S. Weiss, R. G. Ulbrich, D.S. Chemla, Phys. Rev. Lett. **70**, 3307 (1993) and D.S. Chemla, J.-Y. Bigot, M.-A. Mycek, S. Weiss, and W. Schäfer submitted to Phys. Rev., J.-Y. Bigot, M.-A. Mycek, S. Weiss, D.S. Chemla, submitted to Phys. Rev.-B.

[4] P.C. Becker, H.L. Fragnito, C.H. Brito-Cruz, R.L. Fork, J.E. Cunningham, J.E. Henry, C.V. Shank, Phys. Rev. Lett. **61**, 1647 (1988); J.-Y. Bigot, M.T. Portella, R.W. Schoenlein, J.E. Cunningham, C.V. Shank, Phys. Rev. Lett. **67**, 636 (1991)

[5] C. Tanguy, M. Combescot, Phys. Rev. Lett. **68**, 1935 (1992)

[6] J.-P. Foing, D. Hulin, M. Joffre, M.K. Kackson, J.-L. Oudar, C. Tanguy, M. Combescot, Phys. Rev. Lett. **68**, 110 (1992)

[7] W. Schäfer, "Manybody Effetcs in Nonlinear Optics of Semiconductor Structures" in "Optics of Semiconducror Nanostructures" ed. F. Henneberger, S. Schmitt-Rink E.O. Göbel, Akademie Verlag, Berlin (1993) and references therein

[8] I.E. Perakis and D.S. Chemla submitted to Phys. Rev. Lett.

[9] D.B. Tran Thoai and H. Haug, Z. Phys. b91, 199 (1993)

[10] M. Hartman and W.Schäfer Phys. Stat. Sol. b173, 165 (1992)

Implementation of Second-Order Nonlinearities in Semiconductor Waveguides

D.C. Hutchings, C. Kelaidis, J.M. Arnold, J.S. Aitchison, C.N. Ironside,
M. Street and J.H. Marsh
Department of Electronics and Electrical Engineering, University of Glasgow,
Glasgow G12 8QQ, U.K., Tel: 041-339-8855

Semiconductors are known to exhibit large second order nonlinearities (e.g. $d_{14}=200\text{pmV}^{-1}$ for GaAs at $10.6\mu\text{m}$ [1] compared with $d_{15}=5.5\text{pmV}^{-1}$ in LiNbO_3). However, efficient generation of new frequencies has not been possible due to the difficulties of phase-matching as zinc-blende semiconductors do not exhibit birefringence and typically have a large dispersion in the near infrared. One possible quasi phase-matching scheme for second harmonic generation in semiconductors is to use a refractive index grating [2]. However, the generation efficiency of such schemes is poor and Bragg scattering can increase losses. In addition, the high symmetry of zinc-blende semiconductors only gives one non-zero $\chi^{(2)}$ tensor element and therefore restricts the choice of potential device geometries. By breaking the symmetry of the structure, additional (and potentially enhanced) $\chi^{(2)}$ tensor elements can be generated. One particularly promising method for achieving this is to grow asymmetric quantum well structures . For long-wavelength ($10\mu\text{m}$) operation, inter-sub-band transitions with n-doped wells, nonlinear coefficients as large as 360nmV^{-1} have been measured [3]. For near infrared operation, inter-band transitions in intrinsic asymmetric quantum well (AQW) structures can also be used to obtain a second order nonlinearity. Theoretical predictions have concentrated on the heavy-hole transition and obtained nonlinear coefficients of $d_{15}=6\text{pmV}^{-1}$ in coupled quantum wells [4] and $d_{15}=200\text{pmV}^{-1}$ in stepped quantum wells [5]. However an implementation of the d_{15} coefficient in a waveguide geometry would require the excitation of both TE and TM modes. Alternatively, a d_{33} coefficient would permit the excitation in just the TM mode. However, transitions from the heavy-hole sub-bands do not contribute to the d_{33} coefficient due to wavefunction symmetry, but there should still be adequate oscillator strength from the light-hole transitions.

Using an **A.p** perturbation, the second order susceptibility is in general given by,

$$\chi_{ijk}^{(2)}(\omega_1,\omega_2) = \frac{e^3}{2!\hbar^2\varepsilon_0 m_0^3}\frac{i}{(\omega_1+\omega_2)\omega_1\omega_2}S_T\sum_{g,\alpha,\beta}\frac{(\hat{e}_i^*\cdot\mathbf{p}_{g\alpha})(\hat{e}_j\cdot\mathbf{p}_{\alpha\beta})(\hat{e}_k\cdot\mathbf{p}_{\beta g})}{(\Omega_{g\alpha}-\omega_1-\omega_2)(\Omega_{g\beta}-\omega_2)}, \qquad (1)$$

where m_0 is the free electron mass, $\hat{e}_i$ is the unit vector in the direction of the ith polarisation and $\mathbf{p}_{\alpha\beta}$ and $\hbar\Omega_{\alpha\beta}$ are the momentum matrix element and energy difference respectively, taken between the electronic states α and β. Here S_T denotes that the expression which follows it is to be summed over all 6 permutations of the pairs $(i,-\omega_1-\omega_2)$, (j,ω_1) and (k,ω_2). To obtain the electronic states g, α, β, a parabolic band model is used for the conduction band and a 4x4 Luttinger-Kohn Hamiltonian is diagonalised for the valence bands (the split-off band is neglected). Figure 1(a) shows the stepped quantum well (with the calculated energy levels) that will be used as an example here, designed for use at a wavelength of $1.55\mu\text{m}$. The transitions from the $n=1$ valence states to the $n=2$ conduction state are permitted in this structure because of the asymmetric potential. These $\Delta n\neq 0$ transitions are essential in obtaining a finite second order nonlinearity. The calculated dispersion of $\chi^{(2)}$ from equation (1) is shown in figure 1(b). Operating beneath the resonance (to ensure the second harmonic is not absorbed) gives a potentially employable $d_{33}=60\text{pmV}^{-1}$ (although the peak value is around $d_{33}=110\text{pmV}^{-1}$) which is only a factor of 2-3 smaller than the intrinsic d_{14} coefficient for GaAs and predicted peak

values for the d_{15} coefficient in similar structures (in spite of the lack of contribution from heavy-hole transitions).
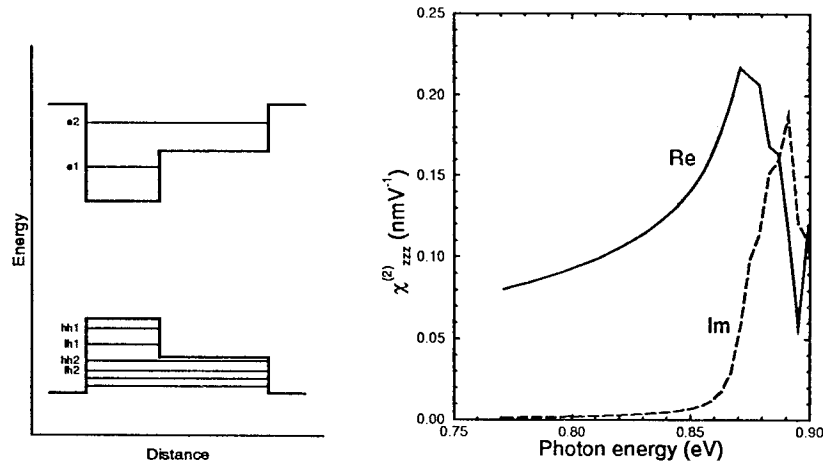
Fig. 1 (a) Schematic of asymmetric stepped quantum well consisting of 4nm $Al_{0.15}Ga_{0.85}As$ and 6nm $Al_{0.33}Ga_{0.67}As$ layers within 20nm $Al_{0.48}Ga_{0.52}As$ barriers showing the energy levels of the bound states. (b) Calculated dispersion of the second order susceptibility $\chi^{(2)}_{zzz}$ for this AQW structure showing both real and imaginary parts.
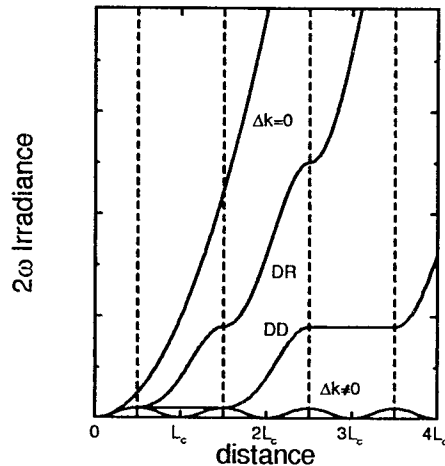
Fig. 2 Schematic showing the initial growth of second harmonic for perfect phase-matching ($\Delta k=0$), non-phase-matched ($\Delta k \neq 0$), and first order quasi phase-matched by domain reversal (DR) and domain disordering (DD). The dashed lines indicate the extent of the domains for quasi phase-matching.

The use of structurely induced second order nonlinearities widens the scope for possible phase matching techniques. Domain reversal is feasible by periodically inverting the asymmetric quantum wells. Practically, this would involve etching and regrowth which would probably lead to substantial propagation losses. A more viable technique is to periodically reduce the size of the nonlinearity (ideally to zero). Fig. 2 shows how SHG would evolve in such a structure compared to domain reversal and ideal phase-matching with a reduction in the effective nonlinear coefficient $d_{DD}=d_{eff}/\pi$. In doped quantum wells for $10\mu m$ operation, the nonlinearity has been reduced by proton implantation [6] which eliminates the carriers. The technique we propose for the near infrared is quantum well intermixing to remove the induced

149

asymmetry. The most promising technique in GaAs/AlGaAs systems is impurity-free vacancy disordering (IFVD) due to the low optical losses [7]. Disordering is realised by depositing an SiO_2 cap on the material and then annealing in a rapid thermal processor. Selectivity across the wafer is achieved by placing a layer of SrF_2 between the SiO_2 and the semiconductor in regions where intermixing is not required [8]. The spatial resolution of the process is more than adequate to define gratings with a pitch ~4µm.

In addition to potential applications for frequency conversion, second-order nonlinearities can be cascaded to produce a nonlinear phase shift which can be controlled through phase-matching [9]. This then can be used to achieve all-optical switching. One possible device design is shown in fig. 3 where the sum of two input frequencies is generated, but because of a set phase mis-match, downconversion subsequently occurs which is, in general, out of phase with the original input [10]. It can be shown that this gives an induced nonlinear phase shift at ω_1 which is independent of the relative phase of the input at ω_2 (i.e. incoherent sources can be used). To induce a phase shift of π at frequency ω_1 in a 1cm long and $8\mu m^2$ cross-section AlGaAs AQW waveguide phase matched by domain disordering (using the optimum phase mis-match $\Delta kL=2\pi$), estimated optical power levels at ω_2 of 4W using $d_{33}=60pmV^{-1}$ and 400mW using $d_{15}=200pmV^{-1}$ [5] are required. This figure should be compared with equivalent all-optical switching devices based on the third-order nonlinearity in AlGaAs where switching power levels of the order of 100W are required.
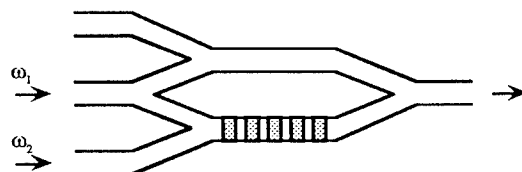
Fig. 3 Schematic of an asymmetric Mach-Zehnder all-optical switch based on a cascaded second order nonlinearity. For semiconductors, quasi phase-matching is employed in the arm where both optical frequencies are present.

References
[1] C. Flytzanis in *Quantum Electronics* Vol. 1, part A, ed. H. Rabin and C.L. Tang (Academic Press, 1975).
[2] J.P. Van der Ziel, M. Ilegems, P.W. Foy and R.M. Mikulyak, Appl. Phys. Lett. **29**, 775 (1976).
[3] P. Boucaud, F.H. Julien, D.D. Yang, J-M. Lourtioz, E. Rosencher, P. Bois and J. Nagle, Appl. Phys. Lett. **57**, 215 (1990).
[4] J. Khurgin, Phys. Rev. B **38**, 4056 (1988).
[5] P.J. Harshman and S. Wang, Appl. Phys. Lett. **60**, 1277 (1992).
[6] S.J.B. Yoo, M.M. Feyer, R.L. Byer and J.S. Harris, Jr., Appl. Phys. Lett. **58**, 1724 (1991).
[7] J.H. Marsh, Semicond. Sci. Tech. **8**, 1136 (1993).
[8] J. Beauvais, J.H. Marsh, A.H.Kean, A.C.Bryce and C. Button, Electron. Lett. **28**, 1670 (1992).
[9] R. DeSalvo, D.J. Hagan, M. Sheik-Bahae, G. Stegeman, E.W. Van Stryland and H. Vanherzeele, Opt. Lett. **17**, 28 (1992).
[10] D.C. Hutchings, J.S. Aitchison and C.N. Ironside, Opt. Lett. **18**, 793 (1993).

Resonant surface second-harmonic generation on Cu(111) by a surface state to image-potential state transition

G. Lüpke,[†] D.J. Bottomley,[‡] and H.M. van Driel,[‡]

[†] Institute of Semiconductor Electronics II,
Rheinisch-Westfälische Technische Hochschule, 52056 Aachen, Germany

[‡] Department of Physics, and Ontario Laser and Lightwave Research Centre,
University of Toronto, Toronto, Ontario, Canada M5S 1A7

Summary

Here we present the first observations of resonant enhancement of $\chi^{(2)}$ from a metal by a surface state-image potential state transition [1]. This conclusion is reached from a systematic experimental investigation of second-harmonic (SH) generation from a clean Cu(111) surface as a function of photon energy, and crystal azimuthal orientation. We also suggest that earlier observations of the sensitivity of the SH resonance in Cu(111) to lattice temperature and bombardment of the surface by ions [2] can be explained by a linewidth broadening associated with electrons in surface states scattering into bulk states, consistent with angle-resolved photoemission measurements [3].

In our experiments a Cu(111) sample was mounted in an ultahigh vacuum chamber (5×10^{-10} Torr base pressure) on a manipulator which could be used to vary the azimuthal orientation of the sample. Surface crystalline order and cleanliness were monitored using low-energy electron-diffraction and Auger electron spectroscopy. For the SH dispersion measurements, we used a synchronously pumped mode-locked dye laser which produced a train of 3-ps pulses at 76 MHz with an average power of 200-500 mW. With three different dyes the wavelength range 775-590 nm ($1.6 < \hbar\omega < 2.1$ eV) could be covered. A p-polarized beam was focused to a 50-μm diameter spot on the sample at an angle of incidence of 67° and p-polarized reflected SH light was detected using a photomultiplier and conventional photon-counting techniques.

Figure 1 shows the SH efficiency of the sample as a function of wavelength obtained for two azimuthal orientations ψ of the sample. The reflected SH efficiency, R, depends on ψ as given by:

$$R \propto | \chi^{(2)}_{eff} |^2 = | [A + B cos(3\psi)] |^2, \qquad (1)$$

for a surface of C_{3v} symmetry [2]. Here ψ is the angle between the plane of incidence and the $[01\bar{1}]$ surface vector, $\chi^{(2)}_{eff}$ is the effective second-order susceptibility, and A and B are linear combinations of χ_{ijk} tensor elements multiplied by angle-of-incidence-dependent Fresnel factors.
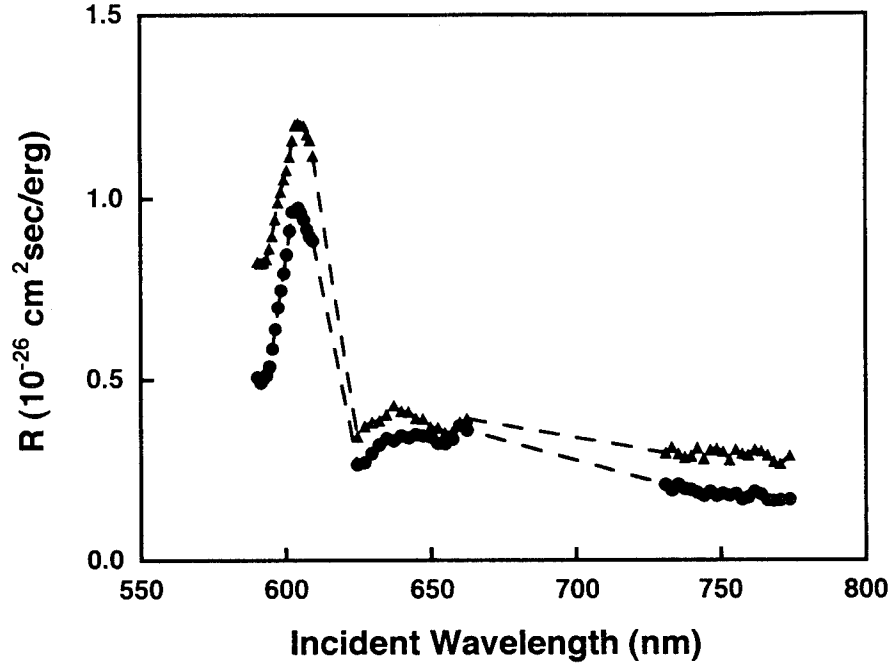
Figure 1: The p-polarized SH efficiency R of the clean Cu(111) surface as a function of wavelength of the p-polarized light incident at 67°. Details see text.

The incident plane in curve 1(a) ($\triangle$) is parallel to the [01$\bar{1}$] direction corresponding to $\psi = 0°$ while the crystal has been rotated $\psi = 30°$ in curve 1(b) ($\bullet$) so that the plane of incidence is parallel to the [11$\bar{2}$]. It follows that $R \propto\mid A + B \mid^2$ in curve 1(a) while $R \propto\mid A \mid^2$ in curve 1(b). Figure 1 indicates that the peak in the SH response near 4.1 eV is entirely due to a resonance in the isotropic coefficient A, whereas the anisotropic coefficient B increases slowly with SH photon energy [1]. Therefore the linear optical parameters can be excluded as a source of the observed SH resonance as they contribute to both A and B. Furthermore, Bloch et al. found that during exposure of the Cu(111) surface to oxygen, the SH efficiency drops by a factor of 10 at wavelengths in the vicinity of the resonance. Therefore, the contribution from the isotropic bulk electric quadrupole term is relatively small at the resonant energy. Thus the strongest candidates for the resonance feature at 4.1 eV are the isotropic surface susceptibility elements of $\chi^{(2)}$.

Figure 2 shows the dispersion relation $E(k_\parallel)$ of the occupied surface state (SS) at the $\overline{\Gamma}$ point of the surface Brillouin zone along with the projected bulk continuum adapted from Ref. [4]. The s-band edge continuum states (L_1) are approximately 4.3 eV above the Fermi level and are too high in energy to be involved in a resonant excitation with the laser frequencies used in these studies. However, the n=1 member of a Rydberg series of image-potential surface states (IS) has exactly the correct energy separation of 4.1 eV from the Fermi level.

We conclude that the observed SH resonance at $2\hbar\omega = 4.1$eV is due to a coup-
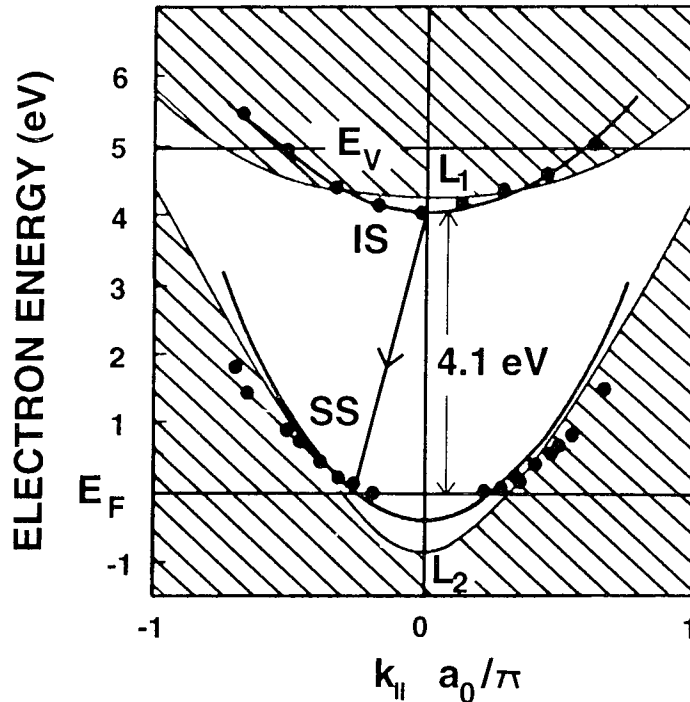
Figure 2: Surface projected band structure adapted from Ref. [4]. Details see text.

ling between the SH photon and an electronic transition between the lowest image potential state and the Gartland-Slagsvold surface state near the Fermi level at the $\bar{\Gamma}$ point of the Cu(111) surface Brillouin zone. This conclusion is supported by high-resolution angle-resolved photoemission measurements on the SS state on Cu(111) demonstrating that its peak width increases on approaching the Fermi energy [3]. Kevan explained the broadening mechanism by considering SS as a defect-induced state which interacts more strongly with the bulk states as its energy approaches that of the bulk continuum near E_F. This explaination is consistent with the SH efficiency of Cu(111) at $2\hbar\omega = 4.1$eV being sensitive to the density of surface defects [2]. A defect-induced energy broadening of the SS state leads to a decrease in the SH efficiency, which in fact has been observed by Bloch et al. after sputtering or annealing of the Cu(111) surface [2].

References

[1] G. Lüpke, D.J. Bottomley, and H.M. van Driel, submitted to Phys. Rev. B.

[2] J. Bloch, G. Lüpke, S. Janz, and H.M. van Driel, Phys. Rev. B **45**, 12011 (1992).

[3] S.D. Kevan, Phys. Rev. Lett. **50**, 526 (1983).

[4] S.L. Hulbert, P.D. Johnson, N.G. Stoffel, W.A. Royer, and N.V. Smith. Phys. Rev. B **31**, 6815 (1985).

Linear and Nonlinear Optical Properties in Fractional-Layer-Superlattice Quantum Wires

Hiroaki Ando, Arturo Chavez-Pirson, Hisao Saito, and Hiroshi Kanbe

NTT Basic Research Laboratories, 3-1, Morinosato Wakamiya,
Atsugi-shi, Kanagawa 243-01 Japan
Tel: +81 462 40 3422

Summary

We present the results of theoretical studies numerically analyzing the linear and non-linear optical features of AlGaAs fractional-layer-superlattice (FLS) quantum wires. The results of the calculation are discussed in terms of quasi-1D quantum confinement effects, and are compared with experimental results.

The fractional-layer superlattice (FLS)[1,2], which has compositional periodicity normal to the direction of crystal growth, has been attracting much attention as a potential material for optical devices. Due to the lateral quantum confinement optical anisotropy normal to the grown surface can be readily observed[3]. The FLS quantum wire is an FLS layer sandwiched by barrier layers, as shown in Fig. 1. We believe it can be classified as a new type of low-dimensional structure. It is known that the compositional distribution in AlGaAs FLS is more gradual than the nominal distribution because of intermixing of Al and Ga. Therefore, in the direction of the FLS periodicity the wavefunctions of electrons and holes penetrate into adjacent wells, and quantum confinement is superlattice-like. The wavefunctions normal to the grown surface are strongly confined within the well, and quantum confinement is quantum-well-like. The quantum confinement dimension in the FLS wire is between 1D and 2D, that is, quasi-1D. Here, we discuss optical properties of the FLS wire from the view point of the asymmetrical quantum confinement in the quasi-1D structure.

To investigate linear and nonlinear optical properties it is necessary to know the detailed conduction and valence subband structures and the wave functions of an electron and a hole generated by optical excitation. A simple effective mass model is used to calculate the conduction subband structures. The valence subband structures resulting from the quantum-confinement induced mixing of heavy-hole and light-hole bands are calculated by diagonalization of the Luttinger-Kohn 4×4 Hamiltonian[4]. To include the quantum-well like confinement effect, strongly confined envelope functions are assumed for electrons (e) and holes (h) in the z direction;

$$\psi_z^i(z) = \sum_m c_m^i \sin\frac{\pi m z}{L_z}, \text{ where } i = e, h.$$

The envelope functions of Bloch form[5] are used in the y direction to take into account superlattice-like behavior.

$$\psi_y^i(y) = e^{-jky} \sum_K c_K^i e^{jKy}, \text{ where } K = 2\pi n/L_y; n = \text{integer}.$$

The Al composition in the FLS layer is assumed to be sinusoidally modulated in the y direction.

Optical anisotropy normal to the grown surface is a good measure to assess the lateral quantum confinement effects in the FLS wires. Figure 2 compares the calculated absorption anisotropy $\alpha_{\parallel-\perp} = \alpha_\parallel - \alpha_\perp$ with the experimental results. Here, we consider linearly polarized light incident along the z direction with electric field vector in the x ($E_\parallel$) and y directions ($E_\perp$). The experimental anisotropy is measured for a $(\text{AlAs})_{1/4}(\text{GaAs})_{3/4}$ FLS quantum wire fabricated by MOCVD[6]. The lateral period L_y and thickness L_z of the

FLS layer are both 8nm. The calculated anisotropy agrees well with the experimental results, reproducing the details of the spectral structures. The good agreement with the experiment confirms the validity of the present theoretical treatment.

Figure 3 compares the calculated optical gain coefficient for an AlGaAs FLS quantum wire with that for a GaAs quantum well (QW). In the calculation the modulation depth of the Al content in the lateral direction is assumed to be $\delta x = 0.1$. The polarization dependence of the gain is a result of the lateral quantum confinement in the FLS wire. The gain spectrum for $E_{\parallel}$ is found to have a more pronounced peak for the FLS wire than that for the QW. This is caused by the modification of the joint density-of-states at the bandedge in going from 2D to quasi-1D. A 3-fold enhancement in the gain coefficient can be expected by incorporating the FLS layer in the well position. The gain spectrum for $E_{\perp}$ has two peaks. The lower energy peak corresponds to the transition between the lowest conduction subband and the heavy-hole-like subband. The higher energy peak is due to the mixed heavy- and light-hole states produced as the result of quasi-1D confinement. This transition has a larger oscillator strength for $E_{\perp}$. Although the Al compositional modulation is as small as 0.1, a large change in the gain spectra is generated by the lateral confinement effects.

Concerning nonlinear gain properties, the higher energy gain peak for $(E_{\perp})$ tends to build up faster than the lower energy peak with increasing carrier density N_c. The crossover energy, where gain values for $E_{\parallel}$ and $E_{\perp}$ are balanced, therefore, shifts to the higher energy side as the carrier concentration increases. Furthermore, not only linear birefringence but also polarization-dependent nonlinear dispersion n_{eh} (nonlinear birefringence; $n_{eh\parallel}$ - $n_{eh\perp}$) is obtainable in the vicinity of the crossover energy, as shown in Fig. 4, corresponding to large anisotropy in nonlinear optical gain.

Existence of this crossover point together with nonlinear gain and dispersion are important from the view point of the application to a novel vertical polarization switch[7]. By incorporating the FLS in a vertical microcavity laser structure, and tuning the optical resonance in the vicinity of the crossover point, small changes in the carrier density N_c induced by electrical or optical means can switch the laser from one linear polarization state to the orthogonal state. It should be emphasized that by using FLS quantum wire not only as a gain media but also as an anisotropic nonlinear media, a simple structure consisting of FLS wire and vertical microcavity will be enough to configure the polarization switch.

In conclusion, we have theoretically investigated linear and nonlinear optical properties of the quasi-1D FLS quantum wire. This theory accurately explains the polarization-dependent absorption spectrum, experimentally assessed for AlGaAs FLS quantum wire. The small lateral modulation of the Al content ($\delta x = 0.1$) is found to change the optical properties markedly and improve the gain characteristics largely. The anisotropic linear and nonlinear properties, brought about by quasi-1D quantum confinement, are expected to lead to novel optical devices which control the polarization state of light.

References

[1] P. M. Petroff, A. C. Gossard, and W. Wiegmann, Appl. Phys. Lett., **45**, 620 (1984).
[2] T. Fukui and H. Saito, Appl. Phys. Lett. **50**, 824 (1987).
[3] A. Chavez-Pirson, J. Yumoto, H. Ando, T. Fukui, and H. Kanbe, Appl. Phys. Lett. **59**, 2654 (1991).
[4] J. M. Luttinger and W. Kohn, Phys. Rev. **97**, 869 (1955).
[5] U. Bockelmann and G. Bastard, Phys. Rev. B **45**, 1688 (1992).
[6] A. Chavez-Pirson, H. Ando, H. Saito, and H. Kanbe, to be published in Appl. Phys. Lett.
[7] A. Chavez-Pirson, H. Ando, H. Saito, and H. Kanbe, Appl. Phys. Lett. **62**, 3082 (1993).
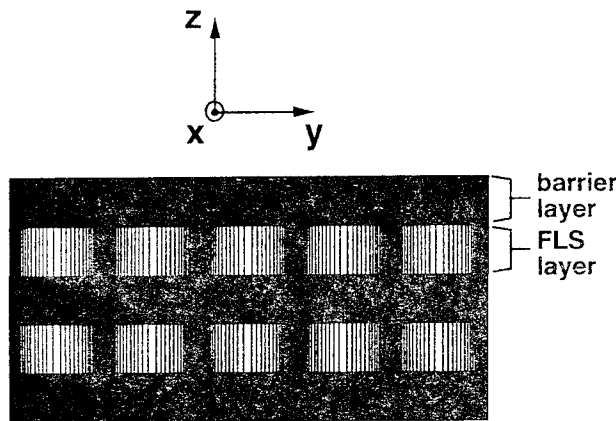
FIG. 1. Schematic drawing of the FLS quantum wire. The quantum confinement is quantum-well-like in the vertical (z) direction, and is superlattice-like in the lateral (y) direction.

FIG. 2. Comparison of calculated absorption anisotropy $\alpha_{\|-\perp} = \alpha_{\|} - \alpha_{\perp}$ with the experimental results. In the calculation the Al content x is assumed to be sinusoidally modulated by $\delta x = 0.08$ with a periodicity of 8 nm in y direction.
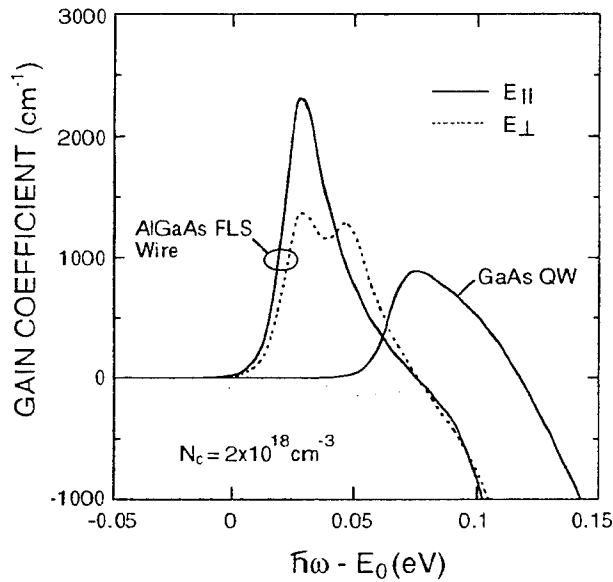
FIG. 3. Gain coefficients in AlGaAs FLS quantum wire and GaAs QW calculated for carrier density of $N_c = 2 \times 10^{18} \mathrm{cm}^{-3}$. The abscissa is the photon energy $\hbar\omega$ with respect to bandgap E_0 of the well material. The FLS layer is assumed to have an average Al content x of 0.25 and modulated by δx of 0.1 with a 16 nm periodicity. The vertical well thicknesses of the FLS quantum wire and the quantum well are both 10 nm.

FIG. 4. Dispersive nonlinearity n_{eh} calculated in gain regime for $N_c = 2 \times 10^{18} \mathrm{cm}^{-3}$. The dispersive nonlinearity is defined as

$n_{eh} = \Delta \bar{n} / \Delta N_c$, where $\Delta \bar{n}$ is the refractive index change induced by the change in carrier density ΔN_c.

Quasi-Phase Matched Second-Harmonic Generation from Asymmetric Coupled Quantum Wells

S. Janz, F. Chatenoud, and R. Normandin

Institute for Microstructural Sciences and Solid State
Optoelectronics Consortium, National Research Council
Montreal Road, Ottawa, Canada, K1A 0R6.
(613) 990-0688

Quasi-phase matched (QPM) second-harmonic (SH) generation in both insulator[1] and semiconductor [2] waveguides has applications ranging from the generation of coherent visible light to optical signal processing.[2,3] QPM compensates the wavevector mismatch between the fundamental and SH light by periodically varying the SH susceptibility, $\chi^{(2)}$, and refractive index, along the SH light propagation direction. It would be very useful if quantum wells could be used to engineer materials with a large $\chi^{(2)}$ which can be easily varied. Large asymmetric quantum well SH susceptibilities have been measured for far infrared wavelengths, where the nonlinear response is dominated by intra-subband transitions. Although there have been several theoretical studies predicting a quantum well $\chi^{(2)}$ comparable to that of $LiNbO_3$[4] or larger[5] in the near infrared and visible wavelength range, there have been no experimental measurements of $\chi^{(2)}$. We use reflection geometry QPM[6] to selectively enhance the SH signal from an asymmetric coupled quantum well (ACQW) superlattice. In addition we present the first measurement, to the best of our knowledge, of $\chi^{(2)}$ in the visible wavelength range for an ACQW.

A 1.0 μm thick ACQW superlattice, shown in Fig. 1, was grown on a (100) $GaAs$ substrate using molecular beam epitaxy. Each ACQW consists of a 3.85 nm $GaAs$ well separated from a 1.3 nm $GaAs$ well by a 0.88 nm $Al_{0.5}Ga_{0.5}As$ barrier. The well and barrier dimensions have been chosen to give the optimal $\chi^{(2)}$, according to the ACQW calculations carried out by Khurgin[4]. The orientation of the quantum well pairs is periodically reversed, thus changing the sign of the ACQW $\chi^{(2)}$, in order to satisfy the reflection QPM condition[6] for $\lambda = 1.319$ μm incident light. Light from a Q-switched $\lambda = 1.319$ μm Nd:Yag laser was incident at 45° on the specimen, and the SH light radiated in the specular direction was detected using conventional photon counting techniques.

Each ACQW pair has the same symmetry as the air/$GaAs$ interface, and hence the same tensor elements, namely $\chi^{(2)}_{zzz}$, $\chi^{(2)}_{zxx} = \chi^{(2)}_{yzy}$ and $\chi^{(2)}_{zxx} = \chi^{(2)}_{zyy}$, will be nonzero[7]. Fig. 2 shows the variation of the p-polarized SH intensity generated by a p-polarized incident beam for both a $GaAs$ reference and the ACQW superlattice, as each specimen was rotated by ψ about its surface normal. The SH intensity variation with rotation
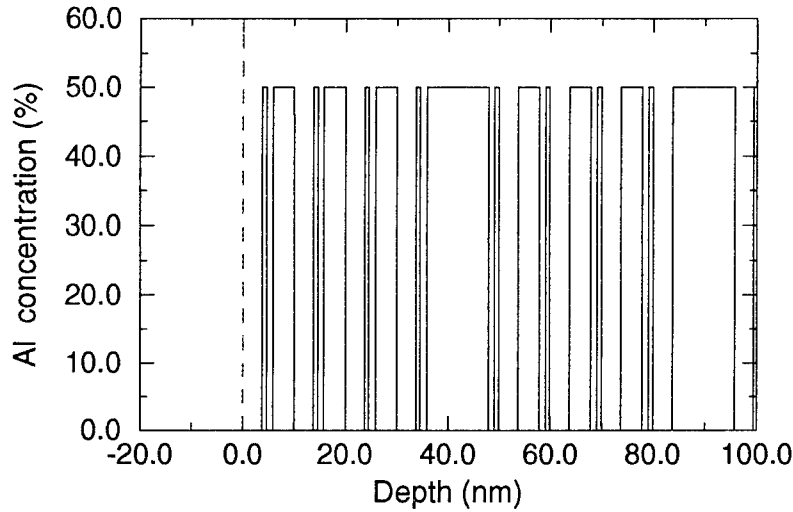
Fig. 1 The *Al* concentration profile of the uppermost unit cell of the asymmetric coupled quantum well (ACQW) superlattice.

angle ψ has the form,

$$I(\psi) = \left| Acos\psi sin\psi + B \right|^2. \tag{1}$$

In homogeneous *GaAs*, A is proportional to the bulk susceptibility $\chi_{xyz}^{(2)}$, while B is due to the surface SH signal. In the ACQW specimen, A is proportional an average of the barrier and quantum well intrinsic bulk susceptibilities, while B includes both surface and ACQW contributions. Since the top layer of the ACQW specimen is also *GaAs*, the surface contribution for both specimens must be identical. A comparison of the best fit of Eq. 1 to the *GaAs* and ACQW data in Fig. 2 indicates that the isotropic component of the SH signal for the ACQW specimen is due primarily to the ACQW superlattice SH response. Measurements were also made of both the s-polarized and p-polarized SH signal from the ACQW superlattice as the incident beam polarization was rotated, with the plane of incidence along the crystal (010) axis. Using this data and the data of Fig. 2, and correcting for the SH signal amplification due to the QPM geometry, the ACQW susceptibilities are estimated to be $|\chi_{yzy}^{(2)}| = 1.5 \times 10^{-11}$ mV^{-1} and $|\chi_{zyy}^{(2)}| = 1.3 \times 10^{-12}$ mV^{-1}. The $\chi_{yzy}^{(2)}$ result is in good agreement with the calculation of Khurgin[4] for similar ACQW structures. On the other hand, the measured value for $\chi_{zyy}^{(2)}$ is comparable to $\chi_{yzy}^{(2)}$, contrary to theoretical considerations[4,5] suggesting that $\chi_{yzy}^{(2)}$ should be much larger than all other components.

In conclusion, we have presented the first measurement of the SH susceptibility of an ACQW superlattice, for SH generation in the visible wavelength range. The measured values of $|\chi_{yzy}^{(2)}| = 1.5 \times 10^{-11}$ mV^{-1} and $|\chi_{zyy}^{(2)}| = 1.3 \times 10^{-11}$ mV^{-1} are comparable to the $\chi^{(2)}$ of *LiNbO$_3$*. These measurements show that it is possible to use quantum
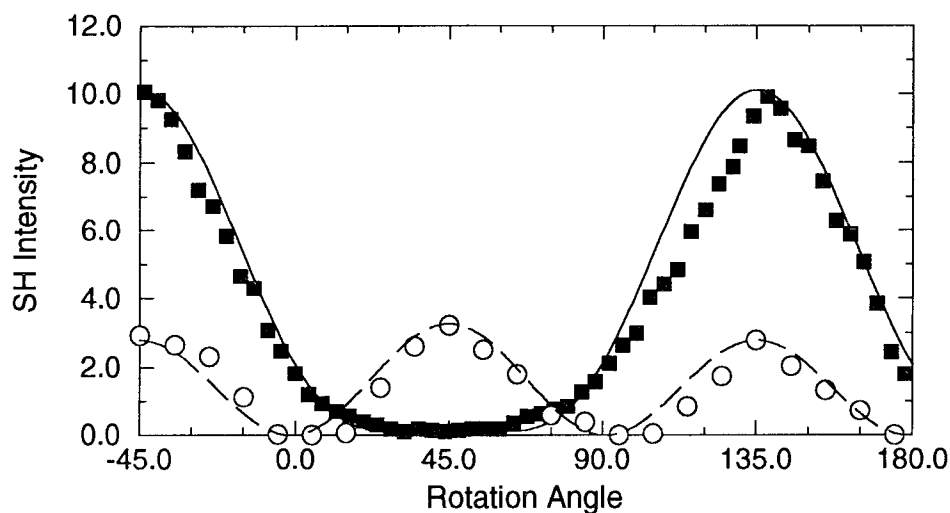
Fig. 2 The variation of the p-polarized SH signal with rotation angle ψ about the surface normal for the ACQW superlattice (squares) and *GaAs* reference (circles), using p-polarized incident light. The smooth curves show the best fits of Eq. 1 to the data.

well engineering to fabricate materials with SH susceptibilities at visible wavelengths comparable to commonly used nonlinear crystals. We have also demonstrated that the use of QPM in a reflection geometry is a practical technique for amplifying the optical SH response of quantum wells and other microstructures. This technique opens new possibilities for applying optical SH and sum-frequency generation to investigate nonlinear optics in semiconductor microstructures.

References

1. M. M. Fejer, G. A. Magel, D. H. Jundt, and R. L. Byer, IEEE J. Quantum Electron. **28**, 2631 (1992), and references therein.
2. R. Normandin, S. Letourneau, F. Chatenoud, and R. Williams, IEEE J. Quantum Electron. **27**, 1520 (1991).
3. M.L. Sundheimer, Ch. Bosshard, E.W. van Stryland, G.I. Stegeman and J.D. Bierlein, Optics Lett. **17**, 1397 (1993).
4. J. Khurgin, Phys. Rev. B **38**, 4056 (1988).
5. P.J. Harshman and S. Wang, Appl. Phys. Lett. **60**, 1277 (1992).
6. S. Janz, C. Fernando, H. Dai, F. Chatenoud, M. Dion, and R. Normandin, Optics Lett. **18**, 589 (1993).
7. T. Stehlin, M. Feller, P. Guyot-Sionnest, and Y.R Shen, Opt. Lett. **13**, 389 (1988).

Femtosecond nonlinear spectroscopy of semiconductor quantum dots: effect of two-electron-hole-pair interaction

S. Hunsche, V. Klimov[+], and H. Kurz

Institut für Halbleitertechnik II, RWTH Aachen, 52056 Aachen, Germany
Tel: +49-241-807896; Fax: +49-241-8888-246; e-mail: hunsche@basl.rwth-aachen.de
[+]Permanent address: Physics Faculty, Moscow State University, 119899 Moscow, Russia

Semiconductor nanocrystals (NCs) can be treated as quasi-zero-dimensional objects or quantum dots.[1] Photo-induced absorption changes of the NCs are usually dominated by state filling. However, Coulomb interaction can also be important in the nonlinear absorption of the NCs. In particular, the two-electron-hole-pair interaction (biexciton effect) may lead to a shift of the energies of the optical transitions from one- to two-pair states. The two-pair interaction energy can be interpreted as biexciton binding energy $\delta E_2 = 2E_1 - E_2$, where E_1 and E_2 are the energies of the one- and two-pair states, respectively. Theoretical studies lead to contradictory results for the sign and magnitude of the two-pair interaction energy.[2,4] Until now, experiments have not given definite evidence for the Coulomb interaction-induced shift of the energy levels of the two-pair states which can be expected to result in increased absorption below ($\delta E_2 > 0$) or above ($\delta E_2 < 0$) the one-pair resonances depending on the sign of the interaction energy. The observation of this effect is usually complicated by strong broadening of the levels of size quantization and bleaching of the one-pair transitions due to state-filling.

We report on measurements of the femtosecond dynamics of differential transmission spectra (DTS) of CdSe NCs excited well above the energy of the lowest optical transition. The effect of the two-pair interaction manifests itself at the initial stage of carrier relaxation, before the lowest electron and hole levels become occupied, as a red-shift of the lowest resonance in the nonlinear absorption spectra.
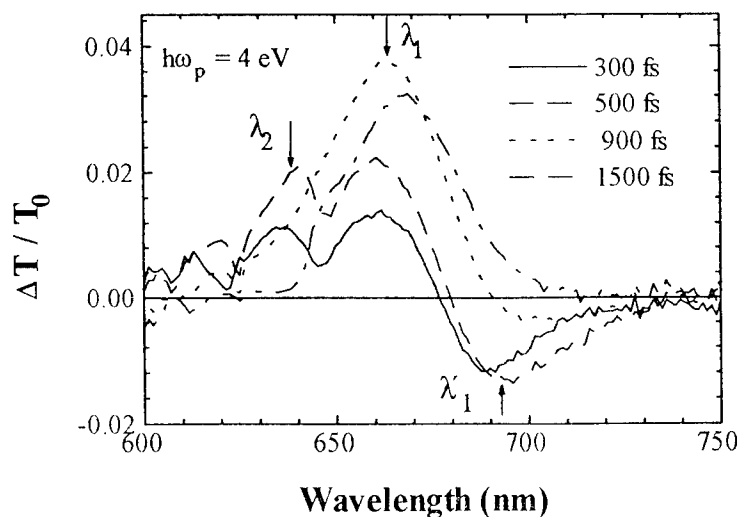
Figure1: DTS of CdSe NCs at different delay times between pump and probe pulses

The samples are CdSe-doped glasses with average radius of the NCs of about 5 nm. The dynamics of the DTS is studied by femtosecond pump and probe measurements (pulse

duration is 80-100 fs, pump photon energy is 4 eV). An optical multichannel analyzer system is used to measure DTS= $[T(\lambda)-T_0(\lambda)]/T_0(\lambda)$, where $T_0(\lambda)$ and $T(\lambda)$ are the transmission spectra of the unexcited and excited sample, respectively. In additional experiments with 2 eV excitation, we have studied the excitation density dependence of the DTS, which allows a determination of the energetic structure of the CdSe NCs in our sample. In addition, from comparison with these data, we estimate that the average excitation density in the measurements presented in this paper is less than one electron-hole pair per NC.

The DTS recorded at small delays between pump and probe pulses (Δt = 200 - 800 fs) exhibit three well resolved features (Fig.1): two bleaching bands at λ_1 and λ_2, and one band of induced absorption λ'_1. In Fig. 2 we show the temporal evolution of the changes of optical density, $-\Delta\alpha d$, derived from the DTS at different wavelengths. The bands λ_2 and λ'_1 are characterized by extremely fast dynamics. Their amplitudes increase within the first 400-500 fs after excitation and then decay during the next 500-600 fs. The band λ_1 exhibits slower dynamics. Its rise time is of about 900 fs, and exponential relaxation time is 2.5ps.
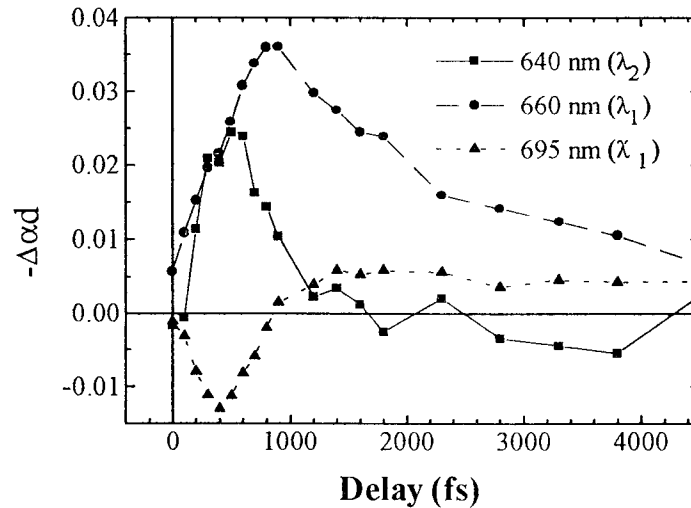
Figure 2: Time dependence of induced absorption changes at the maxima of the λ_1, λ_2, and λ_1' bands in the DTS

The structure and evolution of the DTS can be explained in terms of Coulomb interaction and state filling due to carriers relaxing to the lowest available states. The two bleaching bands λ_1 and λ_2 are attributed to the saturation of the two lowest dipole-allowed one-pair transitions $1s_e$-$1s_h$ and $1p_e$-$1p_h$ coupling electron and hole states. Just after excitation these states are not occupied with carriers. During the energy relaxation carriers reach the 1p states, resulting in the saturation of the corresponding transition (λ_2 bleaching band). Two-pair interaction causes a shift of the energies of the two-pair (biexciton) states including the ground biexciton state. This manifests itself as a bleaching in the range of the lowest resonance (band λ_1) and the induced absorption below it (band λ'_1). The relaxation of the carriers to the lowest 1s states causes the increase of the amplitude of the λ_1 band due to state filling and results in the suppression of the increased absorption below this band.
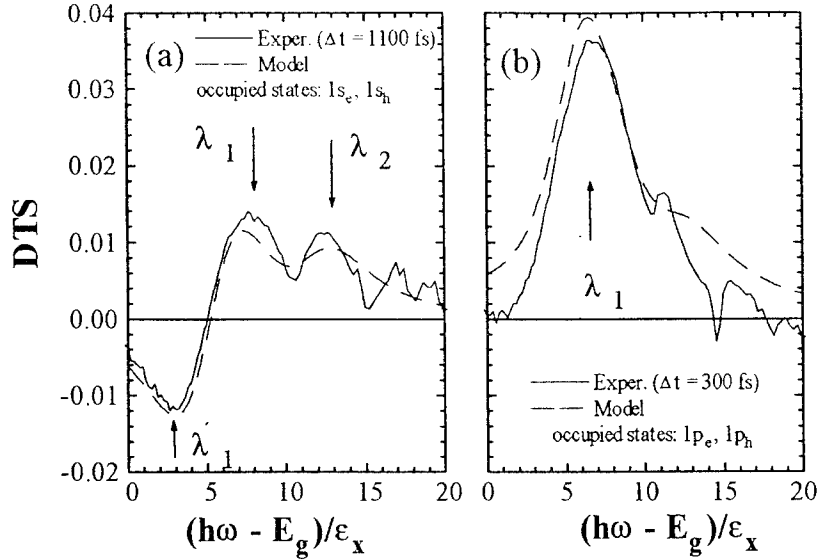
Figure 3: Measured DTS at delays of 300 fs (a) and 1100 fs (b) compared with calculated DTS assuming occupation of either p- or s-states.

The measured DTS are modeled by taking into account six dipole-allowed transitions coupling vacuum state, two one-pair states and three two-pair states. The DTS recorded at small delay ($\Delta t < 600$ fs) can be well described by the calculated spectra assuming occupation of the excited states $1p_e$ and $1p_h$ [Fig.3 (a)]. The spectra observed at longer delay ($\Delta t > 900$ fs) are well fitted assuming that the $1s_e$ and $1s_h$ states become occupied [Fig.3 (b)]. From fitting the experimental spectra we obtain a value of the two-pair interaction energy (biexciton binding energy): $\delta E_2 = 32$ meV. This value is much higher than the biexciton binding energy in bulk CdSe indicating a strongly enhanced attractive interaction of the electron-hole pairs in the NCs.

References:

[1] L. Brus, IEEE J. Quantum Electron. QE-22, 1909 (1986)
[2] L. Banyai, Y.Z. Hu, M. Lindberg, and S.W. Koch, Phys. Rev. B **38**, 8142 (1988)
[3] T. Takahgahara, Phys. Rev. B **39**, 10206 (1989)
[4] Y.Z. Hu, M. Lindberg, and S.W. Koch, Phys. Rev. B **42**, 1713 (1990)

Femtosecond Pulse Compression and Adiabatic Following in Semiconductor Amplifiers

R.A. Indik, J.V. Moloney and R. Binder *

Arizona Center for Mathematical Sciences

Department of Mathematics

University of Arizona

Tucson, Az. 85721

Telephone: (602)-621-6755

Fax: (602)-621-1510

A. Knorr and S.W. Koch

Fachbereich Physik and Zentrum für Materialwissenschaften

Philipps-Universität

Renthof 5, D-35032 Marburg

It has been recently shown that high intensity femtosecond pulses that saturate the gain medium can undergo net absorption when propagating in semiconductor amplifiers [1]. The relevant behavior cannot be captured by a conventional gain saturation model of a semiconductor amplifier [2] but instead requires the resolution of the full many-body dynamics such as bandgap renormalizaion, dynamic Coulomb screening, Pauli blocking etc. [3]. In contrast to uniformly inverted atomic levels, the inverted semiconductor is characterized by an electro-hole plasma which obeys Fermi-Dirac statistics, causing gain below and absorption above the quasi-chemical potential. Therefore after strong pulse excitation, saturation of the gain of the leading part of the pulse leads to absorption of the trailing part by those noninverted states which have a finite spectral (absorptive) overlap with the pulse. Since amplification or absorption can continue indefinitely along the amplifier, it is

unclear how the nonlinear interaction between the pulse and different carrier states manifests itself in the pulse propagation process.

We will report on our studies of a plane wave femtosecond pulse propagating in a semiconductor amplifier over gain lengths well beyond that reported in reference [1]. Preliminary results on the extension of our study to include transverse spatial effects necessary to model realistic waveguiding and broad area amplifier structures will also be discussed. The overall conclusion of our study for a plane wave pulse is that, after initial linear amplification and saturation, the pulse undergoes strong intensity and spectral deformation before settling into a strongly compressed intense superluminal pulse undergoing adiabatic following (AF) with off-resonant noninverted states, well above the chemical potential. In this AF regime the pulse continues to sharpen and grow in intensity. This scenario appears to hold irrespective of the initial pulse intensity or its carrier frequency offset from the gain peak. However, the transient evolution of the pulse intensity and spectrum is very sensitive to the inital detuning of the carrier frequency from the linear gain peak. Dynamic bandgap renormalization leads to a downshift of the peak gain as the carrier density is driven down on the leading edge of the pulse as it saturates. This in turn leads to linear amplification of that part of the pulse spectrum that lies under the maximum of the gain. If the pulse center frequency is initially offset from the renormalized peak gain, we observe strong modulation of the pulse spectrum which in turn modulates the intensity and the pulse transient looks very complicated. We anticipate that these effects will strongly modify the frequency chirp observed across short pulses in semiconductor amplifiers. Figure 1(a) depicts the relevant stages in the pulse intensity evolution over 40 linear gain lengths (reference [1] showed results over 1 gain length) while Figure 1(b) shows the corresponding evolution of the total carrier density.

The dynamics of the field and carriers in the semiconductor amplifier is described by the Maxwell-Semiconductor Bloch equations:

$$\frac{\partial E}{\partial \xi} - \frac{i}{k_0}\frac{\partial^2 E}{\partial x^2} = \frac{id_{cv}\mu_0\omega_0^2}{k_0 V}\sum_q P_q \tag{1}$$

where (η, ξ) are the retarded time and space coordinates [1-4] and we include diffraction in one transverse dimension. The polarization functions P_q are determined from the solution of the Semiconductor-Bloch equations [5]:

$$\frac{\partial P_1}{\partial \eta} = -i(\Delta_q - \omega_p)P_q - i\Omega_q(f_q^e + f_q^h - 1) + \frac{\partial P_q}{\partial \eta}|_{coll} \tag{2}$$

$$\frac{\partial f_q^{e/h}}{\partial \eta} = iP_q^*\Omega_q + c.c. + \frac{\partial f_q^{e/h}}{\partial \eta}|_{coll} \tag{3}$$

with the renormalized Rabi frequency $\Omega_q = \frac{\Omega}{2} + \frac{1}{\hbar}\sum_{q'} V_{q-q'}P_{q'}$. Here $f_{q'}$ and $\Delta_q = \epsilon_q - \frac{1}{\hbar}\sum_{q'} V_{q-q'}(f_{q'}^e + f_{q'}^h)$ denote the distribution functions for electrons or holes and the energy dispersion including the band gap renormalization, respectively. The Coulom potential V_q, is treated in a quasi-statistical screening model. The Rabi frequency $\Omega = d_{cv} \cdot E/\hbar$ is determined by the dipole matrix element d_{cv} and the amplitude of the external electrical field $\tilde{E} = E(\eta, \xi)e^{-i\omega_0 t + ik_0 z}$. For simplicity the collision terms in Eqs. (2) and (3) are approximated in the relation rate approximation using time constants of 60 fs [6].

The inclusion of the diffraction term in the model allows for simulation of femtosecond pulse amplification in waveguided or broad area amplifiers. The computational challenge is much greater here and we are investigating parallel vector supercomputers such as the Cray C-90 and the CM5 Connection Machine for optimal compute performance. The very strong temporal and frequency distortion of plane wave pulses in the temporal domain should manifest also across the transverse Gaussian profile of a finite width pulse. In addition diffractive effects and self-phase modulation should act in concert with these "plane wave" mechanisms to produce some fascinating spatiotemporal evolutions in broad area amplifiers in particular. Figure 2 is the first such result for an injected Gaussian pulse (FWHM =) propagating over 10 linear gain lengths in the amplifier. This propagation distance is insufficient to observe the strong temporal transient leading to the AF regime in Figure 1 but it already indicates the appearance of interesting spatiotemporal features. This particular simulation corresponds to a 150 femtosecond pulse which is strongly saturating in the center. The outer wings undergo strong initial linear amplification and most of the transverse cross-section has reached saturation after 10 gain lengths. Work is in progress to study such spatiotemporal evolutions over longer gain lengths and for lower peak intensity injected pulses.
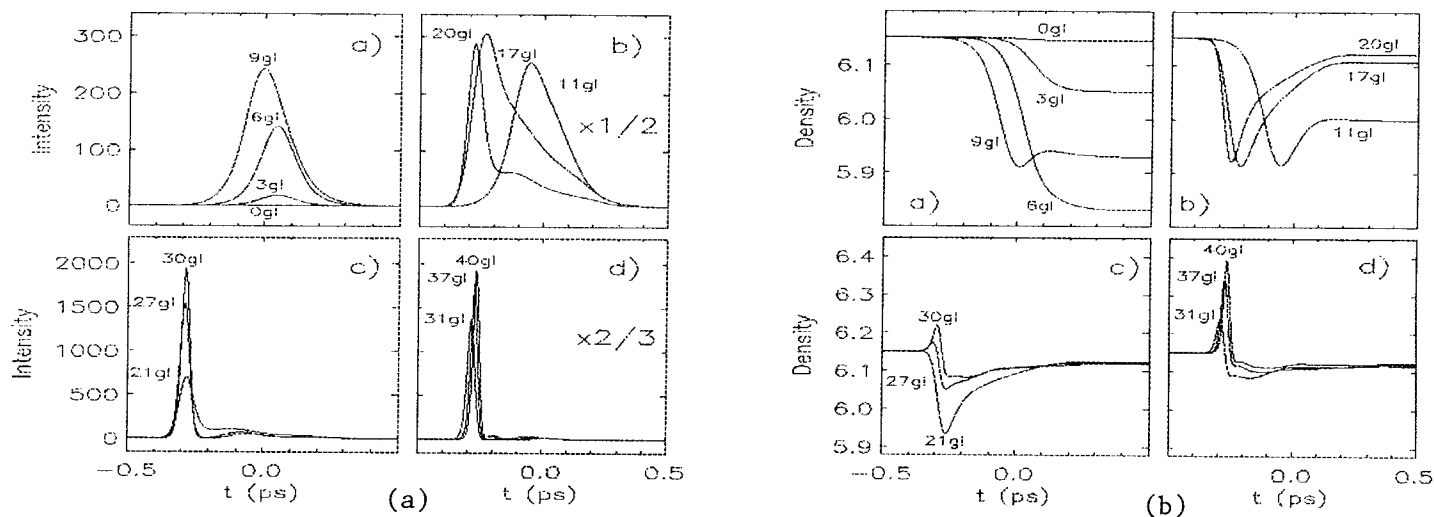
Figure 1. (a) Pulse intensity profiles over 30 gain lengths in the amplifier, (b) corresponding inversion densities.

References

[1] A. Knorr, R. Binder, E.M. Wright and S.W. Koch, *Opt. Lett.*, **18**, 1538 (1993); *Optics and Photonics News*, **4**, 44 (1993).

[2] G.P. Agrawal and N.A. Olsson, *IEEE J. Quant. Electron.*, **25**, 2297 (1989).

[3] H. Haug and S.W. Koch, "Quantum Theory of the Optical and Electronic Properties of Semiconductors", 2nd Edition, (World Scientific, Singapore) (1993).

Effects of carrier relaxation on excitonic nonlinear absorption in GaAs quantum wells

S. Hunsche, K. Leo[*], H. Kurz, and K. Köhler[+]

Institut für Halbleitertechnik II, RWTH Aachen, 52056 Aachen, Germany
Tel: +49-241-807896; Fax: +49-241-8888-246; e-mail: hunsche@basl.rwth-aachen.de
[*]Institut für angewandte Photophysik, TU Dresden, 01062 Dresden, Germany
[+]Fraunhofer Institut für angewandte Festkörperphysik, 79108 Freiburg, Germany

We use time-resolved differential transmission spectroscopy with time-resolution better than 100 fs to study exciton absorption saturation in by optically excited carriers in GaAs/AlGaAs multi quantum wells (MQWs). We perform pump-probe experiments using near infrared pump pulses tunable from 1.44 eV to 1.56 eV and a white-light continuum probe. Pump-induced transmission changes are recorded as differential transmission spectra (DTS). These specra show bleaching of the excitonic transitions at various subband edges due to carrier-induced loss of exciton oscillator strength and broadening of the excitonic absorption lines. The former contribution to the saturation of the exciton absorption peaks can be separated from pure broadening (and shift) of the exciton by integrating the DTS over the width of the broadened exciton line. The main mechanisms leading to exciton bleaching are phase space filling (PSF) and exchange effects, which are directly related to the occupation of carrer states, and long-range Coulomb screening.

The influence of intra-subband carrier relaxation on exciton bleaching was studied in a sample consisting of 40 periods of 10 nm GaAs wells and 20 nm AlGaAs barriers. The pump was tuned to 1.53 eV, below the transition from the second heavy hole subband to the second electron subband (E2H2), creating carriers with a total excess energy of 70 meV in the lowest subbands only. Figure 1 displays DTS at different delay times, showing exciton bleaching at various subband edges.
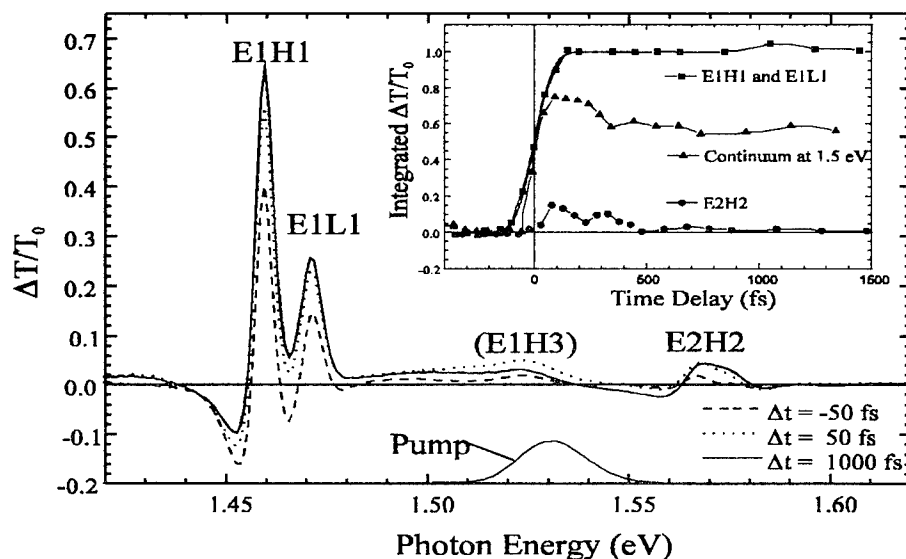
Figure 1: DTS at different time delays after exitation of carriers into the lowest subbands. $N_{exc}=3.9 \times 10^{11}$ cm^{-2}

The inset shows the temporal evolution of the integrated transmission changes, i.e. the loss of oscillator strength, of the transitions corresponding to the first and second electronic subband. Additionally, it shows the transmission change at 1.5 eV that is due to band-filling of continuum states of the lowest subbands. After a very fast increase, this signal relaxes to a quasi-stationary level within 800 fs. This indicates the intrasubband relaxation and cooling of the pump-excited carriers.

In contrast, the integrated transmission change at the lowest subband edges indicates an instantaneous reduction of oscillator strength that reaches its maximum within the pump pulse duration. Obviously, this signal shows no significant influence of the intrasubband carrier relaxation. This is in strong contrast with calculations predicting a distinct dependence of PSF on the carrier temperature.[1,2] According to the existent theory, carrier cooling is expected to result in an increasing efficiency of PSF, which would lead to a delayed increase of the integrated transmission change. This is not observed in our experiment.
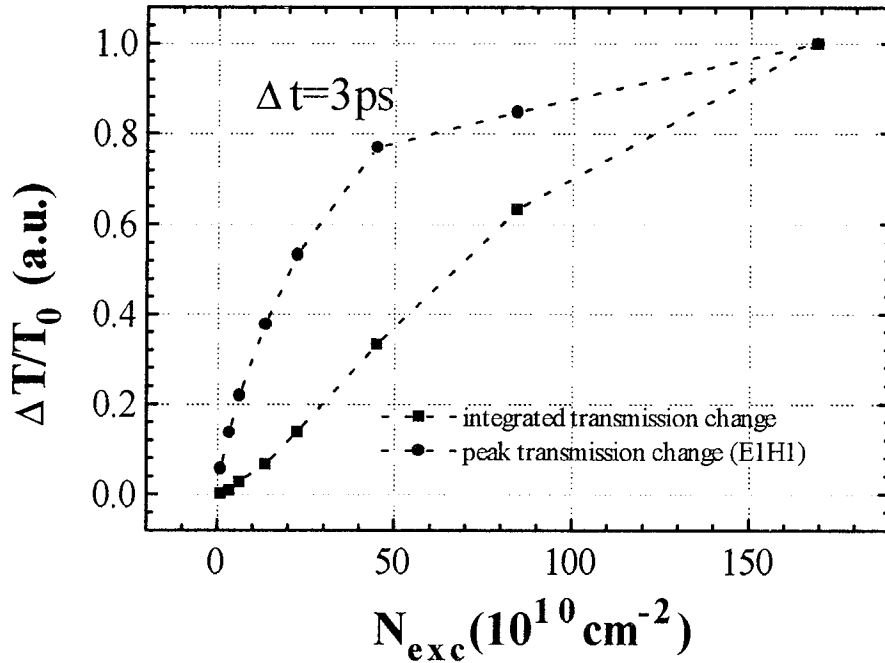
Figure2: Excitation density dependence of integrated and peak transmission change at the E1H1 transition

As no carrier are excited into the second subbands, the E2H2 transition cannot be influenced by PSF, but only by Coulomb screening. The DTS in Fig. 1 indicate a broadening and a slight red-shift of this transition, while the integrated transmission change remains essentially zero. This shows that Coulomb screening does not result in a reduction of the exciton oscillator strength. However, the bleaching of this transition associated with unoccupied subbands shows that exciton absorption saturation cannot be explained in terms of PSF alone. In order to obtain more information about the different contributions to the bleaching, we compare the excitation density dependence of the peak and the integrated transmission change at the E1H1 transition (Fig. 2). The first value contains contributions due to PSF and Coulomb screening, while the latter is given by PSF only. While the latter signal increases roughly linearly up to 10^{12} cm^{-2}, the peak value shows some saturation

already at much lower densities. This different density dependence suggests that pure broadening by Coulomb screening may be the dominant bleaching mechanism at low carrier densities, while PSF becomes more important with increasing density.

Integrated $\Delta T/T_0$

■ E1H1   Simulation:
● E2H2 $\tau_{PUMP}=80$ fs
▲ E3H3 $\tau_{21}=160$ fs

0   500   1000   1500

Time Delay (fs)
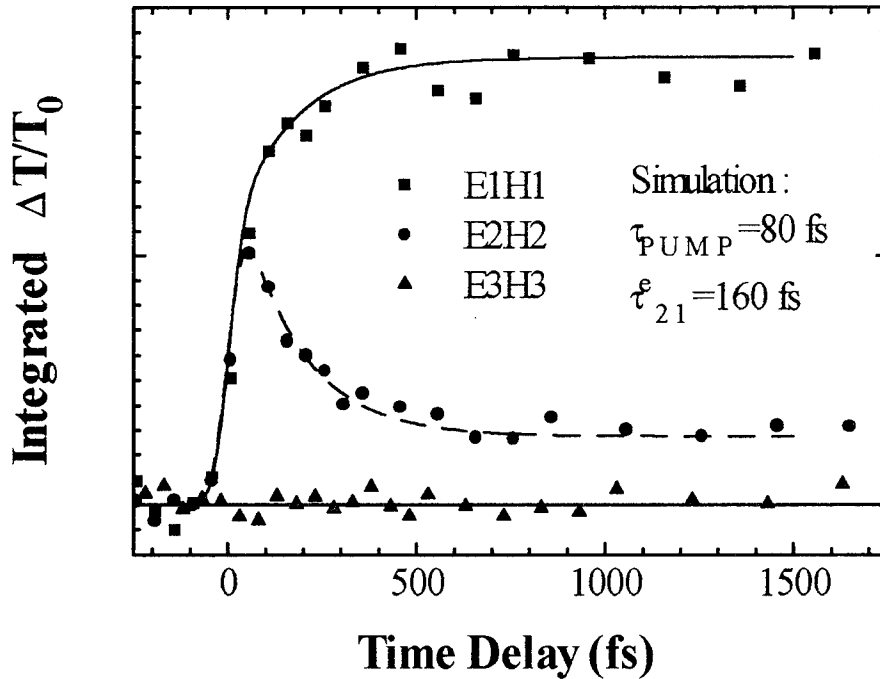
Figure 3: Reduction of exciton oscillator strengths after excitation resonant with the E2H2 transition

The effect of intersubband carrier relaxation has been studied in a MQW sample with 15 nm wells, corresponding to a electron subband splitting of 50 meV. The sample was excited resonantly at the E2H2 transition. Approximately half of the pump-created carriers are excited into the second electron and hole subbands. Figure 3 presents the temporal evolution of the integrated transmission changes at the E1H1, E2H2 and E3H3 transitions. As shown above, these are a measure of the carrier density in the respective subbands. The E3H3 exciton shows no loss of oscillator strength, confirming that no carriers are excited into the third subbands. The bleaching of the E2H2 exciton shows an increase during the pump pulse and a subsequent fast relaxation to a quasi-stationary level. Corresponding to this relaxation, the E1H1 exciton shows a delayed increase. This time dependence can be well explained by a sub-picosecond electron intersubband relaxation, which has been shown to occur for subband splittings larger than the LO phonon energy.[3] From fitting the data, we determine a relaxation time constant of 160 fs.

References:

[1] S. Schmitt-Rink, D.S. Chemla, and D.A.B. Miller, Phys. Rev. B **32**, 6601 (1985)
[2] R. Zimmermann, phys. stat. sol. (b) **146**, 371 (1988)
[3] M.C. Tatham, J.F. Ryan, and C.T. Foxon, Phys. Rev. Lett. **63**, 1637 (1989)

Femtosecond Resonant Second Harmonic Generation (SHG) in Potassium Vapor*

J. Y. Zhang

Department of Physics, Georgia Southern University, Statesboro, GA 30460, USA

K. S. Wong and G. K. Wong

Department of Physics, The Hong Kong University of Science and Technology, Kowloon, HK

and Y. R. Shen

Department of Physics, University of California, Berkeley, CA 94720, USA

It is well-known that the second-order nonlinear effects, such as second harmonic generation (SHG), difference frequency generation (DFG), and sum frequency generation (SFG), in atomic vapors are theoretically forbidden by symmetry on both a microscopic level because the individual atoms in the vapor do not possess a dipole, and on a macroscopic level because the atoms are isotropically distributed. However, SHG is vapor was first observed by Mossberg et al[1] in Tl and then in many other atomic vapors and some noble gases by other groups. Several explanations for this phenomenon have been presented. A model, proposed by Mossberg et al.[1] and later modified by Bethune,[2] attributes it to a dc-field, which is created by laser-induced multi-photon ionization and spatially separation of free photo-electrons from the heavier ions either by the pondermotive potential of the laser or by the kinetic energy of photo-electrons and makes SHG allowed. Such a model is most commonly accepted thus far, although it was called to question by the experimental result of Zhang et al,[3] in which there was no correlation between the SHG and the ionization measured. All experiments reported so far have been carried out by using either nanosecond or picosecond laser pulses.

We report here the first femtosecond SHG in vapor. The experimental study is done in potassium vapor using femtosecond pulses from a mode-locked Ti: sapphire laser. The output of the laser has a quasi-Gaussian beam profile with a pulse width of 100 femtoseconds and a repetition rate of 72 MHz. The output power is split into two parts, 30% as the probe beam and 70% as the pump. Before focusing, two beams are parallel and separated by about 1-cm. They are then focused by a lens with f=20-cm and overlapped near the focal point at an angle of ~0.1 rad. The temporal and spatial overlaps of the two beams are examined and optimized by sum frequency generation (SFG) in a 1-mm thick BBO crystal at the focus. The optical delay between the pump and the probe can be adjusted by a computer-controlled stepping-motor-driven translational stage with a resolution of 6.7 fs/step. The K vapor is prepared by a heat-pipe and protected by 30-50 torr of He. The K vapor pressure can be controlled from 0.1 to 20 torr. The pumping power can be further adjusted by a Glan-prism. The SHG generated from the pump and the probe can be analyzed separately. The detection of the SHG is through a 0.5-m spectrometer and a CCD detector cooled to the liquid nitrogen temperature. The experimental set-up is shown in Figure 1.

Narrow band SHG (with a bandwidth of about 0.35 nm) at 364.2 nm can be detected in the forward direction when the broad band (about 8 nm) Ti: Sapphire laser pulses are focused into the heat-pipe and tuned to the atomic 3s-4d two-photon resonance of potassium. The SHG signal level is rather week and has roughly the same polarization as the pump. Under the optimum condition (vapor pressure of 10 torr and pumping intensity of 5×10^7 w/cm^2) it is about one count per million pump pulses. The four-wave mixing output around 405 nm resulting from mixing of two laser photons and the IR photon generated from the hyper-Raman process 4d$\rightarrow$5p is also observed and is found to be more than two orders of magnitude stronger than the SHG component.

One may suspect that such a low SH signal could be the disguise of a signal from collision

---

*The experimental work is carried out in The Laser and Photonics Laboratory, Physics Dept., HKUST, HK

induced hype Rayleigh scattering or two-photon-induced fluorescence. However, we have found that the SH output is highly directional, proportional to the square of potassium vapor density, and dependent on the pump laser intensity with $I_{SHG} \propto I_{pump}^{4.3}$. The latter result is descried in Fig. 2. No appreciable SHG is detected when the pump is below 25 mW. Thus, the observed SHG appears to be a generic coherent nonlinear optical process.
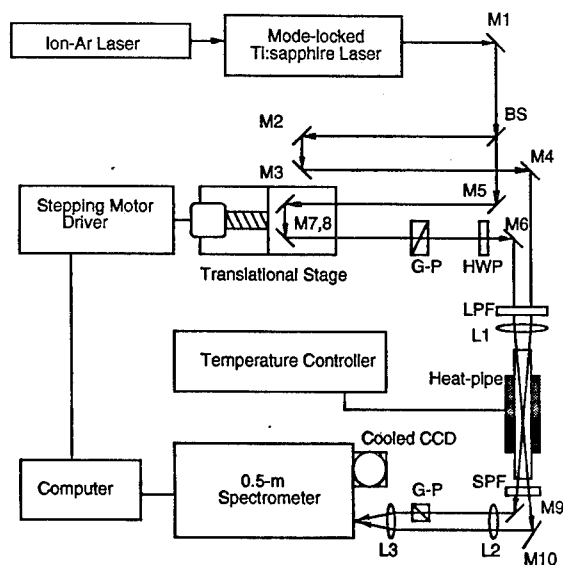
Fig. 1. Experimental arrangement for femtosecond second harmonic generation in potassium vapor
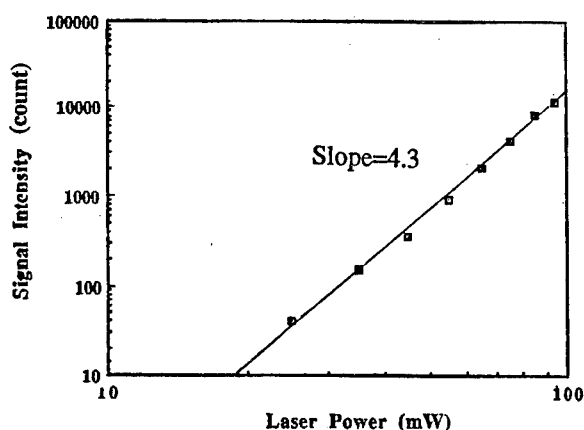
Fig. 2 Dependence of SHG signal on the pump power. A laser power of 100 mw is equivalent to a peak intensity of 5×10^7 W/cm^2 at the focus.

We have studied the effect of the strong pump beam on SHG from the weak probe beam. The intensity of the probe beam is so adjusted that with our detection sensitivity the SHG signal generated by the probe beam alone is hardly detectable. Then the strong pump beam is added and the SHG induced by the pump in the direction of the probe is measured. The effect of the pump on the probe is examined as a function of time-delay (positive and negative). It is found that SHG signal reaches the maximum around zero-delay. The result is presented in Figure 3. At longer delays, the signal drops to ~40% of the maximum. The lower level SHG signal disappears completely when the pump beam is blocked.
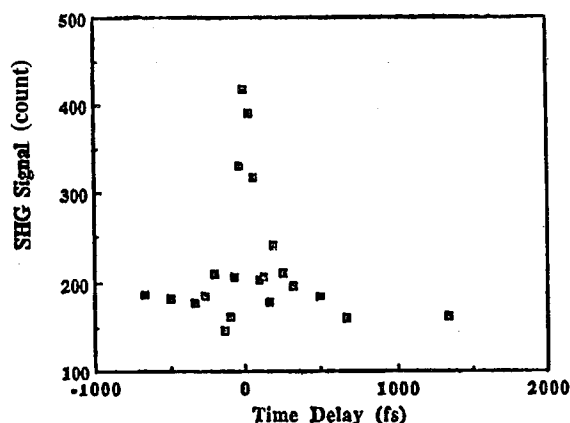
Fig. 3 SHG from the probe beam as a function
of time delay. A negative time delay means that
the pump pulse comes after the probe pulse.

The pump-and-probe result indicates that the pump-induced SHG has a very fast, nearly instantaneous, response as well as a more slowly varying component. This is very similar to the result obtained by picosecond pulse[4]. It can be understood as coherent transient dc-field-induced SHG with the dc-field generated by multiphoton ionization. Obviously, the femtosecond pulse excitation of atomic resonances necessarily requires the consideration of the coherent transient process in the SHG, as has been used to explain resonant SHG in potassium vapor pumped by picosecond pulses[4]. The result could be also affected by the continual presence of some degree of ionization in the medium due to continuous excitations by high-repetition-rate mode-locked laser pulses. Further measurements are being carried out to more closely identify the responsible mechanism.

Reference:

1. T. Mossberg, A. Flusberg and S. R. Hartmann, Opt. Commun. 25, 121 (1978).
2. D. S. Bethune, Phys. Rev. A 23, 3139 (1981).
3. J.-Y. Zhang, H.-T. Zhou and P. Jin, in Resonance Ionization Spectroscopy, T. B. Lucatorto, J. E. Parks, Eds. (Institute of Physics, Gaithersburg, Maryland, USA, 1988) p.29.
4. C. Mullin, D. Kim, and Y. R. Shen (unpublished); C. Mullin, Ph. D. thesis, University of California at Berkeley (1993).

Dephasing-induced nonlinear vibrational spectroscopy

John T. Fourkas, Hitoshi Kawashima and Keith A. Nelson

Department of Chemistry, Massachusetts Institute of Technology, Cambridge, Massachusetts 02139. (617) 253-1562

Advances in infrared laser technology have made it possible, for the first time, to perform nonlinear optical experiments directly on IR-active molecular vibrational modes.[1] As a result, we are only just beginning to appreciate the profound difference between the nonlinear-optical behavior of electronic states and of vibrational states. Here we present an analysis of IR nonlinear optical experiments that predicts a wealth of new, dephasing-induced signals that provide unique information about the interactions between molecular vibrations and their surroundings. We also make a connection between our predictions and echo phenomena observed in anharmonically-coupled classical oscillators.

It has been predicted that nonlinear-optical signals, such as photon echoes, cannot be generated from a quantum harmonic oscillator that is linearly coupled to a harmonic bath.[2] This phenomenon is a direct consequence of a complete destructive interference between the different quantum-mechanical wave-mixing pathways that contribute to the signal. Similar interferences are well known in nonlinear-optical experiments invloving electronic transitions; however, such interferences can be broken by pure dephasing, leading to so-called extra resonances.[3] This suggests that dephasing processes must be taken into account carefully in the analysis of purely vibrational nonlinear optical experiments.

A detailed analysis of a quantum oscillator coupled to a heat bath reveals that both lifetimes and pure-dephasing rates are highly dependent on vibrational quantum number. For a harmonic oscillator, the relative population relaxation rates from various quantum states and the relative pure-dephasing rate of coherences between various quantum levels can be calculated directly. As a consequence of these quantum-number-dependent dephasing

processes, the abovementioned quantum interference is readily broken, creating dephasing-induced vibrational nonlinear-optical signals.

We consider three different third-order nonlinear spectroscopies performed on harmonic oscillators. Two are in the time domain, photon echoes (PE) [1] and transient gratings (TG),[4] and one is in the frequency domain, nearly-degenerate four-wave mixing (NDFWM).[5] In each case, a quantum interference arises from Liouville-space pathways involving excited-state/excited-state absorption at the third interaction, and we find new dephasing-induced phenomena.

In a PE, the signal is produced some delay time after the third interaction. During this time, different mixing pathways involve coherences between different vibrational quantum levels. It is only when these coherences dephase at the same rate that the quantum interference is complete. However, as noted above, both population-relaxation and pure-dephasing rates are dependent on the quantum number. At zero delay between pulses, there is no time for dephasing to occur, and the interference is expected to be complete. However, as the delay time is scanned, the signal builds in with the faster of the two vibrational dephasing time and decays with the slower, revealing extra information about the vibrational dephasing process.

In the TG, the delay time is between the second and third interactions, and the signal comes out beginning immediately after the third interaction. The sample is able to radiate the signal for a time on the order of the vibrational dephasing time T_2. The diffracted signal following an infinitesimally short probe pulse is initially zero, builds in as the different vibrational dephasing rates destroy the quantum interference, and decays with the slower T_2 of the 0-1 vibrational coherence.

In NDFWM one again expects to see no signal unless there exists quantum-number-dependent dephasing. Both the strength and shape of the signal will be dependent on the relative dephasing rates, again yielding extra information about the nature of the dephasing processes.

Finally, we point out interesting parallels between the IR echo and echo phenomena that occur in classical anharmonic oscillators.[6] This class of echoes has been observed in acoustic waves in piezoelectric powders[7], as well as in a cold plasma in a cyclotron[8]. It is thus instructive to consider a classical description of the IR experiment, in which the echo arises from anharmonicity either in the vibration or in its coupling to other intramolecular or

intermolecular modes. Several important features of the classical echo are derived in Ref. [7]: (1) fourth-order anharmonicity is the lowest-order source of the echo; (2) multiple echoes occur; and (3) the echo intesity is null at zero delay time and builds to a maximum at a later delay time, before decaying away. We examine the behavior of a classical system of two coupled modes of the same frequency, where only one mode is IR active. The coupling between the modes is cubic in the active coordinate and linear in the dark coordinate. A perturbative treatment of this system predicts that echo behavior will occur. The phase memory of the active mode is stored in the dark mode until recalled by the "read pulse". Thus, intramolecular vibrational scattering can be the source of the anharmonicity that causes the dephasing-induced echo. IR echoes are therefore a sensitive probe of anharmonic coupling between intramolecular modes, as well as of the intermolecular interactions noted above.

References

[1] D. Zimdars, A. Tokmakoff, S. Chen, S. R. Greenfield, M. D. Fayer, T. I. Smith, and H. A. Schwettman, Phys. Rev. Lett. **70**, 2718 (1993).

[2] Y. Tanimura and S. Mukamel, J. Chem. Phys. **99**, 9496 (1993).

[3] L. Rothberg, Progress in Optics **24**, 39 (1987).

[4] H. J. Eichler, P. Günter, and D. W. Pohl, *Laser-Induced Dynamic Gratings* (Springer-Verlag, Berlin, 1986).

[5] A. R. Bogdan, M. W. Downer, and N. Bloembergen, Opt. Lett. **6**, 348 (1981).

[6] R. W. Gould, Phys. Lett. **19**, 477 (1965).

[7] K. Fossheim, K. Kajimura, T. G. Kazyaka, R. L. Melcher, and N. S. Shiren, Phys. Rev. **B17**, 964 (1978); K. Kajimura in *Physical Acoustics*, v. 16 (Academic, New York, 1982), W. P. Mason and R. N. Thurston, eds., and references therein.

[8] R. M. Hill and D. E. Kaplan, Phys. Rev. Lett. **14**, 1062 (1965).

Nonlinear Contributions in Intracavity Dispersion Measurements

W. H. Knox

AT&T Bell Laboratories Holmdel, NJ 07733

(908) 949-0958 ; (908) 949-2473 (fax) 8fs@spin.att.com

Current state-of-the-art Ti:Sapphire laser systems operate in a dispersion-limited regime at around 10 fs pulsewidth [1]. This remarkable progress has been made as a result of intracavity dispersion optimization, as initial results in self-focusing modelocking produced pulses of ~90 fs duration [2]. The recently developed technique of Frequency-Domain Dispersion (FDD) can provide measurements of the complete intracavity group delay under operating conditions [3]. Since dispersion is a linear optical property, one might wonder whether it is meaningful to measure the dispersion inside a nonlinear system while it is operating. In this paper, we discuss the magnitude and origin of nonlinear corrections to the measured intracavity group delay in FDD measurements. We also raise the general questions - (a) *since a modelocked laser is a nonlinear optical system, is it correct to measure its dispersion when it's lasing ?* ; and (b) *since a modelocked laser is a nonlinear system, is it correct to measure the dispersion when it's not lasing ?*
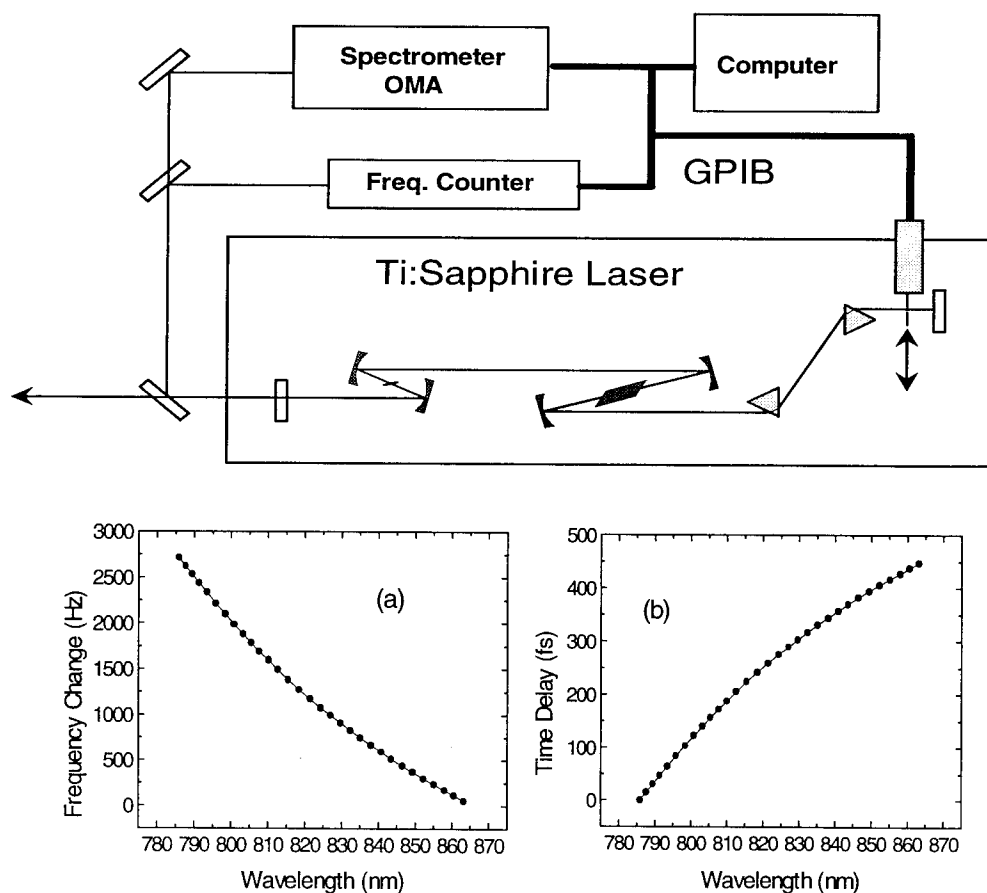
Figure 1. Measurement system for Frequency-Domain Dispersion measurements. A modelocked laser is tuned and its repetition rate is measured at each operating wavelength: (a) frequency change and (b) corresponding group delay change for laser containing SF-10 prisms.

Figure 1 shows the method of FDD [3] applied to measurement of dispersion in a modelocked Ti:Sapphire laser. The laser is tuned and its repetition rate is counted with a digital frequency counter at each wavelength. Figure 1 also shows typical data for cavity repetition rate (a) and the conversion to group delay variation (b). The group delay typically varies by a few hundred femtoseconds as the laser is tuned over a 70 nm bandwidth. This method yields a complete characterization of the group delay. This function can be fitted and integrated to yield the frequency dependence of the phase $\Phi(\omega)$.
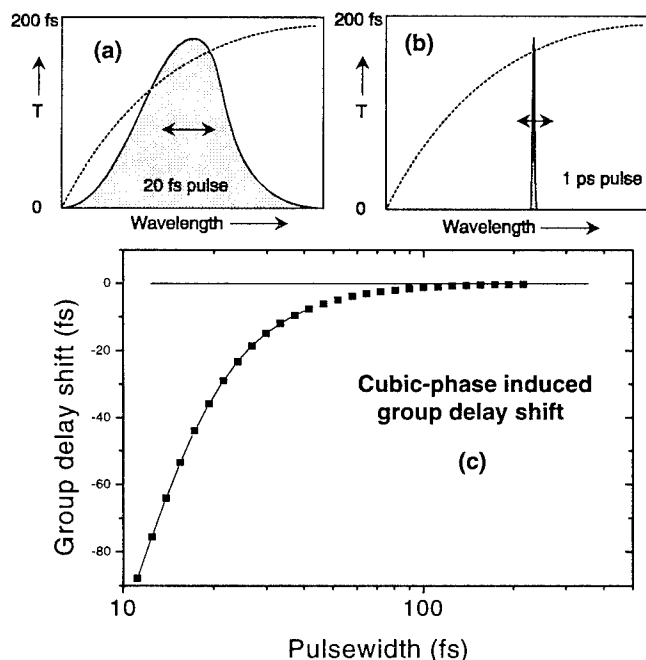
Figure 2. (a) A 20 fs pulse chooses a mean group delay that is averaged over its very large bandwidth. (b) a 1 ps pulse propagates with a group delay that is very close to the group delay at the center wavelength. (c) The net effect is that if the pulsewidth varies as a result of nonlinearity in the cavity as the laser is tuned, a time error is introduced.

There are several possible nonlinear contributions to these signals. First, the nonlinear index of refraction that is responsible for bulk self-focusing itself makes the cavity length intensity-dependent. For a nonlinear phase of π radians which is typical for Ti:Sapphire lasers, the group delay would be increased by one optical period, or 3 fs maximum. Secondly, if there is a cubic phase term in the cavity then the mean group delay becomes dependent on the pulse bandwidth - which is intensity-dependent through the nonlinearity of the modelocking mechanism. This is illustrated in Figure 2. Figure 2a shows that a broad band (20 fs) pulse exhibits a mean group delay that is averaged over the cavity group delay curve, however for a longer pulse, the group delay is almost exactly equal to the group delay at the center frequency (Figure 2b). Figure 2c shows the shift of the mean group delay as a function of pulsewidth for a cavity containing SF10 prisms. Thus, if the pulsewidth is kept longer than 100 fs or so, this error group delay shift is less than a few femtoseconds. Both the explicit nonlinearity and this cubic phase effect therefore do not affect the dispersion parameter $D = \partial T / \partial \lambda$ unless the pulsewidth/bandwidth widely varies during a dispersion scan. Figure 3 summarizes this situation. We note that the filtering action that is required to obtain long pulses can introduce dispersion as well.

As a check on the role of nonlinearities in FDD measurements, we insert some adjustable loss into the cavity and monitor the repetition rate. Figure 4 shows that as the intracavity power is reduced by introducing some adjustable loss, the cavity repetition rate is not measurably shifted. In principle further nonlinearity could be observed in the explicit dependence of the dispersion parameter on the intensity. This is equivalent to the 'shock' term in nonlinear pulse

propagation in fibers. This confirms that for Ti:Sapphire lasers - these nonlinearities contribute less than a few femtoseconds correction to the group delay [4].
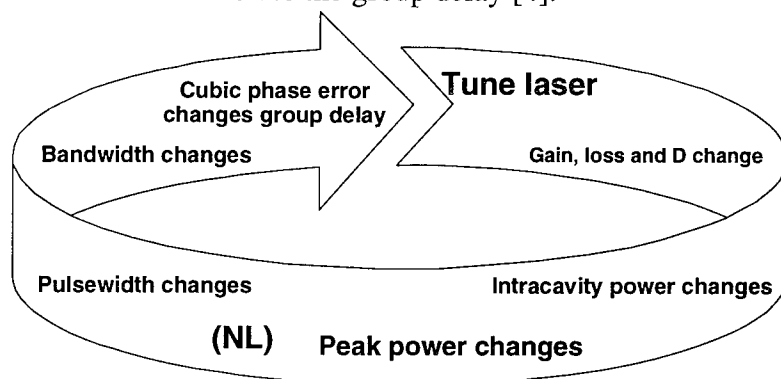
Figure 3. Summary of role of nonlinearity coupled with cubic phase term in producing possible errors in intracavity dispersion measurements. These errors can be minimized by using long pulses for FDD measurements.

Recently, a new technique for measuring intracavity dispersion has been introduced [5]. In this approach, the laser is maintained below threshold and the amplified spontaneous emission (ASE) is cross-correlated with itself after propagating through the cavity one round trip. The result is a complete measurement of the intracavity dispersion in a regime in which the laser is not lasing. In contrast to FDD, this technique only works when the laser is not lasing, since it requires a broadband ASE to obtain the group delay resolution. When applied to laser diodes, some dependence of the group delay with injection current was noted [5]. In such a case, it is likely that the intracavity dispersion will be different when the laser is above threshold. In semiconductors lasers, the carrier distribution changes strongly with injection current, thus changing the index of refraction of the waveguide, and the intracavity dispersion. Then, what is the correct cavity dispersion to describe the operation of the laser above threshold, and what is the best way to measure it ? Also, what goes into the theory ?
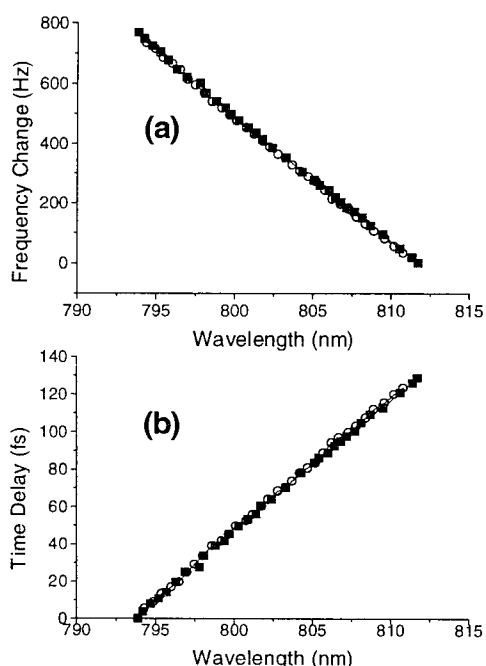
Figure 4. Effect of introducing intracavity loss and lengthening pulsewidth on (a) cavity repetition rate and (b) equivalent change in group delay. No change is detected.

[1] M.T. Asaki, C.P. Huang, D. Garvey, J. Zhou, H.C. Kapteyn and M. M. Murnane, Opt. Lett. 18, 977 (1993) ; Ch. Spielmann, P. F. Curley, T. Brabec, E. Wintner and F. Krausz, Electron. Lett. 28, 1532 (1992); B. Proctor and F. Wise, Appl. Phys. Lett. 62, 470 (1992).
[2] D. E. Spence, P. N. Kean and W. Sibbett, Opt. Lett. 16, 42 (1991).
[3] W. H. Knox, Opt. Lett. 17, 514 (1992).
[4] W. H. Knox and J. P. Gordon, JOSA B10, 2071 (1993).
[5] K. Naganuma, Appl. Phys. Lett. 64, 261 (1993).

Recent Developments in the Measurement of the Intensity and Phase of Ultrashort Pulses Using Frequency-Resolved Optical Gating

K. W. DeLong, David N. Fittinghoff, and Rick Trebino
Sandia National Laboratories, Livermore, CA 94551

James Hunter and William E. White
Lawrence Livermore National Laboratories, Livermore, CA 94550

Daniel J. Kane
Southwest Sciences, Inc., Santa Fe, NM 87501

Recently, we developed a simple and general technique, which we call Frequency-Resolved Optical Gating (FROG), that succeeds in measuring the full intensity and phase evolution of an individual, arbitrary ultrashort pulse.[1-3] In brief, FROG involves measuring the pulse spectrogram, i.e., the spectrum of the signal pulse in an auto- or cross-correlation using any instantaneous nonlinearity, yielding signal intensity vs. delay and frequency. This trace can then be shown to fully and uniquely characterize the pulse—the pulse extraction problem is equivalent to two-dimensional phase retrieval, a solved problem from image science.

In previous work, we have demonstrated FROG on a single-shot basis in the visible and ultraviolet using a polarization-gate (PG) beam geometry, where a newly improved version of our phase-retrieval algorithm operates reliably and quickly and without ambiguity, even in the presence of significant amounts of noise.[4] In this work with lower-intensity pulses, however, we utilize (multi-shot) self-diffraction (SD) and second-harmonic-generation (SHG) FROG arrangements, for which all previously published algorithms[3,5] are unreliable. As a result, we have made significant improvements to these algorithms for these arrangements, including the use of least-squares optimization, generalized projections, Weiner-filtering, and a variety of other techniques. We report significantly improved performance, especially for SHG FROG.

We have also performed an in-depth study, using SHG FROG, of the operation of a Kerr-lens-mode-locked Ti:Sapphire oscillator. We have fully characterized the output train of ~100-fsec, ~2.5-nJ pulses for a wide range of operating parameters, obtaining the pulse intensity and phase evolutions as a function of the lasing wavelength and the amount of glass in the cavity. For most stable operating modes, we typically find little higher-order phase distortion. For operation with much glass, we find almost pure cubic chirp. When some linear chirp is present, we typically also find that chirp of the opposite sign occurs in the wings of the pulse.

Figure 1 shows a typical SHG FROG trace for the pulse train from the Ti:Sapphire laser oscillator. Recall that, using SHG FROG, the trace is necessarily symmetrical in delay and, as a result, has ambiguity in the direction of time. Thus, unlike PG FROG, which directly yields a frequency-vs.-time plot of the pulse, SHG FROG traces require running the algorithm in order to obtain usable information regarding the pulse. Fortunately, the SHG FROG algorithm is fairly robust (although not as robust as our PG FROG algorithm), and the intensity and phase derived for the above FROG trace are shown in Fig. 2. Figure 3 shows a careful comparison of the derived pulse fields with independently taken pulse autocorrelations and spectra, indicating excellent agreement between autocorrelations and spectra calculated for the derived pulses and these experimental measurements. Note that the intensity is smooth and that a small amount of residual quadratic phase (linear

chirp) is present, although it is not possible to determine whether it is positive or negative due to the time-direction ambiguity. Note also that, in the wings of the pulse, the sign of chirp has the opposite sign. This is a common feature of these Ti:Sapphire laser pulses. It is reasonable in view of the self-phase modulation and compression occurring in the laser.

While the laser generally produced pulses similar to that shown above, it was also possible to obtain more complex pulses when much intracavity glass was inserted in the beam. Figure 4 shows a FROG trace with considerable structure. This structure is indicative of spectral cubic chirp. We have recovered this pulse's intensity and phase evolution from its FROG trace (see Fig. 5). It is shows the intensity structure and phase jumps representative of cubic phase vs. frequency.[5] Figure 6 shows the spectrum and phase in the frequency domain, where the cubic phase dependence vs. frequency is more evident.

In conclusion, while FROG has already been shown to be effective for measuring ultrashort pulses of energy greater than about 1 µJ, we believe that, with this work, we are close to achieving with FROG a very simple and general diagnostic for low-energy ultrashort pulses, as well. In addition, our study of the Ti:Sapphire oscillator should shed light on the dynamics of the mode-locking process in this laser.

References

1. D. J. Kane and R. Trebino, IEEE J. Quant. Electron. **29**, 571 (1993).
2. D. J. Kane and R. Trebino, Opt. Lett. **18**, 823 (1993).
3. R. Trebino and D. J. Kane, J. Opt. Soc. Amer. A **10**, 1101 (1993).
4. K. DeLong and R. Trebino, "Improved Ultrashort-Pulse Retrieval Algorithm for Frequency-Resolved Optical Gating," J. Opt. Soc. Amer. A *in press* (1994).
5. J. Paye, M. Ramaswamy, J. Fujimoto, E. Ippen, Opt. Lett. **18**, 1946 (1993).
6. K. W. DeLong, R. Trebino, and D. J. Kane, "A Catalog of Frequency-Resolved-Optical-Gating Traces for Common Ultrashort Pulses," J. Opt. Soc. Amer. B, *in press* (1994).
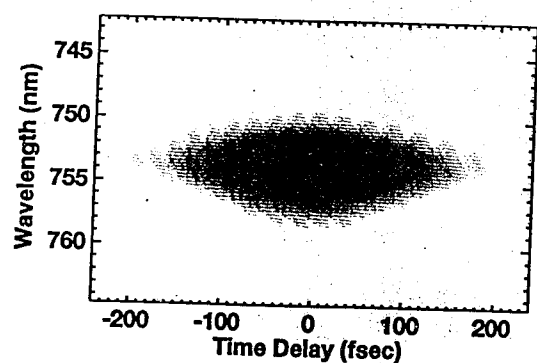
Figure 1. SHG FROG trace for a train of pulses from a Ti:Sapphire laser exhibiting near-transform-limited behavior.
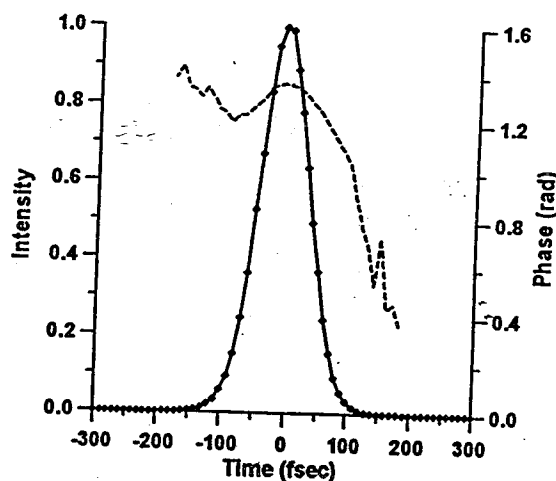
Figure 2. Intensity (solid line) and phase (dashed line) derived for the pulse whose SHG FROG trace is shown in Fig. 1. Note the smooth intensity profile and the small amount of quadratic phase (linear chirp). Note also the opposite sign of chirp in the leading wing of the pulse.
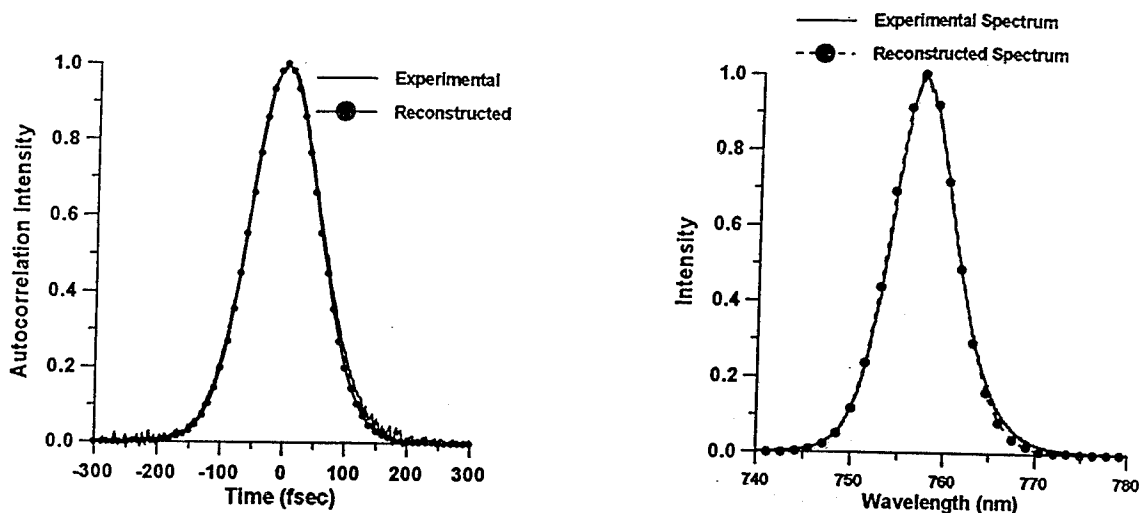
Figure 3. Comparison of the derived and independently measured intensity autocorrelation and spectrum of the pulse in Figs. 1 and 2. Agreement is excellent.
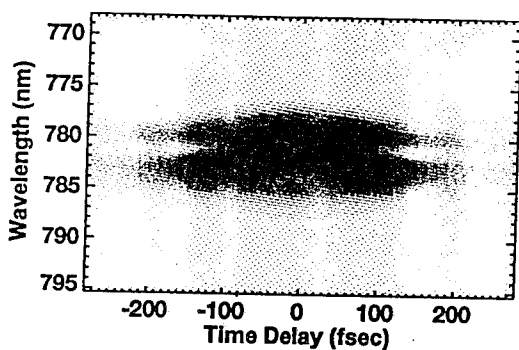
Figure 4. SHG FROG trace for a train of pulses from a Ti:Sapphire laser exhibiting cubic phase vs. frequency. Note the characteristic parabolic group delay vs. frequency (which is symmetrized in this SHG FROG trace due to the time-reversal ambiguity in SHG FROG).
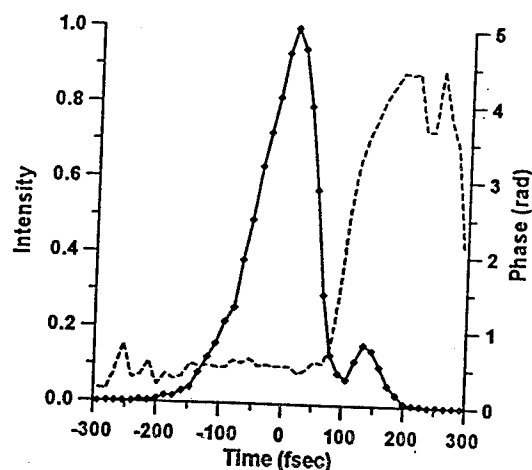
Figure 5. Intensity (solid line) and phase (dashed line) derived for the pulse whose FROG trace is shown in Fig. 4. Note the ~π-phase-shifted satellite pulse, indicative of cubic phase vs. frequency.
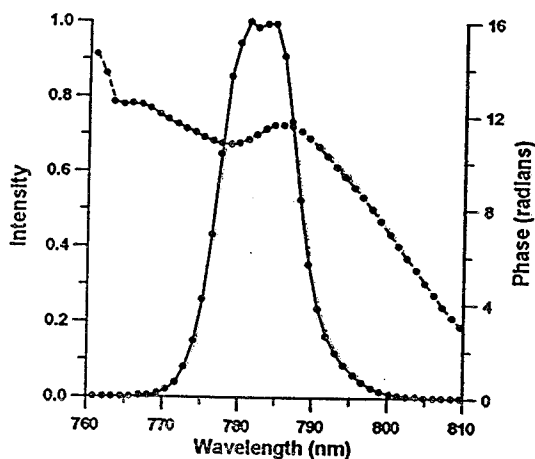
Figure 6. Spectrum (solid line) and phase (dashed line) vs. frequency derived for the pulse whose FROG trace is shown in Fig. 4. Note the smooth intensity and parabolic phase vs. frequency.

Ultrahigh Nonlinear Harmonics in Gases

G. Mainfray, A. L'Huillier, P. Salières, T. Auguste and P. Monot

CEA - SPAM, Bât. 522, C.E. Saclay,
91191 Gif-sur-Yvette cedex, France

The nonlinear interaction of a short laser pulse with neutral gases gives rise to very high-order odd harmonic generation [1]. Coherent radiation wavelengths as short as 7.8 and 7.4 nm have been obtained in Ne, corresponding respectively to the 135th harmonic generated by a Nd-glass laser at 1053 nm [2] and the 109th harmonic generated by a Ti-sapphire laser at 806 nm [3]. The laser intensity used was in the 10^{14}-10^{15} W/cm^2 range depending on the atomic species, the laser wevelength and pulse duration.

The subpicosecond laser pulse is focused into a pulsed gas jet which has an atomic density of about 10^{17} cm^{-3} in the interaction region. The VUV light generated in the nonlinear interaction with the atomic medium is analyzed along the laser axis by using a grating monochromator. The harmonic spectrum has a characteristic universal shape. The yield of the first few harmonics drops rapidly, then it exhibits a plateau where all the harmonics have nearly the same strength. Finally the harmonic spectrum ends with a sharp cut-off. The highest harmonic order produced depends on the highest laser intensity seen by the atom before ionization occurs.

An important insight into the physical understanding of the cut-off has recently been given using a semi-classical approach [4, 5]. In the single-atom response the maximum energy of the emitted harmonic photons is : E_i + 3.2 E_p, where E_i is the atomic ionization energy and E_p the quiver energy of the electron in the laser field. When propagation effects and phase matching are taken into account, the cut-off value is about E_i + 2E_p in good agreement with experimental results [6].

Harmonics in the XUV range are generated with very high spectral brightness because of the ultrafast subpicosecond pulse duration and small transverse dimensions of the XUV beam.

It is also of interest to consider the high-order harmonic spectrum in the time domain. The Fourier transform of a comb of harmonics of similar amplitude, as in the plateau, and extending over 50 eV should give rise to a train of extremely short

duration pulses (10^{-17} - 10^{-16} sec) if all the harmonics have the same phase relationship. If harmonics have non-ideal phases, the subpicosecond envelope will have about 30 attosecond substructures.

Recent compact terawatt laser sources are capable of producing focused intensity of about 10^{18} W/cm^2. At such high intensity the quiver electron velocity becomes relativistic. The nonlinearities in the relativistic quiver motion are expected to generate harmonics of the incident laser field. We present preliminary results on the 3rd, 5th and 7th harmonics produced in a weakly relativistic hydrogen plasma by a 1 psec terawatt laser pulse at 1053 nm.

[1] A. L'HUILLIER, L.A. LOMPRE, G. MAINFRAY and C. MANUS, p. 139 in "Atoms in Intense Laser Fields" ed. M. Gavrila. Academic Press, 1992.

[2] A. L'HUILLIER and Ph. BALCOU, Phys. Rev. Lett., 70, 774 (1993)

[3] J. MACKLIN, J. KMETEC and C. GORDON III, Phys. Rev. Lett., 70, 766 (1993).

[4] J. KRAUSE, K. SCHAFER and K. KULANDER, Phys. Rev. Lett, 68, 3535 (1992).

[5] P. CORKUM, Phys. Rev. Lett., 71, 1994 (1993).

[6] A. L'HUILLIER, M. LEWENSTEIN, P. SALIERES, Ph. BALCOU, M. IVANOV, J. LARSSON and C. WAHLSTROM, Phys. Rev. A, 48, R 3433 (1993).

Effect of Self-diffraction on Erasure Dynamics During Readout at Different Wavelengths and Geometries in Photorefractive Materials

M. Jeganathan, M. C. Bashaw, A. Aharoni and L. Hesselink

Department of Electrical Engineering,

Durand 358, Stanford University, Stanford, CA 94305-4035

Tel : (415) 723-4940; Fax : (415) 725-3377

Certain memory applications based on photorefractive media require the ability to conveniently fix holograms. An attractive alternative is to sufficiently prolong the readout time. Low photo-excitation at long wavelength augmented by self-diffraction can increase readout time by a few orders of magnitude. The interaction of the writing and readout waves, both of the same wavelength, with the photorefractive space charge field has been investigated theoretically [1] and experimentally [2]. Dynamics of beam coupling and self diffraction, in certain geometries, can lead to an initial increase followed by non-exponential decay of the diffracted signal during readout [3]. Here we study how the difference in gain, lifetime, photoexcitation and absorption at *different* wavelengths – which require changing incident angles to satisfy the Bragg condition – affect the decay dynamics of photorefractive gratings.

Initially, gratings are written with two plane waves of intensities I_{g1f} and I_{g2f} at 514.5 nm in a 0.6 x 0.5 x 0.6 mm SBN:60 crystal. The gratings are then read out either at 514.5 nm or 632.8 nm, each in four different geometries as shown in Fig. 1. These experiments have been carried out for several beam ratios, $m = I_{g1f}/I_{g2f}$. Energy transfer from the weak beam to the strong beam results in a grating amplitude that is maximum at $z = 0$ and decreases for increasing z. Readout with the forward propagating 514.5 nm beam in the gain direction leads to an initial increase and then decay of the diffracted signal (Fig. 2). This occurs because the light diffracted from the front of the crystal interferes with the readout beam, writing another photorefractive grating where the original grating is weak. With time, the erasure proceeds from $z = 0$ to $z = d$ with the maximum propagating through the crystal resulting in a prolonged readout. Readout with the counterpropagating I_{g1c} beam leads to a rapid, monotonic but non-exponential, erasure of the grating due to very weak diffraction from the initial interaction. Readout in the loss direction, that is with I_{g1f} or I_{g2c}, leads to new gratings that are π out of phase with the existing grating and therefore an even more rapid decay of the diffracted signal. Qualitatively similar behaviour is observed for readout with the long wavelength (632.8 nm) but quantitatively the behaviour is quite different — both in time-scale and in the details of the dynamics.

The simultaneous numerical solutions [4] to the coupled wave equations and the differential equation for the first harmonic of the space charge field for small modulation approximate the observed behaviour [2]. Figure 3 shows the time dependence of the diffracted signal during readout at 632.8

nm for different configurations. We show fairly good agreement between experiments and theory using parameters determined from experiments and supplemented with those available in the literature [5]. We have neglected the affect of beam fanning in our modeling.

The details of the erasure dynamics depend significantly on the writing beam ratio and the readout geometry. If the pump couples energy to the weak beam, the maximum index amplitude is found at approximately the center of the crystal resulting in non-monotonic erasure in both forward and counter propagating geometries. We propose a simple intuitive and physical interpretation of the above results. These ideas can be used in novel ways to substantially increase the readout time - 3 to 4 orders of magnitude by employing the appropriate readout geometry and wavelength.

References

[1] P. Yeh, *IEEE J. Quant. Elect.*, **25**:484, (1989).

[2] J. M. Heaton and L. Solymar, *IEEE J. Quant. Elect.*, **24**:558, (1988).

[3] L. B. Au and L. Solymar, *Applied Physics B*, **49**:339, (1989).

[4] J. M. Heaton and L. Solymar, *Optica Acta*, **32**:397, (1985).

[5] J. E. Ford, Y. Taketomi, S. H. Lee, D. Bize, R. R. Neurgaonkar, and S. Fainman, SPIE **1148**, page 12 (1989).
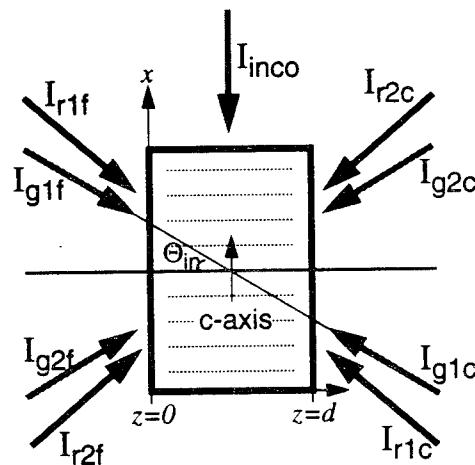
Figure 1 : Various readout geometries used in the experiment. In the subscripts "g" refers to green (514.5 nm), "r" refers to red (632.8 nm), "1" and "2" refer to the two directions, "f" referes to forward and "c" to counter propagating geometry. For incoherent erasure, beam I_{r2f} is used as a probe in the presence of I_{inco}. θ_{in} of approximately 9° leads to a grating period of ~ 0.9 μm.

The Application of Nonlinear Optics in Ocular Biophysics.

Benjamin A. Rockwell, William P. Roach and Mark E. Rogers.
Optical Radiation Division, US Air Force Armstrong Laboratory, AL/OEOP, 8111 18th Street, Brooks Air Force Base, Texas 78235-5215.

Summary of Presentation:

When laser pulses of high peak powers are incident on tissue, nonlinear processes can be observed as the pulses propagate through the tissue. Some of the processes are relatively benign altering only the amplitude and phase of the pulse but leaving the tissue relatively unchanged. Some of the phenomena are much more destructive, leading to irreversible tissue damage. Understanding how such processes occur are important both to laser safety research, where we seek to set exposures that will not damage an individual who inadvertently is exposed to a laser beam, and to medical applications where the surgeon intentionally uses the laser to cause tissue damage for therapeutic effect. It is important to quantitatively correlate the laser parameters such as pulse energy and pulse duration to the amount and type of tissue damage. By better understanding the biophysical process by which high peak power laser pulses cause damage to tissue, the size and location of the damage site can be better controlled as well as the peripheral damage can be limited.

Some applications of nonlinear responses are already used in medicine. Laser-induced breakdown is routinely used to cut fibrous tissue such as the posterior capsule behind the lens of the eye. Ablative processes can be used in the destruction of gall and kidney stones and the removal of plaque inside arteries. Several dermatological techniques such as tattoo removal and removal of possible melanomas use short pulse lasers that generate nonlinear events.

Currently, lasers are commercially obtainable which produce sub-nanosecond laser pulses in the visible and near infrared spectral regions. These wavelengths easily propagate in the eye and can result in retinal damage and functional vision loss if appropriate laser protective measures are not used. Unfortunately, there is no current Air Force or national laser safety standard (ANSI Z136.1-1993) which mandates allowable exposures for pulses shorter than 1 ns in duration. This is due in part to the lack of minimum visible lesion (MVL) data to support standard setting for pulse durations less than one nanosecond. An MVL is defined as the amount of energy necessary to produce a barely perceptible change in the irradiated portion of the retina. The MVL threshold is usually presented as a probability of producing a perceivable change in the retina for 50% of the laser pulses (ED_{50}) and this data forms the basis of the data used to set laser safety standards. According to the increasing sub-nanosecond MVL data base[1,2], one can conclude that extending the current microsecond to nanosecond constant-corneal-fluence-regime ANSI laser safety standard to shorter pulse durations may prove to be imprudent. The present study uses concepts of nonlinear optics to help evaluate ultrashort laser exposures and attempts to understand deviation from the trends in MVL data seen in the femtosecond to microsecond regime.

We first consider how self-focusing can affect the propagation of ultrashort laser pulses in the eye. To assess the effect that nonlinear propagation may have in ocular tissue and therefore on retinal damage, a sensitive and accurate method of determining the nonlinear optical properties in this media is required[3]. As a logical extension of the

z-scan technique, which has been used to determine the nonlinear optical properties for a plethora of optical materials[4,5,6], low n_2 aqueous materials are investigated. We report the nonlinear refractive index (n_2) for rabbit cornea[7], human and rabbit vitreous humor, ultrahigh purity water, and physiological saline using picosecond-visible laser pulses. In the z-scan measurement, self-action effects in the sample as a function of z, the propagation direction, cause the normalized transmittance spectrum recorded to be characterized by either a minimum-maximum or maximum-minimum signature corresponding to positive and negative refractive nonlinearities, respectively. Table I summarizes the measured n_2 values for several relevant ocular and optical materials.

We apply these measured n_2 values to determine the effect self focusing will have on laser pulse propagation in the eye. First note that both the MVL data and the ANSI standard above one nanosecond show two general trends. For exposures longer than 20 μs there is a region where near constant irradiance (W/cm^2) is required for retinal damage. For pulses from 1 ns to 20 μs, diffusion of heat is negligible during the exposure and the fluence (J/cm^2) required for retinal damage is nearly constant. For pulses shorter than one nanosecond, Roach et al.[2] have shown a decrease in the amount of laser fluence necessary to produce laser damage. In this study we calculate the change of spot size and corresponding changes in retinal irradiance due to nonlinear propagation in the eye. We use experimental values for nonlinear refractive indices measured for ocular components with relevant pulse durations[3]. We find that the trend toward decreasing pulse energy incident at the cornea required to produce retinal damage can be explained in part by the effects nonlinear propagation has on the spot size at the retina.

The z-scan measurements were also used to limit the magnitude of the nonlinear absorption coefficient (β). Nonlinear absorption can also be measured using the z-scan[4] technique by removing the aperture before the detector and collecting all of the transmitted light. Using this procedure, no nonlinear absorption was measurable for water, saline or vitreous humor. Using the maximum irradiance used in these absorption measurements and the minimum measurable transmittance change, we can calculate an upper bound on the value for the nonlinear absorption coefficient $\beta < 4 \times 10^{-12}$ cm/W which is consistent with other studies[8]. This value leads us to believe that nonlinear absorption will have at most a slight effect on the irradiance at the retina.

Table I.

	n_2 (esu) [3ps, 580nm]*	n_2 (esu) [60ps, 532nm, Ref 3]
Rabbit Cornea	$(2.5 \pm 0.8) \times 10^{-12}$	
Human Vitreous	$(2.1 \pm 0.8) \times 10^{-13}$	$(1.4 \pm 0.4) \times 10^{-13}$
Rabbit Vitreous	$(4.3 \pm 0.7) \times 10^{-13}$	$(2.7 \pm 0.6) \times 10^{-13}$
Water	$(3.2 \pm 1.7) \times 10^{-13}$	$(1.3 \pm 0.6) \times 10^{-13}$
Saline (0.9%)	$(3.2 \pm 0.9) \times 10^{-13}$	$(1.8 \pm 1.3) \times 10^{-13}$

* tentative data analysis

186

Several other nonlinear phenomena have possible effects on laser retinal damage studies. We have measured the laser induced breakdown thresholds for visible ultrashort laser pulses from several nanoseconds to one hundred femtoseconds. We find that the threshold for this phenomena is above the MVL threshold and therefore does not affect those damage studies, but LIB probably does play a role in suprathreshold damage (e.g. hemorrhagic lesions). We also consider group velocity dispersion, continuum generation and other critical nonlinear phenomena and their possible effects on retinal laser damage.

We conclude that the application of nonlinear optics in biophysics was essential to fully understand trends seen in laser retinal injury for ultrashort laser pulses. Work is continuing to determine the full extent to which the various phenomena studied affect laser retinal damage and the interplay between nonlinear optical effects and other changes in damage mechanisms.

REFERENCES

1   R. Birngruber, C. A. Puliafito, A. Gawande, W. -Z. Lin, R.J. Schoenlein and J. G. Fujimoto, *Femtosecond Laser-Tissue Interactions: Retinal Injury Studies*, IEEE Journal of Quantum Electronics **QE-23**, 1836 (1987).

2   W.P. Roach, C.A. Toth, C.D. Stein, G.D. Noojin, D.J. Stolarski and C.P. Cain, *Minimum visible retinal lesions from pico- and femtosecond laser pulses*, to appear in SPIE Proceedings Vol. **2134**, Laser-Tissue Interaction V, 1994.

3   B.A. Rockwell, W.P. Roach, M.E. Rogers, M.W. Mayo and C.A. Toth, *Nonlinear refraction in vitreous humor*, Opt. Let. **18**, 1792 (1993).

4   Mansoor Sheik-Bahae, Ali A. Said, Tai-Huei Wei, David Hagan and E. W. Van Stryland, *Sensitive Measurement of Optical Nonlinearities Using a Single Beam*, IEEE Journal of Quantum Electronics **QE-26**, 760 (1990).

5   Mansoor Sheik-Bahae, David Crichton Hutchings, David J. Hagan and E. W. Van Stryland, *Dispersion of Bound Electronic Nonlinear Refraction in Solids*, IEEE Journal of Quantum Electronics **QE-27**, 1296 (1991).

6   David Huang, Morrison Ulman, Lucio H. Acioli, Hermann A. Haus and James G. Fujimoto, *Self-focusing-induced saturable loss for laser mode locking*, Opt. Let. **17**, 511 (1992).

7   The animals involved in this study were procured, maintained and used in accordance with the Animal Welfare Act and the "Guide for the Care and Use of Laboratory Animals" prepared by the Institute of Laboratory Animal Resources- National Research Council. Armstrong Laboratory has been fully accredited by the American Association for Accreditation of Laboratory Animal Care (AAALAC) since 1967.

8   H. Nishioka, M. Ishiguro, T. Kawasumi, K. Ueda and H. Takuma, *Single-shot UV autocorrelator that uses two-photon-induced photoacoustic signal in water*, Opt. Let. **18**, 45 (1993).

A two-tone approach for prolonged readout of multiplexed photorefractive holograms

A. Aharoni, M. C. Bashaw and L. Hesselink

Department of Electrical Engineering,
Stanford University, Stanford, CA 94305

Tel. 415 723-2166   FAX 415 725-3377

Photorefractive materials offer important advantages in many optical holography applications, but the recorded images typically remain sensitive to light and therefore erase on readout. Thermal fixing [1, 2], electrical fixing [2, 3], two-photon absorption during grating formation in the presence of a sensitizing wavelength [2, 4], and system-level image refreshing procedures [2, 5, 6] have been used to sustain the recorded image during replay. We propose and demonstrate a novel two-tone holography approach that overcomes the unfavorable speed and poor diffraction efficiency of the thermal and electrical fixing, the complexity of refresh techniques, and the high intensities required for two-photon absorption methods.

In our two-tone approach, holograms are recorded with short wavelength light, typically in the blue-green spectrum for which the photorefractive material is sensitive, and replayed with longer wavelength light, typically in the red-infrared spectrum, for which the material can be essentially inert. The replay light diffracts off of the recorded gratings, but due to significantly reduced photorefractive sensitivity, it introduces minimal erasure. While this concept is well established for plane waves [7], the high Bragg selectivity severely limits the allowable image field of view in these thick media. We overcome this limitation by using a composite red-replay beam consisting of a set of plane waves, offering a piecewise matching to the stored grating over a wide field. This approach overcomes the severe alignment sensitivity and low efficiency of a spherical replay beam [8], allows faster readout than can be affected with a scanning plane-wave reference [9], and avoids page formatting required in interleaving techniques [10].

Figure 1 shows the experimental arrangement. Green light (514 nm) records the holograms in a cerium doped (0.2 mol %) SBN:60 ($S_{60}B_{40}Nb_2O_6$) crystal. A transmission mask encodes a binary data page on the signal beam. A CCD camera and a second Fourier lens detect the replay images.

Replay with plane waves is shown for the green reference beam [Fig. 2(a)] and a red reference beam (633 nm) [Fig. 2(b)]. Scanning is required to access the entire page at the longer wavelength [Fig. 2(c)-(f)]. The red-replay image is confined to a narrow strip whose width is defined by the Bragg selectivity in the plane of reference and signal incidence. The Bragg matching is essentially unaffected by excursions in the perpendicular direction, a property closely related to Bragg degeneracy. Therefore the red-replay strips span the height of the image.

To obtain the full image field we split the red-replay beam into three plane waves that are incident on the crystal at three different replay angles (Fig. 1); this approach is readily extensible to a large number of image components that can conveniently be formed with a beam generator. We use this arrangement to multiplex two images: the photographs of Figures 3(a) and 3(c) show the demultiplexed images as read out by the green recording reference beam, while Figs. 3(b)
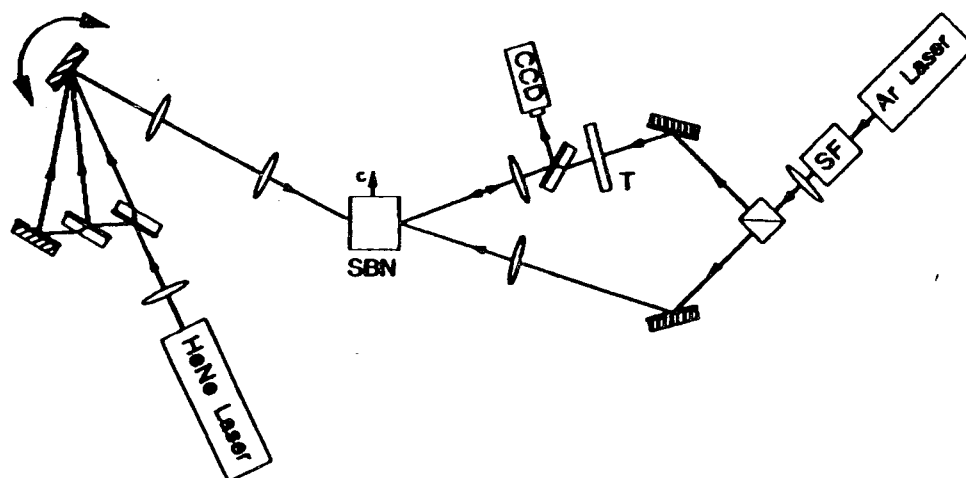
Figure 1: Arrangement for two-tone parallel replay with three Bragg-matched components. The small angular separation between the components is exaggerated for clarity.

and 3(d) show the same images as demultiplexed by a composite red-replay beam. The diffraction efficiencies are on the order of up to 3% and 10% for red and green replay, respectively. For the same intensities, the characteristic erasure times at 633 nm are up to 50 times longer than at 514 nm.

Replay time can be increased further by developing photorefractive materials with lower sensitivities at the replay wavelength. The ability to prolong multiplexed holograms without image field loss by readout at a different wavelength makes ths approach an important optical data processing tool.

References

[1] J.J. Amodei and D.L. Staebler. *Appl. Phys. Lett.*, **18**:540, (1971).

[2] L. Hesselink and M. C. Bashaw. *Opt. and Quantum Electron.*, **25**:S611–S661, (1993).

[3] F. Micheron, C. Mayeux, and J.C. Trotier. *Appl. Opt.*, **13**:784, (1974).

[4] D. von der Linde, A. M. Glass, and K. F. Rodgers. *J. Appl. Phys.*, **47**:217, (1976).

[5] S. Boj, G. Pauliat, and G. Roosen. *Opt. Lett.*, **17**:438–440, (1992).

[6] Y. Qiao and D. Psaltis. *Opt. Lett.*, **17**:1376–1378, (1992).

[7] R. McRuer, J. P. Wilde, L. Hesselink, and J. Goodman. *Opt. Lett.*, **14**:1174–1176, (1989).

[8] H.-C. Külich. *Appl. Opt.*, **31**:2461, (1992).

[9] E. K. Gulanyan, I. R. Dorosh, V. D. Iskin, A. L. Mikaelyan, and M. A. Maiorchuk. *Sov. J. Quantum. Electron.* **9**, 647-649 (1979).

[10] D. Psaltis, F. H. Mok, and H.-Y. S. Li. *Opt. Lett.*, **19**:210–212, (1994).
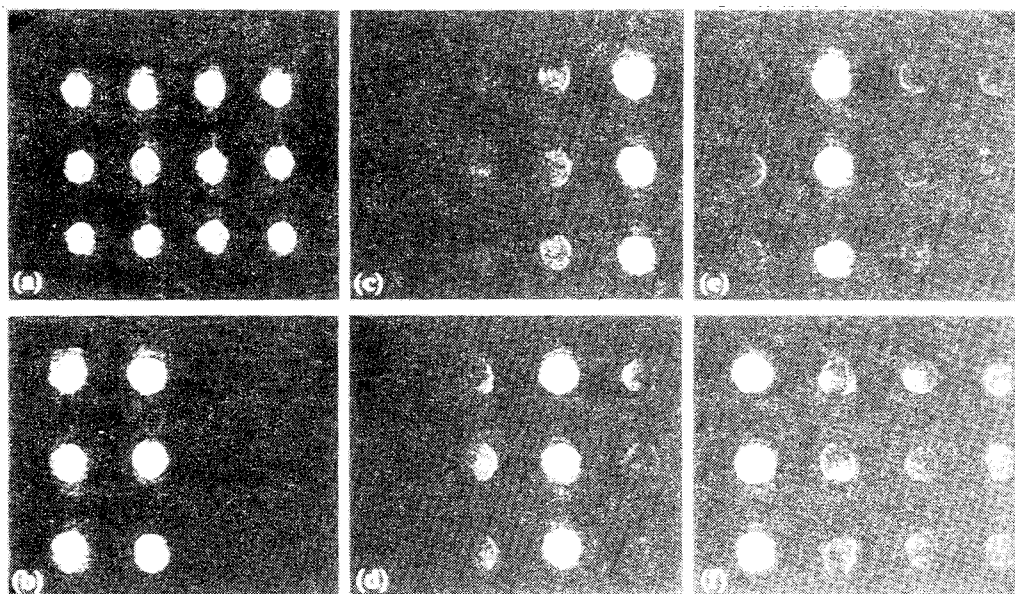
Figure 2: Two-tone replay images, recorded in 514 nm: (a) replay with writing beam at 514 nm; (b) replay with a single 633 nm plane wave; (c)–(f) replay by scanning a single 633 nm plane wave.
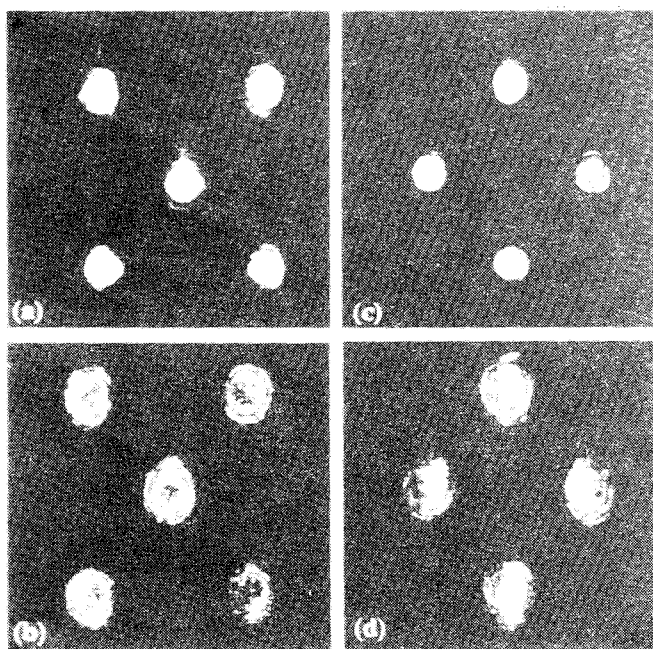
Figure 3: Two-tone parallel readout of two multiplexed images recorded at 514 nm: (a) and (c) green replay; (b) and (d) red replay of corresponding images.

TUP4

Improved second order nonlinear optical polymers by covalent attachment - comparison of four different thermally stable systems

Srinath Kalluri and William H. Steier
Center for Photonic Technology, Department of Electrical Engineering
University of Southern California, Los Angeles, CA 90089-0483

Chengzeng Xu, Bo Wu, Mark W. Becker, Zhixin Yang and Larry R. Dalton
Chemistry Dept., University of Southern California, Los Angeles, CA 90089

Yongqiang Shi and James H. Bechtel
TACAN Corporation, 2330 Faraday Ave., Carlsbad, CA 92008

The practical implementation of polymers into electro-optic and nonlinear optical (NLO) devices requires thermally stable polymers with high optical nonlinearities. The nonlinear moieties (chromophores) can be either doped or covalently incorporated into the different classes of polymer matrices - polyimides, sol-gels, thermosetting, thermoplastic, etc. Although incorporation of covalently attached chromophores along with a means of thermally stabilizing the poling alignment involves difficult synthesis work, its advantages over doping, namely, high chromophore density, reduced phase separation, and improved nonlinearity and thermal stability - make it the route of choice.

We report here on four different approaches to improved long term thermal stability of the poling and the NLO effect. Two crosslinking polymers, one, "side-chain 1" in which the synthesized polymer contains the chromophore as a side chain and is crosslinked during poling to anchor both ends of the chromophore and one, "tri-linked" in which the synthesized chromophore containing prepolymer is crosslinked into a 3D polymer matrix during poling, are discussed. In the second material, the crosslinker also contains the chromophore to increase the chromophore loading. We also report on a polyimide material in which the chromophore is included as a side chain in the polyamic acid precursor polymer and immidization takes place during poling. In the fourth approach, the chromophore is covalently attached to a sol-gel system which is cured during poling.

The "side-chain 1" system: We have incorporated an amino nitro azobenzene chromophore as a sidechain in an MMA-PMMA polymer system [1]. The chromophore was synthesized to be crosslinkable at the free end and links through an iso-cyanate crosslinker to the free crosslinkable ends of other chromophores at elevated temperatures. After corona poling and simultaneous thermal crosslinking near the Tg of the polymer (150°C), the thermal stability and the second harmonic generation d coefficients were measured. We see a 30°C improvement in thermal stability between the crosslinked and uncrosslinked samples (Fig 1). The long term stability of the d coefficient at 100°C was monitored over 250 hours and showed very little decay. A resonance enhanced d_{33} coefficient of 110pm/V was measured at 1.06μm fundamental wavelength and an r_{33} value of 14 pm/V (at $\lambda = 1.3$μm) was extrapolated from the data. We believe that the chromophores anchored at both ends, the high crosslinking density and the high loading density due to covalent incorporation contribute to the enhancement of the stability and nonlinearity.
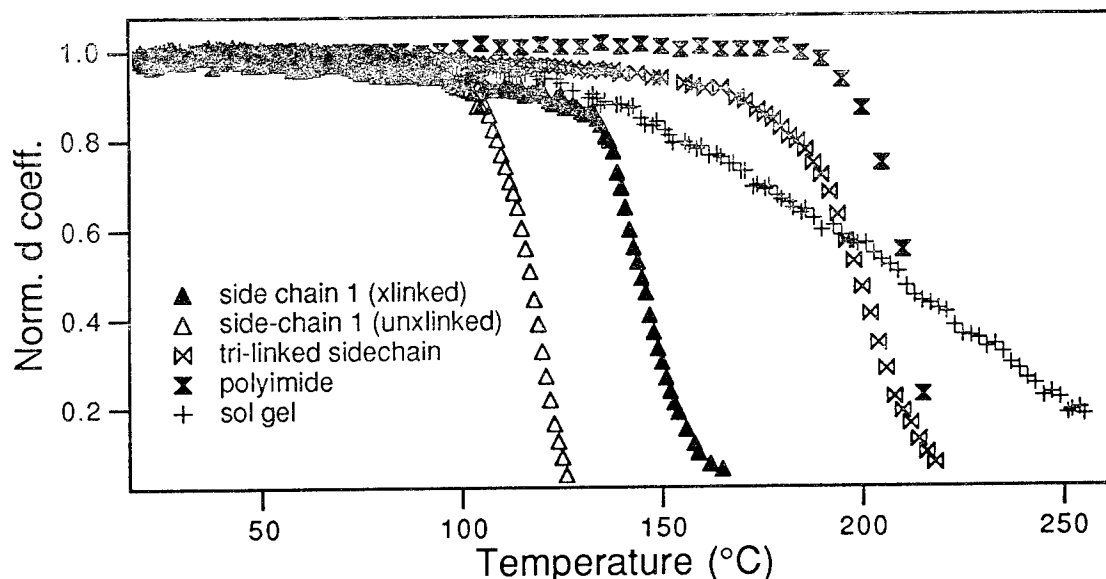
Fig. 1) Stability of the normalized d coefficient when temperature is increased at a rate of 10°C/min.

The "tri-linked" system: We have also explored a novel "tri-linked" polymer system where a trifunctionalized amino-sulfone containing prepolymer crosslinks at high temperatures with a tri-functionalized amino-sulfone crosslinker. The unique feature of this side-chain system is that the polymerization and crosslinking take place in the same thermal heating step and the resultant 3D network has both high crosslinking and high chromophore loading densities. Thermal stability measurements indicate little loss of nonlinearity up to 185°C (Fig 1). The measured d coefficients were moderate. However, with an optimized programming of the temperature and voltage during poling, we expect a significant increase in the NLO effect.

The polyimide system: A disperse red chromophore was covalently incorporated as a sidechain in a polyamic acid precursor polymer [2]. The cured polyimide has a Tg of 205°C. The polymer precursor was corona poled and cured at 220°C - 250°C to complete the imidization. Imidization involves condensation and shrinkage of the polymer network at high temperatures. The resultant collapsed network stabilizes the alignment of the NLO molecules. Thermal stability measurements showed no significant decay of nonlinearity below ~190°C (Fig 1). A r_{33} coefficient of 11pm/V ($\lambda = 1.3\mu m$) was extrapolated from a d_{33} coefficient value of 112pm/V measured at 1.06μm fundamental wavelength. The polyimides show exceptional thermal stability, however the high curing temperatures requires high temperature stability in the chromophores.

The sol-gel system: For this system, we used an amino-sulfone dye, which was functionalized on both ends with nine possible crosslinking sites. After corona poling and thermal curing the NLO moieties which are covalently attached to the gel became part of a rigid network. We measured a d_{33} coefficient of 10-13 pm/V at 1.06μm fundamental wavelength. The measured NLO response is smaller than what is expected from theoretical models for the calculated chromophore loading density of 35%. We attribute this moderate NLO response to increased conductivity at higher temperatures. Stability measurements indicate a slow decrease in nonlinearity starting at around 130°C and up to 60% of the original nonlinearity is retained at 200°C (Fig 1). The polymer also

192

showed long term stability at 100°C over more than 300 hrs. We attribute this dramatic increase in stability over existing sol-gel systems to multiple crosslinking sites which anchor the poled chromophores to a dense matrix. This material system is promising because of the ability to fabricate low loss waveguides. The apparent conductivity problem needs to be addressed however, before significant gains in nonlinearities are achieved.

Each of the various polymer systems has its unique advantages and also presents challeges that need to be addressed. Both the mature systems like the side-chain, main chain, polyimide and novel systems like the sol-gels seem promising for electro-optic applications and we are working on improving the nonlinear properties in many of these polymers, for example by incorporating bigger β chromophores. Table 1 provides a comparison between some of these polymers.

<u>Table 1</u>:　Comparison of NLO properties of the various polymer systems tested in this study

Polymer	λ_{peak}	d_{33} pm/V	Desirable	Problems to solve
side chain 1	472 nm	110	Bigger moieties can be attached by following a generalized synthesis scheme	If corona poling: need precuring to prevent damage
trilinked	~440nm		High crosslinking density High loading density	Compromise between curing time and conductivity
polyimide	460 nm	112	Good thermal, mechanical and chemical stability Excellent optical quality	Required curing T excludes many high β chromophores that degrade at high T
sol-gel	438 nm	10-15	Good thermal, mechanical and chemical stability Good optical quality Possible control of refractive index	Compromise between curing time and conductivity Nonlinearities are small at present

References:

[1]　B. Wu, C. Xu, Y. Ra, L.R. Dalton, S. Kalluri, Y. Shi, W.H. Steier; "Cross-Linkable NLO polymers based on functionalized amino-nitro azobenzene". **Polymer Reprints**, ACS, San Diego, to be published 1994.

[2]　M.W. Becker, L.S. Sapochak, C. Xu, L. R. Dalton, Y. Shi, S. Kalluri, W.H. Steier, A. Jen; "Large and stable NLO effects observed for a polyimide covalently incorporating an NLO chromophore". **Chemistry of Materials**, vol. 6, accepted for publication.

Excited-State $\chi^{(3)}$ Enhancement for a p-Oligophenylene Derivative

L.F. Warren, M.J. Rosker, and H.O. Marcy

Rockwell International Science Center

1049 Camino Dos Rios

Thousand Oaks, CA 91360

805-373-4463

We have reported elsewhere[1] a substantial enhancement in the non-resonant $\chi^{(3)}$ response from a dilute solution of the molecule p-quaterphenyl [(Ph)$_4$] after it has been raised to its first excited singlet electronic state [(Ph)$_4^*$]. Similar behavior was previously observed in diphenylhexatriene by Rodenberger, $et~al.$,[2] although we found that the excited-state $\chi^{(3)}$ signal for (Ph)$_4$ was substantially larger for samples of equal concentration. (Ph)$_4$ displays many desirable characteristics for excited-state NLO applications. These include large absorption at the pump wavelength (~320 nm), separation of the fluorescence and triplet absorption spectral regions from the probe wavelength (~640 nm), and very high photochemical stability.[3-5] (Ph)$_4$ and its higher homologues (Ph)$_n$ suffer, however, in their limited solubilities (e.g., $\leq 5\times10^{-4}$ M for (Ph)$_4$ in dioxane). To achieve a larger figure of merit, $\chi^{(3)}/\alpha$, where α is the absorption constant at the degenerate four-wave mixing (DFWM) wavelength, one must increase this concentration substantially. This follows because, in the unsaturated regime, we expect the $\chi^{(3)}$ enhancement effect to increase with the solution concentration ($[\chi^{(3)}]^* \propto n^* \propto \sigma n_0 I_{pump}$ where n^* is the excited-state population density, n_0 is the ground state density, I_{pump} is the pump intensity, and σ is the cross-section of the ground state at the pump wavelength). We have accomplished this increase in concentration by synthesis of a derivatized form of (Ph)$_4$, diethyl ester of quaterphenylenediacetic acid (QPDA) which is substantially more soluble than the parent molecule. Concentrations greater than 2×10^{-3} M were readily achieved. Here we show that QPDA displays large nonlinearity in its excited-state (QPDA*) similar to (Ph)$_4$. We will also discuss the transient behavior of this nonlinearity as probed by femtosecond time-resolved degenerate four-wave mixing (DFWM); its behavior will be compared to that obtained for the underivatized molecule.

QPDA and it synthesis are shown schematically in Fig. 1. Derivatization at the end positions of the (Ph)$_4$ moiety was chosen as it is less sterically disruptive to the aromatic system (i.e., it avoids twisting of the benzene rings out of the plane) and should therefore leave the electronic structure of (Ph)$_4$ intact. Also the CH$_2$ groups were designed to electronically insulate the aromatic portion of the molecule from the carbonyls (C=O) of the solublizing ester groups. The QPDA samples were made up in a nitrogen glove-bag in anhydrous dioxane (distilled from sodium under N$_2$) at concentrations of 5×10^{-4} M and 2×10^{-3} M. DFWM studies were carried out in the conventional backward counterpropagating pump geometry, with the samples

contained in quartz cells of 50 μm path length, which in essence determined the temporal resolution. The optical source was an amplified, mode-locked dye laser producing approximately 120 fs, 600 mJ pulses at 20 Hz at a wavelength of approximately 640 nm. The pump light was generated by frequency doubling (to ~ 320 nm wavelength) a portion of the amplified light in a 1 mm thick KDP crystal. The remaining amplified light formed the basis of the DFWM experiment.
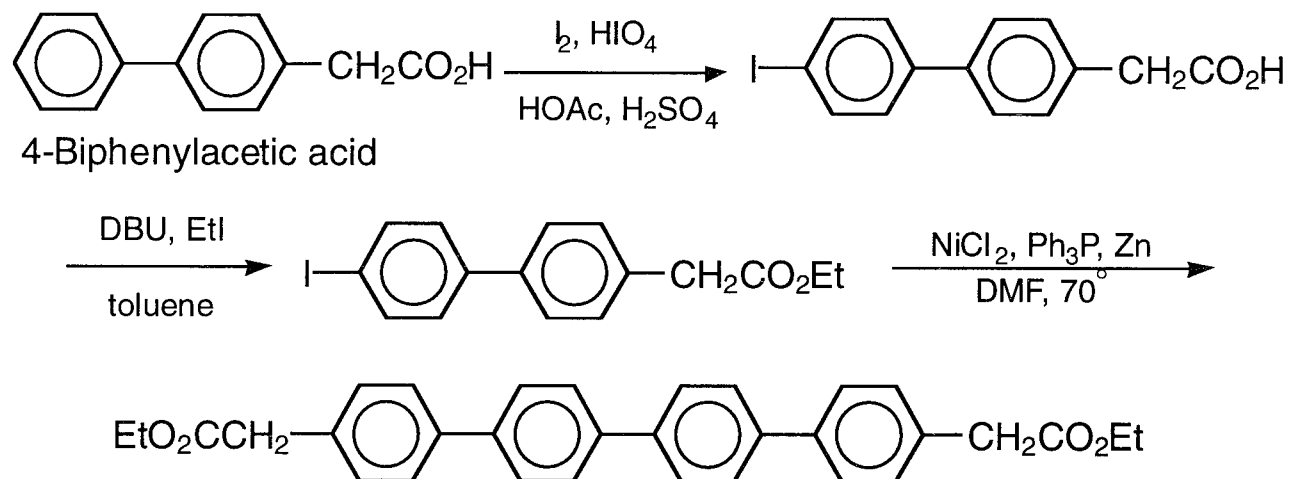
Fig. 1. A schematic representation of the synthesis of diethyl-4,4'''-quaterphenylenediacetate

Figure 2 shows the amount of enhancement of the DFWM signal for QPDA at 640 nm when the pump beam is present relative to the signal obtained for the molecule in the ground state. We observe a factor of over 2000 enhancement for QPDA in dioxane at these concentrations and wavelengths. It is interesting that QPDA has a measurable ground state (i.e., without the pump) DFWM signal; we were unable to detect a signal from the ground state of (Ph)$_4$ larger than that for the dioxane solvent or quartz windows of the cell. Like (Ph)$_4$*, the DFWM signal for QPDA* persists for tens of picoseconds after the grating has been written. For ground-state QPDA, the DFWM signal decays promptly and cannot be resolved in our experiment.

Figure 3 shows the femtosecond time-resolved DFWM response on a longer time scale for both QPDA and (Ph)$_4$ as a function of the relative delay of the readout beam. These results demonstrate (i) that the excited state NLO response is long-lived and (ii) that the response dynamics are similar (but not identical) for QPDA and (Ph)$_4$ in magnitude and in temporal shape. The latter point suggests that this particular derivatization (i.e., QPDA) indeed does not significantly disrupt the electronic structure of (Ph)$_4$. For (Ph)$_4$*, the initial grating decay is non-exponential, but if the first ~20 ps is excluded the decay is fit by an exponential with a time constant of ~ 10 ps. For QPDA*, the initial decay fits well to a time-constant of ~ 20 ps, but after about 30 ps the decay slows dramatically. Another interesting aspect of these data lies in the apparent turn-on time required after the grating is written for the nonlinearity to develop, an effect previously noted for (Ph)$_4$*. The maximum DFWM signal was not achieved until almost

1 ps after the grating was written; such behavior is characteristic of other molecular nonlinearities (e.g., CS_2) and likely indicates that a predominant nonlinear mechanism in the solutions is orientational (i.e., molecular motion) or conformational (i.e., intramolecular motion) in nature. The fact that the turn-on times for (Ph)$_4$ and QPDA are similar argues for a change in conformation (or possibly a solvent-solute interaction) as the responsible mechanism, since any orientational effect would take longer to evolve in the much larger QPDA. Finally, it is interesting to note that initially, the ratio of the DFWM signal from the two QPDA samples is less than the ratio of their concentrations while after ~20 ps the signal ratio is almost exactly four as expected. This aspect of the response dynamics warrants further investigation.
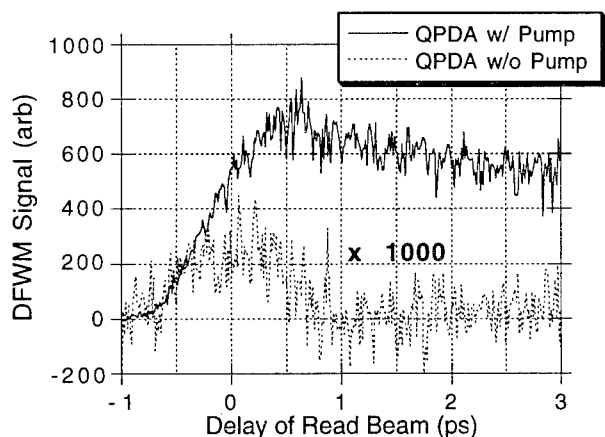
Fig. 2. DFWM signal enhancement and change in response dynamics observed at ~640 nm when QPDA is irradiated at ~320 nm.
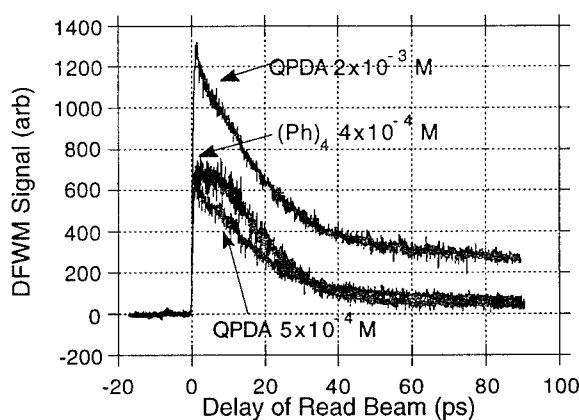
Fig. 3. Comparison of excited-state DFWM signals for (Ph)$_4$ and for QPDA at two different concentrations.

In summary, we have demonstrated that an electronically excited derivative of (Ph)$_4$ displays a large enhancement of its third-order optical nonlinearity like that seen in the parent molecule. These results point us towards the development new materials having even more favorable excited-state nonlinear optical and chemical properties.

References

1. M.J. Rosker, H.O. Marcy, L.F. Warren. *See accompanying summary abstract.*
2. D. C. Rodenberger, J. R. Heflin and A. F. Garito, Nature **359**, 309 (1992).
3. R. S. Taylor and S. Mihailov, Appl. Phys. B **38**, 131 (1985).
4. P. Cassard, R. S. Taylor, P. B. Corkum and A. J. Alcock, Opt. Commun. **38**, 131 (1981).
5. T. G. Pavlopoulos and P. R. Hammond, J. Amer. Chem. Soc. **96**, (1974).

Light-induced Absorption in Photorefractive Strontium-Barium Niobate

Sergei Orlov, Mordechai Segev, Amnon Yariv, and R.R. Neurgaonkar*

California Institute of Technology, 128-95, Pasadena, CA 91125   Tel. (818) 395-4823
*Rockwell International Science Center, 1049 Camino dos Rios, Thousand Oaks, California 91360

Photorefractive (PR) Strontium-Barium Niobate (SBN) has been the subject of extensive research in recent years. Large PR nonlinearities and relatively fast response time at low power levels make this material a preferred candidate for a variety of applications such as optical data storage. Intensity-dependent absorption [1] and related phenomena were discovered and investigated extensively in different PR crystals and at different optical light intensities spanning the range of 1mW/cm^2 to 10^4 W/cm^2. In this study we investigate the light-induced absorption through pump-probe measurement at relatively low optical power densities in photorefractive SBN:60 and SBN:75.

We employ high optical quality 6mm x 6mm x 6mm crystal samples of Cr-doped SBN:60 and Ce-doped SBN:75. In our experimental set-up we use a polarized expanded beam (λ=488 nm) of an argon-ion laser as a pump. The light-induced changes in the absorption coefficient are measured by monitoring the transmitted power of a weak, loosely focused (diameter ~200 μm inside the crystal) probe beam (λ=633 nm) from a low power He-Ne laser. The polarization of both beams is controlled independently by appropriate half-wave plates. Our pump-probe method enables the measurements of both the saturation value of the increase in the absorption and the time response. The incident power of the pump beam is controlled by a variable beam attenuator and is measured with a power meter in the beam path. The pump beam is expanded by a cylindrical lens followed by a spherical lens, which results in a uniform elliptical spot with the area of 0.1cm^2 inside the crystal. The probe beam occupies a much smaller area and is enclosed entirely by the pump inside the crystal. Our measurements are taken in the pulsed regime, i.e. the pump beam is blocked by the mechanical shutter and is switched on only for short periods of time (0.2 to 20 sec). The power of the transmitted probe is monitored and recorded by a storage oscilloscope.

We define the light-induced absorption coefficient α_I in a manner, similar to that of Ref. 1:

$$\frac{I_s(\text{with } I_P \text{ on})}{I_s(\text{with } I_P \text{ off})} = e^{-\alpha_I d} \tag{1}$$

where I_s, I_p are the probe and the pump intensities at the crystal output, respectively, and d is the length of interaction (crystal thickness).

We now perform a series of experiments to measure both the light induced absorption coefficient α_I and its response time τ. First we investigate the absorption of the weak red He-Ne probe induced by the strong green pump in a SBN:60:Cr crystal sample for the different polarizations of both the pump and the probe beams. The steady state values of α_I are shown on Fig.1. The light-induced absorption coefficient saturates at high pump intensities and appears to be fairly insensitive to the polarization of the pump (488 nm) beam. The dependence of α_I on the probe beam polarization is much more dramatic. The data in Fig.1 suggests that for a given pump intensity and polarization: $\alpha_I(\text{extra})/\alpha_I(\text{ord}) = 1.95\pm0.10$. If we assume that these traps are primarily structural defects (e.g., vacancies) rather then impurities and that mutual interaction between them is negligible, the traps and the associated wavefunctions may possess a crystal imparted symmetry, leading to strong polarization effects. Intuitively, one may view the shallow traps as isolated (localized) potential wells with their associated wavefunctions localized differently along the a- and c- axes. This may result in a larger dipole moment (and, consequently, a larger photoionization cross-section) for the light polarized along the c-axis. This explanation, if correct, may also provide useful information about the actual atoms whose absence leads to the shallow traps.

Next, we investigate the build-up rate of the induced absorption, and define it as the inverse of the time required for the signal to reach the (1-1/e) level of its saturation value. Our results are presented in Fig.2. The build-up rate curves are significantly nonlinear with respect to the pump intensity with a pronounced saturation at high pump intensities. For a given polarization of the probe, we observe a shorter response time for the extraordinary polarization of the pump due to the higher absorption of the extraordinary light ($\alpha_{\parallel}$ = 2.0 cm^{-1} at λ= 488 nm) than of the ordinary one ($\alpha_{\perp}$ = 1.5 cm^{-1} at λ= 488 nm). A linear extrapolation to I(pump)=0 at the low intensity branch of the curves gives an estimate of the effective dark decay rate of the population of the shallow traps (due to the thermal ionization) which equals to 30 $\pm$ 5 sec^{-1}. This value is very close to the corresponding data obtained in the BaTiO$_3$ crystals [1]. However, even at moderate intensities (>5 W/cm^2) the response time is about 1.5 to 2 msec, which is significantly shorter than both the PR and the thermal response times for SBN crystals. This enables the very fast recording of photochromic gratings by the light-induced absorption.

We use the same experimental set-up to investigate the induced absorption effect in a PR Ce-doped SBN:75 sample. Because of a very strong PR coupling for an extraordinary light in this material, the light-induced absorption measurements are performed only with the ordinary polarization of the probe beam. Our experimental data, which are shown on Fig. 3 indicate that even low pump intensities (< 5 W/cm^2) induce a large increase in the absorption at the probe wavelength. The linear absorption of the crystal at the pump wavelength (λ = 488 nm) is nearly equal for the extraordinary ($\alpha_{\parallel}$ = 4.7 cm^{-1}) and the ordinary ($\alpha_{\perp}$ = 4.8 cm^{-1}) polarizations. The pump intensity at which the light induced absorption coefficient exhibits saturation appears to be much smaller for the SBN:75. This may explain the intensity dependent diffraction efficiency and intensity dependent wave-coupling observed [2] in some SBN:75 PR crystals. It should be noted that the dark decay (shown in Fig. 4) and the build-up of the light-induced absorption at low light intensities (below saturation) both exhibit a non-exponential temporal behavior. This phenomenon is attributed to the fact that the shallow traps may occupy a broad band rather than a narrow level in the forbidden gap of the crystal. This, in turn, implies that the effective relaxation time depends on the initial distribution of the occupied shallow traps and the decay toward equilibrium obeys a logarithmic, rather than exponential, law within a certain time window [3]. Our direct observations of the dark decay indicate that the relaxation time for the light-induced absorption in SBN:75 may be as long as 3.0 to 5.0 seconds. This clearly indicates that in this material the secondary traps are relatively deep. On the other hand, even at the moderate pump intensities, the build-up of the absorption is very fast and is shorter than 5 msec for pump intensities near 10 W/cm^2.

Finally, we obtain a lower estimate for the density of the shallow levels in the crystal studied using the absorption cross-section s$_{sh}$ evaluated for BaTiO$_3$ [1] s$_{sh}$= 5x10^{-18}cm^2. The lower limit for the density of the secondary traps N$_{sh}$ is given, therefore, by α_I(max)/s$_{sh}$=N$_{sh}$=5x10^{16}-10^{17}cm^{-3}. The actual value may be at least 2-5 times higher, since the approximate formula we use assumes that all the traps are occupied.

In conclusion, we have presented experimental evidence for light-induced, intensity dependent absorption in photorefractive SBN:60 and SBN:75. Large changes in the crystal absorption can be induced even at moderate CW light intensities in the visible range. This fact has a significant impact on applications such as optical data storage where SBN is a potential candidate. Finally, we have found a non-exponential thermal decay of the light induced absorption effect, which suggests that the shallow traps occupy a broad band in the forbidden gap of the SBN:75 crystal.

[1] G.A. Brost, R.A. Motes, and J.R. Rotge, J. Opt. Soc. Am. B 5, 1879 (1988).

[2] J.B. Thaxter and M. Kestigian, Appl. Opt. 13, 913 (1974).

[3] R. Street and J.C. Wooley, Proc. Phys. Soc. A 62, 562 (1949).
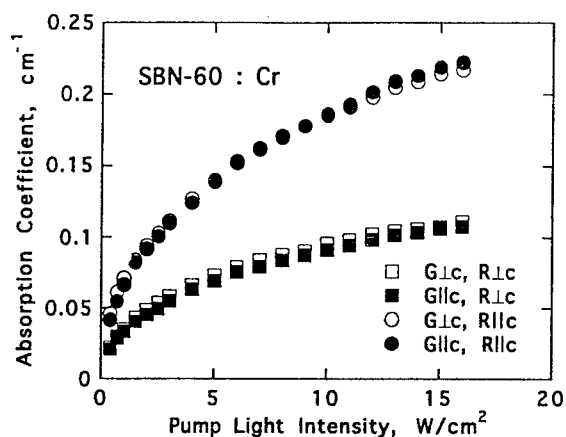
Fig. 1 Light induced absorption at λ=633 nm vs the intensity of the pump (λ=488 nm) in SBN:60:Cr. R (Red) and G (Green) denote the polarization of the probe and the pump respectively. The linear absorption of the red light (λ=633 nm) is $\alpha_{\parallel}$ = 0.4 cm^{-1} for the extraordinary and $\alpha_{\perp}$ = 0.7 cm^{-1} for the ordinary polarization.
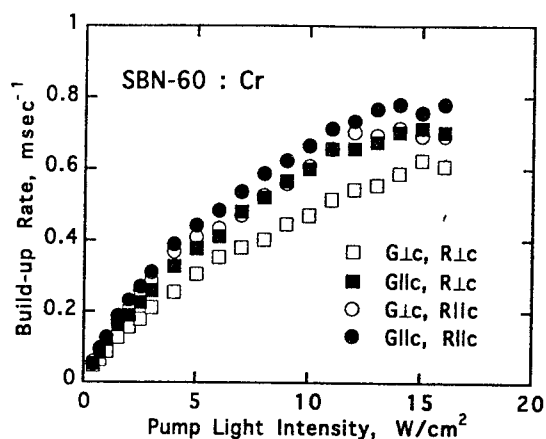
Fig. 2 Build-up rate of the induced absorption at λ=633 nm vs the intensity of the pump beam (λ=488 nm) in SBN:60:Cr. R (Red) and G (Green) denote the polarization of the probe and the pump respectively.
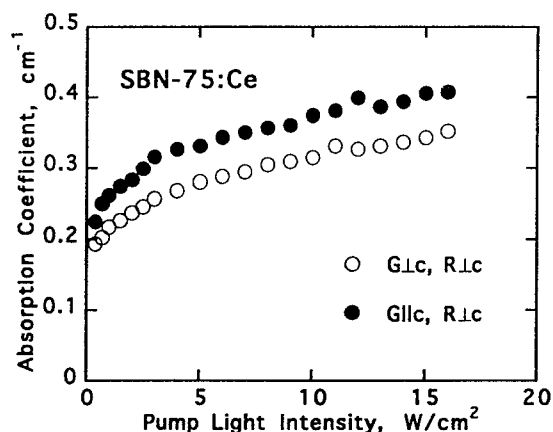
Fig. 3 Light-induced absorption coefficient at λ=633 nm vs the intensity of the pump beam (λ=488 nm) in SBN:75:Ce. G (Green) denotes the polarization of the pump. The probe beam has an ordinary polarization in both cases; the linear absorption coefficient is equal to 0.6 cm^{-1}.
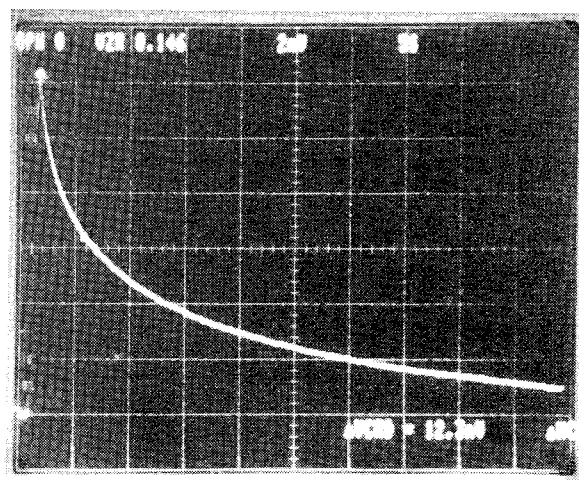
Fig. 4 Nonexponential dark decay of the induced absorption in SBN:75:Ce, after an initial 200 msec pump light pulse. The peak change in the optical absorption at λ = 633 nm is about 0.15 cm^{-1}. The horizontal scale is 5 sec/div.

Thermal Enhancement of Diffraction Efficiency in Cerium Doped Strontium Barium Niobate

Shogo Yagi, Yasuyuki Sugiyama and Iwao Hatakeyama

NTT Interdisciplinary Research Laboratories, Tokai, Ibaraki, 319-11 Japan
Tel: +81-292-87-7565, Fax: +81-292-87-7853

Although Kukhtarev's band transport model[1] well describes almost all behavior related to the photorefractive effect, other origins for this effect, such as ZEFPR[2] and polarization gratings[3], have been reported in recent years. Here, we report an origin which is possibly polarization related, and describe diffraction efficiency enhancement by thermal treatment.

The SBN:Ce (cerium doped strontium barium niobate) was grown using the Czochralski method and was polished to optical quality. To pole the crystal, gold was deposited on its c-surfaces and then an electric field of 500kV/m was applied along the c-axis at 95°C. The crystal was then slowly cooled to room temperature in 30min., and finally the electric field was removed.

All the two wave mixing (TWM) experiments were performed in an acrylic box to avoid any air flow that might cause a fringe pattern fluctuation. The 514.5nm line of an Ar ion laser was used and the intensity ratio of reference/object beams was 1.56. Both beams were horizontally polarized to the c-axis and were oriented so that the grating wave vector was parallel to the c-axis. The grating period was 2.34μm. The object beam was set in the energy gaining direction during TWM. The temperature was controlled to an accuracy of 0.1°C with a Peltier cooler positioned below the crystal.

Figure 1 shows the development of the diffraction efficiency while the crystal was being cooled. The index grating was recorded by continuous exposure at 60°C until the diffraction efficiency saturated. The reference beam for readout was exposed for only 10ms so that the beam would not affect the index grating while reading. Although the diffraction must have suffered a Bragg mismatch when the crystal was cooled since the c-axis expands as shown in Fig. 2, its growth was more than mere compensation for the Bragg mismatch. Also, when the recording was performed at room temperature, the saturated diffraction efficiency was 3.6%, which is lower than that recorded at higher temperature. The solid circles in Fig.1 show the estimated Bragg matched diffraction efficiency using the measured thermal expansion. Here, the phase mismatch was assumed to be $\pi/2$ and the beam coupling during TWM was taken into account[4,5].

Figure 3 shows the temperature dependence of the electro-optic coefficient and the figure of merit. Although it is shown that the $n^3 r_c / \varepsilon$ slightly increases as the crystal is cooled, the increase is not sufficient to explain the enhancement or the weaker diffraction recorded at low temperature. Moreover, we observed no decay in the diffraction efficiency, either for 3 hours at 60°C or for 3 days at 25°C. It had been expected that dark conductivity would cause decay since relatively high dark

conductivity of around 10^{-10} $\Omega^{-1}cm^{-1}$ had been previously reported[6]. Figure 4 shows the decay time (τ) of the diffraction efficiency by light exposure, where τ was proportional to the dielectric constant and was not affected by the thermal excitation term, $exp(-E/k_BT)$, even when the light intensity was as low as 20 $\mu W/cm^2$. The temperature dependence of τ is opposite to those previously reported in $BaTiO_3$ and SBN:Cr[7,8].

All the experiments described above suggest that the photorefractive origin of our SBN:Ce is something other than band transport and charge redistribution. We now postulate that it stems from the polarization grating, which grows when the crystal is cooled after the reversed polarization domain has been seeded at a temperature close to Tc. This might be possible since polarization grating formation in SBN75 without an external field has been reported[3], although the index grating of our experiment was not fixed against light exposure.

In conclusion, the diffraction efficiency of SBN:Ce has been enhanced thermally and the Bragg mismatch has been overcome. The index grating was not fixed against light exposure but against dark conductivity. The origin of this photorefractive effect can not be explained by charge distribution and is possibly caused by the polarization grating.
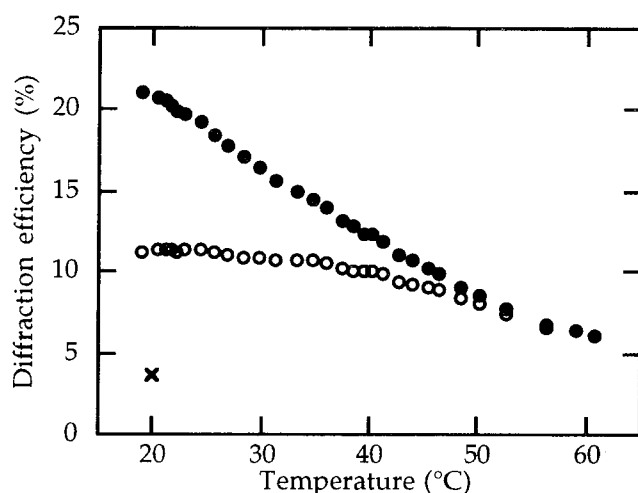
Figure 1 Enhancement of diffraction efficiency

Open circles denote the measured diffraction efficiency. Solid circles are Bragg matched values estimated from the thermal expansion data, where α=5.61cm-1, Γ=11cm-1 and the phase mismatch is assumed to be $\pi/2$.
X denotes the measured diffraction efficiency recorded at 20 °C.
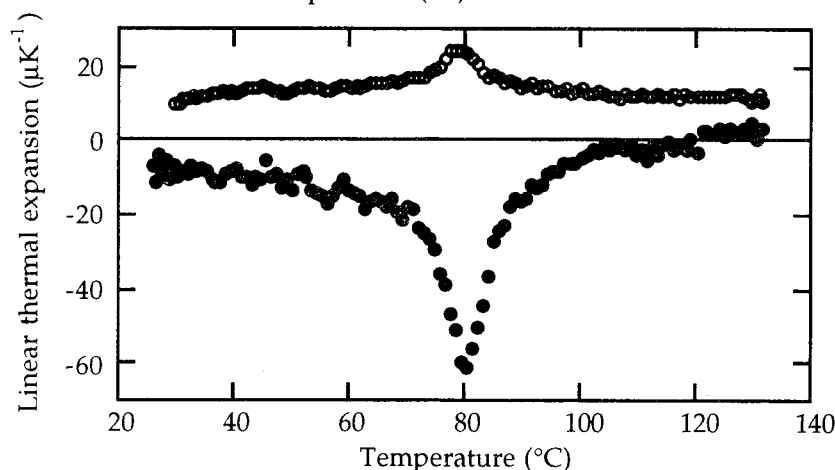
Figure 2 Linear thermal expansion of a- and c-axes of SBN

Open circles show the a-axis expansion. Solid circles show the c-axis expansion. The c-axis has the negative expansion coefficient.
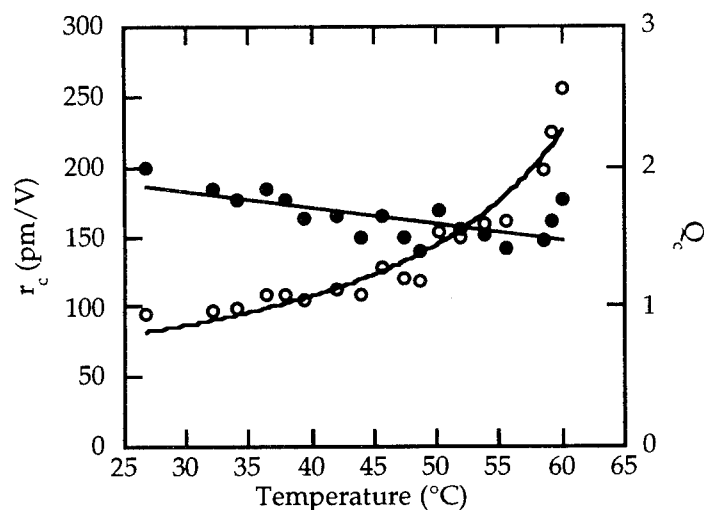
Figure 3 Electro-optic coefficient and figure of merit

Open circles denote the electrooptic coefficient, where $r_c = r_{33} - (n_o/n_e)^3 r_{13}$.
Solid circles denote the figure of merit, $Q_c = n_e^3 r_c / \varepsilon_{33}$
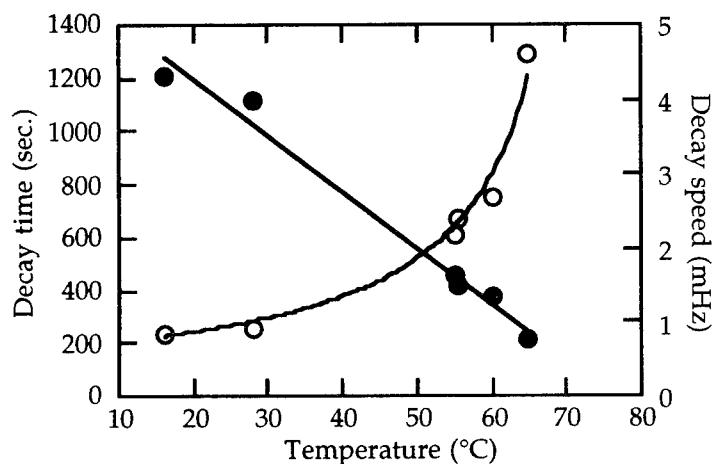
Figure 4 Decay time of diffraction efficiency

Open circles denote the decay time of diffraction efficiency by light exposure. Solid circles denote the inverse of the decay time. The light intensity was 1.46mW/cm^2. Even when the intensity was decreased to $20 \mu \text{W/cm}^2$, the decay time was proportional to $(T_c-T)^{-1}$.

References

1. N.V. Kukhtarev, V.B.Markov, S.G.Odulov, M.S.Soskin, and V.L.Vinetski, Ferroelectrics **22**, 949 (1979)
2. R.Hofmeister, A.Yariv, S.Yagi, and A.Agranat, Phys.Rev.Lett. **69**, 1459 (1992)
3. A.Kewitsch, M.Segev, A.Yariv, and R.Neurgaonkar, Opt.Lett. **18** 534 (1993)
4. R.Hofmeister, A.Yariv, A.Kewitsch, and S.Yagi, Opt.Lett. **17**, 488 (1992)
5. D.Vahey, J.Appl.Phys. **46**, 3510 (1975)
6. M.D.Ewbank, R.R.Neurgankar, W.K.Cory, and J.Feinberg, J.Appl.Phys. **62**, 374 (1987)
7. D.Kirillov and Jack Feinberg, Opt.Lett. **16**, 1520 (1991)
8. K.Sayano, G.Rakuljic, A.Agranat, A.Yariv, and R.R.Neurgaonkar, **14**, 459 (1989)

TUP9

TRANSIENT TWO-WAVE MIXING OF PHOTOREFRACTIVE Bi12SiO20 CRYSTAL WITH A SQUARE A.C. ELECTRIC FIELD

Chong Hoon Kwak and El-Hang Lee
Research Department, Electronics and Telecommunications
Research Institute, P. O. Box 106, Yuseong-gu, Daejeon, Korea
(Tel:+82-42-860-5694, Fax:+82-42-860-5033, e-mail: chkwak@ard.etri.re.kr)

Two wave mixing (TWM) gain in photorefractive materials is one of the most fundamental and attractive aspects of the photorefractive effect. Several techniques for the enhancement of TWM gain have been developed and analysed by many researchers: applied d.c. field technique[1], d.c. field and moving grating technique[2] and applied a.c. field technique[3]. It was shown some time ago by Stepanov *et al.* [3] that TWM gain can be considerably increased by applying a square a.c. electric field instead of a d.c. field. The temporal differential equation describing the build-up of the space-charge field $E_{sc}(t)$ with external applied field $E_0(t)$ takes the following form [2]:

$$\frac{\partial E_{sc}}{\partial t} + gE_{sc} = hm \qquad (1)$$

Here, the coefficients are as follows: $g = \left(1 - i\frac{E_o}{E_q}\right)\bigg/\tau_d\left(1 - i\frac{E_o}{E_M}\right)$ and $h = -E_o/\tau_d\left(1 - i\frac{E_o}{E_M}\right)$, where τ_d is the

Maxwell relaxation time, E_M and E_q are the characteristic electric fields of the material. It is noted that although Eq.(1) is derived for a d.c. applied field (*i.e.*, E_0 = const.), it is still valid for a.c. applied field when the period T (=$2\pi/\Omega$) of a.c. applied field is much longer than the photoelectron lifetime, *i.e.*, $T \gg \tau_e$. In that case, each photoelectron essentially sees a constant applied field during its lifetime. In addition, when the period of the a.c. field is much shorter than the grating build-up time τ_g (approximately equal to Re{1/g}), one may use the time averaging method over the period T to solve Eq.(1) [3]. Then the space-charge field cannot follow the a.c. applied field and the solution becomes independent of the time period T. However, when the period T is comparable with τ_g, the usual time averaging method will not hold, so we require to have the full temporal solution for Esc(t), applicable to the whole frequency range of the a.c. field.

In this paper we developed, for the first time to our knowledge, the corresponding theory describing the buildup of the space-charge field in the presence of square a.c. field and compared with the experimental results of the full temporal variation of the TWM gain for the square applied fields in a photorefractive Bi12SiO20 crystal. Considering the square a.c. field Eo(t) with the time period $T(=2\pi/\Omega)$ as shown in Fig.1, the time varying coefficients g(t) and h(t) in Eq.(1) become constants g^+ and h^+ for each positive half-period of Eo(t)=Eo, and g^- and h^- for each negative half-period of Eo(t)=-Eo, respectively, where E_0 is the amplitude of square applied field. In order to solve Eq.(1), we apply the step-by-step integration in each successive half-period of Eo(t). For the nth period of the applied field Eo(t) (*i.e.*, (n-1)$T \le t \le$ nT) we get the space-charge field $E_n(t)$ for the positive and the negative half-period as:

$$E_n^+(t) = \frac{h^+}{g^+}m\left\{1 - \exp[-g^+(t-(n-1)T)]\right\} + E_n^+((n-1)T)\exp[-g^+(t-(n-1)T)], \text{ for } (n-1)T \le t \le (n-\tfrac{1}{2})T \quad (2a)$$

$$E_n^-(t) = \frac{h^-}{g^-}m\left\{1 - \exp[-g^-(t-(n-\tfrac{1}{2})T)]\right\} + E_n^-((n-\tfrac{1}{2})T)\exp[-g^-(t-(n-\tfrac{1}{2})T)], \text{ for } (n-\tfrac{1}{2})T \le t \le nT \quad (2b)$$

From Eq.(1) we have the following relations: $g^{+*} = g^-$ and $h^{+*} = -h^-$. Before proceeding any further, it is convenient to introduce the steady state values of En(t). Since the steady state of En(t) corresponds to the values for sufficiently large n, we may take the boundary conditions as $E_n^+\left((n-\tfrac{1}{2})T\right) = E_n^-\left((n-\tfrac{1}{2})T\right) \equiv E_\infty^+$ and $E_n^+((n-1)T) = E_n^-(nT) \equiv E_\infty^-$. After simple calculations, we have the real and imaginary part of

$$a_\infty(T) = \frac{g_1h_1 + g_2h_2}{g_1^2 + g_2^2} \, m \left[\coth\left(\frac{g_1T}{2}\right) - \frac{\cos\left(\frac{g_2T}{2}\right)}{\sinh\left(\frac{g_1T}{2}\right)} \right] \tag{3a}$$

$$b_\infty(T) = \frac{g_1h_2 - g_2h_1}{g_1^2 + g_2^2} \, m + \frac{g_1h_1 + g_2h_2}{g_1^2 + g_2^2} \, m \, \frac{\sin\left(\frac{g_2T}{2}\right)}{\sinh\left(\frac{g_1T}{2}\right)} \tag{3b}$$

where we used the following notations: $E_\infty^\pm = \pm a_\infty + ib_\infty$, $g^\pm = g_1 \pm ig_2$ and $h^\pm = \pm h_1 + ih_2$. It should be noted that in the limiting case of $T/2 \ll 1/g_{1,2}$ (i.e., for high frequency limit) Eq.(3) reduces to the same expression derived by the time averaging method[3]. By using the boundary condition of $E_n^-\left((n-\frac{1}{2})T\right) = E_n^+\left((n-\frac{1}{2})T\right)$ and $E_n^+((n-1)T) = E_{n-1}^-((n-1)T)$, we finally get the following expression by using successive iterations:

$$E_n^-(nT) = E_\infty^-\left[1 - \exp[-ng_{av}T]\right] \tag{4a}$$

$$E_n^+\left((n-\frac{1}{2})T\right) = E_\infty^+ - E_\infty^-\exp[-(ng_{av}-\frac{g^-}{2})T] \tag{4b}$$

where $E_0^-(0) = 0$ is taken as the initial condition. On substituting Eq.(4) into Eq.(2) with Eq.(3) we may have the transient solution of the space-charge field Esc(t) for each half-period of applied field. In a photorefractive crystal the effective gain in a two mixing configuration is defined as follows[2]:

$$G = \frac{I_s(\text{with pump beam and AC field})}{I_s(\text{without pump beam and AC field})} = \frac{(1 + \beta)\exp[\Gamma(t)d]}{1 + \beta\exp[\Gamma(t)d]} \tag{5}$$

where $\beta = I_S(0)/I_R(0)$ is the incident intensity beam ratio between the pump beam I_R and the probe beam I_S and d is the interaction length of the crystal. The exponential gain coefficient $\Gamma(t)$ is proportional to the imaginary part of the space-charge field[2].

The full temporal variation of the two wave mixing (TWM) gain is measured in a photorefractive $Bi_{12}SiO_{20}$ crystal grown by Sumitomo ($10 \times 10 \times 10 mm^3$). The experimetal configuration is schematically shown in Fig.1. A beam from an Ar-ion laser beam of 514.5nm wavelength was split into two beams, expanded and collimated. The intensity beam ratio of pump-to-probe beams set to 45 with a total incident intensty of $4.6 mW/cm^2$. The two beams were vertically polarized and were incident on the (110) face of the BSO crystal. The alternating square electric field of up to 7KV/cm amplitude was applied between the (001) faces of the crystal. The interbeam angle between the two incident beams was chosen so as to achieve the optimum gain in experiments at approximately 2°. The frequency range of the applied electric field was 1Hz - 1KHz. Figure 2 shows the typical experimental curves of the time-dependent TWM gain for the repetition rates of 20Hz. Figure 3 shows the theoretical curves for temporal behavior of the TWM gain for square a.c. field of E_0=7KV/cm amplitude with repetition rate of 20Hz. In the calculations we used the following crystal parameters: E_M=0.35KV/cm, grating spacing of 15μm and τ_d =1.3 msec for input intensity of $4.6 mW/cm^2$ and g_1=14.7Hz and g2=37.7Hz for E_0=7KV/cm. One may see that the theory agrees well with the experimental results.

In conclusion, we have developed a theory, based on the Kukhtarev's materials equations, describing the temporal variations of two-wave mixing gain in the presence of a square a.c. field in photorefractive materials. The transient behavior of the two wave mixing gain is also measured in photorefractive $Bi_{12}SiO_{20}$ crystal with a square a.c. applied field of up to 7KV/cm and compared with the theory.

REFERENCES

1. G. C. Valley, J. Opt. Soc. Am. **B1**, 868 (1984).
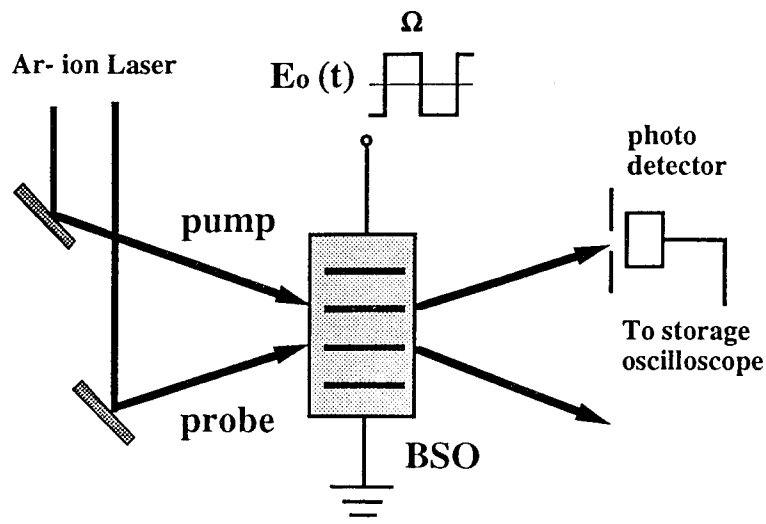
Fig. 1 Experimental geometry for a.c. two-wave mixing.
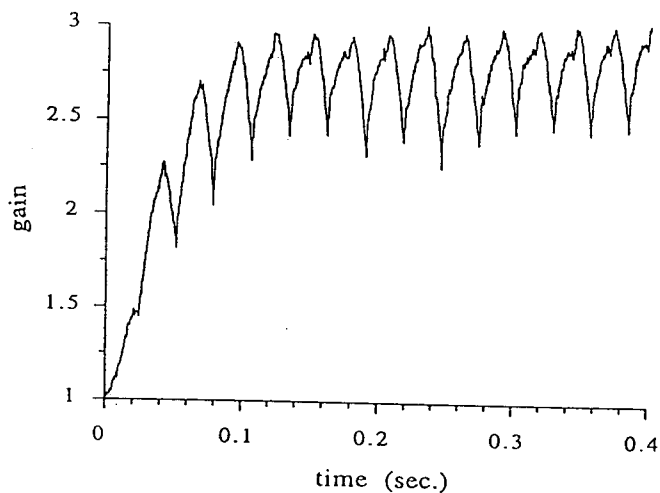
Fig. 2 Experimental time-dependent gain curve in the presence of square a.c. field of 7KV/cm at repetition rate of 20Hz.
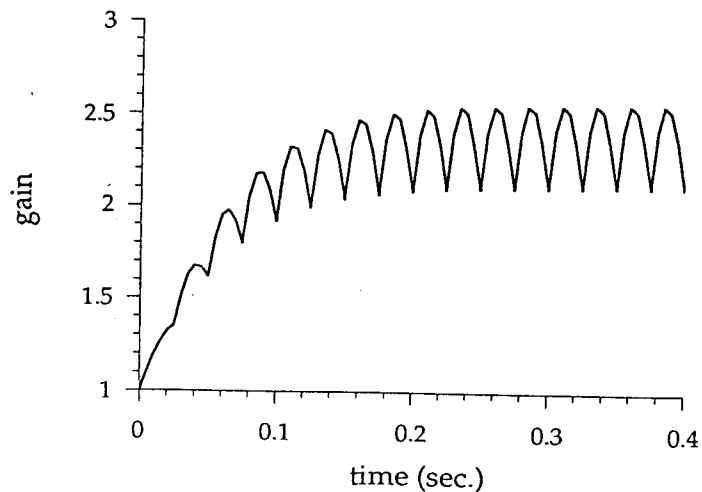
Fig. 3 Theoretical time-dependent gain curve of Fig.2.

Spatial Subharmonics in Photorefractive Materials

Sugie Shim, Chong Hoon Kwak, and El-Hang Lee

Research Department, Electronics & Telecommunications Research Institute, Yusung P.O. Box 106, Daejeon, Korea

Tel.) 82-42-860-6034   e-mail) shim@ard.etri.re.kr

L. Solymar

Holography Group, Department of Engineering Science, University of Oxford, Parks Road, Oxford, OX1 3PJ, UK

Since the first observation of the spatial subharmonics in photorefractive BSO crystal by Mallick *et al.*[1] in 1988, the possible physical mechanism based on the Kukhtarev's materials equations has been intensively investigated. However, most of the work in this field has been concentrated on obtaining the instability condition for the existence of the subharmonic resonances[2, 3]. In this paper we attempt to calculate $K/2$ spatial subharmonic resonances varying the detuning frequencies for several external electric fields and compare the theoretical results with experimental data. A simple theory based on a differential equation which is derived from the materials equations for the space charge field and the coupled mode analysis of the wave equation is developed to describe the subharmonic resonances. The mechanism which is responsible for the subharmonic resonance is assumed to be spontaneous generation caused by the inherent nonlinearity of the photorefractive effect itself[2, 3, 4].

We start with a nonlinear partial differential equation, which is derived from Kukhtarev's materials equations to describe the space charge field E_{SC} in a moving co-ordinate system[2]. The new co-ordinate is set to be $\xi = \Omega t - Kx$, where K is the magnitude of the grating vector and Ω is the amount of frequency detuning. Our differential equation takes the form

$$(1 + \frac{E_{SC}}{E_0})E_{SC}'' - (\frac{E_M}{bE_q} + \frac{E_M}{E_0})E_{SC}' + \frac{E_M}{bE_0}(1 + m\cos\xi)E_{SC}$$
$$= -\frac{E_M}{b}m\cos\xi + \frac{E_M}{E_0 E_q}(E_{SC}')^2, \tag{1}$$

where the primes represent the derivatives with respect to ξ, m is the modulation, E_0 is the external electric field, $b = \Omega\tau_d$. Here, E_M and E_q are characteristic electric fields introduced by Kukhtarev *et al.*[5], and τ_d is the dielectric relaxation time. Diffusion field is neglected since it is sufficiently small compared to the fields of E_0, E_M and E_q. The intensity distribution in the crystal is given by $I_0(1 + m\cos\xi)$ where I_0 is the average intensity. Since E_q and E_0 are large compared to E_M, the last term in the right hand side of Eq. (1) is neglected in the calculation.

In this work we concentrate on the $K/2$ spatial subharmonics and start from the expansion

$$E_{SC} = A_{1/2}\exp(i\xi/2) + A_1\exp(i\xi) + A_{3/2}\exp(i3\xi/2) + c.c.. \tag{2}$$

We skip the contribution from the Fourier component 3/2 for simplicity and substitute Eq. (2) into Eq. (1) to obtain coupled differential equations by equating the exponential terms with the same order. Considering $\exp(i\xi)$ terms, we obtain

$$A_1 = A_{10} + \eta(A_{1/2})^2 \tag{3}$$

with

$$A_{10} = -\frac{mE_M}{2b\{h/b - 1 - (h + \frac{E_M}{E_q b})i\}}, \quad \eta = \frac{1}{4E_0\{h/b - 1 - (h + \frac{E_M}{E_q b})i\}}, \tag{4}$$

where h is defined as E_M/E_0. Investigating $\exp(i\xi/2)$ terms and using Eqs. (3) and (4), we obtain

$$|A_{1/2}|^2 = \frac{(\frac{h}{b} - \frac{1}{4})^2 + (\frac{h}{2} + \frac{E_M}{E_q b})^2 - \frac{(mh)^2}{4b^2} - \frac{25}{16E_0^2}|A_{10}|^2 + \frac{5mh}{8bE_0}(A_{10} + A_{10}^*)}{\{\frac{h}{b} - \frac{1}{4} + (\frac{h}{2} + \frac{E_M}{E_q b})i\}\frac{5}{4E_0}\eta + \{\frac{h}{b} - \frac{1}{4} - (\frac{h}{2} + \frac{E_M}{E_q b})i\}\frac{5}{4E_0}\eta^*}.$$ (5)

For simplicity, $m = 1$ case is considered in the calculation since it gives an optimum condition for generating the spatial subharmonics.

In order to find out the relationship between the output subharmonic intensity distribution and the subharmonic space charge field given by Eqs. (2) and (5), the coupled mode analysis of wave equation is utilized. The solution of the wave equation is assumed to have the form of

$$E(\mathbf{r}, t) = E_1 \exp[-i(K_1 \cdot r - (\omega + \Omega)t)] + E_2 \exp[-i(K_2 \cdot r - \omega t)]$$
$$+ E_{1/2} \exp[-i(K_{1/2} \cdot r - \omega_{1/2} t)],$$ (6)

where ω is the optical frequency, E_1 and E_2 are the amplitudes of the two pump waves and $E_{1/2}$ is that of $K/2$ spatial subharmonic wave, as illustrated in Fig. 1. Using the slowly varying amplitude approximation, we obtain a set of coupled differential equations for E_1, E_2 and $E_{1/2}$. Assuming that there is no pump-beam depletion and no coupling between pump waves it is straightforward to find solutions for the subharmonic waves satisfying the boundary condition of $E_{1/2}|_{z=0} = 0$. Assuming equal pump beam intensities for E_1 and E_2, the output subharmonic intensity in the photorefractive moving gratings is obtained as

$$|E_{1/2}|^2 = (\Gamma L)^2 \sin c^2(\frac{\Delta K L}{2}) I_0 [Re(A_{1/2})]^2,$$ (7)

where $\Gamma = \frac{\mu_0 \epsilon_0 \epsilon_r^2 r_{eff} \omega^2}{2k}$ is the coupling constant, L is the interaction length of the medium, $\sin c(x) \equiv \frac{\sin x}{x}$ and I_0 is the total input beam intensity. It should be noted that the subharmonic intensity comes from the *real* part of $A_{1/2}$ when the equal pump beam intensity is assumed. This gives the same argument with that in the work published by Ringhofer and Solymar[6] although the basic assumptions are different from each other.

Figure 1 shows the schematic diagram of experimental arrangement for observing the subharmonic waves in photorefractive BSO crystal. A beam from an Ar-ion laser at a wavelength of 514.5 nm is expanded, collimated and split into two beams. One of the pump beams is detuned in frequency by applying a triangular signal to a piezoelectric mirror. The comparison of our theoretical results with experimental data for the detuning frequencies of the $K/2$ subharmonic resonances at various E_0 is shown in Fig. 2. The physical parameters of τ_d, E_M and E_q are set to be 6.5 $msec.$, $0.73kV/cm$ and $180kV/cm$, respectively, which are taken from Ref. [3]. Even though the contribution from 3/2 component ($\exp(i3\xi/2)$ terms) is not included in the calculation, the prediction of our simple theory agrees with the experimental data remarkably well.

In conclusion, the optimum detuning frequency of $K/2$ spatial subharmonics in the photorefractive moving gratings is calculated using a simple theory based on materials equations and the coupled mode analysis of wave equation and compared with experimental data which is obtained with the external electric fields varying from 7 kV/cm to 3 kV/cm and detuning frequency varying up to 40 Hz. It is found that as the external electric field decreases the optimum detuning frequency for $K/2$ subharmonics increases and that our simple theory which has no adjustable parameter describes the experimental data very well.
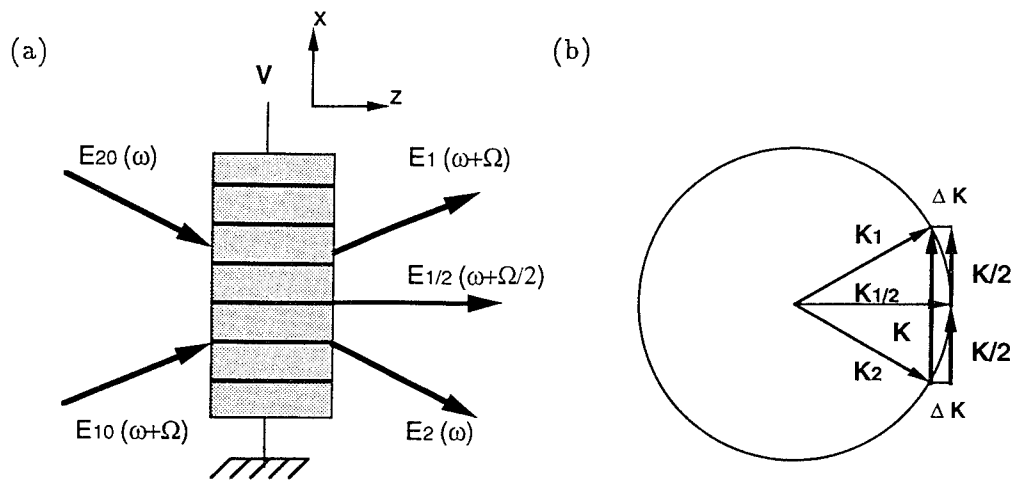
Fig. 1. (a) Schematic diagram of experimental setup for observing spatial subharmonic waves,
(b) Eward sphere representation showing the geometric scheme of spatial subharmonics.
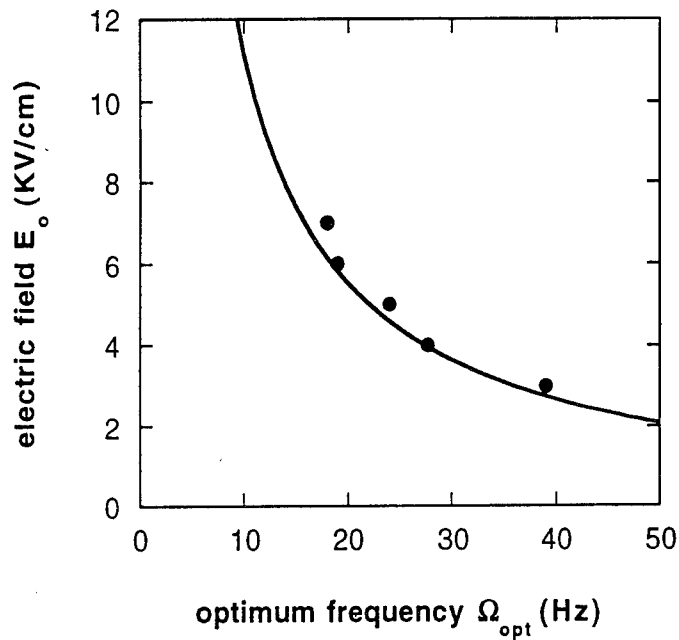
Fig. 2. Comparison of the theoretical
results with the experimental data for
for optimum detuning frequencies of $K/2$
sptial subharmonics at several external
external electric fields. The solid line
represents the theoretical prediction and
the dots represent the experimental data.

References

[1] S. Mallick *et al.*, J. Appl. Phys. **63**, 5660 (1988).

[2] C.H. Kwak, J. Takacs and L. Solymar, Electron. Lett. **28**, 530 (1992).

[3] C.H. Kwak, J. Takacs and L. Solymar, Optics Comm. **96**, 278 (1993).

[4] B.I. Sturman, A. Bledowski, J. Otten and K.H. Ringhofer, J. Opt. Soc. Am. B **9**, 672 (1992).

[5] N.V. Kukhtarev *et al.*, Ferroelectrics **22**, 949 (1979).

[6] K.H. Ringhofer and L. Solymar, Appl. Phys. Lett. **53**, 1039 (1988).

Effects of Photorefractive Phase Conjugate Feedback on Semiconductor Laser Linewidth

Bruce W. Liby

USAF Phillips Laboratory, Semiconductor Laser Applications Branch
Kirtland AFB, NM   87117-5776
TEL: (505)846-4315; FAX (505)846-4313

David   Statman

Department of Physics , Allegheny College, Meadville, PA 16335
TEL: (814)332-2799; FAX:(814)332-0988

John   McInerney

Department of Physics, University College, Cork, Ireland
TEL (+353-21) 276871; FAX: (+353-21) 276949

John K. McIver

Department of Physics and Astronomy, University of New Mexico
Albuquerque, NM 87131
TEL (505)277-8484; FAX: (505)277-1520

Summary

The effect of phase conjugate feedback on semiconductor laser continues to be a topic of interest[1,2]. Phase conjugate feedback has the advantage of self-alignment and aberration correction. These properties result in good coupling back into the laser -- which is not guaranteed with conventional mirror. On the other hand, it has been demonstrated that the round trip phase delay for an external phase conjugate cavity is set by the laser and the phase conjugate mirror, independent of cavity length[3]. In this presentation we consider the impact of this phase delay on the laser diode linewidth.

Agrawal has shown that the linewidth of a single mode in a semiconductor laser with feedback is dependent on the external round trip phase delay and how well the return light is coupled back into the laser cavity[4]. The extent of line broadening or line narrowing is determined by

$$\Delta f/\Delta f_0 = [1 + X \, cos(\phi_0 + \phi_R)]^2 \tag{1}$$

where

$$\phi_0 = \omega_0 \tau + \phi_m, \quad X = \kappa\tau(1 + \alpha^2)^{1/2}, \quad \phi_R = tan^{-1} \alpha. \tag{2}$$

and Δf is the laser linewidth with feedback, Δf_0 is the free running laser linewidth, ω_0 is the free running laser frequency, τ is the round trip time of

flight in the external cavity, ϕ_m is the phase shift due to the external reflector, α is the linewidth parameter, and κ is the feedback coupling rate. When considering phase conjugate feedback to a diode laser, and comparing the results with conventional feedback, it can be seen that κ is not the same for the two cases. Also, while τ can be controlled in the conventional case by the experimentalist, it cannot be controlled in the phase conjugate case.

For a conventional reflector the round trip phase delay is determined by the path length of the external cavity. For any set of laser parameters the narrowing or broadening of the linewidth depends on the position of the external reflector[4]. Therefore, for low external feedback both linewidth narrowing or broadening can take place and can be controlled by changing the length of the external cavity.

A photorefractive self-pumped external cavity has a delay which is independent of the position of the phase conjugate reflector. It is determined by the boundary conditions of the laser and the photorefractive phase conjugate mirror. This phase delay is equal to an integer multiple of 2π;

$$\phi_o + \phi_R = 2n\pi \tag{3}$$

where ω is the frequency of the laser and n is any integer[3]. When this boundary condition is satisfied, the threshold gain is reduced to its minimum value. Imposing the condition on the model developed by Agrawal[4] it is found that the lasing linewidth is always decreased, but not by the maximum amount. This should be contrasted with a conventional reflector where the optimal phase delay is that which compensates the phase due to the linewidth parameter, i.e., the phase delay which produces the maximum linewidth narrowing. Because the complex amplitude of the photorefractive phase conjugate return is itself not conjugate[5], i.e.;

$$A \neq A^* \tag{4}$$

the feedback can be treated in the same manner as a conventional reflector where the total round trip phase delay is restricted to $2n\pi$.

In our experiments a Hitachi HLP1400 laser is coupled to a ring passive phase conjugate mirror (PPCM) that is constrained to unidirectional (Fig. 1). This prevents reflection gratings to be formed in the photorefractive crystal and minimizes the effects of grating competition. The photorefractive material used in the ring PPCM is barium titanate. An etalon is inserted into the external cavity, as shown, to keep the laser single mode even with feedback. For the phase conjugate reflectivities of 0.2% the FWHM linewidth is decreased by 80%. This is shown in Fig. 2

where the decrease in linewidth is clearly seen. Using Eq.'s. 1 and 2, the expected decrease is 73%. It has also been observed that he laser frequency is more stable with the PPCM that with a conventional reflector. There is no frequency jitter of the line center such as that observed with conventional feedback. We suggest here that this is due to the slow response time of the barium titanate. Any jitter from the central lasing frequency does not have enough time to write a new holographic grating. Only that central frequency is coupled back into the laser .
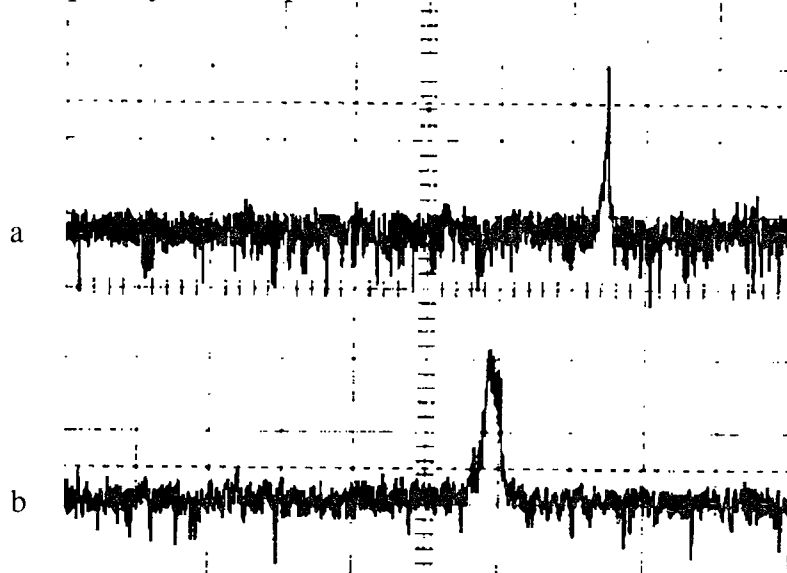
Fig. 2 Linewidth narrowing. a) with feedback, b) free running laser.

References

[1]   E. Jaatinen, W. Krolikowski, and B. Luther-Davies, *J. Opt. Soc. Am. B* **10**, 933 (1993).

[2]   G. P. Agrawal and J. T. Klaus, *Opt. Lett.* **16**, 1325 (1991).

[3]   B. W. Liby and D. Statman, *Opt. Comm.* **101**, 113 (1993).

[4]   G. P. Agrawal, *IEEE J. Quant. Electr.* **QE-20**, 468 (1984).

[5]   J. Feinberg, *Opt. Lett.* **8**, 569 (1983).

Envelope Narrowing from Photorefractive Phase Conjugate Feedback
to a Semiconductor Laser

David Statman, Departments of Physics and Chemistry, Allegheny College, Meadville, PA
16335, Ph. 814-332-2799
Bruce W. Liby, Semiconductor Laser Applications Branch, Phillips Laboratory, PL/LIDA, 3550
Aberdeen SE, Kirtland AFB, NM 87117, Ph. 505-846-4315

Summary

Previous work[1,2] has shown that a popular photorefractive phase conjugator is the ring passive phase conjugator (ring PPCM). The ability of the ring PPCM to reconstruct images is well documented[2]. We have recently demonstrated that the fidelity of this image reconstruction is good[3]. This was accomplished by measuring the ratio of the beam quality of the phase conjugate reflection of a laser diode to the beam quality of the diode laser when a phase aberrator was placed before the ring PPCM. Good optical phase conjugate fidelity suggests that the phase conjugate feedback should couple back into the diode laser quite well. We have also shown, experimentally, that the round trip phase delay for a photorefractive phase conjugator, and indeed any phase conjugator, is an integral multiple of 2π[4]. This phase delay is independent of the position of the reflector. It must be noted, however, that while the fidelity of the phase conjugate feedback, and the $2n\pi$ phase delay are independent of the position of the phase conjugate reflector, the round trip time of flight in the external cavity is dependent on the position of the reflector when it is a ring PPCM. The only requirement is that the $2n\pi$ round trip phase delay be satisfied, i.e., the round trip time of flight must be an integral multiple of the inverse of the frequency, $\tau = n/v = n\lambda/c$. Because the round trip phase delay is constrained, the amount of linewidth narrowing is also constrained[5]. When the round trip time of flight is less than the coherence time of the laser, the linewidth of a single line is also independent of the position of the reflector.

The above work, however, has not considered that the reflectivity of a photorefractive phase conjugator may depend on the intensity of those beams which write the photorefractive gratings[6]. A general rule of thumb is that when the ratio of the rate of photoexcitation to thermal excitation of carriers is greater than unity, the grating strength is independent of the writing intensity. If, however, that ratio is less than unity, then the grating strength is approximately linear with the intensity. The result is that the phase conjugate reflectivity is also dependent on the ratio of the rates of photoexcitation to thermal excitation. Taking account of this effect and its impact on photorefractive feedback, it is seen that the weaker modes of the laser diode will "see" a lower external cavity reflectivity. Those modes too weak to write a photorefractive grating within the crystal will not have a phase conjugate reflection at all. Since all lasing modes undergo the same $2n\pi$ round trip phase delay, the *effective* reflectivity (derived from the output coupler facet reflectivity, the external reflector reflectivity, and the round trip phase delay) is dependent only on the grating strength in the photorefractive phase conjugator,and hence only on the intensity of the laser mode. It must be concluded that for the phase conjugate external cavity, the strongest modes having the greatest *effective* reflectivity will have the greatest decrease in threshold gain. This results in a narrowing of the envelope of the laser diode spectrum. It will also narrow the linewidth of a single mode, but by a very small amount.

We have calculated the general effects of envelope narrowing for a unidirectional ring PPCM. The grating strength was determined using the band transport model for photorefractive materials[7,8]. The reflectivity was calculated based on Kogelnik's expressions for transmission

volume holograms[8]. With the intensity dependent external cavity reflectivity determined, the *effective* reflectivity was then calculated and used to determine the mode intensity. The results of these calculations are shown in Fig. 1. Here the lasing envelope is compared with the multimode spectrum if the external reflectivity were the same for all modes. In both cases there is a $2n\pi$ round trip phase delay. Clearly observable are the effects of envelope narrowing and a slight linewidth narrowing. The photorefractive phase conjugator is acting like a filter which preferentially selects the strongest laser modes. The envelope narrowing effects are more pronounced for lower laser intensity and less pronounced for higher laser intensity.

These effects of envelope narrowing were confirmed experimentally. In our experiments a Hitachi HLP1400 laser diode is coupled to a ring PPCM that is constrained to be unidirectional (Fig. 2). The advantages of such a geometry are described elsewhere[4]. The photorefractive material used is barium titanate. The laser spectrum was compared to that of a laser diode coupled to an external cavity with a dielectric mirror, i.e., we compared the effects of phase conjugate feedback to conventional feedback. In both cases the laser is multimode when coupled to the external cavity. As can be seen in Fig. 3, however, the envelope for the phase conjugate feedback is narrower than that for the conventional case. It can also be seen that in the conventional case the gains for the different longitudinal modes vary with the phase delay as each mode experiences a different round trip phase delay. This is not the case for the phase conjugate cavity because all of the modes experience the same round trip phase delay.

References:

1. M. Cronin-Golomb, B. Fischer, L.O. White, and A. Yariv, IEEE J. Quant. Electr. **QE-20**, 12 (1984).
2. J. Feinberg, Opt. Lett., **10**, 486 (1986)
3. B.W. Liby, J.K. McIver, and D. Statman, Opt. Commun., **101**, 79 (1993).
4. B.W. Liby and D. Statman, Opt. Commun. **101**, 113 (1993).
5. B.W. Liby, D. Statman, and J.K. McIver, submitted to NLO '94.
6. C. Xu, D.Statman, and J.K. McIver, J. Opt. Soc. Am., B, **9**, 1825 (1992).
7. N.V. Kukhtarev, V.B. Markov, S.G. Odulov, M.S. Soskin, and V.L. Vinetskii, Ferroelectrics, **22**, 949 (1979); **22**, 961 (1979).
8. D. Statman, J. Opt. Soc. Am., B, **9**, 849 (1992).
9. H. Kogelnik, Bell Sys. Tech. J., **48**, 2909 (1969).
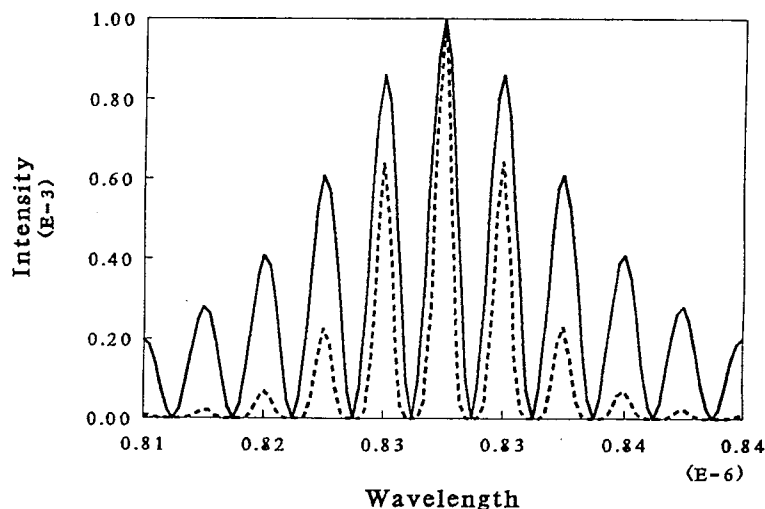
Fig. 1 Calculated envelope narrowing for a diode laser;
solid line: no photoreactive narrowing, dashed line: photorefractive narrowing.
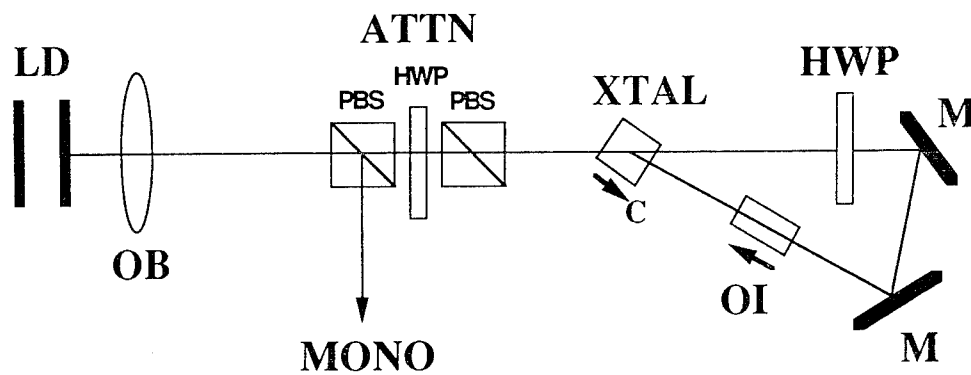
Fig. 2 Experimental set-up. Feedback using a unidirectional ring PPCM.
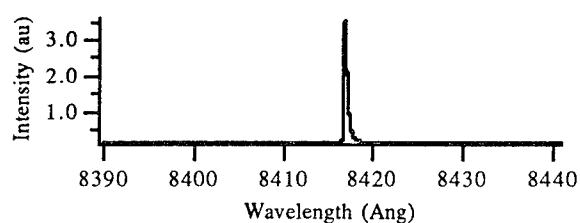
Fig. 3a   Free running laser diode spectrum.
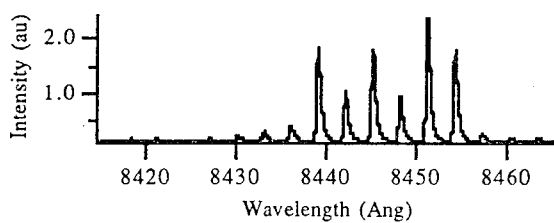
Fig. 3b Laser diode spectrum with conventional feedback.
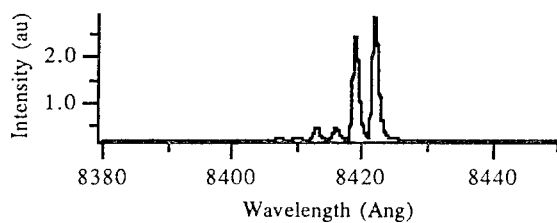
Fig. 3c Laser diode spectrum with phase-conjugate feedback.

TRANSVERSE DYNAMICS OF PHOTOREFRACTIVE OSCILLATORS
AND CLASS-A LASERS

K.Staliunas and C.O.Weiss

Physikalisch-Technische Bundesanstalt, Lab.4.42
Bundesallee 100, 38116 Braunschweig, GERMANY

Tel: +49-531-5924400   FAX: +49-531-5929292
E-mail: STALI426@RZ.Braunschweig.PTB.D400.DE

We report the results of our theoretical and experimental analysis of transverse dynamics of photorefractive oscillators (PRO). Our theoretical, numerical, and experimental analysis shows, that the field dynamics in PROs is very similar to that in Class-A lasers.

An equation of the Complex Ginzburg-Landau type can be derived for the optical field dynamics $E(\vec{r},t)$ in the single- longitudinal- mode PRO:

$$\frac{1}{\gamma}\cdot\frac{\partial E}{\partial t} = (1+i)\cdot E\left[(p-1) - |E|^2\right] - i\cdot p\cdot\left[\beta-d\vec{\nabla}^2-1\right]\cdot E - \frac{p}{4}\cdot\left[\beta-d\vec{\nabla}^2-1\right]^2\cdot E$$

here p is the pump parameter, d is the diffraction constant, β is the cavity detuning, $\vec{\nabla}^2$ the Laplace operator in a two dimensional plane normal to the optical axis of the PRO system, and γ is the relaxation rate of PRO material.

This is the so called Laser Ginzburg-Landau Equation (LGLE) which have been derived from the Maxwell-Bloch equation system for Class-A lasers [1.2]. In addition to terms of the usual Complex Ginzburg-Landau Equation (CGLE), a second order diffusion term (the last term in rhs. of LGLE) is present. Due to this term radiation with certain transverse wave-numbers $\vec{k}_\perp$ ($|\vec{k}_\perp|^2 = (1-\beta)/d$) grows most strongly in the LGLE, this corresponds to the Tilted Wave (TW) excitation in Class-A lasers [3].

The PRO - Class-A laser correspondence is confirmed by numerical integration of the PRO equations [4], and of the LGLE. The experimental observation of transverse field structure emitted by a PRO also shows the properties expected for Class-A lasers. The

tunability to different transverse mode families, the pure transverse mode patterns and square vortex lattices, as well as the periodic and turbulent behavior (also reported in [5]), gives evidence of the PRO - Class-A laser analogy.

We investigate particularly the Square Vortex Lattices (SVL) in PROs and Class-A lasers. The SVL has been shown to appear at the threshold of a laser tuned to a high enough transverse mode family [2]. The SVL in two dimensions is the analog of a Standing Wave (SW) in one dimension. These patterns appears due to the influence of lateral boundaries of PROs or Class-A lasers. Without lateral boundaries the Tilted Wave (TW) is excited in wide aperture Class-A lasers [3].

Further, the destabilization of SVLs and SWs is investigated when increasing of the pump parameter. In the case of one transverse dimension a sharp transition between SW and the TW occurs for a particular value of the pump parameter. The pump parameter corresponding to the transition depends on the transverse size of the system. This SW - TW transition is also interpreted in terms of phase locking between transverse mode families.

(a)   (b)   (c)
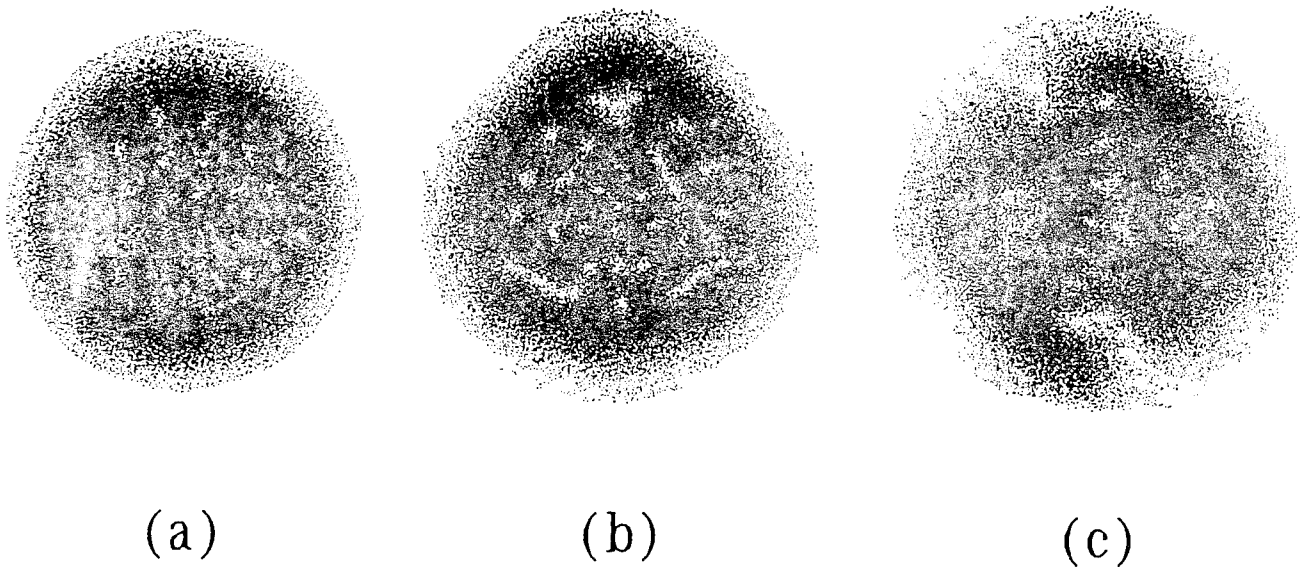
PRO transverse patterns obtained from numerical integration of the LGLE: (a) - stationary vortex lattice, (b) - distorted vortex lattice, (c) - nonstationary (turbulent) pattern.

Also in the case of two transverse dimensions is the SVL replaced by a TW-dominated pattern for large pump values. The SVL-TW transition is in this case more complicated than in the case of one spatial dimension. The transition scenario depends strongly on the shape of lateral boundaries. For square boundaries the increase of pump results in destruction of the SVL and onset of domains of TWs directed oppositely and separated by rows of vortices. For circularly symmetric lateral boundaries the numerical results show that dislocations in the vortex lattice appear first, then nonstationary dynamics sets in. For certain values of the pump parameter stationary TW domains have been also observed numerically.
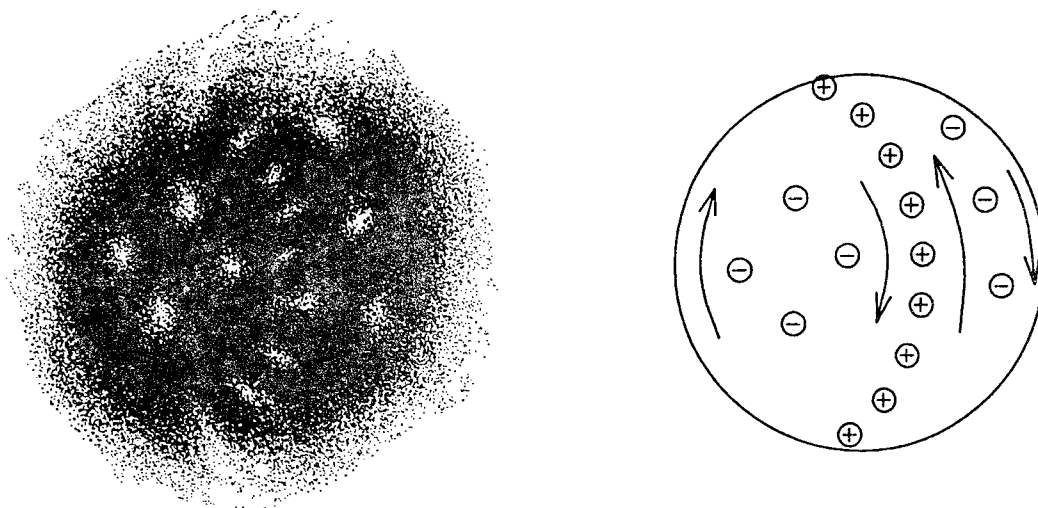
A stationary pattern consisting of domains of TWs directed oppositely and separated by array of vortices

1. K.Staliunas, Phys.Rev. **A48** (1993) 1573.
2. K.Staliunas and C.O.Weiss, "Tilted and Standing Waves and Vortex Lattices in Class-A Laser", Submitted to PRA, 1993.
3. P.K.Jakobsen, J.V.Moloney, A.C.Newell, and R.Indik, Phys.Rev. **A45** (1992) 8129
4. G.D'Alessandro, Phys.Rev. **A46** (1992) 2791.
5. F.T.Arecchi, G.Giacomelli, P.L.Ramazza and S.Residori, Phys.Rev.Lett. **65** (1990) 2531.

Electronic nonlinear optical behaviour of a
grating coupled polymer (4BCMU) waveguide

R.J.Crook, N.P.K.Cotter and J.R.Sambles

Thin Film & Interface Group, Physics Department, University of Exeter, EX4 4QL, UK

Tel: 0392 - 264156

R.Rangel-Rojo, G.Spruce and B.S.Wherrett

Department of Physics, Heriot-Watt University, Riccarton, Edinburgh, EH14 4AS, UK

The nonlinear optical properties of polydiacetylene (PDA) are of interest both fundamentally and technologically. The nonresonant third order susceptibility $\chi^{(3)}$ associated with the nonlinear refractive index n_2 has been found to be relatively large ($>10^{-11}$esu) and ultra-fast ($<$ 1ps). Here we show how the reflectivity response of a grating coupled PDA waveguide can be analysed to yield both the real and the imaginary parts of $\chi^{(3)}$ in a single experiment with the sample in thin film form. Figure 1 shows the absorption spectrum of the blue thermally evaporated P4BCMU with a well defined band-edge at 630nm. The inset shows the experimental waveguide configuration including the optically thick silver layer used to produce the high reflectivities and the low propagation lengths ($\approx$30μm, $<<$beam spot, $r_o = 155\mu$m) allowing a completely rigorous solution of Maxwell's equations [1] in a non-planar system. The laser system is a Nd:YAG operating in TEM$_{oo}$ mode producing 30ps pulses with a 4Hz repetition rate.
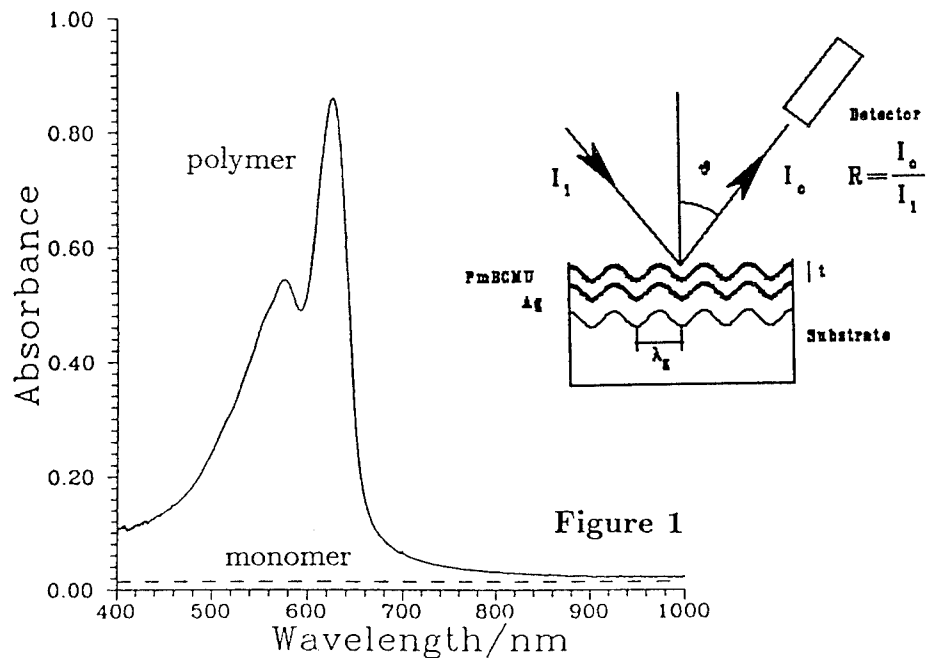
Figure 1

The angular reflectivity scan for the guide at λ =1.064μm using TM-polarized radiation together with the associated electric-field profile at the surface plasmon (SP) coupling angle of 12.84° are shown in figures 2a and 2b respectively. Clearly there has been a decrease in coupling angle $\Delta\theta = -0.10°$ and coupling efficiency $\delta\eta = -20\%$ with increasing irradiance. The fit to the data points for both low (1μJ) and high (10μJ) incident energies is self-consistent, with the polymer dielectric constant ($\epsilon = \epsilon_1 + i\epsilon_2$) allowed to vary as $\epsilon_i = \epsilon_{i0} + \gamma_i|E|^2$ (i=1,2) at each point on the curve where $|E|$ is the local electric field averaged spatially throughout the guide and ϵ_{i0} is the linear value.

Any degeneracies in the fitting procedure are removed by having fitted the data at a wavelength of 632.8nm fixing the thickness of the polymer guide to 0.83μm. These results give values for $\mathrm{Re}(\chi^{(3)}) = -(2.5 \pm 0.4) \times 10^{-11} esu$ which corresponds to $n_2 = -(1.5 \pm 0.2) \times 10^{-4} cm^2 GW^{-1}$ and $\mathrm{Im}(\chi^{(3)}) = (4.0 \pm 0.5) \times 10^{-11} esu$ corresponding to a two-photon absorption coefficient (TPA) of $(28 \pm 4) cmGW^{-1}$. ($\mathrm{Re}(\chi^{(3)}) = 2c\epsilon_o n_o \gamma_1$; $\mathrm{Im}(\chi^{(3)}) = 2c\epsilon_o n_o \gamma_2$; n_o is the linear index and ϵ_o is the permittivity of free-space). Peak local irradiances are around 5 $GWcm^{-2}$.

Figure 2a

Figure 2b
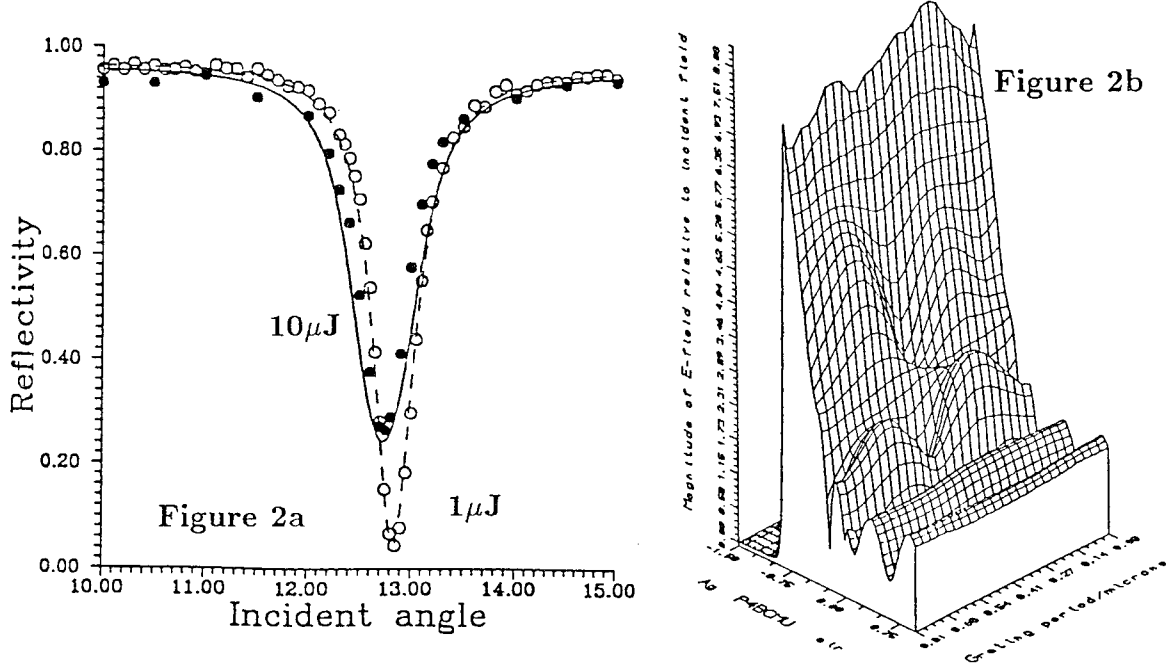
Great care must be taken when assigning an electronic rather than a thermal origin to the observed nonlinearity. Three control experiments are therefore performed to demonstrate the electronic origin of these results. The first experiment concerns the possibility of a thermal perturbation to the surface plasmon coupling conditions. Calculations suggest the electron gas and the lattice of the silver film undergo considerable heating during the 30ps pulse to peak temperatures of around 700K and 200K respectively above room temperature. Work by Van Exter et al [2] allows a prediction of the corresponding changes in ϵ_1 and ϵ_2 for the silver. These are $\Delta\epsilon_1 = +0.10$ (with 80% lattice contribution) and $\Delta\epsilon_2 = +0.15$ (100% lattice). Although these changes are non-negligible, owing to the large dielectric constant of silver at 1.064 μm ($\epsilon_1 = -50$, $\epsilon_2 = 2.80$) calculations show these should not significantly perturb the mode. To confirm this a limiter experiment performed at the SP resonance angle of a substrate | silver interface reveals no irradiance-dependent shift in reflectivity as shown in figure 3.

Damage threshold $\approx 15\mu$J.
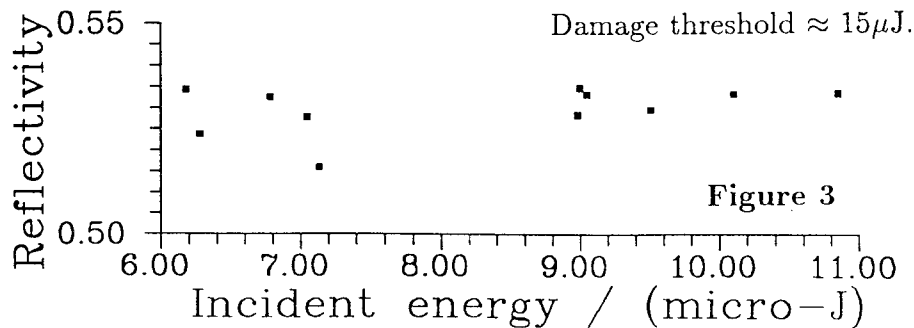
Figure 3

Despite a predicted timescale of ns for the heat generated in the silver to diffuse into the polymer film, concern still remains that this heat transfer could account for the shifts seen in figure 2a. Use is made of the solid-state UV polymerization of PDAs to eliminate this possibility. A *monomer* 4BCMU waveguide is produced with similar thermal properties to the polymer and the shift in reflectivity near the resonance angle monitored with increasing irradiance. The film is then polymerized in situ, effectively switching on the electronic nonlinearity, and the limiter scan repeated near the new resonance angle. The results shown in figure 4 clearly show no nonlinearity for the monomer but a systematic shift for the polymer. On the basis of these results we are confident the observed nonlinear behaviour in the P4BCMU waveguide is electronic in origin. Owing to the relatively large angular half-width of these modes ($\Delta\theta \approx 1°$) the angular detuning from resonance is chosen to maximize $\partial R/\partial\epsilon_i$. This is unnecessary for modes where $\Delta\theta$ is comparable with the observed shifts as is the case with the SP resonance used in figure 3.

Figure 4
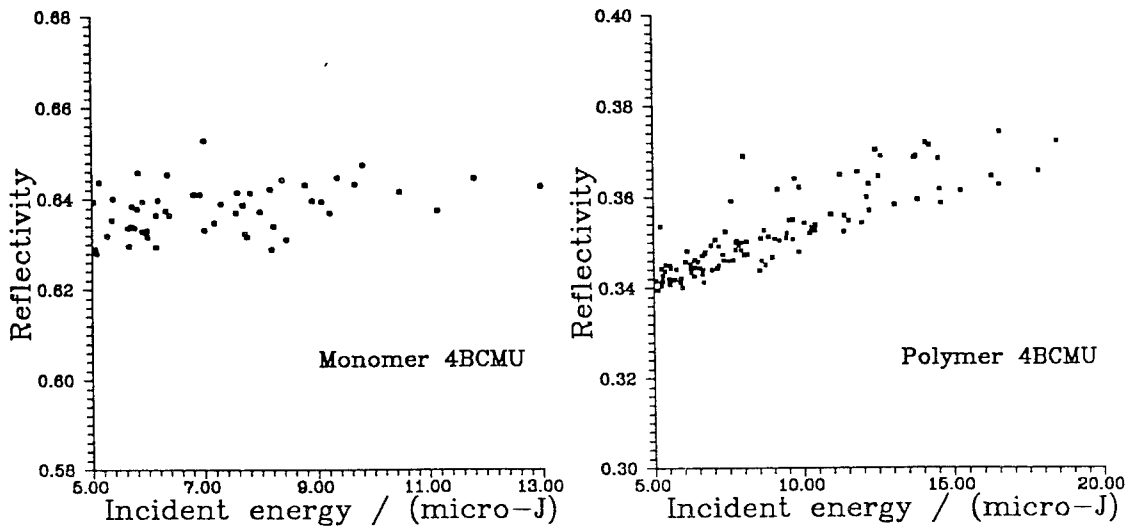
The sign and magnitude of n_2 agree well with a recent self-defocussing experiment giving $n_2 = -(1\text{-}2)\times10^{-4}cm^2GW^{-1}$ [3]. The TPA coefficient lies within the range of reported values $(1.3\text{-}46)cmGW^{-1}$ [4]. It should be noted, however, that these reported TPA results were obtained with red form spun P4BCMU using TE polarization. We believe the anisotropy of the polymer film should make a TE measured TPA value significantly higher ($\times$ 20) than the TM value measured in this work. Clearly this is not consistent with our results and will be the subject of further investigation.

[1] S.J.Elston, G.P.Bryan-Brown and J.R.Sambles, Phys. Rev. B **44**, (1991), 6393

[2] M.van Exter and A.Lagendijk, Phys. Rev. Lett. **60**, (1988), 49

[3] J.Valera, A.Darzi, A.C.Walker, W.Krug, E.Miao, M.Derstine and J.N.Polky , Elect. Lett. **24**, (1990), 222

[4] Nunzi and Grec, J. Appl. Phys. **62**, (1987), 2198

A New Class of Strongly Photorefractive Materials

Richard A. Linke, Tineke Thio, James Chadi and George E. Devlin
NEC Research Institute, Inc., 4 Independence Way
Princeton, New Jersey 08540 phone:(609)951-2632

Certain doped compound semiconductors exhibit persistent photoconductivity (PPC) at low temperatures as a result of the optical ionization of electrons from deep, spatially localized, donor levels known as DX centers (see ref. [1] for a thorough review). We calculate that this release of carriers also produces a refractive index shift (through the plasma effect) which is 30 times larger than that of conventional photorefractive materials. We report the results of diffraction measurements on samples of AlGaAs which support this prediction. The induced index changes can be erased by heating above an annealing temperature determined by the material composition.

Deep donors in AlGaAs exhibit two stable structural states at low temperatures [1-3] as depicted in Figure 1 where the horizontal axis characterizes the position of the donor atom in the lattice. The curve to the left corresponds to the total energy for the usual hydrogenic state of the donor while that to the right corresponds to the donor having captured an electron to become negatively charged [4]. For the $Al_xGa_{(1-x)}As$ system studied here, this DX state is the ground state when $x > 0.22$ and a reduction of the free carrier concentration by many orders of magnitude is observed as the sample temperature is lowered and carriers become trapped in DX centers. [5]

PPC occurs when electrons trapped in DX states are ionized by photons of energy E_{opt}. The

Configuration Coordinate, Q

Figure 1

photo-conversion of all DX centers to ionized shallow donors produces a carrier density equal to the original doping density. Recapture of the electrons, which requires excitation over the capture barrier E_{cap}, does not occur when the temperature is sufficiently low. The carrier concentration remains high indefinitely even after the exciting light source has been removed. [3]. It is this change in carrier concentration which leads to a strong photorefractive effect through an increased polarizability of the free carriers (the plasma effect). If the exposing light intensity is a function of position, as in the formation of a holographic grating, a spatial variation in the degree of ionization of DX centers occurs. We estimate that the electrons liberated by the ionization of DX centers are constrained by Coulombic attraction to remain within ~100nm of the positive ions they leave behind. The resulting spatial variation in refractive index can lead to the formation of a diffraction grating.

We have made a series of measurements on 1.0 μm thick Si doped samples of $Al_{0.27}Ga_{0.73}As$ grown by molecular beam epitaxy on GaAs substrates which were polished on the back to allow for optical transmission. A wafer was cleaved into rectangular samples (2 x 4 mm) for conductance and carrier concentration (Hall effect) measurements and square samples (6 x 6 mm) for optical diffraction measurements.

Samples were put into the highly resistive state, with carriers trapped in DX centers, by cooling in the dark from room temperature to 20K. Carrier concentration, $N(cm^{-3})$, was then measured as a function of exposure to HeNe laser light. Figure 2 shows the change in carrier concen-

tration, $\Delta N (cm^{-3})$, relative to the unexposed case. At saturation, which occurs at a fluence near 1 mJcm^{-2}, ΔN reaches 4×10^{18}cm^{-3}. Below a fluence of ~100 µJcm^{-2}, ΔN is seen to be linear in exposure with a quantum efficiency near unity. Theoretically, the maximum quantum efficiency is 2 since the absorption of each photon by a negatively charged DX center releases *two* electrons into the conduction band. [4]
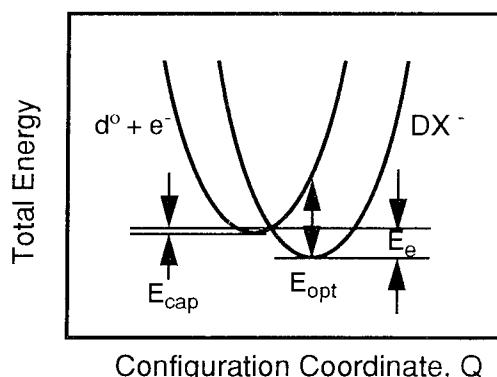
Figure 2

In order to measure the change in refractive index resulting from the carrier concentration change, a diffraction grating was written into the sample using two interfering beams of HeNe laser light. The interference caused a linear fringe pattern at the sample with a grating period of 32 µm. A high degree of conductance anisotropy was found in samples which had been exposed in this way, indicating that a grating in carrier concentration was impressed in the material.

Exposed samples were examined for the presence of a transmission grating using a probe beam at 1.5 µm wavelength. The 0.83 eV energy of the probe photons is too low to cause ionization of the remaining DX centers. A typical measurement of intensity versus diffraction angle is plotted in Figure 3, where zero angle refers to the position of the zeroth order, undiffracted beam (which is attenuated by about 50% by reflections at the sample surfaces). Both first-order diffracted beams are seen in the scan, at the expected angle, with a diffraction efficiency of 1.3×10^{-4}. To our knowledge this is the first observation of diffraction resulting from the photoionization of DX centers. Second order peaks are also visible at about one tenth the efficiency of first order. The baseline scan in Figure 3 was taken after the sample was subjected to a large uniform fluence (>10 mJcm^{-2}) of HeNe laser light to ionize all DX centers. Neither diffraction nor conductivity anisotropy was observed in the sample after this exposure, indicating that the grating was no longer present. Features seen in both scans at -0.7 degrees result from a spurious reflection in the apparatus.

We determine the refractive index change in our 1 µm thick epitaxial sample from the following expression for the diffraction efficiency of a phase grating [6]: $\eta = e^{-\alpha d} sin^2 (\pi \Delta nd/\lambda_0)$. Here α is the absorption coefficient, d is the grating thickness and λ_0 is the read-out wavelength in vacuum (1.5µm). Ignoring the (very low) absorption due to the substrate, we find an index change of $\Delta n = 5.8 \times 10^{-3}$ which is 30 times larger than the Δn reported for conventional photorefractive materials such as BaTiO$_3$ [6].

We now estimate the expected index change due to the plasma effect. There is no conventional photorefractive effect here since both exposed and unexposed regions are electrically neutral. The dielectric constant, $\varepsilon(\omega)$, of a semiconductor is given by: $\varepsilon(\omega) = \varepsilon_0(\omega) - \omega_p^2/\omega^2$. Here ω is the measurement frequency, $\varepsilon_0(\omega)$ is the dielectric constant in the absence of the plasma, and ω_p is the plasma resonance frequency given by $\omega_p^2 = 4\pi Ne^2/m^*$, where N is the carrier density, m^* is the carrier's effective mass, and e is its charge. We find for the expected refractive index change due to a carrier concentration change (for $\omega >> \omega_p$): $\Delta n = -(2\pi \Delta Ne^2)/(n_0 m^* \omega^2)$. Taking a carrier den-

trons in the Γ-band (normalized to the free-electron rest mass) of 0.09, we find an expected index change Δn of 6.5 x 10^{-3} compared with our experimentally determined value of 5.8 x 10^{-3}.
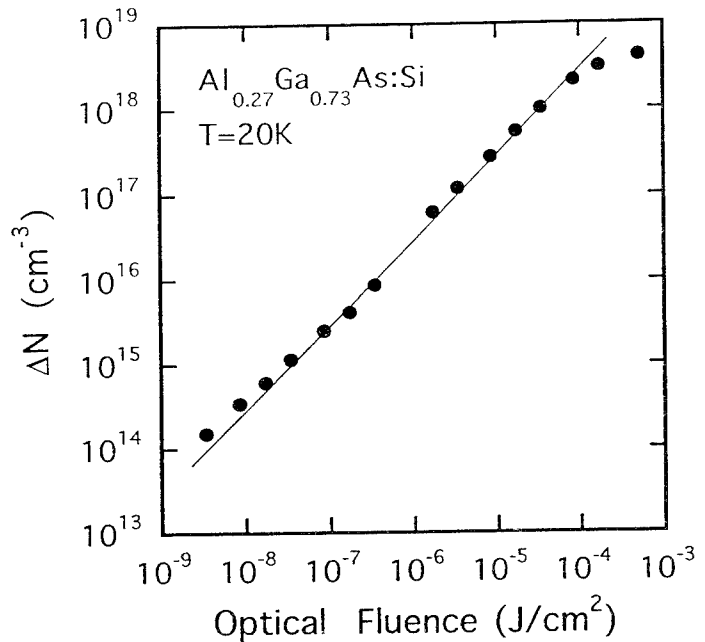
The value of E_{cap} (Fig. 1), which determines the maximum temperature of operation for both PPC and this new photorefractive effect, depends on the material composition. In the $Al_xGa_{(1-x)}As$ system, persistent photoconductivity is stable at liquid nitrogen temperatures for $x \approx 0.3$. Furthermore, PPC at room temperature may be possible with wide bandgap II-VI compounds: DX centers similar to those in AlGaAs have been observed in ZnCdTe:In [7] and PPC has been reported in CdS:Cl at temperatures up to 250K, though it is not currently known whether this is caused by DX centers or by some other mechanism. [8].

In addition to its larger index change, this new effect offers several other advantages over conventional photorefractive materials, e.g., once index changes are "written" they are not erased by subsequent expo-

Figure 3

sures. This significantly reduces the energy required to write and dramatically increases the number of possible stored holograms. [9]. Thermal erasure is possible and we are investigating the possibility of optical erasure.

We would like to thank Dr. M. Mizuta of the NEC Tsukuba laboratory for providing early samples for this study and for his useful advice on techniques for obtaining reliable ohmic contacts. We are grateful to J. Bennett for his technical assistance and to Dr. R. MacDonald for useful discussions and help with sample preparation.

References

[1]P. M. Mooney, J. App. Phys. **67**, R1 (1990).

[2] D. V. Lang and R. A. Logan, Phys. Rev. Lett. **39**, 635 (1977).

[3] D.V. Lang, R.A. Logan and M. Jaros, Phys. Rev. B **19** 1015 (1979).

[4] D. J. Chadi and K. J. Chang, Phys. Rev. B **39**, 10 063 (1989).

[5] N. Chand, T. Henderson, J. Clem, W.T. Masselink, R. FIscher, Y.C. Chang and H. Morkoc, Phys. Rev. B **30**, 4481 (1984).

[6] J. Hong, P. Yeh, D. Psaltis and D. Brady, Optics Lett. **15**, 334 (1990).

[7] K. Khachaturyan, M. Kaminska, E. R. Weber, P. Becla, and R. A. Street, Phys. Rev. B **40**, 6304 (1989).

[8] E. Harnik, Solid State Electronics, **8**, 931 (1965).

[9] D. Psaltis, D. Brady, and K. Wagner, Appl. Optics **27**, 1752 (1988).

DX.non.lin.conf.940221.a
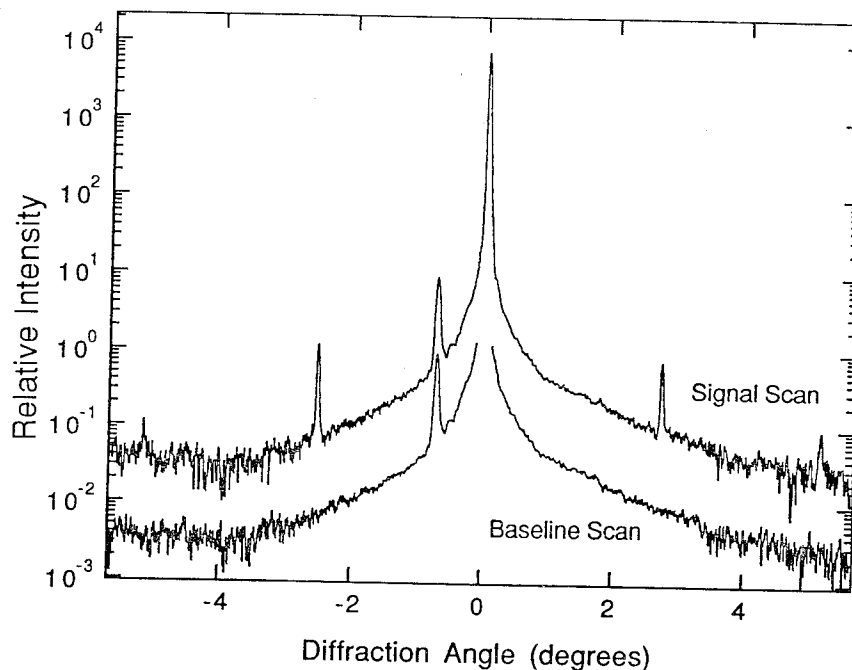
Crosstalk control for multiplex holography

M. C. Bashaw*, J. F. Heanue[†], and L. Hesselink*

*Department of Electrical Engineering,
Stanford University, Stanford, CA 94305-4035

[†]Department of Applied Physics,
Stanford University, Stanford, CA 94305-4090

Tel. 415 723-2166   FAX 415 725-3377

A number of spatially nonlinear-optical materials, such as photorefractive media, are suitable for volume holography. High Bragg selectivity of thick media has led to the development of applications of multiplex volume holography ranging from binary and analog data storage, to associative memory, to neural networks, to optical interconnects. An important consideration is the balance between capacity and noise. We examine here crosstalk for angular, phase-encoded, and wavelength multiplexing for holographic data storage and describe the properties of null-matched arrangement of reference waves, presenting new results for adjacent, sparse, and fractal strategies. We emphasize the impact of signal bandwidth on crosstalk and describe how crosstalk limits storage capacity. We consider first crosstalk due to Bragg mismatch (mismatch-limited crosstalk), and then relate it to other noise sources present in a holographic memory system.

Angular multiplexing is perhaps the most widely studied technique for superimposing pages of holographic data in a medium. For several multiplexing strategies, we are interested in evaluating the capacity using a crosstalk criterion, for which we define the signal-to-crosstalk ratio (SXR) as the ratio between the ensemble average of intensity of the desired signal to the ensemble average of the undesired reconstruction. Early estimates for mismatch-limited crosstalk by Ramberg are based on the average occurrence of crosstalk arising from Bragg mismatch for randomly ordered reference waves, with the signal-to-crosstalk ratio estimated to be [1]:

$$\text{SXR} = \frac{1}{N}\frac{2nL}{\lambda},$$ (1)

in which L is the length of the medium, λ is the wavelength of light in free space, n is the index of refraction, and N is the number of stored holograms.

Angular selectivity is optimized for perpendicular signal and reference wavevectors [2, 3, 4, 5], which is especially important for media in which forward and back scattering dominate. We evaluate a number of angular and other monochromatic multiplexing techniques in which signal and reference wavevectors lying in a plane of incidence are centered essentially normal to perpendicular surfaces of a medium and placed at the nulls of the angular selectivity function. Careful selection of reference reference beams permits significant improvement over the Ramberg limit. For paraxial signal waves, Gu *et al.* place plane reference waves at adjacent nulls, for which [3]:

$$\text{SXR} = \frac{1}{N}\frac{2nL}{\lambda}\frac{1}{\text{n.a.}},$$ (2)

in which n.a. is the numerical aperture of the stored signal.

Because of constraints of peripheral devices, it may be necessary to space the reference waves as sparsely as possible for a given range of reference wavevectors, in which N_B is the maximum number of accessible reference wavevectors for a given optical system [5]. For proper placement of reference waves, the same signal-to-noise ratio may be achieved as for adjacent spacing [Eq. (2)].

We compare these techniques and identify additional strategies to improve crosstalk performance in a holographic storage system. We show that for fractal geometries in which additional reference beams are included out of the plane of incidence, as implemented experimentally by Mok [4], mismatch-limited signal-to-crosstalk ratio can be estimated by

$$\text{SXR} = \frac{N_x}{N} \frac{2nL}{\lambda} \frac{1}{\text{n.a.}},\tag{3}$$

in which N_x is the additional number of rows out of the primary plane of incidence.

We show further that phase-encoded multiplexing of high-bandwidth signals results in modest improvement in mismatch-limited crosstalk over angular multiplexing and compare the strategies outlined here for angular multiplexing to similar strategies for wavelength multiplexing. For example, for wavelength multiplexing in a counterpropagating geometry with adjacent spacing, the mismatch-limited signal-to-crosstalk ratio is estimated to be [6]

$$\text{SXR} = \frac{4}{(\text{n.a.})^2}.\tag{4}$$

We show that for sparse spacing of wavelengths, mismatch-limited crosstalk can be improved, such that

$$\text{SXR} = \frac{N_B}{N} \frac{4}{(\text{n.a.})^2}.\tag{5}$$

The criteria for comparison discussed above are based on ensemble averages of mismatch-limited crosstalk. We discuss the validity of these estimates and the impact of the variance of crosstalk on system performance. Additional sources of crosstalk are dispersion in the response of the medium as a function of grating vector and limitations in the accuracy of peripheral devices. Furthermore, scatter arising from imperfections in the active medium will contribute to noise along with crosstalk. Figure 1 compares the contributions of crosstalk and scatter to overall signal-to-noise for angular multiplexing and shows that only for high-optical-quality materials will crosstalk be the limiting criterion. We discuss how these estimates can be used to evaluate total bit capacity of a volume holographic storage architecture for a number of signal pixel arrangements.

References

[1] E. G. Ramberg. *RCA Review*, **33**:5–53, (1972).

[2] E. N. Leith, A. Kozma, J. Upatnieks, J. Marks, and N. Massey. *Appl. Opt.*, **5**:1303–1311, (1966).

[3] C. Gu, J. Hong, I McMichael, R. Saxena, and F. Mok. *J. Opt. Soc. Am. A*, **9**:1978–1983, (1992).

[4] F. H. Mok. *Opt. Lett.*, **18**:915–917, (1993).

[5] M. C. Bashaw, A. Aharoni, J. F. Walkup, and L. Hesselink. *submitted to J. Opt. Soc. Am. B*.

[6] K. Curtis, C. Gu, and D. Psaltis. *Opt. Lett.*, **18**:1001–1003, (1993).
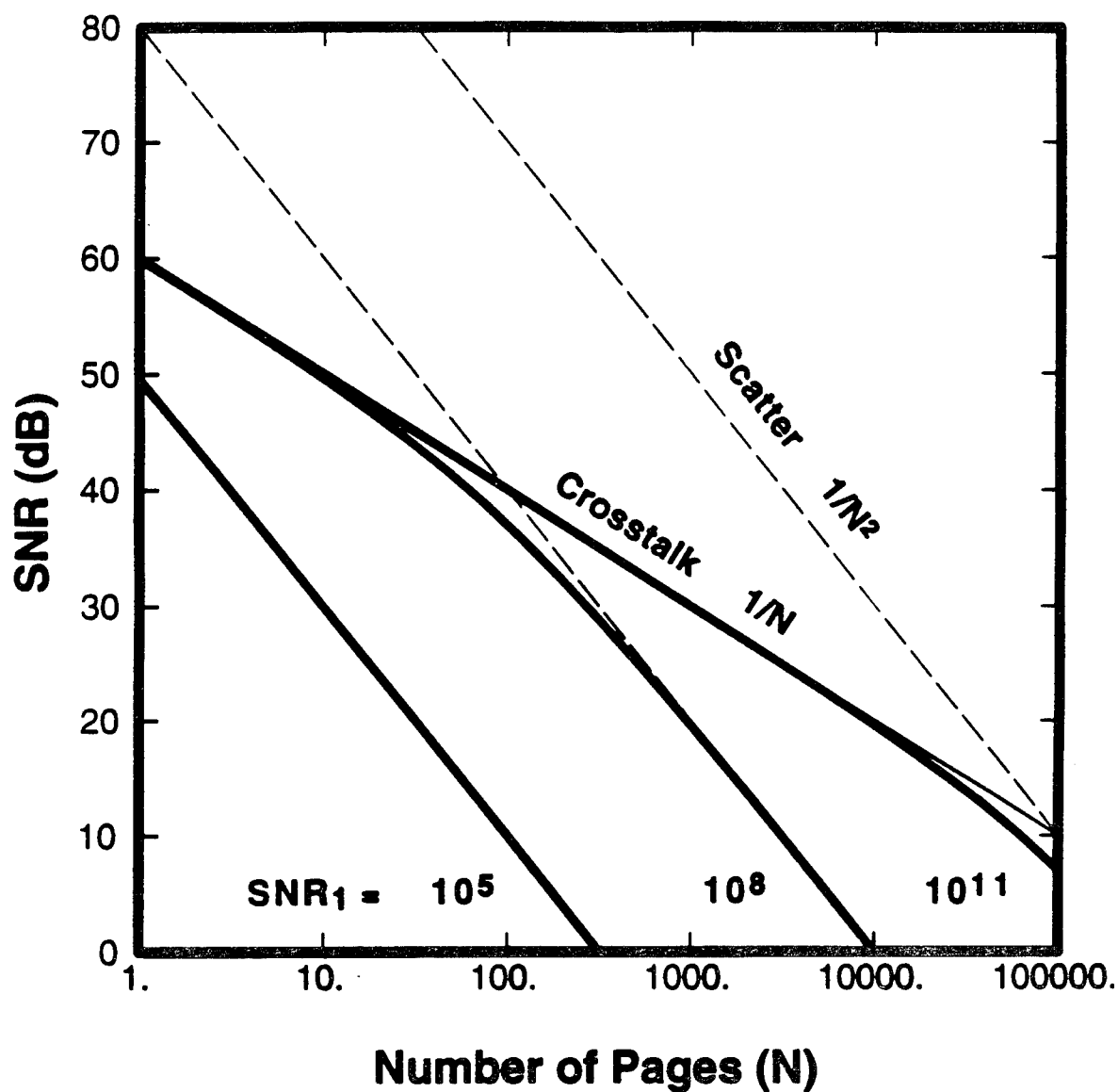
Figure 1: Signal-to-noise ratio (SNR) for angular multiplexing as a function of the number of pages, shown here for 10^5 available pages and signal n.a. $= 0.1$. This corresponds, for example, to a medium with $n = 2.5$, $L = 1$ cm, and $\lambda = 500$ nm, for adjacent multiplexing. The maximum SNR for a single hologram without superposition, SNR_1, is (a) 10^5, (b) 10^8, and (c) 10^{11}. The thin line represents the contribution to SNR due to crosstalk alone, the dashed lines represent the contribution to SNR due to undesired scatter alone, and the thick lines represent the net SNR for each case. (After Bashaw et al. [5].)

Theory of Ultrafast Nonlinear Refraction in Zinc-Blende Semiconductors

D.C. Hutchings

Department of Electronics and Electrical Engineering, University of Glasgow,
Glasgow G12 8QQ, U.K., Tel: 041-339-8855

and B.S. Wherrett

Department of Physics, Heriot-Watt University, Edinburgh EH14 4AS, U.K.

The ultrafast nonlinear refractive index n_2 has been of recent interest, particularly in semiconductors, due to the possibility of fabricating compact, integrated all-optical switching elements [1]. It has shown that n_2 can be obtained by a nonlinear Kramers-Krönig transform of the (nondegenerate) nonlinear absorption (e.g. two-photon absorption) [2]. Applying a two parabolic band model for a semiconductor provides the material scaling and approximate dispersion of n_2 [3], although the resulting quantity has to be scaled by a constant factor to fit experimental data. As has been shown for two-photon absorption [4], this difference is probably due to the neglection of the multiple valence bands near the centre of the Brillioun zone. In this paper, the more realistic bandstructure model of Kane [5] (consisting of a conduction band and heavy-hole, light-hole and split-off valence bands) will be employed in the determination of n_2. Rather than use a nonlinear Kramers-Krönig transform, instead a direct calculation of n_2 will be performed which is numerically simpler and also ensures that all nonresonant terms are properly accounted for.

The nonlinear refractive index n_2 (defined $\Delta n = n_2 I$) for linearly polarised light and isotropic media (Kane bandstructure is isotropic) is given by,

$$n_2(\omega) = \frac{3}{4\varepsilon_0 c n_0^2} \operatorname{Re} \chi_{xxxx}^{(3)}(-\omega, \omega, \omega). \tag{1}$$

From a density matrix treatment based on a $\mathbf{A}.\mathbf{p}$ perturbation, the third-order susceptibility is in general,

$$\chi_{ijkl}^{(3)}(\omega_1, \omega_2, \omega_3) = -\frac{e^4}{3! \hbar^3 \varepsilon_0 m_0^4} \frac{1}{(\omega_1 + \omega_2 + \omega_3)\omega_1 \omega_2 \omega_3}$$

$$\times S_T \sum_{g,\alpha,\beta,\gamma} \frac{\left(\hat{\mathbf{e}}_i^* \cdot \mathbf{p}_{g\alpha}\right)\left(\hat{\mathbf{e}}_j \cdot \mathbf{p}_{\alpha\beta}\right)\left(\hat{\mathbf{e}}_k \cdot \mathbf{p}_{\beta\gamma}\right)\left(\hat{\mathbf{e}}_l \cdot \mathbf{p}_{\gamma g}\right)}{\left(\Omega_{g\alpha} - \omega_1 - \omega_2 - \omega_3\right)\left(\Omega_{g\beta} - \omega_2 - \omega_3\right)\left(\Omega_{g\gamma} - \omega_3\right)}, \tag{2}$$

where m_0 is the free electron mass, $\hat{\mathbf{e}}_i$ is the unit vector in the direction of the ith polarisation and $\mathbf{p}_{\alpha\beta}$ and $\hbar\Omega_{\alpha\beta}$ are the momentum matrix element and energy difference respectively, taken between the electronic states α and β. Here S_T denotes that the expression which follows it is to be summed over all 24 permutations of the pairs $(i, \omega_1 + \omega_2 + \omega_3)$, (j, ω_1), (k, ω_2) and (l, ω_3). Four of these permutations can be associated with two-photon resonant transitions and four more give rise to the triply resonant one-photon band edge nonlinear refraction [6]. The form of $\chi^{(3)}$ given in eq. (2) has been recognised since the 1960's [7]. However the subsequent evaluation for n_2 in solids has not been possible in general due to the fact that some of the terms diverge when one or more of the frequency denominators are zero. We demonstrate that such a summation can be performed by appropriately grouping terms such that cancellation of the divergences is obtained before numerical evaluation.

The resonances in eq. (2) are of two types: real resonances when both the transition frequency and combination of optical frequencies are finite (but cancel) and secular resonances when both the transition frequency and combination of optical frequencies

are both zero. Secular resonances occur solely as a result of expressing the nonlinear susceptibility as a summation of terms in eq. (2) and should cancel. To deal with both forms of resonances, the analytic continuation of ω is taken, $\omega_n \to \omega_n + i\varepsilon$ and the limit $\varepsilon \to +0$ is only considered after the summation. This eliminates the secular resonances and for the real resonances, the real part of $\chi^{(3)}$ is then given by the principal value. The corresponding imaginary part contains the Dirac delta function and at the appropriate frequency provides the two-photon absorption coefficient [8].

There are two equivalent approaches to performing the sum over the electronic states g, α, β, γ in eq. (2) [6]. In the one electron approach [7] the summation is performed as it is set out in eq. (2) ignoring the Pauli exclusion principle for the virtual states α, β, γ. Alternatively the "Pauli-allowed" approach can be employed where the Pauli exclusion principle is applied at each stage and multiple electronic transitions are allowed, but all possible time orderings must be summed over. In the "Pauli-allowed" approach the frequency mis-match at each stage is used for the denominators, but is further complicated by the fact that the reversal of some of the Fermi operators leads to a factor of -1 in some of the terms. However, in spite of its complexity the "Pauli-allowed" approach will be employed as numerically there are divergences in some of the terms in the one electron approach when the optical frequency is equal to an inter-valence band transition (although analytically these divergences cancel).
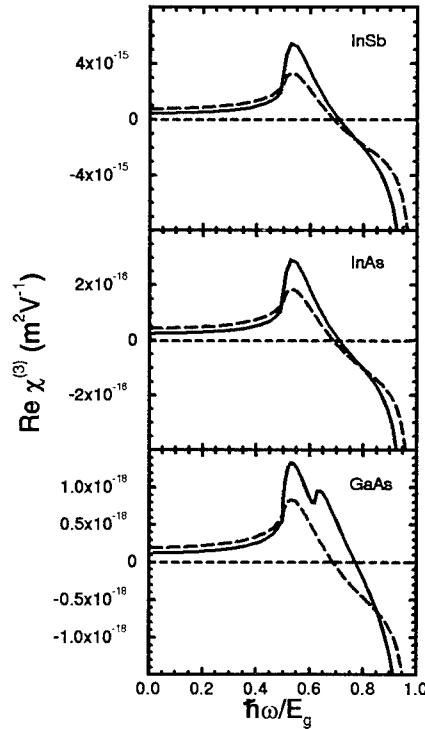
Fig. 1 The calculated dispersion of $\mathrm{Re}\,\chi^{(3)}_{xxxx}$ *for the semiconductors InSb, InAs and GaAs, where the photon energy has been scaled to the bandgap. The solid line is the result of the present calculation and the dashed line is the result of the two parabolic band nonlinear Kramers-Krönig calculation [3] (scaled to semiconductor two-photon absorption data).*

On calculating the real part of $\chi^{(3)}$ for the Kane bandstructure it is found there is a divergence at zero frequency which behaves as ω^{-4}. This divergence can be shown to be proportional to the nonparabolicity integrated over the Brillioun zone [8].

Periodicity dictates that this should vanish for an intrinsic semiconductor and in the present case is purely an artifact of expanding the wavefunctions around the Γ point. This divergence is therefore unphysical and is subtracted from the calculated nonlinear susceptibility.

The result for $\mathrm{Re}\,\chi_{xxxx}^{(3)}$ is shown in fig. 1 for the semiconductors InSb, InAs and GaAs. For comparison, the dashed curves show the result of the nonlinear Kramers-Krönig calculation for two parabolic bands when scaled to semiconductor two-photon absorption data (60% increase to account for the valence band degeneracy). It can be seen that the main difference in comparing these two models is the larger resonance at the two-photon band edge for the Kane bandstructure. This explains the apparently anomalously large value of n_2 measured for ZnTe at 1064nm [3] (although the Z-scan measurements in [3] are consistently a factor of two larger than both theoretical calculations). Another point to note is the second peak in n_2 for GaAs due to the split-off band.

In fig. 2 the dispersion of n_2 is shown in the vicinity of the two-photon edge for $Al_{0.18}Ga_{0.82}As$. The experimental points are the self-phase modulation measurements in [9]. It should be noted that for the present calculation, the values shown are directly from the calculation (i.e. no subsequent fitting has been used). It can be seen that the increased two-photon resonance in n_2 with the Kane bandstructure is required to account for the experimental data. The slight difference between experiment and theory at long wavelengths is likely to be due to band tailing which is not accounted for in the idealised bandstructure model.
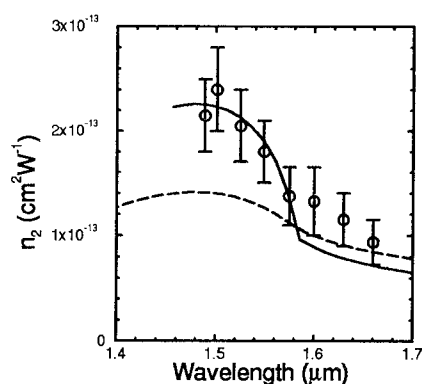
Fig. 2 The dispersion of the nonlinear refractive index n_2 around the two-photon band edge for $Al_{0.18}Ga_{0.82}As$. The solid line is the present calculation, the dashed line the two-parabolic band nonlinear Kramers-Krönig calculation [3] and the experimental points are waveguide self-phase modulation measurements [9].

References
[1] J.S. Aitchison, A.H. Kean, C.N. Ironside, A. Villeneuve and G.I. Stegeman, Electron. Lett. **27**, 1709 (1991).
[2] D.C. Hutchings, M. Sheik-Bahae, D.J. Hagan and E.W. Van Stryland, Opt. Quantum Electron. **24**, 1 (1992).
[3] M. Sheik-Bahae, D.C. Hutchings, D.J. Hagan and E.W. Van Stryland, IEEE J. Quantum Electron. **27**, 1296 (1991).
[4] D.C. Hutchings and E.W. Van Stryland, J. Opt. Soc. Am. B **9**, 2065 (1992).
[5] E.O. Kane, J. Phys. Chem. Solids **1**, 249 (1957).
[6] B.S. Wherrett, Proc. R. Soc. Lond. A **390**, 373 (1983).
[7] P.N. Butcher and T.P. McLean, Proc. Phys. Soc. **81**, 219 (1963).
[8] D.C. Hutchings and B.S. Wherrett, Opt. Mat. **3** (1994).
[9] A. Villeneuve, C.C. Yang, G.I. Stegeman, C.-H. Lin and H.-H. Lin, Appl. Phys. Lett. **62**, 2465 (1993).

Theory of Anisotropy of Two-Photon Absorption in Zinc-Blende Semiconductors

D.C. Hutchings
Department of Electronics and Electrical Engineering, University of Glasgow,
Glasgow G12 8QQ, U.K., Tel: 041-339-8855

and B.S. Wherrett
Department of Physics, Heriot-Watt University, Edinburgh EH14 4AS, U.K.

Two-photon absorption (2PA) in semiconductors is of interest as it provides a nonlinear spectroscopic technique in addition to having important consequences for all-optical switching. Earlier calculations and measurements of 2PA in zinc-blende semiconductors have concentrated on the linearly polarised single-beam case e.g. [1,2], that is ignoring any polarisation dependence. This polarisation dependence can take two forms. First, there is a dependence on the type of optical polarisation employed that in the single beam case gives a difference between linearly and circularly polarised light [3]. This variation can occur even for isotropic media. Second, there is a variation in the 2PA coefficient depending on the relative orientation of the optical polarisation with the crystalline axes which will be the main topic of this paper.

For the cubic symmetry appropriate for zinc-blende structures, there are only four independent non-zero third-order optical susceptibility tensor elements, $\chi^{(3)}_{xxxx}$, $\chi^{(3)}_{xyxy}$, $\chi^{(3)}_{xyyx}$ and $\chi^{(3)}_{xxyy}$. Furthermore for degenerate (single frequency) nonlinear absorption and refraction, permutation symmetry dictates that two of these are equal, $\chi^{(3)}_{xyyx}(-\omega,\omega,\omega) = \chi^{(3)}_{xyxy}(-\omega,\omega,\omega)$ giving just three independent non-zero tensor elements. The 2PA coefficient is directly related to the imaginary part of the third-order susceptibility [3]. For linearly polarised light where the polarisation direction is orientated at (θ,ϕ) with respect to the crystalline axes,

$$\beta^L(\theta,\phi) = \beta^L[001]\left[1 - \frac{\sigma}{2}\left(\sin^2 2\theta + \sin^4\theta\sin^2 2\phi\right)\right], \tag{1}$$

and for circularly polarised light with a propagation direction $(\theta_\kappa,\phi_\kappa)$ with respect to the crystalline axes,

$$\beta^C(\theta_\kappa,\phi_\kappa) = \beta^L[001]\left[1 - \delta - \frac{\sigma}{8}\left(\sin^2 2\theta_\kappa + \sin^4\theta_\kappa\sin^2 2\phi_\kappa\right)\right]. \tag{2}$$

Here the 2PA coefficient has been scaled to its value for linearly polarised light orientated parallel to a principal axis,

$$\beta^L[001] = \frac{3}{2}\frac{\omega}{\varepsilon_0 n_0^2 c^2}\operatorname{Im}\chi^{(3)}_{xxxx}. \tag{3}$$

The two-photon anisotropy parameter σ is conventionally defined as,

$$\sigma = \frac{\operatorname{Im}\chi^{(3)}_{xxxx} - \operatorname{Im}\chi^{(3)}_{xxyy} - 2\operatorname{Im}\chi^{(3)}_{xyxy}}{\operatorname{Im}\chi^{(3)}_{xxxx}} = 2\frac{\beta^L[001] - \beta^L[011]}{\beta^L[001]}, \tag{4}$$

and we also define a two-photon absorption incremental dichroism parameter δ as

$$\delta = \frac{\operatorname{Im}\chi^{(3)}_{xxxx} + \operatorname{Im}\chi^{(3)}_{xxyy} - 2\operatorname{Im}\chi^{(3)}_{xyxy}}{2\operatorname{Im}\chi^{(3)}_{xxxx}} = \frac{\beta^L[001] - \beta^C(\theta_\kappa = 0)}{\beta^L[001]}. \tag{5}$$

These three parameters which can be used to obtain the general 2PA coefficient, $\beta^L[001]$, σ and δ, can be obtained experimentally with just three measurements (two using linear polarisation of different orientations and one with circular polarisation). Theoretically, these parameters can be obtained by calculating the three independent nonlinear susceptibilities.

The three third-order optical susceptibility tensor elements can be determined from a density-matrix treatment [3,4]. For direct-gap semiconductors, the long-wavelength end of the 2PA spectrum is entirely due to electronic states in the vicinity of the zone centre. The band structure of Kane [5] (consisting of a conduction band and heavy-hole, light-hole and split-off valence bands) is sufficient to obtain a linear/circular dichroism in the two-photon absorption coefficient [3]. However, as the resulting bandstructure is completely isotropic, it is insufficient to account for the anisotropy in the 2PA coefficient. Here, we account for the anisotropy in the bandstructure by including the next highest conduction band set (of symmetry Γ_{15}) [6]. For both bandstructure models, the **k.p** plus spin-orbit coupling Hamiltonian is diagonalised numerically and so automatically includes higher order terms in k that gives rise to such effects as nonparabolicity.

Figure 1 shows the calculated spectral dependence of the three independent $\mathrm{Im}\,\chi^{(3)}$ tensor elements for GaAs based on low temperature bandstructure data. It can be seen that the effect of the upper conduction band set is to enhance the off-diagonal elements and to slightly suppress the diagonal elements. The observed change in gradient around $\hbar\omega = 0.95$ eV is due to the threshold of transitions from the split-off valence band.
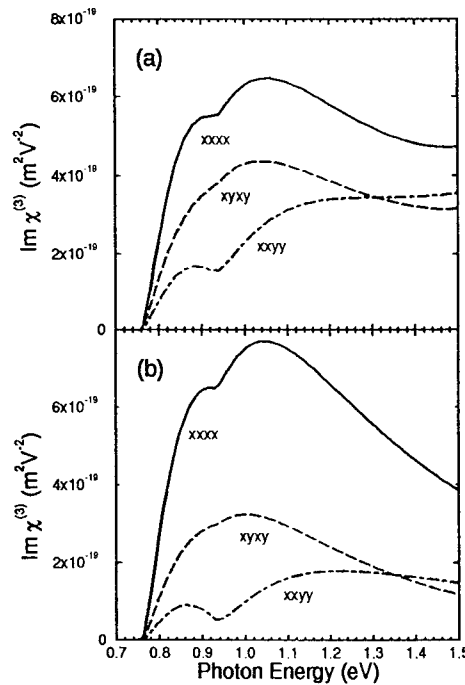
Fig. 1 The calculated spectral dependence of the three independent, degenerate $\mathrm{Im}\,\chi^{(3)}$ tensor elements for GaAs. (a) shows the anisotropic result obtained by including the upper conduction band set Γ^c_{15} and (b) shows the equivalent isotropic result obtained without the upper conduction bands.

The calculated susceptibilities are used to determine the spectral dependence of the anisotropy parameter σ and the incremental dichroism parameter δ for the semiconductors GaAs and InSb (based on low temperature bandstructure data) and are shown in figure 2. It can be seen that σ is always negative indicating that the 2PA coefficient for linearly polarised light has its minimum when the polarisation vector is parallel to the crystal axis. There is a variation of about a factor of 2 in σ from just above the two-photon band to the one-photon edge with the magnitude of σ becoming

large at the two-photon edge due to "allowed-allowed" transitions via the upper conduction bands. For the dichroism parameter δ both the results of the anisotropic and isotropic band structures are shown. The main feature is the minimum at the split-off threshold. The offset between the two curves for GaAs is almost entirely due to the anisotropy; if instead the dichroism is calculated for propagation in the [111] direction (for which there is no angular variation in the 2PA coefficient), one obtains almost identical results from the two bandstructure models.

The 2PA anisotropy values calculated here for GaAs are in good agreement with experimental results (for the same photon energy to band gap ratio). Van der Ziel [6] determined $\sigma = -0.45 \pm 0.06$ at $\hbar\omega = 0.8$ eV by measuring the band edge photoluminescence at low temperatures (-0.48 predicted). Direct measurements include that of Dvorak et al [7], $\sigma = -0.76$ at 950nm (-1.0 predicted) and that of DeSalvo et al [8], $\sigma = -0.74 \pm 0.18$ at 1064nm (-0.9 predicted). A value of $\sigma = -1$ gives a ratio of maximum (polarisation parallel to [111]) to minimum (polarisation parallel to [001]) 2PA coefficients for linearly polarised light of 5/3.
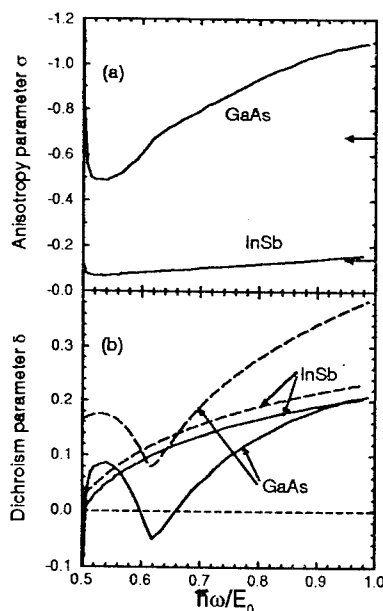
Fig. 2 Spectral dependence of (a) the 2PA anisotropy parameter σ and (b) the incremental dichroism parameter δ for the semiconductors GaAs and InSb. The arrows denote the value of $-2E\left(\Gamma_{15}^v \rightarrow \Gamma_1^c\right) / E\left(\Gamma_{15}^v \rightarrow \Gamma_{15}^c\right)$ which proves to be a useful first estimate of σ [8]. The solid lines correspond to the anisotropic bandstructure model with the upper conduction band set and the dashed lines to the isotropic bandstructure model.

References
[1] M.H. Weiler, Solid State Commun. 39, 937 (1981).
[2] E.W. Van Stryland et al, Opt. Eng. 24, 613 (1985).
[3] D.C. Hutchings and B.S. Wherrett, Opt. Mater. 3 (1994).
[4] D.C. Hutchings and B.S. Wherrett, to be published in Phys. Rev. B (1994).
[5] E.O. Kane, J. Phys. Chem. Solids 1, 249 (1957).
[6] P. Pfeffer and W. Zawadzki, Phys. Rev. B 41, 1561 (1990).
[7] J.P. van der Ziel, Phys. Rev. B 16, 2775 (1977).
[8] M.D. Dvorak, W.A.Schroeder, D.R. Andersen, A.L. Smirl and B.S. Wherrett, to be published in IEEE J. Quantum Electron. (1994).
[9] R. DeSalvo et al, Opt. Lett. 18, 194 (1993).

Theory of the Teraherz Radiation via excitation
of the semiconductor structures above the absorption edge.

J. B. Khurgin

Department of Electrical and Computer Engineering

The Johns Hopkins University Baltimore MD 21218

Below the band gap optical excitation of the ultrashort electrical pulses in the semiconductors due to the optical rectification have been studied by numerous groups. The situation when the excitation pulse is above the bandgap have not been studied up until recently, since, it had been assumed that (a) the response time is determined by the recombination time (i.e. it is slow) and (b) the screening effects will severely attenuate the effect However, in recent results [1,2] strong THZ radiation had been observed.

We have developed the simple theory that explains how high intensity teraherz radiation is obtained in zinc-blende materials and in the two-dimensional structures despite the constraints mentioned above. Our theory uses the combination of Kane **k·p** theory and bond charge theory of the nonlinear susceptibilities.

We have shown that the optical rectification tensor has two different components. The first ultrafast (virtual) component has the "refractive-index-like" dispersion and relatively small magnitude. The second component is real and is associated with the absorption of electron from the bonding orbital of the valence band into the antibonding orbital of the conduction band. The temporal response of this component and its strength are determined primarily by the scattering rates in the valence band. i.e. the second component occurs on the 0.1 ps scale. The dispersion of this component follows the absorption coefficient. When the photon energy surpasses the bandgap energy by more than few meV the second component "overwhelms" the first one. The results of our calculation for GaAs are shown in Fig.1

We have also performed calculations for the strained materials and for the quantum wells showing that in such structures the reversal of the sign of the $\chi^{(2)}$ observed in [2] can take place.

We have also considered the interaction of the materials *with the inversion symmetry* such as silicon, where the Teraherz radiation can be produced by the simultaneous interaction of the light of the fundamental frequency ω and the second harmonic 2ω. This third-order "directional photocurrent" effect does not depend on the orientation of the material, and, although its magnitude is less than the magnitude of the effect in the zinc-blende materials, it can find useful applications in the generation of the submillimiter range microwaves.

References

[1] X-C Zhang, Y. Jin, K. Yang and L-J Scholwalter, Phys. Rev. Lett. 69, 2303 (1992)

[2] T.D. Hewitt, Y. Jin, W. Ellis and X-C Zhang, CLEO-93 technical Digest, paper CWJ61

"Teraherz...", J. B. Khurgin

*
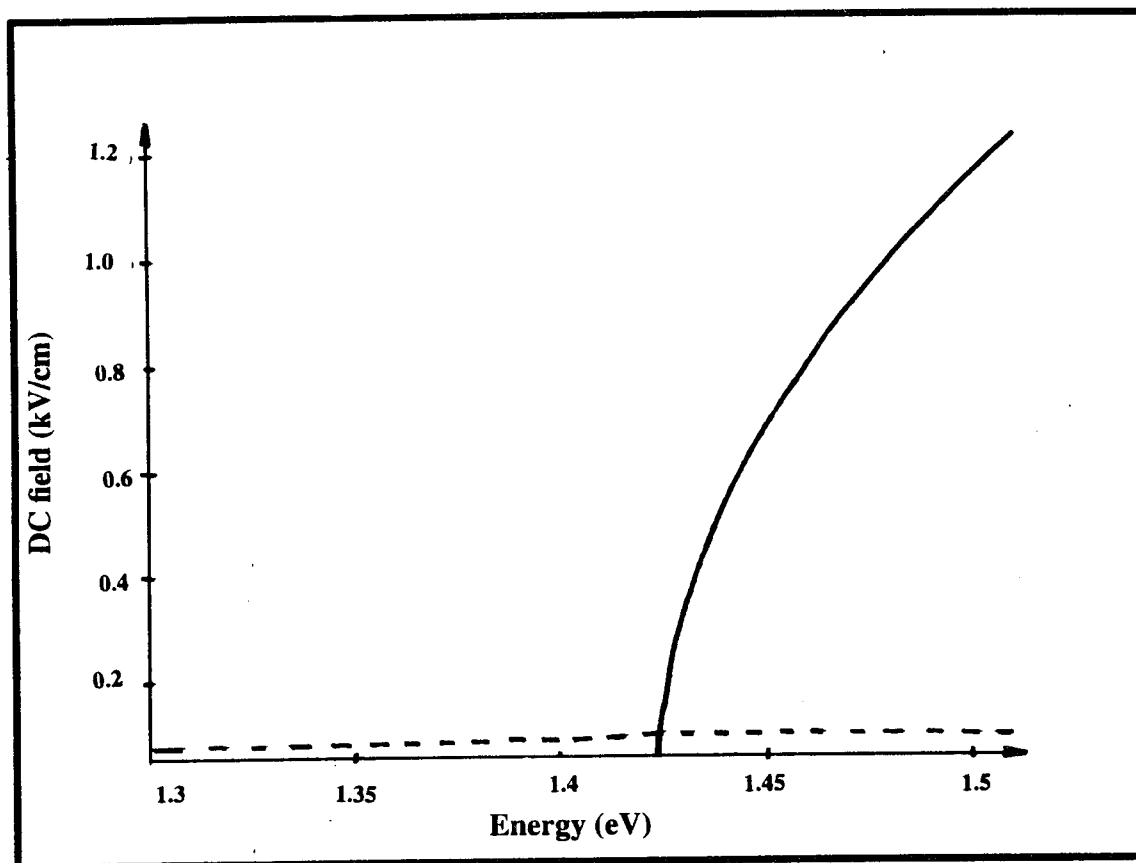
Fig.1 The frequency dependence of DC electric field produces by exciting GaAs with $1MW/cm^2$ laser pulse.

dashed line - the ultrafast component

solid line - the slower component.

"Teraherz...", J. B. Khurgin

235

Observation of intensity-dependent excitonic emission linewidth broadening
in periodic asymmetric coupled three narrow quantum wells

Y. J. Ding[1], A. G. Cui[1], S. J. Lee[2], J. V. D. Veliadis[2],
J. B. Khurgin[2], S. Li[2], and D. S. Katzer[3]

[1]Department of Physics & Astronomy,
Bowling Green State University, Bowling Green, OH 43403.
[2]Department of Electrical & Computer Engineering,
The Johns Hopkins University, Baltimore, MD 21218.
[3]Naval Research Laboratories, Washington, DC 20375.
Telephone: (419) 372-8785

It was demonstrated [1] that excitonic absorption peaks can be significantly broadened at room temperature while their energies stay the same by increasing excitation intensity in multiple quantum well structure. The mechanism for this phenomenon was attributed to bandgap renormalization [1]. Similar phenomenon has not been observed in excitonic emission peaks because they are usually broader than the absorption peaks. Furthermore, the broadening of the excitonic emission peaks is hardly observed even under high excitations since in this case it is usually buried in dominated electron-hole plasma emission [2]. Here, by taking the advantage of an extremely narrow excitonic emission linewidth in a sample of periodic asymmetric coupled three narrow quantum wells, we report our first observation of the broadening of the photoluminescence (PL) excitonic linewidth under the low excitation intensities: 0.54 W/cm^2 - 1.6 KW/cm^2 at low temperature.

The sample was grown by MBE on a semi-insulating GaAs substrate. The expitaxial layers consist of 10 periods, each of which is composed of three narrow asymmetric coupled GaAs quantum wells with the designed thicknesses of 45 Å, 30 Å, and 50 Å, coupled by 40 Å - $Al_{0.3}Ga_{0.7}As$ barriers, see Fig. 1. During the sample growth there is an interruption for 60 seconds at every interface. We measured photoluminescence excitation (PLE) spectra in the temperature range of 4 K - 300 K. In the low temperature range (4 K - 77 K), see Fig. 2, based on our calculations, we have assigned three (primary) sharp peaks to the excitonic emission peaks e_1hh_1, e_2hh_2, and e_3hh_3 for the quantum well width of 50 Å, 45 Å, and 30 Å, respectively, see Fig.2. The shoulders next to these peaks correspond to those for the quantum well widths of 52.8 Å, 47.8 Å, and 32.8 Å, respectively, each of which is one atomic layer thicker than the designed well width. Due to the growth interruption, many tiny growth islands at interfaces join together to form large islands with their sizes larger than the exciton radius corresponding to two different quantum well widths. Because our well width is much narrower than those used previously, the energy separation between the excitonic emission peaks for the well widths of 50 Å and 52.8 Å is larger than the inhomogenous broadening of each peak after the growth is interrupted at every interface. Therefore, we have observed two emission peaks corresponding to those for two different quantum well widths similar to Ref. [3]. For comparison, we plotted a PL spectrum for low laser intensity in the excitation spectrum in Fig. 2. We can see that the main peak in the PL spectrum corresponds to e_1hh_1 for the well width of 52.8 Å and the broad shoulder on the high energy side corresponds to the well width of 50 Å. We did not observe any Stokes shift between the PL peak and PLE peak. This indicates that our sample is of high quality.

We measured the PL spectra for different temperatures and at different excitation intensities, see Fig. 3. At 0.54 W/cm^2 the half width at the half maximum determined from the low energy side is ~ 4.5 Å (0.95 meV). This is the narrowest linewidth obtained so far. When we change the intensity from 0.54 W/cm^2 to 1.6 W/cm^2 at 4 K, we can see that the linewidth of the PL peak increases dramatically. Indeed, it increases from ~0.9 meV to ~4.3 meV. However, the energy of the emission peak stays more or less the same for all the intensities. Based on the measurement of the energy of the PL emission peak as a function of the temperature at a fixed laser intensity, we conclude that the excitons start to participate in the radiative recombination at ~77 K. As the temperature decreases below 77 K, the exciton recombination becomes more and more important and eventually dominates the recombination process below ~25 K. From the above measurement we have determined the binding energy of the $e_1 hh_1$ excitons for the well width of 52.8 Å to be ~5 meV.

Following the argument in Ref. [1], for high density of free carriers the energy of free electron-hole pairs is renormalized, whereas the energy of the excitonic emissions hardly changes because of the charge neutrality of excitons. The binding energy of the excitons measured from the renormalized continuum decreases as the laser intensity increases. As a result, the linewidth of the PL peak is broadened. As mentioned above, the PL linewidth of the first emission peak is the narrowest at low excitation intensity compared with those determined so far. Thus, the same amount of the bandgap renormalization leads to a relatively larger change in the linewidth. This explains why we have observed the large broadening of the PL linewidth after the sample growth was interrupted. When we change the temperature of the lattice from 4 K to 30 K, the linewidth stays unchanged while the peak wavelength shifts significantly. By contrast, in Fig. 3 the peak wavelength stays unchanged when the laser intensity increases. Therefore we can rule out the thermally-induced broadening due to the laser heating of the lattice at low temperatures. Finally, we would like to note that because the emission peak for the well width of 52.8 Å is much weaker than that for the well width of 50 Å in PLE spectra (Fig. 2), we cannot possibly observe the broadening of this peak in PLE or absorption spectra.

This work is supported by AFOSR.

[1]   D. S. Chemla and D. A. B. Miller, J. Opt. Soc. Am. B, **2**, No.7, 1155, (1985).
[2]   G. Tränkle, H. Leier, A. Forchel, H. Haug, C. Ell, and G. Weimann, Phys. Rev. Lett. **58**, 419 (1987).
[3]   K. Fujiwara, K. Kanamoto, and N. Tsukada, Phys. Rev. B, **40**, No.14, 9698, (1989).
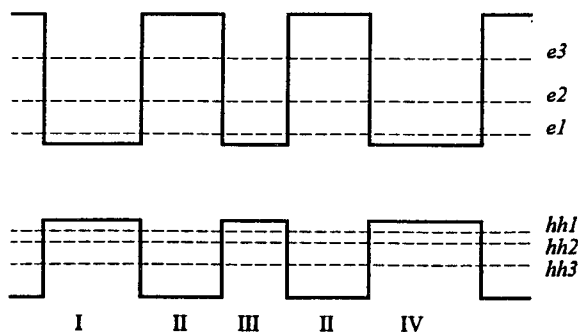
Figure 1.   One unit of periodic asymmetric coupled three narrow quantum well structure. (I) GaAs, 45 Å, (II) $Al_{0.3}Ga_{0.7}As$, 40 Å, (III) GaAs, 30 Å, (IV) GaAs, 50 Å.
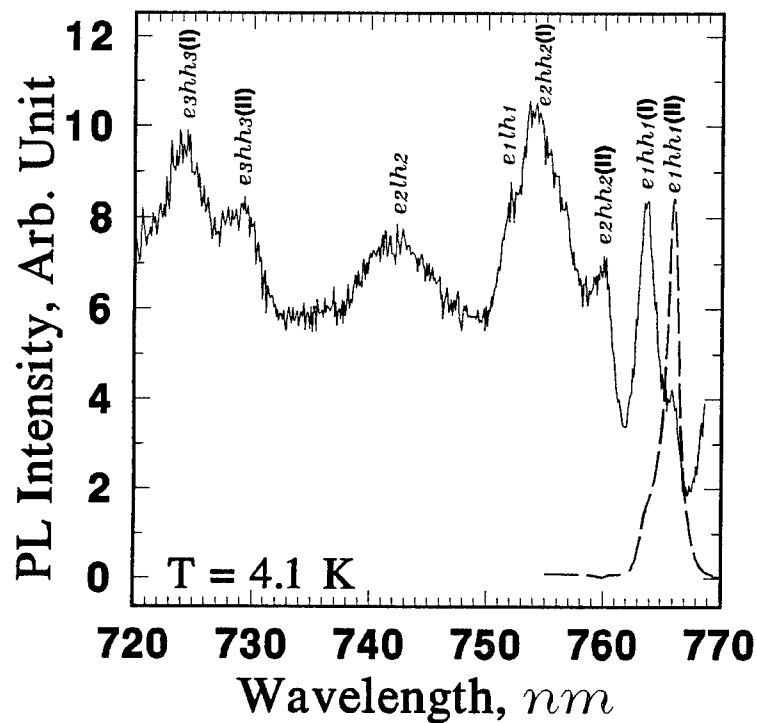
Figure 2. Solid line: excitation spectra at ~1 W/cm^2 at 4.1 K. I - transitions for the designed well widths; II - transitions for the well widths of 1 monolayer thicker than the designed ones. Dashed line: PL spectrum.
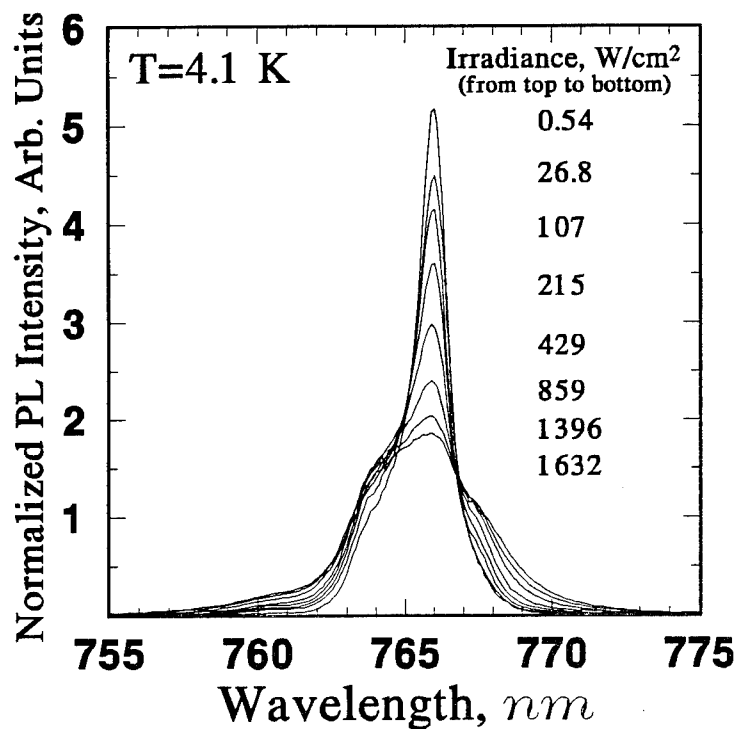
Figure 3. Normalized PL intensity spectra versus laser intensity at 4.1 K. Each curve is normalized by the integrated PL in the entire spectrum range.

Control of Photocurrent Directionality via Interference of Single and Two Photon Absorption in a Semiconductor

H.M. van Driel[*] and A. Haché

Department of Physics,University of Toronto

Toronto, Canada, M5S -1A7

Summary:

In quantum mechanics, if two or more perturbations induce a transition between the same initial and final states of a system, the overall transition probability is determined by the modulus squared of the sum of the transition *amplitudes* for each perturbation. It is therefore possible for interference effects to determine the outcome as it does in. *e.g.*, the classical Young's double slit experiment. If two coherent beams with frequencies ω and 2ω are applied to a system, the interference between the quantum mechanical pathways associated with single and two photon absorption events can lead to final states on the system whose properties are dependent on the relative phase of the beams.

Manykin and Afanas'ev[1] and Gurevich and Khronopulo[2] first showed theoretically how multiple beam, multiphoton absorption can influence the occupancy of excited states. More recently, Brumer and Shapiro[3] showed theoretically that it is possible to control a photochemical reaction via the relative phase of two beams. In a direct extension of this work Kuriziki et al.[4] determined that the photo-ionization of a doublet donor level in a semiconductor prepared in a coherent superposition of states can generate electrons in a preferred momentum state. Electrons flow in a direction which is dictated by the relative phase of the beams creating the superposition and <u>without any external electrical bias</u>. The necessary donor-semiconductor system is not easy to produce and mid-infrared coherent sources of a particular wavelength would be required to observe the effect. Here, we argue that multiple quantum wells or superlattices make it possible to design systems so that one could observe either charged or neutral currents using more readily available beams. We illustrate one such design which should allow neutral electron-hole currents to be generated using beams in the important 1.3-1.5 μm window which is of prime interest in optical communications.

The basic ideas behind coherence control of photocrruent directionality is as follows. For a direct gap semiconductor the transition amplitude between valence and conduction band states is of the form

$$C_{if} = a_1 \vec{A}^{2\omega} \cdot \vec{p}_{vc} + a_2 \vec{A}^{\omega} \cdot \vec{p}_{vc} \vec{A}^{\omega} \cdot \vec{p}_{c'c} \tag{1}$$

where a_1, a_2, are complex constants, c, v label conduction and valence band states, A^{ω} is the vector potential amplitude for the ω beam, $A^{2\omega}$ is that of the 2ω beam and p is the momentum operator; only one intermediate (c') state is considered for the two-photon transition. For collinearly polarized beams of field strength E^{ω} and $E^{2\omega}$

$$C_{if} = b_1 E^{2\omega} p_{vc} \cos\theta \, e^{i\phi_{2\omega}} + b_2 p_{vc'} p_{c'c} (E^{\omega})^2 \cos^2\theta e^{i2\phi_\omega} \qquad (2)$$

where ϕ_ω and $\phi_{2\omega}$ are the phases of the two beams and θ is the angle between the electric fields and the momentum direction. The transition probability is then given by

$$|C_{if}|^2 = A + B\cos(\alpha_{12} + \phi_{2\omega} - 2\phi_\omega) \qquad (3)$$

where α_{12} is related to the relative phase of the complex constants b_1, b_2. Note that A contains the sum of terms involving $\cos^2\theta$ and $\cos^4\theta$ respectively. These lead to anisotropic but <u>non-polar</u> state filling and are related to the independent generation rates of electron-hole pairs via single and two-photon absorption. On the other hand the B "interference" term contains $\cos^3\theta$. If one just considers the generated electrons, integration over all occupied states (i.e. over θ) gives that A leads to no current whereas the polar B term does. It follows that an electron current develops. Similar considerations apply to the holes which will move in the same direction. By varying the relative phase between the two beams, one can influence the directionality of the particle flow. By altering the polarization direction of the beams, one can also change the current <u>vector</u> . A more sophisticated analysis, taking into account details of the bandstructure, and the wavefunctions of the electron and hole states yield the same qualitative results. As Baranova et al.[5] have pointed out in the general context of multiple beam, photo-ionization of media, the bias from using phase-related beams comes not from having the time averaged dc field differ from zero (as it does in a typical electrical circuit) but by having $<E^3> \neq 0$ where E is the total optical field driving the excitation and $<>$ denotes the time average. Hence, although the effect can be understood in terms of the quantum mechanical interference picture presented above, it also has an explanation based on classical but <u>nonlinear</u> electromagnetic theory.

To observe the directionality effect in a semiconductor, one needs an intense fundamental beam to generate the phase-related second harmonic beam and to generate carriers via two-photon absorption. Also, if one wishes to work with common semiconductor materials such as GaAs, Ge or Si or their cousins which have band gaps in the range 0.7-1.8 eV, one needs a fundamental source with photon energy of 0.35-0.9 eV (3 - 1.4 μm). Two years ago we demonstrated the first high average power femtosecond optical parametric oscillator.[6] The system which is pumped by a 100 fs, 1W average power, 80 MHz Ti:sapphire laser, produces pulses as short as 60 fs, tunable between 1.2 and 3 μm with appropriate mirror sets. The output beams have average power up to 300 mW, sufficient to generate 10% conversion to the second harmonic in a BBO crystal. The fundamental output pulses are also sufficiently intense to generate significant two-photon absorption in direct gap semiconductors.

One might hope to observe the effect in a bulk material but the problem of detection of the current flow is non-trivial. One possible method might take advantage of the different masses of electrons and holes which, with the same initial momentum, will tend to spatially separate, following excitation, generating an electric (Dember) field. The particle currents however will persist for only the dephasing time or momentum relaxation time of the carriers which is typically 100 fs. Therefore one would have to detect this field using ultrafast optical techniques such as electro-optic sampling. We are presently performing experiments on asymmetric quantum wells grown on a GaAs substrate. Here, samples with 50 and 80 Å wide GaAs wells are separated by $Al_{0.22}Ga_{0.78}As$ barriers with widths between 150 and 300 Å; $Al_{0.4}Ga_{0.6}As$ barriers are used to separate 10 of these units. When electron and holes are generated via single and two-photon absorption processes (mainly in the $Al_{0.24}Ga_{0.76}As$) they will move into the 50 or 80 Å GaAs wells depending on the beam phases. Because of the different carrier energy levels in the GaAs wells one can detect

which direction the electrons and holes went based on the wavelength of the emitted (even time-integrated!) luminescence. For our samples the experimentally observed luminescence from single beam excitation shows two equal-height peaks with wavelengths of 772 and 797 nm at 295K. It is expected that under two beam excitation the relative heights of the peaks will shift with the relative phase of the two beams. This relative phase which is determined naturally by the second harmonic generation process in the BBO crystal can be controlled downstream by thin optical wedges.

Other samples, geometries, and phase related beams are being considered for other applications. This also applies to using doped materials and performing experiments when, e.g. only one type of carrier is activated so that an electrical current will flow.

REFERENCES

1. E. A. Manykin and A.M. Afanas'ev, Sov. Phys. JETP **25**, 828 (1967).
2. G.L. Gurevich and Yu. G. Khronopulo, Sov. Phys. JETP, **24,** 1012 (1967).
3. P. Brumer and M. Shapiro, Accts. of Chem. Res. **22**, 407 (1989).
4. G. Kurizki, M. Shapiro and P. Brumer, Phys. Rev.B, **39**, 3435 (1989).
5. N. Baranova, A.N. Chudinov and B. Ya Zel'dovich, Optics. Commun., **79,**116 (1990).
6. Q. Fu, G. Mak and H. M. van Driel, Optics Lett., **17**, 1106 (1992).

Enhancement of the near-bandgap nonlinearity using intersubband absorption in quantum wells and dots.

Jacob B. Khurgin and S. Li

Department of Electrical and Computer Engineering
The Johns Hopkins University
Baltimore MD 21218

All optical schemes of information processing have been of major interest to many researchers. It is well known that in order to supply the necessary switching energy, the all-optical processing schemes always require very high optical intensities that are difficult to achieve and/or deliver to the switching element. In contrast, in the electronic devices the switching energy, provided by the bias source, is readily available in virtually unlimited (save for the thermal limitations) amounts. This fundamental advantage of the electrical vs optical bias has directed the recent practical trend away from the all-optical and toward the hybrid devices, the so-called "smart pixels", such as S-SEED [1], FET SEED [2] phototransistor/modulator combinations and others. The concept of smart pixel combines advantages of optics (high degree of parallelism, interconnection ability) with the forementioned advantages of electronics.

Basically, the smart pixel consists of the detector - amplifier (FET, phototransistor e.t.c) and modulator. Often as in SEED's the same element serves dual purpose as both modulator and detector. Then, one can think of the smart pixel as an entity in which the natural optical nonlinearity is enhanced by the gain provided by the built-in electronic circuit. However, the potential of the smart pixel is limited, since as the complexity of the task performed by the system grows, the number of pixels necessary increases beyond the realistic limit and the connection to the power source becomes problematic. At the present stage of miniaturization the smart pixel can not such as real-time holography, where the advantages of optics can be utilized in the most rewarding way.

Thus, it is very important to find the way to deliver the switching power to the "pixel" without hard-wired connections. Far IR radiation (or microwaves [3]) provide such an opportunity. We propose to use the natural thermal nonlinearity of the confined semiconductor materials. the energy for the temperature rise is to be

provided *by the strong incoherent FIR* radiation, but
controlled *by the weak coherent near IR or visible* light.

The proposed structure [Fig.1] consists of the undoped multiple quantum wells (inset) and is split into the separate elements - "pixels", by, say etching the mesa structures. The element is illuminated with weak coherent signal light I_{sig} below the bandgap.

The population of the photogenerated carriers is

$$N_e = I_{sig} \alpha_{sig} \tau_r \lambda_{sig} / hc \tag{1}$$

where α_{sig} is the absorption coefficient at the wavelength λ_{sig}, and τ_r is the recombination time.

The power transferred to the lattice directly from the signal radiation is then

$$P_{sig}=\alpha_{sig}I_{sig}=\frac{N_e hc}{\lambda_{sig}\tau_r}$$ (2)

The photoexcited electrons reside in the ground subband (E_1) of the conduction band, and, by themselves change the absorption and refractive index insignificantly. One can say that the signal have been *recorded,* but it has not been yet "developed".
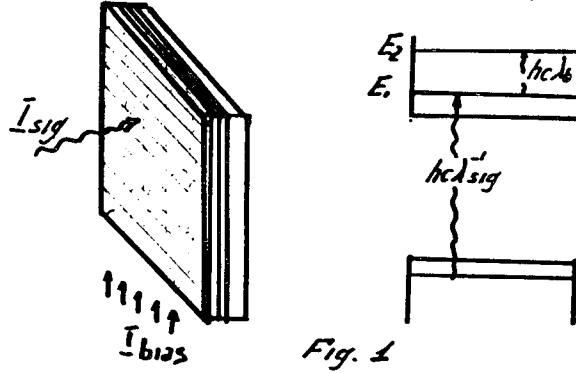
Fig. 1

Now let us introduce the developing agent - the FIR radiation - the "bias" I_{bias} at the wavelength $\lambda_b=hc/(E_2-E_1)$. The "bias" does not to be coherent - the only requirement is that it should be properly polarized to be absorbed between the subbands. Then one can write the balance equation for the population of the subbands 1 and 2

$$\frac{dN_2}{dt} = \sigma_b\lambda_b I_{bias}(N_2-N_1)/hc - \frac{N_2}{\tau_i}$$ (3)

where τ_i is the intersubband relaxation time, the absorption cross section found as

$$\sigma_b=\frac{2\pi}{\lambda_b n}\frac{e^2 z_{12}^2}{\varepsilon_0\Gamma},$$ (4)

$ez_{12}\approx0.18ed$ is the dipole matrix element, Γ is the intersubband linewidth, and $N_2+N_1=N_e$.

The steady-state solution of (3) is

$$N_2=\frac{\frac{1}{2}N_e I_{bias}/I_{sat}}{1+I_{bias}/I_{sat}}$$ (5)

where the saturation intensity is

$$I_{sat}=\frac{\frac{1}{2}hc}{\lambda_b\sigma_b\tau_i}$$ (6)

that for the 100ÅQW with the intersubband absorption around $10\mu m$, and the relaxation time $\tau_i\sim200fs$ is of the order of $10MW/cm^2$ The power transferred to the lattice from the bias radiation can be found as

243

$$P_b = \frac{N_2 hc}{\lambda_b \tau_i} = = \frac{1}{2} P_{sig} \frac{\lambda_{sig} \tau_r}{\lambda_b \tau_i} \frac{I_{bias}/I_{sat}}{1+I_{bias}/I_{sat}} \qquad (7)$$

For the FIR power density below the saturation it can be shown that the power absorbed directly from the signal, and thus the thermal nonlinearity is enhanced by the factor

$$\eta = \frac{P_b}{P_{sig}} = \frac{1}{2} \frac{\lambda_{sig} \tau_r}{\lambda_b \tau_i} I_{bias}/I_{sat} = I_{bias} \sigma_b \tau_r \frac{\lambda_{sig}}{h} = \frac{I_{bias}}{I_0} \qquad (8)$$

where

$$I_0 = \frac{hc}{\lambda_b \sigma_b \tau_r} = I_{sat} \frac{\lambda_b \tau_i}{\lambda_{sig} \tau_r} \qquad (9)$$

This new "cross-saturation" intensity combines large absorption cross-section of the intersubband transition with the long lifetime associated with band-to-band recombination. Assuming $\tau_r \sim 1 ns$ and $\lambda_{sig} \sim 1 \mu m$, $I_0 \sim 10^3 W/cm^2$ - easy to achieve.

Thus the strong local heating will result where the signal light had been absorbed resulting in the local change of the refraction index. The effective nonlinear index of refraction can be introduced and evaluated as

$$n_2 = (dn/dT) \alpha_{sig} \frac{d^2}{\kappa} \frac{I_{bias}}{I_0}$$

where (dn/dT) is the thermooptic coefficient equal to $1.7 \times 10^{-4} K^{-1}$ for *GaAs*, κ is the thermal conductivity and d is the pixel size. For the $10 \mu m$ pixel size the nonlinear index of refraction can be as large as $10^{-3} cmw$ in the presence of $I_{bias} = 1 kW/cm^2$ infrared field. Since we rely upon thermal nonlinearity the speed of the proposed scheme is determined by the heat diffusion time

$$\tau_D \approx d^2 c_p / \kappa$$

where c_p is the heat capacity , For $10 \mu m$ pixel, $\tau_D \sim 1 \mu s$.

This switching time is much shorter that the switching time of the photorefractive process and thus this scheme can be used in such applications as the four-wave mixing and the real-time optical holography. In conclusion, we have shown that intersubband absorption by the photoexcited carriers solves the problem of the delivery of the bias power to the optical switching elements without wires and lithography.

References:

[1] D. A. B. Miller, IEEE J. of Quantum Electron., QE-29, 678, 1993
[2] A. L. Lentine and D. A. B. Miller, IEEE J. of Quantum Electron., QE-29, 655, 1993
[3] S. Li and J. B. Khurgin, Opt. Lett., 18, 1855, 1993

Optical Bistability of Nonlinear Waves in Multilayer Nonlinear Waveguides

Jong-Sool Jeong and Chong Hoon Kwak
Research Department, Electronics and Telecommunications Research Institute,
P.O.Box 106, Yuseong-Ku, Daejeon, Korea
Tel.) +82-042-860-6034   Fax.) +82-042-860-5033

Nonlinear guided waves have received much attention due to its potential application to all-optical signal processing[1,2]. In this paper we analyze the optical bistability of the nonlinear waves and obtain the critical power with varying the thickness of the nonlinear layers in a multilayer nonlinear waveguide system which is composed of five layers including two nonlinear layers covered by semi-infinite clad and substrate, as shown in Fig. 1. The nonlinear dispersion relations are formulated for self-focusing and self-defocusing nonlinear structures using the nonlinear transfer matrix[3].
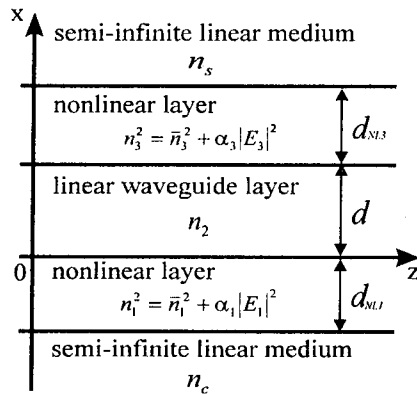
Fig. 1. The schematic drawing of multilayer nonlinear waveguide.

The nonlinear layers have a Kerr-like refractive index of $n^2 = \bar{n}^2 + \alpha|E|^2$, where E is the amplitude of the electric field, $\bar{n}$, the linear refractive index, and α, the nonlinear coefficient of the Kerr-like medium. The electric field in a finite nonlinear layer can be expressed in terms of the Jacobian elliptic functions: *cn* function for self-focusing nonlinear layer and *sn* function for self-defocusing[2]. After manipulating the trial functions adequately, we formulate the nonlinear transfer matrix describing the relation of the tangential components of the electric and magnetic fields at the interfaces of self-focusing and self-defocusing nonlinear layers, as shown in Table I. Applying the boundary conditions at the interfaces, the nonlinear dispersion relation expressed by the elements of nonlinear transfer matrix is given as follows:

$$\tan\left(k_0 d\sqrt{\left|n_2^2 - \beta^2\right|}\right) = \frac{U(\beta, E_0) + V(\beta, E_0)}{1 - U(\beta, E_0)\,V(\beta, E_0)} \qquad \text{for } n_2 > \beta$$

$$\tanh\left(k_0 d\sqrt{\left|n_2^2 - \beta^2\right|}\right) = \frac{-[U(\beta, E_0) + V(\beta, E_0)]}{1 + U(\beta, E_0)\,V(\beta, E_0)} \qquad \text{for } n_2 < \beta$$

(1)

where

$$U(\beta, E_0) = \frac{1}{j\eta_0 \sqrt{\left|n_2^2 - \beta^2\right|}} \frac{r_{21}(\beta, E_0) + j\eta_0 \sqrt{\beta^2 - n_c^2}\, r_{22}(\beta, E_0)}{r_{11}(\beta, E_0) + j\eta_0 \sqrt{\beta^2 - n_c^2}\, r_{12}(\beta, E_0)} ,$$

(2)

$$V(\beta, E_0) = \frac{-1}{j\eta_0 \sqrt{\left|n_2^2 - \beta^2\right|}} \frac{t_{21}(\beta, E_0) + j\eta_0 \sqrt{\beta^2 - n_s^2}\, t_{22}(\beta, E_0)}{t_{11}(\beta, E_0) + j\eta_0 \sqrt{\beta^2 - n_s^2}\, t_{12}(\beta, E_0)}$$

(3)

with wave number k_o, the admittance of free space η_o, the mode index β, the interface electric field E_o. The elements of nonlinear transfer matrix $[r_{ij}]$ and $[t_{ij}]_{(i,j=1,2)}$ are presented in Table I with $\Gamma = \left(n_i^2 - \beta^2\right)^2 + 2\alpha_i C_i \geq 0$ for self-defocusing system where $C_{i(i=c,s)}$ is a constant of integration and the $+ (-)$ sign of off-diagonal elements corresponds to the positive (negative) coordinate.

Table I. Nonlinear transfer matrix elements and their parameters.

	self-focusing	self-defocusing
m	$\left(\Gamma^{1/2} - \left(n_i^2 - \beta^2\right)\right)\big/ 2\,\Gamma^{1/2}$	$\left(\alpha_i C_i - \Gamma^{1/2}\left(n_i^2 - \beta^2\right) - \Gamma\right)\big/ \alpha_i C_i$
q^2	$\left(n_i^2 - \beta^2\right)\big/(1 - 2m)$	$\left(\left(n_i^2 - \beta^2\right) - \Gamma^{1/2}\right)\big/ 2$
A^2	$2mq^2/\alpha_i$	$-\left(\Gamma^{1/2} + \left(n_i^2 - \beta^2\right)\right)\big/ \alpha_i$
$K(x)$	$1 - m\left(1 - E_o^2/A^2\right) sn^2\left(k_o qx\|m\right)$	$1 - m\left(E_o^2/A^2\right) sn^2\left(k_o qx\|m\right)$
$D(x)$	$1 - m\left(1 + E_o^2/A^2\right) sn^2\left(k_o qx\|m\right)$	$1 + m\left(E_o^2/A^2\right) sn^2\left(k_o qx\|m\right)$
$M(x)$	$1 - m\left(1 - E_o^2/A^2\right)\left[1 + cn^2\left(k_o qx\|m\right)\right]$	$\left(1 - m E_o^2/A^2\right) dn^2\left(k_o qx\|m\right)$ $+ m\left(1 - E_o^2/A^2\right) cn^2\left(k_o qx\|m\right)$
$t_{11}(\beta, E_0)$	$cn\left(k_o qx\|m\right)\big/ K(x)$	$cn\left(k_o qx\|m\right) dn\left(k_o qx\|m\right)\big/ K(x)$
$t_{12}(\beta, E_0)$	$\pm j sn\left(k_o qx\|m\right) dn\left(k_o qx\|m\right)\big/\left(\eta_o q K(x)\right)$	$\pm j sn\left(k_o qx\|m\right)\big/\left(\eta_o q K(x)\right)$
$t_{21}(\beta, E_0)$	$\pm j\eta_o q M(x) sn\left(k_o qx\|m\right) dn\left(k_o qx\|m\right)\big/ K^2(x)$	$\pm j\eta_o q M(x) sn\left(k_o qx\|m\right)\big/ K^2(x)$
$t_{22}(\beta, E_0)$	$D(x) cn\left(k_o qx\|m\right)\big/ K^2(x)$	$D(x) cn\left(k_o qx\|m\right) dn\left(k_o qx\|m\right)\big/ K^2(x)$

The dispersion relation of the multilayer nonlinear waveguide shows similar form with that of a linear planar waveguide for both self-focusing and self-defocusing nonlinear systems[4]. The power-dependent mode index β and the electric field E_o at the interfaces between nonlinear layers and cover media are the vital parameters of the nonlinear dispersion relation. After fixing the mode index β, we find the interface electric field using the shooting and matching technique. The pairs of β and E_o are utilized to plot the nonlinear dispersion curve which depicts the dependence of the mode indices on the total guided power.

Since we found that under the our circumstances the self-defocusing system shows no bistabilities, the self-focusing system is only considered and also concentrated on the TE_0 mode, for simplicity, in this work. The parameters of the nonlinear waveguide structure used for numerical

simulation are $\bar{n}_1 = \bar{n}_3 = 1.55$, $n_c = n_s = 1.50$, $n_2 = 1.570$, and $d = 1.2\ \mu\text{m}$. The wavelength considered throughout this calculation is $\lambda = 0.515\mu\text{m}$. Figure 2 shows the optical bistable curves of the nonlinear dispersion relation as a function of the thickness of the nonlinear layers for asymmetrical and symmetrical structures: the nonlinear coefficient of $\alpha_1 = 6.38 \times 10^{-12}\ m^2/V^2$ and $d_{NL3} = 0$ for asymmetrical structure and the coefficients of $\alpha_1 = \alpha_3 = 6.38 \times 10^{-12}\ m^2/V^2$ and $d_{NL1} = d_{NL3}$ for symmetrical structure. The solid curve gives the characteristics of the mode indices for $d_{NL1} = 1.0\mu\text{m}$, the dashed curve, $d_{NL1} = 0.7\mu\text{m}$, and the dotted curve, $d_{NL1} = 0.5\mu\text{m}$, respectively. As the power increases from zero, the field remains in the guided wave confined in the waveguide core until the critical power is reached, and is coupled into the surface wave afterwards. As the power decreases, the field remains in the surface wave until the second critical power is reached, and then there is a discontinuous jump back of the mode index to the low-power value of the field. The critical powers are around 40 mW/mm for symmetrical structure and have nearly double value with respect
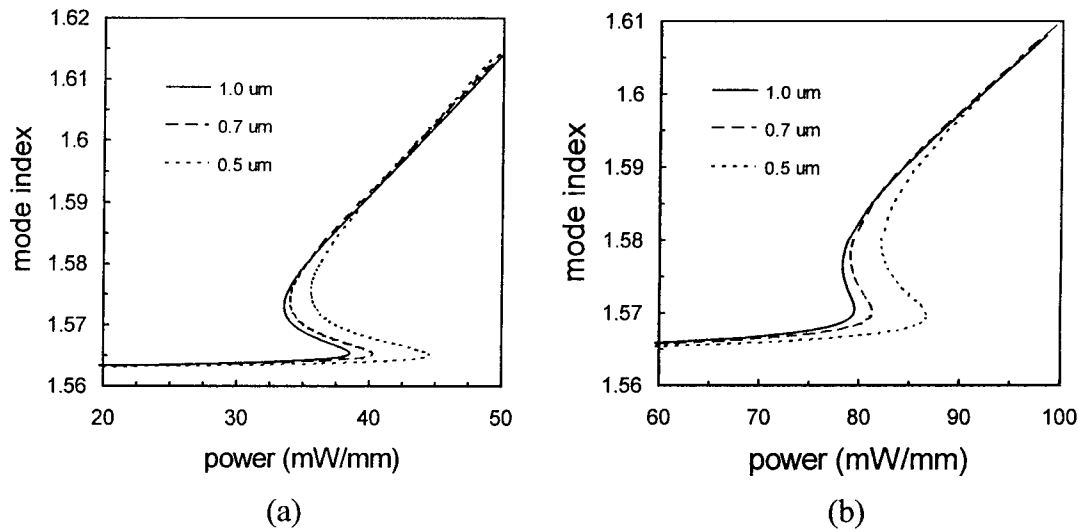
Fig. 2. The bistable curves of nonlinear dispersion relation for (a) asymmetrical structure and (b) symmetrical structure.

to asymmetrical case, *i.e.*, 80 mW/mm for symmetrical structure. The critical powers also increase with decreasing the thickness of the nonlinear layer for both structures as shown in Fig. 2.

In conclusion, we obtained the nonlinear dispersion relation in multilayer nonlinear waveguides by utilizing the method of nonlinear transfer matrix which has the elements of Jacobian elliptic functions. The self-focusing system in multilayer nonlinear waveguide shows the optical bistability of power-dependent mode indices and the critical powers for the optical bistability increase with decreasing the thickness of the nonlinear layers.

REFERENCES
1. C. T. Seaton *et al.*, IEEE J. Quantum Electron. **QE-21**, 774-783 (1985).
2. A. D. Broardman *et al.*, IEEE J. Quantum Electron. **QE-22**, 319-324 (1986).
3. U. Trutschel, *et al.*, IEEE J. Quantum Electron. **QE-25**, 194-200 (1989).
4. J. Jeong *et al.*, submitted to Optical Computing OC'94 (Edinburgh, U.K.).

Observation of fluorescence in the THz frequency region from semi-insulating bulk GaAs excited by ultrashort pulses

Nobuhiko SARUKURA, Zhenlin LIU, and Yusaburo SEGAWA
Photodynamics Research Center, The Institute of Physical and Chemical Research,
Nagamachi Koeji 19-1399, Aoba-ku, Sendai, Miyagi 980, Japan
Telephone: +81 22 228 2012 Facsimile: +81 22 228 2010
Shin-ya KOSHIHARA
Tokyo institute of technology
Yasuhiro KONDO
Department of Applied Physics, Tohoku University,
Aoba, Aramaki, Aoba-ku, Sendai, Miyagi 980, Japan

.*Summary*

THz radiation from various material excited by ultrashort pulse lasers have been intensively studied in the respect of its mechanism and potential application to ultrafast opt-electronics.[1] Especially quantum well sample applied with electrical field was found out to be quite efficient.[2] In this presentation, we will describe the observation of THz radiation not due to the rectification from semi-insulating bulk GaAs excited by ultrashort-laser pulses and its intensity dependence on the 1.5-th power of the excitation intensity.

The experimental set-up consists of picosecond and femtosecond mode-locked Ti:sapphire lasers as the excitation source, a 15-cm focal length mirror for focusing the radiation, a silicon borometer with various low pass filters (10 cm^{-1}, 35 cm^{-1}, 100 cm^{-1}), and a lock-in amplifier. Several GaAs samples with (100) surface with were tested; non doped (semi-insulating) GaAs with over 10^7 Ω cm resistivity, n-type and p-type GaAs with 10^{-3} Ω cm resistivity, and 140-Å GaAs single quantum well (SQW) sample. Only non-doped GaAs and SQW sample emitted THz radiation, however, THz radiation can not be detected from n-type and p-type GaAs samples. This results show that this radiation strongly affected with the conduction type. Comparing non-doped GaAs and SQW sample, bulk sample radiated one-order higher power at the same excitation intensity. This difference may be attributed to the small absorption in the SQW layer.

For these two samples, 1-psec pulses, 100-fsec pulses, and cw-laser light at 787 nm with ~100 mW average power were irradiated in the 3-mm

diameter spot. In the case of cw laser excitation, no radiation can be detected. The fact indicated that this radiation is not due to simple heating. Compared with picosecond and femtosecond case, shorter pulse excitation generated the radiation more efficiently. Using various set of low pass filters, it was found that the power of radiation mostly contained in the region between 10 cm^{-1} to 35 cm^{-1} (0.3 ~ 1.2 THz) even with the use of different pulse duration excitation source. If the radiation are due to rectification, the spectrum should be affected by the excitation pulse duration, and the peak of radiation should locate at 1 THz for 1-psec pulses and 10 THz for 100-fsec pulse. Therefore, this experimental result suggests that the radiation is not due to the rectification, and it should be regarded as a kind of fluorescence.

To clarify the mechanism of this radiation, the fluorescence intensity dependence on excitation power of 1-psec pulses at 787 nm were measured for bulk and SQW GaAs. In both case, the THz-radiation intensity depends clearly on the 1.5-th power of the excitation (Fig. 1). The fluorescence intensity dependence on the excitation wavelength at the same power and the same pulsewidth (1.5 psec) were also obtained and plotted according to the excitation wavelength,[3] and it also shows 1.5 slope (Fig. 2). This coincidence can be well explained in the following way. The excitation density in a unit volume will be proportional to the absorption coefficient, and the THz-radiation intensity depends on this excitation density. Thus it is reasonable that the dependence on the absorption coefficient also indicates 1.5 slope. These two results and the sensitiveness to the doping strongly suggest the photo-carriers play an important role in this fluorescence. But still some more experiments will be needed to explain the mechanism of this radiation.

In conclusion, we have observed THz radiation from GaAs excited by ultrashort pulse laser. This radiation is not due to the optical rectification as observed in other cases. It was found that this radiation is sensitive to the conduction type and it depends on the 1.5-th power of the excitation intensity. But still the mechanism is not clear at present.

References

1. D. H. Auston, Appl. Phys. Lett. 43, 713 (1983).
2. P. Planken, M. C. Nuss, W. H. Knox,
   Appl. Phys. Lett. 61, 2009 (1992).
3. The OSA handbook of optics.
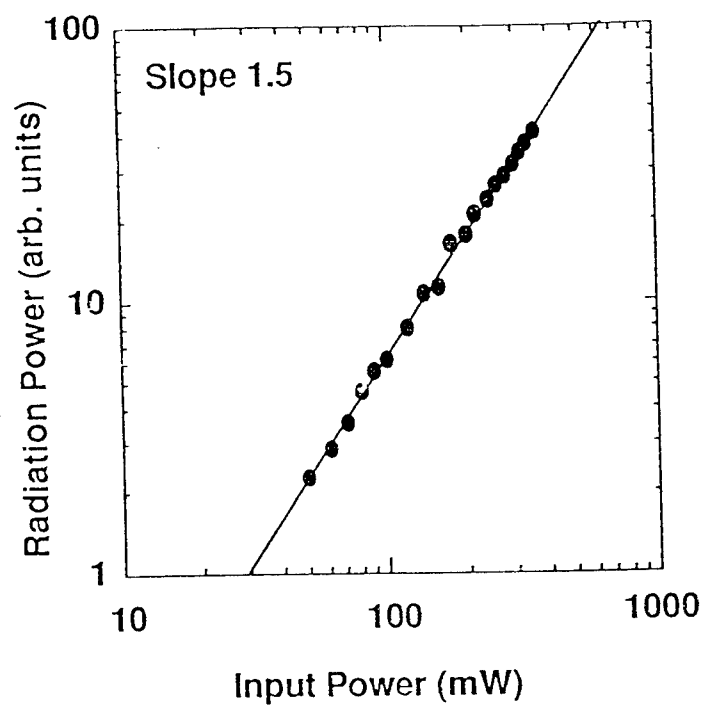
Fig. 1 The dependence on the excitation power.
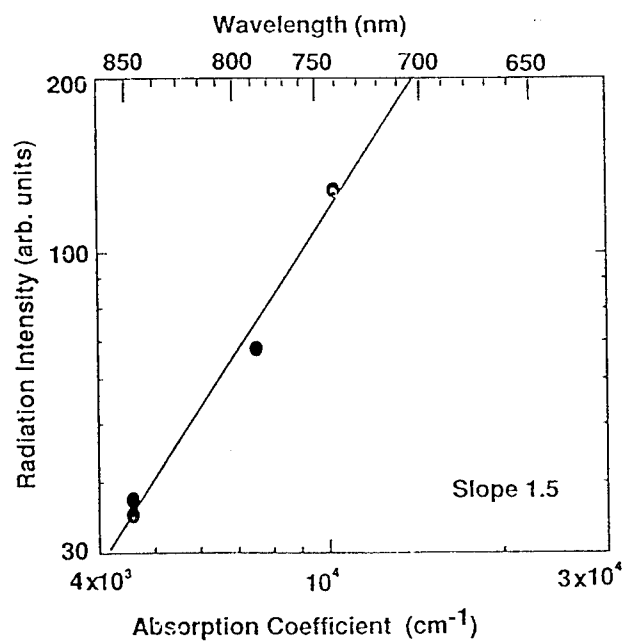
Fig. 2 The dependence on the excitation wavelength.

Optical Nonlinearities at the Bandedge of Amorphous Selenium Clusters

V.P.Mikhailov, K.V.Yumashev, P.V.Prokoshin, S.P.Jmako
*International Laser Center, Belarus State University, 7 Kurchatov Str.,
Minsk 220064, Belarus, Phone/Fax 0172-785726*
V.S.Gurin, M.V.Artemyev
*Physico-Chemical Problems Research Institute, Belarus State University,
14 Leningradskaya Str., Minsk 220080, Belarus, Phone 0172-265608*

The search for new materials with a large nonlinear optical susceptibility and the simple synthesis of selenium clusters of various crystal structure has caused the investigation of nonlinear optical properties of nanometer-size selenium clusters. Samples of PVA films with a-Se clusters on quartz glass were investigated by picosecond pump-probe laser spectroscopy equipment with two photodiode matrices as detectors. Laser pulses with wavelength of 540 nm, duration of 15 ps and repetition frequency of 1 Hz served as pump beam .White continuum was used as probe beam.

Figure 1 shows differential absorption spectra ΔD of a-Se clusters in PVA film obtained at the various delay time between pump and probe pulses and the energy of pump pulse of 80 mJ/cm² . Excitation of a-Se particles results in appearance of induced absorption around E=2.1 eV (Fig.1 shows decay of absorption). Development of induced absorption finished practically after pump pulse action within the resolution time of our picosecond device (15 ps). The decay time of induced absorption is significantly greater than pump pulse duration. Position of maximum in spectra of induced absorption at the energy scale depends on delay time between pump and probe pulses.

In Fig. 2 the kinetics of induced absorption ΔD vs time delay in a-Se clusters are shown for six different energies of photons of probe pulses. From this figure can be made conclusions that the decay time of induced absorption depends on energy of photons and the relaxation of induced absorption at various energies of photons has the exponential character.

Spectral behaviour of decay time τ is presented in Fig. 3. Values of t are independent of photon energy in the range of 2.1 - 2.2 eV and equal to ~ 550 ps. Below 2.1 eV values of t decrease down to 260 ps at 1.75 eV.
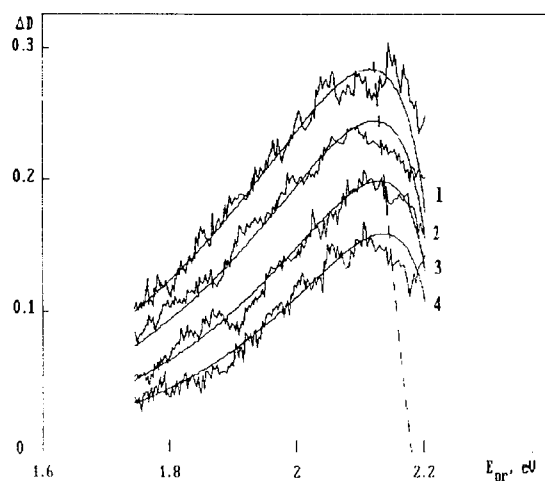
Fig.1. Differential absorption spectra $\Delta D = -\lg(T/T_0)$ of a-Se particles in PVA film at the various delay time t between pump and probe pulses of 15 ps duration. The energy of photons of pump pulse is 2.3 eV and pulse energy is 80 mJ/cm² . T_0 and T are the transmittance of sample before and after pumping. t_d (ps) = 78 (1), 196 (2), 286 (3), 376 (4). Solid lines are the best theoretical fit of experimental curves.

We assume the effect of induced absorption in nanometer-size a-Se clusters can be explained due to realization of the two- photon transition with formation of biexcitons, i.e. two bounded electron-hole pairs. Pump pulse creates the excitons with life time of around few hundreds of picoseconds and observation of probe pulse absorption through that period is conditioned by exciton-biexciton optical transition.

The solid lines in Fig. 1 drawn through the experimental points show the best fit of data using Boltzman energy distribution of excited states.

Fig.2. The kinetics of induced absorption ΔD vs t_d in a-Se particles at the different energy of photons of probe pulses E_{pr} (eV) = 1.75 (1), 2.0 (2), 2.05 (3), 2.1 (4), 2.125 (5), 2.2 (6). All curves are shifted arbitrarily along ordinate.
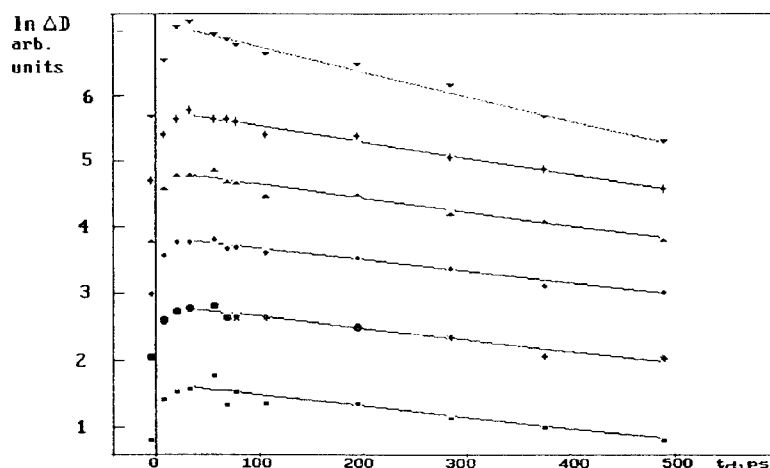
The exponential form of low energetic side in induced absorption spectra (Fig.2) reflects the Boltzman distribution tails of thermalized excitons.

Quasithermal distribution of excitons with some temperature T_x appears at the time less than 15 ps. Shift of maximum in induced absorption spectra reflects the evolution of the effective exciton temperature in semiconductor.
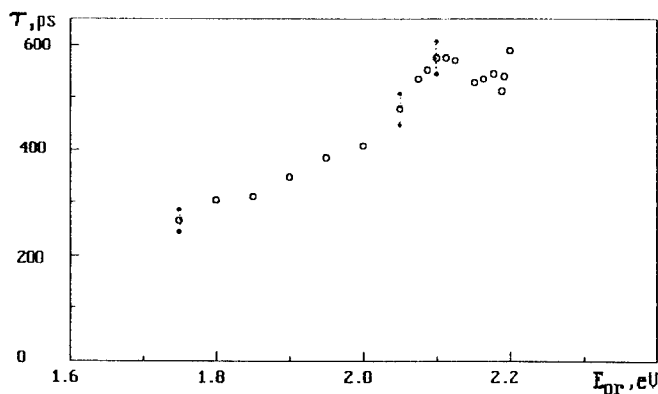
Fig.3. Decay time τ of induced absorption in a-Se particles vs the photon energy E_{pr} of probe pulses.

During the first 450 ps after the pump pulse action T_x reduces from 5900 to 3300 K exponentially with time constant 1085 ± 245 ps and the total number of excitons N_x decreases more than three times. Therefore, reduction of total number of excitons takes place before reaching the thermal equilibrium. Such variation of N_x can be conditioned by surface recombination of excitons in nanometer size clusters of a-Se. Thus the time behaviour of induced absorption is determined by the recombination and cooling of excitons.

Ultrafast Nonlinear Optical Effect in $CuInS_{2x}Se_{2(1-x)}$-Doped Glasses

V.P.Mikhailov, K.V.Yumashev, P.V.Prokoshin, S.P.Jmako
International Laser Center, Belarus State University, 7 Kurchatov Str.,
Minsk 220064, Belarus, Phone/Fax 0172-785726
I.V.Bodnar
Chemistry Department, Radioengineering Institute, 16 Brovki Str.,
Minsk 220600, Belarus, Phone 0172-398957

In this paper we present the experimental studies on ultrafast relaxation of carriers in $CuInS_{2x}Se_{2(1-x)}$-doped glasses under picosecond excitation. We report on transient change of absorption observed in pump-probe experiments and dependence of transmission on the input intensity obtained from a single-beam measurement. Using the laser pulses (15 ps) at 1.15 eV we have studied transient absorption change as a function of excitation intensity. Samples of glasses containing $CuInS_{2x}Se_{2(1-x)}$ microcrystalls with four different values of bandgap (1.06; 1.14; 1.17; 1.22 eV) are selected. The mean crystal diameter in our samples was 5-15 nm.

The transient change of absorption behave differently in different excitation intensity regimes (Fig. 1). At low excitation intensities of ~ 50 MW*cm^{-2} the bleaching effect with recovery time of ~ 11ps was observed for the photon energies slightly exceeding the bandgap. The bleaching was assumed to result from the filling of quantum-well levels in $CuInS_{2x}Se_{2(1-x)}$ microcrystalls. At middle excitation intensity a fast (~40 ps) transition from bleaching to strong induced absorption with relaxation time of ~ 4 ns was observed, which was attributed to two-photon interband transition. At high pump intensities (~10 GW*cm^{-2}) only induced absorption was observed. Bleaching did not occur when the photon energy substantially exceeded the bandgap; the increase of pump level led to an appearance of induced absorption.
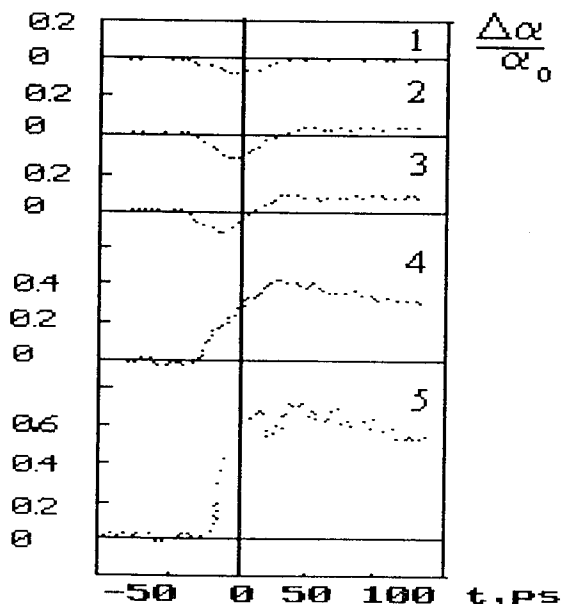
Fig. 1. Transient change of absorption of $CuInS_{1.2}Se_{0.8}$-doped glass after excitation at E_p =1.15 eV. The pump intensities are: (1) 0.06, (2) 0.27, (3) 3.8, (4) 8.2, (5) 19 GW*cm^{-2}. The absorption change $\Delta A/A = -lg(T/T_0)/lg(1/T_0)$ is plotted vs the time delay between pump and probe.

We calculated the dependences of transmission on the input intensity. The suggested theoretical model considers the effects of the single-photon absorption

saturation and two-photon absorption. The theoretical results are in good agreement with experimental data (Fig. 2).

Fig. 2. Measured (dots) and calculated (solid line) dependence of the transmission on the intensity for a $CuInS_{1.0}Se_{1.0}$-doped glass at photon energy of 1.15 eV.
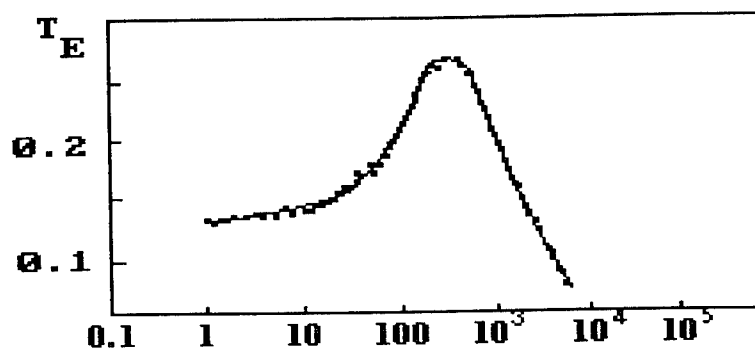
The parameter of two-photon absorption has been estimated to be 0.46 cm/GW for $CuInS_{1.0}Se_{1.0}$-doped glass. Finally, it is shown, that these glasses can be used as saturable absorbers in passively mode locking $YAlO_3$-laser. Ultrashort (16 ps) pulses are obtained.

254

A New Effect of Nonlinear Absorption and Description Using Semiclassical Theory

Chun-Fei Li and Jinhai Si

Department of Physics, Harbin Institute of Technology

Harbin 150001, China

Tel: (86)(451)3621000-4128

FAX: (86)(451)3621048

Summery

Saturable absorption (SA) based on the ground-state absorption at the resonant wavelength has been studied since the 1960's[1]. In these years many people are interested in reverse saturable absorption (RSA) based on the excited-state absorption at the non-resonant wavelength[2-3]. When the pulse width of the incident laser is shorter than intersystem-crossing time (0.1-1 ns), RSA arises from the single first excited-state absorption which is stronger than the ground-state absorption[4].

In this paper we reported a new effect that the nonlinear absorption is changed from RSA into SA at higher fluences of ps laser. SA in this case is due to the singlet second exited-state absorption which is stronger than that of the ground-state or/and the singlet first exited-state.
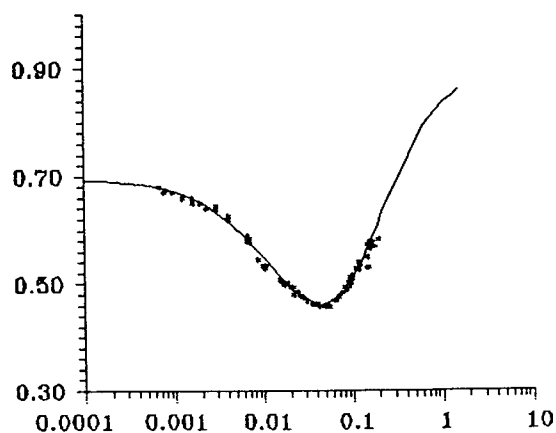
Fig.1. The comparison between experimental data (dots) and theoretical simulation (solid carve) of transmittance versus incident fluences (23 ps at 532 nm) for (TXP)Cd solution in acetonitrile. The change from RSA to SA occurs at fluence of 40 mJ/cm2.
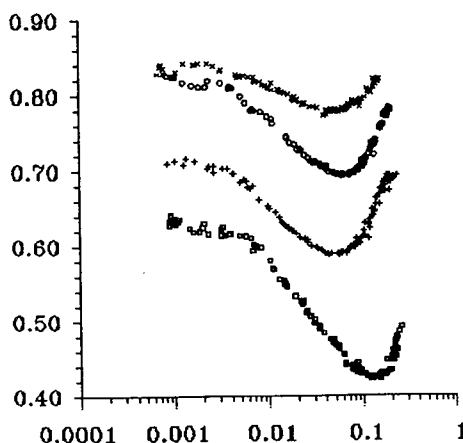
Fig.2. Experimental data of transmittance versus fluence (23 ps pulses at 532 nm) for four samples: □-(TXP)Sm; +-(Cl-TXP)Cd; O-(CH_3-TXP)Cd; ×-(CO_2Na-TXP)Gd.

In our experiments the Nd:YAG laser beam with 23 ps at 532 nm was focused into a cell contained 2 mm thickness (TXP)Cd solution in acetonitrile by a lens with 9 cm focal length.

A experimental curve of the transmittance versus the input fluence for (TXP)Cd is shown in Fig.1. It can be seen that the nonlinear absorption at low fluences is RSA, however the SA occurs above 40 mJ/cm². A set of similar experimental curves with different critical fluence for (TXP)Sm, (Cl-TXP)Cd, (CH₃-TXP)Cd, and (CO₂Na-TXP)Gd are shown in Fig.2.

Fig.3. Seven-lever model for the
organic molecule.
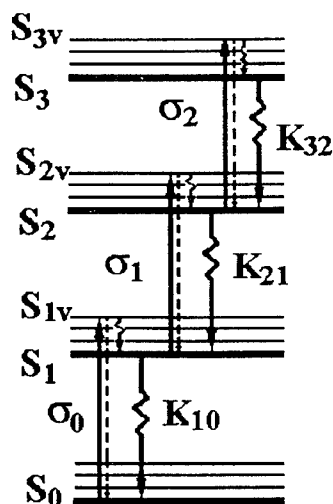
To explain these nonlinear absorption effects, a seven-level model is proposed here, see Fig.3. Molecules in S_0, S_1, and S_2 electronic levels absorb the incident photons with same non-resonant frequency ω and are exited into S_{1v}, S_{2v} and S_{3v} vibronic sub-levels with absorption cross-sections σ_0, σ_1 and σ_2, respectively. Indicating S_0, S_1, S_{1v}, S_2, S_{2v}, S_3, S_{3v} with $|0\rangle$, $|1\rangle$, $|1'\rangle$, $|2\rangle$, $|2'\rangle$, $|3\rangle$, $|3'\rangle$ respectively, the Liouville equation for the density matrix element ρ_{nm} can be written as,

$$\frac{\partial \rho_{nm}}{\partial t} = \frac{1}{i\hbar} \sum_K (H_{nk}\rho_{km} - \rho_{nk}H_{km}),$$ (1)

where Hamiltonian $\hat{H}$ can be written as

$$\hat{H} = \begin{bmatrix} \epsilon_0 & 0 & -\mu_{01'}E & 0 & 0 & 0 & 0 \\ 0 & \epsilon_1 & 0 & 0 & -\mu_{12'}E & 0 & 0 \\ -\mu_{1'0}E & 0 & \epsilon_{1'} & 0 & 0 & 0 & 0 \\ 0 & 0 & 0 & \epsilon_2 & 0 & 0 & -\mu_{23'}E \\ 0 & -\mu_{2'1}E & 0 & 0 & \epsilon_{2'} & 0 & 0 \\ 0 & 0 & 0 & 0 & 0 & \epsilon_3 & 0 \\ 0 & 0 & 0 & -\mu_{3'2}E & 0 & 0 & \epsilon_{3'} \end{bmatrix},$$ (2)

where ϵ_n is the energy of $|n\rangle$ state, E is the monochromatic electric field, and μ_{nm} is the electric dipole matrix element.

Considering the relaxation of each level and neglecting the populations in S_{1v}, S_{2v} and S_{3v}, the diagonal matrix element equations and the light-propagation equation can be obtained from Eq.(1):

256

$$\partial\rho_{11}/\partial t = \sigma_0\phi\rho_{00} - \sigma_1\phi\rho_{11} - K_{10}\rho_{11} + K_{21}\rho_{22}, \tag{3}$$

$$\partial\rho_{22}/\partial t = \sigma_1\phi\rho_{11} - K_{21}\rho_{22}, \tag{4}$$

$$\rho_{00} + \rho_{11} + \rho_{22} = 1, \tag{5}$$

$$\partial\phi/\partial z = -(\sigma_0\rho_{00} + \sigma_1\rho_{11} + \sigma_2\rho_{22})N\phi , \tag{6}$$

where $\phi = I/\hbar\omega$ is the photon flux, N is the total molecular density, K_{nm} is relaxation rate from $|n\rangle$ state to $|m\rangle$ state, and σ_0, σ_1, σ_2 indicate $\sigma_{01'}$, $\sigma_{12'}$, $\sigma_{23'}$, respectively. σ_{nm} is the absorption cross-section from $|n\rangle$ state to $|m\rangle$ state, which microscopic expression can be written as

$$\sigma_{nm} = \frac{\omega T_{mn}\mu_{mn}^2}{\varepsilon_0 nc\hbar[1 + (\omega - \omega_{mn})^2 T_{mn}^2]}, \tag{7}$$

where T_{nm} is a characteristic relaxation time between the states $|n\rangle$ and $|m\rangle$, $\omega_{nm} = (E_n - E_m)/\hbar$.

Using the photophysical parameters of the (TXP)Cd, and assuming Gaussian-shaped temporal and spatial profiles for laser pulses, the Eq. (3)-(6) can be solved numerically. The simulation of energy transmittance versus incident fluence for (TXP)Cd are shown as solid curves in Fig.1, which is consistent with experimental data.

References:

[1] M. Hercher, W. Chu. and D. L. Stockman, IEEE J. Q. E, **QE-4**, 954 (1968).

[2] W. Blau, H. Byrone, W. M. Dennis, Optics Comm. **56**, 25 (1985).

[3] A. Kost, L. Tutt, M. B. Klein, Opt. Lett. **18**, 334 (1993).

[4] Chunfei Li, Lei Zhang, Miao Yang, Hui Wang, Yuxiao Wang, Phys. Rev. A, Vol.49, No.2, (1994).

Generation of Bistable Luminescence Radiation by Thin CdS Films: Experiment and Theory

Bruno Ullrich and Takayoshi Kobayashi
Department of Physics, University of Tokyo, 7-3-1 Hongo, Bunkyo-ku,
Tokyo 113, Japan, Phone: +81/3/3812/2111 Ext. 4156

The availability of efficient optical data links and optical interconnects has lead to a worldwide outburst of excitement in the field of nonlinear photonics in order to find nonlinear materials which are suitable for all-optical (all-OB) bistable logic gates. The research efforts span semiconductors as well organics in various forms (bulk, thin films, quantum wells and microcrystallites) and a considerable amount of nonlinear phenomena (photorefractive effects, photo-thermal bistability, four wave mixing and phase conjugation).[1,2] Recently, a new nonlinear phenomenon was observed: The excitation of thin ($\leq 10\mu m$) CdS films with the 514.5nm Ar^+-laser line generates - besides the well known photo-thermal all-OB in transmission - *all-OB in luminescence* in the near infrared region of the spectrum.[3,4]
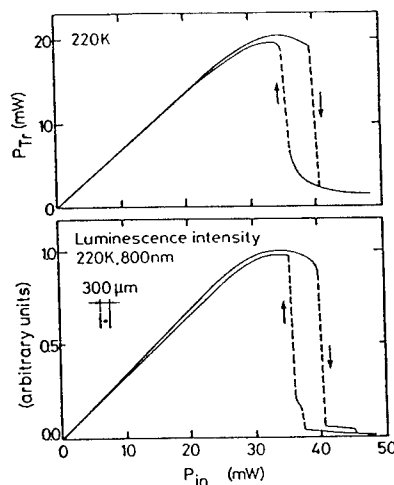
Fig. 1: All-optical bistability of the transmitted power (P_{Tr}) and luminescence intensity at 800nm. Both measurements were taken at 220K. The luminescence signal was recorded in transmission geometry with a monochromator by adjusting the transmitted beam exactly in the middle of the entrance slit as shown in the inset. Both slit widths of entrance and exit of the monochromator were $300\mu m$.

Figure 1 shows the results for transmission and luminescence. It is worthwhile to stress at this point that bistability in luminescence cannot be concluded necessarily from the essentials of photo-thermal bistabilities which are established on the photo-thermal shift of Urbach's tail in the vicinity of the absorption edge.[5] We propose a model based partly on the theory of thermoluminescence by Garlick[6] to explain bistability in luminescence.

For the first time, we present the observation of refractive all-OB bistable switches in luminescence as demonstrated in Fig. 2. A comparison of the experimental conditions of Figs. 1 and 2 shows that the refractive bistabilities cannot be observed if the luminescence of the excited focus is measured but if the direct transmitted beam of the focus is blocked by the entrance slit of the monochromator.
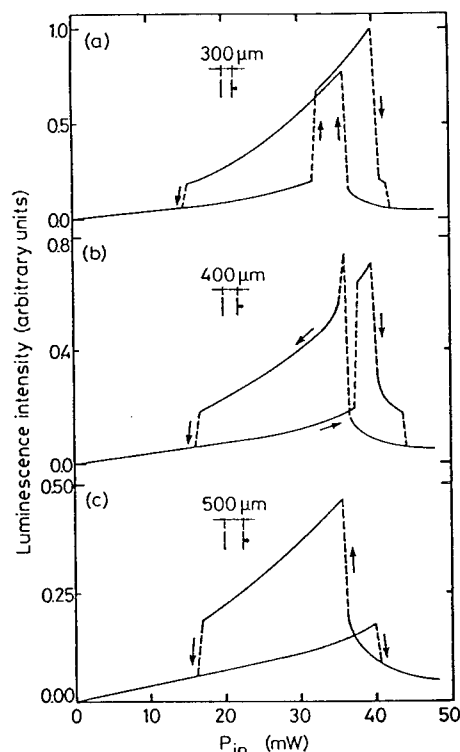
Fig. 2: The dependence of the luminescence intensity on entrance slit widths - (a) 300μm, (b) 400μm and (c) 500μm - of the monochromator. The exit slit width remains untouched at 300μm. Clearly, besides the absorptive bistable switches down pronounced bistable switches up, i.e., refractive bistabilities were observed. Refractive bistability appeared only if the direct transmitted beam of the 514.5nm line was blocked by the entrance slit as depicted in the insets. All measurements were carried out at 800nm and 220K.

In addition, a considerable dependence of the bistable luminescent responses on the entrance slit width is observed. The observation can be explained by the variation of the thermal stress of the surrounding area of the focus of the laser beam during the bistable change of the transparent to the opaque state of the thin CdS film.

An application of bistability in luminescence is discussed. Instead of a monochromator GaAs wafers were used as cut-off filters for the transmitted light in order to measure the integrated luminescence signal (>870nm, i.e. the cut-off wavelength of GaAs at 300K) of the thin CdS film. In Fig. 3 it is shown that the contrasts of the bistable loops in

luminescence depend on the free carrier type of the wafer investigated. It is shown that the differences of the loop contrasts of the bistable luminescence are caused by the the Burstein-Moss shift and bandgap renormalization of n-type and p-type GaAs wafers, respectively.
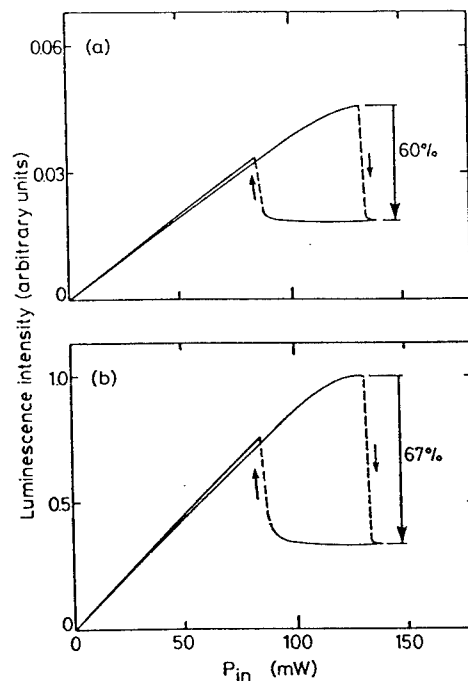
Fig. 3: Bistability in luminescence measured by putting differently doped - (a) p(Zn)-type $(5.8-14 \times 10^{18} cm^{-3})$ and (b) n(Te)-type $(2-15 \times 10^{17} cm^{-3})$ - wafers in the transmitted beam. Obviously, different free carrier types cause different loop contrasts. The temperature of the thin CdS film and the GaAs wafers during the measurement were 150K and 300K, respectively.

In conclusion, the first theoretical interpretation for all-OB in luminescence is presented. This is also the first report of refractive bistability in luminescence. Finally, a novel method is proposed to study the free carrier type of semiconductors by the application of bistability in luminescence.

1. H. M. Gibbs, *Optical Bistability: Controlling Light with Light* (Academic Press, Inc. London, 1985).
2. T. Kobayashi, Nonlinear Opt. **1**, 91 (1991).
3. B. Ullrich, A. Kazlauskas, S. Zerlauth, H. Nguyen Cong and P. Chartier: *Extended Abstracts of the 1993 International Conference on Solid State Devices and Materials, Makuhari,* 1993, p. 669.
4. B. Ullrich, A. Kazlauskas, S. Zerlauth and T. Kobayashi: J. Crystal Growth (in print).
5. B. Ullrich, C. Bouchenaki and S. Roth, Appl. Phys. A **53**, 539 (1991).
6. G. F. J. Garlick in *Handbuch der Physik,* S. Flügge, Ed., (Springer Verlag, Berlin, 1958), Vol. XXVI, p. 1.

Tuesday Papers Not Available

WEDNESDAY, JULY 27

WA: **Photorefractive Applications**

WB: **Photorefractive Materials and Solutions**

WC: **Nonlinear Optical Effects in Fibers**

WP: **Poster Session III**

Nondestructive Testing Using Nonlinear Optically Based Smart-Pixel Processors

David M. Pepper
Hughes Research Laboratories
3011 Malibu Canyon Road
Malibu, CA 90265
310/317-5125

Summary

There is an on-going need in the commercial sector to rapidly and nondestructively inspect components, *ex situ* and *in situ,* under harsh in-factory and field-testing conditions. To motivate this need, we cite below three such examples in rather diverse industrial applications. This will be followed by how optics and, more specifically, how so-called "smart-pixel processors," can augment existing inspection systems — all with the goal of enhancing the performance of the diagnostic. By smart-pixel processors, we imply that multi-pixelated information can be processed in parallel, with differential phase information preserved amongst the pixels. Typically, such processors can be realized via architectures involving phase-conjugate mirrors, either isolated, or in conjunction with spatial light modulators. These systems can, hopefully, lead to more robust and flexible manufacturing diagnostics, resulting in video frame-rate, automated inspection capabilities, with the potential for closed-loop control of the manufacturing process.

One example of an existing inspection need is in the microelectronics industry, where one desires the real-time inspection and quality control of samples consisting of highly complex, yet periodic patterns, such as masks, wafers, active-matrix display panels, and memory chips. The detection and classification of random defects and flaws early during various processing steps can improve the yield and throughput of the assembly line. Flaws typically include surface blemishes (scratches, digs, dust) and breaks (open circuits) in the connecting elements. The challenge is to localize such defects in the presence of the desirable, yet highly complex and periodic, background patterns, typical of step-and-repeat memory chips and pixelated display panels. Currently, various commercial inspection systems exist, which employ concepts such as scatterometry [1] and fixed-mask matched filtering [2]. The former approach involves illuminating the sample with a laser beam and, by measuring the angular dependence of the scattered light, one can infer the statistical distribution of various classes of surface defects. The latter approach involves either holographic filters or image comparison methods, whereby an ideal mask pattern is compared with the sample undergoing inspection. The reference pattern, being a fixed mask, requires precision alignment, magnification control, and distortion-free optical relay systems (either via electromechanical manipulators or via software algorithms). Moreover, as new structures are to be inspected, a catalog of new matched-filter masks are needed as reference structures.

In a series of experiments, both spatial light modulators [3], and real-time holographic materials using photorefractive crystals [4], have been implemented as "all-optical" nonlinear-optical (NLO) processing elements at a spatial Fourier transform plane. The basic idea is that the nonlinear element is biased to provide a thresholding operation at the transform plane — on a

pixel-by-pixel basis — so that intense features (typical of periodic patterns at the object plane) are suppressed, while weak features (typical of random defects at the image plane) are preserved. The NLO element thus functions as an adaptive mask, or filter, free from the alignment constraints of fixed-filter systems. After a second transform operation — with either a second lens or by double-passing the input lens — the defect features remain, while the periodic features are suppressed. Therefore, the viewing of the defects can be enhanced for ease of inspection and/or classification. Being an adaptive filter processor, enables one to inspect a variety of components without the need for reference-filter libraries. The result is a flexible, robust manufacturing diagnostic, with the potential for real-time implementation and process control.

Another general area of concern in the manufacturing and commercial arenas (energy, automotive, aerospace, aging aircraft, etc.) involves the inspection and monitoring of myriad materials processing, including evaluation of metallurgical properties (microstructure and hardness), surface and bulk temperature, thickness, composite material processing (delamination, debonding), and various bonds. Ultrasonic methods constitute one of many diagnostic techniques for such applications. However, in the presence of in-factory conditions such as high temperature, radiation, vibration, and irregular surfaces, conventional techniques such as direct contact and immersion ultrasound may no longer be compatible with these environments. Laser ultrasonics [5] offers a potential technique for ultrasonic inspection without the need for direct contacting, resulting in a nondestructive, long-standoff-distance diagnostic. Significant progress in laser-based ultrasonics has been made over the past decade [6], which may enable this novel diagnostic to find its way into the manufacturing arena. We will discuss some recent advances that involve optical compensation approaches — namely, phase-conjugate mirrors [7] and two-wave mixers [8] — which can further enhance the performance of laser ultrasonic diagnostics, resulting in more robust capabilities so that multi-functional systems can be realized. Finally, we discuss the ability of novel phase-conjugate interferometers to function as compact remote sensors, with the capability to monitor the growth of thin films [9], as well as to sense trace-compound species in free-space and guided-wave geometries [10]. The use of phase-conjugate elements can result in an auto-aligned sensor, with the potential to implement such biosensors and environmental monitoring systems in commercial and manufacturing applications.

References
1. See, for example, J.R. McNeil, et. al, Microlithography World 1(5), 16 ('92).
2. R. Fusek, et. al, Opt. Eng. 24, 731 ('85); M. Taubenblatt, et. al, Appl. Opt. 31, 3354 ('92).
3. R. Cormack, et. al, Opt. Eng. 27, 358 ('88); C. Gaeta, et. al, Opt. Lett. 17, 1797 ('92).
4. E. Ochoa, et al, Opt. Let. 10, 430 ('85); C. Uhrich & L Hesselink, App. Opt. 27, 4497 ('88); A.P. Gosh and R.R. Dube, Opt. Comm. 77, 135 ('90).
5. See, for example, C. Scruby and L. Drain, "Laser Ultrasonics," (Hilgar Press, Bristol, '90).
6. J.-P. Monchalin, IEEE UFFC-33, 485 ('86); ibid., Rev. Prog. QNE, Vol. 12, Plenum ('93).
7. Paul, et. al, App. Phy. Let. 50, 1569 ('87); Matsuda, et al, Jpn.J. App. Phy. 31, L978 ('92).
8. R.K. Ing and J.-P. Monchalin, Appl. Phys. Lett. 59, 3233 ('91).
9. M. Cronin-Golomb, et. al; E. Parshall , et. al; App. Opt. 28, 5196 ('89); and 30, 5090 ('91).
10. D.M. Pepper, Proc. SPIE 1824, 79 ('92).

Application of Phase Conjugation Elements in Optical Signal Processing Networks

Theo Tschudi, Cornelia Denz, Torsten Rauch, Jan Lembcke
Institute of Applied Physics, TH Darmstadt,
Hochschulstrasse 6, 64289 Darmstadt, Germany
Tel: +49-6151-162022
Fax: +49-6151-164123
e-mail: tschudi@gaston.iap.physik.th-darmstadt.de

SUMMARY

Parallel optical information processing systems are well suited for information reduction and preprocessing. Three important specifications for such applications have to be fulfiled: High space-bandwidth-product, amplification for signal restoring, and compensation of aberrations. The introduction of phase-conjugating elements into optical information processing systems will help to realize these specifications. The advantages of phase conjugation in optics, like exact counterpropagation and phase reconstruction, are well known, but the number of experimental realized applications is still small. This report gives a insight into realised applications of phase conjugation. In a first part we report on setups of phase conjugating mirrors in combination with different types of interferometers (Michelson, Sagnac, and Fabry-Perot). Applications on image subtraction, contrast amplification, phase visualisation, and parallel optical feedback systems will be presented. In all our experiments we used $BaTiO_3$ photorefractive crystals and Ar^+-ion laser for pump/signal waves.

In a second part we report on storage of 64 volume holograms in photorefractive $BaTiO_3$ using a novel orthogonal phase encoding storage technique developped in our group. The new kind of volume memories offers enormous data storage densities, fast access times associated with the parallel readout of large memory portions or pages and a potential associative access and data processing in the optical phase.

1. PCM IN A MICHELSON INTERFEROMETER

A folded setup equivalent to a Michelson interferometer with arms of equal length is used. The light of both interferometer arms is directed by mirrors onto a self-pumped phase comjugating mirror, in which it is focused by a lens. The angular selectivity of self-pumped phase conjugation allows the separation of the two arms in a single volume. Inserting images into the two arms of the interferometer allows the realization of parallel optical logic operations like addition, XOR-operation and subtraction. Most promising application is its use as novelty filter.

2. PCM IN A SAGNAC INTERFEROMETER

The use of optical image processing systems depends on the amount of information channels and the nonlinear coupling between channels. We studied the spatial resolution of a phase-conjugating ring-resonator consisting of a Sagnac interferometer and a phase conjugating mirror with high gain. We also examined the contrast function of a set of incoming signals which depends on the gain of the PC resonator and the feedback ratio of the whole system. We obtained about 10^5 independent channels within our system. The transferfunction of the system

is investigated by comparing the power spectrum of the incoming signal and the output signal. Control of coupling strength between channels is possible. We are using ring resonators for the realisation of neural nets and filtering systems.

3. PCM IN A FABRY-PEROT INTERFEROMETER

A Fabry-Perot interferometer of low finesse is used for phase front measurements. While the first mirror of the Fabry-Perot setup is a normal dielectrical one, the second mirror is a self-pumped phase conjugating mirror in which the incoming wave was focused by a internal lens. The interferometer can be regarded as being neutral due to the exact phase front reconstruction via phase conjugation and therefore does not contribute to the interference pattern of the beams. If a phase object is inserted in front of the interferometer into the laser beam, it causes distortions of the wave front, resulting in a change of the interference pattern. This shift can be used to determine the thickness of the phase object. Moreover this setup can prove the quality of phase conjugation.

4. STORAGE OF VOLUME HOLOGRAMS IN PHOTOREFRACTIVE BaTiO$_3$

Reconfigural volume holograms are important for a wide range of multiple data storage applications, including optical interconnection systems, image processing and neural network models. Several techniques for multiplexing to obtain a large number of stored images which can be recalled independently have been developed. But even the most promising of these multiplexing techniques, angular multiplexing using the selectivity of the Bragg-condition, revealed to be limited primarily because of cross-correlation noise. Other problems are not less severe.

In this paper we present an alternative approach implementing a phase coding method of the reference beam. Phase encoding has been discussed for interconnecting vector arrays in thin holograms and to perform array interconnections by correlation of a reference beam with a supplementary phase-coded input beam. In contrast to these investigations, we use a reference beam phase coding method in thick volume holographic media, taking thus full advantage of the selectivity of the Bragg-condition in volume storage media. In our experiments, we stored with pure and deterministic orthogonal phase references 64 images into a photorefractive BaTiO$_3$-crystal. For this we developed a special phase modulator on the basis of a liquid crystal display. Good reconstruction with low crosstalk could be observed. Compared to other multiplexing techniques as angular multiplexing, our method allows high storage capacity without alignement problems. Moreover, easy, light efficient as well as immediate image retrieval without any time delay is possible. Experimental setup and results will be presented. We will especially discuss in detail advantages and disadvantages of this coding method compared to others. In addition, we will present some possibilities to introduce this storage system in combination with a PCM into a assoziative network (latest results).

Adaptive RF Notch Filtering Using Nonlinear Optics

Tallis Y. Chang and John H. Hong

Rockwell Science Center
1049 Camino Dos Rios, A9
Thousand Oaks, CA 91360
(805) 373-4671

Summary

Excising narrowband interference from a broadband received signal is a useful function in modern communication systems [1]. Useful operation requires that the process be adaptive since the frequency location of the interference is not known a priori or may change in time. Nonlinear feedback controlled filters utilizing various algorithms such as Widrow's least-mean-squared-error algorithm [1] have been studied and implemented using both electronic [2] and optical and electro-optical components [3,4]. The hybrid optical systems have demonstrated remarkable performance with interference cancellation ratios exceeding 30 dB [3,4]. The main drawback of these systems, electronic or optical, is the complexity of the architecture which involves some form of nonlinear feedback. The system described in this paper involves no explicit feedback loops and is conceptually simpler than former systems yet offers competitive performance.

In this paper, we present a novel method of achieving adaptive notch filtering using the photorefractive effect in conjunction with an acoustooptic deflector. The frequency of the interference can be unknown, and it does not even have to be temporally stable as long as it falls within the bandwidth of the device. We demonstrate experimentally that our device will achieve 40 dB interference cancellation in a completely adaptive way.

Our new method for adaptive rf notch filtering is conceptually shown in Fig. 1. Two mutually coherent laser beams (I_1 and I_2) probe two different locations of an acoustooptic deflector (AOD). The two locations are chosen such that there is an acoustic (temporal) delay T_a between them, and the AOD is driven by a rf signal to be processed. The two diffracted outputs of the AOD are arbitrarily assigned as the probe and pump beams (I_{probe} and I_{pump} in Fig. 1, respectively) for the next stage of photorefractive two-beam coupling; it is of no significance as to which is the pump and which the probe. When the two beams are combined in a photorefractive crystal, the components that are mutually coherent will interact to transfer energy from the pump to the probe, while the components that are mutually incoherent will not interact, just as described in Sec. II.

To better clarify the experiment, consider the electrical input signal to the deflector be $s_{in}(t) = n(t) + b(t)$ where $n(t)$ represents the narrowband interference component and $b(t)$ the broadband signal component. If we choose the acoustic delay T_a and the photorefractive response time τ such that $1/\Delta f_n > T_a$ and $1/\Delta f_n > \tau$ where Δf_n is the bandwidth of $n(t)$, then the narrowband components will directly couple with one another. Likewise, the inequalities $1/\Delta f_b < T_a$ and $1/\Delta f_b < \tau$ where Δf_b is the bandwidth of $b(t)$ will assure that the broadband components do not interact directly one with the other.

Finally, the output of the filter is obtained when the depleted pump beam (I'_{pump}) is heterodyned with a local reference beam. The reference beam is derived from the laser beams (either I_1 or I_2) incident on the AOD. Ideally, the heterodyned signal will recover $s_{in}(t)$, the electrical input signal to the AOD, minus the component that is mutually coherent in I_{pump} and I_{probe}. In practice, however, the output of the filter is given approximately by

$$s_{out}(t) \approx b(t) + \eta b(t-T_a) + \varepsilon_1 n(t) + \varepsilon_2 n(t-T_a) \tag{1}$$

where η is the diffraction efficiency of the photorefractive grating formed by the coherent component of the signal (i.e., the interference term) and the coefficients ε_1 and ε_2 characterize the interference cancellation performance of the system. Although the broadband components do not directly couple with one another, each diffracts off (fully Bragg-matched) the stable grating formed by the narrowband components with an efficiency η. An unwanted echo of the desired signal exists in the output signal (the term with η in Eq. 1), but it can be electronically filtered out since $\eta < 1$ and the delay T_a is fixed and known.

In our experiments that followed Fig. 1 closely, we used the 514.5 nm Argon laser output, a flint glass acoustooptic modulator with a center frequency of 75 MHz (40 MHz bandwidth), and a cerium-doped $Sr_{0.6}Ba_{0.4}NbO_3$ crystal that was grown at Rockwell Science Center by R. R. Neurgaonkar. The separation between the beams in the AOM gave an acoustic delay of $T_a = 2$ μsec. The heterodyned detector output of the pump beam signal was monitored for several rf signal cases.

The first system test measured the cancellation performance of a sinusoidal interference with no broadband components. This is typically used as a rough measurement of the system performance before broadband components are introduced [3,4]. The interference at 82.4 MHz in frequency was applied to the acoustooptic deflector and the system output (coherently detected pump modulation) was monitored with a spectrum analyzer with the probe blocked (filter inactive) and unblocked (filter active). The inactive and active filter outputs are shown respectively in Figs. 2(a) and 2(b) demonstrating approximately 40 dB of cancellation. The time response of the system was measured by monitoring the output pump intensity as a function of time when the input (interference only) is suddenly switched on and was approximately 5.5 msec at an average total intensity of 10 W/cm^2. If the interference frequency were suddenly changed (within the system bandwidth governed by the acoustooptic deflector bandwidth), the system automatically adapts to the new frequency at this rate.

The system was then tested with an input consisting of both narrowband (sinusoidal) interference and broadband signal by simply using double sideband amplitude modulation of a carrier first with a random sequence signal (zero-mean, uniform distribution at 1 MHz sampling frequency), then a square wave at 500 KHz. The unsuppressed carrier serves in this case as the interference. Figures 3(a) and 3(b) respectively show the inactive and active system output spectra for an input consisting of an interference at 82.4 MHz and the random sequence signal. We have also tested our system with signal center frequency translated to 86.5 MHz and with a square wave signal; we have observed about 40 dB suppression of interference in all cases.

We have described and demonstrated the operation of a novel adaptive rf notch filter using photorefractive two-beam coupling. The simple and yet effective concept yielded interference cancellations of 40 dB while exhibiting both adaptivity to changing frequencies and a rapid response time of 5.5 msec. Our simple design requiring an acoustooptic deflector, a laser, a photodetector and a photorefractive crystal with some minimal optics is very amenable to integrated optical realizations.

References

1. B. Widrow, J. R. Glover, Jr., J. M. McCool, J. Kaunitz, C. S. Williams, R. H. Hearn, J. R. Zeidler, E. Dong, Jr., and R. C. Goodlin, Proc. IEEE **63**, 1692-1716 (1975).
2. D. R. Morgan and S. E. Craig, IEEE Trans. Acoustics, Speech and Sig. Processing, **ASSP-24**, 494-507 (1976).
3. A. Van der Lugt, "Adaptive optical processor," Appl. Opt. **21**, 4005-4011 (1982).
4. D. Psaltis and J. Hong, Appl. Opt. **23**, 3475-3481 (1984).

Fig. 1 Adaptive rf notch filtering using photorefractive two-beam coupling; experimental setup.

Fig. 2 40 dB cancellation of interference at 82.4 MHz with no broadband signal: (a) inactive system output spectrum, (b) active system output spectrum. 10 dB/div. vertical scale.

Fig. 3 35 dB cancellation of interference at 82.4 MHz with computer generated random signal with zero-mean uniform distribution (1 MHz sample frequency): (a) inactive system output spectrum, (b) active system output spectrum. 10 dB/div. vertical scale.

271

Fidelity-Threshold And Critical Slowing Down In Photorefrative Double Phase Conjugate Mirrors

Doruk Engin, Sergei Orlov, Mordechai Segev, and **Amnon Yariv**
California Institute of Technology, 128-95, Pasadena, CA 91125
Tel. (818) 395-4823; Fax (818) 405-0928,

George C. Valley
Hughes Research Laboratories, 3011 Malibu Canyon Road
Malibu, CA 90265

The double phase conjugate mirror[1] is a unique photorefractive device in which two mutually incoherent input beams become phase conjugates of each other. Recently, we developed a model to calculate the temporal and spatial behavior of DPCM[2], predicted and observed[3] a fidelity-threshold. In this work we present a detailed theoretical and experimental study of the DPCM. We characterize its spatial and temporal behavior through the conjugation fidelity and conjugation reflectivity, establish its oscillatory properties and predict critical slowing down near the threshold. This work provides a deeper insight into the stimulated wave mixing process, and will be useful for understanding the limitations of device applications.

Our theoretical and experimental results show that the conjugation fidelity and reflectivity have a different dependence on photorefractive coupling coefficient times length (gain). Fig(1) shows the conjugation fidelity and the conjugation reflectivity as a function of gain. The conjugation fidelity exhibits a sharp jump, which we define as the DPCM fidelity-threshold, while the conjugate reflectivity smoothly increases as the gain is increased past that point. Near this threshold the reflectivity continues to be very small (a sudden, but small, increase in reflectivity is also apparent) while the fidelity is close to unity. Our experimental results[3] confirm this behavior and indicate that above the threshold good fidelity is obtained and stays unchanged as the reflectivity continues to grow with the gain. The difference between the fidelity and reflectivity is also apparent in their temporal evolution. We observe both theoretically and experimentally that the fidelity reaches steady state early in time while the reflectivity continues to grow gradually.

Our calculations point out two major features that characterize the DPCM as an oscillator. The first one is slowing-down of the DPCM temporal response for operation near the threshold (in a similar manner to critical slowing-down in lasers). Fig(1) illustrates the response time of reflectivity as a function of gain. The time required for the reflectivity to reach steady state dramatically slows down near the threshold. The property of decreasing response time with increasing gain is a characteristics of oscillators (in an amplifier, the time response does not diverge at any specific gain value). Our second observation is the sustaining of the conjugation reflectivity after the seed levels are set to zero (for gain values above the threshold). The behavior of DPCM for different gain values is illustrated in Fig(2), where the temporal evolution of the conjugation reflectivities for three different gain values are shown (well above , well below and near the threshold (gain values of 1.63, 0.98, 1.28)). In each case after the system comes to steady state, the seed levels are set to zero. Above the threshold the conjugate reflectivities are not affected (upper curve), while well below the threshold the conjugate reflectivities go to zero. Near the threshold the reflectivity decreases, but remains finite.

Finally, we present the seed level[2] and input intensity ratio dependencies of the gain-threshold. Our calculations show that for low seed level (seed to beam intensity ratio of 10^{-6}) the steady-state fidelity and reflectivity do not vary significantly with seed levels. However, for high seed levels (seed to beam intensity ratio of 10^{-4}) fanning becomes more pronounced, and the calculations show a significant degradation of the phase conjugation. We find that fanning acts as a dissipation process which damps the oscillation, hence "critical slowing down" become less pronounced as the seed level is increased.

Unbalanced input beam intensities result in asymmetric conjugation process where the conjugation fidelity on the side of the weak input beam is greatly reduced, although the intensity of the diffracted strong beam in the direction of the weak beam is large. Specifically, the stronger beam bleaches the fanning (amplified noise) gratings of the weak beam, and enables relatively high conjugation quality on its input side (i.e., high fidelity is obtained for the image originally borne on the strong beam and transferred to the weak beam). The opposite process, however, is not efficient due to unbalanced process, and the weak beam is not able to eliminate the appearance of fanning gratings, which results in the conjugate image embedded in fanning. In our calculations we find that the fidelity as a function of gain on the side of the strong input beam is slightly flattens, but the threshold value is unaffected. On the other hand, the fidelity as a function of gain on the side of the weak input beam is shifted towards higher gain values. Hence, for a given gain value we find more degradation on the side of the weak input beam. The fanning of the strong beam (in a similar manner to large seed level), makes the critical slowing down less pronounced. With larger intensity ratios the peak of the reflectivity response time as a function gain shifts towards higher gain values, confirming the shift in the threshold observed for the fidelities. We also confirmed these results experimentally[3]. Fig(3) shows typical photographs of the phase conjugate images for unbalanced input beams, where (a) and (b) are the images on the sides of the strong and weak inputs, respectively. Additional experimental observations indicate that the fidelity threshold value depends on the resolution of the input beam, and partial conjugation can be observed (in images of varying resolution) at intermediate gain levels.

In conclusion, we present theoretical and experimental results that analyze the double phase conjugation process. We establish the existence of gain-threshold and point out the differences between conjugation fidelity and conjugation reflectivity. We study the oscillatory nature of the DPCM and predict the existence of critical slowing down near the gain-threshold. Our results provide a deeper insight into the stimulated wave mixing process, and are useful for understanding the limitations of device applications, such as image processors, interconnects, interferometers, and coupled-laser devices. Furthermore, our theoretical formulation is general and may be applied to all the stimulated photorefractive processes and all self-pumped phase conjugators.

References

(1) S. Weiss, S. Sternklar and B. Fischer, Opt. Lett. **12**, 114 (1987).

(2) M. Segev, D. Engin, A. Yariv and G. C. Valley, Opt. Lett. **18**, 12 (1993).

(3) S. Orlov, M. Segev, A. Yariv and G. C. Valley, accepted to Opt. Lett.(1994).
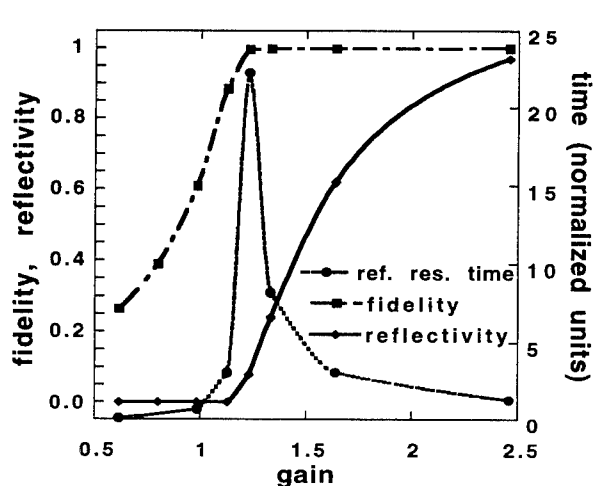
Fig. 1: Conjugation fidelity, conjugation reflectivity, and response time of the conjugation reflectivity (normalized) as a function of gain length product.
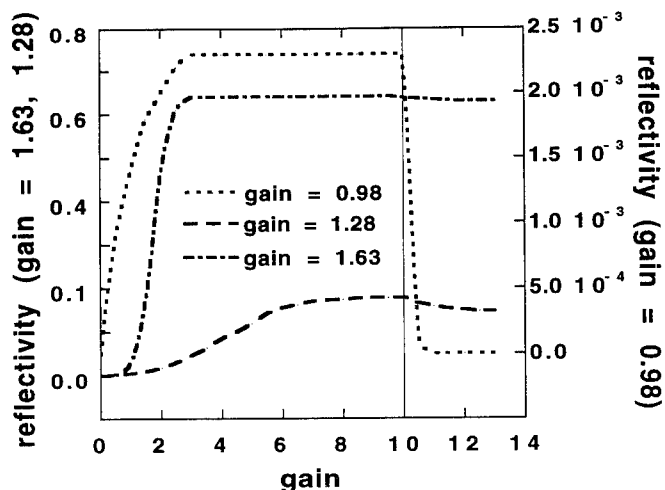
Fig. 2: Conjugation fidelity as a function of time for gain values of (2.71, 1.57, 1.17) for parameters that give a threshold value of 1.62. The left vertical axis corresponds to reflectivities for gain values of (2.71, 1.57), and the right vertical axis corresponds to reflectivities for the gain value of 1.17.
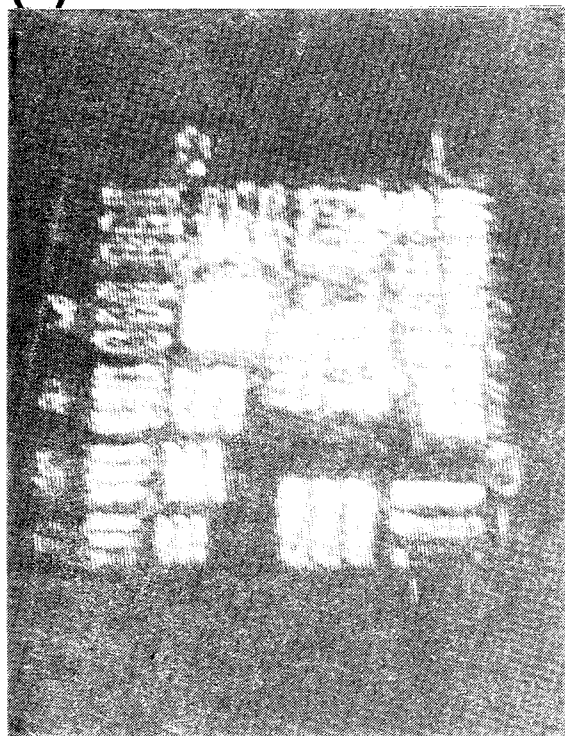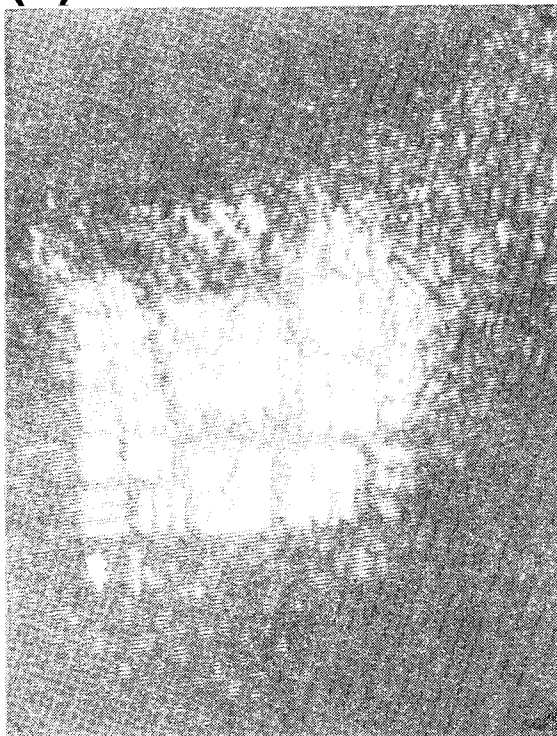
Fig. 3: Phase conjugate images for unbalanced input beams of intensity ratio 1:5; (a) on the side of the strong input beam, (b) on the side of the weak input beam.

High Gain Nondegenerate Two-Wave Mixing in Cr:YAlO$_3$

Ian McMichael, Ragini Saxena, and Tallis Y. Chang
Rockwell International Science Center
1049 Camino Dos Rios
Thousand Oaks, CA 91360
Phone: (805) 373-4508
Fax: (805) 373-4775

Qize Shu and Stephen Rand
Department of Electrical Engineering and Computer Science
University of Michigan
1301 Beal Avenue
Ann Arbor, MI 48109-2122

Jimmy Chen and Harry Tuller
Materials Science & Engineering Department
Massachusetts Institute of Technology
77 Massachusetts Avenue
Cambridge, MA 02139

Summary

Recently we demonstrated a gain of 6 times that was obtained by nondegenerate two-wave mixing in Cr:YAlO$_3$.[1] Here we report new experiments in which a gain of 22 times was achieved by increasing both the interaction length and the doping of the material. To our knowledge, this is the largest cw two-wave mixing gain obtained in a bulk, solid state, non-photorefractive material. Experiments demonstrating high gain, nondegenerate two-wave mixing in new solids using low power cw lasers constitute an essential step in establishing the viability of alternative materials for applications of nonlinear optics in areas such as signal processing. Availability of high gain can bring about rapid progress in experimental research, as occurred with the discovery of photorefractive materials such as barium titanate. To our knowledge however, no one has demonstrated gain comparable to that of photorefractive materials by using a solid state bulk (as opposed to guided wave) Kerr medium with a cw source. We report properties of a candidate material, chromium-doped yttrium aluminate (Cr:YAlO$_3$), that may significantly advance experimental efforts on nonlinear optics in Kerr-like media, much the way basic studies of barium titanate initiated widespread study of nonlinear optics in photorefractive materials. Motivation for the present work was provided by the expectation of new properties that should result from the different nonlinear mechanism (Kerr-like vs. photorefractive), such as improved dynamic range in mutually pumped phase conjugation[2] that is important in wavefront matched heterodyne receivers.[3]

Figure 1 is a simplified schematic of the experiment used to measure gain in nondegenerate two-wave mixing.[4] Light from an argon laser is split into a weak probe beam $I_2(0)$ and a strong pump $I_1(0)$, with a fixed ratio $I_2(0)/I_1(0) = 1/1000$. The frequency of the pump is shifted by approximately 5 Hz with respect to the probe by reflecting it from a mirror mounted to a piezoelectric transducer and driven by a triangle-wave voltage source. The grating formed by the interaction of the pump and probe in the crystal of Cr:YAlO$_3$ results in amplification for the probe when the mirror is moving in one direction, and attenuation when the mirror moves in the opposite direction.
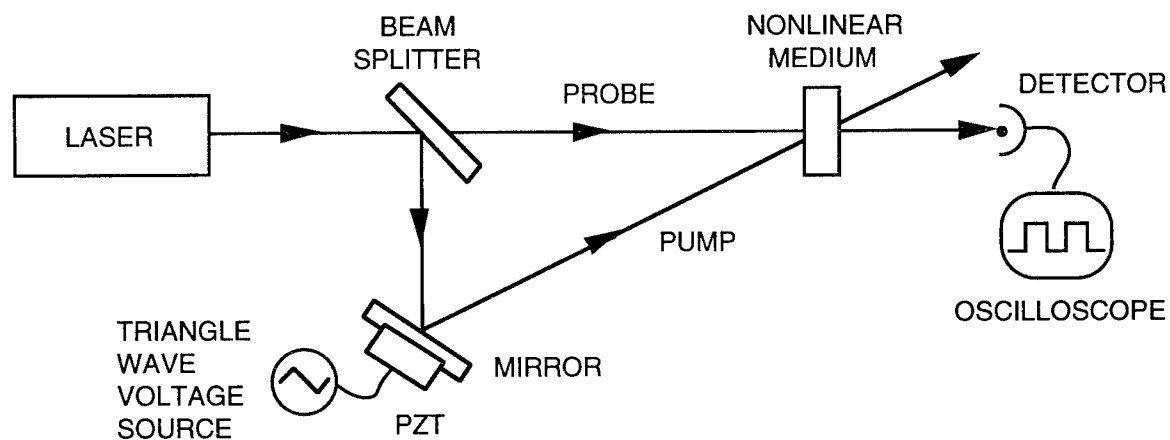
Fig. 1 Schematic of experiment used to measure nondegenerate two-wave mixing gain.

Figure 2 (a) shows a plot of the gain as a function of the intensity of the pump for the range from 0 to 80 W/cm². The circles are the experimental measurements, and the line is a fit of the theoretical form,

$$
\frac{I_2(L)}{I_2(0)} = e^{-\alpha L} \exp\left\{\left(\frac{1-e^{-\alpha L}}{\alpha L}\right)\left[\frac{2\pi n_2 I_1(0)L/\lambda}{\left(1+I_1(0)/I_s\right)^2}\right]\right\}
\tag{1}
$$

with $\alpha L = 0.69$, L = 9.1 mm, $\lambda = 514.5$ nm and $I_S = h\nu/\sigma\tau = 1.27$ kW/cm², where h is Planck's constant, ν is the optical frequency, σ is the absorption cross-section and τ is the metastable state lifetime. Using n_2 as the only adjustable parameter, the fit yields $n_2 = 3.2 \times 10^{-7}$ cm²/W.

(a)   (b)
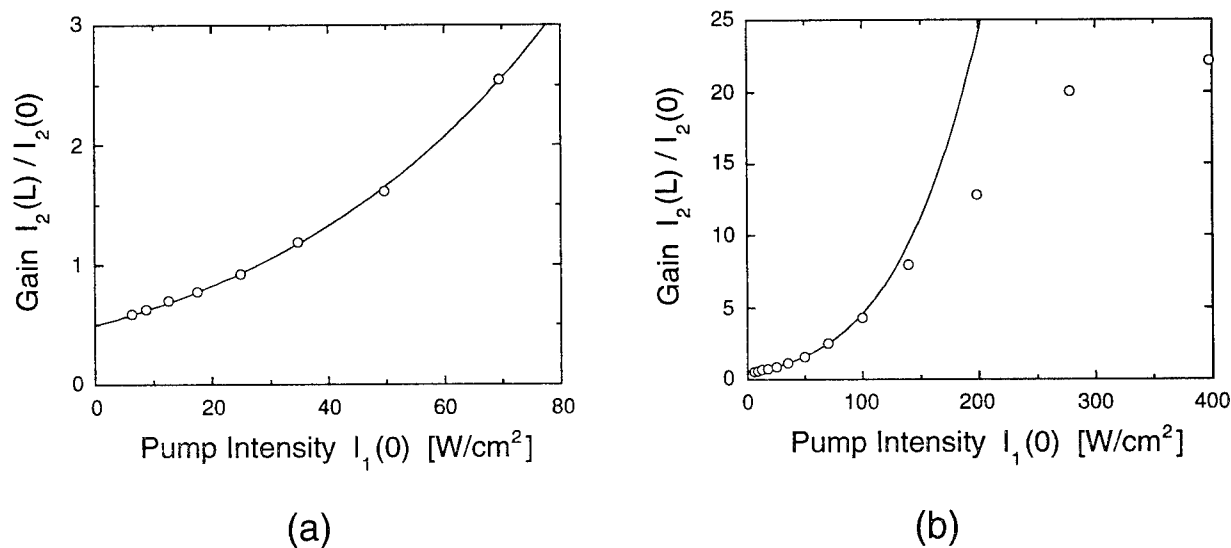
Fig. 2 Gain vs. pump intensity: (a) from 0 to 70 W/cm², and (b) from 0 to 400 W/cm².

Figure 2 (b) shows the gain for the range from 0 to 400 W/cm^2. Using the previously stated parameters and n_2 as determined from the fit for the lower intensity range of Fig. 2(a), the line in Fig. 2(b) represents projections based on the theoretical form expressed by Eq. (1). A gain of 22 times was obtained at approximately 400 W/cm^2, but the measured gain does not increase with intensity as much as theory predicts. (Theory predicts a gain of 200 at 400 W/cm^2.) We believe this is due to "beam break-up" resulting from spatial nonuniformities of the nonlinear refractive index change in the interaction region. As evidence, Fig. 3 shows photographs of the transmitted pump beam with the probe beam off, (a) at low intensity and normal exposure indicating the transmitted beam size, (b) at low intensity and long exposure showing an "X" shaped pattern of linear scattering that is believed to be the result of scattering from surface and bulk defects, and (c) at high intensity and exposure equivalent to case (b) showing both the nonlinear scattering due to nonuniformities in the nonlinear refractive index change, and the linear scattering due to surface and bulk defects. Spatial nonuniformities of the nonlinear refractive index change in the interaction region can be the result of shadows or distortions from surface or bulk defects, or from spatial variations in the Cr-ion concentration.

(a)   (b)   (c)
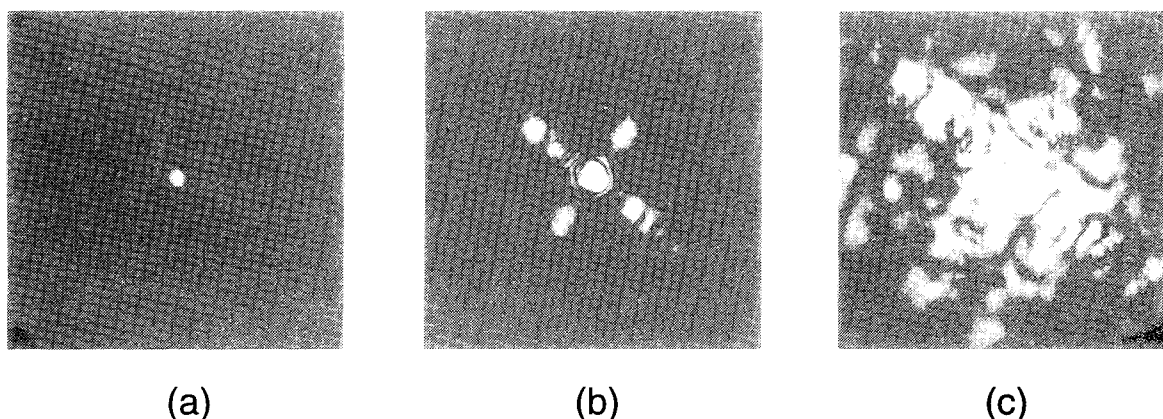
Fig. 3   Photographs of the transmitted pump beam, (a) Gaussian beam size, (b) "X" shaped pattern resulting from linear scattering, and (c) nonlinear scattering.

In conclusion, we have demonstrated a gain of 22 times by nondegenerate two-wave mixing in Cr:YAlO$_3$. The experimentally measured gain appears to be limited by "beam break-up" due to spatial nonuniformities in the nonlinear refractive index change, that are the result of inhomogeneities in the crystal. Theoretical predictions based on our experimental data indicate that gain in excess of 200 times should be possible in Cr:YAlO$_3$ if a homogeneous crystal can be obtained. Due to its potential for such high gain, Cr:YAlO$_3$ is a very promising material for applications of nonlinear optics in areas such as signal processing, making it clear that additional experimental efforts are warranted to explore nonlinear response in solid-state Kerr-like media generally, and to investigate further the potential advantages of materials like Cr:YAlO$_3$ over photorefractive crystals.

References

1. I. McMichael, R. Saxena, T. Chang, R. Neurgoankar, and S. Rand, in *Conference on Lasers and Electro-Optics, 1993* (Optical Society of America, Washington, D.C., 1993), paper CThS34, pp. 514-515.
2. R. Saxena and P. Yeh, J. Opt. Soc. Am. **B 7**, 326 (1990).
3. L. Adams and R. Bondurant, Opt. Lett. **16**, 832 (1991).
4. I. McMichael, P. Yeh, and P. Beckwith, Opt. Lett. **13**, 500 (1988).

Photorefractive properties of rhodium-doped barium titanate

G. D. Bacher, Stuart MacCormack and Jack Feinberg
Departments of Physics and Electrical Engineering,
University of Southern California, Los Angeles, CA 90089-0484
Tel: (213) 740 0870
and
B. A. Wechsler and M. B. Klein
Hughes Research Laboratories
3011 Malibu Canyon Road, Malibu, CA 90265

Undoped barium titanate crystals have a painfully slow photorefractive response time using light in the near infrared, which has discouraged their use with laser-diode devices. Recently, Wechsler *et al.* showed that adding rhodium oxide to the melt produces an additional peak, centered close to 650 nm, in the absorption profile of the resulting $BaTiO_3$ crystals.[1] This additional absorption feature gives the crystals a blue-green color, and, more importantly, it extends their photorefractive response into the near infrared. Earlier, Ross *et al.* observed this enhanced infrared response in $BaTiO_3$ crystals having the same absorption spectrum and observed self-pumped phase conjugation in the CAT geometry out to a wavelength of at least 1.06 μm, with reflectivities of 75% in the near infrared.[2] These IR-enhanced $BaTiO_3$ crystals are now useful for photorefractive device applications at laser diode wavelengths, such as the locking and beam combining of high-power diode lasers, as well as for numerous applications using Nd:YAG lasers.

We have measured the effective trap density, the number of active trap levels, the sign of the dominant charge carrier, and the photorefractive two-beam coupling gain of four rhodium-doped crystals of $BaTiO_3$, all grown at Hughes Research Laboratories. The crystals (labeled 304, 305, 306, and 307) appear blue to deep blue-green, and were grown from melts containing 400, 800, 1600 and 3200 parts per million of RhO_2 respectively. Electron paramagnetic resonance (EPR) measurements confirm the presence of Rh^{4+} centers in these crystals.

Induced transparency/absorption measurements

We cross two beams from an argon-ion laser (λ = 488 nm) in a $BaTiO_3$ crystal. We make the two beams mutually incoherent at the crystal to eliminate any electro-optic or absorption-grating coupling. We measure the change in the absorption of the weak probe beam caused by the presence of the strong pump beam. The results for sample #304 are shown in Fig. 1. The induced absorption (or transparency in this sample) is caused by the redistribution of mobile charges among deep and shallow trapping levels, each level having a different absorption cross section. At low intensities, most charges are in deep trapping sites so the absorption of this deep level dominates. However, higher light intensities populate the shallow trapping levels and this changes the net absorption. For a single deep level and a single shallow level (as is the case for nominally undoped $BaTiO_3$), one sees an induced absorption whose strength saturates at high intensity. However, Fig. 1 shows that in Rh:$BaTiO_3$ #304 there is an induced *transparency* that first increases and then

decreases as the intensity is increased. Such behavior requires the presence of at least one additional trapping level. We postulate that this new mid-level is accessible to infrared photons and so provides the charge reservoir required to generate the photorefractive space-charge field at longer wavelengths.
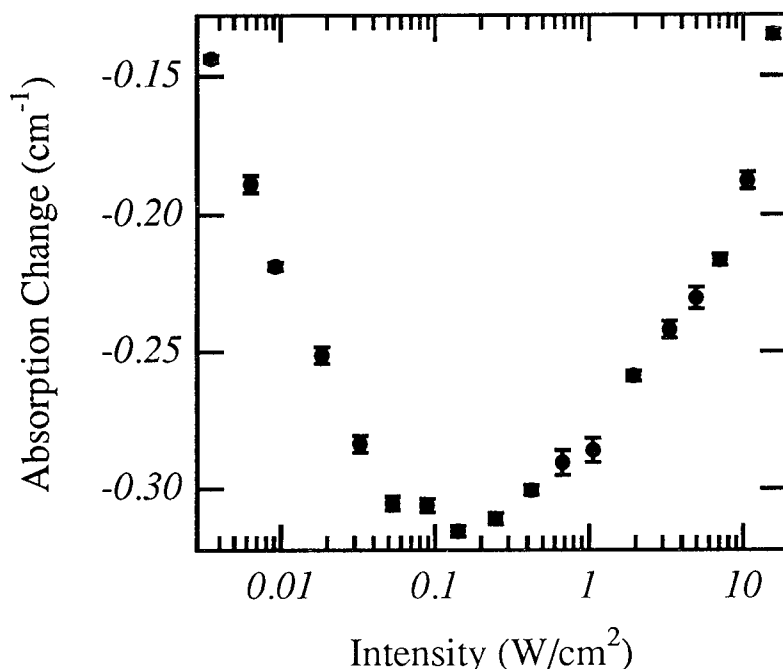
Figure 1) Light-induced transparency in Rh:BaTiO3 sample #304, as a function of light intensity at λ = 488 nm. The shape of the data suggests the presence of at least three active trap levels in this crystal.

Absorption grating measurements

Absorption gratings, caused by the difference in polarizability of empty and full trapping sites, can couple the phase and the amplitude of the two coherent light beams.[3] The complex gain coefficient γ depends on the grating vector k_g according to:

$$\gamma = \left\{ \frac{A\left(k_g / k_o\right)^2 + B}{1 + \left(k_g / k_o\right)^2} \right\} \tag{1}$$

where A is a set of material parameters, B is an offset due to multiple trap levels, and k_o = $(N_{eff} e^2 / (\varepsilon\varepsilon_0 k_B T))^{1/2}$ is the Debye screening wavevector, which contains the crystal's effective trap density N_{eff}. We measure the complex gain γ as a function of k_g (effectively, the beam-crossing angle). (We first make sure to eliminate all electro-optic coupling by carefully choosing the directions of the light beams' polarizations and the crystal's c-axis.) Fitting our data to Eq. 1 yields the effective trap density N_{eff} at the wavelength used. Figure 2 shows the typical dependence of the real and imaginary parts of γ as a function of k_g for sample #304

at the wavelength $\lambda = 488$ nm. For this sample at this wavelength we obtain an effective trap density of 6.2×10^{16} cm^{-3}, which is comparable to the trap density of nominally undoped BaTiO$_3$. We repeat these measurements at a number of different laser wavelengths, from the visible to the near infrared, to determine how the trap density N$_{eff}$ varies with laser wavelength. We will present this data and additional measurements for all our Rh-doped crystals to show how the level of rhodium concentration affects the effective trapping density and other material properties.
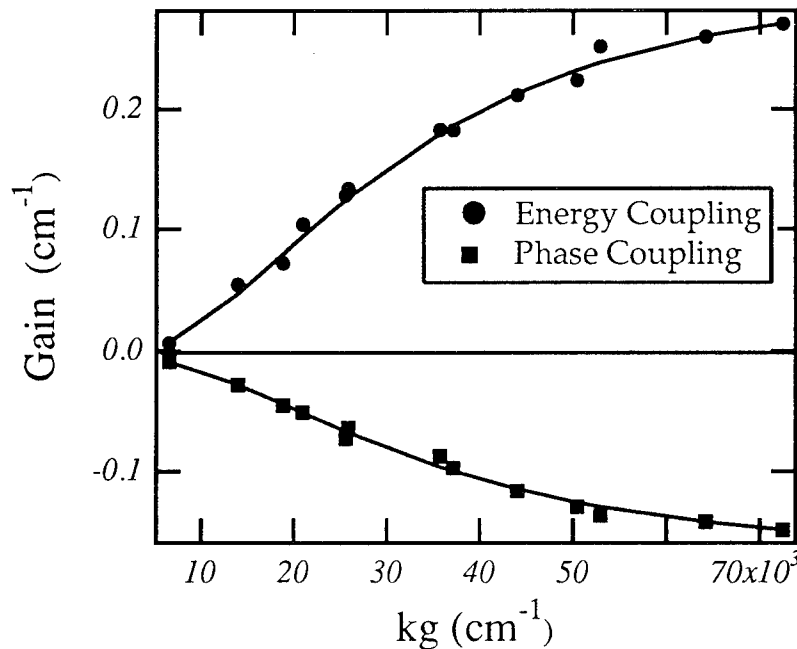
Figure 2) Absorption grating energy and phase coupling as a function of the grating wavevector k$_g$. The lines are fits to Eq. 1. The inflection point of these curves occurs at k$_g$ = k$_o$, and so reveals the effective density N$_{eff}$ of photorefractive charges.

References

1) B. A. Wechsler, M. B. Klein, C. C. Nelson, and R. N. Schwartz, "Spectroscopic and photorefractive properties of infra-red sensitive rhodium-doped barium titanate," accepted January, 1994, for Optics Letters.

2) G. W. Ross, P. Hribek, R. W. Eason, M. H. Garrett, and D. Rytz, "Impurity enhanced self-pumped phase conjugation in the near infrared using 'blue' BaTiO$_3$," Opt. Comm. 101, 60 (1993).

3) R. S. Cudney, R. M. Pierce, G. D. Bacher, and J. Feinberg, "Absorption gratings in photorefractive crystals with multiple levels," J. Opt. Soc. Am. B, 8, 1326 (1991).

Optical and electron paramagnetic resonance investigation of the role of vanadium in photorefractive CdTe:V

Mehrdad Ziari and William H. Steier
Department of Electrical Engineering, University of Southern California
Los Angeles, CA 90089-0483

Robert N. Schwartz and Marvin B. Klein
Hughes Research Laboratories, 3011 Malibu Canyon Road, Malibu, CA 90265

Sudhir B. Trivedi
Brimrose Corporation of America, 7720 Belair Road, Baltimore, MD 21236

Cadmium telluride has been regarded as a material of choice for many envisioned photorefractive applications in the infrared because of its high electrooptic coefficient. We recently demonstrated[1] high beam-coupling gains in CdTe:V using applied electric fields (see Fig. 1). The prospects of using this gain enhancement mechanism in self-pumped phase conjugators and the experimental demonstration[2] of the theoretically predicted high sensitivity of the photorefractive process in CdTe:V has attracted more attention towards the development and the optimization of the photorefractive properties of this material.[3-6] Experience has shown that vanadium is a proper dopant that results in both high resistivity and efficient photoconductive and photorefractive responses over a wide wavelength range in the infrared.[2,3] Further development of this material requires an understanding of the role of V in the photorefractive process. We report on photorefractive characterization, optical absorption, photo-luminescence and electron paramagnetic resonance of vanadium-doped CdTe. The results of these experiments outline the role of vanadium in the photorefractive process. Contrary to other views regarding the role of vanadium,[4] this study establishes that V is substitutionally incorporated on cadmium site in our samples and is a so called "photorefractive center".
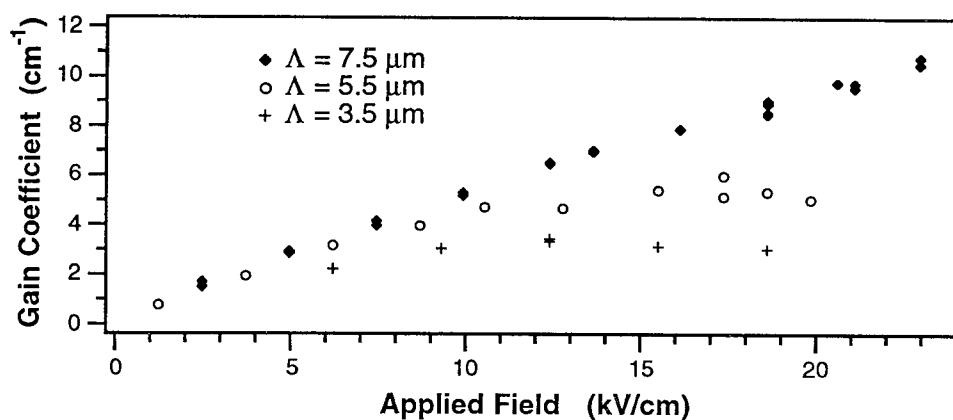
Fig. 1) Gain coefficient vs. applied field for various fringe spacings (Λ) using a square wave at 230 kHz and a beam ratio of 10^4.
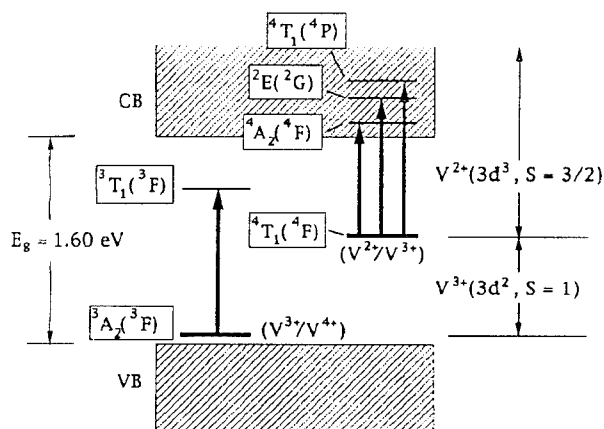
Fig. 2) Combined energy-level band diagram showing internal excitation of substitutional V in CdTe.
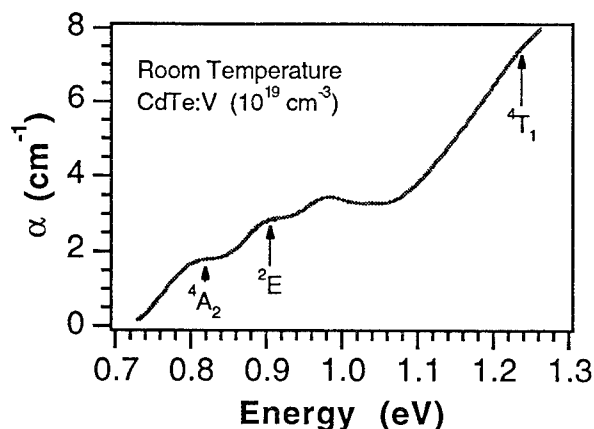
Fig. 3) Optical absorption spectrum of CdTe:V at room temperature. The position of the crystal-field transition energies at 80 K are indicated by arrows.

Theoretical models predict that vanadium should be substitutionally incorporated at the cation site (Cd in CdTe) and be in divalent state.[7] The combined energy-level diagram of CdTe:V in Fig. 2 also shows the crystal-field excited states of V^{2+} that are degenerate with the conduction band. The absorption through these internal excitation channels can result in a conduction electron through self-ionization. The absorption spectrum of CdTe:V is shown in Fig. 3 where the energies corresponding to the internal excitation from the $^4T_1$ ground state to the $^4A_2$, ^2E and $^4T_1$ excited states at 80 K temperature are also marked as reference. Earlier studies[8] report that the photoconductivity spectrum replicates the absorption features that are assigned to internal excitations. This indicates the emission of electrons to the conduction band through self-ionization and makes such internal excitations useful for the photorefractive process. Photoluminescence spectroscopy of our photorefractive CdTe:V reveals the presence of a shallow acceptor at ~0.1 eV above the conduction band. We suspect that this level plays an important role in the charge compensation mechanism and the partial ionization of V^{2+} state.

We observed the electron paramagnetic resonance of V^{3+} ion in CdTe:V at low temperatures.[5] The isotropy of the EPR signal confirms the substitutional incorporation of vanadium in the lattice. The lack of detection of the V^{2+} signal by conventional EPR techniques is not uncommon in semiconductors and it is believed to be due to the broadening of its EPR spectrum by configurational distortions.[5] Furthermore, photoexcitation at 0.51 μm and 1.3 μm resulted in a reduction in EPR signal, suggesting a depopulation of V^{3+} state. This clearly indicates that vanadium is optically active. Note that the low temperature environment of the EPR study limits the direct applicability of its results to the photorefractive and absorption processes at room temperature and it is only regarded as an indication of the presence, the substitutional incorporation and the optical activity of vanadium in CdTe.

Photorefractive properties of CdTe:V at 1.3 and 1.5 μm were characterized by two-beam coupling. The data suggest little or no electron-hole competition at these wavelengths. The sign of the photorefractive carrier was determined by the electrooptic method at 1.06 μm to be that of

electrons. By noting that the direction of energy transfer in two-beam coupling remains the same as wavelength is changed from 1.06 μm to 1.32 μm and to 1.52 μm, we ascertain that electrons are the photorefractive carriers for all these wavelengths. The findings, along with the observation of the absorption features in the 1.3 μm to 1.5μm wavelengths range that are related to internal excitations from V^{2+} state, suggest that photoionization of the V^{2+} state occurs during the photorefractive process.

The characterization of two adjacent samples from the CdTe:V crystal boule reveals that the effective trap density and the amplitude of the absorption features vary along the growth direction. This suggests that the incorporation of vanadium changes along the growth direction. The twinning problem in CdTe and the size requirements for device applications make it necessary to grow large diameter (1-2 cm) crystals. The currently available CdTe:V samples have already exhibited a fast and sensitive response that surpasses other potential photorefractive materials in IR region. However, the wide scale use of CdTe:V as a reliable photorefractive material, we believe, requires further improvement of the growth process and a continuation of efforts in understanding the photorefractive effect in this material.

References:

[1]. M. Ziari, W. H. Steier, P. N. Ranon, M. B. Klein and S. Trivedi, "Enhancement of photorefractive gain at 1.3-1.5 μm in CdTe using alternating electric fields," *J. Opt. Soc. Am. B* , **9,** 1461-1466 (1992).

[2]. A. Partovi, J. Millerd, E. M. Garmire, M. Ziari, W. H. Steier, S. Trivedi and M. B. Klein, "Photorefractivity at 1.5 μm in CdTe:V," *Appl. Phys. Lett.* , **57,** 846-848 (1990).

[3]. E. Rzepka, A. Aoudia, M. Cuniot, A. Lusson, Y. Marfaing, R. Triboulet, G. Bremond, G. Marrakchi, Y. Cherkaoui, M. C. Busch, J. M. Koebel, M. Hage-Ali, P. Siffert, J. Y. Moisan, P. Gravey, N. Wolfer and O. Moine, "Optical and thermal spectroscopy of vanadium doped CdTe and related photorefractive effect," in *Proc. of International Conference on II-VI Compounds and Related Optoelectronic Materials*, (NewPort, R. I., 1993).

[4]. J. P. Zielinger, M. Tapiero, Z. Guelli, G. Roosen, P. Delaye, J. C. Launay and V. Mazoyer, "Optical, photoelectrical, deep level and photorefractive characterization of CdTe:V," *Materials Science and Engineering* , **B16,** 273 (1993).

[5]. R. N. Schwartz, M. Ziari and S. Trivedi, "Electron paramagnetic resonance and optical investigation of photorefractive vanadium-doped CdTe," *Phys. Rev. B* , **49,** 5274 (1994).

[6]. H. J. V. Bardeleben, J. C. Launay and V. Mazoyer, "Defects in photorefractive CdTe:V: An electron paramagnetic resonance study," *Appl. Phys. Lett.* , **63,** 1140-1142 (1993).

[7]. A. Zunger, "Electronic structure of 3d Transition-Atom-Impurities in Semiconductors," in *Solid State Physics*, Vol. 39,, (Academic Press, Orlando, Florida, 1986), pp. 276-464.

[8]. J. M. Baranowski, J. M. Langer and S. Stepanova, "Observation of discrete impurity excited states degenerate with conduction band in CdTe:Ti, CdTe:V and CdSe:Co," in *Proceedings of the International conference on the physics of semiconductors, 11th,* (Warsaw, Poland, 1972), pp. 1008.

Grating Response Time of Photorefractive KNbO$_3$:Rb$^+$

Yuheng Zhang, Scott Campbell, and Pochi Yeh, Department of Electrical and Computer Engineering
University of California at Santa Barbara, Santa Barbara, CA 93106

Dezhong Shen, Xiaoyan Ma, and Jiongyao Chen, Research Institute of Synthetic Crystals
P.O. Box 733, Beijing, China

Photorefractive crystals play an increasingly important role in optical information processing [1, 2]. Some of these crystals have been used in a variety of optical computing applications [3]. The photorefractive response time is a critical issue because it directly determines the processing speed of the devices. Crystals that are widely used at present, such as BaTiO$_3$, LiNbO$_3$, and SBN, etc., are relatively slow when the light intensity is 1W/cm^2. Semiconductor crystals such as GaAs and GaP have a higher speed but suffer from small coupling constants. For high processing speed, KNbO$_3$ has the best promise because it has the highest figure of merit among the oxide photorefractive crystals [4]. Voit *et. al* [5] studied the photorefractive response time of KNbO$_3$:Fe. They found that reduction of the crystal could decrease the response time by several orders of magnitude. However, such KNbO$_3$ crystals often become optically inhomogeneous after reduction [6]. In this paper, we report our investigation of the transient photorefractive response of KNbO$_3$:Rb$^+$ crystals, which exhibit a fast response time while maintaining a significant gain and good optical homogeneity for information processing applications.

Our sample is grown by an improved top seeded solution growth (TSSG) method. By virtue of the fact that Rb$^+$ is of valence +1, the crystal does not go through a reduction treatment, and hence no space inhomogeneities occur. The crystal dimensions are 5.97 x 5.79 x 5.83 (a x b x c) mm^3, and the doping level of Rb$^+$ is 28.9 ppm. Figure 1 depicts our experimental setup to measure the response time of the index gratings. A beam (514.5 nm) from an Ar^{3+} laser is directed through a half wave plate (λ/2) and split by a polarization beam splitter (PBS1) to generate horizontally and vertically polarized beams. The vertically polarized beam is focused and re-expanded by lenses L1 and L2. An acousto-optical modulator is placed near the focal plane of lenses L1 and L2 to modulate the beam. The rise time of the modulated beam is less than 50μs when the modulation period is 100 ms. This modulated beam is then split by a standard 50/50 beam splitter (BS) to form the writing beam pair, W1 and W2. W2 is directly incident into the crystal, while W1 is directed through another polarizing beam splitter (PBS2) and reflected toward the crystal surface. The two write beams are incident symmetrically in the b-c plane of the crystal. The sizes of the writing beams are estimated to be 2 mm in diameter. The horizontally polarized read beam (Re) exiting PBS1 enters the crystal from the back, counter-propagating W2. Because of the difference in the polarization states and frequency, Re does not interfere with W1 or W2. The read beam's diffracted signal counter-propagates W1, passing through PBS2 to reach detector D1. A neutral density filter (NDF) is used to keep the intensity of Re much smaller than that of W1 and W2. In such a configuration, the noise from scattered and surface reflections of W1 and W2 is minimized. The detected signal is then directed to a digital oscilloscope to be stored and analyzed.

A typical wave form of the diffraction response is shown in Fig. 2. The wave form suggests two time constants. The net index modulation as a function of time for such a case can be given by:

$$\Delta n = \Delta n_s [c_1 f_1(t) + c_2 f_2(t)] \tag{1}$$

where Δn_s is the saturation index modulation, $f_1(t)$ and $f_2(t)$ are the exponential time dependencies of the index change of the two species, respectively, and the constants c_1 and c_2 are

the weights for the contributions of each specie. Assuming a small argument, the diffraction efficiency from such an index grating can be written as [7]:

$$\eta \propto \sin^2(l\pi\Delta n \,/\, \lambda\cos\theta) \approx (l\pi \,/\, \lambda\cos\theta)^2 \bullet (\Delta n)^2 \qquad (2)$$

Least-squares curve fits can be performed to match the wave forms from Fig. 2 with Eq. (1) and (2). For grating growth, this gives:

$$\eta = \eta_s[c_1(1 - e^{-t / \tau_1}) + c_2(1 - e^{-t / \tau_2})]^2 \qquad (3)$$

and for grating decay, it gives:

$$\eta = \eta_s(c_1 e^{-t / \tau_1'} + c_2 e^{-t/\tau_2'})^2 \qquad (4)$$

where η_s is the saturation diffraction efficiency, τ_1 and τ_2 are the two grating growth time constants, and τ_1' and τ_2' are the two grating decay time constants.
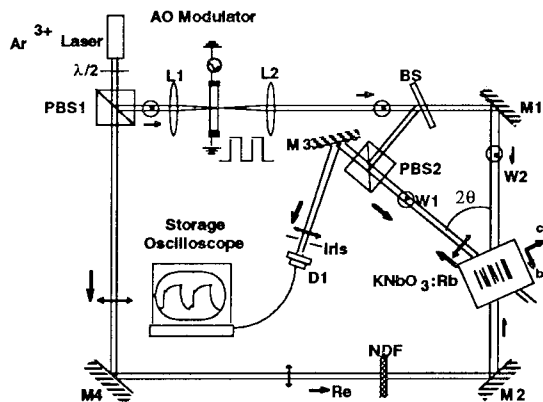
Figure 1. Experimental setup to measure the rise and fall times of the diffraction gratings.
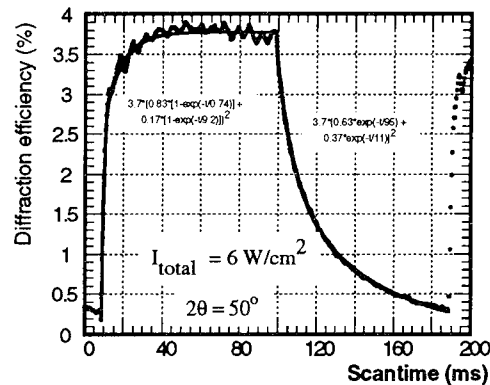
Figure 2. A typical waveform of the rise and fall of diffraction gratings. Circular dots - waveform data; solid line - fitted curve, assuming two rise/fall time constants.

We record the wave forms of the diffraction signals under different writing beam intensities and calculate the portions c_1 and c_2, as well as the time constants τ_1, τ_2, τ_1' and τ_2' using a least-squares scheme. c_1 consistently lies between 60% and 80%, and c_2 between 20% and 40%. The dependence of $1/\tau_1$ on the total light intensity is presented in Fig. 3, where we see a close to linear relation, which agrees with the relaxation approximation [8]. We also study the dependence of the rise time τ_1 on the grating spacing. According to Ref. [1], the rise time of the grating buildup has the following relationship with the grating wave vector K:

$$\tau(K) = \tau_0[1 + (K / K_d)^2] / [1 + (K / K_D)^2] \qquad (5)$$

where is K_D the Debye wave number, and $(K_d)^{-1}$ is the mean free drift length of the charge carriers in the crystal. We vary the angle between the writing beams to measure τ_1, and plot $1/\tau_1$ vs. K^2 ($[4\pi\sin\theta/\lambda]^2$, where λ is the wavelength of the laser). The results are presented in Fig. 4.

285

A nearly-linear relationship is found, which suggests the average drift length (K_d^{-1}) is much smaller than 1μm, hence the dependence of the denominator in (5) on K^2 is very weak. From the slope of this figure, we found the Debye wave number in the crystal to be 5.7 μm^{-1}. Compared with the theoretical limit given by Ref [4], the response time in this study is still more than one order of magnitude larger. Reeves et. al [9] have investigated the coupling constant and transient response of $KNbO_3:Rb^+$. In the same range of light intensity, our results have a speed two orders of magnitude higher than this previous result. Differences in the experimental settings (polarization states, crystal orientation, and doping level) in the two studies are likely the causes of the different results.
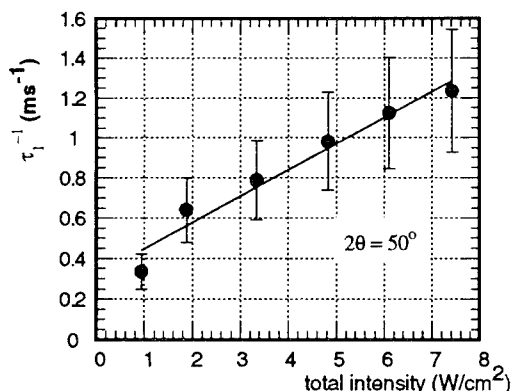
Figure 3. $1/\tau_1$ vs. the total intensity of the writing beams (I_1+I_2).
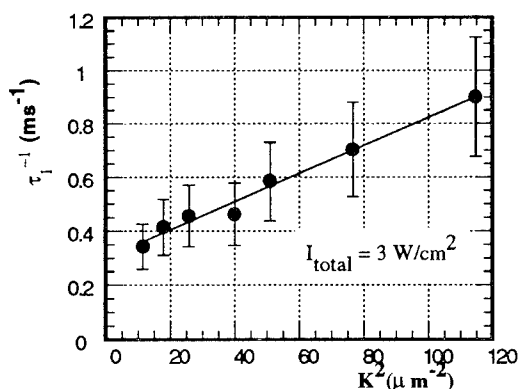
Figure 4. $1/\tau_1$ vs. the square of the grating wave vector K. From this curve the Debye wave number of the charge carrier is estimated, see text.

In summary, we have investigated the response time of the index gratings in $KNbO_3:Rb^+$ crystals. Two charge carrier components appear to contribute to the index grating formation. A sub-millisecond rise time of the larger component (60-80%) is obtained at an intensity of $5W/cm^2$. Our results indicate a significant improvement in the response speed over the previously measured results. This work is supported by Air Force Office of Scientific Research. D. Shen, X. Ma and J. Chen acknowledge the support of an 863 program of China. Pochi Yeh is also a principal technical advisor at Rockwell International Science Center, Thousand Oaks, California.

References

1. P. Yeh, *Introduction to Photorefractive Nonlinear Optics*, John Wiley and sons, 1993;
2. F.T.S. Yu, S. Jutamalia, *Optical Signal Processing, Computing, and Neural Networks*, John Wiley and sons, 1992.
3. P. Yeh, Opt. Eng, **28**(4), 328-343 (1989).
4. P. Yeh, Appl. Opt. **26**, No. 4, 602, (1987).
5. E. Voit, M.Z., Zha, P. Amrhein, and P. G ü nter, Appl. Phys. Lett. **51**(25) 2079-2081, (1987).
6. P.Amrhein, and P. G ü nter *Technical Digest of Photorefractive Materials, Effects, and Devices*, Serial Vol. **14**, 166-169 (1991).
7. H. Kogelnik, Bell Syst. Tech. J **48**, 2909 (1969).
8. P. G ü nter, Physics Reports, **93**, N0. 4, 199-299 (1982).
9. R.J. Reeves, M.G. Jani, B.Jassemnejad, R.C. Powell, G.J. Mizell, W. Fay: Phys. Rev. B. **43**(1), 71-82 (1991).

Photorefractive Spatial Solitons -
Theory and Experiments

Mordechai Segev[1], Galen Duree[2], Gregory Salamo[2],

Bruno Crosignani[3], Paolo Di Porto[3], Amnon Yariv[1]

and Edward Sharp[4].

(1) California Institute of Technology, Applied Physics Dept., m/s 128-95, Pasadena, CA 91125, USA. Telephone: (818) 395-4823, Fax: (818) 405-0928.
(2) University of Arkansas, Physics Dept., Fayetteville, Arkansas, 72701 USA.
(3) Universita dell'Aquila, L'Aquila, and Fondazione Ugo Bordoni, Roma, Italy.
(4) Army Research Laboratory, Fort Belvoir, Virginia 22060.

Summary

The existence of photorefractive (PR) spatial solitons has been predicted by us some two years ago[1,2]. The self-trapping effects occur when diffraction is exactly balanced by self-scattering (two-wave mixing) of the spatial (plane wave) components of the soliton beam. These photorefractive spatial solitons were observed by us recently[3].

Here we present an experimental and theoretical study of the properties of the photorefractive soliton. The major predictions are: (i) independence of the soliton formation of absolute optical intensity or power, (ii) existence in a relatively narrow range of external voltages, the value of which depends on the material properties, (iii) the soliton size may vary significantly with no change in the applied voltage, (iv) the transverse phase of the soliton is always uniform and (v) the PR soliton may be extinguished by either reversing the polarity of the voltage or by uniform background illumination. Our experimental results quantitatively verify all of these predictions. For example, we show in Figs. 1 and 2 a PR soliton with diameters of 33 and 77 micrometers, respectively, in a 6 mm long SBN crystal, with a fixed DC, externally applied, electric field of 400 V/cm. A top-view camera picture of the observation of a PR soliton is shown in Fig. 3 (top) and, for comparison, natural diffraction (bottom). The solitons evolve from arbitrary input intensity and phase profiles. The final (solitary) waveforms, however, are always smooth, regardless of material inhomogeneities, and the transverse phase is always "flat".

We present a theoretical proof that the PR soliton is stable for small perturbations, and breaks up only when the perturbation in the soliton wave-function in on the order of the soliton size. Experimental demonstrations of the soliton stability, its ability to propagate through material inhomogeneities and growth striations are shown in the lower section of Fig. 4. The ripples in the diffracted waveforms (no voltage case) indicate on the small index perturbations. The soliton waveform cross-sections (200 Volts case) are smooth and unperturbed. By varying the location of the input beam we estimate the size of this small perturbation to be roughly ≈ 3 μm wide, which corresponds to one tenth of the soliton cross-section (FWHM ≈ 30 μm). On the other hand, the upper section of Fig. 4 shows the break-up in regions of very large index variations (for example, scratches on the crystal surface). The diffracted waveforms (no voltage case) are now significantly broader and more perturbed. In this case the external voltage (200 volts case) cannot transform into the appropriate trapping space charge field. Instead, it splits the beam into two filaments, each trying to form its own non-diffracting beam but failing to do so due to their mutual, transversely irregular interaction (this experiment is also a good indication that soliton beams which are sufficiently close to each other do interact). We estimate the size and dimensionality of the index perturbation which destroys the soliton by varying the location of the input beam and scanning it in **both** transverse directions. The horizontal direction over which a soliton is not able to form is roughly ≈ 10 μm wide, which corresponds to one third of the soliton size (cross-section).

Finally, we experimentally find that unlike the well-known Kerr solitons, which are stable only in a single transverse dimension, the PR solitons are observed to be stable in both transverse dimensions[3]. This observation drove us to analyze the general case of a 2-transverse-dimensional PR soliton. We will discuss these 2-D self-trapping effects, the origins of the different sizes of the transverse cross-sections, and potential applications.

(1) M. Segev, B. Crosignani, A. Yariv and B. Fischer, "*Spatial solitons in photorefractive media*", **Phys. Rev. Lett. 68**, 923 (1992).
(2) B. Crosignani, M. Segev, D. Engin, P. DiPorto, A. Yariv and G. Salamo, "*Self-trapping of optical beams in photorefractive media*" **JOSA B 10**, 446 (1993).
(3) G. C. Duree, J. L. Shultz, G. J. Salamo, M. Segev, A. Yariv, B. Crosignani, P. DiPorto, E. J. Sharp and R^2 Neurgaonkar, "*Observation of self-trapping of an optical beam due to the photorefractive effect*", **Phys. Rev. Lett. 71**, 533 (1993).
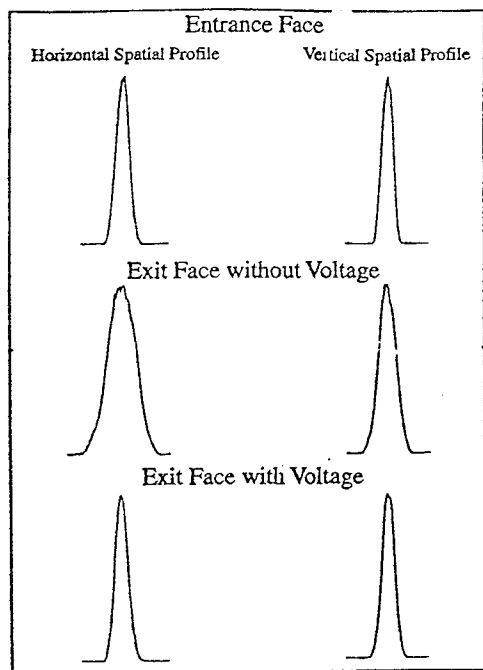
Fig. 1: Input and output profiles of a 33 μm PR soliton in a 6 mm long SBN crystal at 400 V/cm.
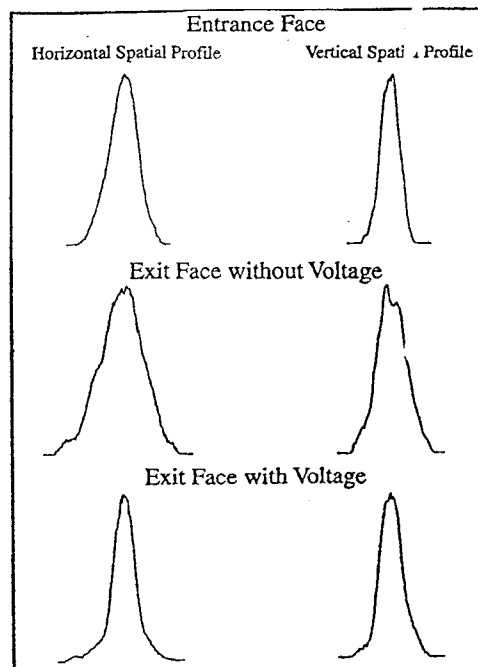
Fig. 2: Input and output profiles of a 77 μm PR soliton in a 6 mm long SBN crystal at 400 V/cm.
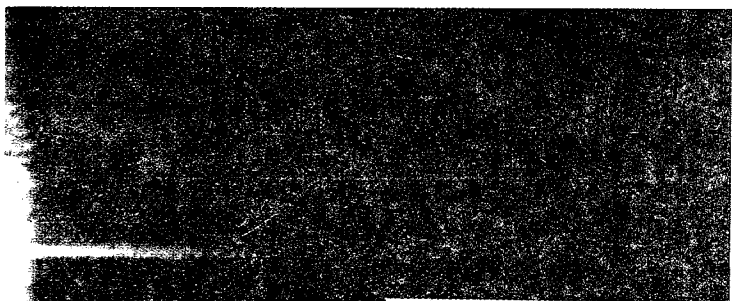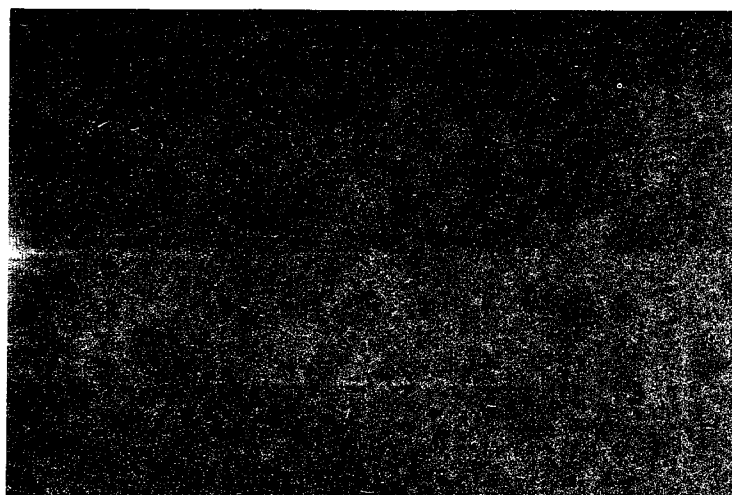
Fig. 3: A top-view photograph of a photorefractive spatial soliton (above) and a normally-diffracting beam— no soliton (below).
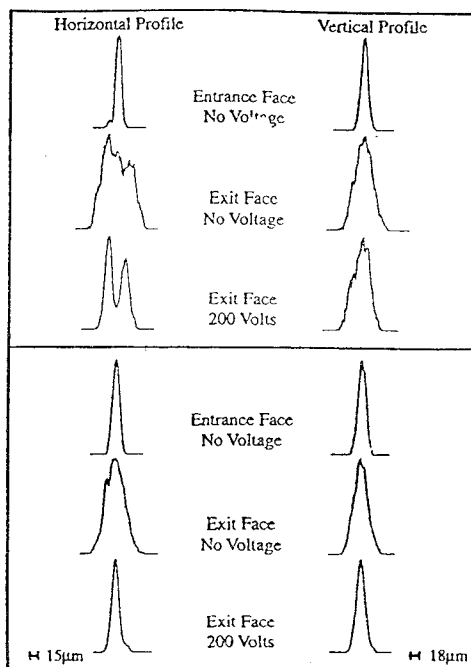
Fig. 4: Input and output profiles of a diffracted and self-trapped beam in a 6 mm long SBN in the presence of large (upper) and small (lower) index perturbations. The waveforms are normalized to their maximal amplitudes.

289

Nonlinear Rotation of 3D Dark Spatial Solitons in a Gaussian Laser Beam

Barry Luther-Davies, Rebecca Powles, Vladimir Tikhonenko

Laser Physics Centre

Research School of Physical Sciences and Engineering

Australian National University, 0200

Australia

Telephone (61) 62 494244

Dark spatial solitons[1] have recently been the subject of intense theoretical and experimental study because of their potential in all-optical switching. The possibility of creating stable light-controllable waveguides which can be used to propagate signal carrying beams has been explored in the case of 2D dark solitons[2]. An extension of this concept of guiding light by light to 3D could allow reconfigurable "optical fibres" to be written in bulk media. However, in the 3D geometry only "black" solitons exist[3], preventing the use of the soliton phase, as in the 2D case, to control the soliton direction and hence that of the induced waveguides. Thus, in the 3D geometry a different means of reconfiguring the soliton induced waveguides is required.

Here we demonstrate non-linearity induced rotation of 3D dark solitons at the output of a non-linear medium. By changing the beam intensity (or the material non-linearity) a 3D soliton embedded off-axis in a Gaussian beam can be made to rotate around that axis by up to 90°. The induced waveguide therefore links a single input port to an array of output ports in a geometry akin to a rotary switch.

In our experiments the non-linear medium was Rubidium vapour irradiated with a CW Ti:sapphire laser (P ~0.4W, Δv ~100MHz, λ ~780nm) tuned near to the D_2 resonance line. In the presence of relatively large Doppler broadening ($\approx$0.75 GHz) and low vapour pressure, it was experimentally confirmed that this line could be treated as single separate resonance for detunings up to 1GHz. This allowed us to employ the model of the two-level atom to estimate the nonlinearity and absorption of the medium. The values of n_2 and γ were typically -1.8×10^{-3} cm^2/W and -0.03cm^{-1} respectively.

Computer-generated holograms were used to generate single or multiple screw dislocations (optical vortices) nested in the Gaussian laser beam[4]. When the beam propagated through the self-defocussing Rubidium vapour the vortices transformed into 3D dark spatial solitons[5]. In a linear medium the position of a vortex relative to the

beam axis changes with propagation distance: the vortex rotating around the axis by 90°
between the beam waist and infinity. The rotation is due to the difference in the phase
evolution of the vortex in comparison with the Gaussian beam in which is it embedded.
As a result the vortex moves around the axis by an amount exactly equalling the Guoy
shift[6] $-arctan[z/z_R]$ where z_R is the Rayleigh length of the beam. This has recently
been confirmed experimentally[7].

The origin of the non-linearity induced rotation has thus a transparent origin.
The defocussing medium flattens the phase fronts of the Gaussian beam increasing z_R
and thus decreasing the amount of vortex rotation that occurs over a given propagation
distance. By careful choice of the initial focussing conditions of the Gaussian beam so
that z_R is considerably shorter than the length of the non-linear medium, large non-
linearity induced rotations can be obtained. As example is given in figure 1 which
shows the evolution of vortex position at the output of the Rb cell as a function of laser
power. Up to 90° rotation was observed. The rotational behaviour proved in excellent
agreement with theoretical models.

This talk will provide details of the theory and experiments on 3D soliton
rotation.

REFERENCES

[1] see for example Yuri S. Kivshar, IEEE Journal of Quantum Electronics, **29**, 250
(1993) and references therein.

[2] B. Luther-Davies, X. Yang, Optics Letters **17**, 496 (1992); B. Luther-Davies, X. Yang,
Optics Letters **17**, 1755 (1992).

[3] A.W.Snyder, L. Poladian, D.J. Mitchell, Optics Letters **17**, 789 (1992).

[4] N.R. Heckenberg, R.McDuff, C.P. Smith, A.G. White, Opt. Lett **17**, 221 (1992).

[5] G.A. Swartzlander Jr. and C.T. Law, Phys. Rev. Lett. **69**, 2503 (1992).

[6] G. Indebetouw, J. Mod. Opt. **40**, 73 (1993).

[7] I.V. Basistiy, V.Yu. Bazhenov, M.S. Soskin, M.V.Vasnetsov, Opt. Commun. **103**, 422
(1993).
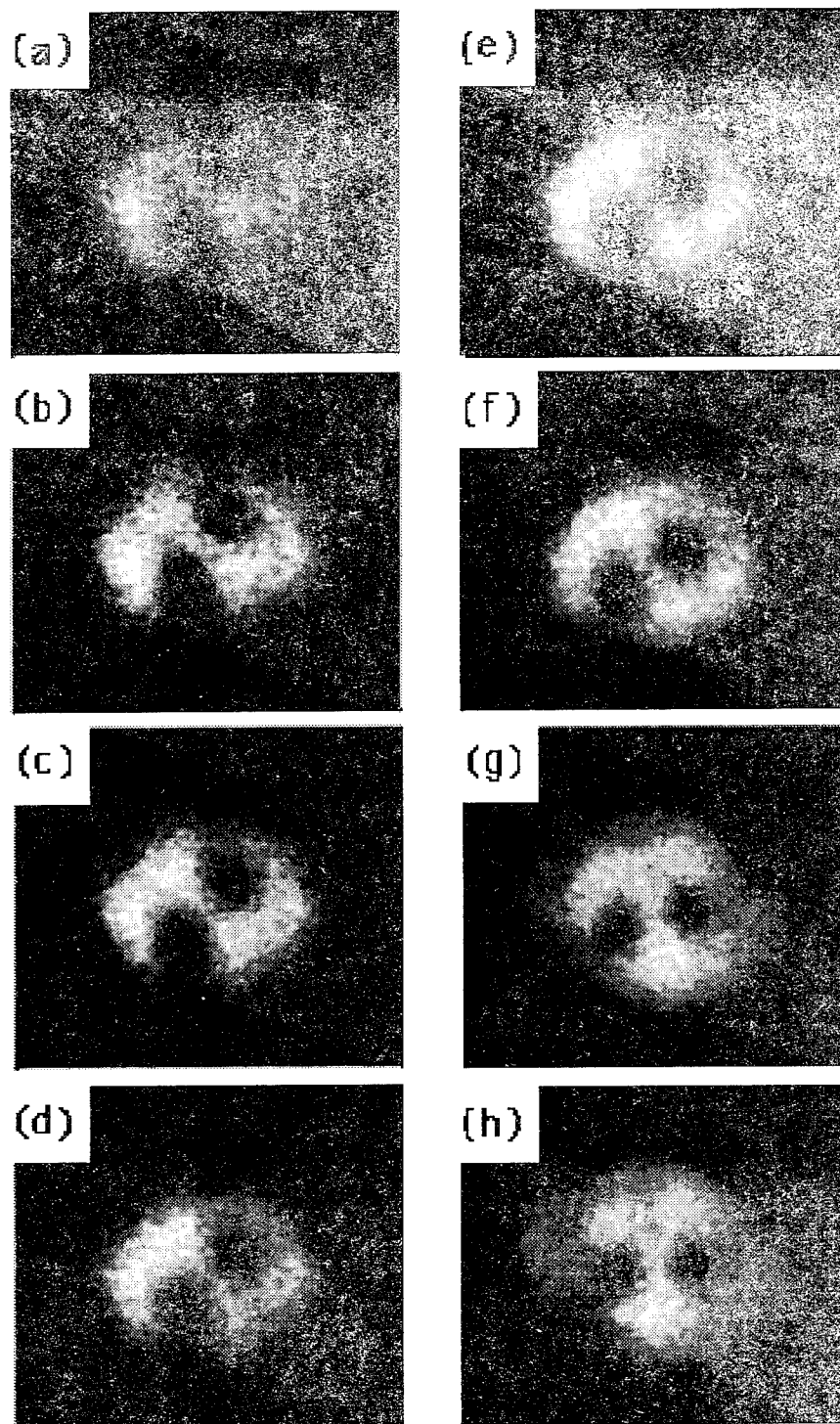
FIGURE CAPTION: Demonstration of clockwise rotation of a pair of off-axis 3D solitons after propagation through the 20cm long Rb vapour cell. The Rb concentration was $0.6 \times 10^{13} cm^{-3}$, laser detuning from Rb $5S-5P_{3/2}(F=2-F=3)$ resonance -0.75GHz, input beam intensities in W/cm^2 were: (a) 0.058; (b) 0.074; (c) 0.12; (d) 0.15; (e) 0.19; (f) 0.25; (g) 0.39; (h) 0.49.

Optically Induced <u>Dynamic</u> Polarization Gratings For Tunable, Quasi-Phase Matched Second Harmonic Generation

Anthony S. Kewitsch, Mordechai Segev and Amnon Yariv
Department of Applied Physics, California Institute of Technology
Pasadena, California 91125
kewitsch_a@caltech.edu
(818) 395 4414 Fax: (818) 405 0928

Gregory J. Salamo and Terry Towe
Department of Physics, University of Arkansas
Fayetteville, Arkansas 72701

Edward J. Sharp
Army Research Laboratory
Fort Belvoir, Virginia 22060

Ratnakar R. Neurgaonkar
Rockwell International Science Center
Thousand Oaks, California 91360

Light interference patterns can photoexcite mobile charge and generate periodic space charge fields with periods of typically 0.1 to 100 microns in photorefractive crystals. The space charge field attains values of 0.1 to 1 kV cm^{-1} in ferroelectrics such as $Sr_{.75}Ba_{.25}Nb_2O_6$ (SBN:75). A fundamental question is whether these periodic space charge fields can spatially modulate the ferroelectric polarization in materials which possess a coercive field of the order of the space charge field. We present experimental evidence demonstrating that this is indeed the case in SBN:75. We observe dynamic domain gratings, which form simultaneously with the build up of the space charge field, and remnant domain gratings, which persist long after the space charge field disappears.

One application of these optically induced polarization gratings is quasi-phase matching (QPM) of a second harmonic process, a technique to compensate for the phase mismatch of the fundamental and second harmonic beams[1,2]. This is typically implemented by modulating the spontaneous polarization and as a consequence modulating the nonlinear coefficients. We experimentally demonstrate tunable QPM using dynamic as well as remnant domain gratings with periods equal to twice the coherence length of the second harmonic process. The origin of this technique lies in our recent demonstration that spatially periodic, photoinduced space charge fields alone can modulate the polarization of the crystal and generate permanent ferroelectric domain gratings in SBN:75 (Refs.3-5). This all-optical technique achieves nearly instantaneously what would normally require complex and lengthy growth and materials processing and has the potential of achieving as large a second harmonic conversion efficiency as more mature technologies. Furthermore, this technique is of fundamental interest because light interference patterns dynamically modify the position of ions within the crystalline unit cell to tailor the optical, electronic, and acoustic properties of the crystal.

In our experiments we exploit the dynamic nature of these domain gratings to perform tunable QPM. The QPM spectral response peak can be shifted across the entire tuning range of the second harmonic, from 440 to 495 nm, by writing gratings with periods ranging from 3.7 to 3.0 microns. Figure 2a illustrates a typical QPM peak centered on 457.25 nm. We predict a full width at half maxima (FWHM) of 0.2 nm for an interaction length of 4.25 mm, in close agreement with the measured FWHM of 0.175 nm from figure 2a. This confirms the uniformity of the grating throughout the entire volume of the crystal, an inherent advantage of this technique.
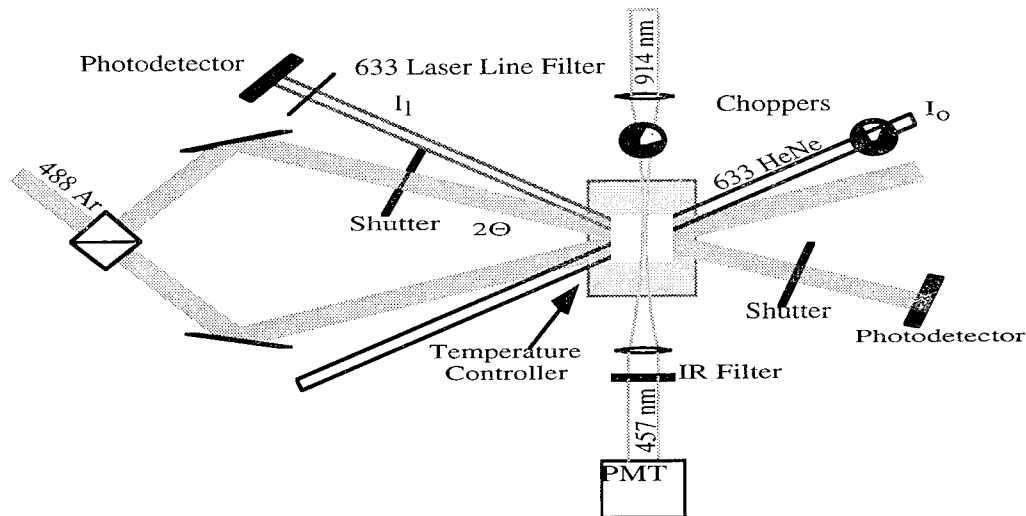
Figure 1: Experimental Setup

The ability to map optical intensity patterns into polarization orientations lends great flexibility and control in tailoring the domain periodicity. Figure 2b is a tuning curve obtained after sequentially recording four gratings within the same volume. The strongest enhancement peak is due to the fourth and final grating recorded (and in the presence of its writing beams). It is apparent that the spectral response is tailored by writing several gratings (either simultaneously or sequentially) with different periods. This figure also indicates that an enhancement of more than a factor of 15 above the non-phase matched second harmonic power can been achieved. While the conversion efficiencies are yet a modest 0.01% at 250 W peak powers, we believe they can be significantly improved as the method is optimized. One method to increase the enhancement is to use higher intensity writing beams, which increases the polarization modulation. In the results presented here, we are limited to writing intensities at or below 1 W cm^{-2}.
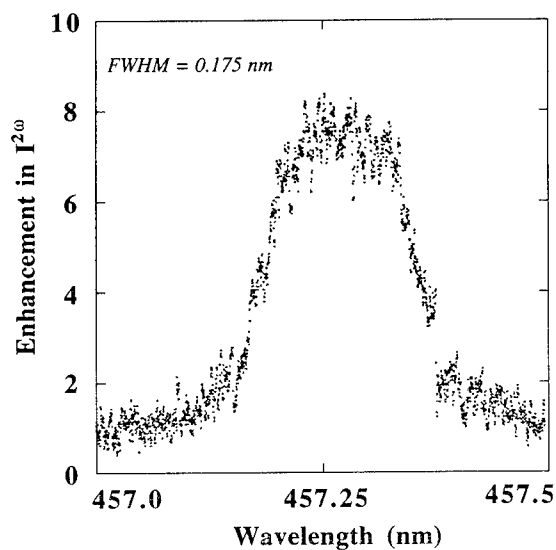
Figure 2a: QPM tuning curve for single grating
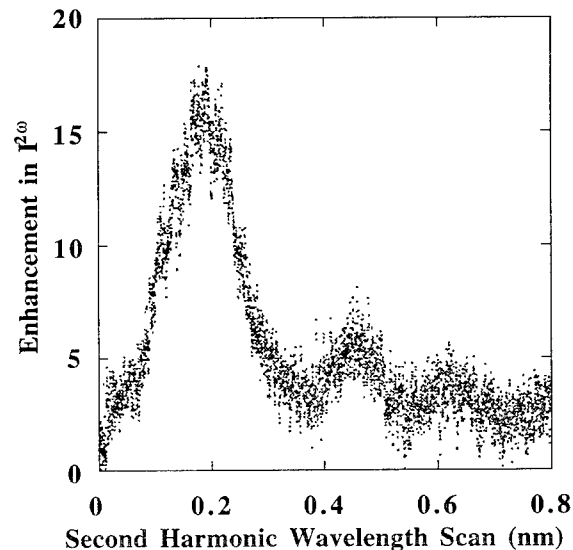
Figure 2b: QPM tuning curve after writing 4 gratings

Figure 3a illustrates time evolution of the second harmonic before, during, and after writing

a domain grating. During the first 60 seconds the only the fundamental beam is entering the crystal, producing a second harmonic power of the order of the expected non-phase matched contribution. Upon illuminating the entire crystal with an optical standing wave of peak intensity of 1 W cm^{-2}, the phase matched polarization grating is generated, as evidenced by the increase in second harmonic power. The transients in the second harmonic enhancement are due to instabilities in phase of the optical interference pattern from vibration, air currents and temperature changes. The crystal is uniformly illuminated after 145 seconds, erasing the space charge field and the dynamic domain grating. The buildup time constant of the QPM peak is approximately inversely proportional to intensity and is consistent with the photorefractive grating buildup times for SBN:75. At 1 W cm^{-2} the buildup time is 0.5 seconds, and at 0.33 W cm^{-2} it is 1.5 seconds. The second harmonic beam exits the crystal in a well collimated, TEM$_{00}$ mode, as depicted in figure 3b. The rapid enhancement of the second harmonic power while recording the volume hologram confirms the presence of dynamic domain gratings in addition to the more typical remnant domain grating given by Δ in figure 3a. Δ is a measure of the polarization hysteresis upon removal of the space charge field. This hysteresis is increased by increasing the writing beam exposure[3], applying a short exposure technique or freezing-in the grating upon cooling.
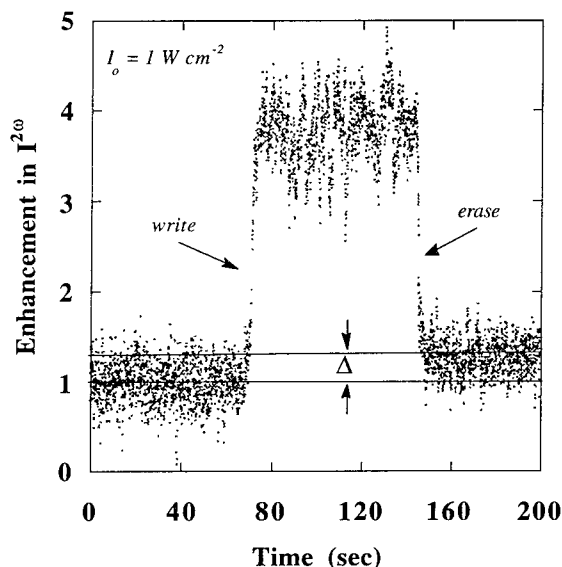
Figure 3a: Time response of buildup and decay
of QPM spectral response peak.
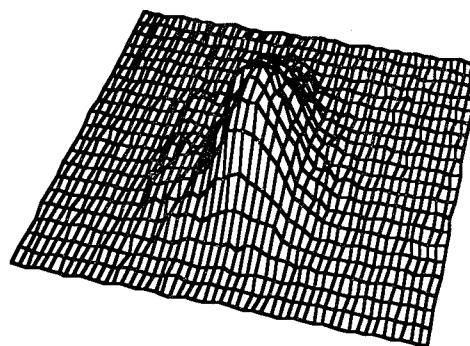
Figure 3b: Second harmonic far field
ntensity profile (TEM$_{00}$ mode, angular
divergence of the order of 1 mrad).

In conclusion, we have presented a technique to optically modulate the ferroelectric polarization on the scale of an optical wavelength in the context of second harmonic generation studies in SBN:75.

[1]   J. A. Armstrong, N. Bloembergen, J. Ducuing, and P. S. Pershan, *Phys. Rev.* **127**, 1918 (1962).
[2]   S. Somekh and A. Yariv, *Opt. Comm.* **6**, 301 (1972).
[3]   A. Kewitsch, M. Segev, A. Yariv, and R. R. Neurgaonkar, *Opt. Lett.* **18**, 1262 (1993).
[4]   A. Kewitsch, M. Segev, A. Yariv, and R. R. Neurgaonkar, *Jap. J. Appl. Phys.* **32**, 5445 (1993).
[5]   A. Kewitsch, M. Segev, A. Yariv, G. Salamo, T. Towe, E. Sharp, and R. R. Neurgaonkar, submitted to *Appl. Phys. Lett.*.

Interrogation of the Lattice Vibrations of Liquids with Femtosecond Raman-Induced Kerr Effect Spectroscopy

Dale McMorrow, Napoleon Thantu, and Joseph S. Melinger
Naval Research Laboratory, Code 6613, Washington, D.C. 20375 (202) 767-3939

William T. Lotshaw and P. Randall Staver
G.E. Research, Rm. KWC 627, 1 River Road, Schenectady, NY 12309 (518) 387-5163

The issue of local order in molecular liquids, and the influence of such order on molecular dynamics and dielectric relaxations in liquids and solutions, is a topic of substantial importance to theoretical representations of the liquid state and interpretations of solvent effects in solute relaxations and chemical reactivity in solutions. In this report we present the results of new studies of intermolecular interactions and dynamics in the liquid state, which interrogate the intermolecular vibrational modes of the local structure of liquids at constant temperature and pressure. Previously [1] we have utilized time and frequency domain analyses of the optical heterodyne detected optical Kerr effect (OHD OKE) to examine the complicated vibrational and Brownian motions of molecules in pure liquids, and identified the intermolecular origin of the low-frequency Raman band in organic liquids (which is typically centered between 10 and 100 cm^{-1}). These bands have been attributed to Raman-active restricted orientational motions, or librations, in non-associated molecular liquids, and exhibit widths in the range of 20 to 100 cm^{-1}.

In this paper we address the question of local order in molecular liquids by investigating the intermolecular dynamics and spectra of a series of dilutions of benzene in carbon tetrachloride (CCl_4) and methylcyclohexane. Benzene is a simple, non-hydrogen-bonding aromatic liquid, and may be considered representative of this class of liquids. Previous work [2] revealed a distinct bimodal structure in the non-diffusive part of the intermolecular Raman spectrum (fig. 3, *vide infra*). Based on symmetry considerations, it was suggested that the low-frequency portion of this bimodal spectrum might be associated with locally ordered structures (dimers or other aggregates) in the bulk liquid. The results of the current study support this interpretation, and provide direct evidence for locally-ordered structures in aromatic liquids.

Experiments were performed using a synchronously pumped continuously tunable Ti:Sapphire laser that generates ≤ 40 fs pulses at average powers ≥ 0.5 W. OHD OKE transients were measured as described elsewhere [1], except that the pure heterodyne signals were isolated for the data analysis [3]. OHD serves to linearize the detected signal in both the pump and probe pulse intensities, permitting application of powerful discrete Fourier-transform (FT) data analysis procedures [1].

Figure 1 shows the OHD OKE transient measured for 9.1% benzene in CCl_4. The purely electronic hyperpolarizability dominates the response near $\tau = 0$, with significant contributions from both benzene and CCl_4 present at positive delays. The prominent oscillations are due to the *intra*molecular vibrational Raman modes of CCl_4 at 217 and 314 cm^{-1}. Analysis of this very complex transient is facilitated by the use of Fourier transform methods, which are described in detail elsewhere [1]. The frequency response function of the OKE transient of fig. 1, deconvoluted from effects of the finite-duration excitation and probing pulses, is shown in fig. 2. The intramolecular Raman modes noted above, and a broad low-frequency band that is associated with the *inter*molecular dynamics of the liquid are evident.

The data of figs. 1 and 2 contain several overlapping contributions that must be separated before a detailed interpretation of the intermolecular dynamics is possible. Since we are interested in the *intermolecular vibrational part* of the response, the Brownian relaxations due to diffusive reorientation are removed using a tail-matching procedure that has been discussed previously [1]. For the 9.1% benzene solution contributions from both solvents can be significant. A reason for choosing CCl_4 as a solvent is the presence
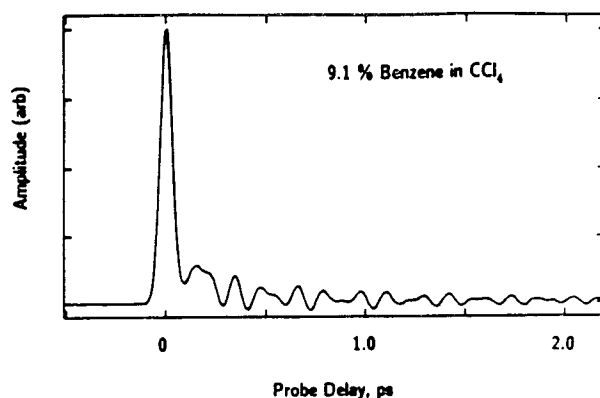
Figure 1. Femtosecond OHD OKE transient measured for a 9.1% solution of benzene in carbon tetrachloride.
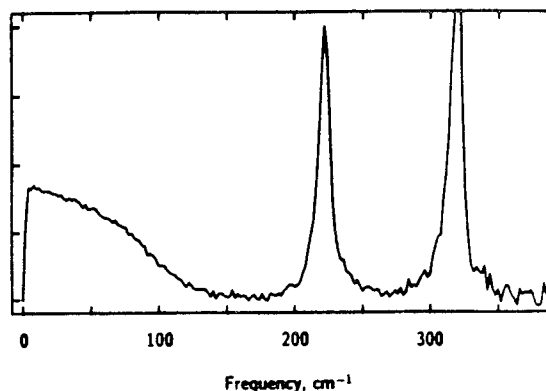
Figure 2. Spectral-density representation of the OHD OKE data of fig. 1.

of strong *intra*molecular resonances that serve as an *internal standard* for removing the CCl_4 contribution from the *inter*molecular part of the spectrum ($\Delta\omega$ <165 cm^{-1}). This operation relies on the principle of linear superposition in the response function and requires the assumption that the intermolecular vibrational spectrum of CCl_4 is not changed significantly in the 9.1% benzene solution. This assumption is reasonable, and is supported by the unaltered lineshape of the intramolecular resonances on dilution.

The upper curve of fig. 3 shows the vibrational Raman part of the benzene OHD OKE deduced from the FT analysis. The shape of this spectrum is the focus of this study. Previously we had attributed this lineshape to a bimodal vibrational response in which, based on the symmetry of the isolated molecule, the low frequency part was attributed to dimers or higher aggregates, and the high-frequency part was attributed to nonaggregated molecules [2]. Dilution of benzene in CCl_4 is expected to reduce the number density of any aggregate structures, resulting in a decrease in the low-frequency amplitude of the vibrational spectrum. The lower curve of fig. 3 shows the vibrational Raman part of the 9.1% benzene/CCl_4 solution with the CCl_4 contribution subtracted off as described in the previous paragraph. The significant decrease in low-frequency amplitude of the 9.1% spectrum supports the dimer/aggregate interpretation of the neat benzene spectrum.

Figure 4 shows the time domain representation of the spectra of fig. 2. The short time portions (<250 fs) of the two transients are very nearly identical, suggesting that
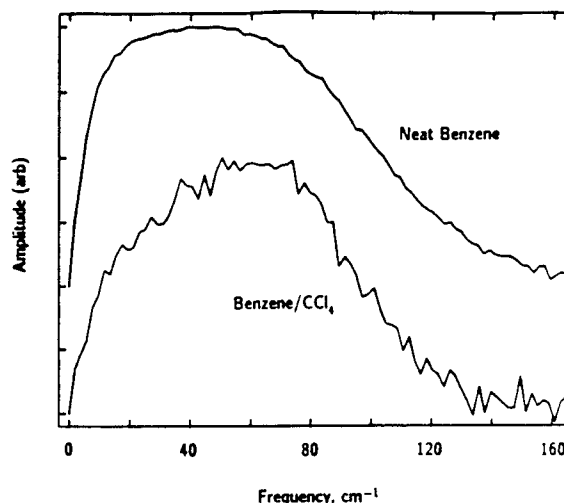
Figure 3. Vibrational part of the intermolecular Raman spectrum for neat benzene (*upper*) and the benzene contribution to the 9.1% solution of benzene in carbon tetrachloride (*lower*) illustrating the rather significant spectral evolution that occurs on dilution.

297

the higher-frequency single-molecule librational degrees of freedom for benzene are not significantly altered in the predominately CCl_4 environment. Significant deviations between the two transients occur, however, for delays greater than 250 fs, with the longer time contributions significantly diminished in the 9.1% solution. These longer-time relaxations, which exhibit a 1/e time constant of 450 fs in neat benzene [2], can be identified with the dynamics of dimer/aggregate structures.
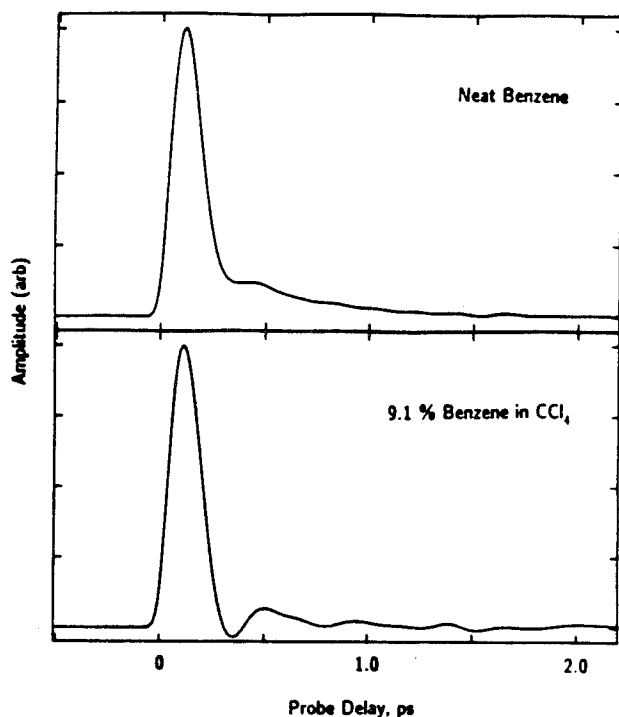
Figure 4. Vibrational part of the intermolecular OHD OKE transient for neat benzene and the 9.1% solution of benzene in carbon tetrachloride.

The changes we observe in the intermolecular Raman spectrum of benzene occur at frequencies less than ~ 50 cm^{-1}, and are difficult to address by spontaneous light scattering due to elastic scattering and background problems. The femtosecond OHD OKE methods are ideally suited to the analyses presented here because the attributes of: i) background supression and phase sensitive signal detection permit isolation of the spectroscopic signal of interest; ii) high sensitivity and signal-to-noise ratio result in the precise characterization of the picosecond Brownian dynamics; and iii) a wide dynamic range and order reduction in the nonlinear response function permit a highly accurate discreet FT analysis of the more complicated elements in the measured transients.

In addition to the data presented here, a complete dilution series has been performed for methylcyclohexane solvent (which exhibits different intermolecular with benzene). At the conference we will address the general utility of femtosecond Raman methods for interrogating the microscopic molecular environment of liquids using the benzene/CCl_4 system as an example. Also, temperature-dependent measurements are in progress, and will be reported.

1. D. McMorrow and W.T. Lotshaw, Chem. Phys. Lett. 174, 85 (1990); J. Phys. Chem. 95, 2028 (1991).
2. D. McMorrow and W.T. Lotshaw, Chem. Phys. Lett. 201, 369 (1993).
3. T.R. Dickson, PhD Thesis, University of Toronto, 1991.

Squeezing with Fiber Sagnac Loop and Sub-Shot-Noise Measurement

H. A. Haus, K. Bergman, L. Boivin, M. Shirasaki, and E. P. Ippen

Department of Electrical Engineering and Computer Science and
Research Laboratory of Electronics, Massachusetts Institute of Technology
Cambridge, Massachusetts 02139 USA

Squeezed states of light are minimum uncertainty states for which the mean square fluctuations in phase and in quadrature with respect to a reference signal are unequal. Among other interesting properties, they provide improved sensitivity of optical interferometric phase measurements. To understand this potential, one must note that quantum theory imposes measurement uncertainty only on a pair of noncommuting variables; the measurement of any one quantum observable could be done with no uncertainty.

Engineering systems usually employ large numbers of photons per measurement to arrive at an acceptable signal to noise ratio. In such situations, the evolution of the operators in the Heisenberg representation can be linearized by writing each operator as the sum of a large c-number and an operator of small expectation value. If higher than first order terms are neglected, the operator equations are linearized. Linear equations do not contain products of operators and thus issues of operator ordering do not arise. But then the equations are indistinguishable from classical linear equations and have the same solutions. In this way a close analogy is established between the quantum problem and the system equations of the classical counterpart. Classical transfer functions can be used, and the superposition principle applies.

Since the application of squeezing is for the reduction of noise in interferometric measurements, it is important to understand how squeezed vacuum can lead to such noise reduction. The measurement of the phase imbalance of a Mach-Zehnder interferometer is made on the output beam splitter on the side which has zero output under balanced conditions (the signal side). The noise of the measurement is due to the zero-point fluctuations entering the "unexcited" side of the input beam splitter. If the measurement of the output signal is with a phase sensitive balanced homodyne detector, squeezed radiation of proper phase fed into the input can reduce the noise. This interpretation of the noise reduction is congruent with the interpretation that the shot noise in a balanced homodyne detector is due to the zero-point fluctuations entering its input port, and not due to the local oscillator photon noise; a balanced detector cancels the local oscillator fluctuations. This point of view follows from the consistent application of the linearization of the operator equations in the Heisenberg representation.

Next consider squeezing by a nonlinear Mach-Zehnder interferometer[1]. A phasor of a coherent state, represented by the probability distribution (Wigner distribution) of its complex amplitude in the phasor plane, entering the interferometer acquires a distribution of phase shift. When the event is represented by a point in the phasor plane of increased amplitude the phase shift is larger, and a smaller phase shift occurs when the point corresponds to a smaller amplitude. The circularly symmetric distribution distorts into an ellipse tangential to the original circle as shown with the two parallel lines that approximate

the circle in the limit of large phasor amplitude. In Figure 1 we remove the net "classical" phase shift due to the average amplitude of the phasor. The inserts follow the evolution of the Wigner distributions through the Mach-Zehnder. The vacuum output port removes the average phasor and produces radiation of zero expectation value. The Mach-Zehnder configuration "filters" out the pump radiation and produces squeezed vacuum.

A simple implementation of the nonlinear interferometer is the fiber Sagnac loop with a 50/50 coupler as shown in Fig. 2[2,3,4]. This configuration is selfstabilized against any index fluctuations on a time scale longer than the traversal time. An input pulse is reflected back into the input port. The vacuum port is excited by the vacuum fluctuations and emits squeezed radiation. Figure 3 shows the evidence for squeezing. In this experiment, the "stabilizing" mirror is swept and the phase between L.O. and squeezed vacuum is changed continuously. The noise is measured with a filter of 40 kHz center frequency and 2 kHz bandwidth. The shot noise level is established by blocking the squeezed vacuum from entering the balanced detector. Any attenuator then injects standard zero-point fluctuations. It is clear from comparison between the two traces, one establishing the shot noise level, the second with repetition of the squeezed radiation, that noise is less than the shot noise level at the instants of favorable phase.

Figure 4 shows the noise spectrum of shot noise and squeezed noise stabilized at the minimum level. The squeezing yields 5.1 dB reduction of the noise below the shot noise level.

These experiments[2,3] were conducted with a fiber that happened to leave the frequency range of 40-90 kHz free of Guided Acoustic Wave Brillouin Scattering (GAWBS)[5]. This scattering is due to the acoustic modes of the fiber near cutoff that are phase matched to the forward Brillouin scattered waves. The GAWBS spectrum is a very sensitive function of the fiber geometry and it is found that in most fibers the convolution of GAWBS to the low frequency measurement window cannot be avoided.

Two ways of overcoming the GAWBS are:

- When two pump pulses delayed by less than 1 ns are used, and one of the pulses is phase reversed before being used as the local, oscillator, the GAWBS cancels.
- With a high pulse repetition rate (> 1 GHz) the GAWBS spectrum does not convolve into the low frequency window.

These schemes have both been tested experimentally and will be reported in detail[6,7].

References

1. M. Shirasaki and H. A. Haus, "Squeezing of pulses in a nonlinear interferometer," *J. Opt. Soc. Amer. B* **7**, 30 (1990).

2. K. Bergman and H. A. Haus, "Squeezing in fibers with optical pulses," *Opt. Lett.* **16**, 663 (1991).

3. C. R. Doerr, K. Bergman, H. A. Haus, and M. Shirasaki, "Stabilization of squeezing with a nonlinear fiber interferometer," CLEO'92, OSA Digest 282 (1992).

4. M. Rosenbluh and R. M. Shelby, "Squeezed optical solitons," *Phys. Rev. Lett.* **66**, 153 (1991).

5. R. M. Shelby, M. D. Levenson, and P. W. Bayer, "Guided acoustic wave Brillouin scattering," *Phys. Rev. B* **31**, 5244 (1985).

6. K. Bergman, C. R. Doerr, H. A. Haus, and M. Shirasaki, "Sub-shot-noise measurement with fiber-squeezed optical pulses," *Opt. Lett.* **18**, 643 (1993).

7. K. Bergman, H. A. Haus, E. P. Ippen, and M. Shirasaki, "Squeezing in a fiber interferometer with a GHz pump," *Opt. Lett.* **19**, 290 (1994).
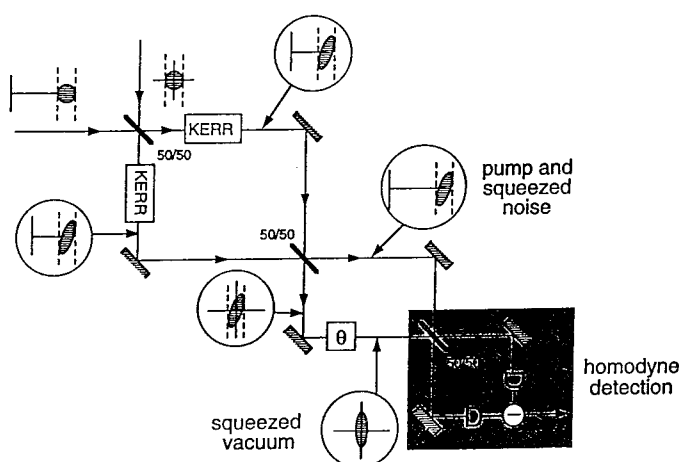
Fig. 1   Squeezing by means of the nonlinear Mach-Zehnder interferometer.
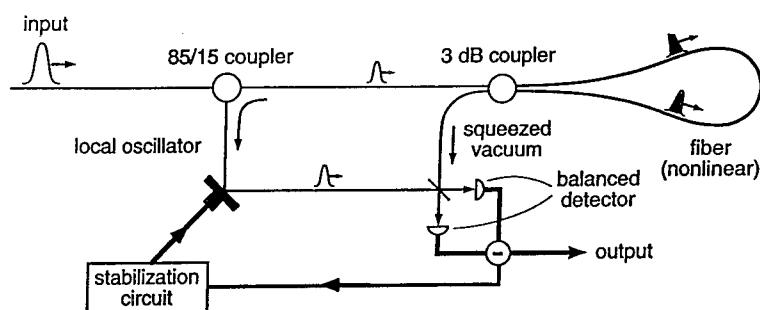
Fig. 2   Experimental configuration

shot noise level

Time (sec)

SHOT-NOISE

Time (sec)

NOISE WITH SWEPT MIRROR

center frequency: 40 kHz
bandwidth: 2 kHz
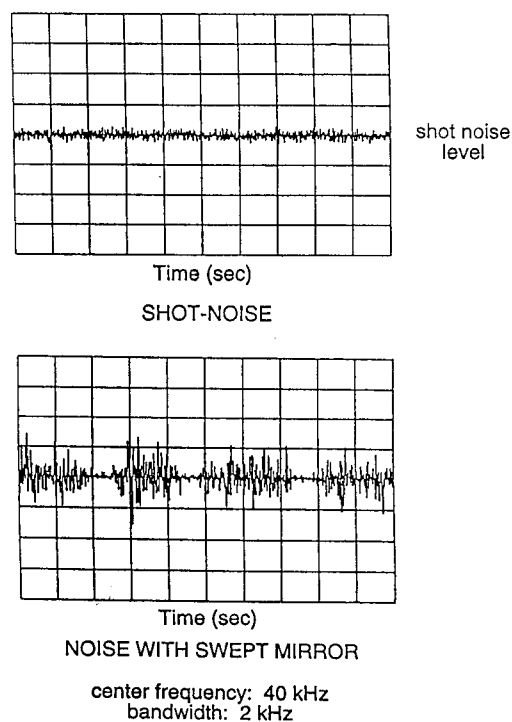
Fig. 3   Evidence of squeezing

55-95 KHz

2.5 dB/div

5 dB

55 kHz   Frequency (4 kHz/div.)   95 kHz
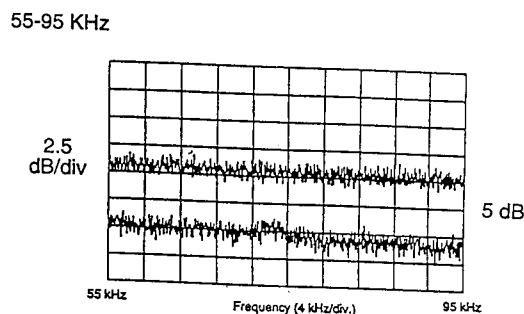
Fig. 4   Quantum noise in homodyne detection with standard zero point fluctuations and with squeezed vacuum.

Optical Fiber Nonlinear Effects in Lightwave Communication Systems

A. R. Chraplyvy and R. W. Tkach

AT&T Bell Laboratories

Crawford Hill laboratory

P. O. Box 400

Holmdel, NJ 07733

Advances in optical amplifier technology have reshaped the lightwave communications landscape. Erbium-doped fiber amplifiers have enabled systems engineers to begin exploiting the enormous transmission capacity of single-mode fibers. However, implementation of optical amplifiers magnify the effects of optical nonlinearities in the transmission fibers. These nonlinearities will limit the information capacity of lightwave communications.

The nonlinearities can be separated into two broad classes. Stimulated scattering processes, such as Brillouin and Raman, cause wavelength conversion of signals. This gives rise to unwanted noise, crosstalk, and power depletion The nonlinear refractive index of silica is the source of such effects as self-phase and cross-phase modulation which produce spectral broadening, and four-photon mixing which mixes signals in wavelength multiplexed systems.

This talk will describe the various optical nonlinearities and discuss the limits imposed by these nonlinearities on the information capacity of lightwave communication systems. Methods for reducing the systems impact of nonlinearities will also be presented.

Liquid Crystal Fibers for Enhanced Nonlinear Optical Processes

I.C. Khoo, H. Li, Y. Liang, P. LoPesti, B. Yarnell, X. Yi, M. Lee
Pennsylvania State University, University Park, PA

Liquid crystals in their various ordered and disordered phases have been shown to possess large optical nonlinearities over a wide temperature and spectral range [1,2]. Consequently, almost all types of nonlinear optical phenomena have been observed. In particular, nonlinear propagation and optical limiting, stimulated back scattering and phase conjugation have been observed in bulk thin film or liquid cells [2].

It is well known that nonlinear optical responses of a material will be greatly enhanced, and the efficiency of the nonlinear phenomena under study could be greatly enhanced if guided wave geometries are employed [3]. In this paper, we report the results of a series of experiments conducted in liquid crystal cored fibers, where we have observed several nonlinear optical phenomena with relatively much lower optical threshold fluence. In particular, passive all-optical limiting action have been found to occur at threshold fluence a few times smaller than their thin film or bulk cell counterpart. Concomitant to these observations, stimulated back scattering and nonlinear pulse propagation effect also appear.

Liquid crystal cored fibers are fabricated by filling glass capillaries with liquid crystal in the isotropic phase. Such fibers of core diameter ranging from 2 to 200 μm have been made. Fiber array composed of parallel assembly of these fibers could also be fabricated by filling commercially available capillary-arrays. Liquid crystal slab waveguides are made by sandwiching a thin film of nematic liquid crystals between two ITO and polymer surface-treated glass slides. We had used both isotropic and ordered (nematic) phase liquid crystals.

Figure 1 shows an experimental setup used for nonlinear propagation and self limiting. The second harmonic of a 20 ns Nd:Yag laser pulse (λ=0.532μm) is focused by a 1 cm focal length lens into an isotropic liquid crystal [EM Chemicals TM74A] fiber. The focal spot is located near the front entrance plane. At low laser energy, the transmitted pulse shape is similar to the input [see photo insert in fig. 1].

Input Pulse
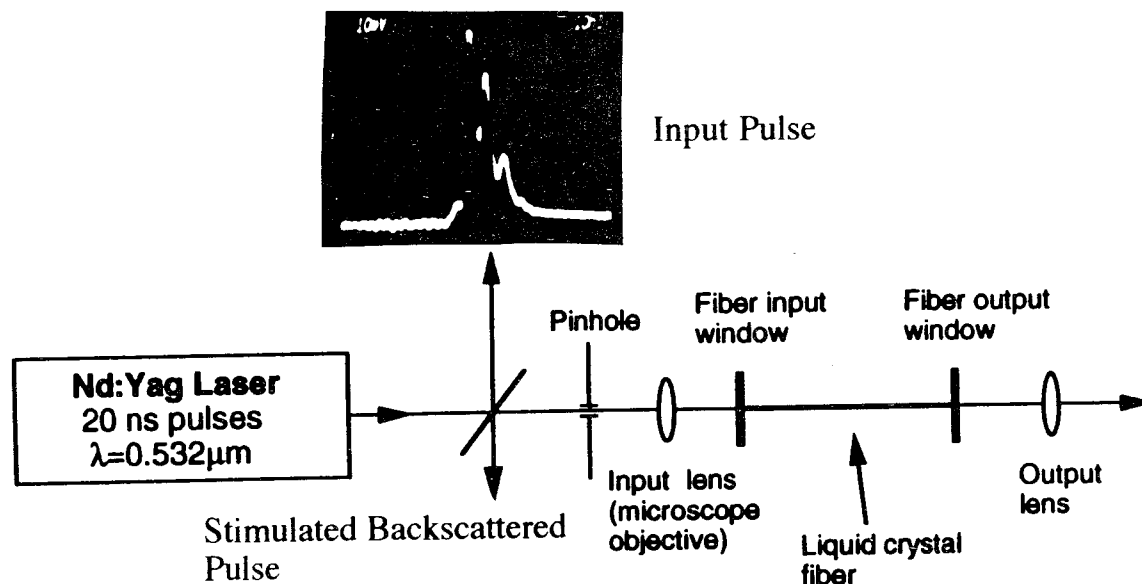
Fig. 1

At high input energies, the transmitted pulse shows obvious sign of limiting effect (See photo insert in figure 2a). As plotted in figure 2a, the transmitted energy versus the input exhibits a typical limiting behavior, with a threshold of 2 μJ for the particular fiber used (core diameter =26μm ; length=3 cm). The (linear) scattering and absorptive losses of the fiber, about 20%, are due to interface reflection and coupling losses. For this case, we note that the threshold input

Fig. 2a

An example of optical self-limiting effect in the transmission of the liquid crystal fiber. The detected output is in arbitrary unit; actual transmission (at low incident power) of the fiber is about 80%.

Fiber core diameter : $26\mu m$

Limiting Threshold Fluence: 0.3 J/cm^2

Fig. 2b

Beam Diameter = 28 um

Limiting Threshold Fluence: 4 J/cm^2
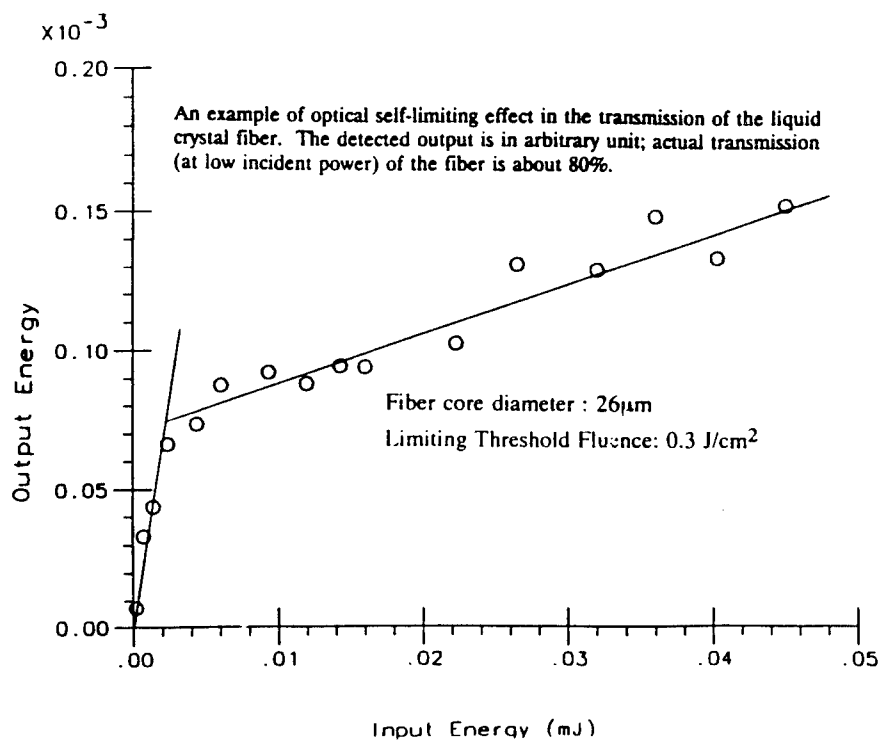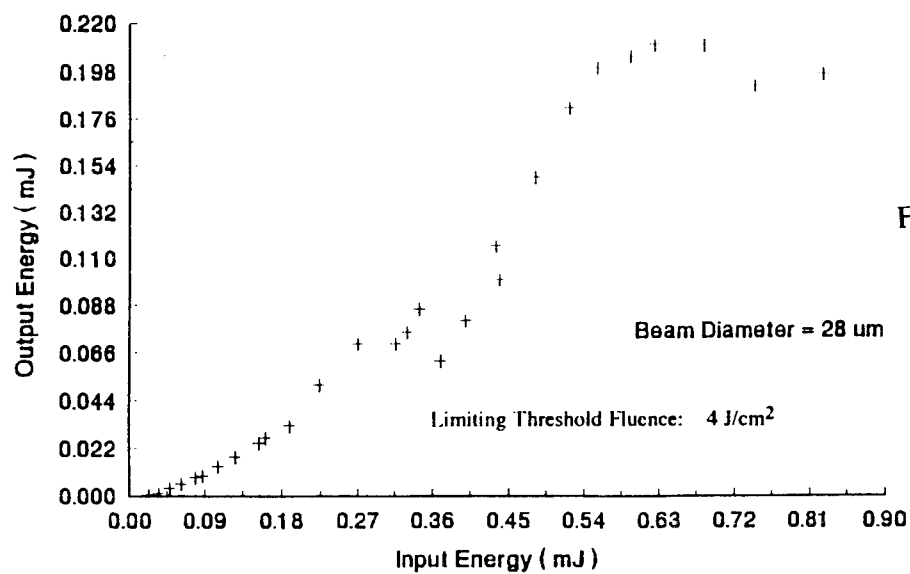
fluence on the liquid crystal fiber is about $0.3\mu J/cm^2$ (focal spot diameter is $26\mu m$). On the other hand, comparative studies in bulk nematic or isotropic liquid crystal samples [4] have shown that the corresponding threshold fluence is at least 10 times larger [c.f. fig.2b for a 2mm thick film of the same liquid crystal used]. The greatly reduced threshold in the liquid crystal fiber is due to the increased interaction region between the laser and the induced density and index change. It is also possible that the intensity dependent laser induced self-lensing effect at the entrance plane of the fiber modifies in an adverse manner the input coupling, and contributed to the self-limiting action.

We have also observed stimulated Brillouin scattering with phase conjugation characteristics in these fibers with threshold on the order of $60\mu J$ or so. Since the thresholds (between $60-80\mu J$)are similar for both TM74A and 5CB, whose absorption constants, α, at $0.532\mu m$ area are very different (α for TM74A is about 0.1 cm^{-1}, whereas α for 5CB is much smaller than 0.1 cm^{-1}), the effect is attributed to stimulated Brillouin scattering (SBS). An
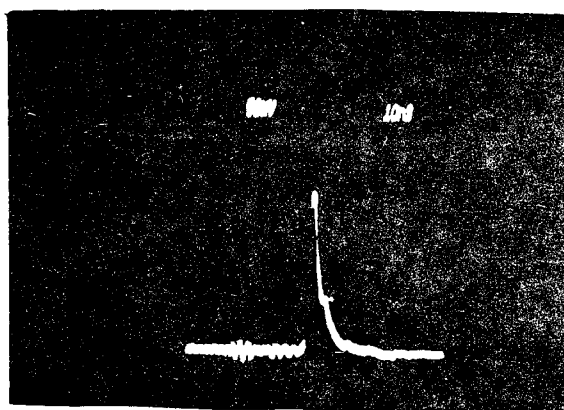
Fig. 3

interesting feature of the observed effect is the aberration correction property associated with SBS, which is manifested in the input-like quality of the backscattered signal. Another interesting feature of the backscattered pulse is that it is significantly compressed [see photo in fig.3]. We will present theoretical analysis of these limiting and stimulated scattering effects which show that liquid crystalline cored fibers will function as very efficient nonlinear optical devices..

References

1.   I. C. Khoo and Y. R. Shen, Optical Engineering 24, p.579 (1985).
2.   I. C. Khoo and S. T. Wu, "Optics and Nonlinear OPtics of Liquid Crystals", (World Scientific, Singapore, 1993).
3.   See, for example, G. I. Stegeman and S.T. Seaton, "Nonlinear Integrated Optics", J. Appl. Phys. 58, p. R57-R78 (1985).
4.   R. G. Lindquist, P. G. LoPresti and I. C. Khoo, SPIE Vol, 1692, p.148-158 (1992).

Ultrafast and efficient optical Kerr effects in chalcogenide glass fibers and the application in all-optical switching

Masaki Asobe, Terutoshi Kanamori*, Kazunori Naganuma, Hiroki Itoh and Toshikuni Kaino

NTT Opto-electronics Laboratories, 3-1 Morinosato-wakamiya, Atsugi, Kanagawa 243-01 Japan
phone: +81 462 40 3243, Fax: +81 462 40 4303
* *NTT Opto-electronics Laboratories, Tokai Naka, Ibaraki, 319-11 Japan*

Nonlinear optical media for all-optical switching should provide for a high degree of nonlinearity, a fast response time, a low rate of transmission loss, and a waveguide structure. Chalcogenide glasses possess this nonlinearity and can be used to form single mode fibers with low transmission loss [1],[2]. We earlier reported on optical Kerr shutter operations using As_2S_3-based glass fibers up to 2-m long [3],[4]. However, switching power for the π phase shift was still high (12~14 W), and the response time of the material was undetermined. This paper reports on the femtosecond nonlinear refractive response in As_2S_3-based glass fibers, and the use of small core fibers with large refractive index differences for reducing switching power. We also demonstrate all-optical switching in a 100-GHz pulse train using a laser diode as a gate pulse source.

A pump-probe measurement was carried out to determine the response time in a material. The experimental setup is shown in Fig. 1. An APM color center laser which generates a 200-fs (FWHM) wide pulse at a wavelength of 1.515 μm was used as the femtosecond pulse source [5]. We used cross polarized lights for the pump and probe [6]. The probe pulse intensity was kept two orders smaller than that of the pump pulse throughout the measurement. We used a short (3-cm-long) fiber for the pump-probe measurement to delimit pulse broadening caused by group velocity dispersion (GVD). The details of this fiber referred to as Fiber C are given in Table 1. The sample fiber had a weak birefringence, which is probably due to photo-induced permanent birefringence [4]. If the polarization of the pump is at an angle ranging from above 0 to under 45 degrees with either fast or slow axies, the Kerr effect will cause changes in the birefringence and lead to polarization changes in the probe. Figure 2 shows a pump-probe trace for a pump power of 490 W and 850 W. For these measurements the polarizer was set to obtain a maximum transmission of the probe pulse in the absence of the pump pulse. The figure shows a fast probe transmission reduction
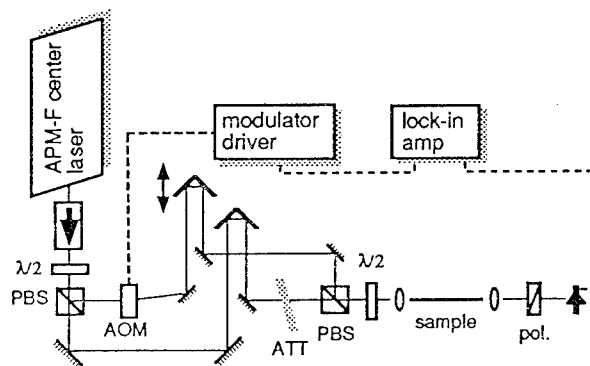
Fig. 1 Experimental setup for pump-probe measurement
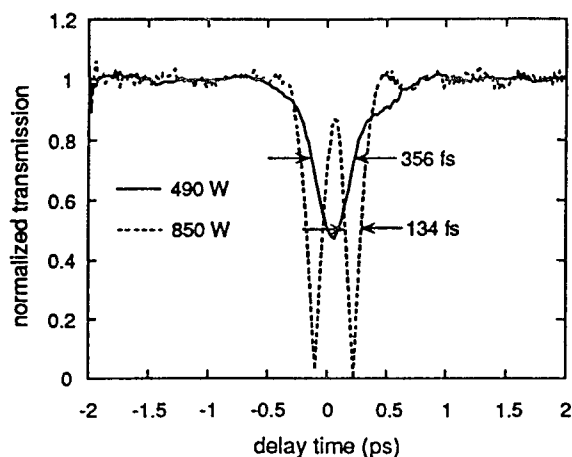
Fig. 2 Pump-probe trace with different pump power

Table 1 characteristics of chlalcogenide glass fiber

Sample	Refractive index difference (%)[*]	Core diameter (μm)	Transmission loss (dB/m)	Fiber length (m)
Fiber A	0.4	5.4	0.9	2.0
Fiber B	0.8	3.6	2.1	2.0
Fiber C	1.3	3.0	3.0	1.2

at a relatively low pump power. The FWHM for the transmission change was 356 fs. This was larger than that of the original pulse width and can be attributed to a pulse broadening in the fiber. When the larger pump power was coupled, a broken up trace with multiple peaks was observed, as shown in Fig. 2. When the probe polarization was aligned to the principle axis, no transmission change was observed. The FWHM in each peak here was 134 fs. These results show that chalcogenide glass has an instantaneous response within a hundred femtoseconds.

There is another speed limitation in all-optical switching caused by GVD. The GVD value for the As_2S_3 glass is 410 ps/kn nm in the 1.55 μm wavelength region [3]. In the picosecond region, pulse broadening is not as noticeable in a fiber of a few meters. Chalcogenide glass fibers thus have one of the highest values for n_2 interaction length product in the picosecond region [7]. Because of this, we conducted an all-optical switching experiment using a picosecond pulse from a laser diode coupled with an erbium doped fiber amplifier (EDFA). To reduce the switching power

sufficiently for laser diode driving, we tried small core fibers with high relative index differences (Δn). We prepared three types of As_2S_3-based single-mode fibers, referred to here as Fibers A, B, and C. Table 1 summarizes the composition and properties in each fiber. The setup for the Kerr shutter experiment is shown in Fig. 3. To measure the switching power for π phase shift, we used a relatively wide (22 ps) signal pulse. By using a 9.6-ps-wide gate pulse, some part of the original 22-ps-wide signal pulse was extracted and the change in the average power of the extracted signal pulse was measured. Fig. 4 shows switched signal pulse energy as a function of the coupled gate power with Fibers A, B, and C. As shown in Fig. 4, switching power for the π phase shift was favorably reduced by
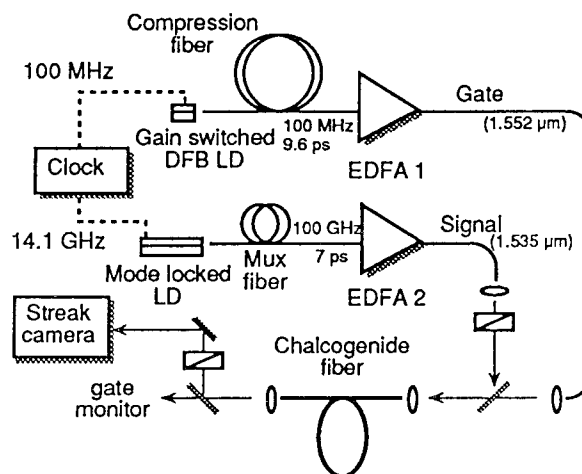
Fig. 3 Experimental setup for all-optical switching using laser diodes

using these high-Δn fibers. The π phase shift was obtained at a gate power of 3 W using the 1.2-m-long Fiber C. From the gate power, the n_2 value is estimated to be 2×10^{-14} (cm^2/W) and is two orders higher than that of a silica fiber [8]. The length of Fiber C was limited by the relatively high loss. This loss is attributed to the scattering loss caused by fiber imperfections such as roughness between the core and cladding. It may be possible to obtain a high-Δ and small-core fiber with a lower loss by reducing the fiber-imperfection loss.

To evaluate the ultrafast switching capability, we performed all-optical switching with a high-repetition signal-pulse train by using Fiber C. Figure 5 shows the temporal waveforms of the switched signal for "normally on" (a), and "normally off" (b). The pulse interval for the signal pulse was 10 ps. As shown in the figures, we were able to switch a 100-GHz signal pulse by using a gate pulse from a laser diode.

These results shows that chalcogenide glass fibers are promising as nonlinear optical media for all-optical switching.

Fig. 5 100-GHz switching with 1.2-m-long fiber

Fig. 4 Switched signal energy as a function of gate power

References

[1] H. Nasu, K. Kubodera, H. Kobayashi, M. Nakamura, and K. Kamiya, *J. Am. Ceram. Soc.*, vol. 73, p. 1794, 1990.

[2] T. Kanamori, Y. Terumuma, S. Takahashi, and T. Miyashita, *IEEE J. Lightwave Technol.*, vol. 2, p. 607, 1984.

[3] M. Asobe, H. Kobayashi, H. Itoh, and T. Kanamori, *Opt. Lett.*, vol. 18, p. 1056, 1993.

[4] M. Asobe, T. Kanamori, K. Kubodera, *IEEE J. Quantum Electron.* vol. 29, p. 2325, 1993.

[5] J. Mark, L. Y. Liu, K. L. Hall, H. A. Haus, and E. P. Ippen, *Opt. Lett.*, vol. 14, p. 48, 1989.

[6] M. N. Islam, C. E. Soccolich, R. E. Slusher, A. F. Levi, W. S. Hobson, and M. G. Young, *J. Appl. Phys.*, vol. 71, p. 1927, 1992.

[7] M. Asobe, K. Naganuma, T. Kaino, T. Kanamori, S. Tomaru, and T. Kurihara, submitted to *Appl. Phys. Lett.*

[8] G. P. Agrawal, Nonlinear Fiber Optics (Academic, New York, 1989).

Exactly solvable model of surface second harmonic generation

Bernardo S. Mendoza
Centro de Investigaciones en Optica, Apartado Postal 948,
37000 León, Guanajuato, México
tel: +(47)17-5823

W. Luis Mochán
Laboratorio de Cuernavaca, Instituto de Física,
Universidad Nacional Autónoma de México,
Apartado Postal 139-B, 62191 Cuernavaca, Morelos, México.
tel: +(73)17-5388

Second harmonic generation (SHG) is a sensitive optical probe of surfaces since the bulk dipolar contribution is suppressed in centrosymmetric crystals [1]. There are different approaches in the literature to study SHG. Sipe et. al.[2] have developed a phenomenological analysis of the surface and bulk susceptibility tensors, identifying their independent components, and the possible functional dependence of the second order reflectance on the incidence and azimuthal angles for different crystal surfaces. However, they did not attempt actual calculations of the susceptibility. Microscopic calculations of the surface response have been performed for simple metals employing hydrodynamic [3,4,5] or self-consistent jellium [6] approximations. Schaich and Mendoza [7] have developed a model that accounts for local field and crystallinity effects in the response of insulators and semiconductors [8], and it has been extended to noble metals [9]. However, there are still very few calculations [10] of the nonlinear spectra of realistic models.

The purpose of the present paper is the development of a simple model that permits the calculation of the second order response and the non-linear reflectance of an arbitrary centrosymmetric semi-infinite system, in terms of its linear response. The calculation involves serious approximations, but we believe it provides useful guidance to the size and the spectral shape of the SHG.

We start by considering a single charge $-e$ bound to its equilibrium position by harmonic forces. In the presence of an harmonic driving field $\vec{E}(\vec{r},t)$ this system acquires a second order dipole and quadrupole moment given by [7]

$$\vec{p}^{(2)}(2\omega) = -\frac{1}{2e}\alpha(\omega)\alpha(2\omega)\nabla E^2, \tag{1}$$

$$Q^{(2)}(2\omega) = -\frac{1}{e}\alpha^2(\omega)\vec{E}\vec{E}, \tag{2}$$

where $\alpha(\omega)$ is the linear polarizability. Now we consider a macroscopic system made up of n of these entities per unit volume, and we will allow n to depend on position, changing rapidly, but continuously near the surface, from its bulk value n_B to its vacuum value of zero. Then, the macroscopic second order polarization $\vec{P}^{(2)}$ is [11]

$$\vec{P}^{(2)} = n\vec{p}^{(2)} - \frac{1}{2}\nabla \cdot nQ^{(2)},$$

using Eq. (1) and Eq. (2) gives,

$$\vec{P}^{(2)} = n\alpha(2\omega)\vec{E}^{(2)} - \frac{n}{2e}\alpha(\omega)\alpha(2\omega)\nabla E^2 + \frac{1}{2e}\alpha^2(\omega)\nabla \cdot (n\vec{E}\vec{E}), \tag{3}$$

where, for consistency, we also added the linear response to the non-linear field $\vec{E}^{(2)}$. At the surface, the normal component of the electric field $E_\perp$ varies rapidly, so that Eq. (3) yields

$$P_\perp^{(2)} = n\alpha(2\omega)E_\perp^{(2)} - \frac{n}{2e}\alpha(\omega)\alpha(2\omega)\partial_\perp E_\perp^2 + \frac{1}{2e}\alpha^2(\omega)\partial_\perp nE_\perp^2. \tag{4}$$

Since the source of the non-linearity is localized near the surface, we have ignored retardation, and we can substitute $E_\perp^{(2)}$ by the depolarization field $-4\pi P_\perp^{(2)}$. Now we write $E_\perp = D_\perp/\epsilon(\omega)$, we ignore the local field

effect in order to write the dielectric function as $\epsilon(\omega) = 1 + 4\pi n\alpha(\omega)$, we assume that the displacement field $D_\perp$ is almost constant within the surface region, and we solve Eq. (4) for $P_\perp^{(2)}$ to obtain

$$P_\perp^{(2)} = \frac{1}{2e\epsilon(2\omega)} \left[-\alpha(\omega)\alpha(2\omega)n\partial_\perp(1/\epsilon^2(\omega)) + \alpha^2(\omega)\partial_\perp(n/\epsilon^2(\omega)) \right] D_\perp^2. \tag{5}$$

The surface susceptibility $\chi_s^{(2)}$ is commonly characterized by two phenomenological parameters, $a(\omega)$ which corresponds to $(\chi_s^{(2)})_{\perp\perp\perp}$ and $b(\omega)$ which corresponds to $(\chi_s^{(2)})_{\|\|\perp}$. We can relate $a(\omega)$ to $P^{(2)}$ through [5]

$$a(\omega) = -64\pi^2 n_B e \left(\frac{\epsilon_B(\omega)}{\epsilon_B(\omega) - 1} \right)^2 \left(\int dr_\perp P_\perp^{(2)} \right) / D_\perp^2, \tag{6}$$

where ϵ_B is the bulk dielectric function. We can perform the integration in Eq. (6) by substituting Eq. (5). It turns out that the integration can be performed analytically, and that *the result is independent of the shape of the density profile* $n(r_\perp)$. The final answer is

$$a(\omega) = 2\frac{(\epsilon_B(2\omega) - \epsilon_B(\omega))(2\epsilon_B(\omega) - \epsilon_B(2\omega) - \epsilon_B(\omega)\epsilon_B(2\omega)) + \epsilon_B^2(\omega)(1 - \epsilon_B(2\omega)) \log(\epsilon_B(\omega)/\epsilon_B(2\omega))}{(\epsilon_B(2\omega) - \epsilon_B(\omega))^2}. \tag{7}$$

Following the same procedure, we obtain that $b(\omega) = -1$, and introducing retardation we also calculate the quadrupolar bulk susceptibility, characterized by the phenomenological parameter [12] $d(\omega) = 1$. We have obtained the same expressions for conducting systems when the spatial dispersion of the electron gas is neglected. Finally, we employ standard formulae [3] to calculate the efficiency of the SHG $\mathcal{R} = I^{(2)}/I_i^2$ where $I^{(2)}$ and I_i denote the second order and the incident intensity respectively.

The results above can be applied to the calculation of the non-linear response of an arbitrary semi-infinite centrosymmetric crystal by simply employing the appropriate values for its dielectric function. For example, in Fig. 1 we show $a(\omega)$ for Ge (ϵ_B is taken from Ref. [13]) and in Fig. 2 we show the corresponding $\mathcal{R}(\omega)$ for $p \to p$ and angle of incidence $\theta = 45°$. We have performed similar calculations for other materials such as diamond whose efficiency turns out to be 5 orders of magnitude smaller.

In summary, by assuming that the polarizability of each microscopic entity is described by Eq. (1) and Eq. (2), by assuming a continuous distribution of these entities and by neglecting the local field effect, we have solved the problem of SHG for a semi-infinite medium obtaining analytical expressions which may be applied to any centrosymmetric system to obtain a first estimate of its non-linear efficiency spectra. The source of the surface non-linearity is the rapid variation of the normal component of the electric field across the surface region. The only input to our calculations is the linear bulk dielectric response, which can be obtained from experiment or from well known calculation schemes.
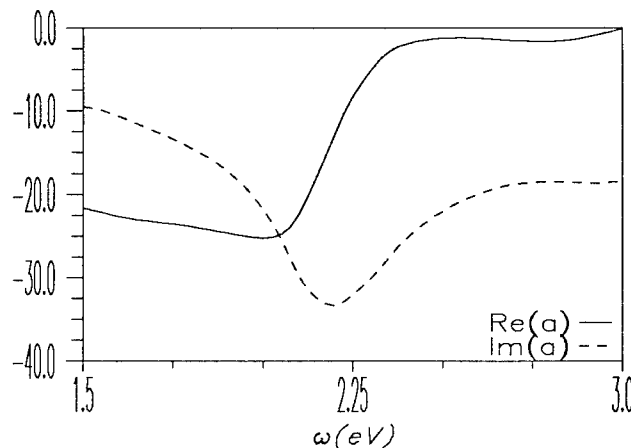
Figure 1. We show the real and imaginary parts of $a(\omega)$ vs. ω for Ge.
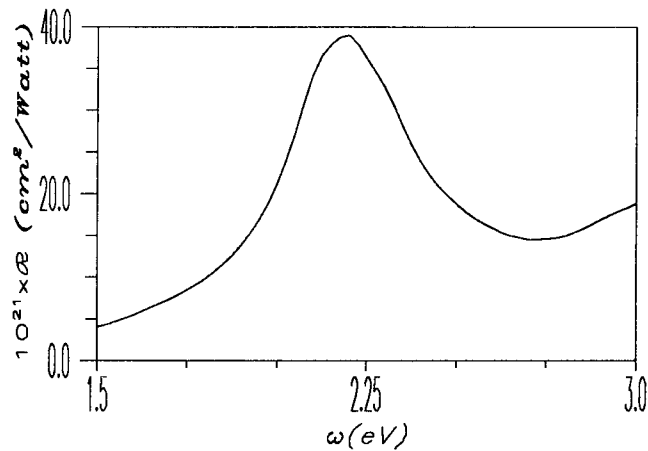
Figure 2. We show the SHG efficiency $\mathcal{R}$ as a function of the fundamental frequency ω for Ge.

ACKNOWLEDGMENTS

REFERENCES

1. R.W.J. Hollering, J.Opt.Soc.Am.B **8**, 374 (1991).

2. J.E. Sipe, D.J. Moss, and H.M. van Driel, Phys.Rev.B **35**, 1129 (1987).

3. M. Corvi and W.L. Schaich, Phys.Rev.B **33**, 3688 (1986).

4. O. Keller, Phys.Rev.B bf 31, 5028 (1985).

5. W.L. Schaich and A. Liebsch, Phys.Rev.B **37**, 6187 (1988).

6. A. Liebsch and W.L. Schaich, Phys.Rev.B **40**, 5401 (1989).

7. W.L. Schaich and B.S. Mendoza, Phys.Rev.B. **45**, 14279 (1992).

8. Bernardo S. Mendoza, J.Phys.: Condens. Matter **5** A181 (1993).

9. W.L. Mochán and Bernardo S. Mendoza, J.Phys.: Condens. Matter **5** A183 (1993).

10. M. Cini, R. Del Sole and L. Reining, Surf.Sci. **287/288**, (1993) 693-698.

11. J.D. Jackson, Classical Electrodynamics, 2nd edition, Wiley, New York.

12. J. Rudnick and E.A. Stern, Phys.Rev.B **4**, 4274 (1971).

13. D. E. Aspnes and A. A. Studna, Phys.Rev.B **27**, 985 (1983).

Extended Parametric Gain Using Twin Core Fiber

Paul B. Lundquist[1] and David R. Andersen[2]
[1]*Department of Physics and Astronomy*
[2]*Department of Electrical and Computer Engineering*
The University of Iowa, Iowa City, IA 52242
319-335-2529

Xiaoping Yang and Barry Luther-Davies
Laser Physics Centre
Research School of Physical Sciences and Engineering
Australian National University, Canberra, ACT 0200, Australia
61-6-249-4255

It is well known that parametric processes can be used to efficiently generate sideband frequencies from a strong pump within a suitable nonlinear medium [1]. However, the bandwidth over which parametric gain can be achieved depends on the ability to phase match the two sidebands with the pump beam. As a consequence, the use of parametric processes to produce tunable frequencies of light is limited by dispersion in the nonlinear material. It could be of great importance to develop methods of extending the tunability of the four-wave mixing process.

In previous work we showed how the tunability of a four-wave mixing process could be extended by coupling to a passive linear wave-guide [2]. Since then we have investigated this new phase matching technique for the specific geometry of a twin-core coupler and have extended our theory to include a correction to the effective dispersion due to the presence of the passive core.

We consider two identical cores in the same cladding, each with radius a, and separated a distance s from center to center. A strong pump beam, weak probe, and a parametrically generated sideband with field amplitudes ϕ_u, ϕ_v, and ϕ_w respectively, propagate along one core. The probe and parametrically generated sideband couple to the linear modes with field amplitudes ϕ_x and ϕ_y in the second core. Parametric generation of the side band is a consequence of the nonlinear correction to the index of refraction for the pump beam. Generally this nonlinearity is described by $n = n_{co}(\omega_u) + n_2|\phi|^2$. The pump beam will not couple to the second core because of self-phase modulation, but the side bands will.

Though the general evolution problem is difficult, with reasonable approximations the it can be linearized. We neglect the transverse derivatives in the treatment of the nonlinearity, and use the undepleted pump and slowly varying amplitude approximations. After redefining the resulting field amplitudes to incorporate a phase change, the following linearized evolution equations are obtained:

$$i\frac{\alpha_v}{(1-\Delta)}\frac{\partial \phi_v}{\partial \zeta} + K_x\phi_x + 2\phi_v + \phi_w^* e^{-i\delta\zeta} = 0 \tag{1}$$

$$i\frac{\alpha_w}{(1+\Delta)}\frac{\partial \phi_w}{\partial \zeta} + K_y\phi_y + 2\phi_w + \phi_v^* e^{-i\delta\zeta} = 0 \tag{2}$$

$$i\frac{\alpha_v}{(1-\Delta)}\frac{\partial\phi_x}{\partial\zeta} + K_x\phi_v = 0 \tag{3}$$

$$i\frac{\alpha_w}{(1+\Delta)}\frac{\partial\phi_y}{\partial\zeta} + K_y\phi_w = 0 \tag{4}$$

where ζ is a normalized length, $\Delta = \frac{(\omega_w - \omega_v)}{2\omega_u}$ is the detuning parameter, δ is the dispersion parameter, and $K_{x,y}$ are coupling constants. The parameters $\alpha_{v,w}$ are corrections which, when $\Delta \ll 1$, are approximately equal to 1. The dispersion parameter is the sum of the nonlinear phase shift in the pump, the single core dispersive propagation mismatch and a phase mismatch correction due to the presence of the passive core. For the geometry of a twin-core fiber we have derived analytic expressions for the coupling constants and the dispersion parameter.

The linearized evolution equations may be cast in matrix form and solved by the eigen-value method. The gain in the system is the maximum real part of the eigenvalues of the resulting evolution matrix. In Figure 1 , we show a map of the gain region in the absence of coupling to the passive core. We see that for Δ small, we can only phase match for parametric gain for $-6 < \delta < -2$. In the presence of weak coupling, gain can be phase matched for δ outside this gain ellipse. As an example, we have made some calculations assuming a $.82\mu m$ wavelength pump in a twin core fiber with $2\mu m$ diameter Germanium doped cores and Florine doped cladding. In Figure 2 we show a trajectory in (δ, Δ) space and the corresponding gain for typical parameters. By comparison with Figure 1 it is apparent that there is an additional gain region due to the core to core coupling. For nearly degenerate frequencies, or stronger coupling a correction to the dispersion parameter may become significant. In Figure 3 we show the gain of a system, and δ as a function of the core to core separation. The separation dependence of δ is entirely due to the correction. For stronger coupling, the correction to δ becomes dominate, eliminating the possibility for gain.

In this talk, we will explain our new phase matching method, present the results of our analytic calculations, and discuss considerations for a practical implementation of this novel technique.

References

[1] R. H. Stolen and J. E. Bjorkholm, "Parametric amplification and frequency conversion in optical fibers," *IEEE J. Quantum Electron.* **QE-18**, 1062-71 (1982).

[2] D. R. Andersen, Xiaoping Yang, Wieslaw Krolikowski, and Barry Luther-Davies, "A Novel Technique for Phase matching Parametric Gain in Nonlinear Waveguides," *J. Opt. Soc. Am. B* , accepted for publication.
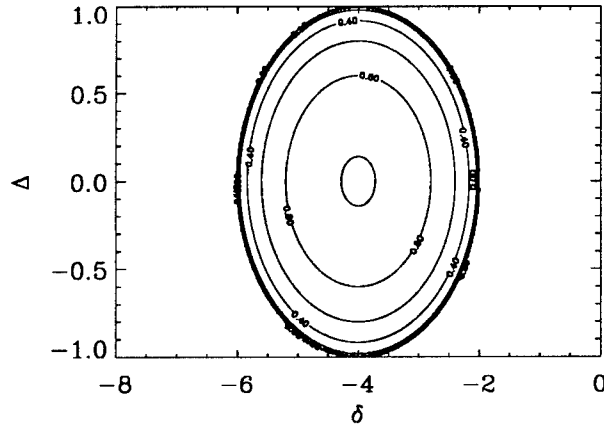
Figure 1: Gain ellipse without coupling to the passive core
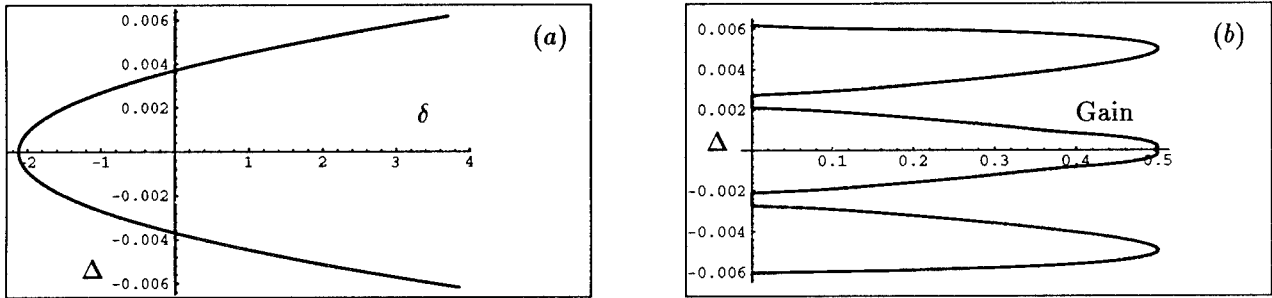
Figure 2: For a typical twin core fiber: (a) the dispersion parameter as a function of detuning, and (b) gain as a function of detuning. Additional gain regions are apparent for $\delta > -2$.
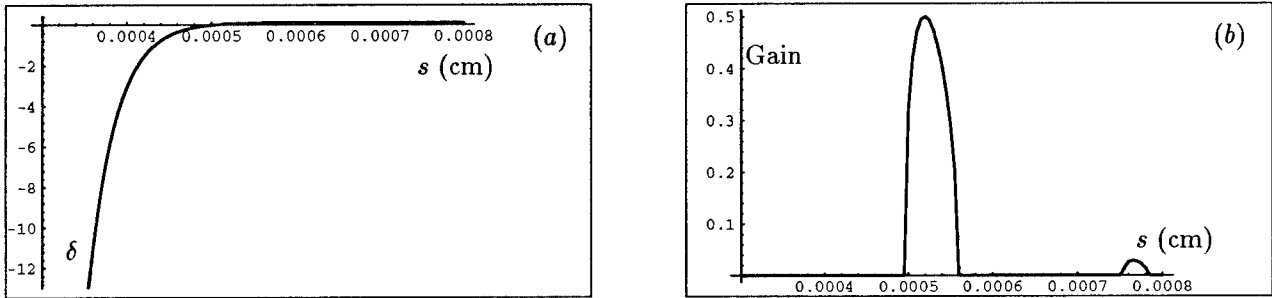
Figure 3: For a typical twin core fiber: (a) the dispersion parameter as a function of the core to core separation, (b) gain as a function of the core to core separation. The separation dependence of the dispersion parameter becomes dominate as the coupling becomes stronger.

Dynamic pulse evolution in self-starting passively mode-locked Ti:sapphire/DDI lasers

Institute of Electro-optical Engineering, National Chiao Tung University
Ci-Ling Pan, Chin-Der Hwang, Nen-Wen Pu, and Jia-Min Shieh
Hsinchu, Taiwan, 30050, Republic of China
Fax: +886-35-716631   E-mail: clpan@cc.nctu.edu.tw

Summary

Detailed measurement on the evolution of the laser pulse width from its onset to the steady state can provide valuable insights on the interplay of various pulse shaping forces. In this study, we have examined the dynamic pulse evolution to the steady state in a passively mode-locked Ti:sapphire laser with intracavity saturable dye absorber. This class of lasers is of interests becuase it is self-starting, robust, and can produce stable, sub-100fs pulses. While previous experimental and theoretical works have shown that the time for such passively mode-locked lasers to reach the steady state is of the order of a few tens of thousand round trips [1-4], the present study reveals the role of various mode-locking mechanisms at a given stage of pulse evolution. In particular, we are able to measure, for the first time to our knowledge, the pulse-shortening speed, S_p, defined as the fractional change in pulse duration per pass, as the pulse evolved.

The experimental appratus is shown in Fig. 1. Our Ti:sapphire laser consists of a linear cavity of six mirrors with a 5% ourput coupler. The gain and absorber folding sections have focusing mirrors of 15 and 5 cm of radii of curvature respectively. Mode-locking was initiated by the saturable dye absorber, DDI. For the cavity without the compensating SF10 prisms, the laser generated picosecond pulses. As the dye concentration increased from 0.84×10^{-4} M to 6.08×10^{-4} M, the steady state pulse width decreased exponentially from ≈ 17.9ps to ≈ 2ps. The pulse width as a function of delay time with respect to the onset of laser action was measured by the time-gating technique described previously [2]. Pulse shortening speeds could also be deduced from the pulse width evolution data. For dye concentration of 0.84×10^{-4} M, 1.25×10^{-4} M, and 6.08×10^{-4} M, the pulse shortening speeds, S_p, are -5×10^{-4}, -1.6×10^{-3}, and -2.3×10^{-3}, at the stage when the laser pulse width, $\tau \approx 200$ps, as opposed to $S_p = -9.4 \times 10^{-5}$, -5.9×10^{-4}, and -1.1×10^{-3}, respectively for $\tau \approx 20$ps. These are in reasonable agreements with theoretical predicted values. With prisms, the laser generated 150fs (gaussian) pulses at 77MHz in the steady state, regardless of dye concentration. The bandwidth-pulsewidth product is 0.45. Fig. 2 illustrates evolution of S_p for the cavity either with or without prisms, at three dye concentration values. Clearly, the saturable dye absorber is a dominant pulse shortening force for pulse width as short as a few picoseconds. The pulse shortening speeds, $S_p = -2.5 \times 10^{-4}$ at the stage when the pulse width evolved to 400fs, are the same for the three different dye concentrations. Our calculations indicate that for $\tau \approx 1$ps, S_p for the

saturable absorber dye and the Kerr-lens mode-locking (KLM) mechanisms are approximately equal and of the order of -1×10^{-4}. For shorter pulses, KLM is the dominant pulse shortening force. As a result, the steady-state fs pulse widths is independent of saturable absorber dye concentrations. By examining Fig. 2, we also find that S_p is four times larger for the cavity with prisms than the cavity without prisms at $\tau \approx 5$ps and dye concentration of 6.08×10^{-4} M. Since the pulse shortening forces due to the saturable dye absorber and KLM are the same for the two cavities, this is strong evidence of the prensence of soliton-like pulse-shaping force by the combined action of SPM and GVD compensation for the cavity with prisms. Recently, we were able to improve our measurements to earlier stage of pulse formation, for τ as long as 1ns. A turning point corresponding to maximum S_p., which shifted with increasing pumping power, was observed (See Fig. 3). This phenomenon can also be understood by noting the pulse-shortening characteristics of the saturable absorber for incident pulses of different peak intensity.

References

1. N. Sarukura and Y. Ishida, "Pulse evolution dynamics of a femtosecond passively mode-locked Ti:sapphire laser," Opt. Lett. vol.17, pp.61-63, 1992.
2. J.-C. Kuo, Jia-Min Shieh, Chin-Der hwang, C.-S.Chang, Ci-Ling Pan and K.-H. Wu, "Pulse-forming dynamics of a cw passively mode-locked Ti:sapphire/DDI laser," *ibid.* , vol.17, pp.334-336, 1992.
3. J. Goodberlet, J.Wang, J.G.Fujimoto and P.A. Schulz, "Starting dynamics of additively-pulse mode locking in the Ti: sapphire laser," *ibid.,*, vol.15, pp.1300-1302, 1990.
4. S. Chen and J. Wang, "Self-starting issues of passive self-focusing mode locking," ibid., pp.1689-1691, 1991
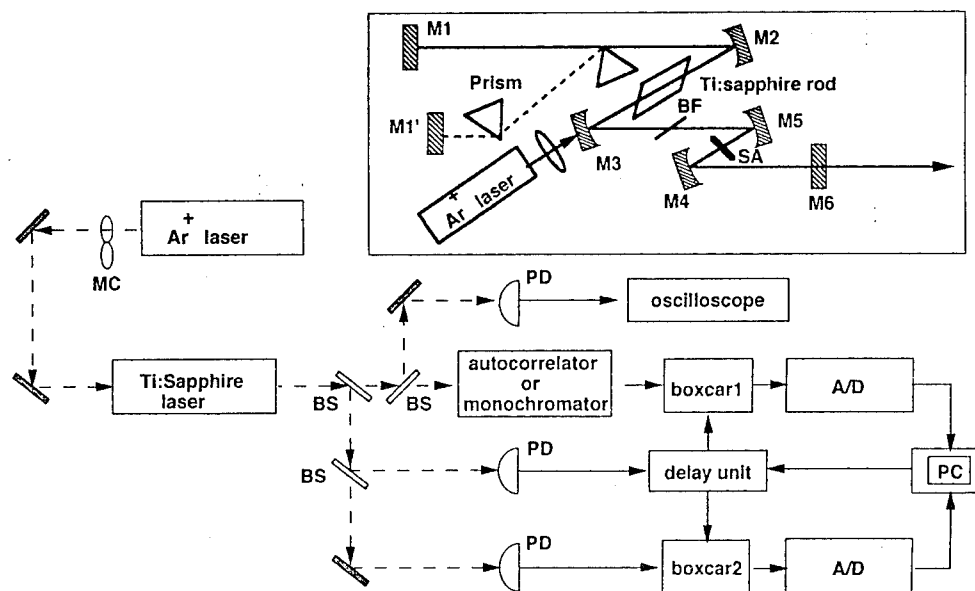
Fig. 1. Block diagram of the experimental setup. MC: mechanical chopper; BS: beam splitter; PD: photodetector; BF: birefringent filter; SA: saturable absorber.

Pulse Shortening Speed (DDI)
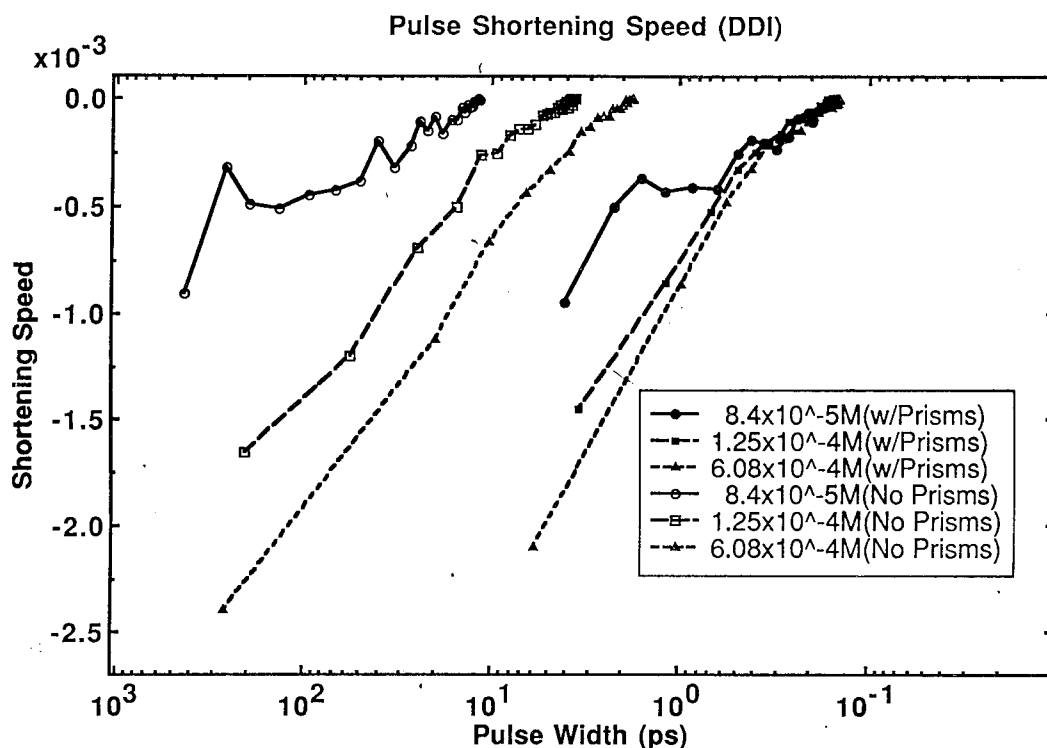
Fig. 2. Pulse shortening speeds as a function of the pulse width as the laser evolves to the steady state for three different dye concentration

Pulse Shortening Speed for 3 Pump Levels
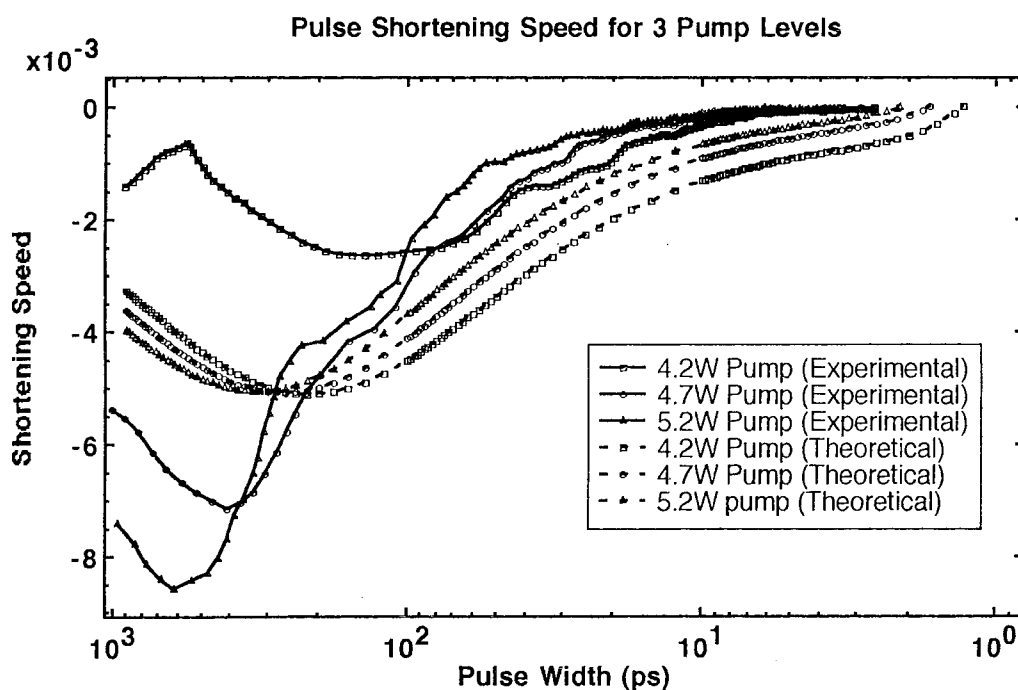
Fig. 3. Experimental and theoretical evolution curves which exhibit maximafor pulse shortening speeds in a cavity without prisms.

Second harmonic generation at conductor surfaces with continuous profiles

W. Luis Mochán

Instituto de Física, Universidad Nacional Autónoma de México,
Apartado Postal 139-B, 62191 Cuernavaca, Morelos, México, tel:+(73)17-5388

Jesús Maytorena

Facultad de Ciencias, Universidad Autónoma del Estado de Morelos,
Av. Universidad s/n, 62000 Cuernavaca, Morelos, México, tel:+(73)17-5388

Bernardo S. Mendoza

Centro de Investigaciones en Optica, Apartado Postal 948,
37000 León, Guanajuato, México, tel:+(47)17-5823

Second harmonic generation (SHG) by centro-symmetric crystals has become a useful tool to study surfaces since their dipolar bulk contribution is suppressed by symmetry. The residual bulk contribution originates from the non-uniformity of the electric field and is usually of a similar order of magnitude as the surface contribution, namely, a factor $(a/\lambda)^2$ smaller than for non-centro-symmetric materials, where a is a distance of the order of atomic dimensions and λ is the wavelength. To distinguish surface from bulk contributions some experiments have concentrated on the anisotropy of the signal [1], and only a few have considered its frequency dependence [2]. Recently, experiments performed on metals immersed in an electrolyte [3] have shown that the surface contributions to SHG depends on the surface electronic distribution. Since a local theory of SHG [4] yields no electronic density profile dependence, spatial dispersion has to be accounted for. In the literature there are calculations for the SHG of free-electron-like metals using either the self-consistent jellium model [5] or the more simple hydrodynamic model [6]. The former calculations have not been performed above $\omega = \omega_p/2$ due to technical difficulties whenever a propagating bulk plasmon at 2ω is excited. The latter calculations have been restricted to discontinuous step profiles, and require that additional boundary conditions be imposed at the density discontinuities. Given the relative simplicity of the hydrodynamic model and the possibilities it offers to go beyond simple jellium models [7], in this paper we extend it to the case of arbitrary surface density profiles.

In the following we concentrate on one component of the nonlinear surface susceptibility tensor χ_2^s, namely $(\chi_2^s)_{\perp\perp\perp}$. The calculations for the other components are analogous. We start from the continuity equation and from Euler's equation for the momentum conservation of a semiinfinite electron fluid of density $n(z)$ moving with velocity field $u(z)$ in the presence of an electric field $E(z)$, namely

$$mn\partial_t u + mnu/\tau + mnu\partial_z u = -neE - \gamma n^{2/3}\partial_z n, \tag{1}$$

where m and $-e$ are the electrons' mass and charge and τ measures their lifetime. The consequtive terms of Eq. (1) correspond to inertial forces, dissipation through friction with the lattice, convective momentum flow, electric force and a pressure gradient. The pressure originates from the density dependence of the average energy of a fermion in a non-interacting homogeneous gas $U/N = 9/10\gamma n^{2/3}$, where $\gamma = (3\pi^2)^{2/3}\hbar^2/(3m)$. To account partially for the Coulomb interaction, E is taken to be the self-consistent field and we neglect exchange and correlation [8]. Here we assume that all vector fields (E, u, etc.) point along the z direction, which we take as the normal to the surface. We also assume that the width of the "surface region" is small when compared to the optical wavelength, so that at this stage of our calculation we may neglect retardation [9] and the variation of the fields along the surface.

Now we make an expansion of n, u, and E in powers of a perturbing oscillating external field $D(z,t) =$

Re $De^{-i\omega t}$. To order zero we obtain

$$E_0 = -\frac{3}{2}\frac{\gamma}{e}n_0^{2/3}, \tag{2}$$

where n_0 is the equilibrium density profile and E_0 plays the role of an effective field that confines the electrons to a semispace. To first order we obtain

$$(\omega_p^2 - \omega^2 - i\omega/\tau)P_1 = \frac{\omega_p^2}{4\pi}[D + \frac{\gamma}{e^2}\partial_z(n_0^{-1/3}\partial_z P_1)], \tag{3}$$

where $\omega_p = \sqrt{4\pi n e^2/m}$ is the (local) plasma frequency and P is the polarization field, related to the electric current $j = -neu$ through $j = \partial_t P$. Finally, for the second order field oscillating at 2ω we obtain

$$
\begin{aligned}
[\omega_p^2 - 2\omega(2\omega + i/\tau)]P_2 &= \frac{\gamma n_0}{m}\partial_z(n_0^{-1/3}\partial_z P_2) - \gamma\frac{n_0}{m}\frac{1}{6e}\partial_z(n_0^{-2/3}\partial_z P_1)^2 \\
&+ \frac{\omega^2}{n_0^2 e}\partial_z(n_0)P_1^2 - \frac{1}{2n_0 e}(3\omega^2 + i\omega/\tau)\partial_z P_1^2.
\end{aligned} \tag{4}
$$

Notice from Eq. (4) that the sources of the surface nonlinear polarization are the spatial derivatives of the ground state density n_0 and of the linear polarization P_1.

The second order differential equations (3) and (4) can be solved analytically in the bulk region where n_0 is z independent and they can be integrated numerically near the surface where n_0 varies from 0 to its bulk value n_B. The bulk and surface solutions may be sewn together by using (additional) boundary conditions which can be obtained from the differential equations themselves [6, 10]. For example, consistency between the order of the singularities that may be present on both sides of Eq. (3) lead immediately to the continuity of the terms under the derivative operator, namely, $P1$ and $n_0^{-1/3}\partial_z P_1$. These boundary conditions are equivalent to those first proposed by Forstmann [11] in order to satisfy energy and charge conservation at sharp boundaries between homogeneous layers.

After solving Eqs. (3) and (4) for $P_1(z)$ and $P_2(z)$ we integrate $P_1(z) - P_1(\infty)$ and $P_2(z)$ over z to get the surface polarizations P_1^s and P_2^s, and the surface susceptibilities $(\chi_1^s)_{\perp\perp} = P_1^s/D$ and $(\chi_2^s)_{\perp\perp\perp} = P_2/D^2$. We have performed similar calculations for all the components of both surface and bulk, linear and nonlinear susceptibilities of this system, and we have employed them to calculate the SHG efficiency.

To illustrate our results we have chosen a simplied form for the equilibrium density: $n_0(z) = n_B$ if $z > z_B$, $n_0(z) = (1 + z/z_B)n_B/2$ if $-z_B < z < z_B$ and $n_0(z) = 0$ if $z < -z_B$; that is, in the selvedge region of width $2z_B$ the density interpolates linearly between its vacuum and bulk values. In Fig. 1 we show the nonlinear efficiency spectra $R_2(\omega) = I(2\omega)/I(\omega)^2$ where I is the optical intensity, calculated for $z_B = 3$ in atomic units, which corresponds very roughly to Al ($r_s = 2.07$). Our results are up to three orders of magnitude larger than those obtained for a single step discontinuous density [6, 9], and display large peaks at $\omega_q/2$, $\omega_d/2$, ω_q and specially at ω_d. The resonance frequencies ω_d and ω_q denote the dipolar and quadrupolar surface collective modes which appear as peaks in the linear surface conductivity [12] $s = -i\omega(\chi_1^s)_{\perp\perp}$. It has been possible to observe multipolar surface modes in EELS experiments [13], although they are strongly shadowed by the monopolar surface plasmon. The number of multipolar resonances, their position and the strength depend on the width of the selvedge and on the shape of the density profile. Currently we are performing similar calculations for more realistic shapes [14].

In summary, we have extended the hydrodynamic model to calculate the linear and non-linear response and the nonlinear efficiency of semiinfinite metals taking account the electronic density profile at their surface. The surface nonlinear susceptibility and its efficiency display a series of very large peaks, several orders of magnitude larger than those obtained for abrupt profiles, corresponding to the excitation of multipolar surface modes at ω and 2ω. Our results suggest that the multipolar modes, which are difficult to observe in electron scattering experiments, might be observed through SHG spectroscopy. We hope this calculation encourages more experiments to measure the frequency dependence of the SHG signal.

References

[1] For example, D. A. Koos, V. L. Shannon, and G. L. Richmond, Phys. Rev. B **47**, 4730 (1993); R. Murphy, M. Yeganeh, K. J. Song, and E. W. Plummer, Phys. Rev. Lett. **63**, 318 (1989).
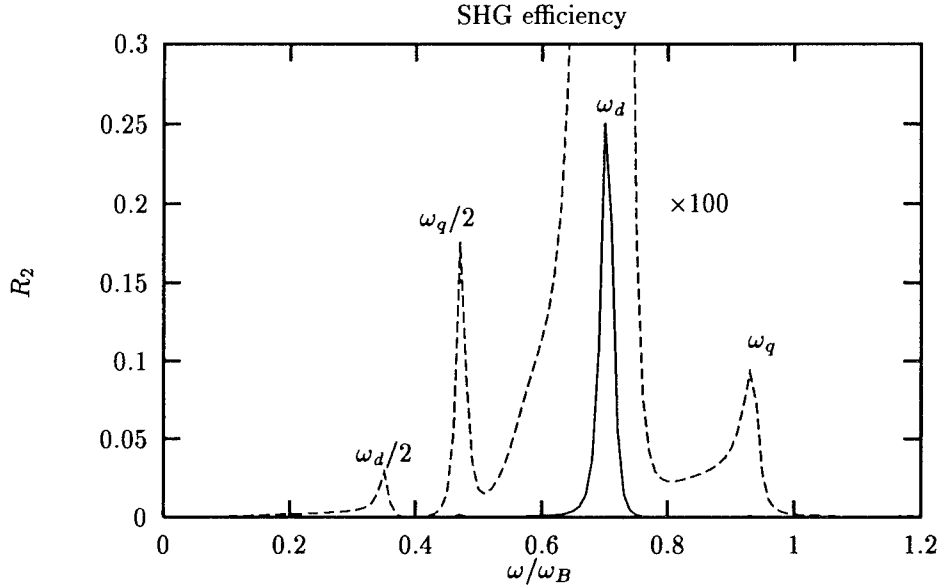
Figure 1: $p - p$ SHG efficiency for light incident at $60°$ on a conductor with $r_s = 2.07$ and with a surface linear profile with $z_B = 3$ in atomic units. The multipolar resonances are indicated.

[2] L. E. Urbach, K. L. Percival, J. M. Hicks, E. W. Plummer, and H.-L. Dai, Phys. Rev. B **45**, 3769 (1992).

[3] P. Guyot-Sionnest, A. Tadjeddine, and A. Liebsch, Phys. Rev. Lett. **64**, 1678 (1990).

[4] B. S. Mendoza and W. L. Mochan, unpublished (submitted to Nonlinear Optics '94).

[5] A. Liebsch and W. L. Schaich, Phys. Rev. B **40**, 5401 (1989).

[6] M. Corvi and W. L. Schaich, Phys. Rev. B **33**, 3688 (1986).

[7] W. Luis mochán and Bernardo S. Mendoza, J. of Phys.: Cond. Mat. **5**, A183 (1993).

[8] A. Chizmesheya and E. Zaremba, Phys. Rev. B **37**, 2805 (1988).

[9] W. L. Schaich and A. Liebsch, Phys. Rev. B **37**, 6187 (1988).

[10] M. del Castillo-Mussot, W. L. Mochán, and Bernardo S. Mendoza, J. of Phys.: Cond. Mat. **5**, A393 (1993).

[11] F. Forstmann and H. Stencshke, Phys. Rev. Lett. **38**, 1365 (1977).

[12] W. Luis Mochán, R. Fuchs, and R. G. Barrera, Phys. Rev. B **27**, 771 (1983).

[13] K.-D. Tsuei, E. W. Plummer, A. Liebsch, E. Pehlke, K. Kempa, and P. Bakshi, Surf. Sci. **247**, 302 (1991).

[14] J. Maytorena, B. S. Mendoza, and W. L. Mochán, unpublished.

Efficient resonant surface-emitting second-harmonic generators and optical power limiters based on multilayers or asymmetric quantum wells

J. B. Khurgin and S. J. Lee
Department of Electrical and Computer Engineering
The Johns Hopkins University, Baltimore, MD 21218
Y. J. Ding
Department of Physics and Astronomy
Bowling Green State University, Bowling Green, OH 43403

Recently, surface-emitting green light was obtained [1] by frequency-doubling infrared laser beam (1.06 μm) in the waveguide based on periodically modulated second-order susceptibility in alternating $Al_xGa_{1-x}As$ and $Al_yGa_{1-y}As$ ($x \neq y$) layers. When a thin layer of AlGaAs is sandwiched between two quarter-wave stacks, large increase in the conversion efficiency was observed [2] though quasi-phasematching was not established. The maximum conversion efficiency so far is still less than 1%/W.

Here, we propose a novel type of devices (Fig. 1) that simultaneously perform two functions: frequency doubling and optical power limiting from different output ports based on resonant second-order susceptibilities in ZnSe/ZnS or AlGaAs/AlGaAs multilayer, or ZnSe/ZnMnSe or GaAs/AlGaAs asymmetric quantum well structures incorporating quarter-wave stacks for resonant enhancement.

To generate second-harmonic light, we need two counterpropagating beams with their polarizations normal to each other (TE and TM) because of the polarization dependence of $\chi^{(2)}$ in bulk materials or asymmetric quantum wells. We can couple a circularly polarized beam into the waveguide to generate these two counterpropagating beams in the waveguide. In the case of frequency doubling, the second-harmonic light emits from the the surface of the multilayer or asymmetric quantum well structures. The quasi-phasematching in multilayers is achieved by growing alternating thin layers in which the single unit consists of two layers possessing different magnitudes of second-order susceptibilities [1]. The quasi-phasematching in asymmetric quantum wells is achieved by growing alternating domains consisting of multiple asymmetric quantum wells in which the single unit consists of two domains that correspond to the opposite symmetries [3]. In both structures, second-order susceptibility can be modulated along the growth direction from one layer or domain to the adjacent one. By properly designing the structures of multilayers or asymmetric quantum wells, we can convert the spectrum of 0.8-2 μm to that of 0.4-1 μm using different materials and structures to avoid the absorption of second-harmonic light by the materials. Because semiconductors are isotropic materials, surface-emitting geometry is probably the only one to achieve quasi-phasematching. We do not need to separate second-harmonic light from fundamental one. Such frequency doublers can be integrated with laser diodes to form a monolithic laser source at short wavelength. We do not need to rotate the sample for a large range of pump wavelengths to maintain quasi-phasematching. We can easily incorporate two quarter-wave stacks into the structures for the Fabry-Perot cavity enhancement.

The conversion efficiency is depicted vs. the input power in Fig. 2. The saturation power can be expressed as

$$P_s = \frac{\lambda_{2\omega}^2 n_\omega^2 n_{2\omega}(1-R_1 R_2)}{8\eta_0[\Delta\chi_0^{(2)}]^2} \frac{d_{eff}}{d} \frac{b}{l}$$

where $\Delta\chi_0^{(2)}$ is the difference of the second-order susceptibilities between adjacent layers for multilayers or between adjacent domains for asymmetric quantum wells, R_1 and R_2 are the reflectivities of the second-harmonic light at two quarter-wave stacks, $\lambda_{2\omega}$ is the second-harmonic wavelength, n_ω and $n_{2\omega}$ are the refractive index for fundamental and second-harmonic wave, η_0 is the vacuum impedance, d_{eff} represents the overlap of the interacting modes, d is the total thickness of the layers, b is the width of the waveguide, and l is the length of the waveguide. When the input power is equal to the saturation power, the conversion efficiency reaches 72%, see Fig. 2. Above the saturation power, the conversion efficiency approaches 100% exponentially. For $P_i = 5P_s$, $\eta \approx 99.4\%$, see Fig. 2.

In the case of optical power limiting (Fig. 3), the output beam is the portion of the input beam that is reflected from the waveguide, propagating along the multilayer or quantum well plane. Optical power limiting is achieved based on the resonant cascaded second-order susceptibilities in multilayers or asymmetric quantum wells (effective third-order nonlinearity) [4]. The advantage of this type of optical power limiters compared with the conventional ones is that they can take much higher input power because the limiting is done by converting the input power into the second-harmonic power (no real absorption is involved). It can be readily shown that the threshold power for power limiting (P_{th}) is the same as the saturation power for second-harmonic generation. Based on the Manley-Rowe relation, we obtain $P_i = P_r + P_{2\omega} + L_\alpha$ where P_i is the input power, P_r is the reflected power, $P_{2\omega}$ is the total second-harmonic power ($=2P_2$), and L_α is the loss which is expected to be low in our structures. Therefore, one device can perform two functions: frequency doubling and optical power limiting through different output ports (Fig. 1).

Following Ref. [1], $\Delta\chi_0^{(2)} \approx 9 \times 10^{-10}$ m/V for GaAs/Al$_{0.8}$Ga$_{0.2}$As multilayers at 1.06 μm. Therefore, we use $\Delta\chi_0^{(2)} \approx 2 \times 10^{-10}$ m/V for estimating the saturation/threshold powers. Consider $d_{eff}/d \approx 10$. If $\lambda_{2\omega} = 0.9\,\mu$m (using GaAs/Al$_{0.8}Ga_{0.2}$As multilayers), $R_{1,2} = 99.99\%$, $b = 10\,\mu$m, $l = 10$ mm, $P_s \approx 1$ W. To efficiently frequency-double 1.32 μm laser light, we replace a single thin layer of Al$_{0.6}$Ga$_{0.4}$As by alternating Al$_{0.5}$Ga$_{0.5}$As/AlAs layers and using quarter-wave stacks with high reflectivities (e.g. $R_{1,2} \approx 99.9\%$) in Ref. [2]. Our estimate shows that two orders of magnitudes of the enhancement on the conversion efficiency is expected. The third example is to generate blue light based on ZnSe/ZnS multilayers. For $\lambda_{2\omega} = 0.49\,\mu$m, $R_{1,2} = 99.99\%$, $b = 10\,\mu$m, $l = 10$ mm, $P_s \approx 130$ mW. The saturation/threshold powers for asymmetric quantum wells, are more or less the same as those for multilayers. We also show that the proposed structure, when used with both TE and TM waves, can act as the coupler, the self-phase modulator, and the optical phase conjugator.

[1] R. Normandin, R. L. Williams, and F. Chatenoud, Electr. Lett. 26, 2088 (1990); D. Vakhshoori, R. J. Fischer, M. Hong, D. L. Sivco, G. J. Zydzik, G. N. S. Chu, and A. Y. Cho, Appl. Phys. Lett. 59, 896 (1991).

[2] R. Lodenkamper, M. L. Bortz, M. M. Fejer, K. Bacher, and J. S. Harris, Jr., Opt. lett. 18, 1798 (1993).

[3] J. Khurgin, Phys. Rev. B38, 4056 (1988).

[4] R. DeSalvo, D. J. Hagan, M. Sheik-Bahae, G. Stegeman, and E. W. VanStryland, Opt. Lett. 17, 28 (1992).
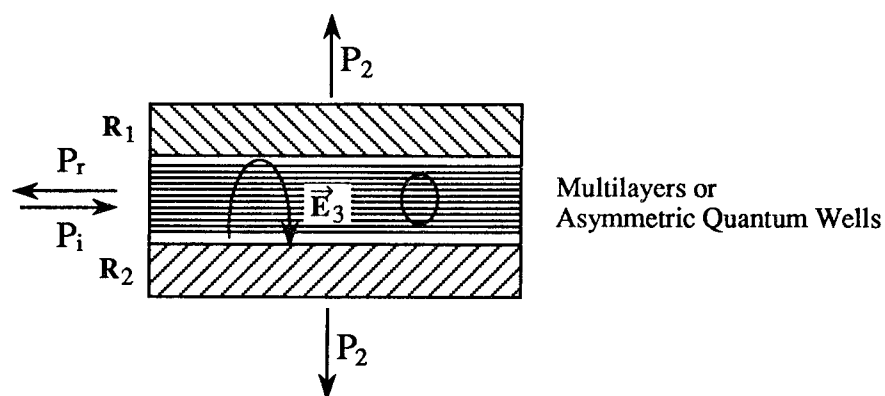
Fig. 1. Configuration of a novel type of devices for frequency doubling and optical power limiting.
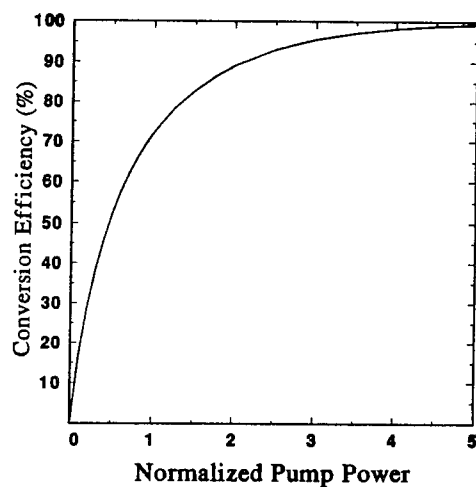
Fig. 2. Second-harmonic conversion efficiency vs. normalized input power (P_i/P_s).
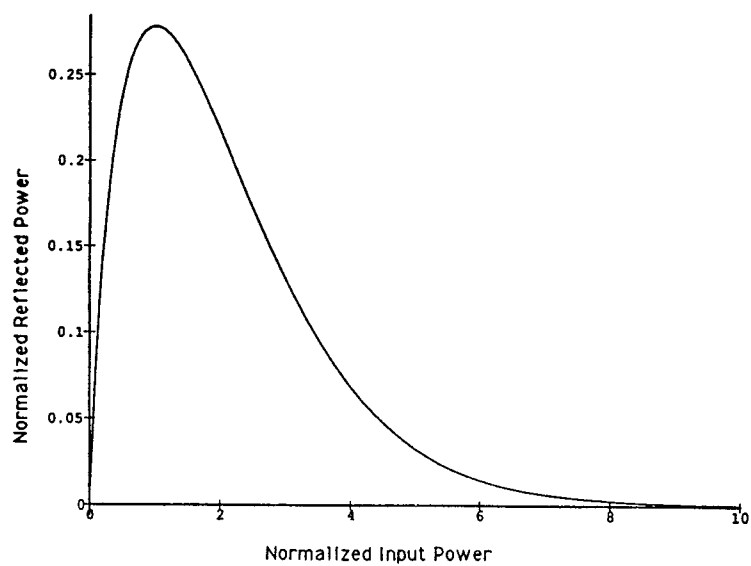
Fig. 3. Normalized reflected power (P_r/P_{th}) vs. normalized input power (P_i/P_{th}) for optical power limiting.

High-Efficiency Frequency Conversion
by
Phased Cascading of Nonlinear Optical Elements

Stephen H. Chakmakjian, Mark T. Gruneisen, Karl Koch, and Gerald T. Moore

Phillips Laboratory PL/LIDN
3550 Aberdeen Avenue S.E.
Kirtland Air Force Base, NM 87117-5776, USA
(505) 846-4750

We present a technique whereby the frequency-doubled output power of a laser system is increased by a factor of two without increasing the size of the pump laser. The technique uses multiple doubling crystals in a tandem arrangement with inter-crystal phase plates to maintain proper phasing of the fields. The result leads to a savings of cost, power, and weight in operational systems. The process is demonstrated with a commercial 19 Watt cw mode-locked Nd:YAG laser and two temperature-tuned lithium triborate (LBO) crystals.

In conventional single-crystal geometries, the conversion efficiency for frequency doubling can be enhanced either by increasing the input intensity or increasing the interaction length. For fixed input power, increasing the intensity by focusing improves the conversion efficiency until the damage threshold of the material is reached or until the diffractive spreading of the tightly focused beams begins to limit the interaction length. Thus, increasing the interaction length of the nonlinear material is an effective method of increasing the conversion efficiency only when tight focusing is not required. For high-peak-power lasers, such as Q-switched or Q-switched mode-locked lasers, a weakly focused beam has sufficient nonlinear drive to produce conversion efficiencies greater than 60%. In the case of low-peak-power lasers, such as continuous-wave or continuous-wave mode-locked lasers, conversion efficiencies are typically limited to less than 30%.
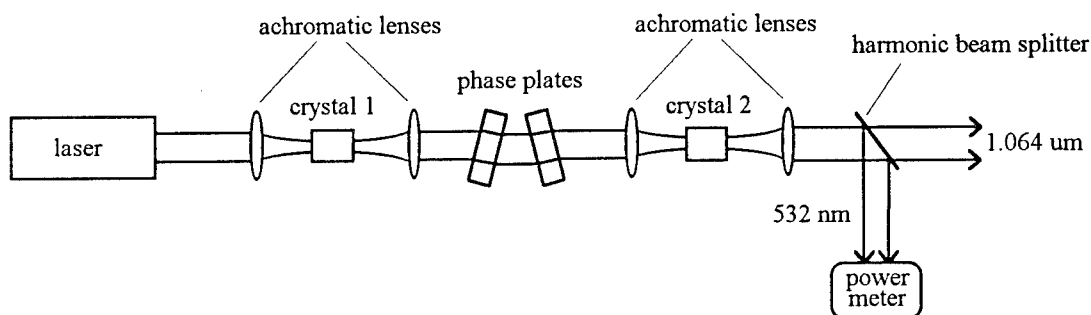
Fig. 1. Experimental setup.

In principle, the conversion efficiency for low-peak-power lasers can be increased by using a second nonlinear element to continue the conversion process. This is done by refocusing the output from the first crystal into a second crystal. A disadvantage of this

approach is that the relative phase difference between the fundamental and second-harmonic waves can change on propagating through the various optical elements, including the air and antireflection coatings. In the worst case, the second-harmonic light generated in the second crystal interferes destructively with that generated in the first crystal leading to complete back-conversion. In our system we implement a second doubling crystal and a phase compensator to cancel these unwanted phase shifts.

A schematic of the system is shown in Figure 1. The pump laser is a 19 Watt average power cw mode-locked Nd:YAG laser that produces 100 picosecond pulses. The peak power of this laser is only 2.5 kilowatts, necessitating tight focusing for efficient frequency doubling. Commercial lasers of this type typically achieve only 25% to 30% doubling efficiency with a single 10 to 20 mm doubling crystal.

The pump wave enters the first element, which consists of a focusing lens, a 15 mm LBO type-I doubling crystal, and a recollimating lens. The pump and second-harmonic waves have the optimum phase difference between them at the exit of the crystal. However, after passing through the recollimating optic, optical coatings, and focusing optics in the system, the phase difference may not be the proper value for continued frequency conversion. In our system we adjust the relative phase of the waves for continued frequency conversion. Once the proper phase difference is achieved the conversion process proceeds as if the two or more nonlinear elements were one contiguous element.
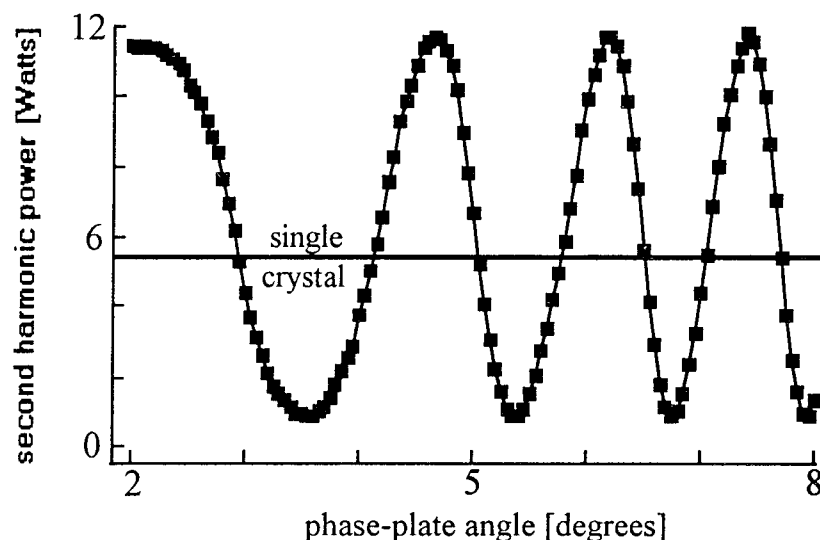
Fig. 2. Measured output power at 532 nm as a function of phase-plate rotation angle for the case of 19 Watts pump power. The maximum second-harmonic power, 12 Watts, corresponds to 63% conversion efficiency.

Phase compensation between the LBO crystals is accomplished using the dispersive properties of two counter-rotating glass plates. The plates provide a relative phase shift between the two optical waves that varies with tilt angle. Counter-rotating plates are used so that no net displacement of the beams occurs as the plates are rotated. Other ways to

accomplish this dispersive phase shift include: a gas pressure cell; a varying path through air; and a variable path through a liquid. Instead of a strictly dispersive device, a birefringent phase compensator may be used to accomplish the relative phase adjustment. Since the first and second-harmonic signals are often orthogonally polarized, an electro-optic phase compensator may be used to achieve the necessary relative phase shift.

In Figure 2 we plot the second-harmonic power as a function of the phase-plate rotation angle. As the glass plates are rotated, a series of interference fringes results in which the output power at the second harmonic varies from about 1 Watt to 12 Watts corresponding to conversion efficiencies from 5% to 63% respectively. The straight line at 5.5 Watts indicates the single-crystal conversion efficiency of roughly 29% typical for laser systems such as this. In an operational system the phase plates would be adjusted to maintain the optimum efficiency of 63%.

We have demonstrated a factor-of-two increase in frequency doubling efficiency using a second nonlinear crystal. In general, this technique may be implemented in any system, however, the most dramatic results are obtained when the single-crystal conversion efficiency is less than 30%. This same technique can be applied to any three-wave mixing, $\chi^{(2)}$ nonlinearity, process where only one relative phase is important. As long as low-peak-power laser applications exist, this technique should prove useful for efficient frequency conversion.

ANTIPHASE DYNAMICS IN INTRACAVITY SECOND HARMONIC GENERATION

Paul Mandel, T. Erneux, D. Pieroux and J.-Y. Wang

Université Libre de Bruxelles, Optique non linéaire théorique,

Campus Plaine, CP 231, B-1050 Bruxelles, Belgium

tel: +32 2 650 5820; fax: +32 2 650 5824; e-mail: PMANDEL@ULB.AC.BE

In the recent years, antiphase dynamics has appeared as a new topic in the study of multimode lasers [1-12]. In particular, Roy, Wiesenfeld and their collaborators have predicted and observed antiphase dynamics in a Nd:YAG laser that also contains a KTP crystal which doubles the frequency of the light emitted by the Nd:YAG crystal [1]. In this set-up, the green light is generated both by frequency doubling and by sum frequency generation from two different longitudinal modes. The control parameter is, in principle, the pump parameter. Another important parameter to control the dynamics is the angle between the fast axes of the two crystals in the cavity. As shown by Roy *et al.* [13], the equations describing these processes can be approximated by the rate equations

$$\tau_c \frac{dI_k}{dt} = (G_k - \alpha_k - g\varepsilon I_k - 2\varepsilon \sum_{j \neq k} \mu_{jk} I_j) I_k \tag{1}$$

$$\tau_f \frac{dG_k}{dt} = \gamma_k - (1 + I_k + \beta \sum_{j \neq k} I_j) G_k \tag{2}$$

where τ_c and τ_f are the cavity round trip time and fluorescence lifetime respectively; I_k and G_k are, respectively, the intensity and gain associated with the kth longitudinal mode; α_k is the cavity loss parameter for the kth mode, γ_k is the small signal gain which is related to the pump rate, β_k is the cross-saturation parameter and g is a geometrical factor whose value depends on the phase delays of the amplifying and doubling crystals and on the angle between the fast axes of these two crystals. The electric field modes can oscillate in one of two orthogonal polarizations. In Eq.(1), $\mu_{jk} = g$ if modes j and k have the same polarization while $\mu_{jk} = 1 - g$ if the modes have orthogonal polarizations; ε is a nonlinear coefficient whose value depends on the properties of the KTP crystal; it describes the conversion efficiency of the fundamental intensity into the doubled intensity.
As shown in [8], antiphase dynamics is already present in the transient relaxation towards equilibrium and in the noise spectrum when noise is added to the steady state.
Of particular interest is the fact that Eqs.(1) and (2) may admit a Hopf

bifurcation at which a steady state becomes unstable. Two different types of solutions are predicted analytically and numerically, depending on the magnitude of the parameter ε.

1/If ε is small (e.g., of the order of 0.00005 as in the original experiments of Roy [1]), the solutions near the Hopf bifurcation are smoothly modulated periodic solutions which display antiphase dynamics. The simplest case of antiphase is one in which N modes are in the same periodic state with period P, each intensity being phase-shifted by P/N from another mode intensity. However, we have discovered a more complex example of response, displayed in Fig.1, where modes 1 and 2 are in antiphase while mode 3 is in phase with the sum of the mode 1 and 2 intensities. Note that mode 3 is not exactly in phase with the sum intensity; the analytical study gives an explicit expression for the very small residual dephasing.

2/If ε is somewhat larger (of the order of 0.05) it is found that the dominant mode of oscillation involves passive Q-switching, i.e., periodic pulses. In this case, antiphase dynamics implies a weak overlap between the pulses of the different modes and may result in an asymmetric influence of a mode on the others [12]. By this, we mean that if there are N modes in one polarization and P modes in the orthogonal polarization, the N modes can be chaotic while the P modes are periodic. An example of this situation is shown in Fig.2. More generally, it appears that perturbations of the N modes affect the P modes but that the P modes can be immune to perturbations from the N modes.

The small ε solution emerges from the Hopf bifurcation. The modulation depth increases from zero at the bifurcation as the pump parameter increases. On the contrary, the larger ε solution emerges from a heteroclinic orbit (infinite period solution). As the control parameter is increased, the pulse period decreases from infinity. These two mechanisms represent two standard ways in which a periodic solution may appear. For both cases, an analytic theory is developed that accounts quite well for the essential aspects of the numerical simulations and the experimental results.

References

[1] K.Wiesenfeld, C.Bracikowski, G.James and R.Roy, Phys. Rev. Lett **65**, 1749 (1990).

[2] C.Bracikowski and R.Roy, Chaos 1 (1991) 49; Phys. Rev. A **43** (1991) 6455.

[3] K.Otsuka, Phys. Rev. Lett. **67** (1991) 1090.

[4] K.Otsuka, Jpn. J. Appl. Phys. **31** (1992) L1546.

[5] K.Otsuka, M.Georgiou and P.Mandel, Jpn. J. Appl. Phys. **31** (1992) L1250.

[6] K.Otsuka, P.Mandel, S.Bielawski, D.Derozier and P.Glorieux Phys. Rev. A **46** (1992) 1692.

[7] S.Bielawski, D. Derozier and P. Glorieux, Phys. Rev. A **46** (1992) 2811.

[8] Wang Jingyi and P.Mandel, Phys. Rev. A **48** (1993) 671.

[9] P.Mandel, M.Georgiou, K.Otsuka and D.Pieroux, Opt. Commun. **100** (1993) 341.

[10] K.Otsuka, P.Mandel, M.Georgiou and C.Etrich, Jpn. J. Appl. Phys. **32** (1993) L318.

[11] D.Pieroux and P.Mandel, *Transient dynamics of a multimode laser: oscillation frequencies and decay rates* Opt. Commun. (in press, 1994).

[12] P.Mandel and Wang Jingyi, *Dynamical independence of pulsed antiphased modes*, Opt. Lett. (1994, in press).

[13] R.Roy, C.Bracikowski and G.James, *Recent Developments in Quantum Optics*, 309, R. Inguva ed. (Plenum press, 1993).

Figure 2. Chaotic antiphased solutions of Eqs.(1) for the case where modes 1 and 2 have the same polarization while mode 3 is in the orthogonal polarization. Parameters are $g = 0.516$, $\beta = 0.292$, $\varepsilon = 5\times10^{-2}$, $\alpha = 0.02$, $\gamma = 0.095$ and $\tau_c/\tau_f = 2\times10^{-3}$.

Figure 1. Periodic antiphased solutions of Eqs.(1) for the case where modes 1 and 2 have the same polarization while mode 3 is in the orthogonal polarization. Parameters are $g = 0.52$, $\beta = 0.6$, $\varepsilon = 5\times10^{-5}$, $\alpha = 0.01$, $\gamma = 0.0124$ and $\tau_c/\tau_f = 2\times10^{-6}$.

Tunable Mid-Infrared Optical Parametric Oscillator

R. B. Jones, B. Brickeen, G.G. Griffith
Northrop Corp.
607 Hicks Rd.
MS L5300
Rolling Meadows, IL 60008
(708) 259-9600

Optical parametric oscillators (OPO) have considerable promise in many applications requiring tunable sources. First demonstrated by Giordmaine and Miller [1] in 1965, progress has been limited by the availability of suitable non-linear materials. In recent years, interest has increased in these devices, as evidenced by the near-simultaneous introduction of commercial devices by several vendors.

Generation of tunable radiation in the mid-infrared spectral range remains difficult, however. There are many scientific and military applications in the 4-5 µm region of the spectrum which require a tunable source in this region. Currently, the 1.06 µm pumped lithium niobate OPO can just reach 4.0 µm, but with energy thresholds of tens or hundreds of millijoules. Current efforts have primarily concentrated on $AgGaSe_2$ or $ZnGeP_2$ OPOs pumped by thullium or holmium lasers at around two microns. High repetition rate operation has been limited in these devices by absorptions in the material. $AgGaSe_2$ in particular has a strong absorption at two microns, which varies somewhat from sample to sample.

Northrop has pursued a two stage approach in order to develop a compact, high repetition rate (~4 kHz) solid state laser/ OPO combination. The approach consists of a non-critically phase matched KTP OPO, pumped by a Nd:YAG or Nd:YLF laser, which oscillates around 1.5 µm, followed by a $AgGaSe_2$ OPO. This approach avoids the $AgGaSe_2$ absorption at two microns while also allowing a simple Nd pump laser. Due to space, weight and power limitations, the pump laser is limited to around 2 mJ per pulse at 4 kHz. Therefore, a low overall threshold is very important for efficient conversion. The non-critically phase matched KTP OPO is well known [2]. This device, due to the lack of extraordinary beam walkoff, allows long interaction lengths with small pump beam spot sizes, and therefore low threshold operation. Komine et. al. have used a Nd:YLF pump (1.05 µm), which generates 1.54 µm from the KTP OPO, with a non-critically phase matched $AgGaSe_2$ OPO [3]. This approach succeeded in generating over 300 mW average power at 3.7 µm. The wavelength of this device contradicts the predictions from the Sellmeier's equations of Bahr [4] or Mikkelsen [5].

The work described here uses a somewhat different approach. A Nd:YAG pump is used, which generates 1.57 µm from the KTP OPO. With two millijoules pump (15 nsec pulse), about 500 µJ of 1.57 µm is generated. The overall threshold of this first stage is about 450 µJ. The 1.57 µm beam is then used to pump a critically phase matched, type I $AgGaSe_2$ OPO, cut at 74 degrees. Due to the high gain and small double refraction angle

of AgGaSe$_2$, the threshold energy of this device is around 200 µJ, even though it is critically phase matched. The overall threshold from 1.06 µm is less than 1 mJ, and the MIR energy is in excess of 50 µJ with 2 mJ overall pump energy. This device is angle tunable from 3.9-4.3 µm. The tuning curve is not in good agreement with any of the published Sellmeier's equations, but appears to be in rough agreement with unpublished data from Cleveland Crystals Inc. (Cleveland OH). Rough measurement suggests that the beam quality is approximately two times diffraction limited.

In this paper, tuning curves, conversion efficiencies, spectra and extension to high repetition rate, high average power operation will be presented.

[1] J. A. Giordmaine and R. C. Miller, Phys. Rev. Lett **14**, 973 (1965).
[2] L. R. Marshall, A. D. Hay, J. J. Kaminskii, and R. Burnham, in Tech. Dig., Adv. Solid State Lasers.
[3] H. Komine, private communication.
[4] G. C. Bahr, Appl. Optics **15**, 313 (1976).
[5] H. Kildal and J. C. Mikkelsen, Opt. Commun. **9**, 315 (1973).

Frequency Conversion by Four-wave Mixing
in Single-mode Fibers

Weishu Wu and Pochi Yeh*

Department of Electrical and Computer Engineering

University of California, Santa Barbara, CA 93106

Sien Chi

Institute of Electro-Optical Engineering

National Chiao Tung University, Hsinchu, Taiwan

Four-wave mixing in optical fibers [1-4] is an important nonlinear process which has a profound effect on optical communications. The mixing may cause some cross-talk problems in a wavelength-division-multiplexing system. On the other hand, the mixing process is useful for frequency conversion. [3] In this paper, we calculate the frequency conversion efficiency and discuss some related issues.

It is known that two waves with frequencies ω_1 and ω_2 in a single-mode fiber will generate a new wave with frequency $\omega_3 = 2\omega_1 - \omega_2$ via partially degenerate four-wave mixing (PDFWM). Four-wave mixing in the regime of no pump depletion has been investigated by previous workers. For the purpose of frequency conversion, it is desirable to maximize the power of the newly generated wave. Therefore, pump depletion has to be taken into account. To achieve this, we solve the coupled mode equations for four-wave mixing in single-mode fibers.

$$\frac{dA_1}{dz} = -i2\gamma A_1^* A_2 A_3 \exp(i\Delta k_{123}z) - \frac{\alpha}{2}A_1$$

$$\frac{dA_2}{dz} = -i\gamma A_1 A_1 A_3^* \exp(-i\Delta k_{123}z) - \frac{\alpha}{2}A_2 \qquad (1)$$

$$\frac{dA_3}{dz} = -i\gamma A_1 A_1 A_2^* \exp(-i\Delta k_{123}z) - \frac{\alpha}{2}A_3$$

where α is the absorption coefficient of the fiber, γ is the nonlinearity coefficient [1] of the four-wave mixing process in the fiber, $\Delta k_{123} = 2k_1 - k_2 - k_3$ is the propagation constant difference describing the phase mismatch of the PDFWM process, A_1, A_2 and A_3 are the amplitudes of three waves, respectively. Under the perfect phase-matching conditions

$\Delta k = 0$, the above coupled equations can be solved exactly. The power of the newly-generated wave is given by

$$P_3(z) = \frac{1}{r} P_2(0) \exp(-\alpha z) \left[\frac{r \sinh^2 \sqrt{r+1} f}{r \cosh^2 \sqrt{r+1} f + 1} \right] \qquad (2)$$

where $r \equiv 2P_2(0)/P_1(0)$, $f = \gamma P_1(0)[1 - \exp(-\alpha z)]/\alpha$, $P_1(0)$ and $P_2(0)$ are the powers at z=0 for ω_1 and ω_2 respectively, . The power coupling as a function of fiber length is plotted in Fig. 1. It can be clearly seen that it is important to choose the fiber length to ensure the maximum conversion. For the typical parameters of the fused-silica fibers, the optimum length is around $1/\alpha$.

(a)   (b)
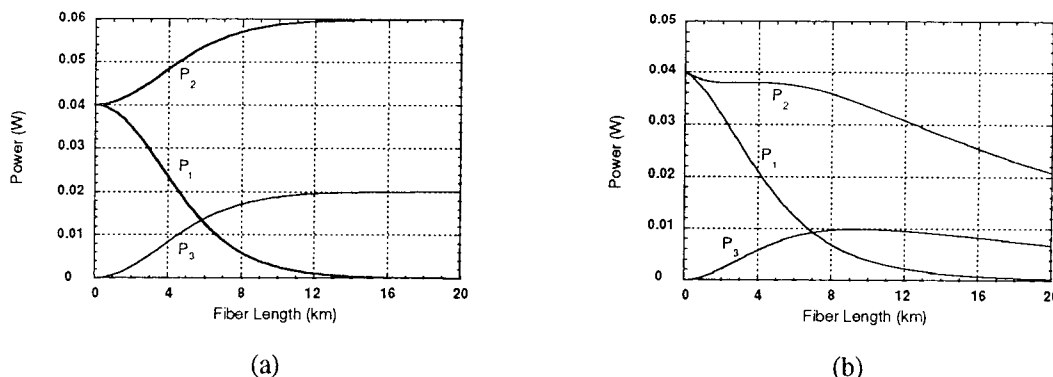
Fig. 1 Power coupling for phase matched PDFWM as a function of the length of a single-mode fiber, (a) in the absence of absorption, and (b) in the presence of absorption.

The phase matching condition is essential to obtain efficient conversion. For partially degenerate four-wave mixing, this can be achieved by choosing the pump frequency ω_1 as the zero-dispersion frequency of the fiber. [4] In addition, the frequency spacing of the two original waves is also an important factor in determining the conversion efficiency to frequency ω_3. When the spacing is small enough, another frequency, $\omega_4 = 2\omega_2 - \omega_1$, can also be generated because the phase mismatch is not large enough to prevent it from building up. Furthermore, it is also possible that ω_3 and / or ω_4 can also act as new pump waves such that new frequency components are further generated. In that case, Eq. (1) should include more terms describing these 'secondary' four-wave mixing processes. By solving them numerically, it turns out that several frequency components can be generated. It also shows that even in the absence of fiber absorption, the power in the desired frequency ω_3 will be reduced or even depleted

by the generation of the new components. In the presence of fiber absorption, ω_4 can still be significantly generated, as illustrated in Fig. 2. This problem can be resolved by increasing the frequency spacing so that the phase mismatch is large enough to prevent these unwanted components from building up. As illustrated in Fig.3, when $\Delta k_{213} = 2k_2 - k_1 - k_3 = 10^{-3}$, which is equivalent to a frequency spacing of between several hundreds of GHz to one THz, the generation of the multiple four-wave mixing processes can be reasonably neglected.
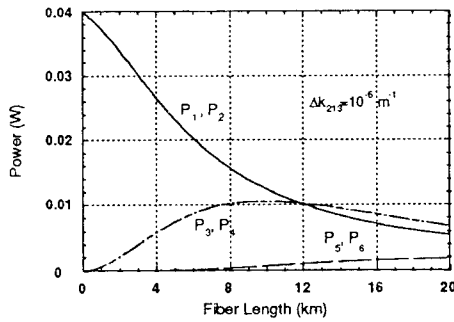
Fig. 2 PDFWM with $\Delta k_{213} = 10^{-6}$ m^{-1} for ω_4 Fig. 3 PDFWM with $\Delta k_{213} = 10^{-3}$ m^{-1} for ω_4
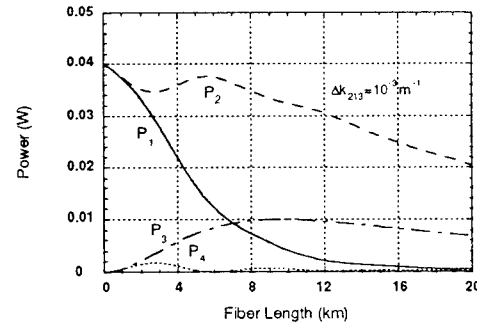
In conclusion, we have investigated the efficiency of frequency conversion via partially degenerate four-wave mixing. We have derived an analytical solution to the partially degenerate four-wave mixing in single-mode fibers when multiple four-wave mixing processes can be neglected. We have shown that efficient conversion can be achieved by carefully choosing the fiber length and the frequency spacing of the two input waves.

1. G. P. Agrawal, *Nonlinear Fiber Optics*, (Academic Press, Inc. London), 1989.
2. K. O. Hill, D. C. Johnson, B. S. Kawasaki, and R. I. MacDonald, J. Appl. Phys. 49, 5098 (1978).
3. K. Inoue and H. Toba, IEEE Photonics Tech. Lett. 40, 69 (1992).
4. K. Inoue, J. Lightwave Tech. 10, 1553 (1992).

Raman-Assisted UV Generation in KTP Frequency Doublers

Chandler J. Kennedy
ProtoPhotonix, Inc.
16 Summerhill La.
Town & Country, MO 63011

Summary

Damage and gray-tracking has been a persistent problem when KTP is used to generate high average power second harmonic from the 1064 nm line of Nd:YAG lasers. The proximate cause of this darkening has been attributed to the change of ionization state of Ti^{+4} to Ti^{+3} which may be induced by sufficiently high energy photons. The source of these photons has been a mystery, since sum frequency generation between 1064 nm and 532 nm to produce UV is not phase matched.

Visual observation of SHG in KTP with small beams at modest power levels reveals a rather striking bright streak of green scattering in the crystal. The usual amber safety goggles which block virtually all the 532 nm light have no effect on the appearance of the green scattering, which must therefore be stokes shifted. A visual spectroscope shows a line at about 553 nm, or a Raman shift of about 700 cm^{-1}. The Raman spectrum of KTP has such a component at 692 cm^{-1}, as well as other lines of lower energy[1], shown in Fig. 1.
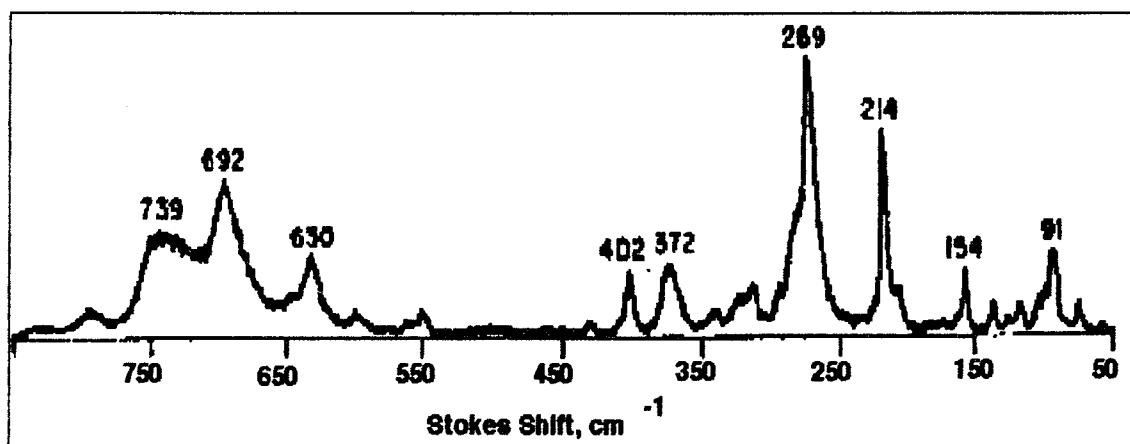
Figure 1. Raman Spectrum of KTP.

An attempt to lase this Raman line in a KTP doubler aroused our suspicions that the Raman process might be implicated in KTP damage. Although occasional flashes of directed stokes light were observed, they were invariably self-terminating and associated with bulk crystal catastrophic damage. We therefore explored the possibility that Raman-shifted light generated in the doubling process was phase matched to produce damaging UV.

We use the published Sellmeyer equations for KTP as follows:

$$n_x^2 = 2.1146 + \frac{0.89188}{1 - \left(\frac{0.20861}{\lambda}\right)^2} - 0.0132\lambda^2$$

$$n_y^2 = 2.1518 + \frac{0.87862}{1 - \left(\frac{0.21801}{\lambda}\right)^2} - 0.01327\lambda^2$$

$$n_z^2 = 2.3136 + \frac{1.0001}{1 - \left(\frac{0.23831}{\lambda}\right)^2} - 0.01679\lambda^2$$

The equation for the index ellipsoid is solved for the directions θ and ϕ.

$$0 = \frac{\sin^2(\theta)\cos^2(\phi)}{x - n_1^{-2}} + \frac{\sin^2(\theta)\sin^2(\phi)}{x - n_2^{-2}} + \frac{\cos^2(\theta)}{x - n_3^{-2}}$$

There are two roots of the equation which we label x and y for the fast and slow polarizations, respectively. Phase matching is indicated by the roots of the following equations which represent Type II, Type I, and complementary (interchanging the polarizations of the two wavelengths) Type II, respectively.

$$R = \left(\frac{1}{\lambda_b x(\lambda_b)} + \frac{1}{\lambda_a y(\lambda_a)}\right)\lambda_c y(\lambda_c) - 1$$

$$P = \left(\frac{1}{\lambda_b x(\lambda_b)} + \frac{1}{\lambda_a x(\lambda_a)}\right)\lambda_c y(\lambda_c) - 1$$

$$Q = \left(\frac{1}{\lambda_b y(\lambda_b)} + \frac{1}{\lambda_a x(\lambda_a)}\right)\lambda_c y(\lambda_c) - 1$$

We select the angles θ and ϕ to be 90° and 26°, respectively. Fig. 2 shows that this is indeed the critical phase match direction for Type II, but also is a Type I phase match for 1064 and 590 nm. Since there is no source for 590 nm radiation, no UV is expected from this interaction.
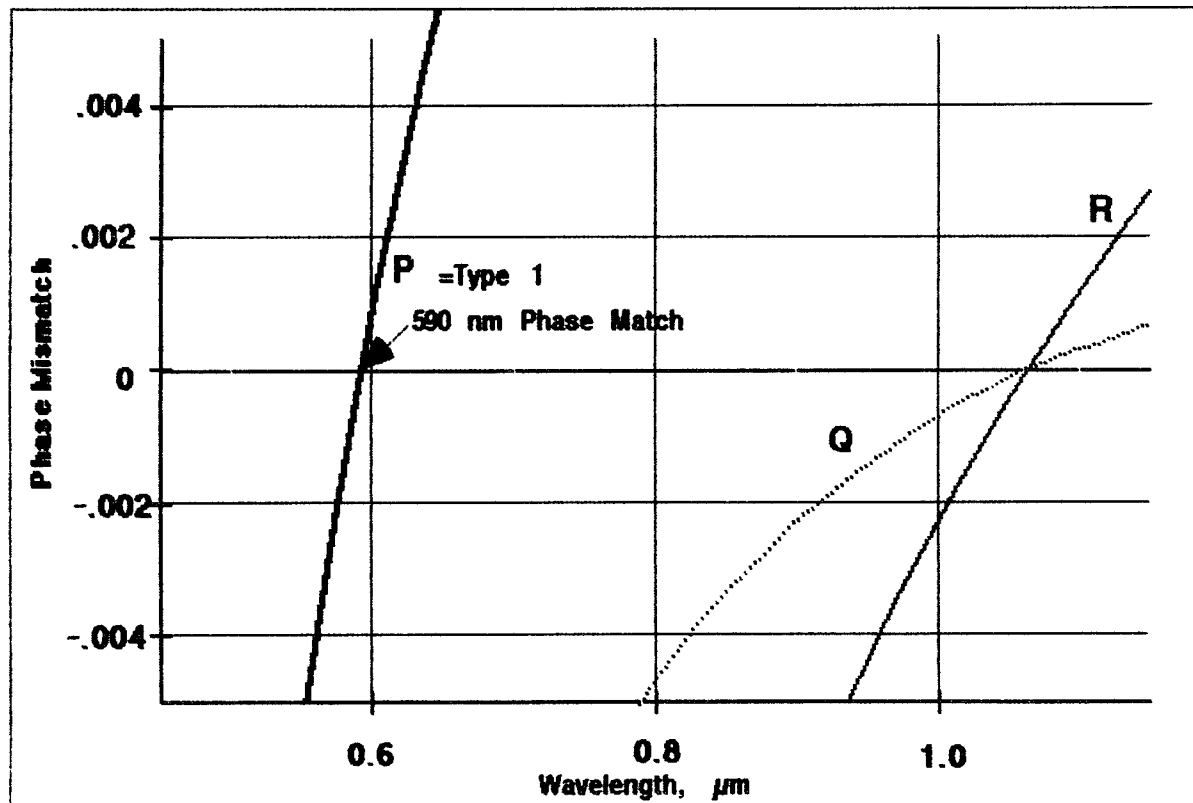
Figure 2. Phase matching graph for 1064 nm source. P is Type I, Q and R are Type II.

However, Raman shifted 1064 nm radiation may exist in some quantity at 1149 nm in KTP. Using this as the source, we see in Fig. 3 that there is a Type I phase match at about 550 nm. Closer inspection shows this to be about 551 nm. This is remarkably close to the Raman shifted 532 nm harmonic at 552 nm. Sum frequency generation would produce UV radiation at about 372 nm. Since this is a Type I interaction, it is necessary for the a and b wavelengths to have the same polarization (x). This polarization is orthogonal to the polarization of the second harmonic (y). However, Raman scattered y-polarized light has components in both x and y in KTP, so that some 552 nm radiation exists in the proper polarization for Type I SFM. 1149 nm light exists in both polarizations because 1064 nm light is in both polarizations as well.
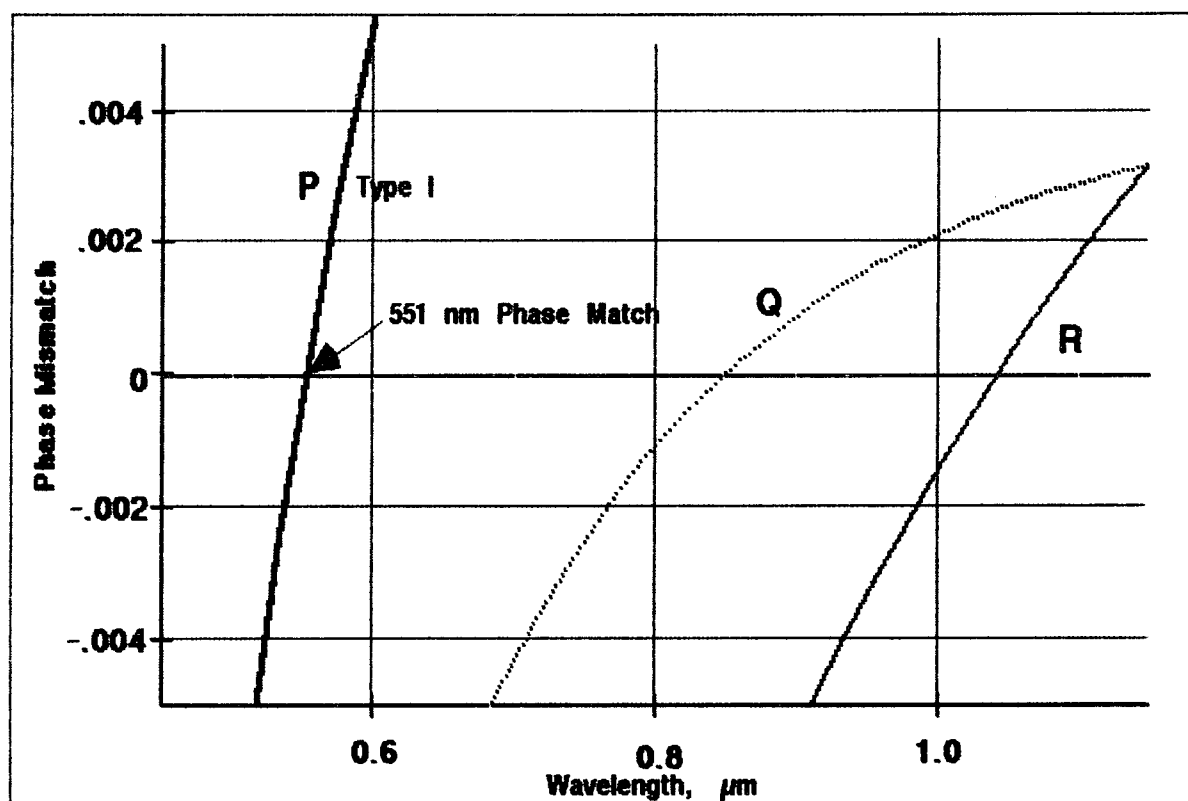
Figure 3. Phase matching chart for 1149 nm source, or Raman shifted 1064 nm.

It would seem, then, that one would expect inadvertent UV generation in KTP doublers from an examination of first principles. The smoking gun, however, is the observation of the UV light at the expected wavelength of 372 nm. The absorption of KTP at this wavelength is not very great, and one should be able to detect and measure its properties, including polarization, with relative ease. Damage, or gray-tracking from exposure to 372 nm radiation can then be established by irradiating the crystal in any direction with an external source.

Reference
[1] G. A. Massey, T. M. Loehr, L. J. Willis, and J. C. Johnson, "Raman and electrooptic properties of potassium titanate phosphate," Applied Optics 19, 4136-4137 (1980).

CROSS-MODULATION DISTORTION
IN SUBCARRIER MULTIPLEXED OPTICAL SYSTEMS

F.V.C. Mendis, M.K. Haldar and J. Wang

Department of Electrical Engineering
National University of Singapore
10 Kent Ridge Crescent, Singapore 0511 (Phone: +65 772-2297)

Introduction

The third-order inter-modulation distortion arising from the non-linear rate equations of a directly driven laser diode of a subcarrier multiplexed (SCM) fiber-optic system has been considered by many researchers [1]-[7]. The inter-modulation products that have been considered are the 3-frequency distortion terms of the form $f_p + f_r - f_q$ and the 2-frequency distortion terms of the form $2f_p - f_r$. Cross-modulation products, i.e. distortion terms of the form $f_p + f_r - f_p$, have not received much consideration. Cross-modulation distortion occurs when the modulation of one carrier is (unintentionally) transferred to another carrier resulting in intelligible crosstalk, as contrasted with the unintelligible crosstalk that results from inter-modulation distortion. We show in this paper that cross-modulation distortion cannot be entirely ignored.

Theory

In a multichannel system comprising N carriers, the inter-modulation distortion (IMD) relative to a carrier of normalized frequency, $f + R\Delta f$, is given for a directly driven laser [4],[7] by:

$$\frac{IMD}{C} = 10\log_{10}\frac{I^4}{16|A|^2}\left[\sum_{\substack{L=Int\left(\frac{R+1}{2}\right)\\L\neq R}}^{Int\left(\frac{N-1+R}{2}\right)}\left|A'_{(2L-R)LL}\right|^2\right.$$

$$+\frac{1}{2}\left\{\sum_{L=0}^{R-1}\sum_{\substack{M=R-L\\M\neq L,M\neq R}}^{N-1}\left|A'_{(L+M-R)LM}+A'_{(L+M-R)ML}\right|^2 + \sum_{L=R+1}^{N-1}\sum_{\substack{M=0\\M\neq L,M\neq R}}^{N-1+R-L}\left|A'_{(L+M-R)LM}+A'_{(L+M-R)ML}\right|^2\right\}\right] \quad (1)$$

Equation (1) may be used to find both the 3-frequency and the 2-frequency 3rd-order intermodulation-distortion-to-carrier-power-ratio for *any* number of carriers. The triple-suffixed amplitude term A' is a complex expression dependent on the laser parameters, and is explained in Equation (32) of [4]. The term in the first line of Equation (1) corresponds to the 2-frequency products, and the term in the second line corresponds to the 3-frequency products.

The cross-modulation distortion (CMD) relative to a carrier of normalized frequency $f + R\Delta f$, obtained by using Equation (36) of [4], may be written as:

$$\frac{CMD}{C} = 10\log_{10}\frac{I^4}{16|A|^2} \sum_{\substack{K=0 \\ K \neq R}}^{N-1}\left|A'_{KRK} + A'_{KKR}\right|^2 \qquad (2)$$

It should be noted that Equations (1) and (2) are valid for systems with memory whereas many expressions reported in the literature are strictly valid only for memoryless systems, which a laser diode (with its dynamic non-linearity) is not. The meanings of all the parameters in Equations (1) and (2) are explained in [4].

Analysis and discussion of results

We compute the IMD/C and CMD/C ratios using Equations (1) and (2) for the following laser parameters. Optical wavelength = 0.835 μm; threshold current, I_{th} = 21 mA; bias current, I_b = 31.5 mA; volume of active region × electron charge, eV_{act} = 1.44×10^{-35} m³C; photon lifetime, τ_p = 2 ps; spontaneous recombination lifetime of carriers, τ_n = 2 ps; carrier density for transparency, N_{om} = 4.6×10^{24} m⁻³; optical gain coefficient, g_o = 10^{-12} s⁻¹m³; confinement factor, Γ = 0.646; fraction of spontaneous emission entering lasing mode, β = 10^{-3}; gain compression factor, ε = 3.8×10^{-23} m³; relaxation frequency at above bias current, f_R = 3.44 GHz.

The results are given in Fig. 1, where the variation of IMD/C and CMD/C (in dB) with the frequency of the first carrier is shown, for a 20 channel system ($N=20$), with a carrier spacing Δf of 40 MHz and an optical modulation depth (OMD) of 5 % per channel. It is noted that the values of these two quantities, whilst being a function of frequency and having the same general shape, are not equal for the two end channels ($R=0$ and 19), this dis-symmetry being due to the fact that the laser is not a memoryless system [7]. The difference in value between IMD/C and CMD/C shows less variation with frequency than either IMD/C or CMD/C : for the centre channel ($R=10$), it is about 8.1 dB; for end channel 1 ($R=0$) it varies between 4.5 dB (which is quite low and occurs at f ~ 1.3 GHz) and 7.3 dB; and for end channel 20 ($R=19$), it varies between 5.8 dB and 7.3 dB. [For a memoryless system, this difference in value can be calculated (based solely on the *number* of IMD and CMD products) to be 6.4 dB and 8.3 dB respectively, for the end and centre channels of a 20 channel system, and is independent of frequency.]

The peaking of the curves near the relaxation frequency (3.44 GHz) of the laser is expected. It is also noted that although the centre channel ($R=10$) has the largest number of distortion products, it does not necessarily have the worst IMD/C and CMD/C values (e.g. for $f < 3.5$ GHz). This is an interesting result. For a system with a larger number of channels (e.g. $N=40$), the difference between IMD/C and CMD/C will increase, while for a smaller number of channels (e.g. $N=10$), this difference will decrease, as is the case for a memoryless system. In fact for $N=10$ and Δf=40 MHz, the difference between IMD/C and CMD/C is only about 2.2 dB at f ~ 1.5 GHz. Also, in general, as the carrier spacing (Δf) increases, the variation with frequency of this difference becomes larger, particularly for the end channels. These numerical results (graphs) are not shown here due to space limitations. It is seen, therefore, that the cross-modulation distortion, hitherto ignored in the literature, can be quite significant, especially for an SCM system with a small number of channels.
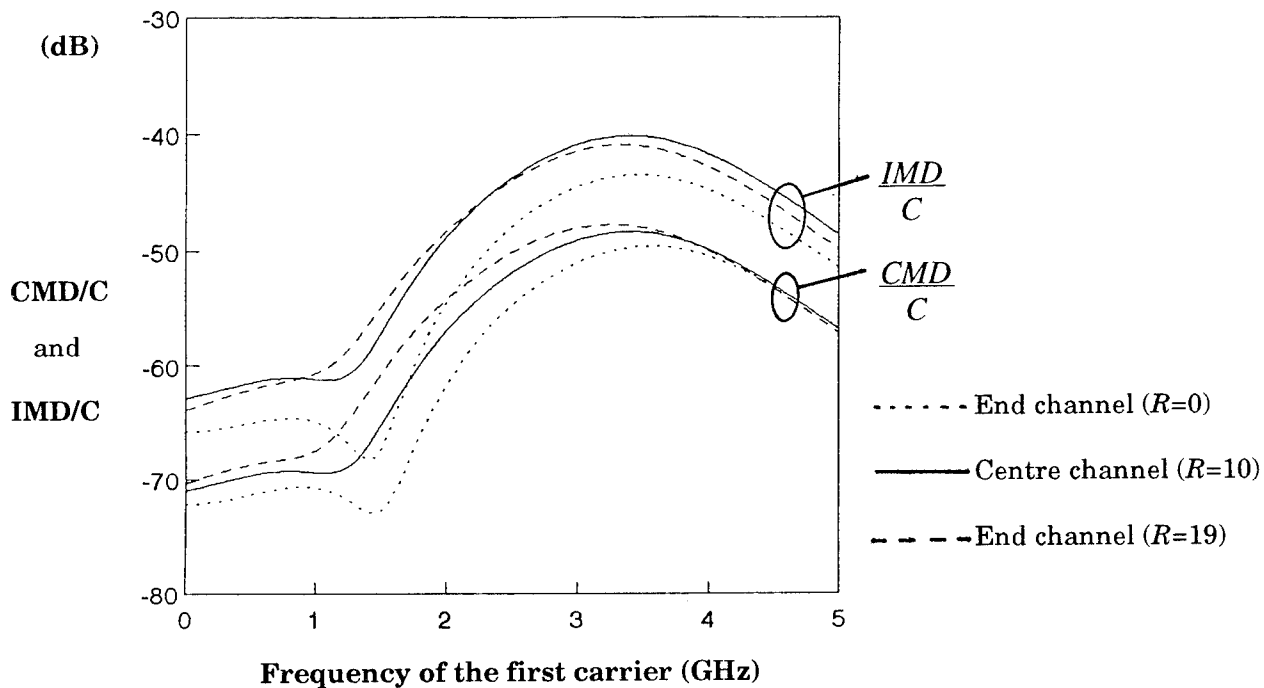
Fig.1 Variation of CMD-to-carrier and IMD-to-carrier ratios for a 20 channel system with a 40 MHz carrier spacing and an OMD of 5 %

Conclusion

Cross-modulation distortion (CMD) arising from the inherent non-linearity of a semiconductor laser diode has been shown to be important in a multi-carrier optical system. The assumption that CMD may be ignored compared to inter-modulation distortion (IMD), which has been the past practice, is not always valid. It has also been shown that CMD (and IMD) are not the same for the two end channels, the dis-symmetry being due to the fact that the laser diode is not memoryless. Likewise, although the centre channel has the largest number of distortion products, it is not always seen to have the worst CMD (and IMD), especially for frequencies less than the relaxation frequency of the laser diode.

References

[1] B. Arnold, "Third order intermodulation products in a CATV system", IEEE Trans. Cable TV, Vol. CATV-2, 1977, pp 67-80.

[2] K.Y. Lau and A. Yariv, "Intermodulation distortion in a directly modulated semiconductor injection laser", Appl. Phys. Lett., Vol. 45, 1984, pp 1034-1036.

[3] P. Iannone and T.E. Darcie, "Multichannel intermodulation distortion in high speed GaInAsP lasers", Electron. Lett., Vol. 23, 1987, pp 1361-1362.

[4] M.K. Haldar, P.S. Kooi, F.V.C. Mendis and Y.L. Guan, "Generalized perturbation analysis of distortion in semiconductor lasers", J. Appl. Phys., Vol. 71, 1992, pp 1102-1108.

[5] J. Helms, "Intermodulation distortions of broadband modulated laser diodes", J. Lightwave Technol., Vol. 10, 1992, pp 1901-1906.

[6] J. Wang, M.K. Haldar and F.V.C. Mendis, "Formula for 2-carrier 3rd-order intermodulation distortion in semiconductor laser diodes", Electron. Lett., Vol. 29, 1993, pp 1341-1343.

[7] F.V.C. Mendis, M.K. Haldar, P.S. Kooi and J. Wang, "Intermodulation distortion in semiconductor lasers in application to subcarrier multiplexed fiber optic video systems", to appear in *Optical Engineering*.

Wavelength domains in bulk Kerr Media

A. P. Sheppard   and   M. Haelterman

Optical Sciences Centre

Australian National University

Canberra 0200, Australia

Ph: +61 6 249 2430   Fax: +61 6 249 5184

Optique Nonlinéare Théorique

Université Libre de Bruxelles

Brussels, Belgium

Fax +32 2 650 5824

It is a fundamental part of nonlinear optics that light beams in nonlinear media affect both their own propagation and the propagation of coincident beams of different wavelength or polarisation. One manifestation of the former effect is self phase modulation and the formation of bright[1] and dark[2] solitons. The latter effect (as cross phase modulation) permits another beam of lesser intensity to be directed by these solitons. This guidance of light by light (neatly explained by considering the soliton as inducing a waveguide for the second beam) has now been realised in the laboratory.[3] The mutual trapping arising when both beams have similar intensity has been shown to lead to many varieties of solitary wave,[4-6] and in particular to the so called polarisation domain walls (PDWs), localised structures separating regions of different polarisation.[7] All this work has been done in a single transverse dimension.

In this paper we consider optical phenomena in two transverse dimensions that arise from nonlinear coupling between two or more copropagating beams of different wavelengths in self defocusing, isotropic Kerr media. We find that the different wavelengths form distinct, stable domain type solitary waves bordered by sharp domain walls that are analogous to PDWs. The domain structures are investigated in several ways. First are the stationary solitary wave solutions, obtained with a physically motivated semi analytical approach. These solutions are composed of a monochromatic circular domain surrounded by a monochromatic region of a different wavelength. The stability of these solitary waves is numerically demonstrated, and then the existence of steerable domain solitary waves is postulated and confirmed. Finally simulations investigating the robustness and dynamical behaviour of the steerable domains are presented.

Of interest are bulk, isotropic materials with a local, self-defocusing Kerr type nonlinearity, with refractive index change given by $\Delta n^2 = \alpha I$. The evolution of a linearly polarised field comprising two different wavelengths is governed by the following coupled equations:[5]

$$ik_1 \frac{\partial U}{\partial z} + \frac{1}{2}\nabla^2 U - \frac{k_1^2 \alpha}{n_1}\left[|U|^2 + \sigma|V|^2\right]U = 0 \tag{1a}$$

$$ik_2 \frac{\partial V}{\partial z} + \frac{1}{2}\nabla^2 V - \frac{k_2^2 \alpha}{n_2}\left[|V|^2 + \sigma|U|^2\right]V = 0 \tag{1b}$$

The Laplacian is taken only over the polar transverse co-ordinates r and φ. z is the longitudinal coordinate. $[U(\mathbf{r}, z), V(\mathbf{r}, z)]$ are the envelopes of the two wavelength components with wave vectors $[k_1, k_2]$ and linear refractive indices $[n_1, n_2]$. The parameter σ is related to the speed of response of the materials. In slow materials $\sigma = 1$ as all wavelengths see the same, slow refractive index change. In fast materials $\sigma = 2$. Although numerical methods are necessary to find solitary wave solutions to these nonintegrable equations, some physical insight can be used to assist and illuminate the numerics.

We now present a simple physical argument to lead us to the menagerie of solutions that exist. Consider a monochromatic circularly symmetric dark soliton[8,9] (known as a 'vortex' soliton, with

an $e^{i\varphi}$ azimuthal dependence) to be formed in u. It is possible to use the waveguide induced by this soliton to guide an arbitrarily weak probe beam of another wavelength.[3] In this way a bound state that comprises both wavelength components is formed. One anticipates that when the power in the probe is increased into the nonlinear regime that this bound state will still exist, although the profile of the original soliton may be altered dramatically to accommodate the other component.

We propose the existence of circularly symmetric stationary solutions of the form $U(r, \varphi, z) = u(r)e^{il\varphi} e^{-i\beta_1 z}$; $V(r, \varphi, z) = v(r)e^{im\varphi} e^{-i\beta_2 z}$ where the envelopes u and v are real functions; β_1 and β_2 their respective propagation constants and l and m are the azimuthal numbers. Using this ansatz we reduce the eqs. 1 to a pair of real ode's that can be solved using standard shooting methods. We find the four types of solitary wave that correspond to permutations of $l, m = 0, 1$. These solutions exist only when the wavelengths are close enough together to satisfy $\sigma^{-1} > k_2^2 n_1 / k_1^2 n_2 < \sigma$. Solutions originating from vortex solitons have $l = 1$, while others beginning as monochromatic plane waves have $l = 0$. Each of these types has a continuous range of solutions up to the limit in which the central region (the domain of the second wavelength) becomes infinitely large. In this limit the solutions represent wavelength domain solitary waves, with a ring shaped domain wall separating the two domains, and both wavelengths appearing as plane waves of amplitudes u_0 and v_0, where $u_0/v_0 = n_1/n_2$.

The existence of these domains relies, in effect, on a simple reversal of the 'grass is greener' philosophy. Each field component at a domain wall sees a lower refractive index on the other side and is therefore happy to keep to its own side of the boundary.

Like many interfaces in physics, the dynamics of these structures are driven by an energy cost per unit length that is associated with the domain walls. The systems therefore evolve to minimise the length of the boundaries, explaining the circular symmetry of the stationary states. Fig. 1 demonstrates the stability of the $l = 0, m = 0$ solitary wave, and shows the system acting to minimise the domain wall length.
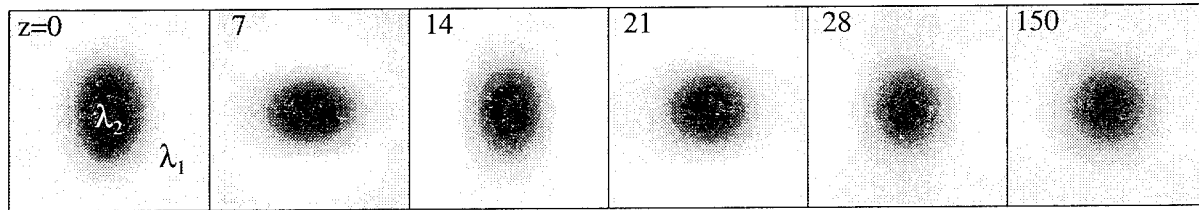
Figure 1: Evolution of an elliptical domain. In light regions the field is predominantly one wavelength component, in dark regions the other. The final box shows the field to have evolved to a circularly symmetric $l = 0, m = 0$ solitary wave.

In order for these new structures be of practical use in switching devices, we need to be able to direct the domains in some way or another. In particular we wish to discover if there are domain solitary waves analogous to grey solitons: solitary waves that propagate unchanged at an angle to the background wave. The wavefronts of the two wavelength components would then be at an angle to one another, preventing the introduction of the simple ansatz used above.

We have conducted preliminary numerical investigations into these objects by launching altered forms of the stationary solutions: the wavefront of the secondary field is oriented at an angle to the primary wavefront. After a transient radiatory period, a stable traveling domain is formed. This result strongly suggests that the stationary wavelength domain solitary waves are part of a larger family of steerable solitary waves, in the same way that the black soliton is only a part of
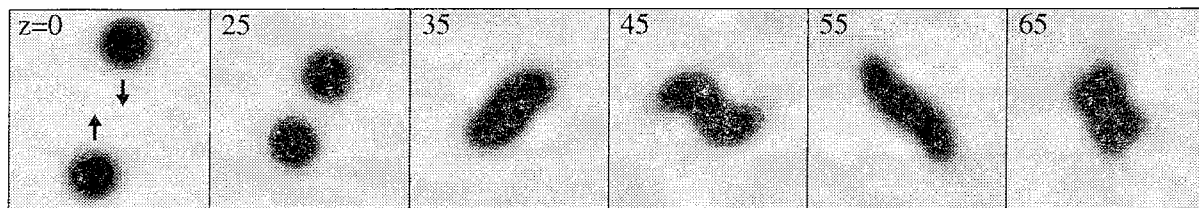
Figure 2: A collision between two travelling domains. The domains attract, spiral about each other, then coalesce and eventually settle to form a single stationary domain (not shown).

the steerable grey soliton family. Fig 2 shows a collision between two small domains that leads to their eventual coalescence, while Fig. 3 shows a small domain annihilating itself against an infinite domain wall. These two results clearly show that simple traveling domains can be destroyed by the forces trying to minimise the domain wall length. Higher order domains, containing topologically trapped 'vortex' nodes may prove to be more robust.

In conclusion we have presented a preliminary study of wavelength domains, both as stationary solitary wave solutions and as dynamically evolving structures.

References

[1] R. Y. Chiao, E. Garmire, and C. H. Townes, *Phys. Rev. Lett.*, **13**, 479 (October 1964).

[2] Y. S. Kivshar, *IEEE J. Quantum Electronics*, **29**, 250 (January 1993).

[3] R. De la Fuente, A. Barthelemy, and C. Froehly, *Optics Letters*, **16**, 793 (June 1991).

[4] D. N. Christodoulides and R. I. Joseph, *Optics Letters*, **13**, 53 (January 1988).

[5] M. V. Tratnik and J. E. Sipe, *Phys. Rev. A*, **38**, 2011 (August 1988).

[6] M. Haelterman, A. P. Sheppard, and A. W. Snyder, *Optics Letters*, **18** (September 1993).

[7] M. Haelterman and A. P. Sheppard, *Optics Letters*, **19**, 96 (January 1994).

[8] A. W. Snyder, L. Poladian, and D. J. Mitchell, *Optics Letters*, **17**, 789 (June 1992).

[9] G. R. Swartzlander and C. T. Law, *Phys. Rev. Lett.*, **69**, 2503 (October 1992).
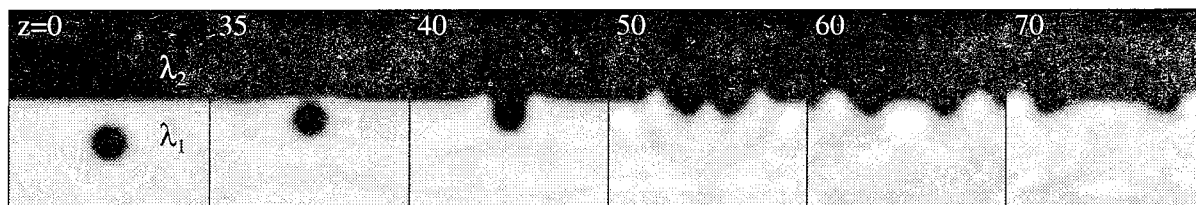
Figure 3: The collision of a circular travelling domain with a quasi-infinite domain wall. The behaviour is strikingly reminiscent of a bubble at the surface of a liquid.

343

Kerr lens effects on transverse mode stability
and active versus passive modelocking in solid state lasers

P. Randall Staver and William T. Lotshaw G.E. Research and Development Center
1 River Road, Room KWC 627 Schenectady, NY 12309
(518) 387-5163

The effects of the nonlinear refractive index as a discriminant between the lowest order (TEM_{00}) transverse mode stability in the passively modelocked and cw operating modes of tunable, solid state laser crystals like Ti:Sapphire and Cr^{3+} or Cr^{4+} doped materials, have recieved much recent attention [1]. This attention has focussed primarily on the intensity dependent focal power in the laser crystal due to the (mostly) nonresonant n_2 and the peak intensity of the oscillating resonator mode. In this report we extend these studies to include resonant and nonresonant n_2 effects due to a synchronous pump laser, and to examine the possibility that the magnitudes, signs, and time dependences of the pump and oscillating wavelength n_2 effects could be manipulated to discriminate between active versus passive modelocking of the tunable laser output, as well as between cw and passive modelocked operation. Active modelocking would reduce or eliminate the need for opto-mechanical optical path stabilization between the pump and tunable laser, and enable wave-mixing experiments/devices such as fs CARS or broadly tunable fs OPO/OPA systems..
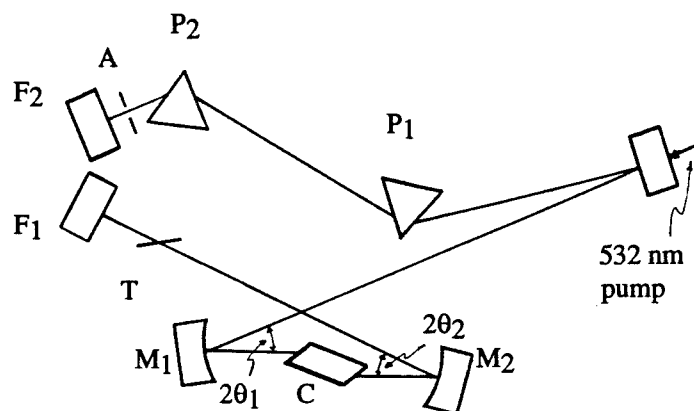
F1: 790-940 nm HR; F2: 7% Output Coupler; M1: 790-940 nm HR, 532 nm HR, 10 cm radius; M2: 790-940 nm HR, 10 cm radius; $P_{1,2}$: Schott F2 glass Brewster prisms $2\theta_{1,2}$: beam included angles at $M_{1,2}$; A: Variable slit; T: $\approx$0.2 mm quartz tuning plate

Figure 1. Ti:Al_2O_3 laser resonator configuration

Our approach to the simulation of the resonator shown in Fig. 1 is to first establish the stability behavior of the passive resonator with respect to resonator symmetry and compensation of passive aberrations through the positions and orientations of the focusing optics, excluding the n_2 of the laser crystal. For all cavity calculations, the *ABCD* matrix method was used [2]. The invariant parameters input to the ray transfer matrix simulation are the radii of curvature for the front surface mirrors $F_{1,2}$ (∞) and $M_{1,2}$ (10 cm.

concave), the length (1 cm.) and refractive index (1.76) of the parallel Brewster faced Ti:Sapphire crystal. The variable parameters are the tilt angles of $M_{1,2}$ and the distances between the curved mirrors M_1 and M_2, and the optics F_1 and M_2, F_2 and M_1, designated L_1 and L_2 respectively. The resonator arm defined by the distance L_2 contains the Brewster prisms $P_{1,2}$ (Schott F2 glass) for compensation of group velocity dispersion in the experimental laser. These elements were omitted from the simulations presented here because the aberrations induced by them is negligible.

The results of the ray transfer matrix simulation of the passive resonator in figure 1 for an asymmetric cavity, where L_1 and L_2 are 56.4 and 128 cm. respectively, revealed a branched stability diagram for the fundamental transverse mode as a function of the M_1-M_2 mirror spacing in both the tangential and sagittal planes (data not shown). Furthermore, the manipulations of adjusting the spacing and tilt angles of the curved mirrors M_1 and M_2, in order to compensate for aberrations due to the Brewster-faced laser rod and front surface mirrors, resulted in the prediction of unique values of these parameters for generating a symmetric mode at the flat mirrors $F_{1,2}$, and provided an alignment diagnostic for setting them which we verified experimentally. We then added the laser crystal n_2 to the simulation in order to examine the *cw* versus modelocked discriminant imposed by the laser rod Kerr lens.

Many techniques have been implemented in order to simulate the behavior of the crystal nonlinearity [3]. Most of them are based on the quadratic duct method, [2], and do not treat specifically the case of elliptical beams except for [1].

Bridges, et. al. [1]; however, show that this ellipticity leads to nonlinear coupling between the tangential and sagittal mode radii and significantly alters their characteristics, which we have confirmed. Our analysis follows after that described in [1] where the nonlinear medium is divided into *n* segments.
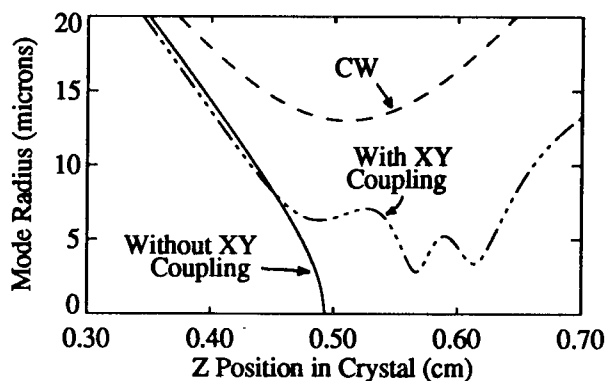
Figure 2. Sagittal mode propagation in Ti:Sapphire crystal for elliptical *cw* mode, elliptical modelocked mode with and without *x-y* coupling.

Figure 2 summarizes the propagation of the laser mode through the $Ti:Al_2O_3$ crystal (*n* =1000) in the sagittal and tangential planes for an average output power of 0.48 W and a pulse duration of 40 fs when the nonlinear refractive index is included. The oscillatory behavior near the focus is a direct result of the nonlinear coupling between the

tangential and sagittal mode radii through the n_2 of the laser crystal. If this coupling is removed, or the mode made symmetric, the beam exhibits catastrophic self-focusing and collapses to the axis, a behavior that is often predicted by non-coupled approximations [4]. The convergence of this simulation of the laser rod focal power due to the n_2 Kerr lens effect is critically dependent upon the values of the mode parameters at the n segment boundaries, and hence the value of n. This dependence is shown in figure 3, where the average output power of the laser is 0.50 W at a 40 fs pulse duration.
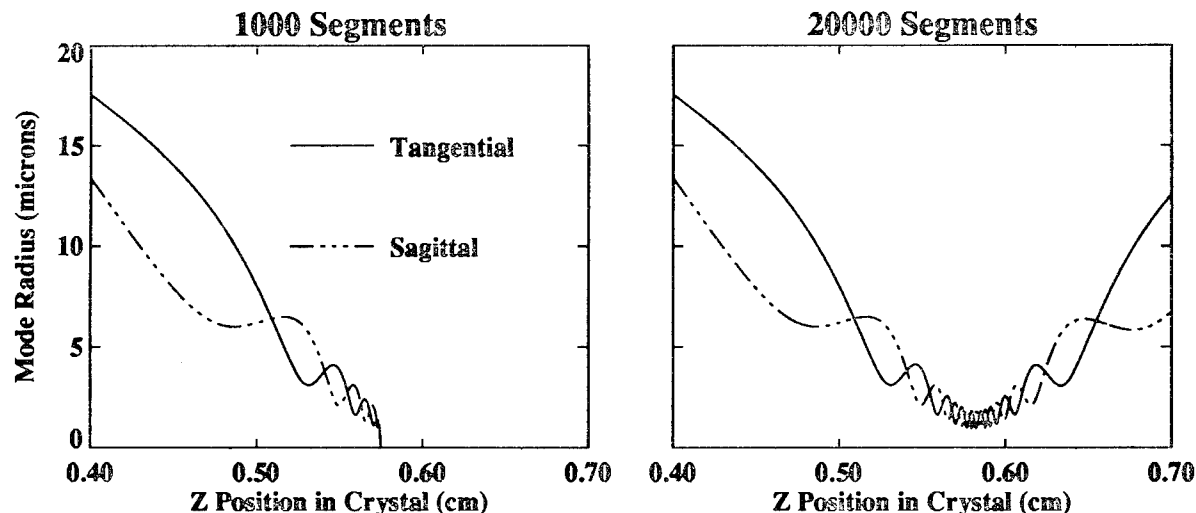
Figure 3. Propagation of the elliptical resonator mode through the Ti:Sapphire laser crystal divided into 1000 segments (left) and 20,000 segments (right).

The convergence of this calculation of the lens properties of the laser crystal is crucial to the accurate ABCD simulation of the mode behavior elsewhere in the resonator, and hence to the resulting discrimination between *cw* and modelocked operation. The results of these simulations, suitably modified to account for thermal and nonresonant n_2 effects due to the pump mode and the effects of quadratic dispersion [5,6], will be presented in support of experimental performance data on the synchronously pumped resonator depicted in figure 1, which generates tunable, $\leq$ 40 fs pulses at average powers of approximately 0.6 W (5 W pump).

1. Bridges, Boyd, Agrawal, "Effect of beam ellipticity on self-mode locking in lasers," Optics Letters, 18, pp. 2026-2028, (1993).
2. A. Siegman, Lasers (University Science, Mill Valley, Ca, 1986), Chapters 15 and 20.
3. V. Magni, G. Cerullo, S. De Silvestri, "ABCD matrix analysis of propagation of gaussian beams through Kerr media," Optics Communications, 96, 348-355, (1993).
4. Boyd, Nonlinear Optics (Academic Press, Inc., New York, NY, 1992), pp. 257-262.
5. A. G. Kostenbauder, "Ray-Pulse Matrices: A Rational Treatment for Dispersive Optical Systems," IEEE Journal Of Quantum Electronics. 26, pp. 1148-1157 (1990).
6. J. Chilla, O. Martinez, "Spatial-temporal analysis of the self-mode-locked Ti:sapphire laser,", J. Opt. Soc. Am. B, 10, pp. 638-643 (1993).

ENHANCED FIBER SQUEEZING VIA LOCAL-OSCILLATOR PULSE COMPRESSION

Jeffrey H. Shapiro

Department of Electrical Engineering and Computer Science
Massachusetts Institute of Technology
Cambridge, MA 02139-4307

Lance G. Joneckis

Laboratory for Physical Sciences
University of Maryland
College Park, MD 20740

Although continuous-wave (cw) fiber experiments were among the very first squeezed-light demonstrations, only 0.58 dB of quadrature-noise reduction has been seen to date in such configurations [1]. Significant advantages accrue in fiber squeezing if the cw pump is replaced by a periodic stream of short pulses. Pulsed squeezing in fibers has produced over 5 dB of noise reduction in a fiber loop-mirror Mach-Zehnder interferometer (MZI) [2]. This value, however, does not approach the fundamental limit on fiber squeezing, which stems from the finite time-constant of the quantum Kerr interaction [3]. For a 50 m-length standard single-mode silica fiber the fundamental limit is expected to lie near 18 dB of squeezing. In the pulsed MZI configuration, with a pump pulse whose temporal distribution is Gaussian, the time-dependent phase-orientation and eccentricity of the homodyne-detection noise ellipse limits the observed squeezing [4]. Indeed, because these experiments use the bright-fringe output from the loop-mirror MZI as their homodyne-detection local-oscillator (LO) beam, they can produce only 8.73 dB of noise reduction under the most ideal conditions. In this paper we shall show that the preceding Gaussian-pulse-profile limit on fiber squeezing can be circumvented via LO pulse compression.

Squeezed-state generation in optical fiber is usually described by instantaneous-interaction, quantum four-wave mixing (FWM). However, a quantum theory for propagation in fiber must include a Kerr-effect time constant if the correct classical limit of self-phase modulation (SPM) is to be recovered. Both quantum FWM and classical SPM can be obtained, within their respective regions of validity, from a coarse-grained time quantum theory—with τ_K-second granularity—for propagation in lossless, dispersionless single-mode fiber subject to the Kerr effect [3]. All fiber-squeezing experiments performed to date have operated in the FWM limit. However it appears that the transition zone—wherein the predictions of the FWM theory begin to diverge from those of the full, coarse-grained time quantum SPM theory—may be experimentally accessible.

For cw coherent-state inputs, both the FWM and SPM theories imply frequency-independent homodyne spectra out to frequencies comparable with τ_K^{-1} [3]. Similar behavior obtains for repetitively-pulsed, coherent-state pumps if the low-frequency spectra are calculated from individual pulses as follows. The minimum normalized (shot-noise level = 1) homodyne-measurement noise level, for a coherent-state input field $E_{IN}(t)$, is given by

$$S_{min}(0) = 1 + 2(S_{OUT}^{(n)}(0) - |S_{OUT}^{(p)}(0)|), \tag{1}$$

where $S_{OUT}^{(n)}(0)$ is the normally-ordered output-noise spectrum

$$S_{OUT}^{(n)}(0) = \begin{cases} (\kappa L)^2 \int_{-\infty}^{\infty} dt\, |E_{LO}(t)|^2 |E_{IN}(t)|^4, & \text{FWM} \\[2mm] \tau_K \int_{-\infty}^{\infty} dt\, |E_{LO}(t)|^2 |E_{IN}(t)|^2 \left(1 - \exp[2\mathrm{Re}[iR]|E_{IN}(t)|^2]\right), & \text{SPM,} \end{cases} \tag{2}$$

$S_{OUT}^{(p)}(0)$ is the phase-sensitive output-noise spectrum,

$$S_{OUT}^{(p)}(0) = \begin{cases} i\kappa L \int_{-\infty}^{\infty} dt\, E_{LO}^{*\,2}(t) E_{IN}^2(t)(1 + i\kappa L|E_{IN}(t)|^2) \exp(2i\kappa L|E_{IN}(t)|^2), & \text{FWM} \\[2mm] \tau_K \int_{-\infty}^{\infty} dt\, E_{LO}^{*\,2}(t) E_{IN}^2(t) \left(\exp[2iR'|E_{IN}(t)|^2 + i\phi_q] - \exp[2iR|E_{IN}(t)|^2]\right), & \text{SPM} \end{cases} \tag{3}$$

and $E_{LO}(t)$ is the normalized ($\int_{-\infty}^{\infty} dt\, |E_{LO}(t)|^2 = 1$) temporal profile of the local oscillator. The classical nonlinear phase shift at time t is $\phi_c(t) = \kappa L |E_{IN}(t)|^2$ for an L m-long fiber, and $iR \equiv [\exp(i\phi_q) - 1]\tau_K$, $2iR' \equiv [\exp(i2\phi_q) - 1]\tau_K$, with $\phi_q \equiv \kappa L/\tau_K$ being the nonlinear phase shift for a single photon in a τ_K-second-duration mode. In the calculations that follow we will employ a normalized fiber length $L_K \equiv \phi_q/2\pi$, and a normalized input power $N_K \equiv |E_{IN}(0)|^2 \tau_K/\hbar\omega$. Because we use photon-units field operators, N_K is the average number of input photons in a τ_K-second-duration mode. Note that the peak classical nonlinear phase shift is $\phi_c = 2\pi N_K L_K$.

In loop-mirror fiber-squeezing experiments the MZI's bright-fringe output pulse—augmented with an adjustable phase bias—is used as the LO pulse for homodyne detection of the MZI's dark-fringe output. Figure 1 shows the theoretically predicted performance of the ideal device with $L_K = 10^{-6}$ ($L \approx 25\,\text{m}$, for $\tau_K = 1\,\text{fs}$) for both square and Gaussian pump pulses. The square pulse, which is equivalent to cw operation, yields optimum squeezing performance: in the FWM theory a square-pulse input yields unlimited squeezing as N_K grows; in the SPM theory the square-pulse input reaches the fundamental squeezing limit of $S_{min}(0) \approx -20\,\text{dB}$. On the other hand, a Gaussian pulse, even in the FWM theory, shows squeezing limited to $S_{min}(0) = 1 - \sqrt{3}/2 \approx -8.73\,\text{dB}$. This Gaussian-pulse FWM result does *not* improve with increased fiber length or input power. The SPM theory is slightly worse; for the case shown it has the characteristic upturn just before it reaches the FWM theory's noise minimum.

The Gaussian-profile pump pulse creates a time-varying orientation and eccentricity to the dark-fringe's squeezing ellipse. As a result, when the bright-fringe pulse is used as the homodyne-detection LO, the observed squeezing suffers for two reasons. First, the low-noise quadrature of the dark fringe is not sampled at all time instants. Second, even with sampling at the correct phase shift, the degree of dark-fringe squeezing varies during the pulse with (in FWM) the strongest squeezing occurring at the pulse's peak. With LO pulse compression, however, both of these effects can be ameliorated. In particular, a shorter LO pulse will encounter a smaller phase rotation of the dark-fringe's low-noise quadrature, and it can be arranged to sample only the strongest squeezing on dark-fringe output. Figure 2 shows the expected squeezing for two possible approaches to LO pulse compression: (1) when the LO pulse is a transform-limited Gaussian whose duration is a factor of r shorter than that of the input pulse; and (2) when the LO pulse is the transform-limited Gaussian obtained by grating-pair pulse compression of the Gaussian pulse produced by propagating the pump pulse through nL meters of fiber. The former could be realized by splitting the output from a femtosecond laser, using one part for the LO, and spectrally shaping the remainder to produce a much longer pump pulse for the loop-mirror MZI. The latter could be realized by passing the MZI's bright-fringe output into an auxiliary fiber of appropriate length and then grating-pair compressing the resulting output to create the LO.

As seen in Fig. 2, neither the $r = 10$ nor the $n = 1$ cases offer any enhancement of the observed squeezing. In fact, both perform *worse* than using the bright-fringe output as the LO, whose behavior is shown by the curve labeled "Output LO." On the other hand, for $r = 100$ and for $n = 2, 3$ there is significant improvement over the standard bright-fringe LO.

To quantify how these results vary with fiber length, we show, in Fig. 3, the maximum attainable squeezing $s_{opt} \equiv -10\log\{\min_{\phi_c}[S_{min}^{SPM}(0)]\}$ versus normalized fiber length. Figure 3 also plots the classical nonlinear peak phase shifts at which these optimum squeezing values occur. The squeezing enhancements resulting from a compressed LO are for the most part fiber-length insensitive until they asymptotically approach the fundamental limit set by the square pulse.

References

[1] R.M. Shelby, M.D. Levenson, R.G. DeVoe, S.H. Perlmutter, and D.F. Walls, Phys. Rev. Lett. **57**, 691 (1986).

[2] K. Bergman and H.A. Haus, Opt. Lett. **16**, 663 (1991).

[3] L.J. Joneckis, and J.H. Shapiro, J. Opt. Soc. B **10**, 1102 (1993).

[4] M. Shirasaki, and H.A. Haus, J. Opt. Soc. B **7**, 30 (1990).
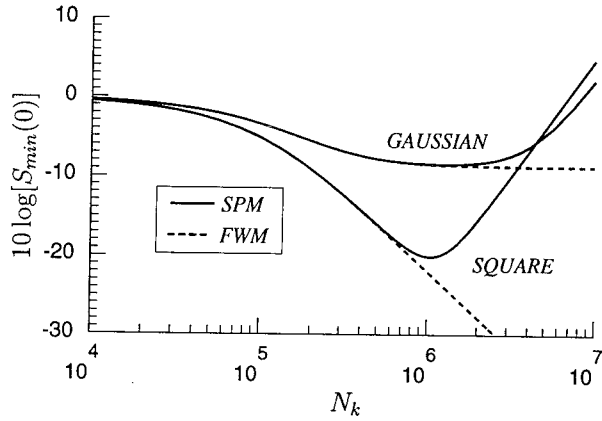
Fig. 1. Minimum low-frequency, homodyne-measurement noise spectra for a coherent-state input to a fiber length $L_K = 10^{-6}$ ($L \approx 25$ meters for $\tau_K = 1$ fs) versus normalized input power for square and Gaussian pulses. The solid curves are the coarse-grained time SPM theory; the dashed curves are the instantaneous-interaction FWM theory.
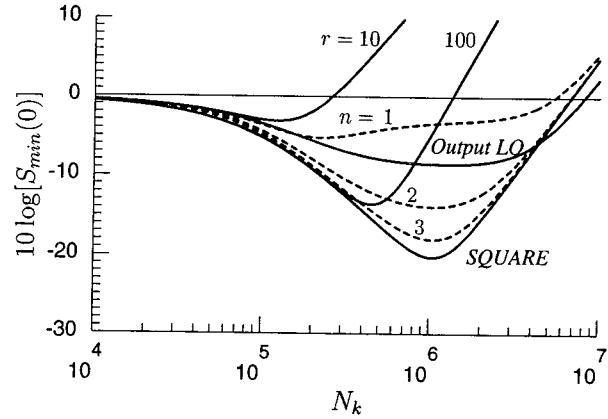
Fig. 2. Minimum low-frequency, homodyne-measurement noise spectra for a coherent-state input to a normalized fiber length $L_K = 10^{-6}$ versus normalized input power for Gaussian pulses with transform-limited, compressed local oscillators. The $r = 10, 100$ curves are for LO pulses which are r-fold compressions of the pump pulse. The $n = 1, 2, 3$ curves are for LO pulses which are ideal, grating-pair compressions of the pump pulse after it has propagated through a fiber of normalized length nL_K. Also shown, for purposes of comparison, are the two SPM curves shown in Fig. 1. The horizontal line at zero ordinate is the shot-noise limit.
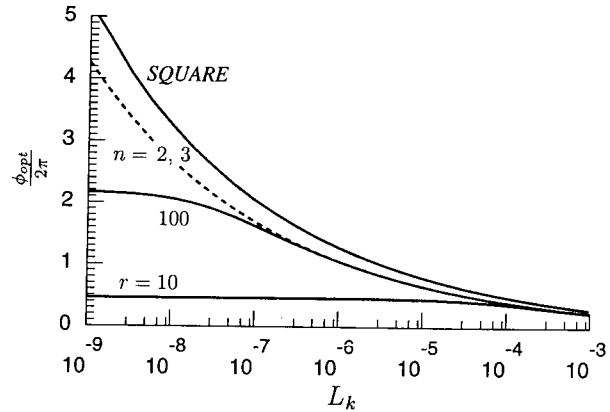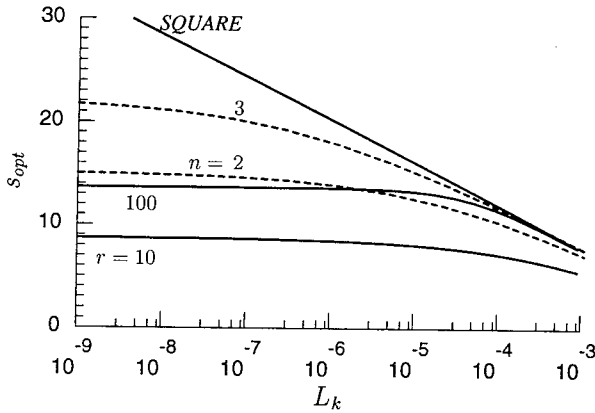
Fig. 3. The SPM theory's optimum squeezing factor, $s_{opt}(L_K)$, and the corresponding classical nonlinear phase shift, ϕ_{opt}, versus normalized fiber length. The $r = 10, 100$ curves are for LO pulses which are r-fold compressions of the pump pulse. The $n = 2, 3$ curves are for LO pulses which are ideal, grating-pair compressions of the pump pulse after it has propagated through a fiber of normalized length nL_K. The square-pulse curve represents the SPM theory's fundamental limit on fiber squeezing.

SEMICLASSICAL vs. QUANTUM BEHAVIOR IN FOURTH-ORDER INTERFERENCE

Jeffrey H. Shapiro

Department of Electrical Engineering and Computer Science
Massachusetts Institute of Technology
Cambridge, MA 02139-4307

Ke-Xun Sun

Edward Ginzton Laboratory
Stanford University
Stanford, CA 94305-4085

Parametric interactions in $\chi^{(2)}$ crystals have proven to be rich sources of nonclassical light-beam phenomena: squeezed-state generation using an optical parametric amplifier (OPA), photon-twins production from an optical parametric oscillator (OPO), and fourth-order interference experiments using signal and idler beams from a parametric down converter. Satisfactory quantum theories for all of the preceding nonclassical light-beam phenomena are available, but a unified formalism encompassing them all has yet to appear. In particular, both OPA squeezing and OPO twin beams are easily understood in terms of their field-quadrature spectra, but fourth-order interference is generally treated via correlated, single-photon wave packets. More importantly, whereas the well-known semiclassical, "shot-noise" limits of optical homodyne detection and differenced direct detection provide clear-cut boundaries beyond which purely quantum phenomena can be claimed in OPA and OPO experiments, the corresponding semiclassical bounds on fourth-order interference are, we believe, not widely appreciated. In this paper we explore semiclassical and quantum descriptions of fourth-order interference that are built upon classical and quantum Gaussian-state models for the signal and idler outputs from a parametric down converter [1]. Our approach unifies the analysis of fourth-order interference with those for squeezing and photon twins. It also demonstrates that a purely-quantum fourth-order interference effect can be claimed at fringe visibilities substantially below the commonly accepted threshold of 50%. We start with a pair of models—one quantum and one classical—for the signal and idler fields produced by parametric down conversion.

Quantum Field Model

Let $\hat{E}_S(t)$ and $\hat{E}_I(t)$ be the positive-frequency signal and idler field operators, respectively, at the output of the parametric down converter. These operators commute with each other (and with each other's adjoint) and individually satisfy the usual δ-function commutator rule. The joint density operator for the signal and idler is a zero-mean-field Gaussian state which is completely characterized by the following normally-ordered and phase-sensitive correlations for $j = S, I$ and $k = S, I$:

$$\langle \hat{E}_j^\dagger(t+\tau)\hat{E}_k(t)\rangle = \delta_{jk}\exp(i\omega_j\tau)\int \frac{d\omega}{2\pi}\mathcal{P}(\omega)e^{i\omega\tau}, \tag{1}$$

$$\langle \hat{E}_j(t+\tau)\hat{E}_k(t)\rangle = (1-\delta_{jk})\exp[-i(\omega_P t + \omega_j\tau)]\int \frac{d\omega}{2\pi}\sqrt{\mathcal{P}(\omega)[\mathcal{P}(\omega)+1]}e^{-i\omega\tau}, \tag{2}$$

where ω_S, ω_I are the center frequencies of the signal and idler beams, δ_{jk} is the Kronecker delta function and $\mathcal{P}(\omega) \geq 0$ is the common, signal and idler spectrum. We shall assume that $\mathcal{P}(\omega)$ is an even function of ω, and we note that a frequency-dependent phase factor could be included inside the integral in the phase-sensitive correlation.

Classical Field Model

The classical field model that most closely mimics the preceding quantum model corresponds to classically-random, positive-frequency, photon-units signal and idler fields, $E_S(t)$ and $E_I(t)$, respectively. These fields comprise a pair of zero-mean, complex-valued, jointly-Gaussian random processes, which are completely

characterized by the following normally-ordered and phase-sensitive correlations for $j = S, I$, and $k = S, I$:

$$\langle E_j^*(t + \tau) E_k(t) \rangle = \delta_{jk} \exp(-i\omega_j \tau) \int \frac{d\omega}{2\pi} \mathcal{P}(\omega) e^{i\omega\tau}, \tag{3}$$

$$\langle E_j(t + \tau) E_k(t) \rangle = (1 - \delta_{jk}) \exp[-i(\omega_P t + \omega_j \tau)] \int \frac{d\omega}{2\pi} \mathcal{P}(\omega) e^{-i\omega\tau}, \tag{4}$$

where the angle brackets now denote classical ensemble average, instead of quantum average.

When the preceding quantum and classical field models are used, respectively, in conjunction with standard quantum and semiclassical theories of photodetection it is a simple matter to derive the following results for squeezing, photon twins, and fourth-order interference.

Quadrature-Noise Squeezing

For a degenerate parametric down converter—one whose signal and idler frequencies coincide—unity quantum efficiency homodyne detection of the 50/50 combination of the signal and idler beams yields a phase-sensitive photocurrent noise whose spectrum at the optimum (noise-minimizing) local-oscillator (LO) phase is

$$S_{min}(\omega) = \begin{cases} q^2 P_{LO} \left[\sqrt{1 + \mathcal{P}(\omega)} - \sqrt{\mathcal{P}(\omega)} \right]^2, & \text{quantum theory,} \\ \\ q^2 P_{LO}, & \text{semiclassical theory.} \end{cases} \tag{5}$$

where P_{LO} is the local oscillator's photon flux, and q is the electron charge. Thus, the semiclassical noise-level always equals or exceeds the shot-noise limit, $q^2 P_{LO}$, whereas the quantum theory can have noise lower than the shot-noise limit.

Photon Twins

When the signal and idler beams from a parametric down converter are separately detected by unity quantum efficiency photon counters, the signal−idler photon count difference over a T-sec-duration interval is a zero-mean random variable, ΔN_T, whose variance obeys

$$\langle \Delta N_T^2 \rangle / T = 2P, \quad \text{for all } T, \tag{6}$$

in the semiclassical theory, whereas the quantum theory predicts

$$\langle \Delta N_T^2 \rangle / T \to \begin{cases} 2P, & \text{as } \Delta\omega T \to 0 \\ \\ 0, & \text{as } \Delta\omega T \to \infty, \end{cases} \tag{7}$$

where $2P$ is the signal+idler average photon flux from the down converter—and hence the shot-noise limit for this measurement—and $\Delta\omega$ is the common signal/idler fluorescence bandwidth. Thus, the semiclassical per-unit-time photocount variance is always shot-noise limited, but the quantum expression drops substantially below this limit, once the counting interval is long enough to sense the nonclassical entanglement of the signal and idler beams.

Fourth-Order Interference

The recent dispersion-cancellation experiment of Steinberg, Kwiat, and Chiao [2] has a simple explanation in our Gaussian-state formalism. Their data shows a pronounced, transform-limited, fourth-order coincidence-rate dip at zero delay when the signal beam from a nondegenerate parametric down converter is dispersed, delayed and 50/50 combined with the down-converter's idler beam prior to photodetection. Our formalism gives the following predictions for $C(T; \tau_g)$, the coincidence rate as a function of delay T, in the Steinberg, Kwiat, and Chiao experiment:

$$C(T; \tau_g) = \begin{cases} P \left\{ \sqrt{\pi} P \tau_g + 2^{-1} \left[1 - \exp(-\Delta\omega^2 T^2 / 2) \right] \right\}, & \text{quantum theory} \\ \\ \sqrt{\pi} P^2 \tau_g \left\{ 1 + (2\Delta\omega\tau_g)^{-1} \left[1 - \exp(-\Delta\omega^2 T^2 / 4) \right] \right\}, & \text{semiclassical theory} \end{cases} \tag{8}$$

where τ_g is the coincidence gate's duration. This result assumes that $\mathcal{P}(\omega)$ is a Gaussian spectrum, and that operation is in the low-photon-flux regime, with $\tau_g \gg T$ and $\Delta\omega\tau_g \gg 1$; these conditions prevail in the Steinberg, Kwiat, and Chiao experiment.

351

Both the quantum and semiclassical formulas show complete dispersion cancellation in the transform-limited widths of their minima at $T = 0$. Note that there is nothing intrinsically quantum mechanical about this dispersion cancellation. Its origin is easily traced to the fact that the four correlation functions appearing in bowels of our calculations are dispersion-broadened, chirped-Gaussian functions. The negative contributions to that give rise to the coincidence-rate dip derive from signal/idler cross-terms which, when integrated over the τ_g-sec gate interval, behave like the matched-filter pulse compressors found in chirped-pulse radar systems.

For the low photon-fluxes prototypical of parametric down conversion, nanosecond gate durations will give $P\tau_g \ll 1$, hence the $T = 0$ coincidence-rate dip in the quantum theory constitutes an essentially 100%-visibility white-light fringe, viz., we have that

$$\gamma \equiv \frac{\max_T[C(T;\tau_g)] - \min_T[C(T;\tau_g)]}{\max_T[C(T;\tau_g)] + \min_T[C(T;\tau_g)]} \tag{9}$$

$$= 1/[1 + 4\sqrt{\pi}P\tau_g] \approx 1, \quad \text{for } P\tau_g \ll 1. \tag{10}$$

In the semiclassical model, however, the white-light fringe at $T = 0$ is completely masked, i.e., we have that

$$\gamma = 1/[1 + 4\Delta\omega\tau_g] \ll 1, \quad \text{for } \Delta\omega\tau_g \gg 1. \tag{11}$$

Thus, a Steinberg, Kwiat, and Chiao dispersion-cancellation experiment that is performed on Gaussian-state light in the low-photon-flux regime can be said to show a nonclassical effect even with fringe visibilities substantially less than 50%.

Restricting our semiclassical vs. quantum fringe-visibility comparison to Gaussian-state light is very reasonable. As shown in [1], this restriction includes the *only* classical-field model that reproduces *all* the signal-only and idler-only photodetection statistics of the quantum model. Nevertheless, let us briefly address the non-ergodic classical-field model which prior studies have asserted yields 50% fourth-order fringe visibility.

In lieu of our classical field model, we now assume that $E_S(t)$ and $E_I(t)$ are classically-random, positive-frequency, photon-units signal and idler fields obeying

$$E_S(t) = \sqrt{P}\exp[-i(\omega_S + \tilde{\omega})t - i\tilde{\theta}], \tag{12}$$

$$E_I(t) = \sqrt{P}\exp[-i(\omega_I - \tilde{\omega})t + i\tilde{\theta}], \tag{13}$$

where $\tilde{\omega}$ and $\tilde{\theta}$ are statistically-independent random variables, with the former being Gaussian with mean zero and variance $\Delta\omega^2$, and the latter being uniformly distributed on $[0, 2\pi]$. This model is not ergodic, but if $\tilde{\omega}$ and $\tilde{\theta}$ are made slowly-varying functions of time, we can still use an ensemble average analysis as representative of a real, time-average measurement.

Continuing our assumption that $\Delta\omega\tau_g \gg 1$ holds, we find that the non-ergodic classical field model predicts a low-photon-flux regime coincidence rate given by

$$C(T;\tau_g) = P^2\sqrt{\pi}\tau_g \left[1 - (\sqrt{8}\Delta\omega\tau_g)^{-1}\exp(-T^2/4\tau_g^2)\right]. \tag{14}$$

This result is very different from the low-photon-flux quantum behavior we exhibited earlier. First of all, the peak coincidence rate is proportional to P^2, not to P. Second, the dip at $T = 0$ is coincidence-gate limited, not transform limited. Finally, the fringe-visibility is much smaller than 50%. Indeed, the non-ergodic model's fringe visibility is similar to that found earlier for our Gaussian-state classical-field model.

References

[1] J.H. Shapiro, and K.-X. Sun, "Semiclassical vs. quantum behavior in fourth-order interference," to appear in J. Opt. Soc. Am. B.

[2] A.M. Steinberg, P.G. Kwiat, and R.Y. Chiao, Phys. Rev. Lett. **68**, 2421 (1992).

WP16

Multiphoton Photochemistry and Resonant Laser Ignition of Reactive Gases

Brad E. Forch
ATTN: AMSRL-WT-PC
U.S. Army Research Laboratory
Aberdeen Proving Ground, Maryland 21005-5066
(410) 278-7067

SUMMARY

There are several known gas phase laser ignition mechanisms which are thermal (laser heating of the gases), photochemical (laser photolytic production of radicals which are important in exothermic chemical reactions), non-resonance spark formation (laser gas breakdown) and resonance microplasma formation (wavelength-specific formation of a spark through photochemical processes). The ignition process depends on the deposition of a minimum energy (Calcote, et al., 1952) that is sufficient to achieve self propagation of the flame front when the ignition source is removed. The form and rate of energy input into the combustion process can also influence the success of the ignition event (Lavid, et al., 1985). Recent ignition work in reactive gas-phase mixtures illustrates that the operating wavelength of the laser (particularly in the ultraviolet UV) can determine the potential for photochemistry to occur (Chou, et al., 1991; Lavid, et al., 1985; Lucas, et al., 1987; Maas, et al., 1986, Raffel, et al., 1985, Forch, et al., 1991; Forch, et al., 1990, Forch, et al., 1987, Forch, et al., 1986). This work has lead to the development of a new ignition method called resonant laser microplasma ignition (Forch, et al., 1991; Forch, et al., 1990, Forch, et al., 1987, Forch,et al., 1986) . Wavelength specific multiphoton laser photolytic and excitation processes create excess populations of radicals, ions, electrons and reactive species which enhance ignition. In our previous gas-phase investigations a tunable laser system was used to ignite premixed reactive gaseous flows of H_2/O_2, H_2/N_2O, and D_2/O_2. It was found that UV laser photolysis of either fuel or oxidizer molecules produced H and O radicals which could be resonantly photoexcited and photoionized to produce a laser microplasma of sufficient intensity to achieve ignition. The amount of incident laser energy (ILE) that was required to ignite the mixtures was found to be a minimum at wavelengths which correspond to the location of two-photon excitation transitions (Figure 1. (a.-b.)) of atomic hydrogen and atomic oxygen near 243 nm and 225.6 nm respectively.

The ignition mechanism consists of three concurrent processes which occur during a single ca. 10 ns laser pulse: 1.) photodissociation of the fuel or oxidizer component to produced ground-state H or O atom; 2.) resonant two-photon excitation of the atoms and photoionization to produce free electrons; 3.) resonance formation of a laser-produced microplasma which serves as an ignition source. Specifically, photodissociation of O_2 or N_2O produces ground electronic state oxygen $2p^4$ ($^3P_{2,1,0}$) which are the well-known three ground-electronic spin-orbit-split states. The ground state fine structure components are well separated (the three ground state fine structure components are a triplet and are spaced at relative energies of 0, 158.5 and 226.5 cm^{-1}) the excited state $2p^33p(^3P_{2,1,0})$ splittings are only 0.54 and 0.16 cm^{-1} and could not be resolved so only single peaks were observed whose intensities are summed over the upper oxygen $2p^33p(^3P_J)$ states. Absorption of a third photon is sufficient to achieve ionization and drive the resonant formation of a microplasma. Plots of the ILE required for ignition versus wavelength revealed three minima which correspond exactly to the spectral positions of these two-photon allowed transitions $2p^4$ ($^3P_{2,1,0}$)$\rightarrow 2p^33p(^3P_{2,1,0})$. Photodissociation of H_2 or D_2 produces ground-electronic-state 1S atomic hydrogen. Resonance two-photon excitation of the atoms to the lowest excited electronic state (near-degenerate $2S_{1/2}$, $2P_{1/2}$, $2P_{3/2}$ levels) and ionization through the absorption of a third photon likewise serves as the basis for the formation of a microplasma. Plots of the ILE required to ignite the mixtures as a function of laser excitation wavelength showed two minima whose spectral locations correspond exactly to the two-photon excitation wavelengths of H and D at 243.07 nm and 243.0 nm respectively.

Resonance laser microplasma ignition affords a distinct advantage over non-resonant gas breakdown (spark formation) in terms of the energy threshold for ignition and extraction of the minimum energy required for ignition. Laser-induced gas breakdown occurs through non-resonant ionization of the gas, collision-
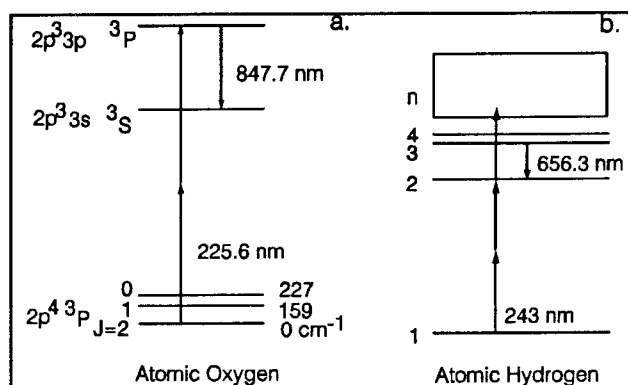
Figure 1. Simple energy level diagrams for a. atomic oxygen and b. atomic hydrogen.

induced cascade ionization and subsequent spark formation driven by inverse bremsstrahlung (Smith, et al., 1976). The threshold for non-resonant gas breakdown in an initially transparent non-absorbing gas typically exceeds the requisite minimum ignition energy for a reactive gaseous mixture and therefore the extraction of the minimum ignition energy from this measurement may be difficult. This is because the laser power density at which ionization, electron production and spark formation occurs in a non-resonant process simply exceeds the minimum energy required to ignite the mixture. Typically a very intense spark or blast wave is formed which can extinguish combustion or lead to a detonation. Resonance laser microplasma ignition provides a means of photochemically producing radicals and seed electrons very early on in the laser pulse well below the energy threshold for ignition and gas breakdown. Resonance excitation and ionization of the radicals produces a very weak and controllable microplasma (laser spark) below the threshold for ignition. The laser energy can then be gradually increased to the point that the microplasma grows to sufficient intensity for ignition to occur. Furthermore, with a resonant laser source it is easy to produce a visible well-controlled microplasma within the mixture that will not cause ignition until additional energy is supplied to the laser pulse. At the ignition threshold a certain amount of energy has been deposited in a sufficiently short time period such that self-sustaining ignition occurs which allows the ignition kernel to propagate into a stabilized combustion subsequent to the termination of the laser pulse.

The measurement of the incident laser energy required for the ignition of reactive gaseous mixtures is simple since the amount of energy delivered to the laser focal volume can be determined with an energy meter. The measurement of the minimum ignition energy is far more difficult since the multiphoton absorption, photodissociation, photoexcitation and photoionization processes which form the laser microplasmas exhibit a highly nonlinear dependence on laser intensity which make absorption measurements difficult. The primary goal of this work is to determine what fraction of the ILE that drives the formation of the microplasma and ignition is absorbed in the ignition event. The fraction of energy absorbed is the minimum ignition energy under these experimental conditions. Although a distinct wavelength dependence on the ILE required for ignition was observed in our past work, an additional motivation of this work is to ascertain that if once a minimum ignition energy has been deposited is there a selective enhancement in ignition which is wavelength dependent.

In this work a tunable laser system which operates in the ultraviolet (UV) has been utilized to ignite premixed reactive gaseous flows of H_2/O_2, D_2/O_2 and CH_4/N_2O in a jet burner at atmospheric pressure. Multiphoton UV photodissociation of the fuel or oxidizer molecules produced ground state radicals (H and O atoms). Resonance enhanced multiphoton excitation and ionization of these radicals formed a laser-produced microplasma which served as an ignition source. Time-
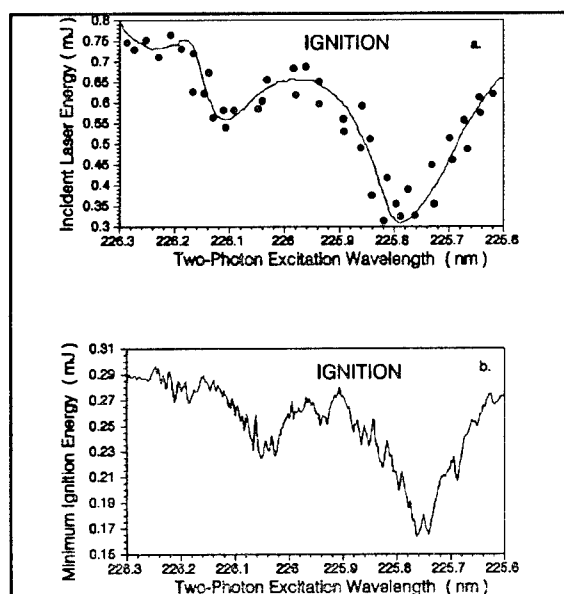
Figure 2. Plots of a. ILE versus wavelength and b. minimum ignition energy versus wavelength for H_2/O_2 ($\Phi = 0.7$).
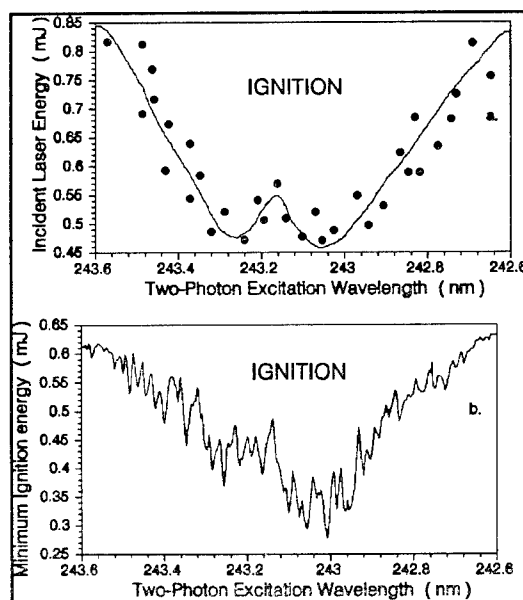
Figure 3. Plots of a. ILE versus wavelength and b. minimum ignition energy versus wavelength for $H_2,D_2/O_2$ ($\Phi = 0.7$).

resolved absorption techniques were utilized to determine minimum ignition energies for the gaseous mixtures when the laser was tuned to resonance two-photon excitation transitions of H and O atoms near 243 nm and 225.6 nm respectively

Figures 2,3. The minimum ignition energy was found to be wavelength dependent and was the least when the laser was tuned to the resonant two-photon excitation transitions. These results suggest that ignition is not only dependent upon the absorption of a certain minimum amount of energy but is also photochemically enhanced by the production of ground and excited-state radicals and ions which participate in exothermic chemical chain-branching reactions in the early stages of ignition. The microplasmas were also characterized using emission, photoaucoustic and ionization spectroscopies.

ACKNOWLEDGEMENTS

REFERENCES

Chou, M-S. and Zukowski, T.J.:1991, "Ignition of $H_2/O_2/NH_3$, $H_2/Air/NH_3$ and $CH_4/O_2/NH_3$ Mixtures by Excimer-Laser-Photolysis of NH_3", *Comb. and Flame*, Vol. **87**, pp. 191-202.

Forch, B.E. and Miziolek, A.W.: 1991, "Laser-Based Ignition of H_2/O_2 and D_2/O_2 Premixed Gases Through Resonant Multiphoton Excitation of H and D Atoms Near 243 nm," *Comb. Flame*, Vol. **85**, pp. 254-262.

Forch, B.E., Morris, J.B. and Miziolek, A.W.: 1990, "Laser-Induced Fluorescence and Ionization Techniques for Combustion Diagnostics," invited book chapter in *Laser Techniques in Luminescence Spectroscopy*, ed. Vo-Dinh and Eastwood, ASTM Pub. STP 1066, pp. 50-68.

Forch, B.E. and Miziolek, A.W., 1987, "Ultraviolet Laser Ignition of Premixed Gases by Efficient and Resonant Multiphoton Photochemical Formation of Microplasmas," *Comb. Sci. and Tech.*, Vol. **52**, pp. 151-159.

Forch, B.E and Miziolek, A.W.: 1986, "Oxygen-Atom Two-Photon Resonance Effects in Multiphoton Photochemical Ignition of Premixed H_2/O_2 Flows," *Opt. Lett.*, Vol. **11**, pp. 129-131.

Lavid, M.L. and Stevens, J.g..: 1985, "Photochemical Ignition of Premixed Hydrogen/Oxidizer Mixtures with Excimer Lasers", *Comb. Flame*, Vol. **60**, pp. 195-202.

Lucas, D., Dunn-Rankin, D., Hom, K. and Brown, N.J.: 1987, "Ignition by Excimer Laser Photolysis of Ozone", *Comb. and Flame*, Vol. **69**, pp. 171-184.

Maas, U., Raffel, B. and Wolfrum: 1986, "Observation and Simulation of Laser Induced Ignition Processes in O_2-O_3 and H_2-O_2 Mixtures", *Twenty-First Symposium (Internation) on Combustion*", 1986, pp. 1869-1876, Combustion Institute, Pittsburg.

Raffel, B., Warntaz, B., and Wolfrum, J.: 1985, "Experimental Study of Laser-Induced Ignition in O_2/O_3 Mixtures," *Appl. Phys.*, B37, pp. 189-195.

Nd:YALO-Amplifier Above 100 Watts Average Output Power With High Beam Quality Via Phase Conjugation

H.J. Eichler, A. Haase, R. Macdonald and R. Menzel

Optisches Institut, Technische Universität Berlin[*)]
Straße des 17. Juni 135, 10623 Berlin, Germany
Phone: (30) 314-22498, Fax: (30) 314-26888

Nd:laser with good beam quality via phase conjugating SBS-mirrors can be realized as oscillators [1] and for higher output powers as systems of Master Oscillator and Power Amplifier. MOPAs were described using Nd:YAG slab geometries in multi-pass arrangements [e.g. 2]. With these setups average output powers of more than 100 Watts were reported [2, 3] with pulse energies in the range of 1 J to 25 J.

To reduce the complexity of higher power Nd-MOPAs we developed a scheme with a single Nd:YAG rod [4]. The thermal lens of the highly pumped laser rod with focal lengths of less than 30 cm could be perfectly compensated by the aid of the phase conjugating SBS-mirror. But in high power Nd:YAG laser rods a strong birefringence occurs. This leeds to a depolarization of the incident laser light even after the first pass [5]. Therefore a scheme with two optical isolation stages was used to extract all amplified energy and to protect the oscillator from backscattered amplifier radiation. Although this scheme operated well and we were able to extract 100 Watts from this single rod Nd:YAG amplifier, the beam quality of the output was restricted somewhat to about 2 times the diffraction limit (better than 2*DL).

Therefore we set up a single rod amplifier based on a $YAlO_3$-crystal with 9.5 mm diameter , 152 mm length and 1.0 at.% Neodymium doping as active material. This Nd:YALO crystal is optically highly anisotropic and shows therefore no remarkable stress birefringence. On the other side the thermal lensing of this material is roughly two times higher than for Nd:YAG (see Fig. 1). But this disadvantage of a higher thermal lensing could be compensated with the phase conjugating mirror.
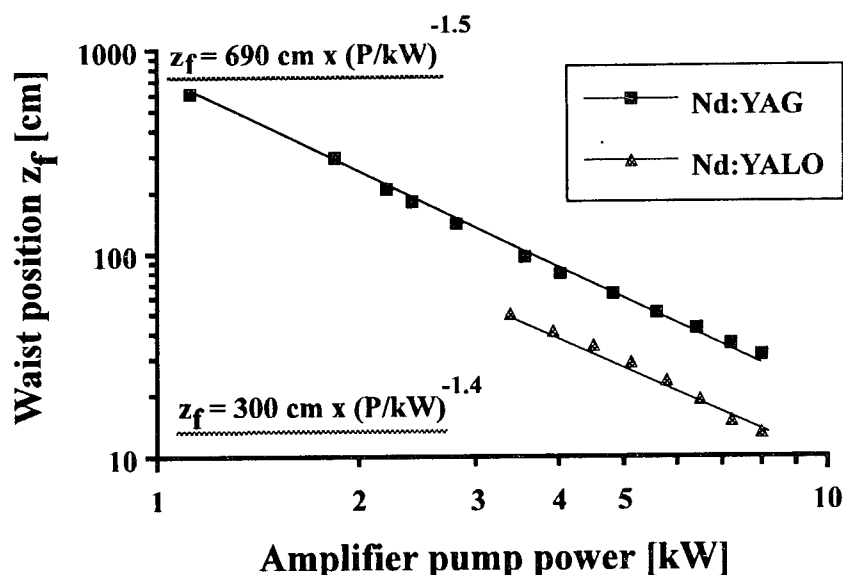
Fig.1:   Thermal lensing of Nd:YAG and Nd:YALO rods as a function of electrical pump power

A 45 degree Faraday rotator was used to couple out the amplified light in combination with a polarizer. As SBS-material we used CS_2. Because of astigmatic thermal lensing the Nd:YALO oscillator showed an slightly elliptical transversal beam profile. In the vertical direction the beam was 1.3 times diffraction limited and in the horizontal 1.1 times. The flashlamps were driven with a repetition rate up to 100 Hz. During each flash a burst of 3 to 40 Q-switch pulses of different amplitudes ocurred adjustible by the time delay of oscillator and amplifier.

The thermal lens of the YALO-amplifier could be perfectly compensated in the double pass arrangement by the phase conjugating SBS-mirror as measured in a distance of 5.2 m behind the amplifier rod (see figure 2).
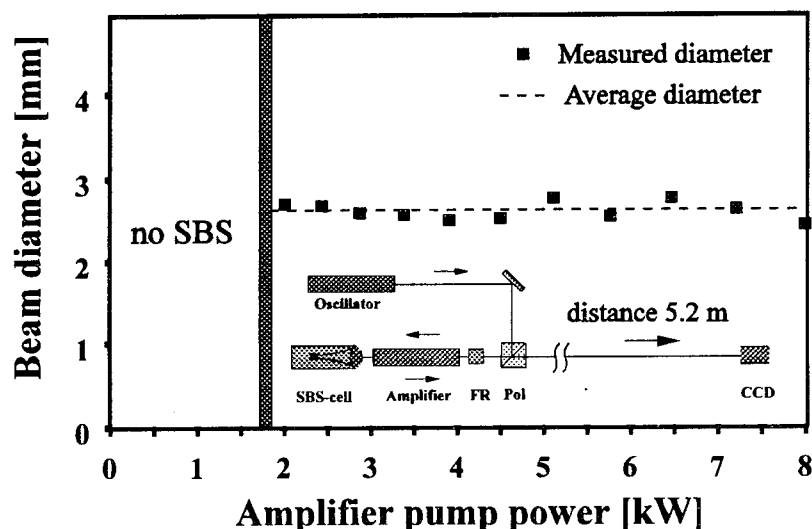
Fig.2:   Measured beam diameter of the amplified light in a distance of 5.2 m as a function of the electrical input power. The dashed line represents the average diameter of 2.6 mm.

Demonstration of Accumulated Photon Echoes by using Synchrotron Radiation

H. Itoh[1], and S. Nakanishi[1], M. Kawase[2], H. Fukuda[3], H. Nakatsuka[3], and M. Kamada[4]

[1]*Department of Physics, Kagawa University, Takamatsu 760, Japan*

[2]*Department of Chemistry, Kagawa University, Takamatsu 760, Japan*

[3]*Institute of Applied Physics, University of Tsukuba, Tsukuba 305, Japan*

[4]*UVSOR Facility, Institute for Molecular Science, Okazaki 444, Japan*

1. Introduction

Synchrotron radiation (SR) can be applied as an excitation source of the accumulated photon echoes. The accumulated photon echoes of sulforohdamine 640 (SRh640) doped in polyvinyl alcohol film (PVA) was successfully observed by exciting the sample with the SR and employing the phase modulation method [1]. When we used the SR passed through a bandpass filter with the bandwidth of about 13 nm, the photon echo decay curve was obtained with a time resolution of 133 fs. In addition, when the bandpass filter was removed, the field autocorrelation time of the SR beam decreased to about 3 fs.

2. Theory

When the sample is collinearly excited by the two SR beams, $E_1(t) = E(t)$ and $E_2(t) = E(t - \tau)$, the power spectrum $S(\omega)$ of the excitation in the sample is expressed as follows,

$$S(\omega) = \lim_{T \to \infty} \frac{1}{T} \left| \int_{-T/2}^{T/2} (E_1(t) + E_2(t)) e^{i\omega t} dt \right|^2 = S_0(\omega)[1 + \cos(\omega\tau)], \quad (1)$$

where $S_0(\omega)$ is the power spectrum of the SR itself. If the inhomogeneous broadening is sufficiently broader than the homogeneous broadening of the sample and excitation spectrum, the population grating $H(\omega)$ formed by $S(\omega)$ is

$$H(\omega) \propto \int_{-\infty}^{\infty} \frac{\gamma}{\gamma^2 + (\omega - \omega')^2} S(\omega) d\omega' \quad (2),$$

where γ means the inverse of the dephasing time T_2. The polarization induced by $H(\omega)$, which contributes to the echo signals, is as follows,

$$P_2(\omega, t) \propto \int_{-\infty}^{\infty} H(\omega) E_2(t') e^{(-i\omega - \gamma)(t - t')} dt'. \quad (3)$$

By integrating over the inhomogeneous distribution $g(\omega)$, a macroscopic third-order electric dipole moment $< P_2(t) >$ is obtained. Because of the phase modulation

method, $E_2(t)$ is rewritten by $E_2(t)\exp[iM\sin(ft)]$ so that the echo signal $I(\tau)$ is expressed as follows,

$$I(\tau) = \left[J_0^2(M) + 2J_0(M)J_2(M)\cos(2ft) + \cdots\right]e^{-2\gamma\tau}, \tag{4}$$

where $J_i(M)$ denotes the i-th order Bessel function, and M means the index of the phase modulation induced by the piezoelectric transducer. Note that the echo signal of $2f$-component is proportional to the product of the zeroth- and the second-order Bessel functions [2].

3. Experiment

The experiment was performed at a beam line 8A of UVSOR facility, Institute for Molecular Science, Okazaki, Japan. The SR beam was focussed with a concave mirror with the horizontal and vertical focal length of 2.8 m and 2.6 m, respectively. The electron storage ring was operated with the electron energy of 750 MeV and the beam current of 200 mA. The output SR pulses had the repetition rate of about 90 MHz and the time duration of 1.5 ns [3]. The SR beam was filtered by the bandpass filter with center wavelength of 605 nm and bandwidth of 13 nm. After the filter, the SR beam was introduced to a Michelson interferometer in order to split it into two beams (the power of 2.2 and 0.8 μW), and one beam was temporally delayed relative to the other beam which was phase modulated at f=6.5 kHz. The collinearly overlapped two beams were focused onto the sample and the transmitted beams were detected by a PIN photodiode whose output was fed into a lock-in amplifier. The echo signal was obtained in the $2f$-component of the lock-in detected signal. The filtered SR beam was resonant to the 0-0 transition between S_0 and S_1 levels of SRh640 in PVA.

4. Results

We first measured the field autocorrelation of the SR beam that determines the time resolution in the photon echo experiment. Figure 1(a) shows the autocorrelation obtained for the SR beam used in our experiment. In this measurement, the sample was removed and the signal of f-component was detected. The correlation time (FWHM) of the filtered SR was measured to be 133 fs, which clearly indicates that the photon echo decay can be measured with a time resolution of about 130 fs. Figure 1(b) displays the field correlation when the bandpass filter was eliminated, indicating the field correlation time of about 3 fs.

Figure 2 shows the accumulated photon echo decay on a logarithmic scale measured for SRh640 in PVA at 29 K, where the delay time τ was scanned from 1.2 ps to 10 ps. The T_2 obtained in Fig. 2 is approximately 4.8 ps. This decay curve is normalized with the SR beam intensity by assuming that the intensity is proportional to the beam current in the storage ring. In the measurement we took ten data into a computer at a fixed delay time after accumulating a population grating for 60 sec. Then the accumulated population grating was erased by slowly changing

the delay time τ to the next sampling delay time with the two excitation beams on, which took 60 sec.

Using a dye laser pumped by a Q-switched YAG laser, we also examined whether this T_2 of 4.8 ps is reasonable for SRh640 at 29 K. The T_2 was thus measured at the sample temperature from 10 K to 30 K. The solid circles in Fig. 3 show the T_2 measured by the incoherent ns dye laser and a solid square represents the T_2 of 4.8 ps observed by the SR. The square point just lies on the fitting line of $T_2 \propto T^{-1.7}$, which confirms the validity of the T_2 measured by the SR.

This work is performed under the Joint Studies Program of the Institute for Molecular Science, Japan.

References

[1] S. Saikan, K. Uchikawa and H. Ohsawa, Opt. Lett. **16**, 10 (1991).

[2] A. Wakamiya, Master thesis, University of Tsukuba, Japan (1993).

[3] M. Watanabe, Nucl. Instrum. & Methods Phys. Res. A **246**, 15 (1986).
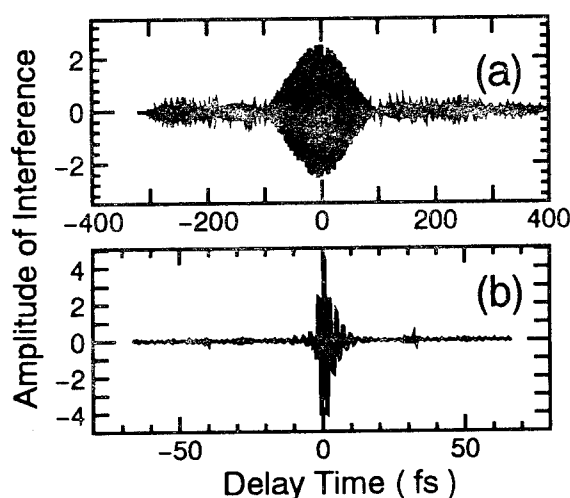
Fig. 1. Autocorrelation trace of the SR beam (a) with the bandwidth of 13nm at 605 nm (the correlation time of 133 fs) and (b) with the widest bandwidth (the correlation time of 3 fs).
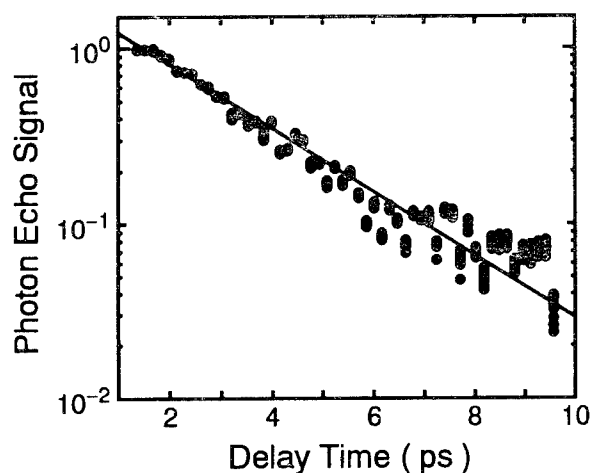
Fig. 2. Accumulated photon echo decay for SRh640 doped in PVA at 29 K.
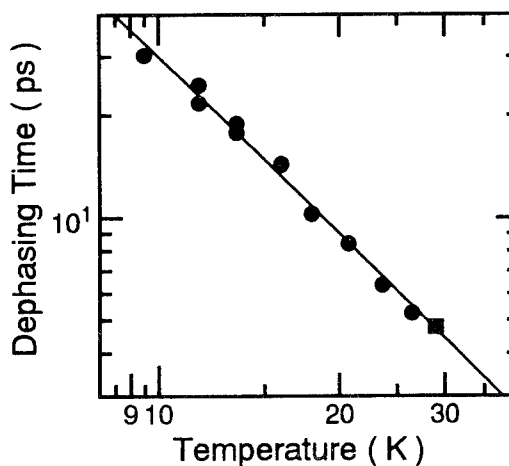
Fig. 3. Dephasing time versus the sample temperature. Solid circles and a square represent the T_2 measured by the ns incoherent dye laser and the SR, respectively.

CHARACTERISTICS OF SELF-PUMPED PHASE CONJUGATION IN A GAIN MEDIUM

R.P.M. Green, G.J. Crofts and M.J. Damzen

The Blackett Laboratory, Imperial College, London SW7 2BZ, U.K.
Tele. No. 071-589 5111

SUMMARY

Self-pumped phase conjugation using a nonlinear material in a self-intersecting loop geometry are attractive for their simplicity and efficiency. Loop systems based on photorefractive media [1] and Brillouin-active media [2,3] have been most extensively investigated. Several investigation have also been made of gain-media in loop geometries [4,5,6] although several issues relating to conjugation fidelity and the implementation of this device as a practical laser source have not been fully addressed. We present the results of investigation of the spatial, temporal and energy characteristics of the solid-state gain medium Nd:YAG in a loop configuration.

One of the investigated configurations is shown in Figure 1. A (transmission) gain-grating is formed in a flashlamp-pumped Nd:YAG amplifier (A_1) by a self-intersecting input beam (E_{in}) consisting of a linearly-polarised pulse in a TEM_{oo} single-longitudinal mode with FWHM duration 17ns. The grating diffraction efficiency (η) can be optimised by controlling the forward loop transmission factor (T_f) with a Faraday rotator and half-wave plate combination. The backward transmission factor (T_b) through this combination is approximately unity resulting in unidirection laser oscillation in the backward (conjugate) direction when the loop threshold condition is achieved $\eta G T_b > 1$, where G is the gain of an additional loop amplifier module (A_2). The amplifier rods (A_1 and A_2) were 100mm long by 6.35mm in diameter with small-signal single-pass gains up to 100, a beam crossing angle ~10mrad to achieve good overlap in amplifier A_1,and a loop roundtrip time $\approx$ 5ns.

The threshold input pulse energy was as low as ~10μJ for generation of a backward oscillation signal. For an input pulse up to ~10 millijoules the output energy was as high as 300mJ in a TEM_{oo} spatial mode and in the form of a single-longitudinal-mode pulse with duration ~10ns. The output pulse typically emerged approximately 30ns after the input pulse had entered the loop system. At higher input pulse energies, higher output energy could be achieved (up to 500mJ) but the spatial quality degraded from the diffraction-limit. Even in the case when the output was of the form of a diffraction-limited TEM_{oo} mode the

mode diameter was not generally the same as the input but was a function of the input pulse energy.

A fuller test of the phase conjugating ability of the loop amplifier consisted of i) inserting an aberrator (phase plate) in the loop and ii) using a non-TEM_{oo} input beam. The introduction of the loop phase plate (in location shown in Figure1) resulted in the distortion of the input beam as shown in Figure 2a however the output beam quality was almost unchanged and still a high-quality TEM_{oo} mode as shown in Figure 2b. The correction of the loop phase aberrations (~10-20x diffraction-limit) is a dramatic demonstration of the excellent corrective ability of the gain conjugator. The introduction of a non-TEM_{oo} beam was produce by passing the TEM_{oo} input beam through a pair of crossed wires giving a four-lobed beam with diffractive fringing in the transmitted beam. With suitable adjustment of the input energy it possible to reproduce the dominant four-lobe structure in the conjugate beam. It was noted that by decentralising the cross wires such that the relative intensity of the input lobes were not equal that the higher intensity lobes were much more efficiently reflected than the weaker lobes. This can be qualitatively understood since the diffraction efficiency of a gain grating depends on the strength of the interfering writing beams.

As a general conclusion of our present studies, the system has good corrective ability of loop aberrations and this is very promising for high-average power scaling of solid-state laser systems in which thermally-induced phase distortion is a major consideration for beam quality. The loop conjugator should be considered as an adaptive laser resonator with a holographic grating element formed by the self-intersecting beam. Such a system can produce output energy at least two orders of magnitude higher than a high-quality injecting pulse. The application of this device as a phase conjugator of input radiation with severe aberration is not so clear according to our present results but more work is still required to ascertain its full potential.

References

[1] A.A. Zozulya, IEEE J.Quantum Electron., QE-29, 538 (1993)
[2] V.I. Odintsov and L.F. Rogacheva, JETP Lett., 36, 344 (1983)
[3] M.S. Barashkov et al, Sov. J.Quantum Electron., 20, 631 (1990)
[4] I.M. Bel'dyugin et al, Sov. J. Quantum Electron., 14, 602 (1984)
[5] M.J. Damzen, R.P.M. Green and G.J. Crofts, Opt. Lett., 19, 34 (1994)
[6] V.A. Berenberg et al, Opt Spectro., 65, 302 (1988)
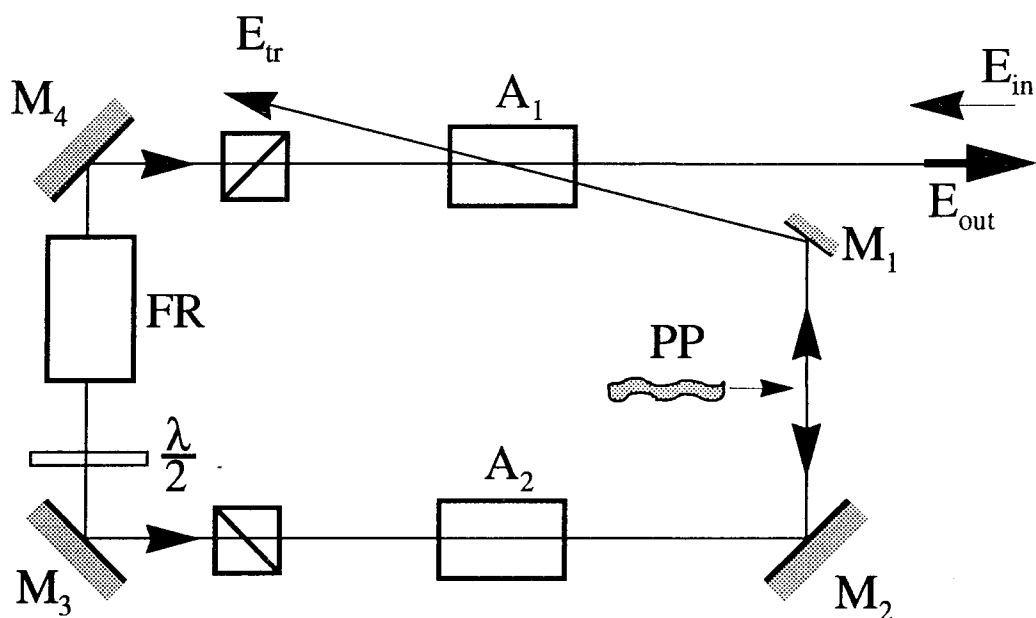
Figure 1. Schematic diagram of experimental laser system
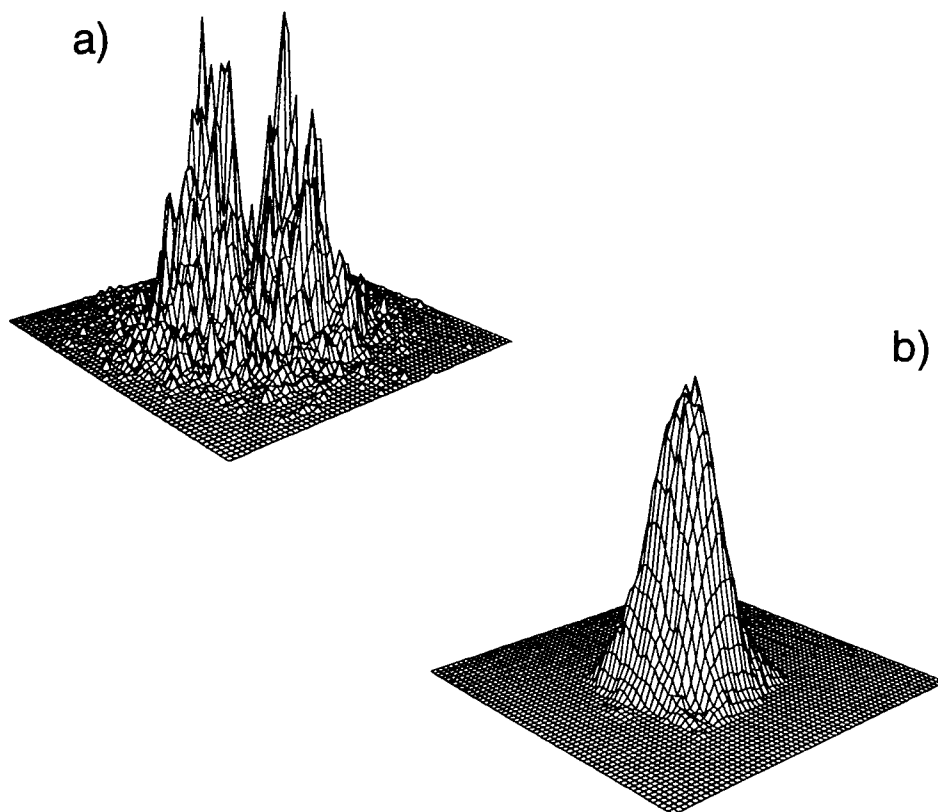
Figure 2. Spatial beam profiles with a loop phase aberrator.
a) Incident aberrated loop beam, b) Compensated backward conjugate beam.

SBS Threshold Reduction Using Feedback

John J. Ottusch and David A. Rockwell

Hughes Research Laboratories

3011 Malibu Canyon Road, Malibu, CA 90265

(310) 317-5000

(310) 317-5483 (FAX)

Ordinary self-pumped phase conjugate mirrors (PCMs) that employ stimulated Brillouin scattering (SBS) turn on when the gain exponent ($G = gIL$) is in the range of 25 to 30. Feedback makes it possible to reduce this threshold gain considerably. A number of theories have been developed to describe SBS with feedback, most of which are specific to highly aberrated pump beams and steady-state conditions. These theories predict that by introducing feedback the gain threshold can be reduced to as little as $G_{th} = 0.35$ [1]. Recently, Scott [2] proposed a theory of SBS with feedback that departs from previous theoretical approaches. First, it specifically focuses on Gaussian beams. Second, it explicitly recognizes that the nonlinear medium has a finite response time; consequently the evolution of the nonlinear process is limited by the finite duration of the pump pulse. Although these theoretical features provide new insights into SBS with feedback, further analysis is required to bring the theory into agreement with our measurements, some of which were motivated by discussions with Scott.

We performed several experiments involving SBS with feedback using focused, nearly diffraction-limited pump beams. Figure 1 shows two variations of the loop arrangement for SBS with 100% feedback in which the first-pass transmitted pump beam is recycled and

(a)   (b)
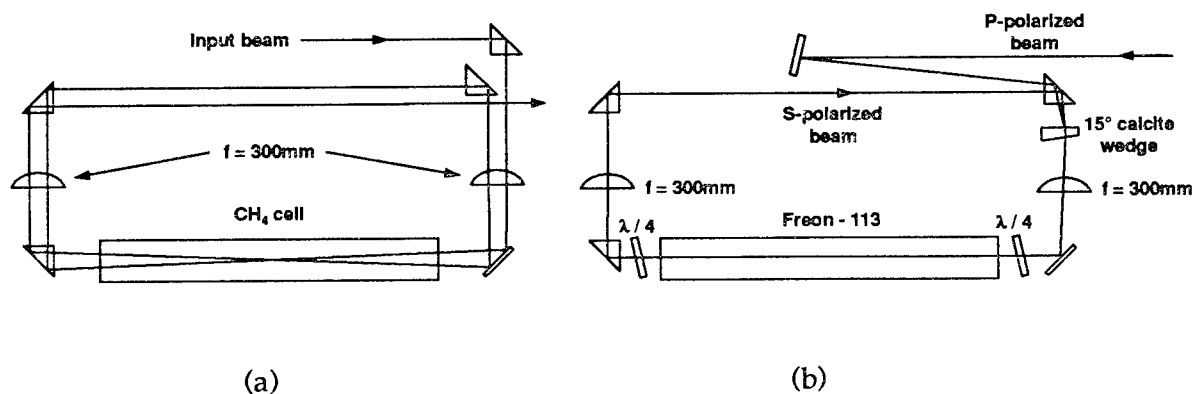
Figure 1. Loop geometries for SBS with feedback.

refocused to the same point as the focused first pass pump beam. In Fig. 1(a), all beams are linearly polarized, and a 20 mrad angle separates the first and second passes. In Fig. 1(b), quarter-wave retardation plates make the polarization of the transmitted pump beam orthogonal to that of the incident pump beam so the two beams can be made to overlap exactly inside the interaction region, again with negligible loss. This scheme also differs from the first in that the beam polarizations allow only the Stokes beams produced by Brillouin-enhanced four-wave mixing to contribute to the phase conjugate output.

Figure 2. SBS threshold reduction factor as a function of the ratio of the pump pulse duration and the phonon lifetime, t_{pump} / t_{phonon}. The calculated TRF (shown as a line) is 7.7 in the steady-state limit.

In the first case, using CH_4 as the SBS medium, it was possible to measure the threshold reduction factor (the SBS threshold without feedback vs. with feedback) for several different values of t_{pump} / t_{phonon} by independently varying the pump pulse width and the acoustic lifetime (which depends on CH_4 pressure). According to Scott's theory, the SBS threshold power is lowest for very long pulses (i.e. closest to steady-state conditions) and increases monotonically as t_{pump} / t_{phonon} decreases (for very short pulses, i.e. $t_{pump} / t_{phonon} \sim 1$, the theory is no longer appropriate). From the theory of transient stimulated scattering [3] we can calculate the threshold power for SBS without feedback. The ratio is the calculated threshold reduction factor (TRF). Figure 2 shows the comparison between theory and experiment. The measured SBS TRF does not exhibit the consistently increasing trend as a function of t_{pump} / t_{phonon} predicted by the theory; it was always about 2.5. When we changed to a faster-responding SBS medium, namely Freon-113, we expected an even greater improvement in TRF. However, the measured SBS TRF for Freon-113 was only 3.

When Freon-113 was used in the feedback geometry of Figure 1b, the SBS TRF doubled to 6. Representative data are shown in Figure 3. We also observed that higher-order Stokes could be

Figure 3. Stokes energy vs. pump energy with and without feedback. Geometry is that of Figure 1b. Pump pulse FWHM is 160ns. SBS medium is Freon-113.

produced using this geometry (in contrast to standard SBS generators which don't employ feedback). By increasing the pump power we eventually reached the point where the Stokes beam was strong enough to generate its own Stokes-shifted beam. In our experiment, the threshold power for second Stokes was about 5 times the threshold power for first Stokes. This second Stokes beam propagates in the same direction as the pump beam. Increasing the pump power produced still higher Stokes orders.

Figure 4. Comparison of pulse shapes: a) pump, b) Stokes with feedback, and c) Stokes without feedback. SBS medium is Freon-113 (phonon lifetime ~ 0.7ns)

The temporal coherence properties of the output Stokes signal are also affected by feedback. Without feedback, phase jumps occur randomly on a time scale of tens of phonon lifetimes [4]. They manifest themselves in the Stokes pulse shape as sudden intensity fluctuations (see Figure 4). Properly-phased feedback eliminates phase jumps altogether.

We gratefully acknowledge Andrew Scott for many technical discussions and for sharing the details of his theory prior to publication. We also acknowledge German Pasmanik for suggesting the loop geometry of Fig. 1(b).

References

1. D. A. Nikolaev and V. I. Odintsov, Sov. J. Quantum Electron., 19 (9), 1209 (1989).

2. A. Scott, in Technical Digest, Conf. on Lasers and Electro-Optics, (Optical Society of America, Washington, DC, 1993), paper CThJ3.

3. M. G. Raymer and J. Mostowski, Phys. Rev. A, 24 (4), 1980 (1981).

4. M. S. Mangir, J. J. Ottusch, D. C. Jones, and D. A. Rockwell, Phys. Rev. Lett. 68, 1702 (1992).

UV Laser Source for Remote Spectroscopy by Multiple Nonlinear Conversion of a Nd:YAG Laser

E. Gregor, J. Sorce, K.V. Palombo D.W. Mordaunt and M Ehritz

Hughes Aircraft Company Building E1, M. S. B 118, P. O. Box 902
El Segundo, CA 90245
310-616-3955

Laser sources in the ultraviolet (UV) spectrum specifically in the range from 250 nm to 350 nm, are of great interest for long range remote fluorescence spectroscopy. The detection at a stand-off range of biological and organic compounds is accomplished by monitoring the returned energy in the fluorescence spectrum of the compound in question. A multiple UV wavelength laser or a tunable laser source provides the ability to improve the discrimination between compounds with similar spectra. Vibrational stimulated Raman scattering (VSRS) in the UV has been reported in 1979 using excimer lasers (223 nm, 248 nm and 308 nm)(Ref. 1), but with limited efficiency (25%).

We report here our experimental results of efficient (87%) rotational stimulated Raman scattering (RSRS) and vibrational stimulated Raman scattering (VSRS) using the fourth harmonic from a phase conjugated master oscillator power amplifier Nd:YAG laser with high beam quality . We present experimental data obtained for Hydrogen and Deuterium gases used as Raman mediums.
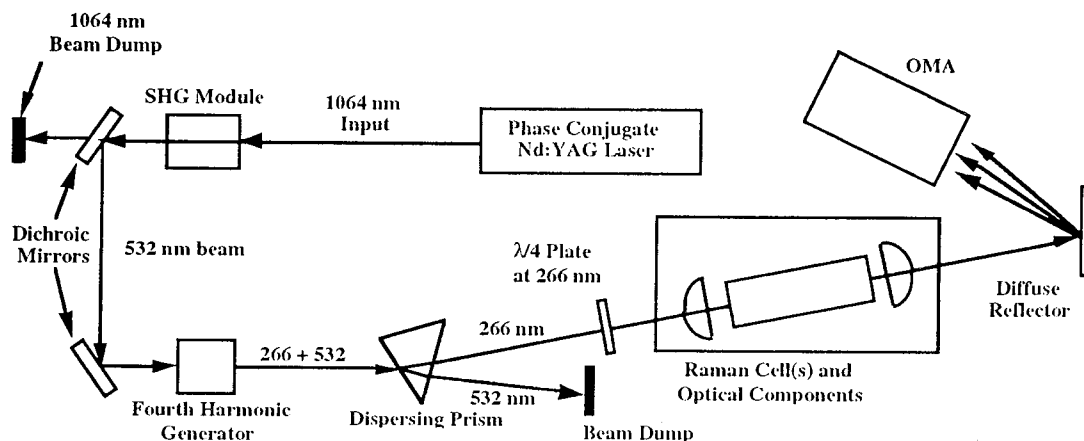
Figure 1. Optical diagram of the UV Raman laser with multiple wavelength output.

The phase conjugate laser used in these experiments was reported previously (Ref. 2,3,4,5) and features high beam quality for efficient second harmonic, fourth harmonic

and VSRS/RSRS conversion. Our present experimental setup is depicted in Figure 1. The 1064 nm beam is doubled twice to generate the fourth harmonic at 266 nm. This wavelength is separated from the remaining 532 nm using a prism and then focused into a Raman gas cell. The output from the Raman cell is recollimated and the wavelength distribution is measured with an Optical Multichannel Analyzer (OMA). The laser has near diffraction limited beam quality and 4 to 6 longitudinal modes. The pulse width is 20 ns in the UV and the 100 mJ beam was used at 1 Hz .

Raman Line	Wavelength (nm)	% of Output
RP	266	13
R1	270	25
R2	275	23
R3	279	13
R4	283	3
V1A1	294	2
V1	299	4
V1R1	304	3
V1R2	310	4
V1R3	316	2

RP = Residual pump energy
Rn = nth order rotational Stokes line
Vn = nth order vibrational Stokes line
An = nth order rotational anti-Stokes line
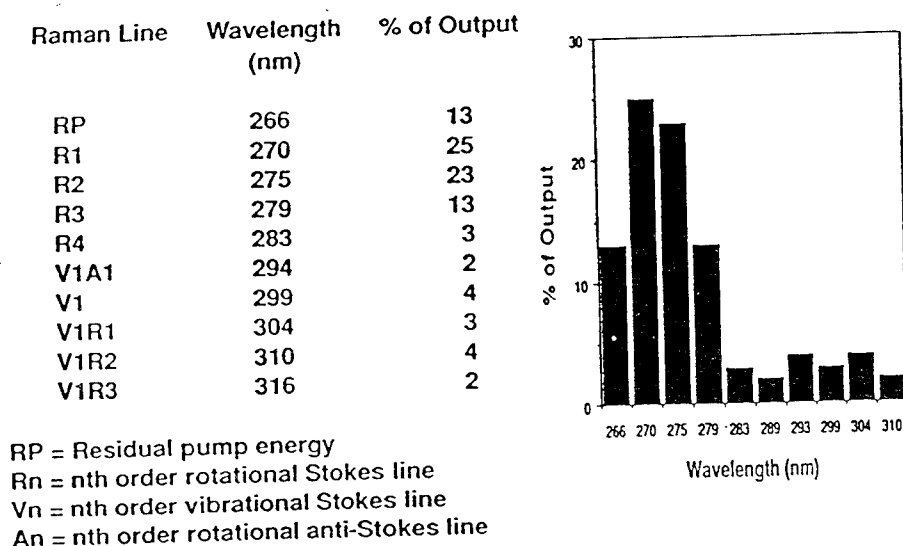
Figure 2. UV rotational stimulated Raman conversion in Hydrogen gas using the 266 nm pump laser with 87% efficiency.

For RSRS the 266 nm laser beam was circular polarized and VSRS was suppressed by the use of lower pressures and larger f/numbers. In Figure 2 we show our results using Hydrogen gas as the Raman medium. Efficient conversion to the Raman lines reached up to 87%.

For efficient VSRS the laser beam was linearly polarized and the pressures were optimized at a higher level and the f/numbers were lower. In Figure 3a we show typical results using Deuterium gas. However, at the UV wavelength of 266 nm the VSRS gain is 6 to 8 times higher then for example at 532 nm and efficient VSRS is obtained at low pressures (54 atm). The first (289 nm) and the second (316 nm) Stokes lines are efficiently generated. By reducing the pressure to 2 atm a combination of RSRS and VSRS are obtained (Figure 3b).
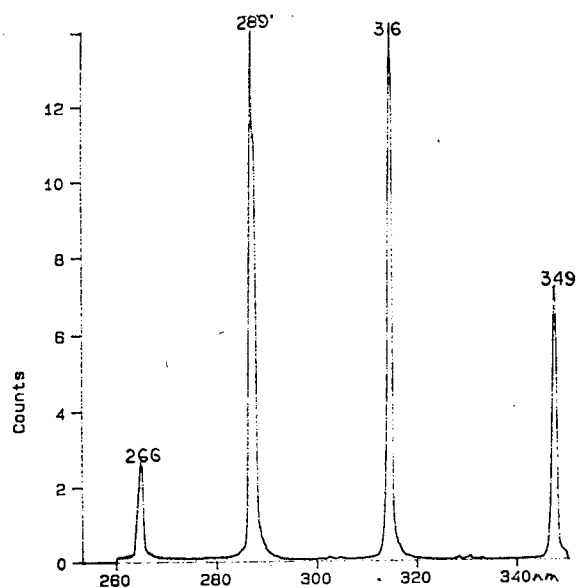
Figure 3a. Vibrational stimulated Raman conversion in Deuterium gas using a 266 nm pump laser (calibrated relative output energy with >80% into Raman lines)
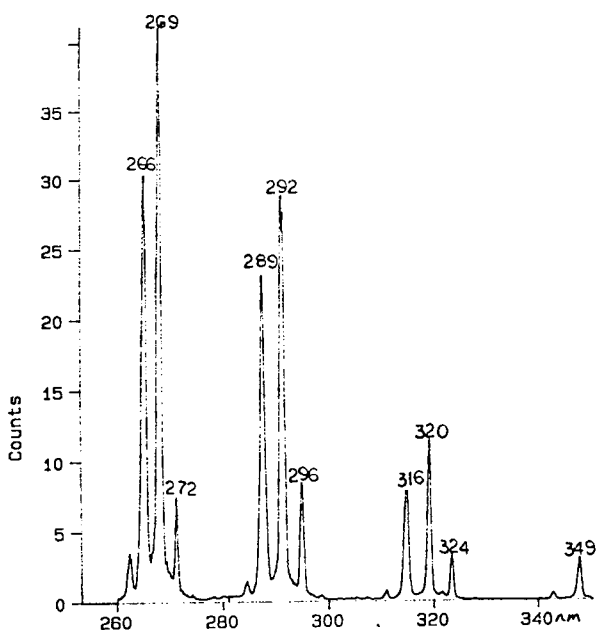
Figure 3b. Rotational and vibrational Raman conversion in Deuterium gas using a 266 nm pump laser.(calibrated relative output energy with >80% into Raman lines)

In conclusion, we have experimentally demonstrated an efficient approach for a multi-wavelength UV source based on the solid state Nd:YAG laser using second harmonic, fourth harmonic and vibrational and rotational stimulated Raman scattering. With the advances in efficiency of the diode pumped Nd:YAG laser and the new high optical quality UV transparent efficient crystals (BBO) efficient UV solid state laser sources are achievable. When these UV lasers are combined with the mature Raman technology, multiple wavelengths in the 250 nm to 350 nm range are efficiently obtained. This spectral range is of special interest for long range remote fluorescence spectroscopy of organic and biological compounds in the atmosphere.

REFERENCES
1. T.R. Loree, R.C.Sze, D.L. Barker, and P.B. Scott: IEEE J. QE. 15, 337 (1979)
2. S.C. Matthews, J.S. Sorce: SPIE Proc.1220, Nonlinear Optics, (1990)
3. E. Gregor, D.W. Mordaunt, O. Kahan, A.R. Muir, and M. Palombo: SPIE Proc. 1627, Solid State Lasers III, 65 (1992)
4. J.S. Sorce, K. Palombo, S.C. Matthews, and E. Gregor: OSA Proc. 13, Advanced Solid-State Lasers, (1992)
5 E. Gregor, D.W. Mordaunt, and K.V. Strahm: OSA Proc. 6, Advanced Solid-State Lasers, (1991).

BEAM COMBINATION IN RAMAN AMPLIFIERS

Jessica Digman
DRA Fort Halstead, Sevenoaks, Kent , TN14 7BP
United Kingdom
Tel. (0959) 515093

Richard Hollins
DRA Malvern, Great Malvern, Worcs. WR14 3PS
United Kingdom
Tel. (0684) 894471

The energy capability of pulsed laser systems can be extended by using a Raman amplifier to combine the energy of several pump beams into a single output [1]. Energy is extracted from the pump beam(s) by the amplification of a Raman shifted Stokes seed pulse. Beam combination has particular application to neodymium based visible lasers in which the pulse energy can be limited by the damage threshold of the second harmonic generating crystal.

The properties of a Raman amplifier pumped by frequency doubled Nd:YAG have been investigated experimentally using the geometry shown in Figure 1. The $4155cm^{-1}$ vibrational shift in hydrogen was used to generate Stokes radiation at 683nm. Combination of energy from two separate (but mutually coherent) pump beams into a single Stokes output has been successfully demonstrated. The Stokes energy extraction for amplifiers driven by single and double pump beams are shown Figure 2. Amplified Stokes beams of very high spatial quality were obtained when a single pump was used; interference effects produced some distortion of the output in the two beam system (Figure 3).

The effect of the spatial, temporal and phase characteristics of the incident beams has been investigated theoretically. Results show that serious limitations in efficiency are imposed by the Gaussian spatial profile and the broad bandwidth of the laser used in the experiments. In the latter case, the presence of many longitudinal modes inhibits Stokes growth in the early stages of the amplifier due to the lack of correlation between the injected Stokes signal and pump [2]. With sufficient gain-length, the phases of the Stokes modes evolve so that the two fields become correlated. This process is illustrated in Figure 4 in which the phase difference, $\Phi_p-\Phi_s$, between each pump-Stokes mode converges to a common value.

1. Partanen and Shaw,"High power forward Raman amplifiers employing low pressure gases in light guides. (i) Theory and applications," JOSA B, **3**,10,(1986).

2. Eggleston and Byer, "Steady state stimulated Raman scattering by a multimode laser," IEEE JQE, **QE-16**,8,(1980).

Figure 1a. Raman beam combination experimental layout

Nd:YAG OSCILLATOR

532 nm PUMP

SHG

Nd:YAG AMPLIFIER

SHG

Nd:YAG AMPLIFIER

RAMAN GENERATOR

STOKES SEED 683 nm

RAMAN AMPLIFIER

FILTER
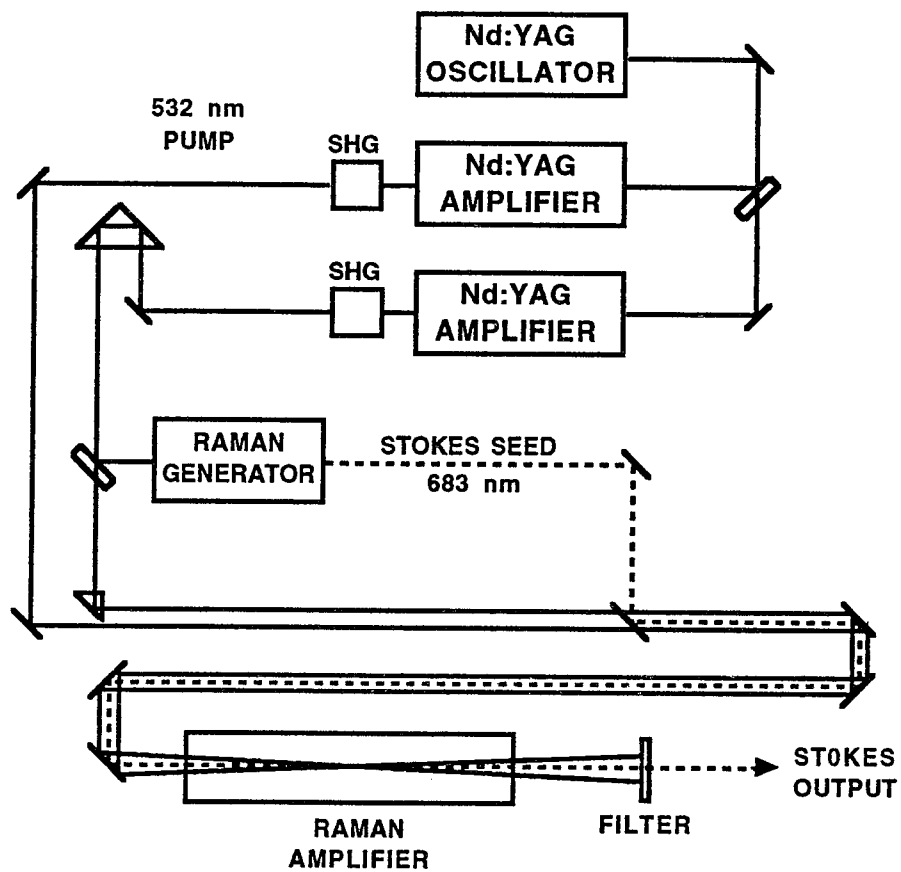
STOKES OUTPUT

Figure 1b. Amplifier cell geometry

PUMP 1

SEED

PUMP 2

RAMAN AMPLIFIER CELL
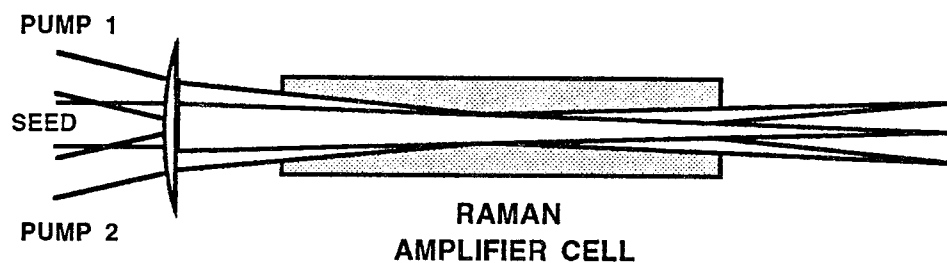
Figure 2. Beam combination experimental results: comparison between one and two beam pumping
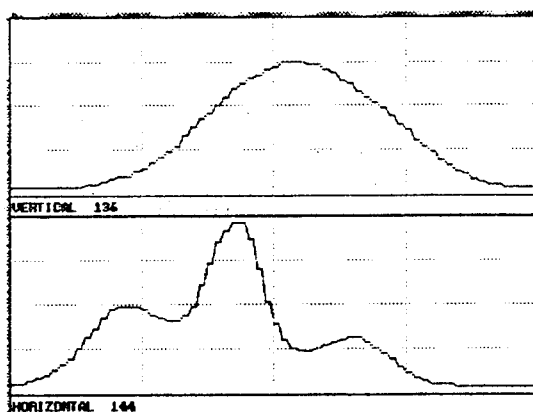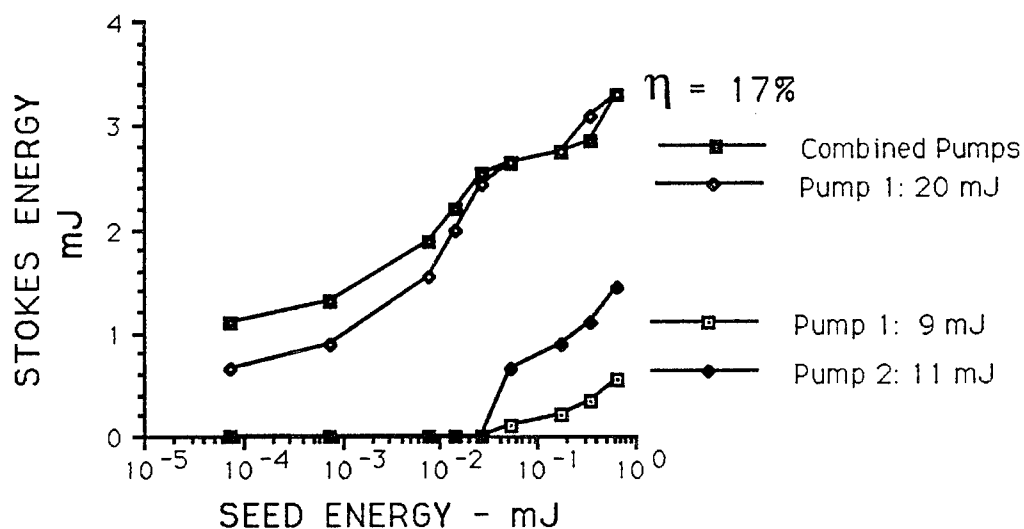
Figure 3. Cross-sections through Stokes output spatial profile

Figure 4. Phase-pulling during Raman amplification

PHASE PLOT: 20 MODES

$\Phi_p - \Phi_s$
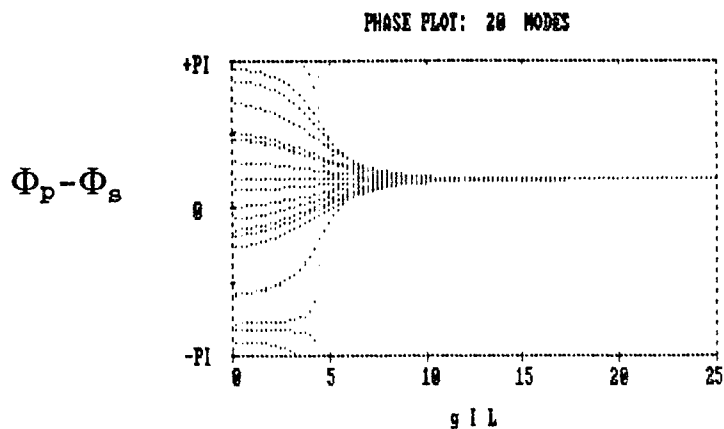
How quickly self-Raman effects and third-order dispersion destroy squeezing

Yinchieh Lai and Shinn-Sheng Yu

Institute of Electro-Optical Engineering, National Chiao-Tung University

Hsinchu, Taiwan, Republic of China

Tel:886-35-712121 ex 4277   Fax:886-35-716631   E-mail: yclai@cc.nctu.edu.tw

Pulse squeezed state generation using optical fibers has attracted a lot of attention recently. By using a fiber loop interferometer, pulse squeezed vacuum has been successfully generated at the 1.3 μm wavelength with 5 dB squeezing observed[1] and has been successfully generated at the 1.55 μm wavelength with 1.1 dB squeezing observed[2]. In the squeezing experiment at 1.3 μm, pulses from a modelocked YAG laser with a 20 ps pulseduration were used. At this wavelength, the group velocity dispersion is close to zero. In the squeezing experiment at 1.55 μm, pulses from a modelocked color-center laser with a 200 fs pulseduration were used. The group velocity dispersion is negative and the pulses propagated inside the optical fiber are actually optical solitons. In going from longer pulses to shorter pulses, one gains the advantages of a high peak power at the same pulse energy and thus a shorter propagation distance in order to achievable appreciable squeezing. However, it is well known that when the pulseduration is getting shorter, the self-Raman effects[3,4] and third order dispersion will start to affect pulse propagation. Physically, both self-Raman effects and third order dispersion cause additional perturbations to the optical field and thus one would naturally expect that they will eventually destroy squeezing. The problem is how quick the destruction is. This is the question we would like to answer in the present paper.

Recently, based on our previous work[5], we have developed a general quantum theory of nonlinear pulse propagation. We also worked out a self-consistent quantum theory of self-Raman effects in optical fibers. Our approach was based on the linearization approximation, the conservation of commutator brackets, and the concept of adjoint systems. A general, self-consistent scheme was developed to quantize nonlinear optical pulse propagation problems and a general computation procedure ("the backpropagation method") was developed to calculate the quantum uncertainties of the inner product between any given function and the (perturbed) field operator. By utilizing these results, we can calculate the magnitude of squeezing when an optical pulse propagates through the optical fiber in the presence of self-Raman effects and third-order dispersion. The following three situations have been considered :

1. 50 fs and 100 fs (FWHM) solitons.

2. 100 fs, 200 fs, and 1000 fs (FWHM) sech pulses with zero group velocity dispersion.

3. 100 fs, 200 fs, 1000 fs and 20 ps (FWHM) square pulses with zero group velocity dispersion.

Due to the limitation of space, in this summary we only show the results for 50 fs solitons, 1000 fs sech pulses and 20 ps square pulses. The dotted lines are results without self-Raman effects and third-order dispersion. The lines labeled "KR" are results with self-Raman effects only. The lines labeled "D3" are results with third-order dispersion only. The lines labeled "KR+D3" are results with both self-Raman effects and third-order dispersion.

Based on our results, we would like to make the following comments :

1. The influences of self-Raman effects and third-order dispersion on squeezing are mainly due to the transformation of the original quantum noise.

2. For solitons, the squeezing ratio is more sensitive to the self-Raman effects than to the third-order dispersion. This is due to the existence of second-order dispersion.

3. The self-Raman effects alone have big impacts only when the pulse duration is below 100 fs. However, if the third order dispersion is also present, then they can generate some combined influences.

4. For sech pulses at zero dispersion, with no self-Raman effects and third-order dispersion, the squeezing ratio saturate after reaching 0.16. Physically this is due to the build-up of chirp across the pulse and is an disadvantage to work in the zero dispersion regime.

5. At zero dispersion, the build-up of chirp across the pulse can be reduced using square pulses. However, the improvement is limited due to the third-order dispersion.

Since in our calculation we did not include in the effects of loss and additional classical noises (i.e., noises due to Guided Acoustic Wave Brillouin Scattering[6]), the results given here represent the lower limits of the squeezing ratio at different situations. It is straightforward to include in these additional effects in our formulation since our theory are applicable to general pulse propagation problems. Finally, our results seem to suggest that solitons are the only qualified candidates for achieving very large squeezing using optical fibers.

References

1. K. Bergman and H.A. Haus, *Opt. Lett.* **16**, 663(1991).

2. M. Rosenbluh and R. M. Shelby, *Phys. Rev. Lett.* **66**, 153(1991).

3. J. P. Gordon, *Opt. Lett.* **11**, 662(1986).

4. R.H. Stolen, J.P. Gordon, W.J. Tomlinson, and H.A. Haus, *J. Opt. Soc. Am. B* **6**, 1159(1989).

5. Y. Lai, *J. Opt. Soc. Am. B* **10**, 475(1993).

6. R.M. Shelby, M.D. Levenson, and P.W. Bayer, *Phys. Rev. B* **31**, 5244(1985).

classical nonlinear phase shift
(normalized propagation distance)
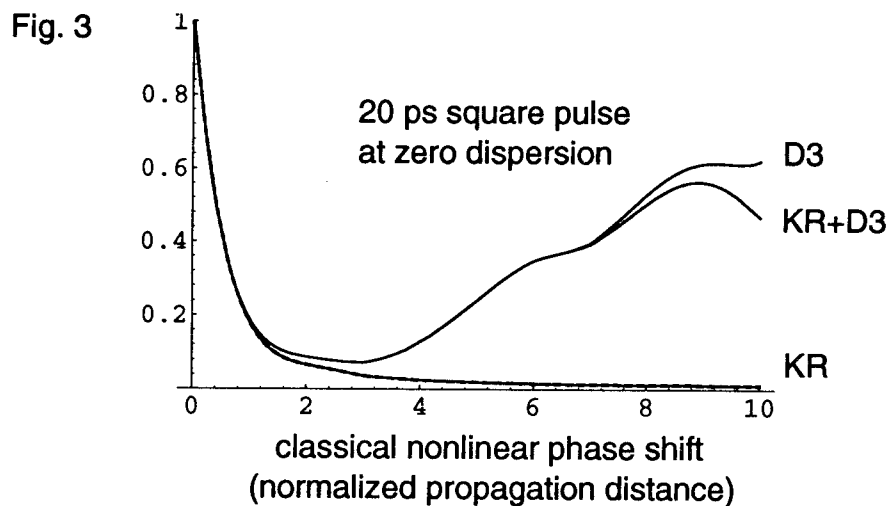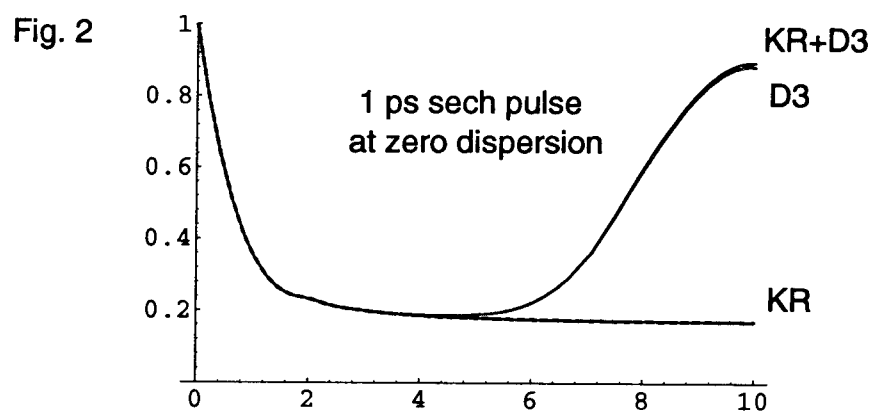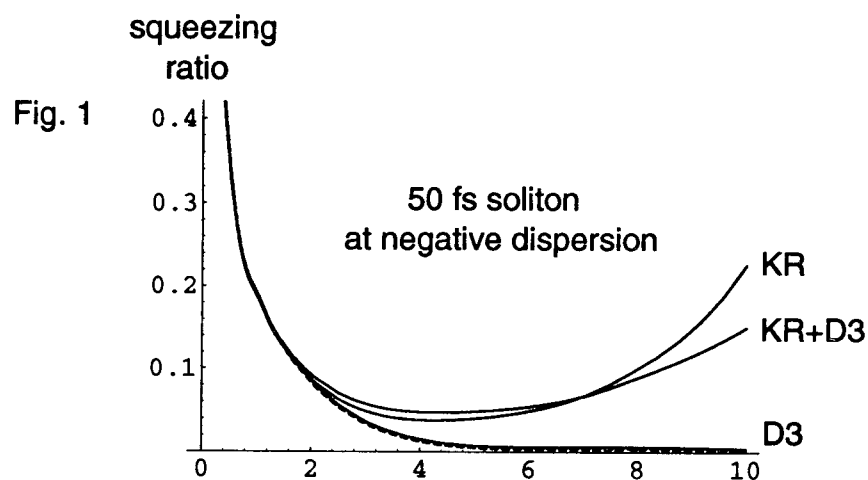
Low Power Visible-Near Infrared (0.4mm-5mm) Self-Starting Phase Conjugation with Liquid Crystal

Y. Liang, H. Li, I.C. Khoo

Pennsylvania State University, University PArk, PA

Self-starting optical phase conjugation (SSOPC) is an interesting process which has good application potentials. It has been observed in several material systems, e.g., photorefractive materials [1], atomic sodium [2], and nematic liquid crystals [3] with low power lasers, and Brillouin cells [4] with high power lasers. Among these materials, nematic liquid crystals with their broadband (visible-infrared) birefringence are prime candidates for realizing low power SSOPC in spectral regime not accessible by the others. This was indeed demonstrated recently [3] using stimulated thermal scattering effect. Although the process could be applicable over a very wide spectral regime owing to the broadband birefringence and large thermal index gradient of nematic, a major drawback is the high sensitivity of the process to the temperature vicinity to T_c, the nematic to isotropic phase transition temperature. This requires very stable temperature control, and imposes limitations on the incident laser power used and therefore the efficiency of the process.

In this paper, we report the first observation, to out knowledge, of self-starting optical phase conjugation effect in a nematic liquid crystal using stimulated orientational scattering effect. The orientational fluctuations in nematics naturally provide an efficient energy coupling between the ordinary and the extraordinary waves (c.f. Figure 1).
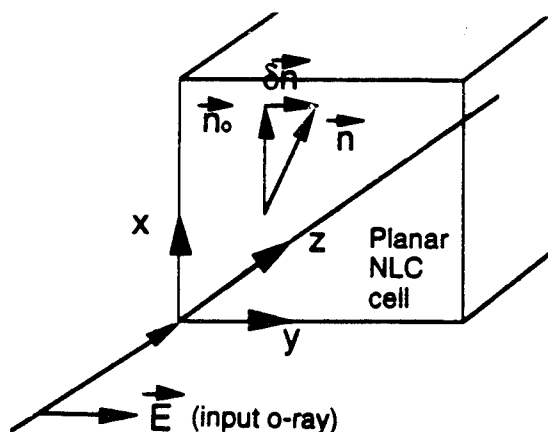
Figure 1. Director axis fluctuation causes e-o wave scatterings in a planar aligned nematic liquid crystal sample.

The experiment set-up is shown in Figure 2. The liquid crystal we used is pure E-7 (EM Chemicals) which has nematic to isotropic phase transition of 63°C. The experiment is done at room temperature. The LC sample is 200µm thick and planar aligned. The incident beam is linearly polarized with its polarization vector making an angle of 45° to the director axis of the liquid crystal. A polarizer is placed behind the NLC cell, so that the reflected beam is also linearly polarized with its polarization perpendicular to that of the incident beam. The phase conjugation signal is taken out by a beam splitter and observed in the far field.

When the power of incident beam is small ($<$ 600mW), there is only noise background. As the pump power increases to about 600mW, a bright spot of phase conjugated signal appears from the fuzzy noise field (see the photo insert in Figure 2). We noticed that in spite of the aberrations imparted by the input laser beam and gas approximately the same divergence. The efficiency of the phase conjugation reflection is measured to be a few percents at the power used, with an onset time of about 20ms.

Because of the broadband birefringence of liquid crystal [Figure 3], and the low sensitivity

of the two-wave mixing gain on the wavelength, the process can be realized in a rather broad spectrum, from the visible, through the diode-laser wavelength, to the infrared. In particular, since
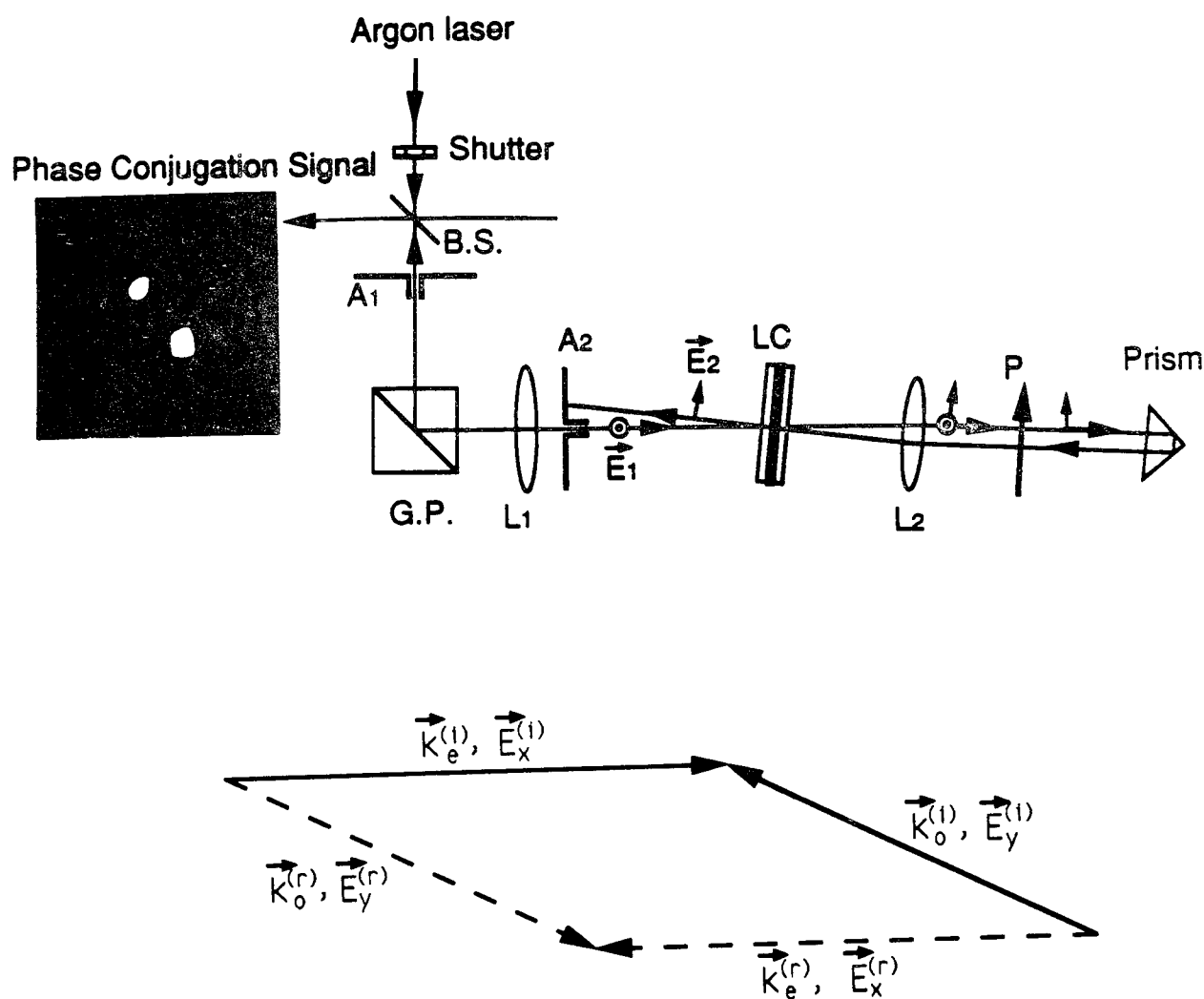
Figure 2. Schematic depiction of the experimental set-up used in the SOS self-starting phase conjugation effect and the wave vector phase matching condition.. [LC: liquid crystal, $L_{1,2}$: lens, P: polarizer, B.S.: beam splitter, G.P.: Glan Prism, $M_{1,2}$: mirrors, $A_{1,2}$: pin holes] Photo insert shows the obtained phase conjugation reflection. Double dots are due to the glass splitter used.
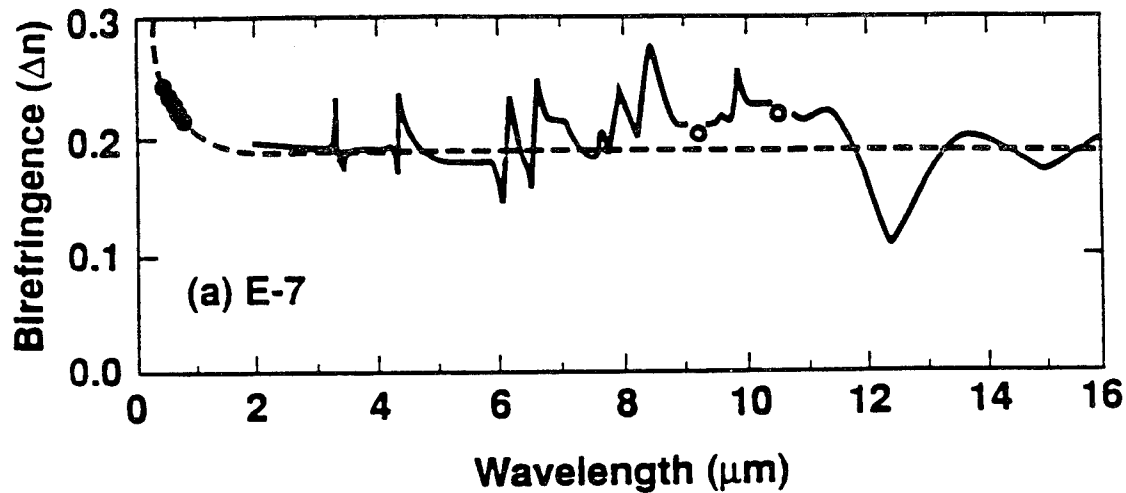
Figure 3. Broadband birefringence of the liquid crystal E7 from 0.4μm - 16μm.

the absorption and scattering loss of nematics such as E7 are quite low in the 0.4μm - 5μm area, application of the SSOPC effects observed here to phase conjugating devices in this spectrum regime are clearly feasible [5]. We will presenting quantitative theoretical estimates of the threshold and device performance characteristics.

Reference

1. M. Cronin-Golomb, B. Fisher, J. O. White, and A. Yariv, IEEE J. Quantum Electron.JQE-20, 12 (1984).
2.C. J. Gaeta, J. F. Lam and R. C. Lind, Opt. Lett. 14, 245 (1989); M. Vallet, M. Pinard and G. Grynberg, Opt. Lett. 16, 1071 (1991).
3. I. C. Khoo, H. Li, and Y. Liang, Opt. Lett., 18, 1490 (1993).
4. See for example, B. Ya. Zeldovich,N. F. Pilipetsky and V. V. Shkunov, in " Principles of Phase Conjugation," Springer-Verlag, Berlin (1995)
5. I. C. Khoo and S. T. Wu, Optics and Nonlinear Optics of Liquid Crystals, (World Scientific, Singapore, 1993).

Dual-wavelength-pumped Raman conversion of broad band lasers

Tsuneo Nakata, Harunobu Itoh, Tadashi Yamada, and Fumihiko Kannari
Department of Electrical Engineering, Keio University
3-14-1 Hiyoshi, Kohoku-ku, Yokohama 223, Japan
telephone:+81-45-563-1141 ex. 3301

In a recent paper[1] we have proposed dual-wavelength-pumped Raman-resonant four-wave mixing, where an intense secondary pump and its Stokes radiation are applied in addition to the primary pump laser with a proper phase matching angle to enhance the Raman phonon amplitude (see Fig. 1). This method enables one to efficiently up- or down-convert a primary pump laser light whose intensity is not high enough to induce an efficient nonlinear frequency conversion by itself. This feature is particularly useful for converting a laser wavelength in VUV spectrum region, where a high-power laser source can hardly be developed. We have carried out numerical calculations on the dual-wave pumped Raman process assuming an F_2 laser with the wavelength of 157.6 nm for the primary pump, and a KrF excimer laser (248 nm) for the secondary pump. More than 80% theoretical efficiencies are possible for either Stokes or anti-Stokes conversion [2]. These analyses were carried out by assuming single-frequency radiations for all the pumps and Raman-converted components. However, this assumption is inappropriate for the conversion of VUV lasers, since conventional spectrum narrowing methods (e.g. ethalon, injection locking) are inapplicable in this spectrum region. For example, a typical line width of a free-running F_2 laser is 10~50 pm.

In this paper we present a numerical analysis of dual-wavelength-pumped Raman process taking account of a finite band width for the primary pump laser, while still assuming a single frequency laser for the secondary pump laser. This assumption is much more realistic than that in the previous analyses [1], because in practical experiments one can use a narrow band laser in visible or UV spectral region as the secondary pump source. The dual-wavelength pumped Raman-resonant four-wave mixing with a broad-band primary pumping laser can be described in a cw analysis by deriving coupled equations describing spatial evolution of self-correlation functions of the primary pump and its Stokes field components. The Fourier transform of the self-correlation function corresponds to the spectrum profile. These self-correlation functions are coupled through a cross-correlation function of the relevant fields.

Figure 2 shows evolutions of the self-correlation functions $\langle F_i^*(t')F_i(t)\rangle$, where F_i's are the complex field envelope for i-th wave (i=0 for primary pump, i=-1 for 1st Stokes of primary pump). An F_2 laser with the spectral width of 100 pm (FWHM) and the intensity of 4 MW/cm^2 was assumed for the primary pump, and a single-frequency KrF excimer laser (λ=248nm) with the intensity of 40 MW/cm^2 was assumed for the secondary pump. The Stokes field of the *secondary* pump is seeded in the phase-matched direction with the intensity of 0.4 MW/cm^2. The Raman medium is assumed to be H_2 gas with a density of 20 amagats. The self-correlation functions at |t-t'|=0 corresponds to the intensity. Therefore, one can observe that an almost complete conversion from the pump to the Stokes occurs at a certain propagation distance z, as in the results obtained with a single-frequency laser [1]. One can also see that the profiles of the self-correlation functions of the primary pump and its Stokes waves are kept almost the same as that of the incident primary pump radiation at z=0. Therefore, the spectrum of the primary pump laser is maintained in the the Stokes spectrum. This is quite natural because a strong phase-locking occurs in the dual-wave pumped Raman process with an intense secondary pump that fixes the relative phase of a primary pump and its Stokes waves to that of a secondary pump and its Stokes waves. This is also verified analytically from the coupling equations.

Figure 3 shows similar calculation results to Fig. 2, but with an increased primary pump bandwidth of 1.0 nm (FWHM) and a medium density of 60 amagats. All the other parameters are fixed as those used in Fig. 1. Different conversion property from that in Fig. 1 is observed. At the

end of propagation (z~11.5cm), the self-correlation function width of the Stokes beam is slightly wider than that of the pump self-correlation function, therefore the Stokes field becomes a narrower band width than the pumping field. In turn, the complete intensity conversion from the primary pump to the Stokes, which is observed in Fig. 2, is not found in Fig. 3. These are caused by wavelength dispersion, which makes a *cross*-correlation function between the pump and the Stokes asymmetric with respect to t and t'. This dispersion effect arises from a time-derivative term in the coupled equations [1], which gives only small contribution in the single-frequency pumping. Contribution of the time-derivative term increases as the phase fluctuation of the pump laser increases. Theoretical discussions on the dispersion effect, as well as numerically determined conditions for optimizing the spectral narrowing effect, will be given at the presentation.

[1] T. Nakata and F. Kannari, J. Opt. Soc. Am. B10, 1870 (1993).
[2] T. Nakata, T. Yamada, and F. Kannari, digest of papers presented in QELS'93, Baltimore, ML (1993) paper QTuK34.
[3] A. P. Hickman, J. A. Paisner, and W. K. Bischel, Phys. Rev. A33, 1788 (1986).
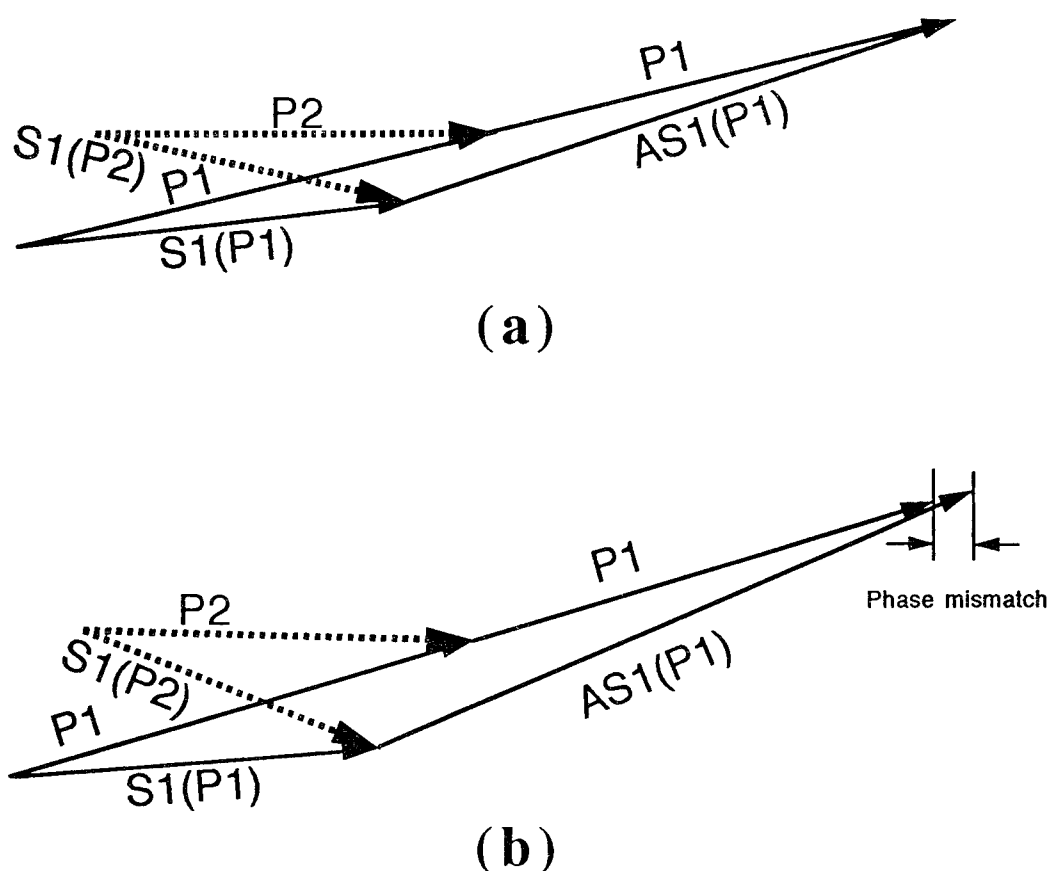
Fig. 1 Phase-matched wave-vector configuration for dual-wavelength-pumped Raman-resonant four-wave mixing (a). Selective enhancement of Stokes conversion of the primary pump is possible by introducing a significant phase-mismatch for the anti-Stokes process (b).
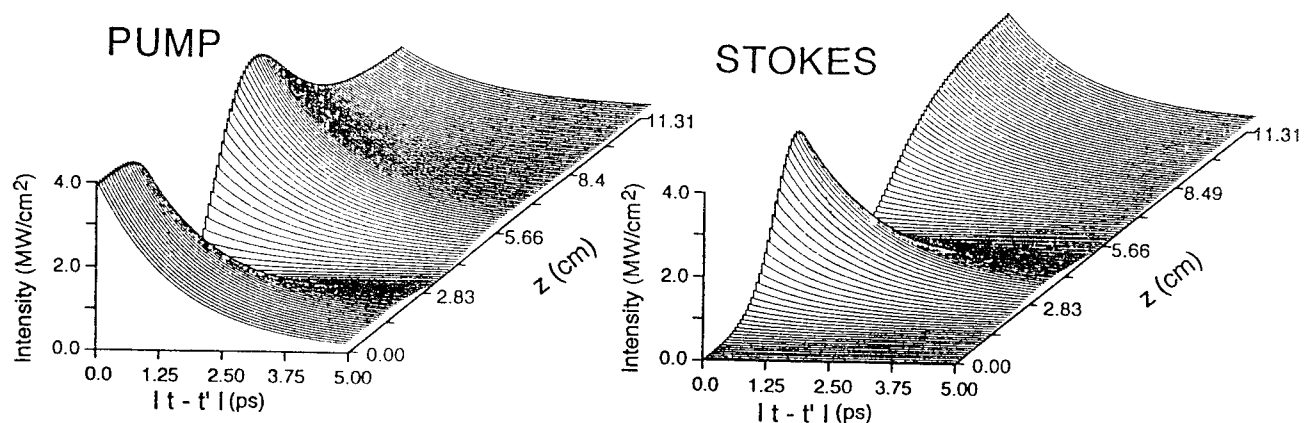
Fig. 2 Self-correlation functions of the primary pump $<F_0^*(t')F_0(t)>$ (left) and its Stokes $<F_{-1}^*(t')F_{-1}(t)>$ (right) fields plotted along the time interval |t-t'| and the propagation distance z. The primary pump band width and the medium density at z=0 are 0.1 nm and 20 amagats, respectively. Other boundary conditions are given in the text.
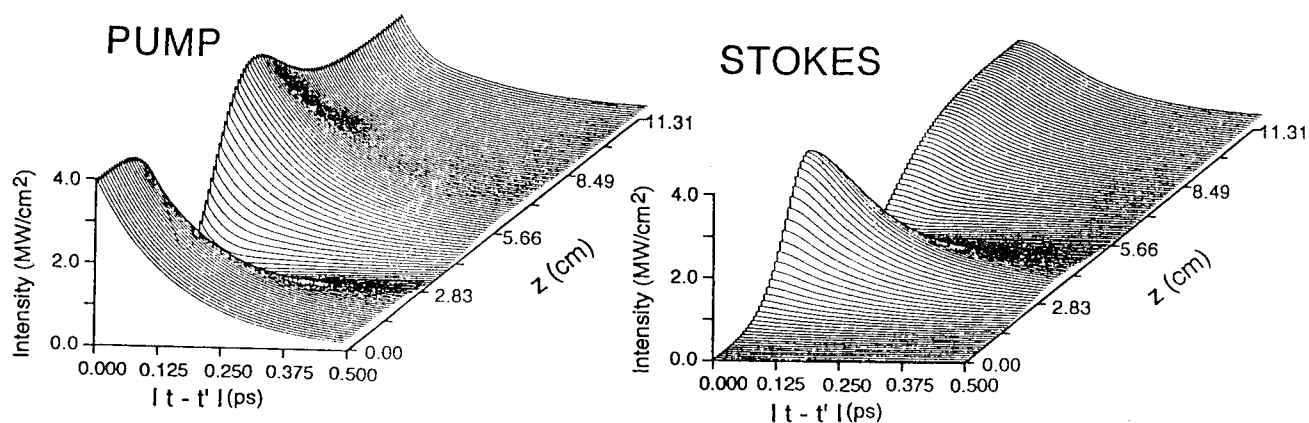
Fig. 3 Self-correlation functions of primary pump and its Stokes fields, for the case with the incident pump laser bandwidth of 1.0 nm and the medium density of 60 amagats. Other boundary conditions are unchanged from Fig. 2. Notice that the numbers on |t-t'| axis are 10 times smaller than those in Fig. 2.

Brillouin Induced Mutually Pumped Phase Conjugation in Reflection Geometry

R. Saxena and I. McMichael
Rockwell International Science Center
Thousand Oaks, CA 91360
(805) 373-4157

SUMMARY

A mutually pumped phase conjugator (MPPC) generates the phase-conjugate replicas of *two* incoherent incident beams. Each input beam is converted into the phase-conjugate replica of the other by Bragg diffraction off a shared grating. In photorefractive media, several configurations differing in their number of internal reflections from the crystal surfaces were demonstrated;[1] for efficient operation, the two incoherent beams must have comparable input intensities. However, applications like phase-conjugate heterodyne detection[2] require the device to work for large imbalance of input beam intensities, when a weak optical signal from a remote transmitter is combined with the strong beam from a local oscillator. A modest extension of the dynamic range can be obtained by increasing the photorefractive gain;[1] however, it is desirable to extend the dynamic range of the device to several orders of magnitude.

MPPC has also been studied in electrostrictive Kerr media by utilizing the Brillouin gain in a transmission geometry.[3] An advantage of MPPC in electrostrictive Kerr media over photorefractive media is the large dynamic range of input beam ratio over which the process will occur. This is because if one beam intensity is large enough to satisfy the threshold condition for the total beam intensity, then a small intensity of the second beam will initiate the process of MPPC. However, none of this work has been corroborated experimentally. There has been recent theoretical and experimental work on MPPC in electrostrictive Kerr media using the reflection geometry.[4] That large dynamic range was also possible in reflection geometry was discussed in Ref. 4, but here we present the first solutions to the transcendental equation that illustrate this possibility.
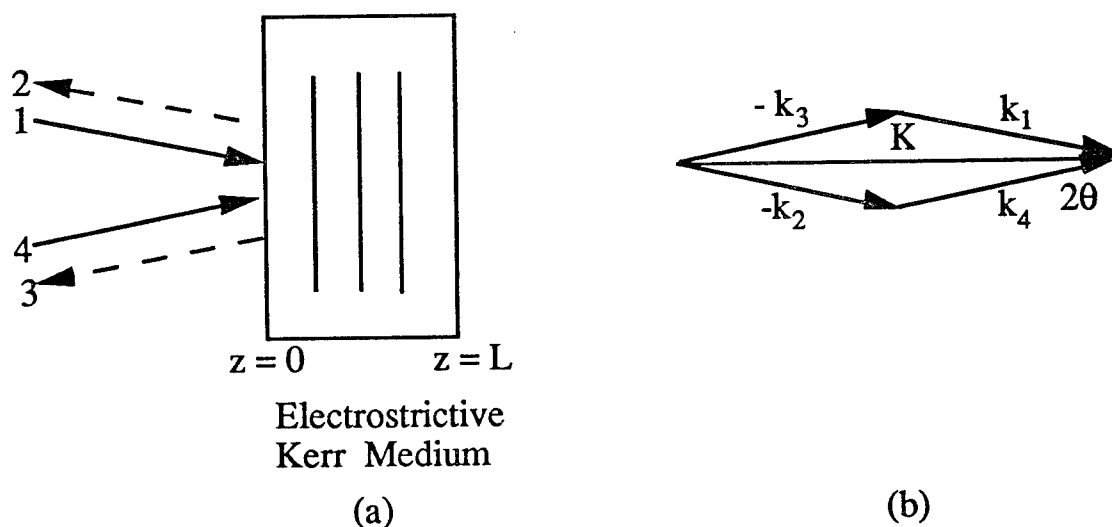
Fig. 1 (a) Schematic diagram showing MPPC using reflection gratings in an electrostrictive Kerr medium. (b) Wave vector diagram for MPPC using reflection gratings.

The geometry for the nonlinear interaction responsible for MPPC is shown in Fig.1(a) and Fig.1(b). Input beams 1 and 4 are a pair of mutually incoherent beams that enter through the front face of the nonlinear medium and intersect at an angle 2θ. Acoustic phonons that are initially present in a transparent Kerr medium like CS_2 due to thermal and quantum noise cause Stokes scattering of the input beams in all directions. Also, a photon from each input beam can be spontaneously converted into a frequency downshifted Stokes photon and an acoustic phonon. The coherently generated Stokes waves will interfere with the input beam to produce interference patterns which travel at the acoustic velocity, and which drive acoustic waves by electrostriction.[5] These acoustic waves induce index gratings in the medium, and the index grating that diffracts each incoherent input beam into the phase-conjugated output of the other input beam beam will be reinforced by both the beams. Hence this mutual index grating has the maximum gain compared to all the other possible gratings, and we label the corresponding Stokes scattered wave of input beam 1 as beam 3, beam 3 being the phase-conjugate of input beam 4. Similarly, the relevant Stokes wave of input beam 4 is beam 2, and this is the phase-conjugate of pump beam 1. Coupled-wave equations for the complex beam amplitudes A_i (i=1 to 4) describe the energy exchanged between the various beams at steady-state:

$$\frac{dA_1}{dz} = -\frac{g}{2} (A_1 A_3^* + A_2^* A_4) A_3$$

$$\frac{dA_2}{dz} = -\frac{g}{2} (A_1^* A_3 + A_2 A_4^*) A_4$$

$$\frac{dA_3}{dz} = -\frac{g}{2} (A_1^* A_3 + A_2 A_4^*) A_1$$

$$\frac{dA_4}{dz} = -\frac{g}{2} (A_1 A_3^* + A_2^* A_4) A_2 \quad , \tag{1}$$

where g is the Brillouin gain coefficient. Assuming non-zero Stokes seeds at the z = L backplane that arise from the mutual scattering of each input beam in a direction counterpropagating to the other input beam: $A_{2L} = f A_4(L)$, $A_{3L} = f A_1(L)$, f being the mutual scattering coefficient that is equal in amplitude and phase for both the pumps, we obtain the following transcendental equation for the phase-conjugate reflectivity $R \equiv |A_3(0)/A_{40}^*|^2$:

$$R = q |f|^2 \exp[G(1-R/q)] \tag{2}$$

Here q is the intensity ratio of the two incoherent beams at the z= 0 input plane: $q \equiv I_{10}/I_{40}$, and $G \equiv g(I_{10}+I_{40})L$ is the total Brillouin gain. The phase-conjugate reflectivity S in the other arm is equal to $|A_2(0)/A_{10}^*|^2$ and is related to R by: $S = R/q^2$. The device transmissivity T measures the fraction of each input beam that is converted into the phase-conjugate output of the other beam, and is equal for both inputs. Note that if $|f|^2 = 0$, i.e., $I_{2L} = I_{3L} = 0$, then the phase-conjugate reflectivities R and S are equal to zero. Hence finite seed values of the Stokes waves are required for MPPC to work in reflection geometry. Fig. 2 is a plot of the solutions of Eq. (2) showing the phase-conjugate reflectivities R, S and transmissivity T as a function of the input intensity ratio q on a log-log scale, for a fixed value of Brillouin gain $G_4=18$ satisfied by the strong input beam 4. This is below the threshold value required for self-SBS (~ 23) of input beam 4. We take $|f|^2 = 10^{-12}$ for noise induced Stokes scattering. Increasing q is equivalent to

increasing I_{10}, keeping I_{40} and hence G_4 fixed. Note that the weak input beam I_{10} ($q = 10^{-6}$) is phase-conjugated with a reflectivity greater than unity. ($S = 60$). Since S is inversely proportional to I_{10}, S decreases with increasing q for $q \leq 10^{-1}$. As q is further increased, the total Brillouin gain increases, leading to increased conversion of input beam I_{40} into the Stokes beam $I_2(0)$, as seen by the increase in T. This compensates for the decrease of S with increasing I_{10}, so that S actually increases for a limited range of q values. When the total Brillouin gain is enough to convert most of the input beams into their Stokes waves, then any further increase in q results in decreasing S once again. R is a monotonically increasing function of q because its denominator I_{40} is a fixed quantity, and increase in I_{10} results in more conversion of this input beam into its Stokes wave $I_3(0)$.
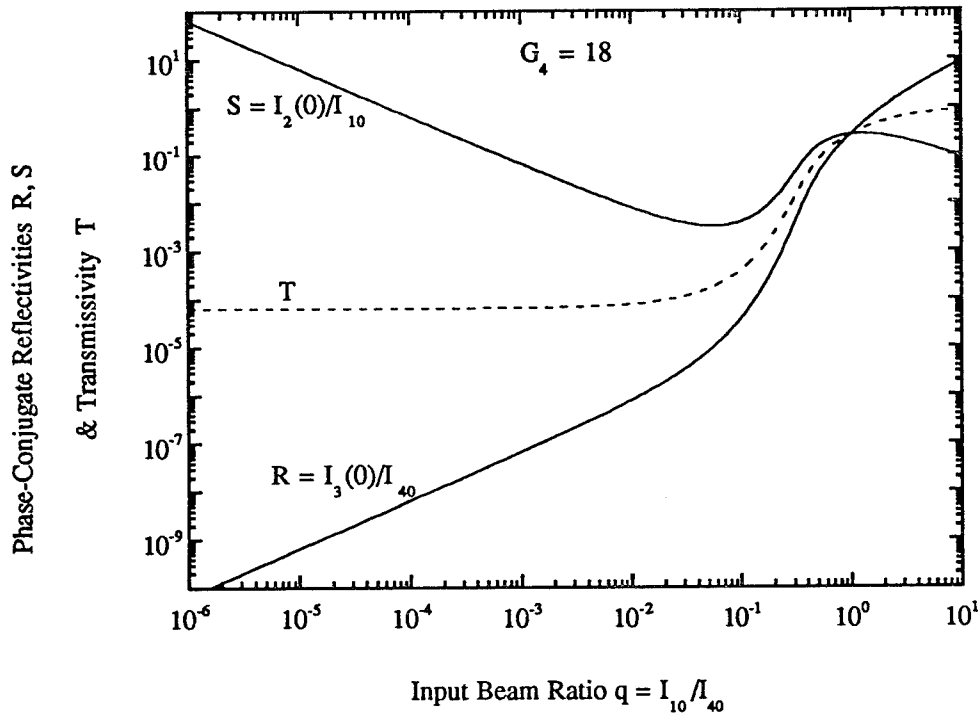
Fig. 2 Phase-conjugate reflectivities R, S and transmissivity T as a function of intensity ratio of the two input beams q, for $|f|^2 = 10^{-12}$ and $G_4 = 18$.

In conclusion, we studied Brillouin induced MPPC in the reflection geometry and obtained solutions illustrating that a weak beam can be phase-conjugated with reflectivities larger than unity. The technique works for a large dynamic range of input beam ratio as the intensity of the weak input beam is increased, while the intensity of the strong incoherent input beam is kept constant below the threshold value for self-SBS.

REFERENCES

1. S. Sternklar, S. Weiss and B. Fischer, Opt. Eng. **26**, 423 (1987)
2. L. E. Adams and R. S. Bondurant, Opt. Lett. **16**, 832 (1991).
3. R. Saxena and P. Yeh, J. Opt. Soc. Am. B **7**, 326 (1990).
4. S. Sternklar, Opt. Lett. **17**, 1403 (1992).
5. A. M. Scott and K. D. Ridley, IEEE J. Quanum Electron. **QE-25**, 438 (1989).

Effects of Stimulated Raman Scattering on Kerr Switching Profiles in a Nonlinear Fiber Loop Mirror

Hak Kyu Lee, Kyong Hon Kim, Seo Yeon Park, and El-Hang Lee
Electronics and Telecommunications Research Institute, P.O. Box 106,
Yuseong-gu, Taejon, 305-600, Korea; Phone :+82-42-860-6032

The nonlinear fiber loop mirror (NFLM) switches based on the Kerr effects of fibers has received a considerable attention for their potential application as high speed all-optical signal processing devices. High power pump beams needed for the NFLM switches to induce large nonlinear refractive index change in the fiber may cause other nonlinear processes such as the stimulated Raman scattering(SRS), the modulation instability(MI), and the parametric mixing. Therefore, it is important to investigate the effects of other nonlinear processes on the switching profiles of the NFLM. In this presentation we report the detailed characteristics of Kerr switching profiles of the NFLMs under high power pumping. Pumping powers to induce a 3π phase shift in the fibers was strong enough to generate SRS and MI.

The experimental set-up used in our experiments is shown in Fig. 1. The nonlinear fiber used in the NFLM was a 500-m long polarization maintaining fiber. A cw probe beam from a 1530-nm DFB laser diode was split into two counterpropagating beams, I_{s1} and I_{s2}, entering into the NFLM through a 3 dB fiber coupler. 1053-nm mode-locked Nd:YLF laser pulses of a 100 ps pulse width and 76 MHz repetition rate used as pump pulses, and coupled into the NFLM via a WDM coupler1 whose coupling ratios were 100 : 0 and 5 : 95 at the probe and pump beam wavelengths, respectively. The pump beam exits from the NFLM through a WDM coupler2 which is identical to the WDM coupler1. The switched profiles of the probe beam and the spectral profiles of the pump beam were measured by a high speed photodiode and an optical spectrum analyzer, respectively.

Fig. 2 (a)-(d) show the switched probe beam profiles of the NFLM switches and the spectral profile of the outcoming pump beams from the NFLM at various pump powers of 130, 330, 600, and 850 mW, for which the equivalent phase shifts are 0.5π, 1.3π, 2.3π, and 3.3π, respectively.
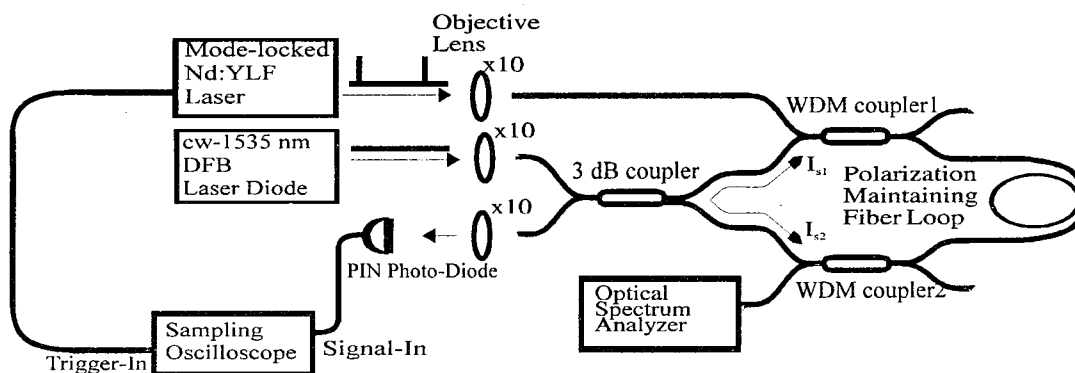
Fig. 1 Experimental set-up for measurements of the effects of SRS on the switching profiles of the nonlinear fiber loop mirror.

The Kerr switching profile can be written as

$$I_s = \frac{1}{2}[1 - \cos\{\phi_1(t) - \phi_2\}] \tag{1}$$

where $\phi_1(t)$ and ϕ_2 are the phase shifts of the copropagating probe beam, I_{s1}, and the counterpropagating probe beam, I_{s2}, with the pump beam, respectively. The peak value of $\phi_1(t)$ saturates to ϕ_{1sat} due to the walk-off effect between pump beam and I_{s1}.[1] The ϕ_{1sat} is proportional to the peak intensity of the pump beam times the pump pulse width and inversely proportional to the group delay difference, τ (in ns/km), between the pump and probe beams. The phase shift, ϕ_2, is proportional to the average intensity of pump beam times fiber length, L.[2] The temporal duration of the Kerr switching profile equals to τ L. For our 500-m long polarization maintaining fiber the group delay difference between a 1053-nm pump wavelength and a 1535-nm probe wavelength was 7.0 ns/km, and the temporal duration of Kerr switching profile was 3.5 ns. The phase shift, ϕ_2, was about 18 % of ϕ_{1sat}, and causes the background floating on the switching profiles. The gradually decreasing section of the switching profile in Fig. 2 (a) is attributed to the intensity decrease along the fiber caused by its optical loss, 1.7 dB /km.

Fig. 2 (b) shows a completely switched case, in which ϕ_{1sat} is 1.3 π. It is shown that there is a background level floating as much as 13 % of the peak value because of $\phi_2 = 0.23 \pi$. An 1103-nm SRS signal appears in the pump spectrum, but its energy is not strong enough to influence the switching profile. The measured threshold power to generate the SRS was 270 mW.

Fig. 2 (c) shows the switched profile and pump spectrum for $\phi_{1sat} = 2.3 \pi$. Two side lobes appear in the pump spectra, and its wavelength shift from the center wavelength is 13 nm. Since the pump wavelength was at the normal dispersion region, it represents the cross-phase modulation induced modulation instability(MI) through the interaction between the pump and SRS pulses. The side lobes shown in the Raman spectra behave as expected according to the typical MI theory [3], although the red shift is not resolvable because of the self-phase modulation induced broadening on the SRS pulse. The measured threshold power to generate the MI was about 450 mW. In the switched temporal profile, however, the effect of SRS and MI can not be shown clearly. The peaks shown in the leading and trailing edges of the switched profile indicate that the corresponding phase shift difference between $\phi_1(t)$ and ϕ_2 is π. The gradually increasing section in the middle of the switched probe beam profile represents that the phase difference between ϕ_{1sat} and ϕ_2 decreases from 2 π to π due to the fiber loss.

For the pump beam power of 600 mW which cause a phase shift $\phi_{1sat} = 3.3 \pi$, the SRS signal appears strong, and depletes the 1053-nm pump beam, which eventually influences the Kerr switching profiles. Fig. 2 (d) shows the output profiles which result from the interaction among the probe, pump, and SRS beams in the fiber. The energy conversion rate from the pump pulse to the SRS pulse was measured to be about 40 %. The SRS pulse moves faster than the pump pulse in the normal dispersion region of the fiber. The measured group delay difference between the SRS and pump beams was 2

ns/km, and thus the group delay difference between the probe and SRS beams was 5 ns/km. The SRS pulse leaves from the 500-m long fiber earlier than the pump pulse as much as 1 ns. Before SRS pulse leaves the fiber both the pump and SRS pluses contribute to affect the switching profile. Since the total energy is conserved, the switched temporal profile is the same as in the case where the pump propagates along the fiber without the energy conversion to SRS. Due to the fiber loss the phase shift difference, ϕ_{1sat}- ϕ_2, decreased from 2.6 π to 2 π. After SRS pulse leaves the fiber, only the pump beam, portion of which was depleted by the SRS, contributes to affect the switching profile. The phase shift difference rapidly decreases from 2 π to π, and the switched output intensity rapidly increases from 0 to 1, which is shown near the trailing edge of the switching profile in Fig. 2 (d).

By comparing Fig. 2 (c) with Fig. 2 (d) one can see that the switched probe beam intensities near the trailing edge of the two switched profiles do not change even though the input pump power increases from 600 to 850 mW. This is mainly due to the conversion of the pump pulse to the SRS pulse energy by as much as the amount of the pump power increment.

References

[1] T. Morioka and M. Saruwatari, Opt. Eng. **29**, 200 (1990).
[2] M. Jinno and T. Matsumoto, IEEE Photon. Tech. Lett. **2**, 349 (1990).
[3] G. P. Agrawal, *Nonlinear Fiber Optics* (Academic Press, New York 1988), Chapter 7.
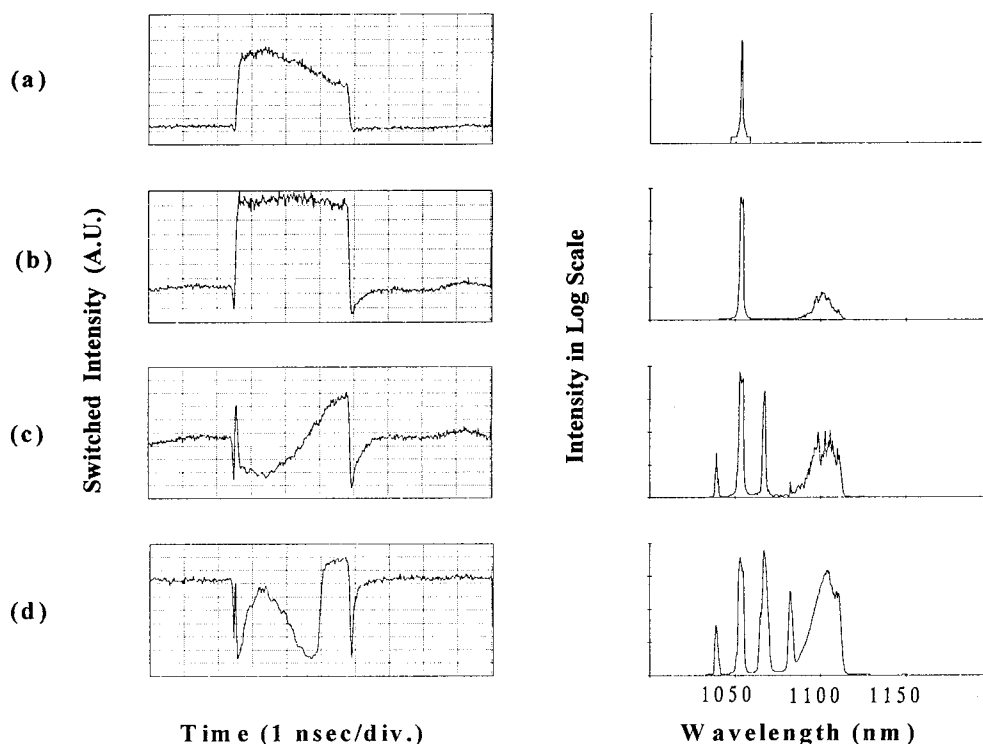
Fig. 2 Measured Kerr switching profiles and pump beam spectra for various incident pump powers of (a) 130 mW, (b) 330 mW, (c) 600 mW, and (d) 850 mW.

Fast Polarization Self-Modulation in a Vertical-Cavity Surface-Emitting Laser

Shijun Jiang, George Pan, and Mario Dagenais

Department of Electrical Engineering and Joint Program for Advanced Electronic Materials
University of Maryland, College Park, MD 20742
Tel: (301) 405-3684

Robert A. Morgan

AT&T Bell Laboratories, Solid-State Technology Center, Breinigsville, PA 18031

For many applications, it is important to modulate a semiconductor laser at very high rates ($\geq$ tens GHz). It usually requires the use of high speed electronics and operating the laser at high currents, unless some passive mode locking techniques are used. Recently, a technique based on the self-modulation of the polarization in an edge-emitting semiconductor laser was used for generating high frequency optical pulses without requiring high-speed electronics[1,2]. Demonstration of polarization self-modulation using a vertical-cavity surface-emitting laser (VCSEL) is particularly appealing because VCSELs are well suited for two dimensional array applications including optical interconnection and optical storage[3,4] and because they exhibit different intrinsic polarization properties from edge-emitting lasers [5,6].

The structure of the GaAs/AlGaAs VCSEL used in our experiment is similar to that described in Ref. 4. The VCSEL is operated CW at room temperature and lases at a wavelength of about 835 nm. The output light from a VCSEL is linearly polarized along either the <011> or the <01$\bar{1}$> (denoted by $P_{||}$ and $P_{\perp}$ modes) crystal direction. These two modes are nearly degenerate because of the symmetrical circular active region[6,7].

The experimental setup used to study polarization self-modulation in a VCSEL is shown in Fig. 1. The extended cavity is formed by the VCSEL and a partial reflecting mirror (R= 65%), with a zero order quarter-wave plate inserted in between. The optical axis of the quarter-wave plate is oriented at 45 degrees with respect to the polarization directions of $P_{||}$ and $P_{\perp}$. After one complete round-trip through the extended cavity, the quarter-wave plate acts to change the polarization state of the retroreflected light by 90 degree (from $P_{||}$ to $P_{\perp}$ and vice versa). This polarization-rotated feedback light forces the polarization of the laser to switch[7]. Therefore $P_{||}$ (or $P_{\perp}$) is the dominant mode every other extended cavity round-trip. i.e., the polarization of the VCSEL oscillates between the two cross polarization modes every extended cavity round-trip time. To detect the polarization self-modulation signals, another quarter-wave plate is placed outside the extended cavity to convert the circularly polarized light transmitted through the partial reflecting mirror back into linearly polarized $P_{||}$ (or $P_{\perp}$) light. This light is then resolved into its $P_{||}$ and $P_{\perp}$ components by means of a polarizing beamsplitter. Each polarized signal is detected by an avalanche photodiode (APD). The signal from the APD is amplified by a broadband amplifier and displayed on an oscilloscope and/or an RF spectrum analyzer.

As discussed above, each polarized mode is dominant every other extended cavity round-trip time, τ_r. Therefore the modulation frequency f_m of the self-modulated signal is governed by

$$f_m = \frac{1}{2\tau_r} = \frac{c}{2 \times 2 L_{eff}}$$
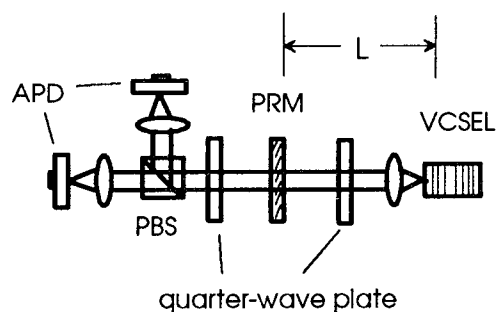
Fig.1 Schematic diagram of the experimental setup.
(PRM) partial reflecting Mirror, (PBS) polarizing
beamsplitter, (APD) avalanche photodiode.
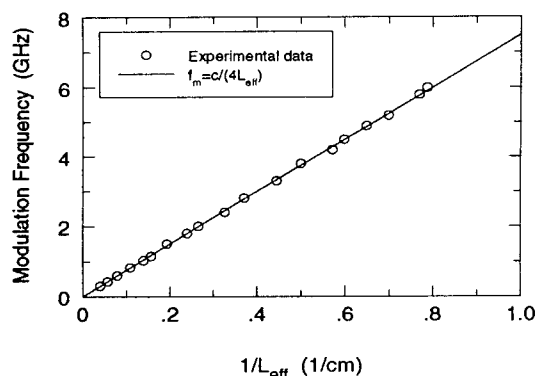
Fig.2 Plot of modulation frequency versus
the effective extended cavity length L_{eff}.

where c is the speed of light in vacuum, L_{eff} is the effective extended cavity length and is given by

$$L_{eff} = L + l + (n_{glass} - 1) \times (d_{lens} + d_{QWP}).$$ L and l are the lengths of the extended cavity and the VCSEL chip, respectively, n_{glass} is the refractive index of glass, d_{lens} and d_{QWP} are the thicknesses of the collimating lens and the quarter-wave plate, respectively. Fig. 4 shows the measured modulation frequency as a function of the effective length of the extended cavity. The theoretical prediction is indicated by a solid line and agrees well with the experimental observation.

The physical principle behind polarization switching in a VCSEL is based on an external feedback-induced frequency locking mechanism. Since the VCSEL has a very high ($\cong 99.5\%$) top mirror reflectivity, the origin of our polarization self switching is different from the one that was previously studied[1,2], where the quarter-wave plate was an integral part of an external ring cavity formed by an anti-reflection coated semiconductor laser (~ 1%) and four mirrors. In our case, however, the quarter-wave plate changes the polarization state of the retroreflected light externally. This polarization-rotated feedback light then induces an injection locking in the VCSEL and leads to a switching of the polarization state[7]. It should be stressed that this switching does not require the critical biasing of the injected current.

Fig. 3 shows typical oscilloscope waveforms of the measured $P_{||}$ and $P_{\perp}$ modulated light signals for an extended cavity length of 16.5 cm, corresponding to a repetition rate of about 450 MHz. The modulation depth is measured to be 80%, which is partly limited by the quarter-wave plates whose operation wavelength is not optimized to the lasing wavelength of the VCSEL. In addition, it can be seen from the figure that the $P_{||}$ and $P_{\perp}$ modulated lights have nearly the same amplitude. This means that two nearly equal amplitude complementary high frequency modulation signals can be generated simultaneously by using a VCSEL with the very simple setup shown in Fig. 1.

In the experiment, we have successfully observed polarization self-modulation signals with a repetition rate up to 6 GHz. The oscilloscope waveforms of the modulation signals at frequencies exceeding 1.5 GHz are not available because of the bandwidth limitation of the oscilloscope (Tektronix 7104). Instead, those signals are measured with an RF spectrum analyzer. Fig. 4 shows a RF spectrum of a modulated signal at a frequency of 6 GHz. An optical switching energy of order 1 fJ is extracted from these measurements.

The maximum observable self-modulation frequency is currently limited by the physical length of the setup. However, since the polarization self-modulation results from the alternate polarization switching between the two cross polarization modes, it is a two-mode switching process. The two-mode
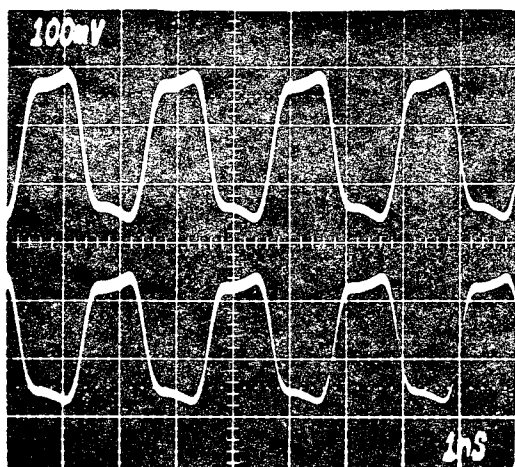
Fig. 3   Oscilloscope waveform of polarization
self-modulation signal at a frequency of 450 MHz.
upper trace: $P_{||}$ light, lower trace: $P_{\perp}$ light.
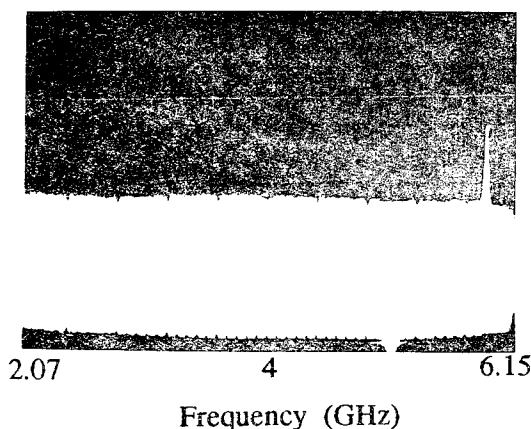
Fig.4   RF Spectrum of a polarization self-
modulation signal at 6 GHz. Vertical scale
is 10 dB/div.

switching involves a gain competition mechanism between the two laser modes. The total concentration of carriers inside the cavity is kept almost constant during the switching. Therefore, the switching speed is primarily limited by the cavity lifetime(photon lifetime) rather than by the carrier lifetime[8]. It has been theoretically predicted[9] that the speed of the polarization switching in a semiconductor laser can be as high as 100 GHz. Since the cavity lifetime in a VCSEL can be shorter than that in a conventional edge-emitting laser, the polarization switching speed in a VCSEL can be expected to be faster than that in edge-emitting laser. Moreover, the difference in optical gain between the two quasi-degenerated polarization modes is very small in a VCSEL, which could also lead to a faster switching speed and lower switching energy. Therefore, our approach is potentially scalable to ultrahigh speed operation (100 GHz or beyond) by integrating a VCSEL with a polarization switching component. The implementation of this is presently under way. We believe that it may lead to potential applications in ultrahigh speed optical clocks and optical storage.

References

1. W. H. Loh, Y. Ozeki and C. L. Tang, Appl. Phys. Lett., **56**, 2613 (1990).
2. W. H. Loh, A.T. Schremer and C. L. Tang, IEEE Photon. Tech. Lett., **3**, 467 (1990).
3. J. L. Jewell, J. P. Harbison, A. Scherer, Y. H. Lee and L. T. Florez, IEEE J. Quantum. Electron., **QE-27**, 1332 (1991).
4. R. A. Morgan, L. M. F. Chirovsky, M. W. Focht, G. Guth, M. T. Asom, R. E. Leibenguth, K. C. Robinson, Y. H. Lee and J. L. Jewell, Proc. SPIE **1562**, 149 (1991).
5. M. Shimizu, F. Koyama and K. Iga, Japanese Journal of Appl. Phys., **27**, 1774 (1988).
6. F. Koyama, K. Morito, and K. Iga, IEEE J. Quantum. Electron., **QE-27**, 1410 (1991).
7. Z. Pan, S. Jiang, M. Dagenais, R. A. Morgan, K. Kojima, M. T. Asom, R. E. Leibenguth, G. D. Guth and M. W. Focht, Appl. Phys. Lett., **63**, 2999 (1993).
8. C. L. Tang, A. Schremer and T. Fujita, Appl. Phys. Lett., **51**, 1392 (1987).
9. W. H. Loh and C . L. Tang, IEEE J. Quantum. Electron., **QE-27**, 389 (1991).

Efficient Frequency Conversion of cw Mode Locked Tunable ps Pulses in the Visible and Near Infrared Spectral Region

U. Socha, J. Hussong and R. Beigang

Fachbereich Physik

Universität Kaiserslautern

Postfach 3049

D - 67653 Kaiserslautern

Tel.: (049) 631 205 2180

Fax: (049) 631 205 3300

Summary

Generation of ultrashort light pulses tunable in the whole visible and infrared spectral region is of considerable interest for a wide range of applications. Nonlinear frequency mixing techniques are well suited to generate such ultrashort tunable light pulses with a high repetition rate in these wavelength ranges. In particular, second harmonic, sum and difference frequency generation allow for the generation of tunable light pulses in a wide wavelength range depending on the laser sources used. Femtosecond pulses, e. g. , have been generated in the wavelength range from 1.3 µm to 1.6 µm by difference frequency mixing of the cw mode locked radiation of a Nd:YAG laser and a dye laser [1,2]. In this contribution we report on the generation of tunable picosecond pulses in the wavelength range from 620 nm to 680 nm, 725 nm to 900 nm, and 2.6 µm to 4 µm by frequency conversion processes between the cw mode locked radiation of a NaCl:OH color center laser and a Nd:YAG laser which is also

used as the pump source for the color center laser.

The color center laser produced pulses of 5 ps length at a repetition rate of 76 MHz with an average power of approximately 2 W. It was tunable with a birefringent filter from 1.45 µm to 1.8 µm. The color center laser was synchronously pumped by a cw mode locked Nd:YAG laser (90 ps pulse length, repetition rate 76 MHz, average power 20 W). 8 W of the pump radiation was used for pumping whereas the remaining 12 W were used for the mixing experiment. The pulses from the color center laser and the Nd:YAG laser were synchronized in time with an optical delay line and after proper alignment of the polarization overlapped and focussed into the nonlinear crystal.

There are several crystals which can be used for frequency mixing 1.64 µm and 1.45 µm ...1.8 µm radiation, e. g. $LiJO_3$, KTP, $AgGaS_2$ and $KNbO_3$. We have chosen $KNbO_3$ because of the high nonlinearity, the relativly large acceptance bandwidth and the good thermal properties. With a single $KNbO_3$ crystal cut in the xz-plane ($\Theta = 40°$) the following nonlinear processes are possible by adjusting the proper polarization of the two interacting wavelengths:

1. second harmonic generation of the color center laser (oo-e, type I),
2. sum frequency generation (oo-e, type I),
3. difference frequency generation(eo-e, type II).

A typical tuning curve of the difference frequency signal as a function of the color center laser wavelength is shown in Fig. 1.
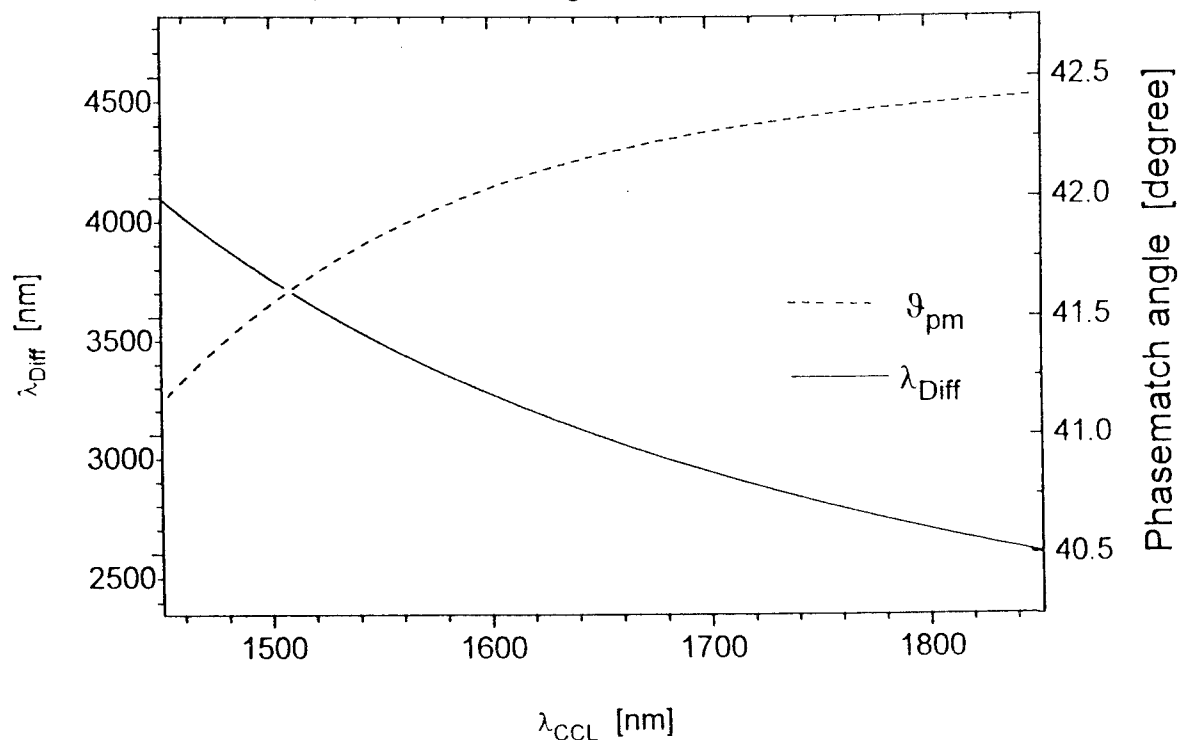
Fig. 1 Tuning curve of the difference frequency process between the radiation of the color center laser and the Nd:YAG laser as a function of color center laser wavelength. The phase match angle is shown on the right hand side of the figure.

A total wavelength range from 2.6 µm to 4 µm can be covered, in principle, using type I (oo-e) difference frequency mixing. We have generated up to 50 mW average power infrared radiation between 3 µm and 4 µm using a 7.8 mm long xz-cut $KNbO_3$ crystal.

The crystal was AR coated on both sides for 1.6 µm and 1.064 µm.

In the case of sum frequency generation with the same crystal we have obtained up to 300 mW of average power in the wavelength range from 620 nm to 680 nm. The second harmonic generation of the color center laser radiation resulted in up to 220 mW between 725 nm and 900 nm.

The pulse width for all processes is mainly determined by the pulse width of the color center laser and was around 6 ps. Group velocity mismatch (GVM) between the three interacting wavelengths does not lead to an increase in pulselength for crystal lengths and wavelength used in this experiment. Group velocity mismatch can also be neglected for ps pulses.
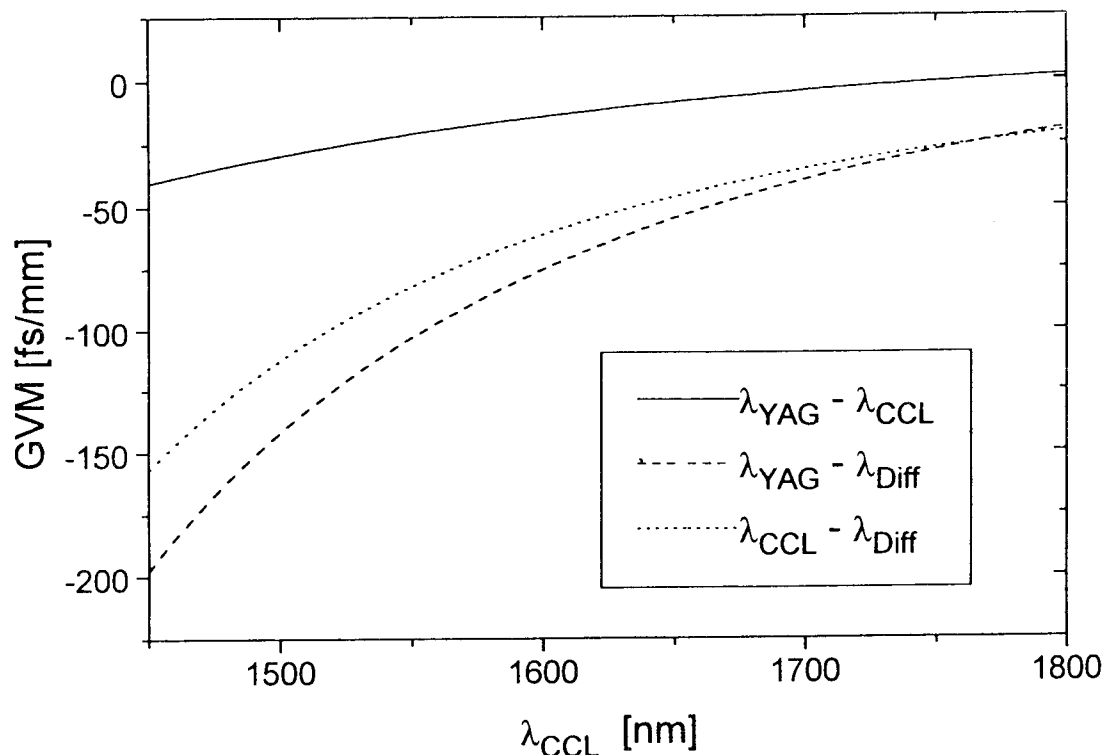
Fig. 2 Group velocity mismatch (GVM) between $\lambda_{Nd:YAG}$, λ_{CCL}, and λ_{Diff} in KNbO$_3$

The limiting factors in the conversion efficiency are the small acceptance angle of about 0.026° and the walk-off angle of 3.5°. Therefore a tight focus will not result in a higher conversion efficiency.

In summary we have shown that a cw mode locked NaCl:OH color center laser can be used to generate tunable pulses between 620 nm to 680 nm, 725 nm to 900 nm, and 2.6 µm to 4 µm by frequency mixing with ps radiation from a cw mode locked Nd:YAG laser. The pump laser for the color center laser itself can be used as the second source for the mixing process so that no extra ps source for the mixing process is required. Using a xz-cut KNbO$_3$ crystal 41° average output powers of 300 mW in the wavelength range from 620 nm to 680 nm and up to 50 mW in the wavelength range from 3 µm to 4 µm were obtained.

1. A. Mokhtari, L. Fini, and J. Chesnoy
   Opt. Commun. 61, 421 (1987)
2. K Kurokawa and M. Nakazawa
   Appl. Phys. Lett. 55, 7 (1989)

Coherent phonon-polaritons as a probe of anharmonic lattice vibrations

H.J. Bakker, S. Hunsche, and H. Kurz

Institut für Halbleitertechnik II, RWTH Aachen, 52056 Aachen, Germany
Tel: +49-241-807896; Fax: +49-241-8888-246; e-mail: hunsche@basl.rwth-aachen.de

We investigate the dielectric properties of $LiTaO_3$ and $LiNbO_3$ in the THz regime by measuring the dynamics of coherently generated phonon-polaritons. The dielectric response of these ferroelectric crystals is dominated by the lowest-energy lattice vibration of A_1 symmetry. This so-called ferroelectric mode is associated with a strong absorption peak at 6 THz (200 cm^{-1}) in $LiTaO_3$ and at 7.5 THz (250 cm^{-1}) in $LiNbO_3$. The properties of these vibrations are strongly affected by the displacement of ions which occurs when the lattice temperature approaches the ferroelectric phase transition temperature. The dielectric properties of $LiTaO_3$ and $LiNbO_3$ can be described by modelling these modes with a microcopic vibrational potential within one unit cell.[1] The structure of this potential determines critically the polariton response. Therefore, the experimental determination of the phonon-polariton dispersion and damping provides information about the microscopic properties of $LiTaO_3$ and $LiNbO_3$.

Coherent polariton wavepackets are excited and probed in a three-beam pump-probe set-up, using intense femtosecond laser pulses derived from an amplified CPM laser (pulse duration τ_{pu} = 60 fs, bandwitdh $\Delta h\nu_{pu} \approx$ 44 meV, λ_{max} = 625 nm, $E_{puls} \approx$ 5 μJ). Two pump pulses are focused onto the sample under a chosen angle to a common focus of 200 μm. Polaritons are impulsively generated by difference-frequency generation within the bandwidth of the pump pulses. The wavevector k_p of the polaritons is given by the angle between the pump beams. The generation process is phase-matched for the frequency that is given by the polariton dispersion $\omega(k_p)$ and creates two counterpropagating polariton wave packets. Due to the electro-optic effect the polaritons are associated with a refractive index grating that diffracts the time-delayed probe pulse. Interference of the diffracted light with background scattered light results in a heterodyne detection, leading to a signal that oscillates with the frequency of the polariton. The polariton dispersion is determined by varying the angle between the pump pulses.

Figure 1: Time-resolved measurement of phononpolariton beats in $LiNbO_3$. The inset shows the Fourier transform of the oscillating signal.
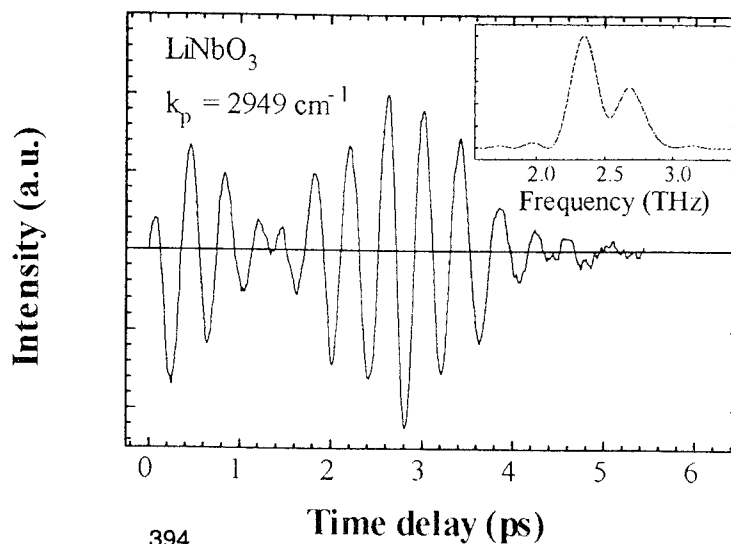
At certain wavevectors, the oscillating signal becomes irregular and shows a beating structure, as shown in Fig. 1. The inset shows the Fourier transform of the oscillating signal. This demonstrates that two polariton frequencies are generated, and that polaritons with a frequency of 2.4 THz cannot be excited. This effect is explained by a weak resonance at 2.4 THz which is associated with an avoided crossing in the polariton dispersion, i.e. a splitting into two dispersion branches. Near this avoided crossing, polaritons in the upper and lower branch can be excited with comparable efficiency, leading to polariton beats.[2] In LiNbO$_3$, our data indicate four resonances at 1.3 THz, 2.4 THz, 3.4 THz, and 4.1 THz. In LiTaO$_3$, we find a weak resonance at 1 THz. This is clearly visible in the experimentally determined polariton dispersions which are indicated by the dots in Figs. 2 and 3. The frequencies of these resonances are much below the frequencies of all fundamental phonon modes.
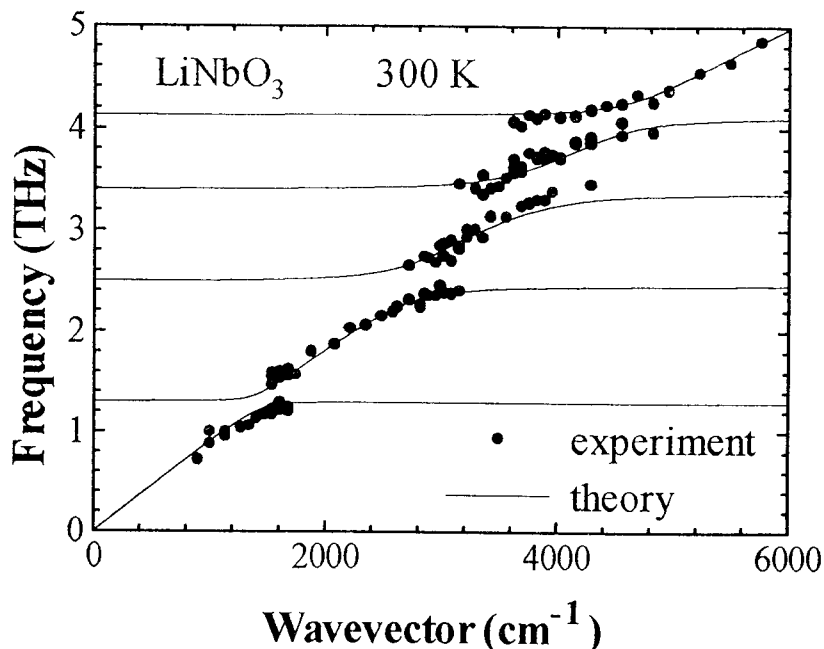
Figure 2: Phonon-polariton dispersion in LiNbO$_3$.

The presence of these low-frequency resonances can be explained by a strong anharmonicity of the ferroelectric mode. It has been found, that this lattice vibration can be described by a vibrational potential that contains three minima within one unit cell and is tilted due to the local electric field in the ferroelectric phase. The fundamental phonon frequency corresponds to transitions between states that are localized in the lowest well of this potential. Excited states which are delocalized over several wells have a much lower energy separation, resulting in low-frequency resonances in the dielectric function. The measured frequencies and absorption strengths of these resonances allow a precise determination of the shape of the vibrational potential in LiNbO$_3$ and LiTaO$_3$. The polariton dispersions calculated from these potentials are shown as lines in Figs. 2 and 3.

The resonances at 1 THz in LiTaO$_3$ and 1.3 THz in LiNbO$_3$ are identified as tunneling resonances that correspond to classically forbidden oscillations of the Li$^+$ ion between two potential wells. The triple-well potential also provides a correct description of the ferroelectric phase transition and the temperature dependence of the dielectric response. This has been verified by measurements of the polariton dispersion and damping in LiTaO$_3$ at various temperatures.[3]
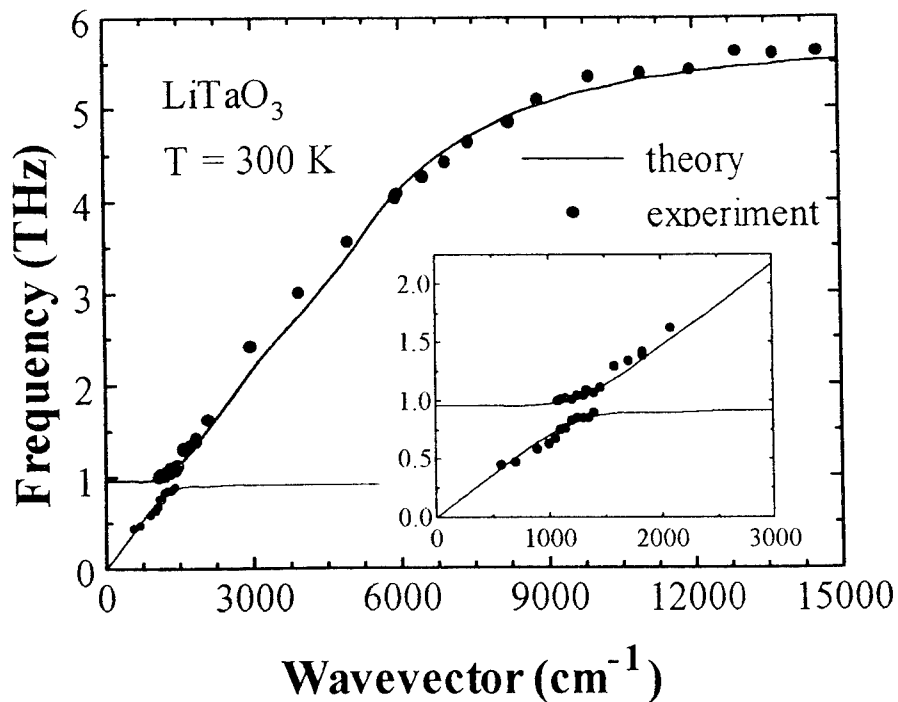
Figure 3: Phonon-polariton dispersion LiTaO₃.

In conclusion, we study the THz dielectric response of $LiTaO_3$ and $LiNbO_3$ with coherent phonon polaritons. We obtain microscopic information about the anharmonicity of the ferroelectric phonon mode. This is relevant for a basic understanding of ferroelectricity in these materials.

References:

[1] M.E. Lines, Phys Rev. B **2**, 698 (1970)
[2] H.J. Bakker, S. Hunsche, and H. Kurz, Phys. Rev. Lett **69**, 2823 (1992)
[3] H.J. Bakker, S. Hunsche, and H. Kurz, Phys. Rev. B **48**, 13524 (1993)

PROPAGATION AND SWITCHING OF ULTRA-SHORT PULSES IN NONLINEAR FIBER COUPLERS

Nail Akhmediev

Optical Sciences Centre, Institute of Advanced Studies
The Australian National University, Canberra, ACT 2601, Australia
Tel: 61 (06) 249-0191

J. M. Soto-Crespo
Instituto de Óptica, C.S.I.C.
Serrano 121, 28006 Madrid, Spain

Although much work has already been done to understand the processes taking place in a nonlinear fiber coupler, the theory of this device is still incomplete. Only special (and simple) cases have been considered using numerical [1]-[5] or semi-analytical [6]-[9] approaches. On the other hand, experimental data have shown that pulse propagation on this device is not always so simple. For example, the pulse can break up into smaller pulses; this effect, which leads to incomplete self-switching, cannot be explained using simple theories. Hence, a more elaborate approach based on the theory of Hamiltonian dynamical systems is needed.

The systematic investigation of a Hamiltonian dynamical system should consist of the following steps (either analytically or numerically): (i) Finding the stationary solutions (singular points); (ii) Investigation of their stability (establishing the type of point); (iii) Study of the evolution of the unstable states, and (iv) solution of the initial value problem. Step (i) of this sequence has been done previously in Ref.[10], where the full set of soliton states for the coupled set of nonlinear Schrödinger equations has been found and a bifurcation diagram for them has been constructed. Step (ii) has been partly (for symmetric and antisymmetric states in a limited range of parameters) done in Ref.[4]. A comprehensive study of the stability properties of the full set of soliton states has been completed in [11]. Step (iii), and partially step (iv), are accomplished in this work.

The results from steps (iii) and (iv) can be found asymptotically for large distances of propagation, where the soliton states are well separated from the radiation and from each other. This is analogous to a single NLSE where asymptotic results can be predicted from the spectrum of the inverse scattering problem. At short propagation distances there is still a strong interaction between the different parts of the solution, and so each case has to be considered separately. Both cases, i.e. short and long couplers, can be interesting in practice. Note also that we are considering here only the cases when two or more soliton states are well-separated at the output. The cases when they are superimposed on each other are more complicated and require more numerical simulations to understand the processes in the coupler.

Pulse propagation in a dual-core fiber coupler, including the effects of dispersion to second order and self-phase modulation can be described in terms of two linearly-coupled

nonlinear Schrödinger equations:

$$\begin{cases} iU_\xi + \frac{1}{2}U_{\tau\tau} + |U|^2U + KV = 0 \\ iV_\xi + \frac{1}{2}V_{\tau\tau} + |V|^2V + KU = 0 \end{cases} \tag{1}$$

where $U(\xi,\tau)$ and $V(\xi,\tau)$ are the electric field envelopes, K is the normalized coupling coefficient between the two cores, ξ is the normalized longitudinal coordinate, τ is the normalized retarded time, and the equations are written assuming anomalous group velocity dispersion (GVD).

An invariant of Eqs.(1) is the Hamiltonian:

$$H = \int_{-\infty}^{\infty} [\frac{|U_\tau|^2 + |V_\tau|^2}{2} - \frac{|U|^4 - |V|^4}{2} - K(UV^* + U^*V)]d\tau \tag{2}$$

Using Eq.(2) Eqs.(1) can be written in a canonical form:

$$iU_\xi = \frac{\delta H}{\delta U^*}, \quad iV_\xi = \frac{\delta H}{\delta V^*} \tag{3}$$

Eqs.(2) and (3) define the Hamiltonian dynamical system on an infinite-dimensional phase-space of two complex functions U, V decreasing to zero at infinity.

Eqs. (1) have stationary solutions. In particular, the set of Eqs.(1) has symmetric and antisymmetric solutions. In addition to symmetric and antisymmetric states, the set of Eqs.(1) has also asymmetric solutions with unequal field components. There are no analytic solutions for them, but they can be found numerically (see Ref.[10]). There are two different families of asymmetric solutions. They have been named in Ref.[10]: A-and B-type asymmetric states. The A- and B-type asymmetric states split off from the symmetric and antisymmetric states at bifurcation points. An exhaustive study of the stability of all of these types of soliton states can be found in Ref.[11].

By using the approach of nonlinear dynamical systems generalized to systems with infinite degrees of freedom, it is possible to predict qualitatively the behaviour of pulses propagating along a nonlinear directional coupler. Depending on the initial energy of the signal at the input, the output pulses are always close to one of the stable soliton states: to a symmetric state below the point of bifurcation or to an asymmetric A-state above the point of minimum energy. Although the total energy of the input signal is conserved, we can consider the central (signal) pulse as having energy losses related to the emission of radiation from the central pulse. Radiation plays an essential role in the processes of pulse transformations, allowing the pulses to adjust their energies to those corresponding to the stable soliton states. Stable soliton states are always excited with small perturbations unless the initial condition is an exact soliton state. The perturbation behaves oscillatorily because its growth rate is purely imaginary for stable states. Hence, arbitrary initial conditions produce periodic motion around stable soliton states after the radiation is emitted. This general idea can be applied to any particular case.

The antisymmetric states split off into two A-type asymmetric soliton states. The surplus energy is radiated in the form of small subpulses. The two asymmetric A-type states separate from each other. This means that two A-type states will appear at the output with certain delay, which depends on the length of the coupler. The sequence of

appearance of the two asymmetric A-type states is defined by the sign of the perturbation in the initial conditions.

For smooth initial pulses launched into one of two cores, there can be different regimes depending on the initial energy of the signal: (i) If the total energy of the input pulses is lower than some Q_o ($Q_o = Q_M + Q_R$, where Q_M is the energy at the point of bifurcation and $Q_R \approx 0.1Q_M$ is the radiated energy), then the field will consist of radiation (which decreases the amount of energy in the signal) and periodic oscillations around a stable symmetric state. The oscillations gradually decay with propagation so that the signal converges to the symmetric soliton state. This convergence is slower for smaller initial energies. For very low initial energies, the oscillations have larger amplitudes and are nondecaying. In the linear limit, the coupler swaps the energy of the pulses between the channels as in the case of CW initial conditions; and (ii) If the energy of the initial pulse is higher than Q_o, then the propagating field consists of radiation and periodic oscillations around an asymmetric A-type state. We can observe the unequal pulse amplitudes at the output of the coupler. There is an intermediate range of energies where symmetric and asymmetric states exist at the same value of energy. It can happen in this case that the motion consists of periodic oscillations around both symmetric and asymmetric soliton states simultaneously. If the energy of the initial pulse is much higher than Q_o, so that it is enough to excite two or more soliton states, then several soliton states will appear.

References

[1] B.Daino, G.Gregory, S.Wabnitz, *J.Appl.Phys.*, **58**, 4512 (1985).

[2] A.W.Snyder, D.J.Mitchell, L.Poladian, D.R.Rowland, *J.Opt.Soc.Am.*, **B 8**, (1991).

[3] S.Trillo, S.Wabnitz, E.M.Wright and G.I.Stegeman, *Opt.Lett.*, **13**, 672 (1988)

[4] E.M.Wright, G.I.Stegeman, S.Wabnitz, *Phys.Rev.*, A **40**, 4455 (1989)

[5] G.D.Peng and A.Ankiewicz, *Int.J.Nonlinear Opt. Phys.*, **1**, 135 (1992).

[6] F.Kh.Abdullaev, R.M.Abrarov and S.A.Darmanyan, *Opt.Lett.*, **14**, 131 (1989).

[7] C.Pare, M.Florjanczyk, *Phys.Rev.*, A,**41**,6287 (1990).

[8] Y.S.Kivshar, B.A.Malomed, *Opt.Lett.* **14**, 1365 (1989).

[9] P.L.Chu, G.S.Peng and B.A.Malomed, *Optics Letters*, **18**, 328 (1993).

[10] N.N.Akhmediev, and A.Ankiewicz, *Phys.Rev.Lett.*,**70**, 2395 (1993).

[11] J.M.Soto-Crespo, N.N.Akhmediev, *Phys.Rev.*, **E 48**, 4710 (1993).

Femtosecond Pulse Splitting, Supercontinuum Generation and Conical Emission in Normally Dispersive Media

G.G. Luther, J.V. Moloney E.M. Wright and A.C. Newell

Arizona Center for Mathematical Sciences

Department of Mathematics

University of Arizona

Tucson, Az. 85721

Telephone: (602)-621-6755

Fax: (602)-621-1510

Conical emission has long been associated with spectral super broadening [1] (SSB) and has been attributed to four-photon coupling[3]. Recent laboratory experiments[2] demonstrate that SSB correlates with the threshold for self-focusing (SF). Both these experiments and several numerical studies suggest that SF is inhibited by normal group velocity dispersion NGVD. Near this threshold SSB, conical emission and pulse splitting occur explosively.

We will report on a self-consistent theory of critical self-focusing in the presence of normal group velocity dispersion. The underlying physical phenomena are all contained in the spatiotemporal dynamics of short laser pulses described by the nonlinear Schrödinger equation (NLS),

$$2ik\frac{\partial A}{\partial z} + \frac{\partial k}{\partial \omega}\frac{\partial A}{\partial t} + \nabla^2 A - k\frac{\partial^2 k}{\partial \omega^2}\frac{\partial A}{\partial t^2} + 2k^2\frac{n_2}{n_0}|A|^2 A = 0. \tag{1}$$

where $k'' = \partial^2 k/\partial \omega^2|_{\omega_0} > 0$ for NGVD. We will show that the conical emission predicted by this equation is due to a fundamental four-wave interaction that promotes the transport of energy to a

band of modes with finite frequency and energy shifts. This mechanism was originally identified in the break-up of one dimensional envelope solitons of ocean surface waves by transverse perturbations [4]. These modes are closely related to those of the modulational instability (MI) of the condensate or uniform plane wave solution. Pulse splitting, spectral broadening and conical emission are intimately related, and each is a consequence of this wave interaction. Figure 1(a) shows a contour of the pulse intensity and far-field spectrum (in θ and ω) just at the instant of splitting and Figure 1(b) depicts the same quantities just after the pulse splits. Notice the strong spectral features in the (θ-ω) plane that emerge along the intersecting straight lines which is simply the locus of four wave resonant vectors satisfying the relation $\gamma^2\Omega^2 = \kappa^2$ where Ω is the shift in frequency and κ the shift in wavenumber. It is easy to see from this figure that a spectrally filtered far-field will exhibit conical emission at the blue and red-shifted ends of the generated supercontinuum with the diameter of the cone increasing with frequency shift from the center outwards in either direction.

We will also show that complex spatiotemporal evolution of the pulse up to and just beyond the splitting point can be captured by a simple set of coupled ordinary differential equations whose phase portraits give quantitative information on the critical focusing and pulse splitting process. The singular perturbation method we use is motivated by the idea that the initial 2D transverse self-focusing (2D collapse) has a universal self-similar form which can act as the relevant transverse mode as long as the dispersion (NGVD) is initially weak. The simple theory yields quantitative agreement with the full numerical simulation of the above NLS equation even beyond the splitting point. Prelimianry results on the effect of Raman scattering on critical focusing show that the "effective" refractive index can oscillate in sign for certain realistic experimental situations and lead to strong temporal modulation along the self-focusing pulse.

References

[1] R.R. Alfano and S.L. Shapiro, *Phys. Rev. Lett.*, **24**, 584 (1970); R.R. Alfano, Ed. "The Supercontinuum Laser Source" *Springer Verlag, New York* (1989).

[2] P.B. Corkum and C. Rolland,, *IEEE J. Quant. Electron.*, **25**, 22634 (1989); F.A. Ilkov, L. Sh. Ilkova and L. Chin, *Opt. Lett.*, **18**, 681 (1993)

[3] R.Y. Chiao, P.L. Kelley, and E. Garmire, *Phys. Rev. Lett.* **17**, 1158 (1966).

[4] O.M. Phillips, "Dynamics of the Upper Ocean", (Cambridge University Press, 1977).
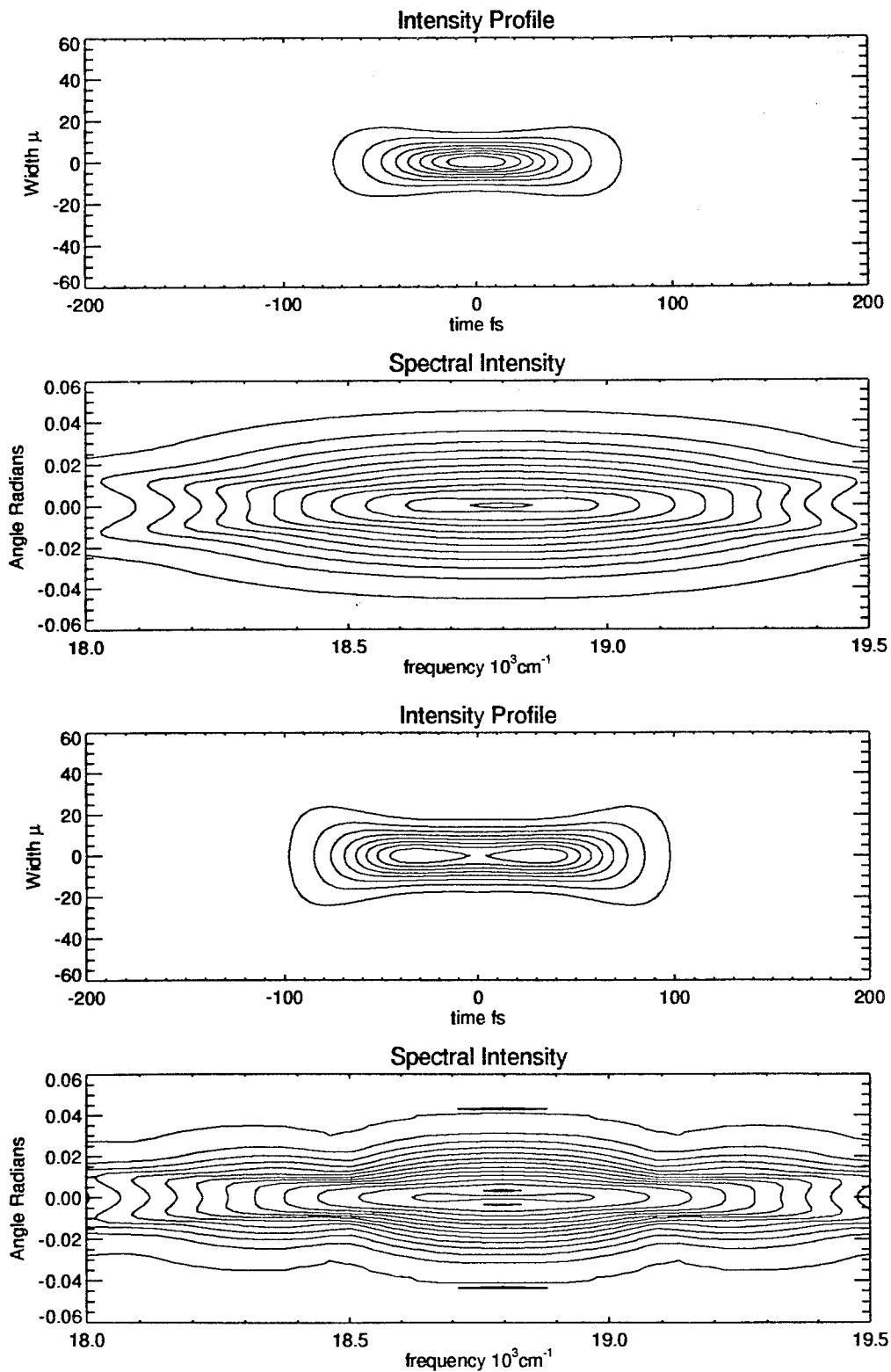
Figure 1(a) Pulse intensity contours (r,t) at the moment preceding splitting and accompanying superbroadened spectrum (k,ω). (b) The same graph after the pulse split.

Generation of subpicosecond infrared laser pulses produced by optical switching from low temperature grown gallium arsenide

J. Meyer and A.Y. Elezzabi, Department of Physics, The University of British Columbia, Vancouver, B.C., Canada, V6T 1Z1, Tel.:(604) 822 6577

The generation of ultra short pulses at the CO_2-laser wavelength can provide a unique and indispensable tool in the investigation of several interesting fundamental processes which occur in picosecond and femtosecond time scales. We are interested in the application of such pulses for the investigation of semiconductor properties, for example: the measurement of kinetics of non equilibrium electron-hole plasmas, fast carrier relaxation times, time-resolved transport properties inside semiconductor buried structures and interfaces and induced intraband coherence effects in quantum wells.

Pico/femtosecond optical semiconductor switching using both a reflection and a transmission switch for 10.6 µm has been used before to produce pulses as short as 130fs[1]. However, for many experiments, for example those involving intra cavity switching it is desirable to operate with a single reflection switch. To this end we investigated many semiconductor surface structures in this talk we will discuss the fastest and most reliable structure investigated which is capable to generate 10µm pulses shorter than 500fs.

The CO_2-laser pulse is created by reflection from a transient metallic-like semiconductor plasma. The speed of this switching technique relies on the ultra short carrier life time (≤ 0.5ps) in low temperature molecular beam epitaxy (MBE) grown GaAs (LT-GaAs)[2]. Subpicosecond recombination time is achieved through the introduction of high density As-recombination centers during the growth of GaAs. Our experiments show that LT-GaAs, grown under the following conditions is ideally suited for optical semiconductor switching of below band gap IR radiation.

The LT-GaAs layer is grown by MBE on a semi-insulating GaAs substrate. The substrate is treated in an UV generated ozone atmosphere for 4 minutes to remove any residual organics from the wafer surface. The oxide is desorbed thermally in the MBE growth chamber which roughens the surface of the substrate. The surface is smoothed by growing a 2µm thick (1µm/hr) GaAs buffer layer at a temperature of 600°C. Next, a 100nm thick GaAs temperature-transition layer is grown on the buffer layer. During this growth the substrate temperature is lowered from 600°C to 320°C in 6 min. Following this, a layer of LT-GaAs is grown at 320°C with an As_2 to Ga at various flux ratios, typically of 3:1. For most of our experiments a 200nm thickness of LT-GaAs is sufficient, which corresponds to the absorption depth of 600nm radiation. Then the sample is heated from 320°C to 550°C in 3 min and annealed for 6 min at 550°C under As_2 flux. The substrate temperature is measured to within ±1°C using diffuse reflectance spectroscopy[3].

The resultant LT-GaAs layer and GaAs substrate is transparent to IR radiation. However, once illuminated with a visible laser pulse with sufficient energy fluence to produce an electron-hole plasma density $\geq 10^{19}$cm^{-3} the layer becomes reflective to CO_2-laser radiation in a time less than the visible pulse duration. Significant reflectivity will persist as long as the carrier density is $\geq 10^{19}$cm^{-3}. As precipitates in the LT-GaAs layer act as ultra fast recombination centers. If enough As (~1%) is introduced in the layer it is possible to reduce the carrier density below 10^{19}cm^{-3} in less than 0.5ps. Thus it is possible to reflect subpicosecond IR pulses.

One series of experiments was performed in the following way. Single mode, polarized radiation from a 35W cw-CO_2-laser, operated on a single gain line (P20) is focused to a spot size of 1.2 mm^2 onto the LT-GaAs layer at Brewster's angle of incidence (~72°). This way we obtained a contrast ratio between the reflected pulse and remnant reflected background radiation of 10^4:1. The excitation of the switch is provided by a laser system consisting of a synchronously mode-locked dye laser (616nm, 370fs, 82MHz) followed by a three stage dye (Rh640) amplifier chain which is pumped by the frequency doubled output of a Nd:YAG regenerative amplifier. The system delivers 1mJ, 450fs pulses at 616nm with a repetition rate of 10Hz. A 50:50 beamsplitter splits the output into two pulses. One pulse (control pulse) is concentrated to a 2mm diameter spot on the LT-GaAs layer completely covering the CO_2-laser spot. This generates the ultra short IR pulse. The angular separation between the IR- and control beams is kept to a minimum (~5°) in order to prevent wave front distortion of the reflected IR pulse during switch out.

The following cross correlation technique was used to measure the temporal IR pulse shape. A 50 μm thin Si semiconductor wafer acting as a cut off switch is placed at normal incidence with respect to the focused IR and second optical pulses which has passed through a variable optical delay line. Pure Si transmits the IR radiation except for 30% surface reflection losses. However, upon irradiation by the visible pulse free carriers are generated over the absorption depth of 2.8μm. Due to the induced IR reflection and free carrier absorption the IR transmission of the wafer changes from 0.7 to zero at the applied irradiance within a time of ~100fs, measured in a separate experiment and remains unrecovered for ~20ns. The transmitted IR radiation is recollimated and detected by a Cu:Ge IR detector-GHz-amplifier combination. The detected signals are integrated, digitized and stored on a computer in combination with the simultaneously monitored and digitized visible pulse energy. By varying the optical delay of the second visible pulse we obtain the cross correlation signal between the IR pulse and the optical gate whose first derivative effectively displays the IR pulse shape.

These cross correlation measurements can be compared with calculations based on a theoretical model in which the free carriers are generated exponentially decreasing in density both in the LT-GaAs and the buffer layers by a Gaussian pulse of 450fs FWHM convoluted with the following free carrier dynamics. The carriers in the LT-GaAs layer recombine exponentially with a lifetime of 0.5ps while the carriers in the exponential tail in the buffer layer diffuse at $D=20cm^2$/s both towards the bulk and towards the LT layer. The resulting evolution of the carrier density is calculated and the amplitude reflectivity is found by integrating over the reflectivity of infinitesimal density steps using the Drude model. The intensity reflectivity is then integrated from zero to time t to simulate the cross correlation measurements. The resulting pulse shape is very sensitive to the assumed LT-life time and the FWHM of the optical pulse.

The following figure shows a typical result of the experiment (points with standard error of at least 20 measurements) and the model prediction (full curves) in which the maximum free carrier density reached was $5\times10^{19}cm^{-3}$. The curves indicate a 1ps IR pulse followed by a long low intensity tail due the diffusing carriers in the buffer layer. Furthermore the results indicate that the described experiment in comparison with the model calculations can provide a good determination of the free carrier relaxation time. Shorter pulses as is predicted by the model can be attained at lower visible pulse fluence, however experiments become much more difficult due to the rapidly decreasing detected IR pulse energies. The experiments would be greatly improved if control pulses of duration much shorter than the free carrier lifetime (e.g. 100fs) were to be used. Finally

we would like to point out that by reflecting far infra red pulses of $\lambda > 100 \mu m$ off the described switch pulses of less than one optical cycle can be produced.
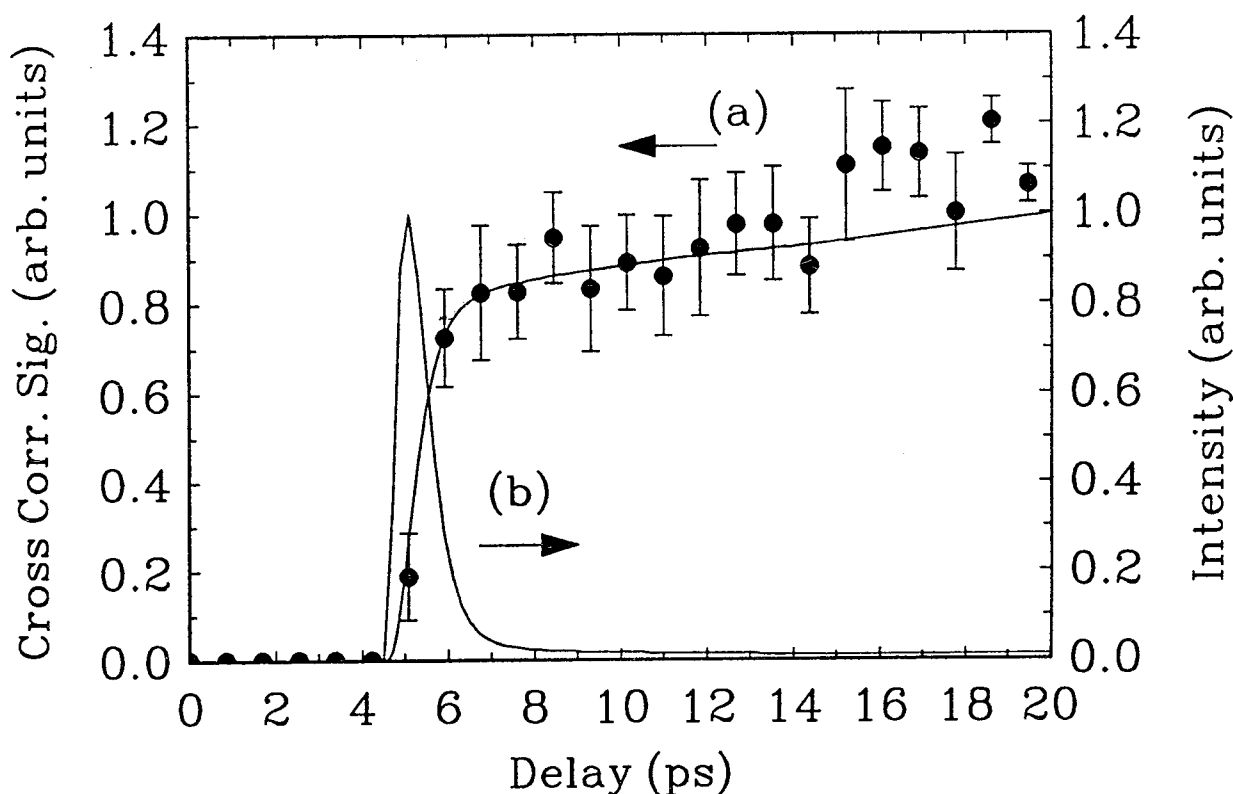
In a second series of experiments we measure the spectrum of the ultra short reflected IR pulse using an IR monochromator-pyro-electric-array combination. Sacrificing statistics these experiments had to be carried out using a pulsed hybrid CO_2-laser operating at a maximum repetition rate of one Hz. Details of the spectrum, including a possible chirp will be reported.

The authors thank T. Tiedje for the use of the MBE machine, S.R. Johnson for growing the samples and acknowledge the assistance of S. Knotek, D. DiTomaso, and T. Felton. This work is supported by the Natural Science and Research Council of Canada.

[1]P.B. Corcum, Opt.Lett., **8**, 514 (1983); IEEE J.Quant.Electron., **21**, 216, (1985).

[2]E.S. Harmon, M.R. Melloch, J.M. Woodall, D.D. Nolte, N. Otsuka, and C.L. Chang, Appl.Phys.Lett., **63**, 2248, (1993); M.Y. Frankel, B. Tadayon, and T.F. Carruthers, Appl.Phys.Lett., **62**, 255 (1993); X.Q. Zhou, H.M. van Driel, W.W. Rühle, Z. Gogolak, and K. Ploog, Appl.Phys.Lett., **61**, 3020 (1992).

[3]S.R. Johnson, C. Lavoie, T. Tiedje, and J. Mackenzie, J.Vac.Sci.Tecnol., **B11**, 1007 (1993).

Wednesday Papers Not Available

THURSDAY, JULY 28

THA: **Applications of Nonlinear Optics**
THB: **Holographic Optical Storage**

A Solid-State Three-Dimensional Upconversion Display

E. A. Downing, L. Hesselink

Dept. of Electrical Engineering, Stanford University, Stanford, California 94305-4035
415-725-3288; 415-725-3377 (fax)

R. M. Macfarlane

IBM Research Division, Almaden Research Center, 650 Harry Rd, San Jose, California 95120

We demonstrate a novel solid-state three-dimensional display using rare earth doped heavy metal fluoride glass as the active medium.   In this device, two laser beams intersect inside a bulk glass at room temperature to address a pixel in three-dimensional space. The two-step resonant upconversion process requires two different infrared wavelengths to produce visible radiation. In this manner, a pixel can be addressed only at the intersection of the two laser beams. By scanning the intersection of these beams inside the display material, true three-dimensional figures can be drawn.[1] For practical applications with high bit densities and low power pump lasers, high upconversion efficiency is necessary. Recent work on upconversion in fluoride glasses, motivated by fiber amplifier and short wavelength laser development, has identified fluoride glass hosts and rare earth dopants as systems that have high radiative recombination rates and high upconversion efficiencies.   In this presentation we demonstrate three-dimensional displays in both trivalent praseodymium (Pr^{3+}:ZBLAN) and in trivalent thulium (Tm^{3+}:ZBLAN) doped bulk fluoride glass.

Bulk heavy metal fluoride glass samples were fabricated using the reactive atmosphere processing technique. We chose ZBLAN as the host due to its stability in the vitreous phase, transparency in the infrared, and the ability to incorporate high rare earth dopant concentrations. Starting mole percentages used in the samples were 53% ZrF_4 * 20% BaF_3 * (4-x)% LaF_3 * 3% AlF * 20% NaF * x% rare earth, with x ranging from .1% to 2% PrF_3 and TmF_3. Samples were melted in vitreous carbon crucibles at 850 degrees C in a chlorine gas atmosphere for 1.5 hours, then quenched. Typical sample volumes of 1 cubic cm weighing roughly 4 grams were used.

The upconversion fluorescence spectra were measured using two-step photoexcitation which populates the $^3P_0$ and $^3P_1$ levels in praseodymium and the $^1G_4$ and $^1D_2$ levels in thulium. Figure 1 shows the energy levels of Pr^{3+} and Tm^{3+} doped ZBLAN glass populated by the laser wavelengths used.   The population of the $^1D_2$ level in Tm can arise from a combination of two-step upconversion and cross-relaxation processes.
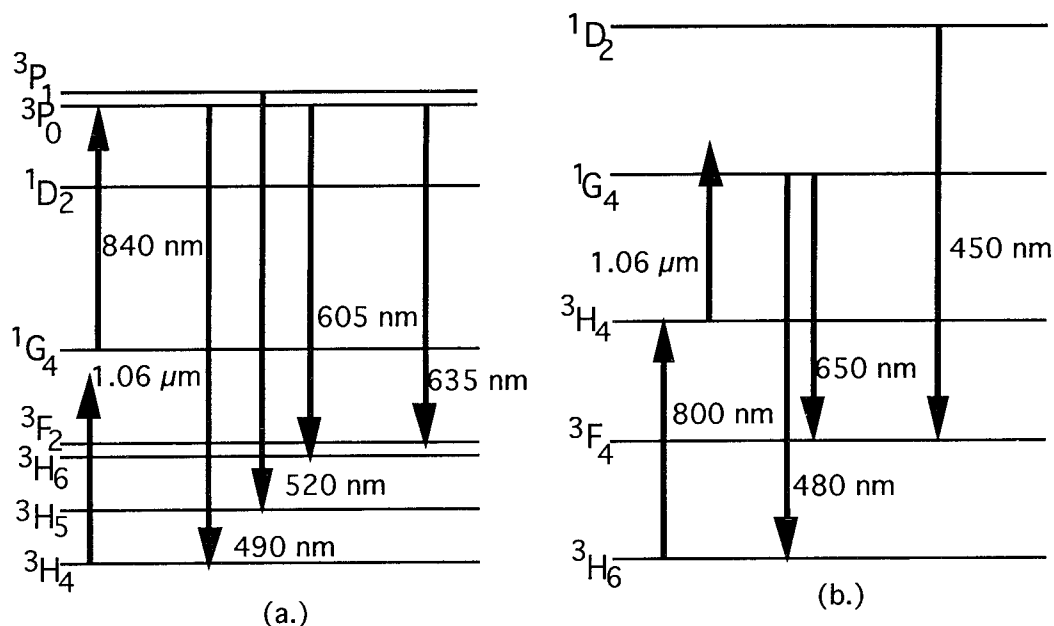
Figure 1. (a) Energy level diagram for Pr^{3+} doped ZBLAN glass using pump wavelengths of 1064 nm and 840 nm; (b) Energy level diagram of Tm^{3+} doped ZBLAN glass using pump wavelengths of 800 nm and 1064 nm.

The upconverted fluorescence spectra of Pr:ZBLAN excited with cw pump wavelengths of 1064 nm and 840 nm and of Tm:ZBLAN excited with 800 nm and 1064 nm are shown in figure 2. The Pr:ZBLAN spectrum is similar to that obtained from argon ion laser pumping and from two-photon excitation using other wavelengths.[2-5] Contrast ratios between single frequency upconversion and two-photon upconversion will be discussed.
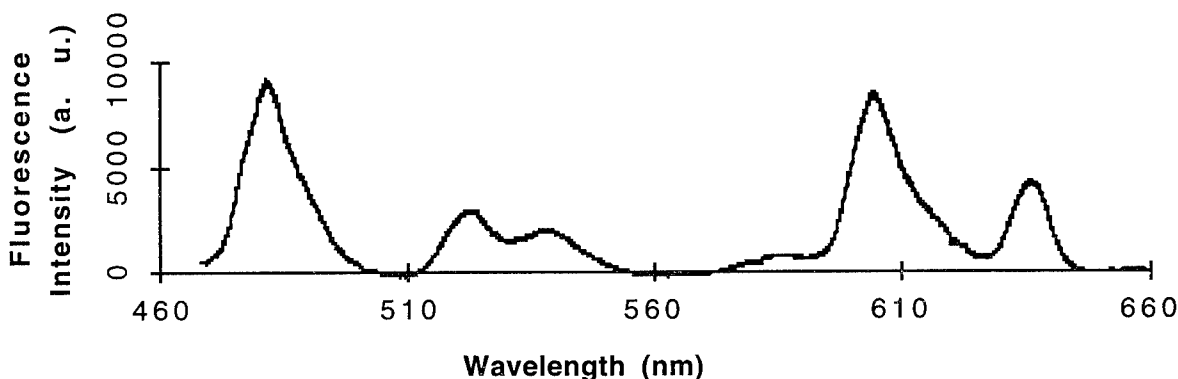
Figure 2. (a) Fluorescence spectrum of Pr^{3+} doped ZBLAN glass pumped at 1064 nm and 840 nm.
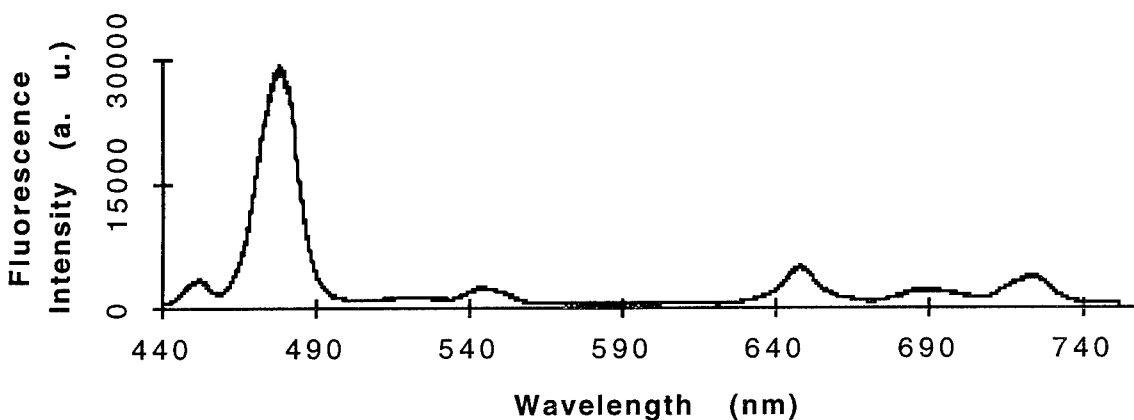
Figure 2. (b) Fluorescence spectrum of Tm^{3+} doped ZBLAN glass pumped at 800 nm and 1064 nm.

As a device demonstration we used a rotating mirror and refractive optics to scan the laser pump beams into the praseodymium doped glass sample, as shown in figure 3. The 1064 nm beam was reflected at a near normal incident angle from a mirror mounted on a 3600 RPM electric motor. This beam was focused to a 50 micron spot and scanned conically inside the sample. The 840 nm laser beam was focused cylindrically into a 50 micron thick stationary plane. Circles and ellipses on the order of 5 mm in diameter were drawn inside the sample by intersecting the cone and plane to form conic sections. Addressing of 300 50-micron pixels was done at a scan rate of 60 Hz. Simple calculations show that given present upconversion efficiencies, we should be able to address 30,000 pixels with sufficient brightness and bandwidth to be suitable for desk-top viewing under normal room lighting conditions. In the presentation we will discuss relative efficiencies of different dopants and glass hosts and additionally the merits of different excitation and scanning schemes.
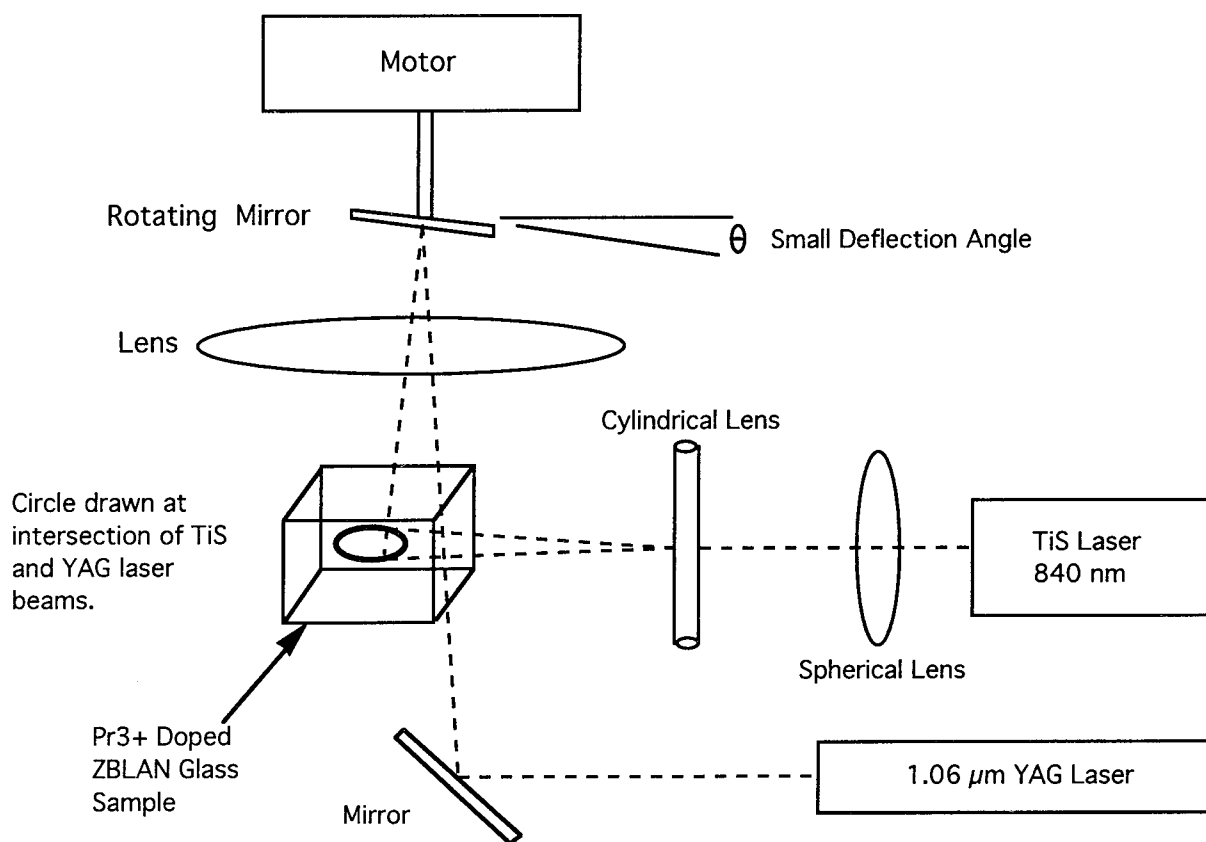
Figure 3. Diagram of scanning system used to draw circles in Pr^{3+} doped ZBLAN glass.

1. J. D. Lewis, C. M. Verber, R. B. McGhee, IEEE Trans. Electron Devices. Vol. Ed-18, No 9, Sept. 1971.

2. M. Eyal, E. Greenberg, R. Reisfeld, Chem. Phys. Lett. **117**, 108 (1985).

3. J. Y. Allain, M. Monerie, H. Poignant, Electron. Lett. **27**, 189 (1991).

4. R. G. Smart, J. N. Carter, A. C. Tropper, D. C. Hanna, Opt. Comm. **86**, 333 (1991).

5. R. G. Smart, D. C. Hanna, A. C. Tropper, Electron. Lett. **27**, 1307 (1991).

A versatile all-optical modulator based on nonlinear Mach-Zehnder interferometers

Gijs J.M. Krijnen, Alain Villeneuve, George I. Stegeman,
Paul V. Lambeck* and Hugo J.W.M. Hoekstra*

Center for Research and Education in Electro-Optics and Lasers
University of Central Florida, 12424 Research Parkway, Orlando, Florida 32826
Tel: 407-658-3991 / Fax: 407-658-355.

*Lightwave Devices Group, MESA Institute, University of Twente
P.O. Box 217, 7500 AE Enschede The Netherlands

Introduction

High bit rate communication systems of the future will demand ultrafast devices for routing signals, controlling polarisation, converting wavelengths and performing logical functions. Without doubt it is a great benefit when all this can be done completely in the optical domain. In this paper we describe a device based on a Nonlinear Mach-Zehnder interferometer (NMI) which exploits cross-phase modulation (XPM) of two co-propagating modes in bimodal branches. This is in contrast to the device as introduced in [1] which exploits XPM of orthogonally polarised modes of monomode waveguides. The advantage of the new concept is the fact that the device becomes polarisation independent while keeping phase insensitive by using different propagation constants of the modes of the bimodal branches.

Basic operation

A schematic lay-out of the proposed Nonlinear Mach-Zehnder interferometer is shown in Figure 1. The structure is assumed to consist of materials with Kerr nonlinearities. It has three inputs; the middle one is used for insertion of a probe beam (P_p), the two outer waveguides for insertion of control beams (P_c^1 and P_c^2). The probe beam is equally divided
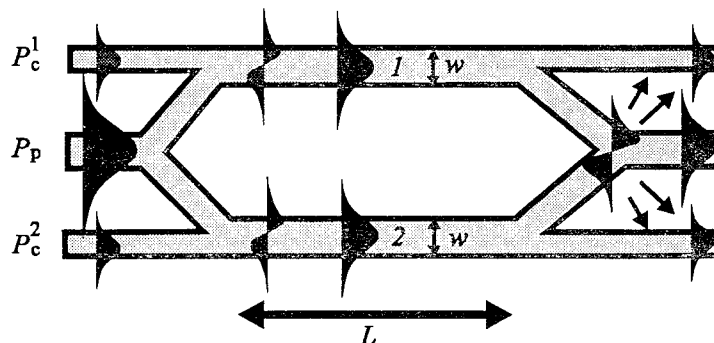
Figure 1: Schematic lay-out of the proposed NMI.

over two branches by the central Y-junction and each of them is also the wider input of an asymmetrical Y-junction. When carefully designed [2] these latter Y-junctions cause the modes from the wider input channel and the smaller input channel to convert adiabatically into the fundamental and first order modes respectively of the bimodal waveguides 1 and 2. So when both probe and control power are inputted as fundamental and first order modes they will co-propagate through the bimodal sections and induce mutual phase changes by XPM. At the end of the branches the fundamental mode (the probe) and the first order mode (the control) are separated with the same asymmetrical Y-junctions, now used in reversed direction since they act as mode-splitters in this direction. The fundamental modes propagate into the centre Y-junction at the output where they will recombine. The in-phase parts will add up to form the fundamental mode of the output. The transmission of the probe can be given by:

$$\frac{P_{out}}{P_{in}} = \cos^2(\Delta\phi/2) \tag{1}$$

412

where $\Delta\phi$ is the phase difference of the two fundamental modes at the end of the branches. The phase of the fundamental modes at the end of the branches is determined by the propagation constant and the self-phase modulation (SPM) of the probe mode and the XPM by the control. Using the expressions for the nonlinear polarisation and restricting the terms to those at $\omega=\omega_0$ (the frequency of the light used) which are independent of the propagation co-ordinate, the nonlinear induced phase change of the probe modes is given by [3]:

$$\Delta\phi_p^i(L,P_p,P_c^i) = (Q_{pp}^i\frac{P_p}{2} + 2Q_{pc}^iP_c^i)L \qquad \{i=1,2\} \qquad (2)$$

where i denotes the branch and L is the length of the branches. The nonlinear coupling coefficients are given by the well-known overlap integrals:

$$Q_{\mu\nu}^i = \frac{\omega\varepsilon_0}{2}\int\limits_{x=-\infty}^{\infty}\int\limits_{y=-\infty}^{\infty}n_0n_{2e}|E_\mu^i(x,y)|^2|E_\nu^i(x,y)|^2dxdy \qquad \{\nu,\mu = p,c\} \qquad (3)$$

where E_ν^i and E_μ^i denote the normalised fields of modes ν and μ in branch i and where n_{2e} is the nonlinear Kerr-index. Assuming that the branches are identical the phase difference at the output is given by:

$$\Delta\phi = \Delta\phi_p^1 - \Delta\phi_p^2 = 2Q_{ps}(P_c^1 - P_c^2)L \qquad (4)$$

For the case of one input (i.e. say $P_c^2=0$) the switching power is found for $\Delta\phi=\pi$:

$$P_s = \frac{\pi}{2Q_{pc}L} \qquad (5)$$

It is worthwhile remarking that for isotropic waveguide structures the field profiles are not strongly depending on the polarisation. There is, however, in general a dependence of n_{2e} on the polarisation direction thus making the nonlinear coupling coefficients polarisation sensitive. Nevertheless, since the switching curves are rather flat around $P=P_s$, according to (1) more than 93% switching can be obtained by taking P_s as the average value of the P_s-values for cross- and equipolarised beams. Furthermore by avoiding working in the proximity of any resonance's, the dispersion of n_{2e} will be relative small thus making the device operate at a range of wavelengths even when using different probe and control wavelengths. Finally $\Delta\phi$ is independent of P_p implying that, according to this first order analysis, any probe power can be switched by the controls. Hence, the device enables modulation, amplification and wavelength and polarisation conversion at one time.

Numerical results

As an example of the proposed concept we numerically investigated a possible implementation of the structure in $Al_xGa_{1-x}As$ technology. The waveguide geometry comprises a 40% Al substrate, a 1.0 μm thick 18% Al film layer and a 1.5 μm thick 30% Al cladding layer, etched down to 0.35 μm in the regions adjacent to the waveguides. Taking these concentrations the bandgap energy will be a little higher than 2 times the photon energy for 1.55 μm wavelength thus virtually eliminating two-photon absorption [4]. Refractive indices and nonlinearities were calculated using expressions as given in [5]. The mode profiles of the waveguides were analysed by means of a Finite Difference scheme [6]. Results of these calculations were compared to those of Nonlinear Effective Index calculations [7] showing very good similarity with regard to the field profiles and the nonlinear coupling coefficients. This implies that further analysis of the device lay-out could be pursued by applying two dimensional BPM calculations.

413

The Y-junctions were optimised using simple approximate expressions [8]. It was found that 0.15 degrees branching angles in combination with 2 and 2.5 µm wide input waveguides gives a Mode Conversion Factor of ≈ 2. This on its turn should yield a mode selectivity of ≈ 26 dB which indeed was nearly (24 dB) observed in Enhanced Finite Difference Beam Propagation (EFDBPM) calculations [9]. A branch to branch separation of 20 µm was found to give sufficient decoupling (-60 dB) of the modes in the two branches of the NMI. Aiming at a total device length of 2.5 cm and reserving 4 mm for the centre output waveguide in order to allow the radiation modes to spread out in the environment, a branch length of 1.5 cm resulted. The CW performance of the described structure was analysed by means of EFDBPM calculation. P_p was taken to be fixed at 200 W whereas P_c^1 was varied between 0 and 100 W. Figure 2 top shows the calculated transmission curve for P_p versus P_c^1. The transmission clearly shows a strong modulation due to the weaker signal beam leading to an almost absence of power (0.02 %) in the output for $P_c^1 = 22$ W. This is illustrated in the middle part of Figure 2 which shows $|E(x,z)|$ as obtained by EFDBPM. Finally we studied the modulation of a 200 fs long probe pulse ($P_{peak} = 1$ W) by a 1 ps long signal pulse ($P_{peak} = 45$ W) by means of a split-step Fourier method [10]. Figure 2, bottom, shows that the probe pulse is fairly equally modulated over the complete length of the pulse without any substantial pulse break-up
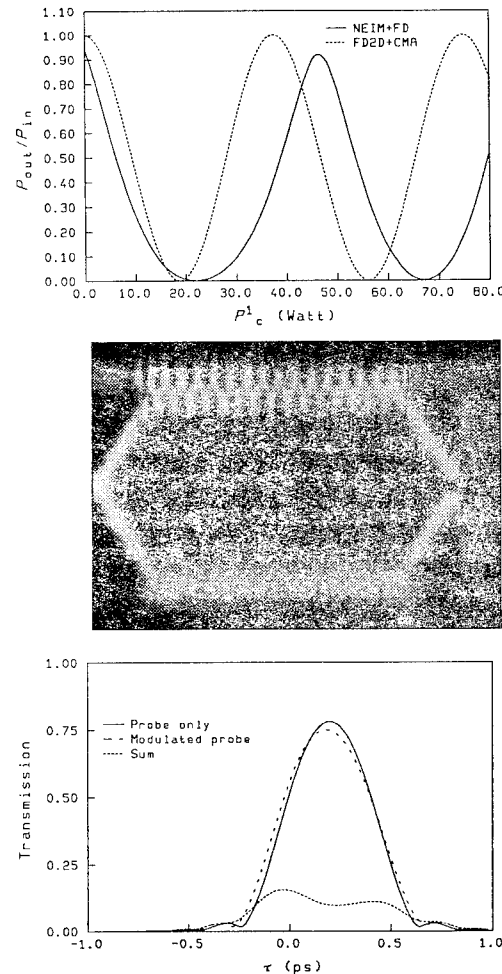
Figure 2: Top: Transmission of a 200 W probe beam versus input signal. Middle: modulus of the electric field (P_p=200 W, P_c^1 = 22 W). Bottom: calculated pulses.

Acknowledgement

References

[1]   A. Lattes, H. Haus, F. Leonberger and E. Ippen, IEEE J. Q. Elect., Vol-19, 1983, p1718.
[2]   W. Burns and F. Milton, IEEE J. Q. Elect., Vol-11, 1975, p32.
[3]   Y. Silberberg and G. Stegeman, Appl. Phys. Lett., Vol-51, 1987, p1230.
[4]   A. Villeneuve, C. Yang, G. Stegeman, C. Lin and H. Lin, Appl. Phys. Lett, Vol-62, 1993, p2465.
[5]   M. Sheik-Bahae, D. Crichton Huntings, D. Hagan, E. van Stryland, IEEE J. Q. Elect., Vol-27, 1991, p1296.
[6]   E. Schweig and W. Bridges, IEEE Trans. Microw T. Techn., Vol-MIT-32, no 5, may 1984, p531.
[7]   G. Krijnen, H. Hoekstra and P. Lambeck, accepted for publication in IEEE J. L. T.
[8]   G. Krijnen, H. Hoekstra, P. Lambeck and T. Popma, Elect. Lett. Vol-28, 1992, p2072.
[9]   H. Hoekstra, G. Krijnen and P. Lambeck, Opt. Comm. 94, 1992, p506.
[10]   See for example: G. Agrawal, "Nonlinear fiber optics", Academic press, ISBN 0-12-045140-9.

COMPENSATION FOR DISTORTIONS AND DEPOLARIZATION
OF A MULTI-MODE FIBER
USING A BRILLOUIN PHASE-CONJUGATE MIRROR

Steven C. Matthews
Hughes Electro-Optical Systems
2000 E. El Segundo Blvd.
El Segundo, CA 90245
and
David A. Rockwell
Hughes Research Laboratories
3011 Malibu Canyon Road
Malibu, CA 90265

Multi-mode optical fibers are being increasingly utilized for high-power solid-state laser beam delivery. While the benefits of such a flexible beam-delivery system are highly appealing in many applications, multi-mode fibers with lengths of more than ~ 1 meter produce a severely distorted and highly depolarized output beam, even when the initial high-power laser beam is nearly diffraction-limited and linearly polarized. These distortions (and also possibly the depolarization) can limit the utility of fiber beam delivery.

Over the past decade, the ability of nonlinear optical phase conjugation (NOPC) to compensate fiber distortions and depolarization has been established by several experimental demonstrations that utilized a photorefractive phase-conjugate mirror (PCM). The first such report was that of Dunning and Lind[1] in 1982. More recently, Luther-Davies et al.[2] reported the successful use of phase conjugation to compensate fiber distortions and depolarization in a phase-conjugate oscillator configuration that was specifically aimed at laser beam-delivery applications. From an applications perspective, these previous demonstrations suffered from two practical disadvantages inherent in the use of a photorefractive PCM. First, because of the relatively slow response times of such conjugators, the compensation "washes out" if the fiber-induced distortions change too quickly. Second, available photorefractive conjugators are not effective at the 1.06 μm wavelength of the Nd:YAG laser. Because NOPC has been established as a viable approach for compensating distortions and depolarization in high-power solid-state lasers,[3] we have investigated the practicality of using a Brillouin PCM to achieve comparable compensation of multi-mode fibers. Indeed, as is detailed below, we find that excellent compensation can be achieved.

The experimental apparatus is shown in Figure 1. We used a linearly polarized Nd:YAG oscillator and single pass amplifier, producing a beam ~ 1.5 times diffraction-limited and operating in a single longitudinal mode with a pulse duration of 20 nsec. A combination of a half-wave plate and polarizing beam splitter (BS1) allowed us to divide the laser power among two beams, with a continuously adjustable splitting ratio. One beam, the signal beam, passed through a second beam splitter (BS2, an uncoated glass wedge) and was coupled into a 2 m graded index fiber (NA~0.33, d = 380 μm, Fiberguide Industries) through a (down-collimating) imaging telescope of magnification M=10. The use of an image-relay telescope to couple into and out of the fiber allowed us to perform diagnostics on the entire radiation pattern returning from the fiber, i.e., we could analyze the full NA of the fiber.

Following a single pass through the fiber, the signal beam was highly aberrated (>100 times diffraction-limited) and totally depolarized, i.e. half of the power was contained in each of the two orthogonal polarization states. This distorted, depolarized beam then propagated to the PCM, which was based on the scheme originally demonstrated by Basov et al.[4] Specifically, a calcite wedge separated the signal beam into two orthogonally polarized components, and the polarization of one of the components was rotated by 90°. Hence, the two beams were co-polarized as they

entered the PCM, which consisted of a hollow quartz capillary (0.8 mm ID, 20 cm long) filled with liquid $TiCl_4$.

The conjugate beam passed back through the fiber and was coupled by BS2 into the diagnostics that were used to analyze the angular distribution of the return beam. As our primary beam-quality diagnostic, we measured the "energy in the bucket," i.e. the fraction β of the total beam energy that was contained within a far-field angular cone of full width θ. This diagnostic approach is essential in this type of measurement because of its sensitivity to very weak levels of radiation that might be spread over a broad solid angle as large as the fiber numerical aperture. We also analyzed the degree of polarization in the input and output beams.

Figure 1 also indicates that BS1 produced a reference beam, which had a power of 600 kW; its function was to turn on the PCM, which had an SBS threshold of ~ 80 to 100 kW (as measured using the reference beam). The use of this reference beam was necessitated by the requirement to maintain the signal-beam power below ~ 15 kW to preclude the onset of SBS in the fiber. The simultaneous presence within the light guide of the signal beam as well as the reference beam and its Stokes-shifted, phase-conjugate reflection led to the creation of a conjugate to the signal beam via Brillouin-enhanced four-wave mixing (BEFWM).[5] Once the PCM was turned on, the signal beam achieved essentially the same reflectivity (~ 40 %) and conjugation fidelity as the reference beam, in agreement with earlier observations using a similar arrangement.[6,7]
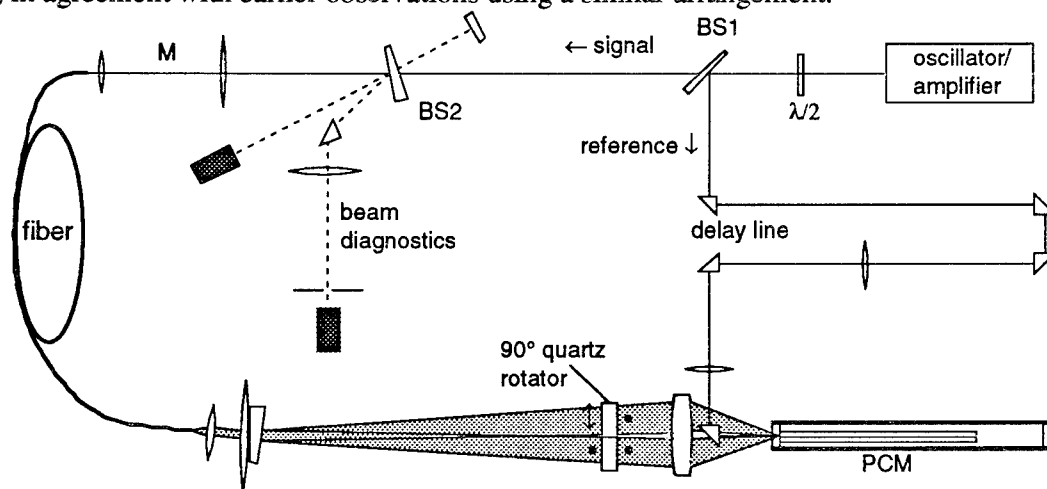
Figure 1. Schematic of experimental apparatus used to demonstrate that Brillouin phase conjugation can compensate the distortions and depolarization induced by a 2 m long multi-mode fiber.

Upon examining the output beam following its second pass through the fiber, we found excellent compensation: 70 % of the output beam was contained within a spot having approximately the same divergence as the input signal, and the residual depolarization was less than 1 %. This is seen in Figure 2, which shows the energy in the bucket for the input and return beams. If we define the conjugation fidelity as the ratio β_{out}/β_{in}, we see the fidelity is about 70 % in the range of 2 to 4 mrad. When the experiment was subsequently repeated using a 2 m step-index fiber, essentially the same results were obtained in terms of the fidelity and residual depolarization.

The far field of the return beam consisted of a central spike, the phase conjugated portion of the return, surrounded by a pedestal containing the non-conjugated (and unpolarized) portion. Since the non-conjugated portion essentially filled the mode volume of the fiber, the full angle of this pedestal was approximately 2(NA)/M = 66 mrad, or about 10 times broader than the ~ 6 mrad

full width of the base of the central spike (see Figure 2). Since the pedestal has only ~ 40 % as much energy as the spike (i.e. the ratio of 0.3 to 0.7) and its energy was spread over a spot with 100 times more area, the pedestal intensity is approximately 0.4 % of the peak intensity of the central spike. Because of this low intensity, the pedestal is expected to be of minimal consequence in applications.
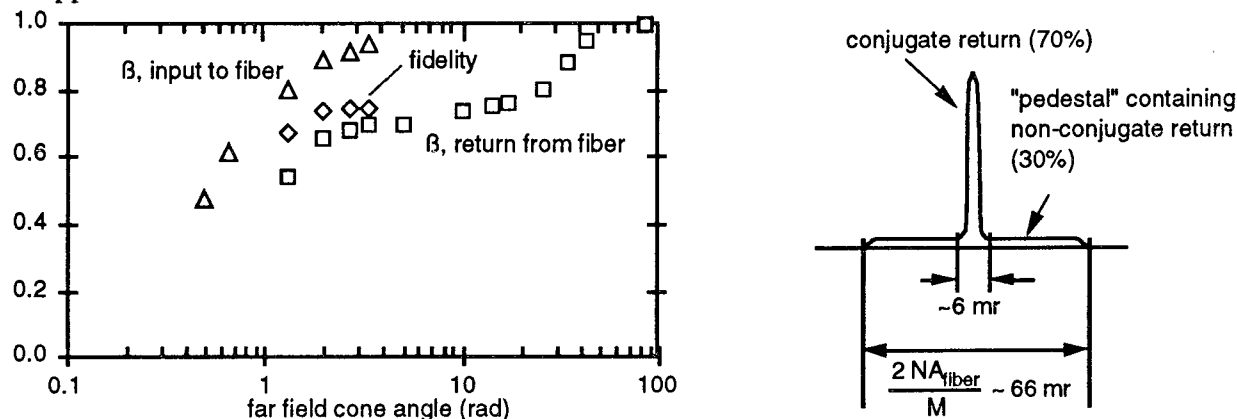
Figure 2. Energy fraction ß as a function of the far-field cone angle, for the signal input to the fiber, and for that returned through the fiber after reflection from the PCM. The fidelity is the ratio of these two quantities, about 70% in the 2 to 4 mrad range. Note the log scale, which shows the angular extent of the non-conjugate "pedestal" to be equivalent to the full NA of the fiber.

In summary, we have used Brillouin phase conjugation to demonstrate compensation of phase aberrations and depolarization induced by a multi-mode fiber, and we have achieved a high degree of fidelity. Although the relatively weak signal-beam power led to our selection of a PCM based on BEFWM, with its associated complexities, simple SBS PCMs are capable of thresholds much less than those of the present device. For example, the use of longer capillaries (lengths of several meters) with smaller cross sections (100 μm) has been shown[8] to yield SBS threshold powers as low as ~ 100 W.

The authors would like to acknowledge many helpful technical discussions with H. W. Bruesselbach, D. C. Jones, M. S. Mangir, and J. J. Ottusch, as well as the technical support of R. F. Chapman and R. H. Sipman.

REFERENCES
1. G. J. Dunning and R. C. Lind, "Demonstration of image transmission through fibers by optical phase conjugation," Opt. Lett. **7**, 558-560 (1982).
2. B. Luther-Davies, A. Liebman, and A. Maddever, "Single-mode resonator incorporating an internal multimode optical fiber and a phase-conjugate reflector", J. Opt. Soc. Am. B **7**, 1216-1220 (1990).
3. D. A. Rockwell, "A review of phase-conjugate solid-state lasers," IEEE J. Quantum Electron. **24**, 1124-1140 (1988).
4. N. G. Basov, V. F. Efimkov, I. G. Zubarev, A. V. Kotov, S. I. Mikhailov, and M. G. Smirnov, "Inversion of the wavefront in SMBS of a depolarized pump," Pis'ma Zh. Eksp. Teor. Fiz. **28**, 215-219 (1978) [transl. JETP Lett. **28**, 197-201 (1978)].
5. A. M. Scott and K. D. Ridley, "A review of Brillouin-enhanced four-wave mixing," IEEE J. Quantum Electron. **25**, 438-459 (1989).
6. N. G. Basov, I. G. Zubarev, A. V. Kotov, S. I. Mikhailov, and M. G. Smirnov, "Small-signal wavefront reversal in nonthreshold reflection from a Brillouin mirror," Kvant. Elektron. **6**, 394-397 (1979) [transl. Sov. J. Quantum Electron. **9**, 237-239 (1979)].
7. V. V. Ragulskii, "Wavefront inversion of weak beams in stimulated scattering," Pis'ma Zh. Tekh, Fiz. **5**, 251-254 (1979) [transl. Sov. Tech. Phys. Lett. **5**, 100-101 (1979)].
8. D. C. Jones, M. S. Mangir, and D. A. Rockwell, "Stimulated Brillouin scattering phase-conjugate mirror having a peak-power threshold < 100 W," Conference on Lasers and Electro-Optics, 1993, Vol. 11. OSA Technical Digest Series (Optical Society of America, Washington, D.C. 1993) p. 426.

A SINGLE-LONGITUDINAL-MODE HOLOGRAPHIC SOLID-STATE LASER OSCILLATOR

M.J. Damzen, R.P.M. Green and G.J. Crofts

The Blackett Laboratory, Imperial College,London SW7 2BZ, U.K.
Tele. No. 071-589 5111

SUMMARY

We present the results of a laser resonator design that uses a 3-D volume gain grating formed by spatial hole-burning [1]. The induced gain-grating can be considered a dynamic holographic element with diffractive properties that provide both spectral and spatial mode control of a high-gain flashlamp-pumped Nd:YAG laser system. The dynamic parametric growth of the grating initiated from amplified spontaneous emission in the cavity produces a self Q-switching resulting in short pulse formation.

The cavity configuration (Figure 1) has a 4% reflectivity output coupler and the back cavity reflector is the diffractive gain grating that is produced by spatial hole burning in a Nd:YAG amplifier module (A_1) in a self-intersecting loop geometry [2,3]. To achieve optimum grating diffraction efficiency and dominantly unidirectional lasing a Faraday element is incorporated in the loop. An additional Nd:YAG amplifier module is also necessary in the loop to achieve lasing threshold when using the low reflectivity output coupler of this resonator.

The dynamics of the resonator can be considered as follows. The initial gain-grating starts from spontaneous emission which weakly diffracts intracavity flux in the loop element. Regenerative intracavity radiation that gives constructive interference to enhance the growth of the grating will be preferentially selected. This parametric feedback process is self-enhancing and gives a high spatial and spectral selectivity to the intracavity radiation. Above a threshold inversion in the Nd:YAG amplifiers the diffraction efficiency of the gain-grating enhanced by the additional loop amplifier causes the system to achieve threshold for oscillation from the 4% output coupler. The feasibility of a self-intersecting loop geometry gain-grating having such a high amplified reflectivity >25, as required in this system for lasing threshold with a 4% output reflector, has been predicted theoretically [3] as well as confirmed experimentally [4].

Our experimental system consisted of two Nd:YAG amplifier rods (A_1 and A_2) 100mm long by 6.35mm diameter and small-signal single-pass gains up to ~100, oscillator round-trip time ~9ns (consisting of ~5ns self-intersecting loop time and ~4ns double-pass time from output coupler to gain-grating amplifier) and 10Hz repetition rate. At highest amplifier gains, the cavity output consisted of 10ns pulses with up to 600mJ energy. The pulses were temporally smooth (as shown in

Figure 2) which, together with a Fabry-Perot measurement showing their spectral content was less than its resolution-limit ~ 1GHz, indicates single-longitudinal-mode operation and possibly close to a transform-limited linewidth (~44MHz). We note that this is achieved without any conventional line-narrowing elements and the short pulse duration is also achieved without a conventional Q-switching device. The short duration is achieved by parametric growth of the gain-grating and hence of the cavity-Q when the amplifier gains are above threshold. The narrow linewidth operation is a consequence of the long coherence length requirement of the self-intersecting loop for optimum grating writing. Our modelling of this system indicates that both transmission and reflection type gain gratings are involved in the oscillation dynamics.

The spatial mode of the system under these conditions was not TEM_{oo} since no mode control was incorporated in the resonator. Despite this, phase conjugate oscillation was evidenced to be occurring by the relative insensitivity of the output mode to the introduction of a phase plate within the self-intersecting loop. The system ran on a TEM_{oo} diffraction-limited mode when an aperture was placed near the output coupler. In this case, the output energy was reduced to ~200mJ due to the smaller mode volume and hence less extraction of the available gain volume. A Gaussian variable reflectivity output coupler was also used and resulted in a TEM_{oo} output but again in a small mode volume and reduced energy. This was despite the Gaussian reflector having a divergent curvature which is used to achieved large mode volume extraction in conventional resonator systems. In this adaptive resonator, the self-forming grating "rear cavity reflector" can adjust its effective radius of curvature to maintain a stable resonator with a confined mode size. Hence a different strategy would appear to be necessary to achieve large mode volume, diffraction-limited spatial output from these self-adaptive resonators.

In conclusion, we have successfully demonstrated a high-energy Nd:YAG self-adaptive laser resonator based on saturable gain-gratings that produce narrow linewidth and short pulse duration without requirement of any conventional line-narrowing elements or Q-switching element.

References
[1] R.P.M. Green, G.J. Crofts and M.J. Damzen, Opt. Commun.,102, 288 (1993)
[2] I.M. Bel'dyugin et al, Sov. J. Quantum Electron., 14, 602 (1984)
[3] M.J. Damzen, R.P.M. Green and G.J. Crofts, Opt. Lett., 19, (1994)
[4] R.P.M. Green, G.J. Crofts and M.J. Damzen, "Single-mode operation of a uni-directional holographic ring resonator", submitted to Optics Letters.

Figure 1. Schematic diagram of experimental laser system

FWHM=10ns

Time (nsecs)
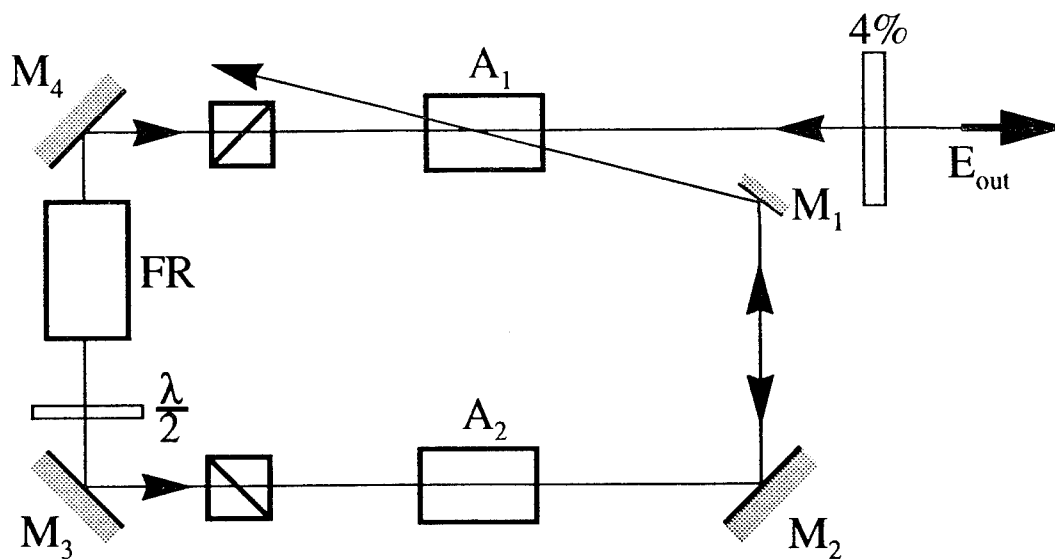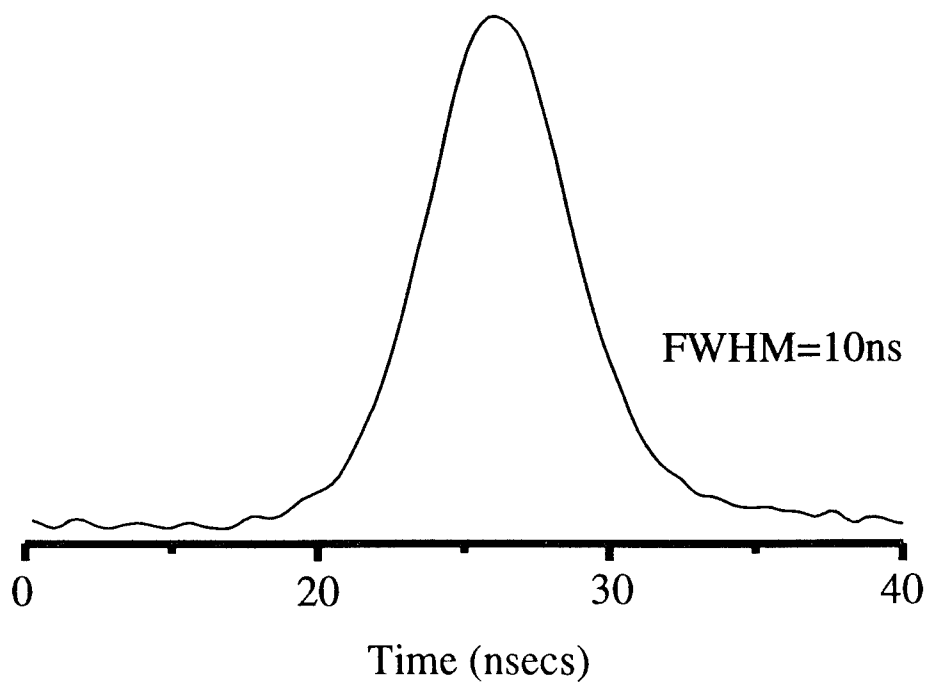
Figure 2. Temporal output of laser system

Hologram Restoration and Enhancement in Photorefractive Media

Pochi Yeh
Department of Electrical and Computer Engineering
University of California, Santa Barbara, CA 93106

Claire Gu
Department of Electrical Engineering
The Pennsylvania State University, PA 16802

Chau-Jern Cheng and Ken Y. Hsu
Institute of Electro-Optical Engineering
National Chiao Tung University, Hsinchu, Taiwan

It is well known that volume index gratings and holograms can be recorded by using optical interferometric techniques in photorefractive media [1]. These index gratings and holograms can also be erased by the illumination of light. The dynamic nature of these index gratings and holograms offers unique capability in many advanced applications, including real time image processing, optical phase conjugation, optical neural networks, etc [1]. In many of the applications, several holograms must be recorded sequentially in a photorefractive medium. As a result of the optical erasure, the amplitudes of the previously recorded holograms may decay exponentially during the subsequent recording stages. There has been proposals for the equalization of the amplitude of holograms by using a properly designed exposure schedule and even the sustainment of decaying holograms by using re-recording schemes [2-4]. Here, we propose and analyze a new and simple optical method for the enhancement and restoration of decaying holograms in photorefractive media.

Consider the readout of a photo-induced volume index grating or hologram in a photorefractive medium by using a laser beam. A diffracted beam bearing the image information is produced provided the reading beam is incident along the Bragg angle. As a result of the photorefractive effect, the diffracted beam and the reading beam will jointly induce a new index grating or hologram which bears exactly the same information as the existing one. During the readout process, while the existing hologram is being erased exponentially, the new hologram formed by the diffracted beam and the reading beam jointly is growing exponentially. The photorefractive medium is oriented such that the photo-induced index grating or hologram produced by the simultaneous presence of the reading beam and the diffracted beam is in phase with the existing grating or hologram and is thus reinforcing the amplitude of the hologram for a short period of time. The transient enhancement of the hologram manifests itself in terms of an increase in the diffraction efficiency for a short period of time. Continued reading of the hologram by a single readout beam for a long period of time leads to a decay of the hologram eventually. In what follows, we consider an optical method which utilizes the transient gain of the hologram to achieve a steady state enhancement of the hologram.

Referring to Fig. 1, we consider a readout of a photo-induced hologram in a photorefractive medium by using a pulsed laser. The diffracted beam, which bears the image information, is then retro-reflected by the phase conjugate mirror. The pulse length (or exposure time) and the repetition rate are selected such that there is no physical overlap between the incident pulse and the phase conjugated pulse inside the photorefractive medium. The hologram is first readout by the incident laser pulse for a short duration of time t producing an image bearing diffracted beam. When the diffracted beam is retro-reflected by the phase conjugator, the hologram is then readout by the retro-reflected beam for another short period of time t producing a phase conjugate version of the original laser pulse. The exposure time t is chosen so that the amplitude of the hologram is enhanced at the end of the first readout and further enhanced at the end of the second readout. Thus there is a net gain in the amplitude of the hologram during the first cycle. If the process continues, further increase in the amplitude of hologram is possible until a saturation of

the grating amplitude is reached. In what follows, we analyze the temporal growth and the spatial variation of the hologram in the bulk of a photorefractive medium. For simplicity, we consider the case of a single photo-induced volume index grating in a photorefractive medium.

A plane wave with amplitude A_1 is incident upon the photorefractive grating long a direction that exactly satisfies the Bragg condition (see Fig. 1). As a result of the Bragg scattering, a diffracted wave with amplitude A_2 is generated. The spatio-temporal equations of the two beams in the photorefractive medium can be written approximately [5]

$$\frac{\partial A_1}{\partial z} = -\frac{\Gamma}{2}GA_2, \qquad\qquad \frac{\partial A_2}{\partial z} = \frac{\Gamma^*}{2}G^*A_1, \qquad\qquad (1)$$

$$\frac{\partial G}{\partial t} = -\frac{1}{\tau}(G - \frac{A_1 A_2^*}{I_0}), \qquad\qquad (2)$$

where Γ is the photorefractive coupling constant, G is a measure of the relative amplitude of the photorefractive index grating, $I_0 = |A_1|^2 + |A_2|^2$ is the total intensity and τ is the time constant of photorefractive crystal. To understand the spatial and temporal variation of the index grating, let us examine Eq. (2) for the relative grating amplitude G. Near the entrance face ($z = 0$) of the medium, A_2 grows spatially from zero. Thus the right hand side of Eq. (2) is always negative for small z, indicating a decay of the grating amplitude. As A_2 grows spatially in the bulk of the medium due to diffraction, the right hand side of Eq. (2) becomes positive leading to an enhancement of the index grating. Generally speaking, more enhancement is obtained if the initial index grating is concentrated near the incident side of the medium. There will be no enhancement if the initial index grating distribution is concentrated near the exit side of the medium. The grating amplitude distribution is modified as a result of the readout. We note that as a result of the readout the diffraction efficiency is increased and the center of gravity of the index grating is pushed toward the exit face ($z = L$) of the crystal. Such a new distribution is not suitable for further enhancement via continued readout. If the index grating is now read from the exit face ($z = L$), the grating amplitude can be further enhanced based on the above discussion. To continuously enhance the grating amplitude, the index grating must be readout alternately from both sides of the medium. For the case of a hologram which consists of many grating components, a phase conjugate mirror is essential to ensure the readout from the rear of the medium. Our analysis also indicates that the steady-state grating is independent of the shape and level of the initial grating. For the case of an initially uniform grating, it can be shown analytically that the grating can be enhanced provided $\Gamma L > 4$ according to Eqs. (1)-(2).

We now consider the dependence of the steady-state diffraction efficiency η_s on the coupling strength ΓL and the exposure duration t. Fig. 2(a) shows the steady-state diffraction efficiency η_s as a function of the coupling strength ΓL. The result shows that there exists a threshold value ΓL for a non-zero steady-state grating. Fig. 2(b) plots the steady-state diffraction efficiency η_s as a function of the exposure duration t in each readout. The results in Fig. 2(b) indicate that the steady-state diffraction efficiency decreases when the exposure duration per readout increases, due to the erasure during readout. We also note that there is a cutoff exposure time beyond which the grating will eventually be erased by the reading beams, leading to a steady-state diffraction efficiency of 0.

By examining Fig. 2, we further note that the diffraction efficiency as a function of ΓL bears a strong resemblance to that of a mutually pumped phase conjugator (MPPC)[1,6-9]. In fact, for an extremely small exposure time ($t \ll \tau$), the diffraction efficiency becomes identical to that of an MPPC [1,6] with a threshold of $\Gamma L=4$. for equal pump intensities. In addition, the steady state index grating as shown in Fig. 2 is also similar to that of an MPPC[1]. The process of alternating readout of an index grating from both sides of the crystal is equivalent to an MPPC with pulsed pump beams. It is known that steady state MPPC exists even with pulsed pump beams[10]. This is

often achieved by first initiating the process of MPPC with cw laser beams. Upon reaching the steady state, the pump beams can then be modulated temporally so that only one of the pump beams is on at any given time. This is exactly identical to our alternating readout scheme for the enhancement of the gratings. The only difference is that we start the process from the very beginning with an extremely weak grating. Thus our results can be employed to explain the initiation and the growth of the MPPC process from an extremely weak grating (or hologram) which may be a small component of a noisy fanning hologram.

In conclusion, we have proposed and analyzed a new and simple optical method for the enhancement and restoration of decaying holograms in photorefractive media. The results indicate that extremely weak holograms can be enhanced provided that the two-beam coupling is sufficiently strong. Steady-state photorefractive holograms can be maintained continuously without decay by using a double-side alternating readout schedule in conjunction with a phase conjugator. The result also provides an explanation for the formation of mutually pumped phase conjugation in terms of the successive enhancement of an initial noise grating.

References

1. See, for example, P. Yeh, "Introduction to Photorefractive Nonlinear Optics," (Wiley, 1993).
2. D. Psaltis, D. Brady, and K. Wagner, Appl. Opt. **27**, 1752 (1988).
3. Y. Taketomi, J. E. Ford, H. Sasaki, J. Ma, Y. Fainman, and S. H. Lee, Opt. Lett. **16**, 1774 (1991); Opt. Lett. **16**, 1874 (1991).
4. Y. Qiao, D. Psaltis, C. Gu, J. Hong, P. Yeh, and R. R. Neurgaonkar, J. Appl. Phys. **70**, 4648 (1991); Y. Qiao and D. Psaltis, Opt. Lett. **17**, 1376 (1992).
5. C. Gu, J. Hong, and P. Yeh, J. Opt. Soc. Am. **B9**, 1473 (1992); D. M. Lininger, D. D. Crouch, P. J. Martin, and D. Z. Anderson, Opt. Commun **76**, 89 (1990).
6. M. Cronin-Golomb, B. Fischer, J. O. White, and A. Yariv, IEEE J. Quantum Electron. **QE-20**, 12(1984).
7. S. Weiss, S. Sternklar, and B. Fischer, Opt. Lett. **12**, 114 (1987); S. Sternklar, S. Weiss, M. Segev, and B. Fischer, Opt. Lett. **11**, 528 (1986).
8. P. Yeh, T. T. Chang, and M. D. Ewbank, J. Opt. Soc. Am. **B5**, 1743 (1988); M. D. Ewbank, Opt. Lett. **13**, 47 (1988); M. D. Ewbank, R. A. Vazquez, R. R. Neurgaonkar, and J. Feinberg, J. Opt. Soc. Am. **B7**, 2306 (1990).
9. M. Segev, D. Engin, A. Yariv, and G. C. Valley, Opt. Lett. 18, 1828 (1993).
10. M. D. Ewbank, private communication.
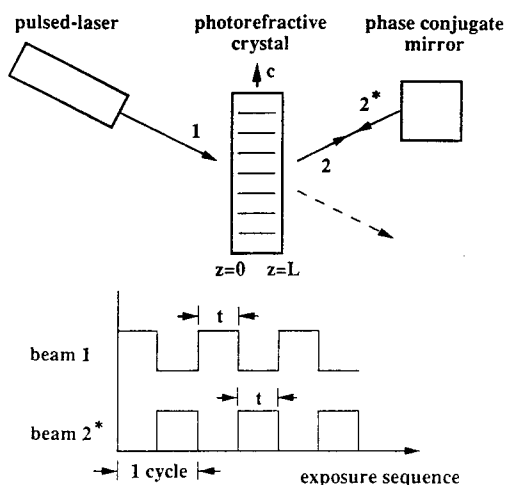
Fig. 1 Schematic diagram of the double-side readout configuration. The lower figure shows the alternating readout scheme.
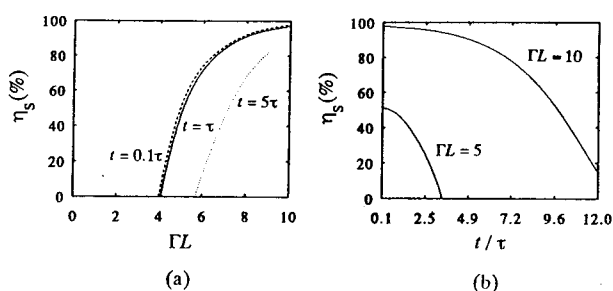

Fig. 2 (a) Steady-state diffraction efficiency η_s as a function of the coupling strength ΓL for various cases of exposure time t per readout and (b) Steady-state diffraction efficiency η_s versus the normalized exposure time t / τ per readout for various cases of photorefractive coupling strength ΓL.

Compact Volume Holographic Memory System
with Rapid Acoustooptic Addressing

Ian McMichael, William Christian, John Hong,
Tallis Y. Chang, Ratnakgar Neurgaonkar and Monte Khoshnevisan

Rockwell International Science Center
1049 Camino dos Rios, A9
Thousand Oaks, CA 91360
(805) 373-4508

SUMMARY

The concept of storing data in the form of multiplexed holographic gratings in volume media had been proposed during the sixties [1-3] and developed with limited success. With recent advances in the growth and preparation of holographic materials along with the maturation of associated device technologies such as spatial light modulators and detector arrays, the realization of working memory systems that are capable of delivering the perfomance levels for long term storage applications is now possible. We at Rockwell have been developing a compact volume holographic memory system for use in avionics and other applications using a design that incorporates a pair of acoustooptic devices in a spatio-angularly multiplexed design to achieve high data storage capacity and rapid random access to stored data.

The currently known common-volume multiplexing techniques of angular encoding, wavelength encoding, phase encoding, and electric field encoding allow holograms recorded in the same medium volume to be independently read out with minimal crosstalk. There are practical limits to the number of holograms which can be stored in this fashion due to the finite dynamic range in photorefractive crystals [4,5] and the inverse square law dependence of the diffraction efficiency of each hologram on the number of superposed holograms which is a consequence of photorefractive cross-erasure encountered during the multiple exposure sequence [6]. Off-Bragg crosstalk can also grow as a function of the number of stored holograms and thereby limit the storage capacity [7]. As an example, if the nominal volume of the storage crystal is of the order of 1 cm^3, the recording of 10,000 holograms [8] in most photorefractors will result in a diffraction efficiency of about 10^{-6} for each hologram beyond which reliable detection will be difficult using realistic readout laser intensities. Thus, if each hologram (page) contains 10^6 bits of information, the storage capacity of each common volume will be limited to 10 Gbits because of the practical reasons listed above.

Our approach is to spatially multiplex many such common volume storage units to ultimately achieve high aggregate capacity in architectures devoid of mechanically steered devices so as to enable both rapid access (10 μsec) and high data transfer rates (1 Gbit/sec). In the angularly multiplexed approach, the beam is steered nonmechanically by acoustooptic deflectors which can steer a given beam to one of one thousand angular positions within a switching time of about 10 μsecs. Layers or boxes of such common volume storage units are arrayed in geometries similar to that shown in Figure 1 where a "coarse" address directs the reading or writing beams to the appropriate layer or box and the "fine" address corresponds to the particular holographic page within the chosen common volume unit.

Our early efforts in holographic optical storage were focused on theoretical studies of the limitations on storage capacity [4,5,7], and on experimental demonstration of fast non-mechanical access. A demonstrator capable of data transfer rate at the optical level exceeding 1 Gbit/s was constructed using one layer of $LiNbO_3$ as the storage medium. The demonstrator used an acousto-optic beam deflector for rapid non-mechanical access to several hundred angularly multiplexed pages at rates in excess of 50,000 pages per second. With each page consisting of an array of 320 x 220 pixels, this corresponds to readout at a rate of 3.5 Gbits/sec.

In addition to the storage of digital data, storage of analog information in the form of detailed highway maps was also demonstrated.

Figure 2 is a simplified schematic showing a more recent system that implements several layers in a spatioangularly addressed system. In the actual design, the system is folded to save space, but for the purposes of clarity in its presentation, the system is shown unfolded in the figure. The total system dimensions are of the order of 12"x8"x5", including the laser and most of the electronics. To achieve high speed random access addressing, both inter-layer and intra-layer addressing are accomplished using acoustooptic devices.

An important issue that is associated with all volume holographic memory systems that use photorefractive materials is that of long term data retention. Holograms written in photorefractive materials diminish in strength due to two mechanisms: i) optical erasure from further writing or readout exposure, ii) dark erasure due to finite dark conductivity. Fixing in SBN crystals has been accomplished using various means [9,10] by which the holographic gratings can be made nearly impervious to optical erasure so that nondestructive readout can be performed. We have conducted fixing experiments in which we demonstrated both resistance to optical erasure as well as long term data stability. For example, a holographic grating that was fixed in our laboratory has exhibited undiminished strength over a period of six months during which the grating was periodically probed with readout light, demonstrating tolerance to both erasure mechanisms.

We will describe in more detail the design and operation of our compact holographic memory demonstrator and in fixing holographic gratings in SBN.

REFERENCES

1. E. N. Leith, A. Kozma, J. Upatnieks, J. Marks, N. Massey, Appl. Opt. V.5, p.1303 (1966).
2. J. P. VanHeerden, Appl. Opt. V.2, p.393 (1963).
3. E. G. Ramberg, RCA Review V.33, p.53 (1972).
4. T. Y. Chang, J. H. Hong, F. Vachss, R. McGraw, J. Opt. Soc. Am. B, V.9, No.9, p.1744 (1992).
5. J. H. Hong, P. Yeh, D. Psaltis, D. Brady, Opt. Lett., V.15, No.6, p.344 (1990).
6. D. Psaltis, K. Wagner, D. Brady, Appl. Opt. V.27, p.1752 (1988).
7. C. Gu, J. Hong, I. McMichael, R. Saxena, F. H. Mok, J. Opt. Soc. Am. A, V.9, p.1978 (1992).
8. F. H. Mok, Opt. Lett. V.18, p.915 (1993).
9. Yong Qiao, S. Orlov, D. Psaltis, R. R. Neurgaonkar, Opt. Lett. V.18, p.1004 (1993).
10. A. Kewitsch, M. Segev, A. Yariv, R. R. Neurgaonkar, Opt. Lett. V.18, p.1262 (1993).
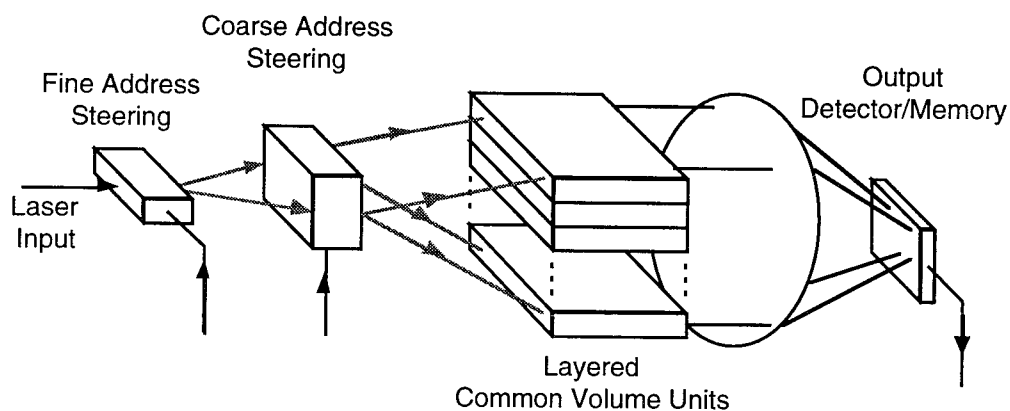
Figure 1
Spatial Multiplexing to Augment Storage Capacity (see text)
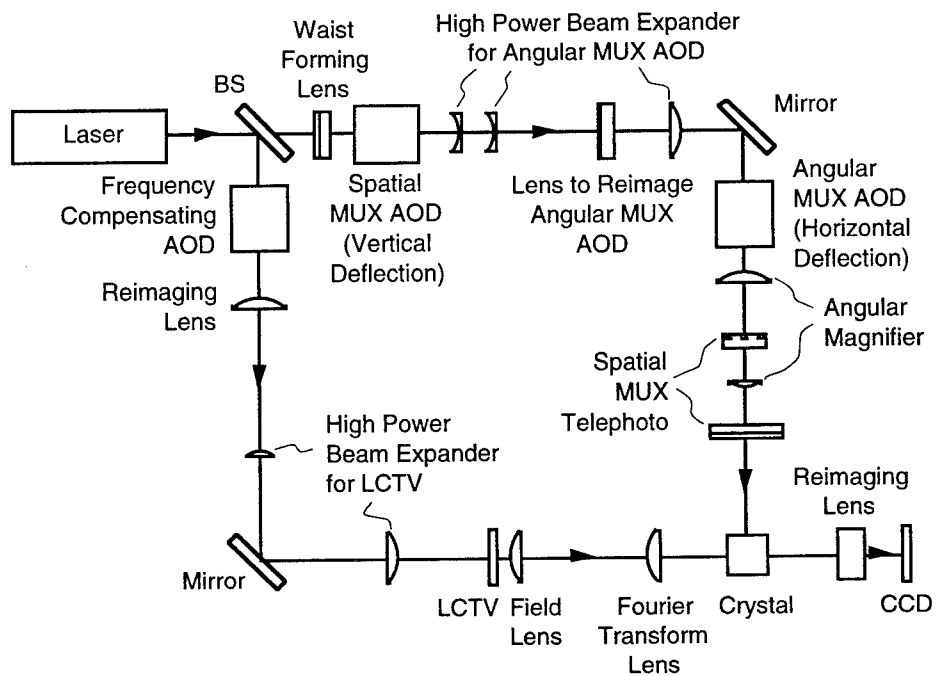
Figure 2 Schematic of the prototype holographic storage demonstrator.

Recall of Linear Combinations of Stored Data Pages Using Phase Code Multiplexing in Volume Holography

J. F. Heanue[†], M. C. Bashaw[‡], and L. Hesselink[‡]

[†]Department of Applied Physics, Stanford University, Stanford, CA 94305-4090

[‡]Department of Electrical Engineering, Stanford University, Stanford, CA 94305-4035

Tel. 415 723-9127 FAX 415 725-3377

Recently, phase code multiplexed data storage in volume holographic media has been investigated as an alternative to angular or wavelength multiplexing[1]. Phase code multiplexing allows implementation with fixed geometry and wavelength, resulting in potentially fast access times and the possibility of cascading in an optical system. In addition, it has been suggested that use of partial phase codes can be used to directly reconstruct certain sums and differences of stored images[2]. We demonstrate the recall of arbitrary linear combinations of stored data pages by using a compound phase and amplitude modulator in the reference beam path.

Phase code multiplexing involves storing M images, $|S_1\rangle, \ldots, |S_M\rangle$, with M reference waves, $|R_1\rangle, \ldots, |R_M\rangle$. Each reference wave consists of N plane wave components. It is assumed that the geometry is held fixed, so that the amplitude and phase, but not direction, of each component may be varied. The different reference waves can be represented by N-element vectors,

$$|R_m\rangle = |r_1^m e^{j\phi_1^m}, \quad r_2^m e^{j\phi_2^m}, \quad \ldots \quad r_N^m e^{j\phi_N^m}\rangle, \tag{1}$$

where r_n^m and ϕ_n^m are the amplitude and phase, respectively, of the nth plane-wave component of the mth reference wave.

If the different plane-wave components of the reference waves are separated by a sufficiently large angle, Bragg-mismatched reconstruction can be neglected. If in addition, dispersion in the spatial frequency response of the medium is negligible and all gratings are recorded to the same strength, readout with reference wave $|R_p\rangle$ results in an output signal

$$|S_{out}\rangle = B_0 \sum_{m=1}^{M} \langle R_p | R_m\rangle |S_m\rangle, \tag{2}$$

where B_0 is a constant. When the amplitudes and phases of the reference waves are chosen such that each $|R_m\rangle$ is a member of a set of orthogonal vectors, the output is given by $|S_{out}\rangle = B_0 |S_m\rangle$.

The possibility of recalling linear combinations of stored images is apparent from the above representation of the phase-encoding process. When readout is performed with $|R_{out}\rangle = \sum a_i |R_i\rangle$, the output is $B_0 \sum a_i |S_i\rangle$. Recall of arbitrary linear combinations of stored data pages is possible in a system capable of generating the necessary reference waves $|R_{out}\rangle$. To demonstrate the recall of combinations of stored data pages, we multiplexed three images in an Fe-doped $LiNbO_3$ crystal using three different discrete Walsh functions as the phase codes.

427
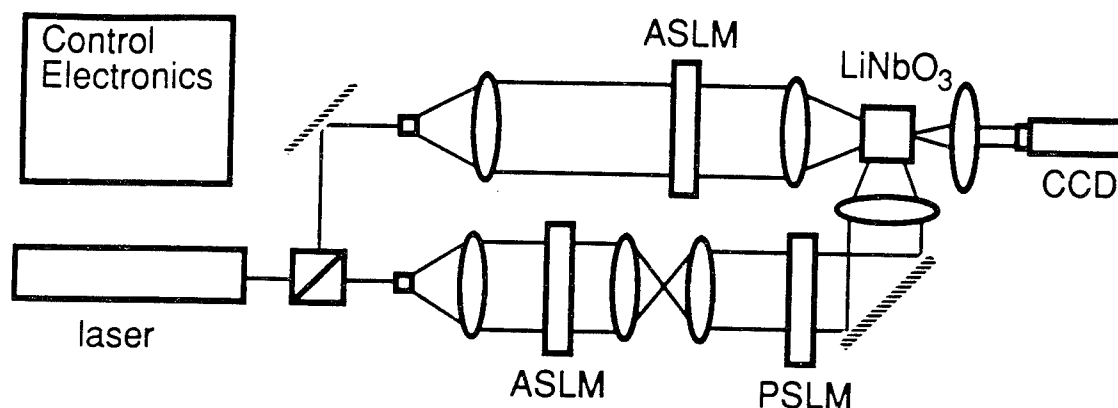
Figure 1: Experimental arrangement.

The reference beam path included an amplitude spatial light modulator which was imaged onto a phase spatial light modulator, as shown in Figure 1. During recording, the ASLM was set for maximum transmission. During recall, both the PSLM and ASLM were used to compose the desired reference waves. The reconstructions of each of the three images is shown in Figure 2. Figure 3 shows the recall of two different combinations, $|image2 - image3|$ and $|2 \times image1 + image2|$. Note that the CCD camera used in the experiment detects intensity, so we are limited to detecting the absolute value of the desired combination.

The ability to perform page-wise arithmetic operations is of great use in both binary and grey-scale image processing. It allows operations such as averaging or background subtraction to be performed without pixel-by-pixel computation. The combination of stored data pages is a linear process; therefore, the data can be stored having undergone any linear transformation and still be recalled correctly. For example, the data page may be Fourier-transformed or discrete-cosine transformed before being stored. The recalled signal will be a linear combination of the transforms of each page and can be inverse transformed to give the desired result. In addition, a system capable of generating reference waves with both specified phase and amplitude modulation can be used to correct for dispersion in the spatial frequency response of a recording medium[3].

References

[1] C. Denz, G. Pauliat, G. Roosen, and T. Tschudi. "Volume Hologram Multiplexing Using a Deterministic Phase Encoding Technique". *Opt. Commun.*, **85**:171–176, (1991).

[2] J. Lembcke, C. Denz, T. H. Barnes, and T. Tschudi. "Multiple Image Storage Using Phase Encoding–Latest Results", in *Proceedings of the Conference on Photorefractive Materials*, held Kiev, Ukraine, 1993, paper SaC02.

[3] M. C. Bashaw, A. Aharoni, J. F. Walkup, and L. Hesselink. "Crosstalk Considerations for Angular and Phase-Encoded Multiplexing in Volume Holography", to be published.
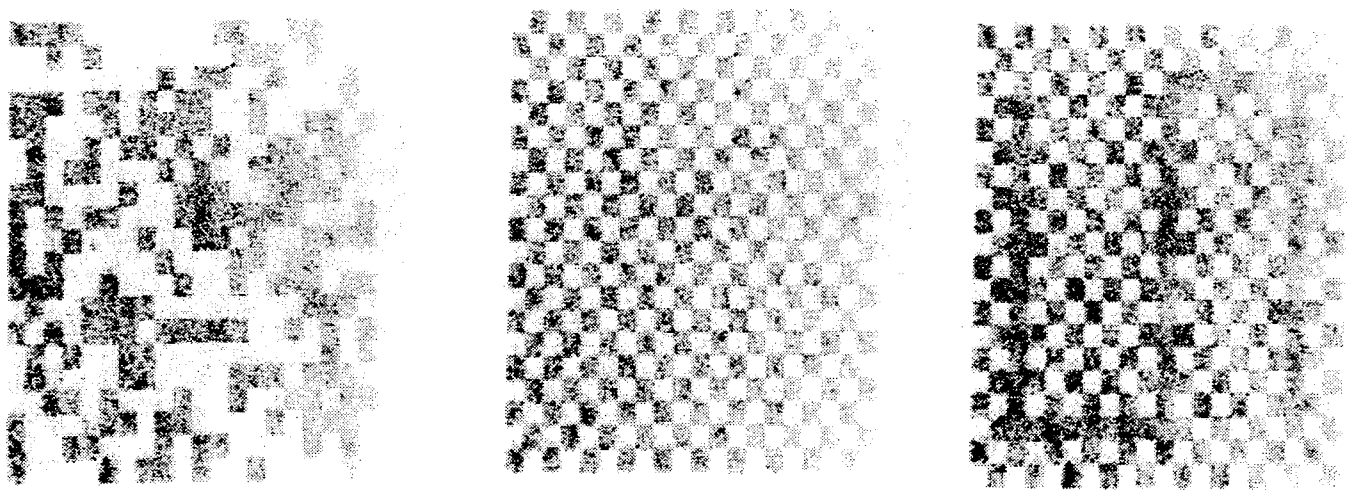
Figure 2: The reconstructions of each of the three stored images. (480x440 pixels)
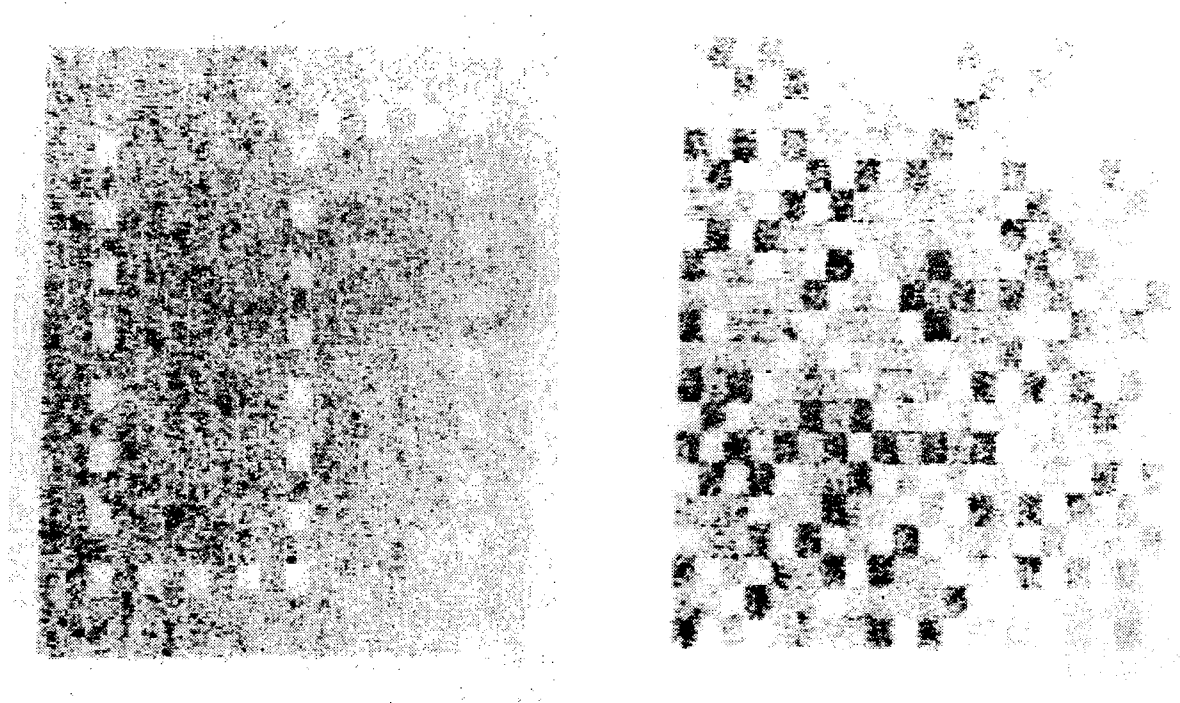
Figure 3: Two linear combinations: a) $|image2 - image3|$, b) $|2 \times image1 + image2|$.

Optical Self-Enhancement of Photorefractive Holograms

Scott Campbell and Pochi Yeh
Electrical and Computer Engineering Department, University of California
Santa Barbara, CA 93106   (805) 893-7015

Claire Gu
Electrical Engineering Department, The Pennsylvania State University
University Park, PA 16802-2705   (814) 863-4256

Shuian Huei Lin, Chau-Jern Chen, and Ken Y. Hsu
Institute of Electro-Optical Engineering, National Chiao Tung University
Hsinchu, Taiwan

It is well known that dynamic volume holograms, such as those stored in photorefractive crystals, decay upon readout [1]. Though such a property can be useful in many real-time processing applications, it is often a drawback in optical data storage applications when an information set may be recalled multiple times or during the sequential storage of multiple holograms. There have been approaches for the sustainment of decaying holograms via re-recording as well as exposure schedule algorithms for the storage of multiple holograms [2,3]. In this paper, we present experimental results verifying a novel optical proposal for the enhancement and restoration of decaying holograms in photorefractive media [4].

Consider the Bragg-matched readout of a photo-induced volume index grating in a photorefractive media by a laser beam. The portion of the readout beam that diffracts off of the grating does so in such a way that the interference pattern between the diffracted beam and the readout beam is exactly in phase with the interference pattern that originally wrote the grating. As a result, the readout beam and its diffracted beam write a volume index grating exactly in phase with the one they are reading. During readout, this new grating is growing in strength exponentially while the original grating is decaying exponentially. If the two-beam coupling gain, ΓL, in the photorefractive media is sufficiently large, then the net transient result can be an increase in the overall index modulation depth [4,5]. Continued reading of the hologram by a single read beam leads to its eventual decay. If, however, after a time period, t, the read beam is shut off and a phase conjugate of the diffracted beam is turned on for the same time period, then the grating can continue to be enhanced by this second beam. Continued toggling between the read beam and its phase conjugated diffracted beam in this manner will strengthen the grating up to a steady state level, η_s. This steady state level is determined by the crystal's two-beam coupling gain and the duration of each toggling sequence compared with the crystal's time constant, τ. Conceptually, the index grating amplitude will "slosh" from one side of the crystal to the other as each respective enhancement beam is activated.

Our experimental investigations into the theories proposed in Ref. [4] were performed utilizing a Coherent Innova 300 Ar^{+3} laser at 514.5 nm and a number of undoped and cerium doped barium titanate crystals, obtained from the Institute of Physics, Chinese Academy of Sciences, Beijing. Figure 1 diagrams the set up utilized, where plane waves were used to write and read index gratings in the crystals. Beams A_1 and A_2^* enter through their respective toggling shutters S_1 and S_2, reflecting off of beam splitters BS to enter the photorefractive crystal. Detectors D_1 and D_2 then detect the respective diffracted signals, sending this data to a computer for storage and analysis. This computer also controls shutter operations. Two approaches were exercized in achieving steady state diffraction efficiencies: case one which toggled the beams whenever the respective diffracted signal fell to a given percentage of its maximum value during a

given toggle cycle, and case two which toggled the beams at a set fraction of the crystal's photorefractive response time. Figure 2(a) shows a typical plot of the data taken under case one, where the beams were toggled at 95% of their achieved maximum and the crystal utilized was a 45 degree cut undoped sample. Slight assymetries, especially evident near saturation, are due to fanning losses which differ for the two beams in this type of crystal. Data for case two is given in Fig. 2(b), which shows relative peak and average saturation diffraction efficiencies as a function of t/τ values utilizing the same crystal as in case one.

It should be noted that the enhancement of gratings is a simple case of the enhancement of holograms. Enhancing holograms, with all of their spatial frequencies, is a task requiring more attention being given to generation of the phase conjugate of the diffracted beam. Indeed, if the object beam is utilized as the original enhancing beam, then its diffracted beam could be a simple plane wave, which would be easy to phase conjugate. It can also be noted that selective characteristics of index holograms can be enhanced while undesireable characteristics are dimished or erased simply by spatial filtering of the diffracted read beam somewhere inbetween the stored hologram and the diffracted beam's phase conjugate mirror. Under such circumstances, optical information processing can be achieved during the enhancement process. Such a filtering scheme would be necessary, in fact, for the preservation of relative grating amplitudes in a hologram.

In conclusion, we have shown experimental verification of novel concepts for the optical enhancement of photorefractive gratings. We have also proposed how these concepts can be utilized for dynamic optical information processing of data stored within a photorefractive crystal.
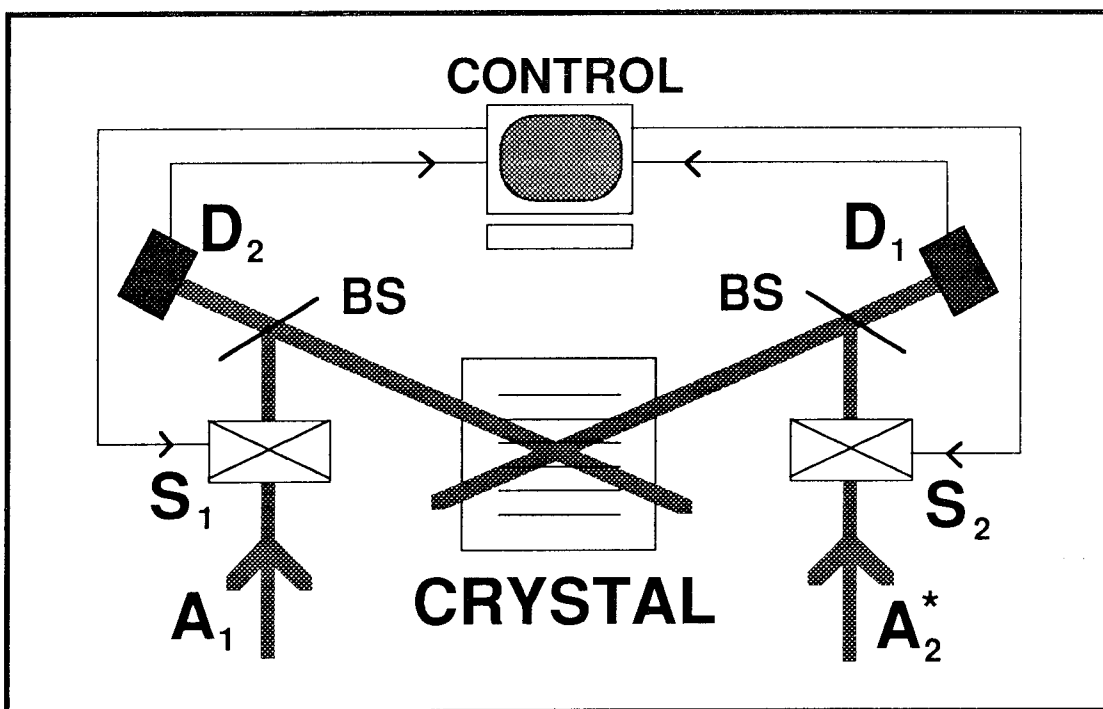
Figure 1. Experimental set up for studying optical self-enhancement of photorefractive gratings. The Crystal is 45 deg. cut, undoped barium titanate. Beams A_1 and A_2^* are phase conjugates of one another's diffracted beams. They are toggled by shutters S_1 and S_2, respectively, in accordance to the Control decision concerning the signals detected at detectors D_1 and D_2, respectively.
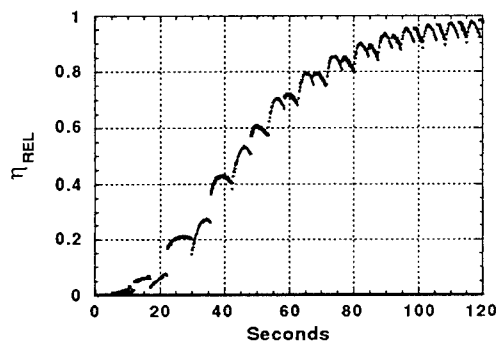
(a)
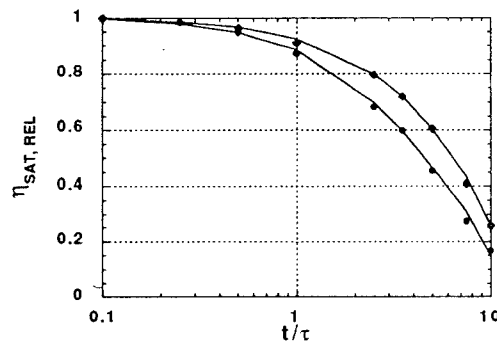
(b)

Figure 2. (a) Experimental data for beam toggling at 95% of local diffraction maximum. Diffraction is seen to quickly rise, peak out, and begin falling before the shutters toggle to the other beam. The assymetry in the two beam diffraction curves is due to beam fanning, which is stronger for one beam than it is for the other, due to the crystal's special cut.

(b) Experimental data for beam toggling at various fractions of the crystal's photorefractive response time. The diamonds represent peak saturation values and the circles represent average saturation values at given t/τ ratios. In both (a) and (b), the gratings grew from noise (zero initial grating amplitudes).

References:
1. See, for example, P. Yeh, "Introduction to Photorefractive Nonlinear Optics," (Wiley, 1993).
2. D. Psaltis, D. Brady, and K. Wagner, Appl. Opt. **27**, 1752 (1988).
3. Y. Taketomi, J. E. Ford, H. Sasaki, J. Ma, Y. Fainman, and S. H. Lee, Opt. Lett. **16**, 1774 (1991); Opt. Lett. **16**, 1874 (1991).
4. P. Yeh, C. Gu, C. J. Cheng, and K. Y. Hsu, submitted to Opt. Lett., Dec. 1993.
5. C. Gu, J. Hong, and P. Yeh, Opt. Soc. Am. **B9**, 1473 (1992); D. M. Lininger, D. D. Crouch, P.J. Martin, and D. Z. Anderson, Opt. Comm. **76**, 89 (1990).

A New Method for Holographic Data Storage in Photopolymer Films

A. Pu, K. Curtis, D. Psaltis
California Institute of Technology, Pasadena, CA

Conventional holographic storage methods, such as angle or wavelength multiplexing, superimpose multiple holograms in the volume of the recording material. The number of holograms that can be stored is typically proportional to the thickness of the material. Recently, photopolymer films have been developed that are inexpensive, easy to fix and have a relatively large dynamic range, making them good candidates for high density data storage. An example of this material is DuPont's HRF-150-38 photopolymer film [1,2]. The storage density achievable with these materials is limited due to their thickness of tens of microns. In this paper we present two results. First, a new holographic multiplexing method (peristrophic multiplexing) that significantly increases the storage density achievable in thin films is demonstrated. In addition, an exposure schedule that maximizes the utilization of available dynamic range of the photopolymer is derived.

The setup used to demonstrate peristrophic multiplexing is shown in Figure 1. The setup is similar to a conventional angle multiplexing arrangement, where either the angle of the reference beam is scanned or the material is rotated around the y-axis. For peristrophic multiplexing, the material is rotated around the z-axis instead. After each hologram exposure, the material is rotated in plane. The rotation shifts the reconstructed image off the detector or the stored hologram becomes non-Bragg matched, allowing for another hologram to be stored at the same location. This process repeats until the maximum rotation angle of 180° is reached. For materials greater than ~1mm in thickness, the Bragg match criterion will determine the required peristrophic rotation angle before a new hologram can be stored at the same location. Otherwise, the reconstructed image is shifted off the detector first with the rotation. Peristrophic multiplexing can also be realized by rotating both recording beams around the z-axis. To further increase the storage density, other multiplexing techniques can be combined with peristrophic multiplexing.

An exposure schedule for the HRF-150-38 photopolymer was derived by first measuring the diffraction efficiency versus the exposure energy as shown in Figure 2. The amplitude of the recorded gratings can be obtained by taking the square-root of the diffraction efficiency. This curve can then be fitted for $E>E_o$ to the following equation,

$$A(t) = A_{sat}\left(1 - e^{-\left(\frac{E-E_0}{\tau}\right)}\right) \qquad (1)$$

where E is the exposure energy . The slope of equation (1) multiplied by the exposure energy gives the amplitude of the written grating. By setting the mth hologram's grating amplitude equal to the $m-1^{th}$ grating amplitude, a recursive formula can be derived that results in M holograms with equal diffraction efficiencies. The exposure energy for the mth hologram is given by Equation (2), where E_m and E_{m-1} are the exposure energies for the mth and $m-1^{th}$ holograms, respectively.

$$E_m = E_{m-1}e^{\frac{E_{m-1}}{\tau}} \qquad (2)$$

The dynamic range is fully utilized by scaling the initial recording energy to $E_1=\tau/M$, where M is the total number of holograms to be recorded.

Peristrophic multiplexing was demonstrated using the setup shown in Figure 1. A second rotation stage was added to rotate the material in the y-axis in order to implement angle multiplexing as well. The signal and reference beam were initially incident on the film at $\pm 30°$ to the normal (z-axis). Cartoons were presented to the optical system by using a spatial light modulator (SLM). The photopolymer to be exposed was located in-between the Fourier plane and the image plane to ensure uniformity of the presented image. The peristrophic rotation required to filter out a stored hologram was experimentally determined to be ~3° while the rotation required to Bragg mis-match an angle multiplexed hologram was also ~3°. For each peristrophic multiplexing position, five angle multiplexed holograms were stored. A total of 295 holograms were recorded in about a half cm^2 area with an average diffraction efficiency of better than 10^{-6}. Figure 3 shows the reconstruction of one of the 295 holograms.

In summary, we have demonstrated that peristrophic multiplexing makes it possible to store several hundred holograms in thin films. Whereas previously this capability was only possible with materials ~1cm thick. Therefore, this approach makes it possible to fabricate compact 3-D holographic disks with high storage density.
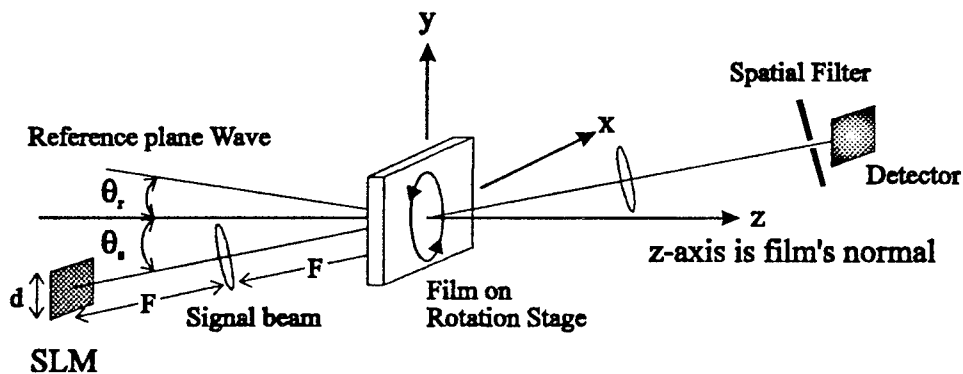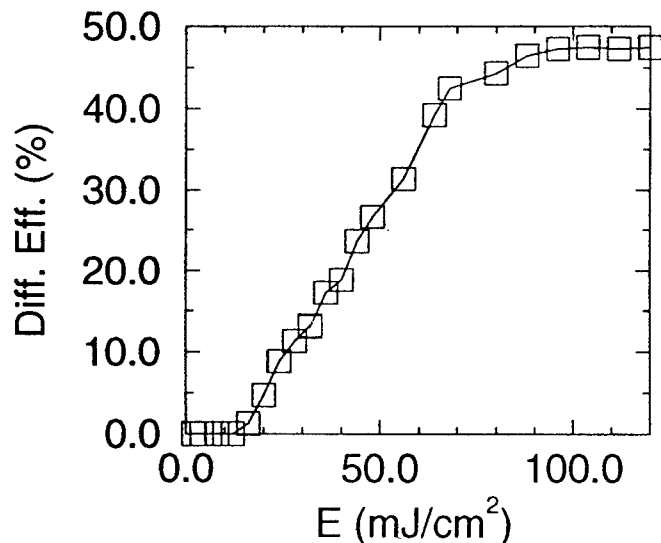
Figure 1: Peristrophic multiplexing setup.

Figure 2: The diffraction efficiency as a function of exposure energy.

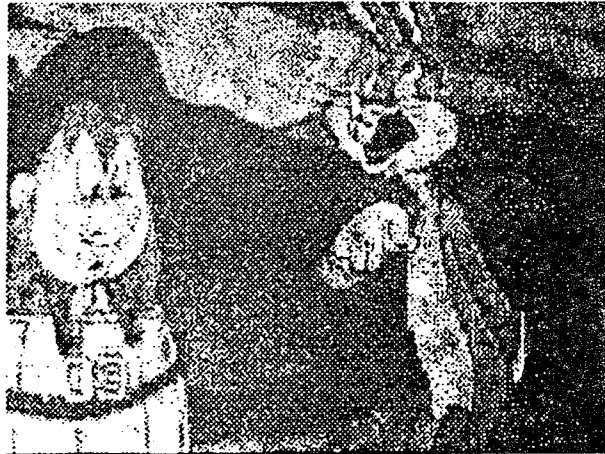Figure 3: One reconstructed hologram out of 295.

References

1. W. K. Smothers, T. J. Trout, A. M. Weber, D. J. Mickish, 2nd Int. Conf. on Holographic Systems, Bath, UK (1989).
2. K. Curtis and D. Psaltis, Applied Optics, 31, 7425 (1992).

Cross-talk Noise and Storage Density in Holographic Memory

Xianmin Yi and **Pochi Yeh**
Electrical and Computer Engineering, University of California, Santa Barbara, CA 93106

Claire Gu
Electrical Engineering, Pennsylvania State University, University Park, PA 16802

Optical data storage in volume holographic media has been an important and exciting area of research. This is driven mainly by the prospect of an enormous storage density of $\sim 1/\lambda^3$ bits per unit volume. In the spectral regime of visible light, this translates into a storage density of several terabits per cubic centimeter. In practical applications such as optical image processing, and pattern classification, the storage capacity is limited by the cross-talk noise between holograms and pixels. Several aspects of the cross-talk noise have been addressed by previous workers[1-5]. Assuming an infinite transverse dimension of the medium, Gu et. al. have considered the effect of the thickness of the crystal on the storage capacity, and obtained limitations on the total number and the physical size of the holograms that can be stored in the crystal with a certain signal-to-noise ratio[1,2]. In addition, Yariv has analyzed the problem of interpixel cross-talk noise in orthogonal wavelength-multiplexed volume holographic data storage[4]. Although some aspects of the cross-talk noise have been investigated, a general theory leading to quantitative results on storage capacity in terms of number of bits per unit volume is not available. In this paper, we present a general analysis of the storage capacity by considering the effect of finite transverse size of the crystal on the storage capacity, and employing a statistical method to evaluate the cross talk noise. We obtain, for the first time, expressions for the cross-talk limited storage capacity in terms of the number of bits per unit volume. The results are then employed to compare angle multiplexing and wavelength multiplexing.

Fig. 1 shows a typical recording and readout configuration for optical storage where Fourier transform holograms are stored in a volume holographic medium. The input and output array of pixels are shown in Fig.2. It is assumed that the input pixels can only be on or off with no gray levels and the phases of the on-pixels are random. At the output plane, an array of point detectors is used. We first consider the intrapage interpixel cross-talk caused by the finite transverse size of the crystal. An arbitrary input pattern consisting of an array of square pixels is stored in the holographic medium. By using standard Fourier-optics analysis, we obtain the optical amplitude of the reconstructed image in the output plane. By virtue of diffraction, each pixel of the input pattern is transformed into a sinc-like pattern with a series of side lopes. Thus the reconstructed image is not an exact replica of the input pattern. It consists of a signal amplitude and a noise amplitude. The physical overlap of these pixel images is the source of interpixel cross-talk. Without loss of generality, let us examine the image amplitude of the input pattern at the origin $(0,0)$. The signal amplitude and the noise amplitude can be written

$$U_s = A_0 [\int dx \operatorname{sinc}(\frac{D}{\lambda f} x) \operatorname{rect}(\frac{x}{\delta})]^2 \tag{1}$$

$$U_n = \sum_{\substack{m=1 \\ m \neq (0,0)}}^{N^2} A_m \exp(i\phi_m) \int dx_o \operatorname{sinc}(\frac{D}{\lambda f} x_o) \operatorname{rect}(\frac{x_o - m_x S}{\delta}) \int dy_o \operatorname{sinc}(\frac{D}{\lambda f} y_o) \operatorname{rect}(\frac{y_o - m_y S}{\delta}) \tag{2}$$

respectively, where $A_m \exp(i\phi_m)$ is the amplitude for the m-th pixel with a random phase, δ is the width of each pixel, S is the period of the pixel array, D is the transverse size of the crystal, f is the focal length, and $\lambda f/D$ is the width of the side lopes of the sinc function. By evaluating the integral in Eq. (2) we find that the interpixel cross-talk noise is critically dependent on the ratio between δ and $\lambda f/D$. When the pixel size is an odd integral multiple of the width of the

sinc function side lope, i.e., $\delta = (2k-1)\lambda f / D$ (where k is a positive integer), the noise is maximum. The signal-to-noise ratio (defined as the ratio of the signal intensity $|U_s|^2$ to the variance of the noise $E\{|U_n - E\{U_n\}|^2\}$) can be written

$$SNR_{odd} = \frac{3\pi^2}{8}(\frac{DS}{\lambda f})^2 .$$ (3)

When the pixel size is an even integral multiple of the width of the sinc function side lope, i.e., $\delta = 2k\lambda f / D$, the noise terms in Eq. (2) are minimum. The total noise has a finite upper limit when all the input pixels are in phase. The signal-to-noise ratio (defined as the ratio of the signal intensity $|U_s|^2$ to the upper limit of the total noise intensity) can be written

$$SNR_{even} = (\frac{3}{4}\frac{D^2 S^2}{\lambda^2 f^2})^2$$ (4)

According to Eqs. (3) and (4), we note that the finite transverse size of the crystal leads to the intrapage interpixel cross-talk noise which imposes a limitation on the pixel separation in each hologram. It is known that the finite thickness of the crystal leads to an interpage cross-talk noise which in turn limits the total number and physical size of the holograms that can be stored in the crystal[1,2]. Combining Eqs. (3) and (4) with those previous results, we can obtain the storage density in terms of the total number of bits per unit volume.

In the case of wavelength multiplexing, the limitations imposed by the interpage cross-talk are $\Delta v = c/(2t)$ and $SNR_{pa} = 2f^2/area^2$, where Δv is the frequency separation of adjacent holograms, c is the light velocity in vacuum, t is the thickness of the crystal, SNR_{pa} is the signal-to-noise ratio due to interpage cross-talk noise, f is the focal length and $area$ is the area of the input plane ($NS \times NS$). Assuming the wavelength tuning range is from $\lambda_o/2$ to λ_o, the ratio $\delta D / \lambda f$ will vary by a factor of 2. Thus the SNR varies between SNR_{odd} and SNR_{even}. The storage density for wavelength multiplexing is between the following two limits

$$\rho_\lambda(\min) = \frac{3\pi^2}{2}\frac{1}{(SNR_{pa}SNR_{odd})}\frac{1}{\lambda_o^3} \quad \text{and} \quad \rho_\lambda(\max) = \frac{3}{(SNR_{pa}\sqrt{SNR_{even}})}\frac{1}{\lambda_o^3}$$ (5)

Because of the variation in wavelength, the maximum storage density, which represents an upper limit, can not be achieved in practice.

In the case of angle multiplexing, the limitation imposed by the interpage cross-talk is $SNR_{pa} = (2tf)/(\lambda d_y N_h)$, where d_y is the size of the output plane in the y direction and N_h is the number of holograms[1]. The interpage cross-talk only gives limitation on one dimension of the output plane. The other dimension is limited by the paraxial approximation. Let $\alpha = d_x/f$, where d_x is the size of the output plane in the x direction. The storage density for angle multiplexing is between the following two limits

$$\rho_\theta(\min) = \frac{3\pi^2}{4}\frac{\alpha}{SNR_{pa}SNR_{odd}}\frac{1}{\lambda^3} \quad \text{and} \quad \rho_\theta(\max) = \frac{3}{2}\frac{\alpha}{SNR_{pa}\sqrt{SNR_{even}}}\frac{1}{\lambda^3}$$ (6)

In angle multiplexing, we can adjust λ and f to satisfy the condition for minimum intrapage interpixel cross-talk. Thus, the maximum storage density is practically achievable.

By allowing a bit error rate of 10^{-9} which corresponds to $SNR_{pa} = SNR_{odd} = 150$, $SNR_{even} = 4$, and using $\alpha = 0.2$, we obtain $\rho_\lambda(\min) = 7 \times 10^{-4} / \lambda_o^3$, $\rho_\lambda(\max) = 0.01 / \lambda_o^3$, $\rho_\theta(\min) = 7 \times 10^{-5} / \lambda^3 = 5 \times 10^{-4} / \lambda_0^3$, and $\rho_\theta(\max) = 10^{-3} / \lambda^3 = 8 \times 10^{-3} / \lambda_0^3$, where we assume $\lambda = \lambda_0 / 2$ for angle multiplexing.

In conclusion, we present a statistical analysis of the cross-talk limited storage capacity for both angle and wavelength multiplexed holographic memory. We obtain, for the first time, expressions for the storage capacity in terms of the number of bits per unit volume. It is found that they are reduced from the ultimate storage capacity of λ^{-3} by a factor of the signal to noise ratio. The results also indicate that angle multiplexing has more degree of freedom to be optimized to reduce the intrapage interpixel cross-talk noise.

References:

1. C. Gu, J. Hong, I. McMichael, R. Saxena, and F. H. Mok, J. Opt. Soc. Am. A **9**, 1978 (1992).
2. K. Curtis, C. Gu, and D. Psaltis, Opt. Lett. **18**, 1001 (1993).
3. G. A. Rakuljic, V. Leyva, and A. Yariv, Opt. Lett. **17**, 1471 (1992).
4. A. Yariv, Opt. Lett. **18**, 652 (1993).
5. G. P. Nordin, P. Asthana, Opt. Lett. **18**, 1553 (1993).
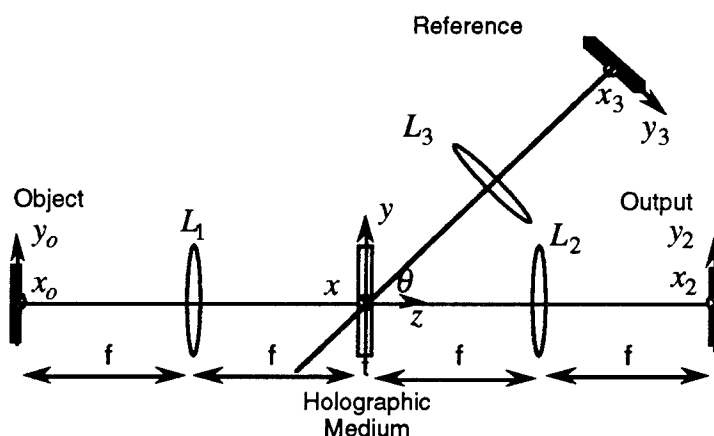
Fig.1 Recording and readout geometry for angle multiplexing (e.g. $\theta = \pi/2$) and wavelength multiplexing (e.g. $\theta = 0$).

(a)   (b)
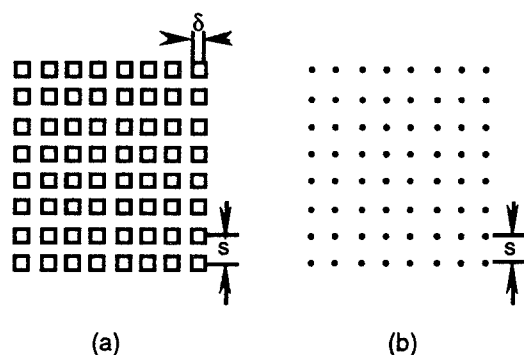
Fig.2 Input (a) and output (b) configurations.

Thursday Papers Not Available

THA1 Frequency Doubled Nd:Yag Laser for General Surgery: From the Research Lab to Commercial Product

THA2 Up-conversion Lasers

THA5 Threshold Reduction Techniques for SBS Phase Conjugation

FRIDAY, JULY 29

FA: **Fundamental Quantum Processes in NLO**

FB: **Nonlinear Optical Materials-Inorganics**

Are Time- and Frequency-Domain Nonlinear Spectroscopies Related by a Fourier Transform?

Rick Trebino
Combustion Research Facility, Sandia National Laboratories
Livermore, CA 94551, (510) 294-2893, FAX (510) 294-2276

John T. Fourkas
Department of Chemistry, University of Texas
Austin, TX 78712, (512) 471-5001, FAX (512) 471-8696

Alfred M. Levine
Applied Science Department, College of Staten Island
Staten Island, NY 10301

It is commonly believed that nonlinear-spectroscopic techniques involving nearly monochromatic beams, in which one or more beam frequencies are varied, are in some sense the "Fourier transforms" of techniques involving ultrashort pulses, in which one or more pulse delays are varied. While it is well known that many effects (inhomogeneous broadening, saturation, imperfect light sources, etc.) can complicate the relationship between such techniques, it is still felt that at some fundamental level, in the absence of these effects, the Fourier-transform relationship of these "conjugate techniques" remains valid. Indeed, nearly all nonlinear-optics textbooks include a section "proving" the validity of the Fourier transform in each order of perturbative nonlinear spectroscopy. Butcher,[1] for example, in his classic work on nonlinear optics, *defined* the frequency-domain nonlinear susceptibility, $\chi^{(n)}(\omega_1, \dots, \omega_n)$, to be the n-dimensional Fourier transform of the time-domain nonlinear response function, $R^{(n)}(\tau_1, \dots, \tau_n)$.

Given, however, that semi-classical nonlinear-optical perturbation theory gives specific expressions for the response in time-domain experiments and the susceptibility in frequency-domain experiments,[2] a reasonable question is *"Are $\chi^{(n)}(\omega_1, \dots, \omega_n)$ and $R^{(n)}(\tau_1, \dots, \tau_n)$, as given by semi-classical nonlinear-optical perturbation theory, n-dimensional Fourier transforms of each other for corresponding frequency- and time-domain nonlinear-spectroscopic interactions?"*

We find that, while the above Fourier transform does hold for *classical* problems, it fails badly in *semi-classical* nonlinear spectroscopy.

An easy-to-derive result is that each Feynman diagram yields a term that contributes to both time- and frequency-domain interactions, and these terms are, indeed, related by an n-dimensional Fourier transform. However, because each of these pairs of terms involves a different set of conjugate variables, the Fourier-transform relationship does not survive. Thus, *we find that, unless a single time-ordering contributes to each nonlinear-optical interaction, $\chi^{(n)}(\omega_1, \dots, \omega_n)$ and $R^{(n)}(\tau_1, \dots, \tau_n)$ are still not n-dimensional*

Fourier transforms of each other. In general, it is difficult to find cases where only a single time-ordering contributes.

Figures 1 and 2 show, as an example, two techniques that are commonly considered Fourier transforms: the transient-grating (TG) technique[3] and nearly degenerate four-wave mixing (NDFWM),[4,5] which frequently involve the same diagrams. The breakdown of the Fourier-transform relationship for these techniques occurs at the first interaction, in which the time and frequency conjugate variables are $\tau_1 \equiv t_2 - t_1$ and ω_1, respectively, for the first and third diagrams in Fig. 2 and $-\tau_1$ and $-\omega_2$, respectively, for the second and fourth diagrams. It is the second interaction, however, that is important in these experiments, and the susceptibility's dependence on the relevant variable, $\omega_1 - \omega_2$, can be shown to be *proportional* to the Fourier transform of the response's dependence on $\tau_2 \equiv t_3 - t_2$, a somewhat weaker condition, but perhaps acceptable.

Unfortunately, at low pressure, *the proportionality "constant" is a function of the variables of interest, and the resonances actually cancel out!* Specifically, in the absence of pure dephasing, the NDFWM susceptibility is well known to be constant due to perfect cancellation of these factors when all time-orderings are included.[5] In the TG response, on the other hand, the time-orderings constructively interfere, yielding strong oscillations even at very low pressures. TG results for sodium are shown in Fig. 3, and NDFWM results have been observed experimentally many times (see, for example, Bloembergen, et al.[5]).

We will discuss the consequences of these unintuitive results. We will also discuss cases in which an n-dimensional Fourier transform can be assumed to hold, but for which unintuitive behavior is also obtained. An example of this latter effect involves time- and frequency-domain CARS, in which the width of a frequency-domain CARS spectrum is not related to the decay time constant in time-domain CARS.

References

1. P.N. Butcher, "Nonlinear-Optical Phenomena," Bulletin 200, Engineering Experiment Station, Ohio State University.
2. T.K. Yee and T.K. Gustafson, "Diagrammatic Analysis of the Density Operator for Nonlinear-Optical Calculations: Pulsed and cw Responses," Phys. Rev. A, vol. 18, pp. 1597-1617 (1978).
3. D.W. Phillion, D.J. Kuizenga, and A.E. Siegman, "Subnanosecond Relaxation Time Measurements Using a Transient Induced Grating Method," Appl. Phys. Lett., vol. 27, pp. 85-87 (1975).
4. R. Trebino, C.E. Barker, and A.E. Siegman, "Tunable-Laser-Induced Gratings for the Measurement of Ultrafast Phenomena," J. Quant. Electron., vol. QE-22, pp. 1413-1430 (1986).
5. N. Bloembergen, A.R. Bogdan, and M.W. Downer, "Collision-Induced Coherence in Four-Wave Light Mixing," in *Laser Spectroscopy V*, eds. A.R.W. McKellar, T. Oka, and B.P. Stoicheff, (Springer-Verlag, Berlin, 1981).
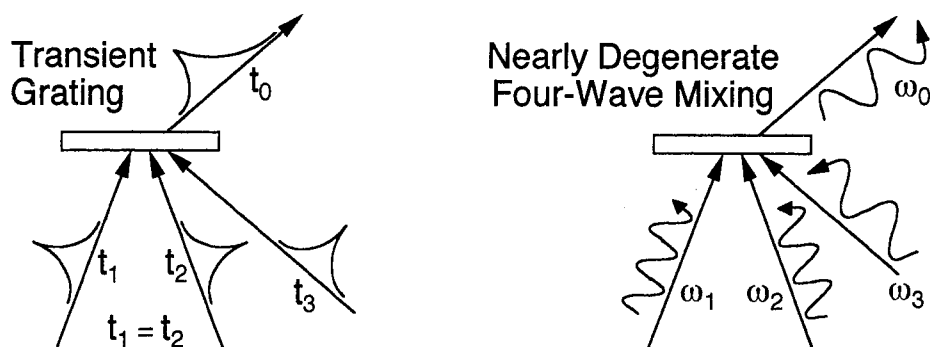
Figure 1.   Examples of time- and frequency-domain methods that are generally considered "Fourier-transform-pair techniques." Beam diagrams illustrate the transient-grating (TG) and nearly-degenerate four-wave mixing (NDFWM) techniques. These methods are used as an example in this work, but the breakdown of the Fourier-transform relationship is general and applies to all such pairs of methods.
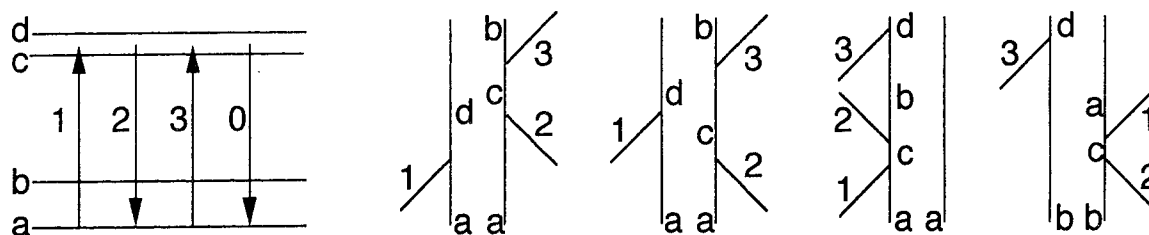
Figure 2.   Most important Feynman diagrams (time-orderings) contributing to the induced polarization in the transient-grating and nearly degenerate four-wave-mixing techniques. At left is shown a simple energy-conservation diagram for these processes, illustrating the possible study of ground-state or excited-state resonances.

Fig. 3. Experimental (squared-modulus) response for a one-color, time-domain transient-grating experiment involving the excitation and probing of the sodium D_1 line at very low pressure. Inset is the numerically computed Fourier transform of this response, showing the 1.77-GHz ground-state hyperfine splitting and the excited-state 189-MHz hyperfine splitting. In the frequency domain (See Bloembergen, et al.[5]), the signal strength is not the Fourier transform of this experimental result; instead it is constant for this experiment. Indeed, these two-photon resonances are absent from the susceptibility.
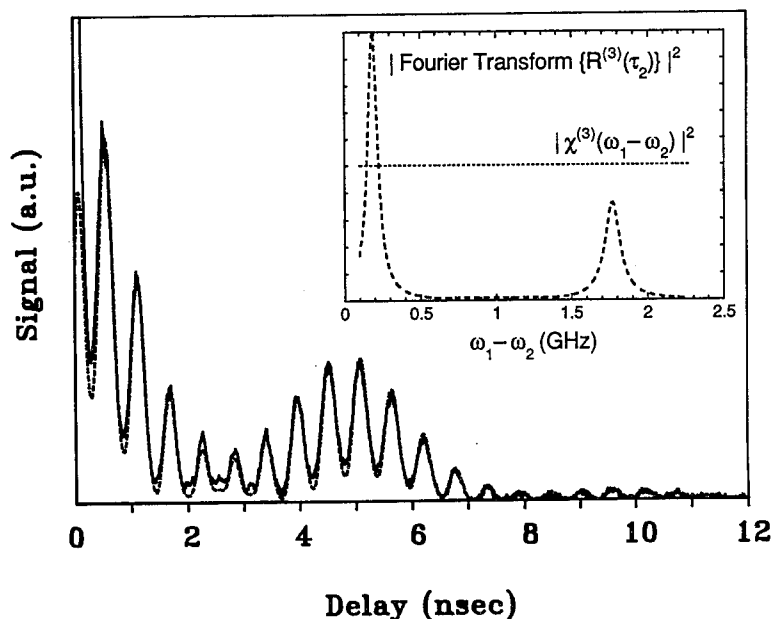
Quantum Optics of Dielectric Media

P.W. Milonni

Theoretical Division

Los Alamos National Laboratory

Los Alamos, New Mexico 87545

The quantization of the electromagnetic field in dielectric media goes back to work of Ginzburg and Jauch and Watson in the 1940s. Ginzburg, in particular, applied his formalism to problems of transition radiation and the Cerenkov effect. The theory of the electromagnetic field in dielectric media has attracted renewed attention in recent years, with particular emphasis given to (a) general radiative processes and the effect of local (Lorentz-Lorenz) field corrections; (b) the general form of the interaction Hamiltonian; and (c) the effect of local field corrections on nonlinear optical susceptibilities.

In this work the field is quantized in a simple and straightforward way based on the classical expression for the energy density,

$$u_\omega = \frac{1}{16\pi} \left[\frac{d}{d\omega}(\epsilon\omega)|\mathbf{E}_\omega|^2 + \frac{d}{d\omega}(\mu\omega)|\mathbf{H}_\omega|^2 \right],$$

for the case of weak absorption. The quantized fields lead to expressions for spontaneous and stimulated emission rates, and gain and absorption coefficients, for the general case of a dispersive dielectric host medium. Local field corrections, when they apply, arise in the same manner as in classical electromagnetic theory. The theory also leads to a radiative level shift dependent on the dispersion of the dielectric, and this shift may be interpreted as a van der Waals interaction between the guest atom and the atoms of the host medium.

Contrary to the frequent statement that it is the electric displacement vector rather than the electric field that should be used in the electric dipole interaction, it is shown that use of the displacement vector leads in fact to an incorrect result for an atom embedded in a dielectric host, and the reason for this is explained from both physical and formal perspectives. The theory is also applied to the modification of nonlinear susceptibilities by local fields.

Realistic Measurement of Phase

H. Paul

Arbeitsgruppe "Nichtklassische Strahlung"

der Max–Planck–Gesellschaft

an der Humboldt–Universität zu Berlin

Jägerstraße 10/11, 10117 Berlin

Germany

One of the most delicate problems in quantum optics is the proper description of the phase of a single–mode radiation field. The formal problem of introducing a (strictly) Hermitian phase operator could be ultimately solved only by resorting to an artificial finite–dimensional Hilbert space [1]. From a more practical point of view, it will be felt even more unsatisfactory that no experimental scheme for an "ideal" phase measurement could be devised. Actually, both the theoretical and the experimental difficulties have a common root: Since an electromagnetic field couples to matter via the electric field strength which comprises both (real) amplitude and phase, the phase cannot be determined from a single measurement, even in classical optics. So in order to make contact with reality, one will have to turn the tables: One will first devise an experimental scheme for phase measurement, thus giving an operational definition of phase, and afterwards search for the proper quantum–mechanical description of the experimental procedure. In fact, several such schemes which differ distinctly in their experimental setup have already been proposed and even partly realized. In this paper, I will describe them in some detail and present the outlines of their theoretical analysis.

The first to discuss a realistic phase measuring device were Bandilla and Paul [2],

who as early as 1969 proposed to amplify, with the help of a laser (or parametric) amplifier, the microscopic field to be investigated to a macroscopic level, where classical phase measurement techniques can readily be applied. Since any amplifier unavoidably adds noise to the amplified signal, this type of phase measurement is necessarily of noisy (fuzzy) character.

Fifteen years later Shapiro and Wagner [3] analyzed a heterodyne detection scheme which allows simultaneous, however noisy, observations of both the phase and the amplitude of a signal field. Their basic idea was to mix the signal, by means of a weakly reflecting mirror, with a strong coherent field (local oscillator) whose frequency is shifted by a certain amount $\Delta\nu$. The mixed field is sent to a photodetector. Its photocurrent contains an alternating current oscillating at the difference frequency $\Delta\nu$ — it is just the beat signal — and the amplitudes of this alternating current, corresponding to the components oscillating as $\cos(2\pi\Delta\nu t)$ and $\sin(2\pi\Delta\nu t)$ respectively, are determined separately by well known electronic techniques. By repeating this measurement many times, one can determine a distribution function for those amplitudes x and p. Passing to polar coordinates one gets a distribution function for both the amplitude (radius) and the phase (polar angle) of the signal field. Averaging, in particular, over the amplitude yields a phase distribution. Also in the present case undesired noise enters the experimental device: One has to notice that a beat signal with beat frequency $\Delta\nu$ originates also from the empty field mode which is the image, with respect to frequency, of the signal mode, which makes the measurement noisy.

Only recently, Noh, Fougères and Mandel [4] proposed and, moreover, realized a different experimental scheme which is closely related to classical phase measurement. Also in this case two variables are measured simultaneously, namely two field quadra-

ture components x and p. This is achieved by dividing, with the help of a 50 : 50 beam splitter, the original field into two parts and measuring x one of them and p on the other. Those two independent measurements can be performed making use of the balanced homodyne detection technique. When the local oscillators employed in those detection schemes are strong, one can analyse the experiment along the same lines as in the heterodyne–detection scheme [3]. Also this measurement is noisy, due to vacuum fluctuations that enter the unused input port of the beam splitter.

Actually it could be shown that all three schemes are physically perfectly equivalent, the measured distribution for x and p being the Q function for the original field. They share the common feature that they make possible a simultaneous, however noisy, measurement of two canonically conjugate variables.

References

[1] D. T. Pegg and S. M. Barnett, Europhys. Lett. **6**, 483 (1988); S. M. Barnett and D. T. Pegg, J. Mod. Opt. **36**, 7 (1989).

[2] A. Bandilla and H. Paul, Ann. Phys. (Lpzg.) **23**, 323 (1969); H. Paul, Fortschr. Phys. **22**, 657 (1974).

[3] J. H. Shapiro and S. S. Wagner, IEEE J. Quantum Electron. **QE-20**, 803 (1984).

[4] J. W. Noh, A. Fougères, and L. Mandel, Phys. Rev. Lett. **67**, 1426 (1991); Phys. Rev. **A 45**, 424 (1992).

CONTROLLING QUANTUM FLUCTUATIONS BY

ELECTROMAGNETIC FIELD INDUCED COHERENCES

G.S. AGARWAL

University of Hyderabad, Hyderabad, INDIA

It is well established that a Λ - system under the action of two intense fields and in the absence of collisions ends up in a state known as coherent population trapping state[1] (CPT state). This state has well defined coherence between the two lower levels of the Λ - system and has found many different applications. In this paper I demonstrate the utility of this coherence in controlling quantum fluctuations.

As a first application I consider the production of twin beams[2] i.e. beams which are identical not only in their mean amplitudes but also in their quantum statistics. The last fact is expressed mathematically in terms of the P-distribution for the joint density matrix of the two beams. The P-distribution has the structure.

$$P(\alpha_1, \alpha_2) = \delta^{(2)} (\alpha_1 - \alpha_2) \, f(\alpha_1).$$

This is obtained by considering the quantum dynamical evolution of the weak fields on the two transitions of the Λ - system. The master equation is derived and the coefficients in the master equation depend to all orders on the strength of the two pump fields. The presence of the coherence between two lower states of the Λ - system leads to correlation between the two modes. The correlation is especially pronounced and survives even in the steady state if the frequencies of the two modes satisfy the Raman condition.

As a second application we consider how we can use the coherence between two ground states to transfer[3] energy from

the pump field to the signal field without addition of quantum noise. In other words an initial coherent state of the signal transforms into a coherent state with larger field amplitude. This is in contrast to the normal amplification process where an input coherent state is transformed into a mixture of coherent state and noise photons, which are inherent in the amplification process.

Generalization of the above results to the case of pulsed excitation will be discussed.

1.   G. Alzetta, A. Gozzini, L. Moi and G. Orriols, Nuov. Cimento 36B, 5 (1976); H.M. Gray, R.M. Whitley and C.R. Stroud Jr., Opt. Lett. 3, 218 (1978).

2.   G.S. Agarwal, Phys. Rev. Letters 71, 1351 (1993).

3.   G.S. Agarwal, M.O. Scully and H. Walther, Opt. Commun. to be published.

A NEW ERA FOR SPONTANEOUS EMISSION:
THE SINGLE-MODE LIGHT-EMITTING-DIODE

by
E. Yablonovitch
UCLA Electrical Engineering Department
405 Hilgard Ave.
Los Angeles, CA 90024-1594
tel. (310)206-2240
FAX: (310)206-8495

As we learn to engineer spontaneous emission, it begins to assume many of the roles previously reserved for stimulated emission. While interest in low-threshold semiconductor laser diodes has grown, e.g. for optical interconnects, its spontaneously luminescent half-brother, the light-emitting-diode (LED) has begun to re-emerge in a new form. In this new form the LED is surrounded by an optical cavity. The idea is for the optical cavity to make available only a single electromagnetic mode for the output spontaneous emission from the semiconductor diode.

With all the spontaneous emission funneled into a single optical mode, the LED can begin to have many of the coherence and statistical properties normally associated with above-threshold lasing. The essential point is that the spontaneous emission factor, which measures the proportion of spontaneous emission going into the preferred electromagnetic mode, should approach unity. (A closely related concept is that of the "zero-threshold laser", in which the high spontaneous emission factor produces a very soft and indistinct threshold characteristic in the light output-versus-current input curve of laser diodes.)

The idea is to combine the advantages of the LED which is thresholdless and highly reliable, with those of the semiconductor laser which is coherent and very efficient.

The essential ingredient for these concepts is a single mode electromagnetic micro-resonator which captures all the spontaneous emission from the LED active region. There has been great progress, recently, in designing and making dielectric resonators employing

the concepts of photonic band structure. A photonic bandgap can occur in a 3-dimensionally periodic structure (a photonic crystal), which does to photon waves what a semiconductor crystal does to electron waves; it creates a forbidden band of energies irrespective of propagation direction in space. By introducing a defect into the otherwise perfect photonic crystal, a local electromagnetic mode forms in the forbidden gap region. In keeping with the electronic analogy, the defect mode can be either acceptor-type or donor-type.

Figure 1 shows a cross-sectional view of an acceptor defect in a practical photonic crystal. We have been fabricating a 3-dimensional photonic band structure in GaAs and will review our progress. In addition, we will consider some other types of dielectric resonator structures which are derived from millimeter wave technology[1]. These include various types of microscopic dielectric buttons, disks, and cylinders. The behaviour of these dielectric resonator structures in LED's are being tested by observing their spontaneous emission behaviour under optical pumping.

We will present our experimental results on the spontaneous emission from various types of microscopic dielectric structures, which have been designed for the goal of being useful for making a single-mode LED.

1. "Dielectric Resonators", ed. by D. Kajfez and P. Guillon (Artech House, Norwood, Mass., 1986)

2. E. Yablonovitch, T. J. Gmitter and K. M. Leung, Phys. Rev. Lett. 67, 2295 (1991).

FIGURE CAPTION

Figure 1: A $<1,\bar{1},0>$ cross-sectional view of our face-centered-cubic photonic crystal[2] consisting of non-spherical "air-atoms" centered on the large dots. Dielectric material is represented by the shaded area. The rectangular dashed line is a face-diagonal cross-section of the unit cube. We selected an acceptor defect as shown, centered in the unit cube. It consists of a missing horizontal slice in a single vertical rib.
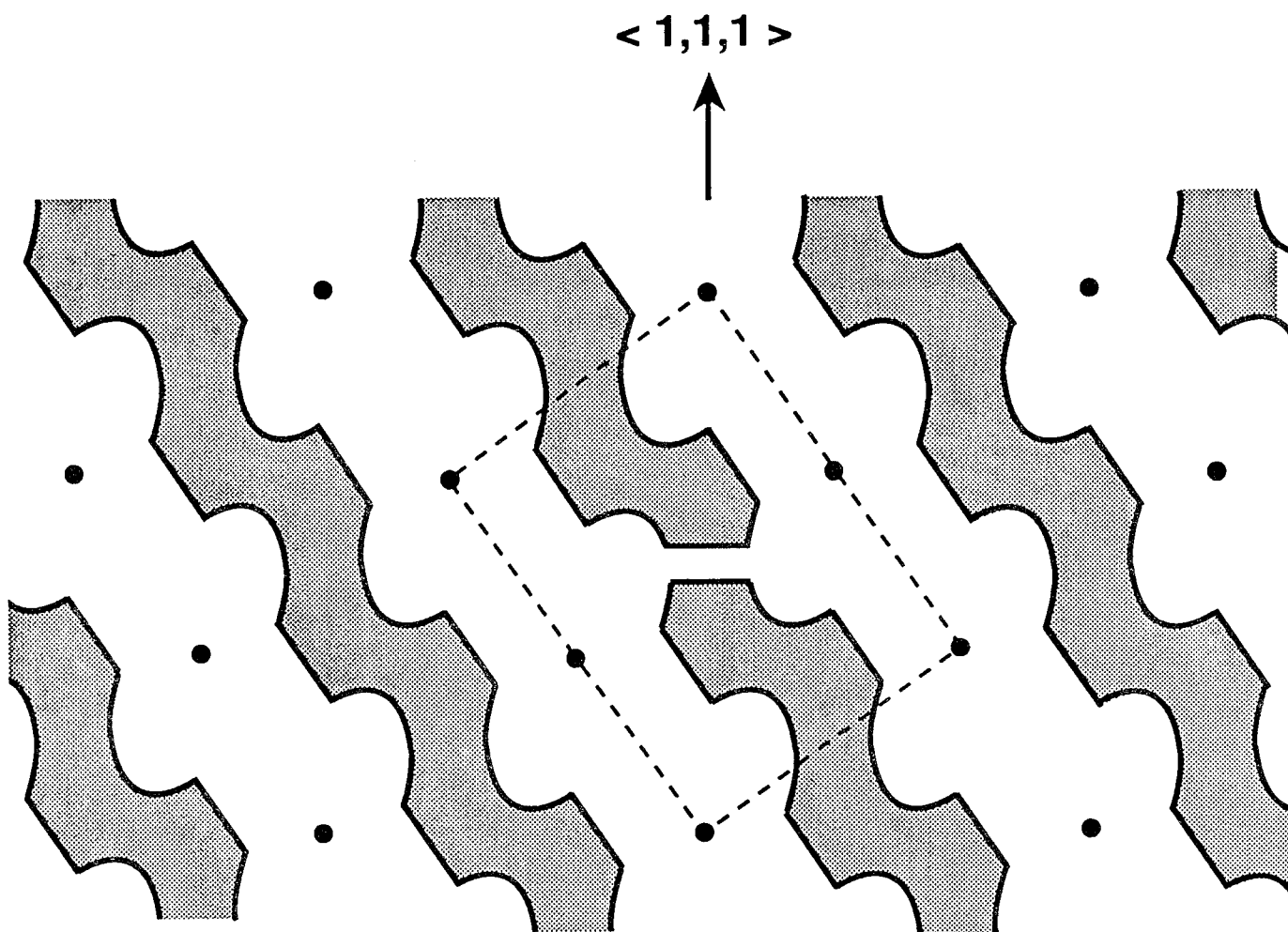
Frequency-Àgile Materials for Visible and Near IR Frequency Conversion

L.K. Cheng, L.T. Cheng, J.D. Bierlein and R. Harlow
Central Science and Engineering, DuPont Co., Inc., P.O. Box 80306, Wilmington, DE 19880-0306

The nonlinear optical crystal $KTiOPO_4$ (KTP) has long been a favorite among device designers for generating coherent radiation in the visible and near infrared. Recent development of its isomorphs, such as $KTiOAsO_4$ (KTA), $CsTiOAsO_4$ (CTA) and $K_{1-x}Ti_{1-x}Nb_xOPO_4$ (Nb:KTP) further enhances the attractiveness of these light sources in practical applications by providing more material flexibility. Like KTP, these isomorphs possess large nonlinearity and favorable temperature bandwidths. Their linear optical properties, such as the crystal birefringence and infrared, however differ significantly from KTP and lead to phase matching characteristics that complement KTP in many important applications. For instance in the generation of ~2 μm radiation using a Nd:YAG pumped OPO, the smaller crystal birefringence of CTA increases the phase matching angle in the x-z plane (θ~75° in CTA compares to θ~51.5° in KTP), leading to a theoretically higher effective nonlinearity and smaller beam walkoff.[1] Similarly, the nearly 1 μm wider infrared transparency of the arsenate isomorphs should effectively eliminate the thermal loading problem associated with the ~3.5 μm idler absorption in a Nd:YAG pumped high power KTP OPO.[2,3]

More importantly, as these isomorphs are isostructural, they can readily form solid-solutions and do so with favorable partition coefficients ($0.5 < \kappa < 1.2$). Table 1 lists the birefringence of these isomorphs, their crystal birefringences n_z-n_x at 632 nm, their x-propagating SHG cutoffs, and the theoretical birefringence tuning rates. This ability to fine tune the crystal birefringence via solid-solution composition-tuning is particularly attractive as it offers the potential of angle-noncritical phase matching over a broad wavelength range (~0.45-3.6 μm). Whereas the crystal series KTA, RTA ($RbTiOAsO_4$), and CTA offers a systematic decrease in the crystal birefringence,[4] substantial birefringence increases are found for the crystal series KTP, Na:KTP ($Na_xK_{1-x}TiOPO_4$)[5], Nb:KTP and Ta:KTP ($K_{1-x}Ti_{1-x}Ta_xOPO_4$).[6] For highly doped

crystals (e.g. ~14.6%Nb:KTP), a ~100 nm blue-shift in the SHG cutoff wavelength (from 0.994 μm to 0.890 μm) has already been reported. This has led to renewed interests in the use of bulk KTP isomorphs as compact blue-green light sources.

Although our solid-solution birefringence tuning approach appears promising, important material issues concerning compositional uniformity needs to be addressed. In this regard, two aspects of these isomorphs should prove advantageous: First, with appropriately chosen solid-solution combinations, the birefringence tuning rate is reasonably small that compositional fluctuation becomes more tolerable. For instance, with the $KTiOP_xAs_{1-x}O_4$ solid-solution, a 10^{-4} birefringence change corresponds to a (P_xAs_{1-x}) compositional change of $\Delta x \sim 3\%$. Second, KTP isomorphs are grown from a *dilute* solution where the crystal yield amounts to only a fraction (~7 weight%) of the melt. With near unity partition coefficient, the melt composition remains essentially unchanged throughout the crystal growth run. Again, using the previous $KTiOP_xAs_{1-x}O_4$ solid-solution example, the concentration of $(P_{x'}As_{1-x'})$ in our $K_6(P_{x'}As_{1-x'})_4O_{13}$ flux out-numbered Ti (as in $KTiOP_xAs_{1-x}O_4$ crystal) 10-to-1. Thus, throughout a typical crystal growth run, the near unity partition coefficient ($\kappa \sim x/x' \sim 0.88$ for P) leads to a maximum *theoretical* change in the flux composition x' of less than 0.01, or a $< 0.3 \times 10^{-4}$ birefringence change. Preliminary crystal growth experiments have yielded 5-22 mm long crystals of $KTiOP_xAs_{1-x}O_4$ and $K_{1-x}Ti_{1-x}Nb_xOPO_4$ crystals with respectable optical uniformity ($\Delta \lambda.l < 2$ nm-cm). Refinement of the crystal growth process should yield even more encouraging result.

In summary, we reported the possible use of solid-solutions of KTP isomorphs for frequency conversion applications. These materials promise exceptional design flexibility and frequency agility as their phase matching properties can be compositionally tuned for optimal device performance.

Table 1: Birefringences, SHG cutoffs and tuning rates of KTP isomorphs.

Crystal	n_z-n_x	SHG cutoff along x [μm]	Tuning rate $\partial(n_z$-$n_x)/\partial x$ [10^{-4}/%]
14.6%Nb:KTP	0.1466	n.a.	
KTiOPO$_4$	0.1022	1.082	30.4
RbTiOPO$_4$	0.0975	1.147	0.47
TlTiOPO$_4$	0.0674	n.a.	3.01
KTiOAsO$_4$	0.0965	1.134	
RbTiOAsO$_4$	0.0891	1.243	0.74
CsTiOAsO$_4$	0.0812	1.548	0.79

n.a. = not available; *italics* denote calculated values.

1. L.T. Cheng, L.K. Cheng, J.D. Bierlein and F.C. Zumsteg, Appl. Phys. Lett. **63**, 2618 (1993).
2. W.R. Bosenberg, L.K. Cheng and J.D. Bierlein, in *Topical Meeting on Solid State Lasers*, New Orlean, 1992 (Optical Society of America),
3. K. Kato, IEEE J. of Quantum Electron. **27**, 1137 (1991).
4. L.T. Cheng, L.K. Cheng, J.D. Bierlein and J. Parise, Appl. Phys. Lett. **64**, 1 (1994).
5. G.M. Loiacono, R.A. Stolzenberger and D.N. Loiacono, Appl. Phys. Lett. 16 (1994).
6. L.K. Cheng, L.T. Cheng, R.L. Harlow and J.D. Bierlein, **64**, 155 (1994).

Nonlinear Optical Properties of Thin Film Composite Materials

R. W. Boyd,[1] G. L. Fischer,[1] R J. Gehr,[1] Varada Iruvanti,[1]
S. A. Jenekhe,[2] J. A. Osaheni,[2] and J. E. Sipe[3]

[1] *Institute of Optics, University of Rochester, Rochester, NY 14627*
716-275-2329 (voice), 716-273-1075 (fax), boyd@optics.rochester.edu

[2] *Dept. of Chemical Engineering, University of Rochester, Rochester, NY 14627*

[3] *Dept. of Physics, University of Toronto, Toronto, Ontario, Canada*

There is great need for materials with large optical nonlinear coefficients for use nonlinear optics and photonics. Recently, several groups[1] have proposed the use of composite materials as a means of achieving large values of the third-order susceptibility $\chi^{(3)}$. One proposal, due to two of the present authors,[2] involves forming a composite of alternating layers of two different materials with layer thicknesses much smaller than an optical wavelength. If the linear refractive indices of these two components are different, the electric field strength of an optical field polarized perpendicular to the plane of the layers will be nonuniformly distributed between the two constituent materials. The field strength will exceed the spatially averaged field strength in the material with the smaller linear refractive index, and if this material is the more nonlinear of the two then the effective $\chi^{(3)}$ value of the composite material can exceed that of either component. For the situation in which the two linear refractive indices differ by a factor of two, the value of $\chi^{(3)}$ can thereby be enhanced by a factor of ten.

This enhancement is maximized if the light propagates through the material as a TM guided wave. The enhancement will be reduced if the light propagates through the material at some oblique angle. However, the angular dependence of the nonlinear optical response can offer a means to determine quantitatively the extent to which the $\chi^{(3)}$ susceptibility is enhanced. In the present paper, we report the results of our experimental study of this angular dependence. We find that the angular dependence is in good qualitative agreement with theoretical predictions.

We have formed a composite of alternating layers of titanium dioxide and the nonlinear optical polymer PBZT (poly (paraphenylene benzobisthiazo)).[3] Samples are formed by spin casting onto glass substrates. Here titanium dioxide constitutes the high-index component having essentially linear response. It is spin cast from a sol gel precursor and is cured for 24 hours at 200 C to yield a material with a refractive index of approximately 2.2. The PBZT is also spin cast and is cured for 24 hours under vacuum at 70

C. It has a linear refractive index of 1.7 and a $\chi^{(3)}$ of 5×10^{-11} esu. Layer thicknesses of 50 nm are used. The sample used in the measurements reported below contains five layers of each material.

The nonlinear optical response of these materials is measured as a function of the angle of incidence using the z-scan method. The experimental setup is shown in Fig. 1. Measurements are performed at a wavelength of 1.9 μm to avoid two-photon absorption in the polymer. This wavelength was obtained by Raman shifting the output of a Nd:YAG laser in a hydrogen cell. Results of this measurement are shown in Fig. 2. Here the nonlinear phase shift as determined by the z-scan measurement is plotted as a function of the angle of incidence for both TM (p-polarized) and TE (s-polarized) light. Also shown is our best theoretical fit to the data. Note that for TM waves the nonlinear phase shift first increases with angle and then decreases as the Fresnel transmission coefficient drops to zero at grazing incidence. The increase in nonlinear phase shift occurs both because of the increase in transmission near Brewster's angle and because $\chi^{(3)}$ increases with angle of incidence. However, we cannot explain our data by assuming that the increase is due solely to the former effect.

References

1. K. C. Rustagi and C. Flytzanis, Opt. Lett. **10**, 511, (1985); G. S. Agarwal and S. Dutta Gupta, Phys. Rev. A **38**, 5678 (1988); and J. W. Haus, R. Inguva, and C. M. Bowden, Phys. Rev. A **40**, 5729 (1989).

2. R. W. Boyd and J. E. Sipe, to appear in J. Opt. Soc. Am. B, 1994.

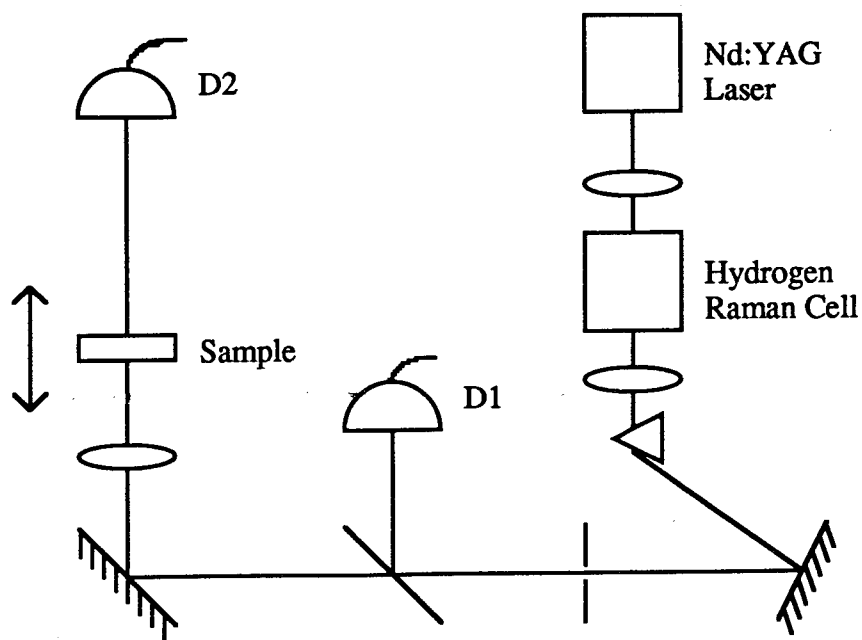3. H. Vanherzeele, J. S. Meth, S. A. Jenekhe, M. F. Roberts, Appl. Phys. Lett. **58**, 663 (1991).
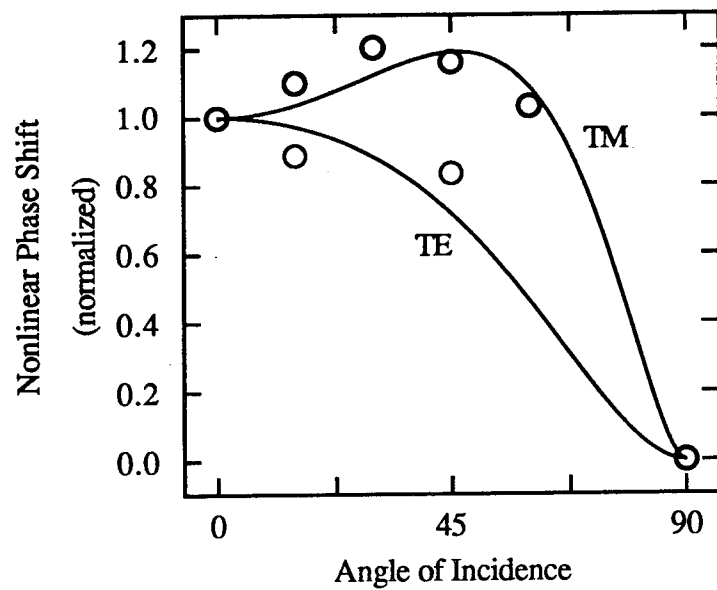
Figure 1: Experimental setup.

Figure 2: Angular dependence of nonlinear phase shift.

Boromalate Salts: A New Family of Solution-Grown Crystals for Nonlinear Optical Applications for the UV, Visible, and Near-IR

H.O. Marcy, M.J. Rosker, L.F. Warren, and P.H. Cunningham
Rockwell International Science Center
1049 Camino Dos Rios
Thousand Oaks, CA 91360
805-373-4153

A continuing need exists to develop new optical materials useful for frequency conversion in the UV to near-IR spectral range. This need is particularly acute with regards to systems requiring large apertures and/or high average powers. This paper reports our preliminary results for a new and promising family of solution-grown nonlinear optical (NLO) materials based on salts of the boromalate anion. Crystals of this family which we have characterized to date include lithium boromalate ($LiBC_8H_8O_{10}$), potassium boromalate hydrate ($KBC_8H_8O_{10} \cdot H_2O$), sodium boromalate ($NaBC_8H_8O_{10}$), guanidinium boromalate ($CN_3H_3BC_8H_8O_{10}$), and ammonium boromalate ($NH_4BC_8H_8O_{10}$). The boromalate salts, with the exception of potassium boromalate hydrate (KBM) which is known to be monoclinic $P2_1$,[1] are crystals whose structure and optical properties have not previously been examined.

The boromalate salts are examples of "semiorganic" NLO materials, i.e., crystals in which the typically high optical nonlinearity of a purely organic material is combined with the potentially favorable mechanical and thermal properties of an inorganic[2,3] Much recent work[4,5] has demonstrated that organic crystals can have very large nonlinear susceptibilities relative to inorganic crystals, but their use is impeded by their low optical transparencies, poor mechanical properties, low laser damage thresholds. It has also proven difficult to produce and process large crystals of organics. Purely inorganic NLO materials typically have excellent mechanical and thermal properties but often possess relatively modest optical nonlinearities due to their lack of extended π-electron delocalization. In semiorganics, polarizable organic molecules are stoichiometrically bound within an inorganic host, e.g., an organic ion/inorganic counterion salt, such as L-arginine phosphate[6], or an organic ligand/metal ion complex, such as zinc tris(thiourea) sulfate (ZTS).[2] Imparting ionic character to large NLO response organic molecules via complexation and/or salt formation works to improve the mechanical and optical properties of the crystals of these materials and also provides a high degree of design flexibility for NLO effects utilizing simple synthesis and screening techniques.

The boromalate salts were identified in our ongoing survey of semiorganic materials as a family of potentially useful NLO crystals. The salts were crystallized from aqueous solutions containing 2:1:1 molar ratios of L-malic acid to boric acid to the appropriate alkali cation (the latter incorporated as the hydroxide or carbonate). -A schematic representation of the boromalate anion is shown in Fig. 1. Based upon the crystal structure of the potassium salt KBM,[1] the hydroxyl group and adjacent carboxylate hydrogen of each L-malic acid are deprotonated, and two of these dianions tetrahedrally coordinate to the boron(3+) atom, leaving a net minus one charge on the boromalate complex anion. Crystals of salts of this acentric anion are assured of being noncentrosymmetric due to the chirality of the malic acid units. The principal nonlinearities of the boromalates are assumed to arise from delocalized π-electrons associated with the carboxylate functionalities (C=O). More complete determinations of the boromalate salt structure-property relationships are in progress.
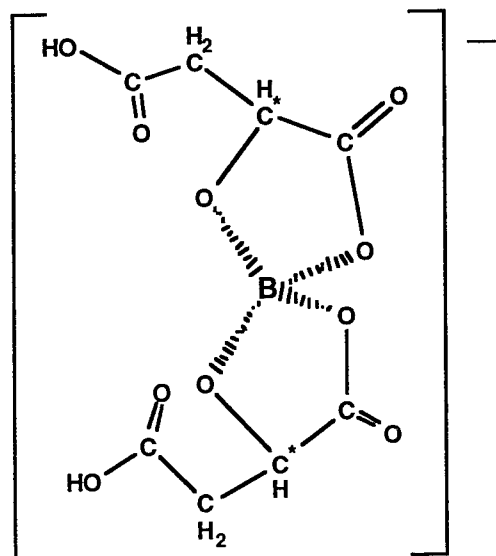
Fig. 1. A representation of the boromalate anion. The trivalent boron atom is tetrahedrally coordinated. C* is the chiral carbon atom of the malate anion.
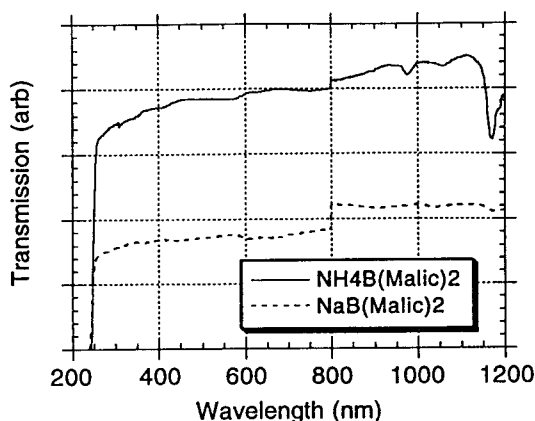
Fig. 2. Transmission spectra for ammonia boromalate and sodium boromalate on unpolished samples of 1.7 mm and 4.1 mm respectively. The anomaly at 800 nm is due to a grating change in the spectrometer

The single crystal boromalate salts reported here are optically transparent between about 250 nm and 1300 nm (see Fig. 2). We observe experimentally that these salts are biaxial in nature. The measured Type I and Type II 1064 nm SHG PM loci and the corresponding variations of the effective nonlinearities for KBM are shown in Fig. 3. In this figure, $\theta = 0$, $\phi = 0$ corresponds to propagation along the dielectric axis having the smallest refractive index and $\theta = 0°$, $\phi = 90°$ corresponds to propagation along the dielectric axis having the highest refractive index. These data were measured on a ~1 mm diameter sphere of KBM using a computer automated version of the direct phase matching (DPM) technique described in Ref. 7. Preliminary analysis of our DPM data indicates that KBM has an effective nonlinearity larger than that of potassium dihydrogen phosphate (KDP) and is less angularly sensitive at the locations of maximum d_{eff}. The DPM technique was also applied to crystals of ammonium boromalate (NHBM) and indicated a similar nonlinearity and birefringence. More precise determinations of d_{eff} and $\delta\Delta k/\delta\theta$ as well as measurements of the refractive index dispersion will be made on cut plates and oriented prisms. The general shape of the phase matching loci indicate that the KBM and NHBM probably have sufficient birefringence to phase match for a number of parametric processes between 300 and 1300 nm, including SHG of 1064 nm light and sum frequency mixing of 1064 nm and 532 nm to produce 355 nm light. Measurements on other members of the boromalate family will also be reported.

The single crystal boromalate salts reported here are optically transparent between about 250 nm and 1300 nm (see Fig. 2). We observe experimentally that these salts are biaxial in nature. The measured Type I and Type II 1064 nm SHG PM loci and the corresponding variations of the effective nonlinearities for KBM are shown in Fig. 3. In this figure, $\theta = 0$, $\phi = 0$ corresponds to propagation along the dielectric axis having the smallest refractive index and $\theta = 0°$, $\phi = 90°$ corresponds to propagation along the dielectric axis having the highest refractive index. These data were measured on a ~1 mm diameter sphere of KBM using a computer automated version of the direct phase matching (DPM) technique described in Ref. 7. Preliminary analysis of our

463

DPM data indicates that KBM has an effective nonlinearity larger than that of potassium dihydrogen phosphate (KDP) and is less angularly sensitive at the locations of maximum d_{eff}. The DPM technique was also applied to crystals of ammonium boromalate (NHBM) and indicated a similar nonlinearity and birefringence. More precise determinations of d_{eff} and $\delta\Delta k/\delta\theta$ as well as measurements of the refractive index dispersion will be made on cut plates and oriented prisms. The general shape of the phase matching loci indicate that the KBM and NHBM probably have sufficient birefringence to phase match for a number of parametric processes between 300 and 1300 nm, including SHG of 1064 nm light and sum frequency mixing of 1064 nm and 532 nm to produce 355 nm light. Measurements on other members of the boromalate family will also be reported.

These preliminary results suggest that boromalate-based semiorganic salts show promise as new NLO materials for frequency conversion in the near-IR to near-UV. Because the angular sensitivity appears to be small and relatively constant, the power threshold figure of merit[6] is expected to compare favorably with high temperature melt-grown materials, such as BBO. These results serve to further validate the semiorganic approach to developing solution-grown alternatives to these latter materials.

Fig 3. Measured (a) phase matching loci (b) singular sensitivity and (c) SHG intensity for KBM. Solid circles are Type I, open triangles are Type II phase matching.

References

1. R.A. Mariezcurrena and S.A. Rasmussen, Acta Cryst. **B29** 1035-1040, (1973).
2. H. O. Marcy, L. F. Warren, M. S. Webb, C. A. Ebbers, S. P. Velsko, G. C. Kennedy and C. C. Catella, *Appl. Opt.* <u>31</u>, 5051-5060 (1992).
3. L. F. Warren, in <u>Electronic Materials -- Our Future</u>, edited by R. E. Allred, R. J. Martinez and K. B. Wischmann, Proceedings of the 4th International SAMPE Electronics Conference, <u>4</u>, (Society for the Advancement of Material and Process Engineering, Covina, CA, 1990) p. 388-396.
4. G. R. Meredith, in <u>Nonlinear Optical Properties of Organic and Polymeric Materials</u>, edited by D. J. Williams, ACS Symposium Series, <u>233</u>, (American Chemical Society, Washington, DC, 1982) p. 27-56.
5. <u>Materials for Nonlinear Optics -- Chemical Perspectives</u>, edited by S. R. Marder, J. E. Sohn and G. D. Stucky, Vol. 455, (American Chemical Society, Washington, DC, 1991).
6. D. Eimerl, *IEEE J. Quantum Elect.* <u>QE-23</u>, 575-592 (1987).
7. S. P. Velsko, *Opt. Eng.* <u>28</u>, 76-84 (1989)

Electric Field Measurements Associated
with Second Harmonic Generation in Thin Film Waveguides

John J. Kester and Iyad Dajani
Frank J. Seiler Research Laboratory
U.S. Air Force Academy, CO 80840-6272
(719) 472-3122

Ulf Osterberg and Peter Weitzman
Thayer School of Engineering
Dartmouth College
Hanover NH 03755
(603) 646-3486

The observation of second harmonic generation (SHG) in planar[1] and fiber optic[2] waveguides of germania doped silica has been linked to the formation of an internal DC electric field[3]. Models predict that an internal static electric field is produced by a modification of the optical properties of the waveguide material through the interaction of fundamental laser light at frequency ω and second harmonic light at frequency 2ω waveguiding along the same optical path.[3] This pre-conditioning of the waveguide material is often called "seeding". After the removal of the second harmonic "seed" beam, the induced static but spatially varying electric field produces a phase-matched effective second order susceptibility which allows SHG.

We are investigating the process by which these induced static electric fields are produced in the waveguide material. Most of the models for the production of this field rely on a photoionization process within the waveguide which has a preferential photoejection direction, i.e., a net current flow. Our work models the current that produces the static electric field and measures the electric fields outside the waveguide surface that are produced by this internal current flow.

The experimental setup for the measurement of photoinduced currents is similar to those experiments which apply an external electric field to induce SHG with only the incident fundamental laser light.[4,5] The proper phase matching conditions for generation of the second harmonic light require that the internal electric field have a periodicity, Δz, given by

$$\Delta z = \left| \frac{2\pi}{2\beta_\omega - \beta_{2\omega}} \right|$$

where β_ω and $\beta_{2\omega}$ are the propagation constants for the fundamental and second harmonic light, respectively. For a 6m% germania-doped silica waveguide having a thickness of 3.5 microns on a silica substrate the appropriate indices of refraction require a periodicity of approximately 26 microns. Figure 1 shows the design of an interdigitated electrode. The actual electrode structure had a 26 micron periodicity and 400 digits. This electrode structure was placed approximately 0.5 microns above the waveguide surface. The electrode digits were directed approximately

normal to the waveguide path. The orientation of the digits relative the waveguide path was adjusted to produce the phase-matching conditions needed for the particular waveguide selected.

Interdigitated Electrode
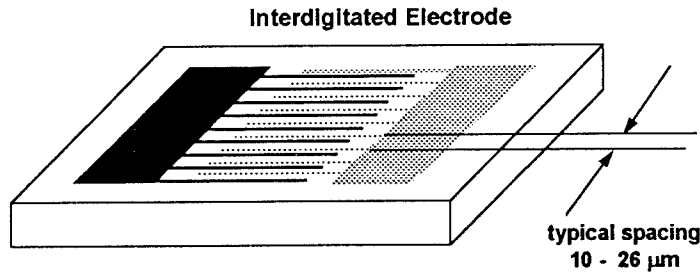
Figure 1. Chrome interdigitated electrode structure on glass substrate

Part of the output of Q-switched and mode-locked Nd:YAG laser at 1.06 microns is frequency doubled in a KTP crystal as shown in Figure 2.   These beams are independently prism-coupled into the waveguide film with p-polarization.   Currents produced by photoionization within the film generate an electric field outside the waveguide that are sensed by the interdigitated electrodes as an induced current.
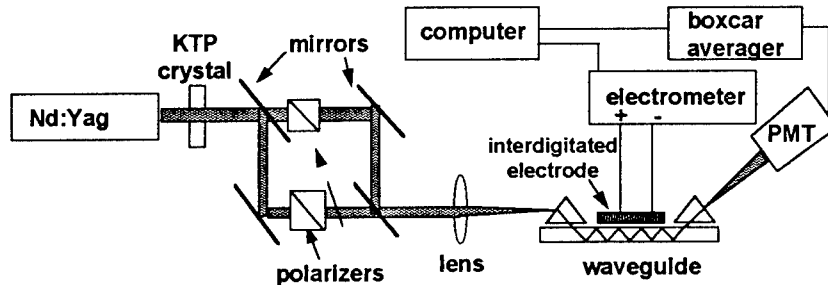
Figure 2. Experimental setup

The photoinduced current normal to the direction of propagation, j_y, in the waveguide is produced by a multi-photon interaction of fundamental and second harmonic light with the material given by

$$j_y(y,z) = \sigma^{(3)} E_{opt}(y,z)$$

where $\sigma^{(3)}$ is the third order conductivity and E_{opt} is the optical DC field in the waveguide that produces the asymmetry in the photocurrent. The third order nonlinear conductivity corresponds to the four-wave mixing model that produces the optical DC field given by

$$E_{opt}(y,z) \propto E_\omega^2(y) E_{2\omega}^*(y) e^{i(2\beta_\omega - \beta_{2\omega})z} + c.c.$$

where E is the field due to a particular waveguiding mode and the exponential term satisfies the phase matching conditions and, thus, dictating spatial variation of the final static internal field as a function of z along the waveguiding path.   The fields outside the waveguide will increase as a

function of time until the photoinduced current is canceled by the backfield due to charge separation.[6]

The interdigitated electrodes were aligned by a rotary movement relative to the waveguide path to optimize the phase matching conditions. Phase matching conditions were tested by observing film generated SHG when only the fundamental light was incident as a function of voltage applied to the electrodes.[4,5] With the electrodes optimally oriented both the fundamental and second harmonic were co-propagated in the waveguide. The fields produced outside the waveguide due to the internal charge separation generated a current in the interdigitated electrodes. The current induced in the electrodes as a function of the illumination conditions is shown in Figure 3. This figure shows preliminary data that indicates that only when both the fundamental and second harmonic are waveguiding do we see a current induced into the electrodes. The observation of these currents suggests the presence of the photocurrents and the build up of a static internal field.
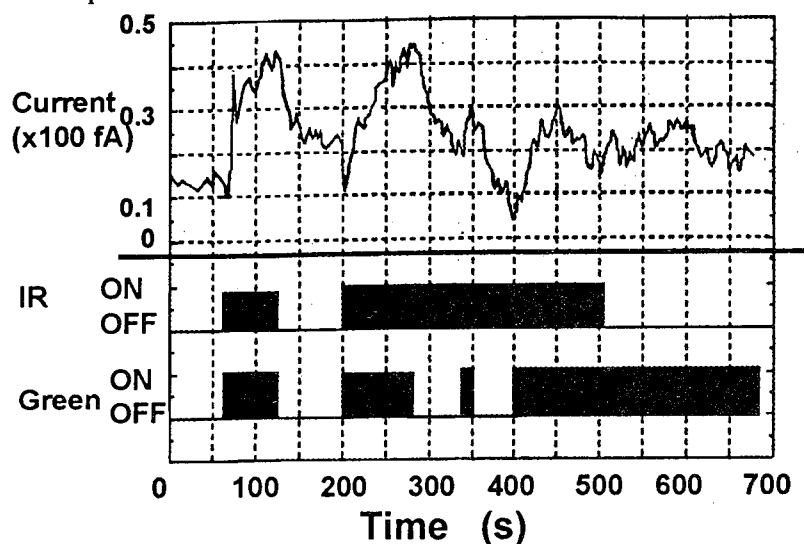
Figure 3. Current measured in interdigitated electrodes as a function of fundamental and second harmonic intensities.

Preliminary calculations indicate that the fields that are generated outside the waveguide and their spatial dependence will depend on the type of spatial charge distribution that is producing it. Additional measurements of the external field as a function of waveguiding light intensity may allow us to predict the exact charge distribution and the multi-photon dependence.

References

1. J.J. Kester, P. J. Wolf, and W.R. White, Opt. Lett. 17, 1779 (1992).
2. U. Osterberg and W. Margulis, Opt. Lett. 11, 516 (1986).
3. R.H. Stolen in Nonlinear Waves in Solid State Physics, A.D. Boardman, ed. (Plenum, NY 1990), pp.297-324.
4. R. Kashyap, J. Opt. Soc. Am. B, 6, 313 (1989).
5. P.S. Weitzman, J.J. Kester, U. Osterberg, (submitted)
6. B. Ehrlich-Holl, D.M. Krol, R.H. Stolen, and H.W.K. Tom, Opt. Lett. 17, 396 (1992).

Friday Papers Not Available

FA5   Emission Processes in Microcavities

FB5   Developing New UV NLO Crystals Using Molecular Engineering Approach

NLO '94 Authors

Abe, S.	MP24	Clays, K.	MA3	Green, R.	WP19 THA7
Agarwal, G.	FA4	Collins, M.	MP16	Gregor, E.	WP21
Agranovich, V.	MP16	Cory, W.	TUP16	Gregory, D.	MP19
Aharoni, A.	TUP1 TUP3	Cotter, N.	TUP14	Griffith, G.	WP8
Aitchison, J.	TUA5	Cristian, W.	THB2	Gruneisen, M.	WP6
Akhmediev, N.	MP22 WP31	Crofts, G.	WP19 THA7	Grynberg, G.	MB1
Alsing, P.	MB4 MP8	Crook, R.	TUP14	Gu, C.	THB1 THB4 THB6
Andersen, D.	WP2	Crosignami, B.	WB4	Gurin, V.	TUP25
Ando, H.	TUA7	Cui, A.	TUP20	Haase, A.	WP17
Arnold, J.	TUA5	Cunningham, P.	FB3	Hache, A.	TUP21
Artemyev, M.	TUP25	Curtis, K.	THB5	Haelterman, M.	MP2 WP12
Asobe, M.	WC5	Dagenais, M.	WP28	Hagan, D.	MC6
Assanto, G.	MC6	Dajani, I.	FB4	Haldar, M.	WP11
Atkins, T.	MP19	Dalton, L.	TUP4	Han, K.	MP28
Bacher, G.	WB1	Damzen, M.	WP19 THA7	Hanna, D.	THA2
Bakker, H.	WP30	Danlewski, H.	MP1	Hanna, D.	THA2
Banerjee, P.	MP4	Dapkus, P.	TUA2	Harken, D.	TUA1
Bartschke, J.	MC3	De Martini, F.	FA5	Hatakeyama, I.	TUP8
Bashaw, M.	TUP1 TUP3 THB3	De La Cruz, S.	MP18	Hattori. Y.	MP26
Becher, C.	MC3	DeLong, K.	TUC4	Haus, H.	TUC1 WC2
Bechtel, J.	TUP4	Devlin, G.	TUP15	He, Q.	MP18
Becker, M.	TUP4	Di Porto, P.	WB4	Heanue, J.	THB3
Beier, B.	MC3	Digman, J.	WP22	Hendershot, D.	MP21
Beigang, R.	WP29	Ding, Y.	TUP20 WP5	Hesselink, L.	TUP1 TUP3
Bennet, C.	MB2	Dong, C.	WA6		THB3 THA3
Beyer, D.	MA4	Dong, S.	MP25	Hoekstra, H.	THA4
Binder, R.	TUB3	Downing, E.	THA3	Hollins, R.	WP22
Bjorkman, C.	MP15	Du, Q.	MP12	Hong, H.	MP17
Bodnar, I.	TUP26	Dubovitsky, S.	TUA2	Hong, J.	WA3 THB2
Boller, K.	MC3	Duree, G.	WB4	Hsu, K.	THB4 THB1
Bortz, M.	MC1	Dvorak, M.	MP21	Huang, J.	MP29 MP30
Borutszky, A.	MC5	Ehritz, M.	WP21	Huang, X.	TUA1
Bottomly, D.	TUA6	Eich, M.	MA4	Hunsche, S.	TUB2 TUB4 WP30
Boyd, R.	FB2	Eichler, H.	WP17	Hunter, J.	TUC4
Brickeen, B.	WP8	Elezzabi, A.	WP33	Hussong, J.	WP29
Bruckmeier, R.	MC4	Emmerichs, U.	MP15	Hutchings, D.	TUP17 TUP18 TUA5
Bubeck, C.	MA7	Engin, D.	WA4	Hwang, C.	WP3
Buryak, A.	MP22	Erneux, T.	WP7	Indik, R.	TUB3
Calleja, E.	TUA1	Fainman, Y.	MP7	Ippen, E.	TUC1
Campbell, S.	WB3 THB4	Feinberg, J.	MP18 WB1	Ironside, C.	TUA5
Cartwright, A.	TUA1	Feng, Q.	MP6	Iruvanti, V.	FB2
Chadi, J.	TUP15	Fiedler, K.	MC4	Itoh, H.	WP18 WP25 WC5
Chakmakjian, S.	WP6	Firth, W.	MP5 MP9	Janz, W.	TUA8
Chang, T.	WA5 THB2	Fischer, G.	FB2	Jeganathan, M.	TUP1
Chang, T.	TUP16 WA3	Fittinghoff, D.	TUC4	Jenekhe, S.	FB2
Chang, C.	MP29	Fix, A.	MC5	Jeong, J.	TUP23
Chaplin, R.	MP14	Flytzanis, C.	TUB1	Jia, W.	MP10
Chatenoud, F.	TUA8	Forch, B.	WP16	Jiang, S.	WP28
Chaves-Pirson, A.	TUA7	Fourkas, J.	TUB6 FA1	Jmako, S.	TUP25 TUP26
Chemla, D.	TUA4	Freeman, R.	TUC6	Joint Group	WA6
Chen, C.	THB4 FB5	Fukada, H.	WP18	Joneckis, L.	WP14
Chen, J.	WA5 WB3	Gao, X.	MP25	Jones, R.	WP8
Cheng, L.	FB1	Gavrielides, A.	MB4 MP8	Justus, B.	MP21
Cheng, C.	THB1	Geddes, J.	MP5	Kaino, T.	WC5
Cheung, E.	MC7	Geerlings, P.	MP20	Kalluri, S.	TUP4
Chi, S.	WP9	Gehr, R.	FB2	Kamada, M.	WP18
Chien, C.	MP3	Goeritz, G.	MC5	Kanamori, T.	WC5
Chraplyvy, A.	WC3	Gong, Q.	MP25	Kanbe, H.	TUA7
Chu, P.	MP14	Gonzalez-Sanz, F.	TUA1	Kane, D.	TUC4

469

Kannari, F.	WP25	Lundquist, P.	WP2	Osterberg, U.	FB4
Kashihara. S.	TUP24	Lupke, G.	MP15 TUA6	Ottusch, J.	WP20
Katzer, D.	TUP20	Luther, G.	WP32	Palombo, K.	WP21
Kauranen, M.	MA5 MP11	Luther-Davies, B.	MP23 WB5 WP2	Pan, C.	WP3
Kawase, M.	WP18	Lytel, R.	MA1	Pan, G.	WP28
Kawashima, H.	TUB6	Ma, S.	MP28	Park, S.	WP27
Kelaidis, C.	TUA5	Ma, X.	WB3	Park, N.	TUA3
Keller, U.	TUC2	Ma, J.	MP7	Paschotta, R.	MC4
Kennedy, C.	WP10	MacCormack, S.	WB1	Paul, H.	FA3
Kester, J.	FB4	Macdonald, R.	MP1 WP17	Paulus, W.	MA4
Kewitsch, A.	WB6	Macfarlane, R.	THA3	Peng, G.	MP14
Khoo, I.	WC4 WP24	Mainfray	TUC5	Pepper, D.	WA1
Khoshnevisan, M.	THB2	Mandel, P.	WP7	Persoons, A.	MA5 MP11
Khurgin, J.	TUP19 TUP20	Mandel, L.	FA2	Pieroux, D.	WP7
	TUP22 WP5	Marcy, H.	MA4 TUP5 TUP6 FB3	Powles, R.	WB5
Kim, D.	MC2	Marsh, J.	TUA5	Prokoshin, P.	TUP25 TUP26
Kim, K.	WP27	Mathur, A.	TUA2	Psaltis, D.	THB5 TUP16
Klein, M.	WB1 WB2	Matthews, S.	THA6	Pu, N.	WP3
Klimov, V.	TUB2	Maytorena, J.	WP4	Pu, A.	THB5
Knappe, R.	MC3	McCallum, D.	TUA1	Rand, S.	WA5
Knorr, A.	TUB3	McDonald, J.	MP19	Rangel-Rojo, R.	TUP14
Knox, W.	TUC3	McInerney, J.	TUP11	Reardon, J.	MP19
Kobayashi, T.	TUP28 MP13	McIver, J.	TUP11	Rikken, G.	MP20
	MP26 MP27	McMichael, I.	WA5 WP26 THB2	Ringsdorf, H.	MA4
Koch, S.	TUB3	McMorrow, D.	WB7	Roach, W.	TUP2
Koch, K.	MC7 WP6	Melinger, J.	WB7	Rockwell, B.	TUP2
Kondo, Y.	TUP24	Mendis, F.	WP11	Rockwell, D.	WP20 THA6
Koroteev, N.	MB3	Mendoza, B.	WP1 WP4	Rogers, M.	TUP2
Kovanis, V.	MB4 MP8	Menzel, R.	WP17	Rosker, M.	MA4 TUP5 TUP6 FB3
Krijnen, G.	THA4	Meyer, J.	WP33	Sacedon, A.	TUA1
Kuizenger, D.	THA1	Meyer, C.	MP15	Saito, H.	TUA7
Kukhtarev, N.	MP4	Mikhailov, V.	TUP25 TUP26	Salamo, G.	WB4 WB6
Kurz, H.	MP15 TUB2 TUB4	Miller, B.	TUA3	Sambles, J.	TUP14
	WP30 TUB4	Minoshima, K.	MP27	Samoc, A.	MP23
Kwak, C.	TUP9 TUP10 TUP23	Miranda, P.	MP12	Samoc, M.	MP23
Lai, Y.	MP3 WP23	Misawa, K.	MP13 MP27	Sanchez-Rojas, J.	TUA1
Lambeck, P.	THA4	Miyata, S.	MA2	Sarukura, N.	TUP24
Latif, A.	MP14	Mlynek, J.	MC4	Sasabe, H.	MA6
Law, C.	MB3	Mochan, W.	WP1	Sasaki, H.	MP7
Lee, M.	MP17 WC4	Mochan, W.	WP4	Saxena, R.	WA5 WP26
Lee, K.	MP17	Mollenaur, L.	WC1	Scheidt, M.	MC3
Lee, H.	WP27	Moloney, J.	MP5 MP6	Schiek, R.	MC2
Lee, S.	MP7 TUP20 WP5		TUB3 WP32	Schildkraut, J.	MA3
Lee, E.	TUP9 TUP10 WP27	Moore, G.	MC7 WP6	Schwartz, R.	WB2
Lega, J.	MP6	Mordaunt, D.	WP21	Scott, A.	THA5
Leo, K.	TUB4	Morgan, R.	WP28	Scroggie, A.	MP9
Levine, A.	FA1	Munoz, E.	TUA1	Sefler, G.	MP12
Li, C.	TUP27	Naganuma, K.	WC5	Segawa, Y.	TUP24
Li, S.	TUP20 TUP22	Nakanishi, S.	WP18	Segev, M.	TUP7 WA4
Li, H.	WC4 WP24	Nakata, T.	WP25		WB4 WB6
Liang, Y.	WC4 WP24	Nakatsuka, H.	WP18	Seitzs, M.	MA4
Liao, C.	MP29	Nelson, K.	TUB6	Shakin, V.	MP24
Liby, B.	TUP11 TUP12	Nelson, L.	TUC1	Shapiro, J.	WP14 WP15
Lin, S.	THB4	Neurgaonkar, R.	TUP7 TUP16	Sharp, E.	WB4 WB6
Linke, R.	TUP15		WB6 THB2	Sheik-Bahae, M.	MC6
Liu, J.	MB4	Newell, A.	MP6 WP32	Shen, D.	WB3
Liu, Z.	TUP24	Newkirk, M.	TUA3	Shen, Y.	TUB5 MP30 MP12
Liu, H.	MP10 MP18	Normandin, R.	TUA8	Sheppard, A.	MP2 WP12
LoPesti, P.	WC4	Oliver, E.	MP19	Shi, Y.	TUP4
Lotshaw, W.	WB7 MP13	Oliver, J.	TUP16	Shieh, J.	WP3
Lu, X.	MP28	Orlov, S.	TUP7 WA4	Shim, S.	TUP10
Lucovsky, G.	MP15	Osaheni, J.	FB2	Shimoda, S.	MA2

Shu, Q.	WA5	Warren, L.	MA4 TUP5 TUP6 FB3	
Si, J.	TUP27	Watanabe, T.	MA2	
Simpson, T.	MB4	Wechsler, B.	WB1	
Sipe, J.	FB2	Weiss, C.	TUP12	
Smirl, A.	TUA1	Weitzman, P.	FB4	
Socha, U.	WP29	Whang, W.	MP29	
Solymar, L.	TUP10	Wherret, B.	TUP14 TUP17 TUP18	
Sorce, J.	WP21	White, W.	TUC4	
Soto-Crespo, J.	WP31	Whitney, W.	THA5	
Spruce, G.	TUP14	Wildt, D.	MC5	
Staliunas, K.	TUP12	Williams, D.	MA3	
Statman, D.	TUP11 TUP12	Wolter, F.	MP15	
Staver, P.	WB7 WP13	Wong, G.	TUB5	
Stegeman, G.	MC2 MC6 THA4	Wong, K.	TUB5	
Steier, W.	TUA2 WB2	Woodruff, M.	MP23	
Steir, W.	TUP4	Wright, E.	MP5 WP32	
Street, M.	TUA5	Wu, M.	MP30	
Sugiyama, Y.	TUP8	Wu, W.	WP9	
Sun, K.	WP15	Wu, B.	TUP4 FB5	
Sundheimer, M.	MC2	Wu, X.	WA6	
Swartzlander, G. Jr.	MB3	Xu, C.	TUP4	
Taiji, M.	MP27	Yablonovitch, E.	FA6	
Talanina, I.	MP16	Yagi, S.	TUP8	
Tamura, K.	TUC1	Yamada, T.	WP25	
Tao, X.T.	MA2	Yang, Z.	TUP4	
Thantu, N.	WB7	Yang, G.	WA6	
Thienpont, H.	MP20	Yang, X.	WP2	
Thio, T.	TUP15	Yang, S.	MP25	
Tikhonenko, V.	WB5	Yao, Z.	MP28	
Tkach, R.	WC3	Yariv, A.	TUP7 WA4	
Toruellas, W.	MC6		WB4 WB6	
Towe, T.	WB6	Yarnell, B.	WC4	
Trebino, R.	TUC4 FA1	Yasuda, T.	MP15	
Trivedi, S.	WB2	Yeh, P.	MP18 WB3 WP9	
Tschudi, T.	WA2		THB1 THB4 THB6	
Tuller, H.	WA5	Yi, X.	WC4 THB6	
Ukuda, H.	MA2	Yoon, C.	MP17	
Ullrich, B.	TUP28	Yoshizawa, M.	MP26	
Urschel, R.	MC5	Yu, L.	FB5	
Vahala, K.	TUA3	Yu, H.	MP4	
Valley. G.	WA4	Yu, S.	WP23	
van Driel, H.	TUP21 TUA6	Yumashev, K.	TUP25 TUP26	
Van Stryland, E.	MC6	Zeng, W.	FB5	
Veliadis, V.	TUP20	Zhang, H.	WA6	
Verbandt, Y.	MP20	Zhang, F.	TUB7	
Verbiest, T.	MA5 MP11	Zhang, Y.	WB3	
Veretennicoff, I.	MP20	Zhang, J.	TUB5	
Villeneuvve, A.	THA4	Zhang, Z.	MP28 TUB7	
Wada, T.	MA6	Zheng, J.	TUB7	
Wallenstein, R.	MC3 MC5	Zhou, J.	FB5 TUA3	
Wang, D.	MP25	Zhu, Y.	WA6	
Wang, G.	MP28	Ziari, M.	WB2	
Wang, J.	MP3 TUB7	Zou, D.C.	MA2	
	WP11 WP7			
Wang, W.	MP28 TUB7			
Wang, X.	TUB7			
Wang, Y.	FB5			
Wang, Z.	MC6			